January 2013

One Dimensional Stochastic Coating Growth Kinetics of PEG 3400 onto Ammonium Nitrate in a Fluidized Bed

Brandon Smeltzer
University of South Florida, bbsmeltzer@gmail.com

One Dimensional Stochastic Coating Growth Kinetics of PEG 3400 onto Ammonium Nitrate in a Fluidized Bed

by

Brandon Blair Smeltzer

A dissertation submitted in partial fulfillment
of the requirements for the degree of
Doctor of Philosophy
Department of Chemical and Biomedical Engineering
College of Engineering
University of South Florida

Major Professor: Aydin K. Sunol, Ph.D.
Scott W. Campbell, Ph.D.
Dmitry Goldgof, Ph.D.
Jennifer Sinclair-Curtis, Ph.D.
Sermin G. Sunol, Ph.D.
Ryan Toomey, Ph.D.

Date of Approval:
November 18, 2013

Keywords: dimensionless number, distribution, heat transfer, hydrodynamics, probability

DEDICATION

This dissertation is dedicated to my family. This was not a journey made alone.

ACKNOWLEDGMENTS

There are several people I would like to acknowledge for their help in completing this work. First, I would like to thank Dr. Aydin Sunol for giving me the opportunity to do graduate research. Thank you for your encouragement, guidance, and also providing an opportunity to teach Plant Design.

I would also like to thank my colleagues in the Environmentally Friendly Engineering Systems group for their help and support. Thank you to my friends Dr. Raquel Carvallo and Dr. Wade Mack, and Haitao Li for the advice and encouragement. Thank you to Dr. Keyur Patel for being patient with my myriad of Matlab questions. I would also like to thank Aaron Driscoll for his patience with the countless number of Matlab questions I presented to him as well.

I would also like to thank Dr. Yusuf Emirov for his assistance with the AFM measurements. I would like to thank Sandy Pettit for her assistance with the FTIR spectra. I would like to thank Donovan Industries, Temptroll, and the Chemical and Biomedical Engineering Department at USF for the financial support. I would also like to thank Dr. Peter Hede, Dr. Karen Hapgood, and Dr. Kevin Cronin for their gracious correspondence.

Finally, and most importantly, I want to thank my family. Thank you for providing patience, perspective, and understanding at the low points and celebrating the highlights with me. I could not have done this without you and a simple, powerful nickname. I love you all!

TABLE OF CONTENTS

LIST OF TABLES

LIST OF FIGURES

ABSTRACT

Fluidized beds represent a cost effective, scalable technology invaluable to the chemical processing community as part of the global scheme of particle design. However, despite wide spread use and multiple approaches (empirical and mechanistic) to modeling a fluidized bed coating process, operations must be done at different scales due to changes within the balance of phenomenological forces (e.g. gravity, buoyancy, drag, surface tension, viscosity, kinetic energy).

Ammonium nitrate is synthetic compound that has multiple applications such as fertilizer, rocket fuel, and self-cooling applications. Ammonium nitrate has five temperature dependent crystal structures that are accompanied by a change in density. The density fluctuations can result in altered solid properties including cracking and agglomeration (also called caking). The presence of a coating on the ammonium nitrate surface can serve multiple functions including: acting as a barrier between moisture in the air and the ammonium nitrate – thus preventing deliquescence, preventing unwanted agglomeration between ammonium nitrate particles, and potentially providing a means of controlled release.

Polyethylene glycol (PEG) with a molecular weight of 3400 was used as the coating material for this work. PEG 3400 is a biodegradable water soluble polymer that is part of a class of polymers used in cosmetics, pharmaceuticals, soaps, and phase change materials (PCM's). PEG 3400 also has a partially amorphous structure which also makes it an attractive candidate as a coating for ammonium nitrate. The solvent used for PEG 3400 was water.

In this work, a stochastic modeling approach is used to determine the following outputs for both the top spray and Wurster orientation fluidized beds: the coating efficiency, the final particle size distribution, and the coating thickness distribution. Coating efficiencies were determined with isothermal calorimetry and UV/Vis absorbance. With the aid of two tunable parameters, which are functions of the fluidized bed geometry and the fluidization air flow rate, the coating growth kinetics model matches the experimental coating efficiency for both orientations to about ±1%. A sensitivity analysis done for the coating growth model shows that the particle porosity, liquid-solid contact angle, and the simulation control volume height have the most significant impact on the calculated average coating thickness. SEM and AFM analysis proved the ammonium nitrate particle morphology changes from a smooth to rough texture following the coating operation.

CHAPTER 1

INTRODUCTION

The purpose of this chapter is to provide an understanding of particle coating. Techniques developed for particle coating will be discussed with a particular focus on the fluidized bed technique. A brief outline providing motivation for coating ammonium nitrate with a water soluble polymer will be given. An overview of the objectives of this research and the ensuing chapters will also be presented.

1.1 Particle Coating and Particle Coating Techniques

Particle coating, also called microencapsulation, is a process in which one material is encased within another material on a very small magnitude scale (usually 10^{-6} m). The terms microencapsulation and particle coating are considered equivalent for this work and particle coating will be used throughout the remainder of this dissertation. Particle coating is an important part of several chemical industries including: food, pharmaceuticals, and agriculture. Particle coating processes provide the means necessary for applications such as taste masking, controlled release, longer shelf life, easier handling, and aesthetics [1]. Another function provided by particle coating includes providing an extra barrier against heat, moisture, air and light degradation [2]. Particle coatings may take different forms as shown in Figure 1.1[3].

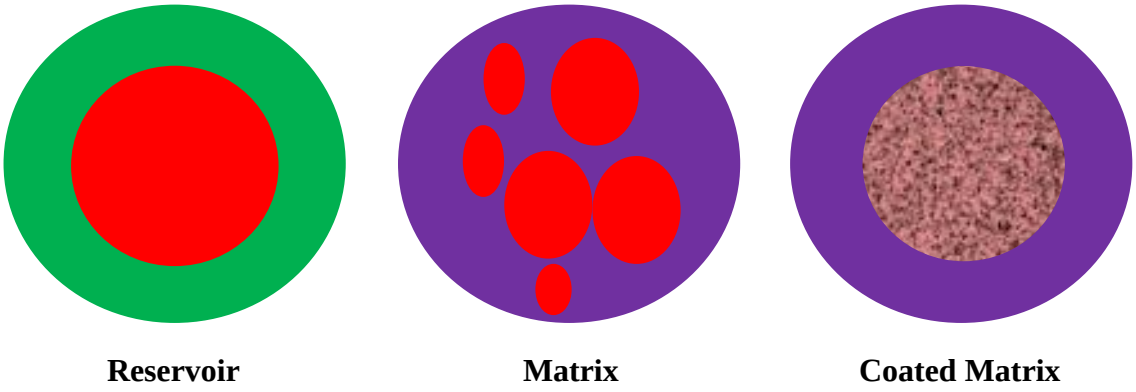

Figure 1.1 Different Classifications of Particle Coating

The reservoir coating is also known by several other names: mono-core, single core, core-shell and capsule. In the matrix coating, several particles are coated together as one conglomerate or unit. The coated matrix form is a combination of the reservoir and matrix coating [3]. Multicore or poly-core coatings are another form of particle coating that can be done where each layer of coating, when applied properly acts as part of the core particle for the next layer of coating. Figure 1.2 shows an example of multicore coating for a solid rocket fuel propellant application [4].

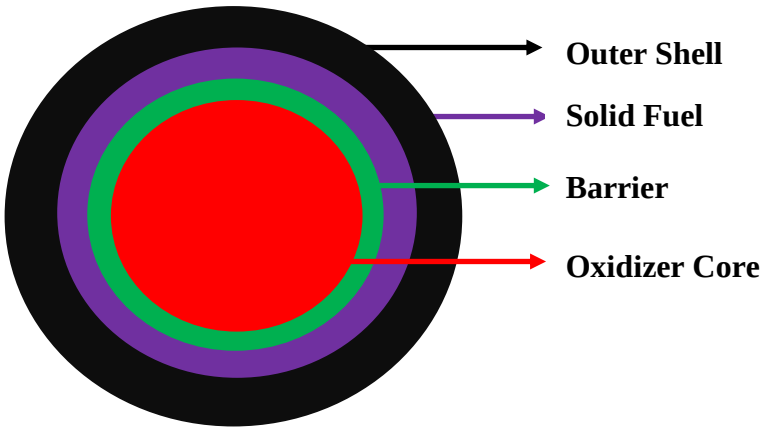

Figure 1.2 Multicore Particle Coating for Solid Rocket Fuel Propellant

Spherical particles are not the only solid geometries coated for various applications as additional examples are shown in Figure 1.3.

Figure 1.3 Additional Sample Geometries

While the function of the particle coating is important, the method by which the particle coating is done also significant. The properties of the coated particles are dependent on the coating method used. Table 1.1 shows the various types of particle coating methods available with applications, advantages, and disadvantages for each method. In addition, the particle size range typically used and the typical loading for each method is also mentioned [3,5-7].

Table 1.1 Particle Coating Methods

Coating Procedure	Applications	Advantages	Disadvantages	Particle Size Range [µm]	Loading [%]
Spray Coating	Flavor oils	Technology well known, inexpensive, straightforward	Encapsulant water solubility, energy intensive process	10-400	5-50
Spray Chilling/Cooling	Organic/Inorganic salts, enzymes, flavors	Least expensive technology	Imperfect coating – active ingredient still exposed on surface	20-200	10-20
Spinning Disk/Centrifugal Coextrusion	Food industry	Continuous high speed process	Scale up issues	200-5000	20-50
Extrusion	Volatile, unstable flavors	Long shelf life	Large particle size formed 500-1000 µm, high loading	150-8000	70-90
Fluidized Bed	Agriculture, food stuffs, pharmaceuticals	Ability to coat any kind of particle with a shell material	High electrostatic forces of small particles can interfere with coating process	5-5000	5-50
Coacervation	Flavor oils, fish oils, nutrients, vitamins, enzymes, preservatives	High payloads achievable ~99%	Very expensive, crosslinking with glutaldehyde	10-800	40-90
Alginate Beads	Food industry	Very mild, easy preparation for lab scale	Expensive, scale up issues, porous microcapsules	50-1000	1-50
Liposomes	Pharmaceuticals	Stable for water soluble materials, targeted delivery	Lipid bilayer breaks down at 50^{o}C, scale up issues	10-1000	5-50
Rapid Expansion Supercritical Solution (RESS)	Enzymes, flavors, pharmaceuticals	<100µm coating possible, very rapid, pressure or temperature swing	Solubility of shell materials is very low, removal of co-solvent	10-400	20-50

Table 1.1 Continued

Supercritical Anti-Solvent (SAS) or Gas Anti-Solvent (GAS)	Enzymes,dyes, flavors, pharmaceuticals	Used when coating material not soluble in supercritical fluid, coating induced by milder pressure swing or temperature swing vs. RESS	Solvent removal step may be long	10-400	20-50
Inclusion Encapsulation	Flavors, vitamins	Unique release characteristics	Low payloads with cyclodextrin	0.001–0.01	5-15

While Table 1.1 shows several particle coating methods available to the scientific community, the fluidized bed technique is a very attractive particle coating method due to the capability of coating any kind of particle. The main drawback to most of the coating methods outlined in Table 1.1 revolves around economics. Some methods have scale up issues, while others face higher expenses due to energy requirements with water as the solvent. Poor shell material solubility can also lead to higher coating operation cost. Fluidized beds are not always privy to these drawbacks because the coating-solvent system can be chosen by the design engineer and problems with large scale operations have been studied [8].

As Table 1.2 shows, there are other characteristics of fluidized beds that make them attractive to various industries [9].

Table 1.2 Advantageous Fluidized Bed Characteristics

Advantages	**Comments/Examples**	**Reference**
Ease of Automatic Control Implementation	Particle Size Measurement Pressure Drop Solids Flow, Solids Volume Fraction Temperature	10-12
Rapid Mixing of Solids	Axial and Radial Diffusivity Measurements Mixing Index	13-15
High Heat and Mass Transfer Rates	Localized Particle Heat Transfer Coefficients (glass, FCC, silica) Surface Averaged Heat Transfer Coefficients for Circulating Fluidized Bed Heat Transfer Coefficient Dependent on Particle Size, Superficial Gas Velocity, and Slightly on Gas Thermal Conductivity	16-18
Can be Scaled to Large Operations	Dimensional Scaling Laws Developed Scaleup Validation Done by Pressure Drop Measurements or External Visualization Methods (e.g. High Speed Cameras, Optics, Capacitance) 0.5kg to 24kg batch size (Coating) 5kg to 120kg batch size (Agglomeration)	19-21

While there are many characteristics that make fluidized beds a good candidate for particle coating operations, there are some drawbacks to fluidized beds as shown in Table 1.3 [9].

Table 1.3 Disadvantages of Fluidized Bed Characteristics

Disadvantages	Comments/Examples	Reference
Can Be Difficult to Develop Accurate Models for Gas Flow	Different Fluidization Regimes Involve Diverse Modeling Methodologies (e.g. Two Phase Model for Bubbling Regime vs. Plug Flow or Ideal CSTR for Turbulent Regime) Observation of Smooth Transitions to Different Fluidization Regimes Rather than Sharply as Determined by Boundary Correlations Computation Power/Time	22
Non-Uniform Particle Residence Times	Residence Times Vary Due to Different Solids Flow Regimes Identified in CFB Particle Residence Times in Wurster Fluidized Bed Dependent on Particle Size, Fluidization Flow Rate and Temperature, and Bed Geometry	23-24
Vessel Erosion Can Be Severe	Reduction of Service Life Finnie Model for Erosion Caused by Single Particle Factors Include: Operating Conditions (Flow Rate and Temperature), Particle Properties (Diameter, Distribution, and Hardness) and Mechanical Design (Distributor Design, Geometries, and Feed Locations)	25-26

Table 1.3 Continued

Friable Particles Can Lead to High Levels of Entrainment	Two Mechanisms for Entrainment in Bubbling Fluidized Bed: Particle Carry Over and Ejection From Bubble Wake Due to Bubble Coalescence Particles with Higher Cohesive Forces Will Have Lower Levels of Entrainment in a Fluidized Bed Compared to Particles with a Low Magnitude Cohesive Force	27-28
Scale Up Issues	Bed Defluidization Bubble Growth, Coalescence, and Breakup Erosion of Fluidized Bed Internals/Walls Gas Bypassing and Channeling Fouling Particle Elutriation Poor Particle Size Distribution Prediction Poor Solids Mixing	29-30

Fluidized beds exhibit excellent temperature control due to very high heat transfer coefficients between the gas and solid phases. Fluidized beds allow for rapid mixing of solids. A direct result of superior temperature control and rapid mixing is isothermal conditions whether the operation is particle coating or a reaction. Fluidized beds can also be run continuously [9].

1.2 Challenges in Fluidized Bed Particle Coating

There are a few obstacles that must be avoided when using fluidized bed technology including: high pressure drop, excessive fluidizing gas or liquid coating flow rates, low fluidizing gas flow rates. These obstacles tend to arise due to an improper balance of the forces that occur during a fluidized bed coating process. Among the outcomes of an improper balance of forces that occur during a fluidized bed coating operation are: particle agglomeration, bed

defluidization, and excessive spray drying of coating liquid. Figure 1.4 illustrates the potential pathways of a fluidized bed coating operation.

Some of the issues concerning fluidized bed coating operational issues revolve around the fluidizing gas flow. Significant pressure drops can severely alter the performance of a fluidized bed to the point that fluidization is extremely difficult. Large pressure drops inside a fluidized bed indicate slugging is taking place. Slugging inside a fluidized bed leads to poor gas-solids mixing and lowered heat and mass transfer capabilities [9]. Poor contacting between the gas and solid due to excessive bubbling is also a problem resulting in lower heat and mass transfer rates. Residence times inside the fluidized bed during continuous operations will be different due to the variety of particle sizes present [9]. Excessive spray drying of the liquid coating solution may occur if heat and mass transfer rates are too high relative to the liquid coating spray rate [31]. When spray drying occurs the coating efficiency of the fluidized bed operation is lowered resulting in longer operation times [31].

In addition to problems incurred via the fluidizing gas flow, there are also issues in fluidized bed coating operations regarding the liquid coating incorporation. A liquid coating flow rate that is too high can result in particle agglomeration rather than particle coating. Agglomeration occurs when the viscous forces of the liquid are higher in magnitude compared to the kinetic energy of colliding particles [32].

Ideal Fluidized Bed Coating Pathway: Even Distribution of Coating Material Over Entire Batch

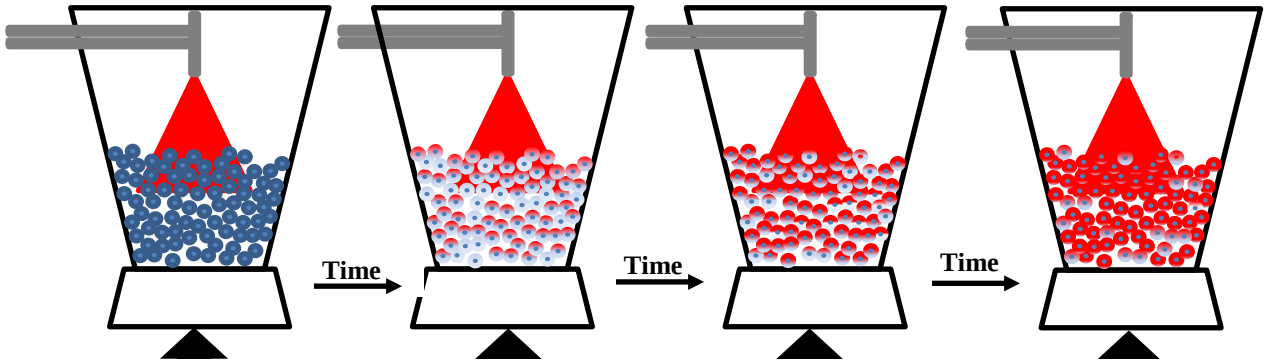

Potential Unwanted Fluidized Bed Coating Pathway: Particle Agglomeration Resulting From Combination of High Liquid Coating Solution Flow Rate and Low Fluidization Flow Rate/High Relative Humidity/Low Temperature Leading to Lower Excess Kinetic Energy for Particle Collisions

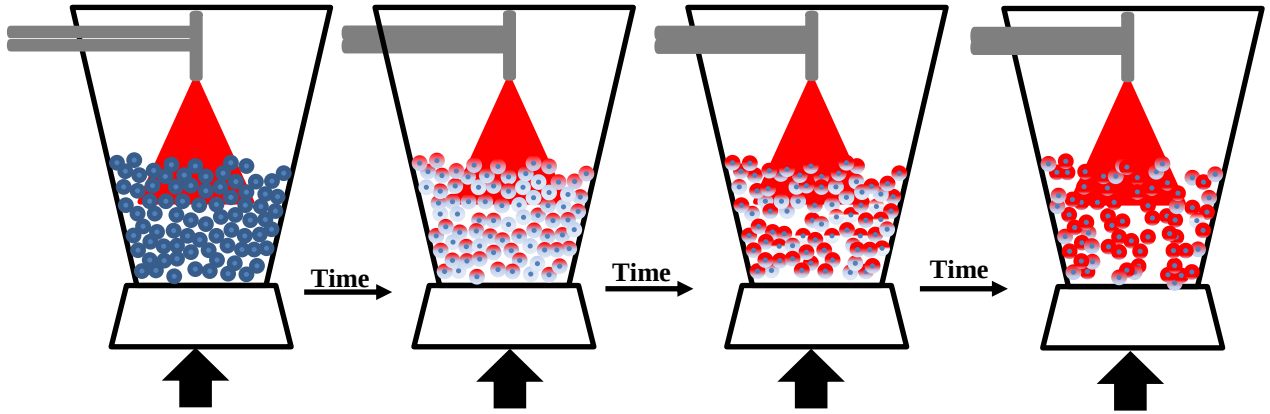

Figure 1.4 Fluidized Bed Coating Pathways

Potential Unwanted Fluidized Bed Coating Pathway: Bed Defluidization Due to Particle Over-Wetting Resulting from Combination of High Liquid Coating Solution Flow Rate and Insufficient Fluidization Flow Rate/Relative Humidity/Temperature Combination

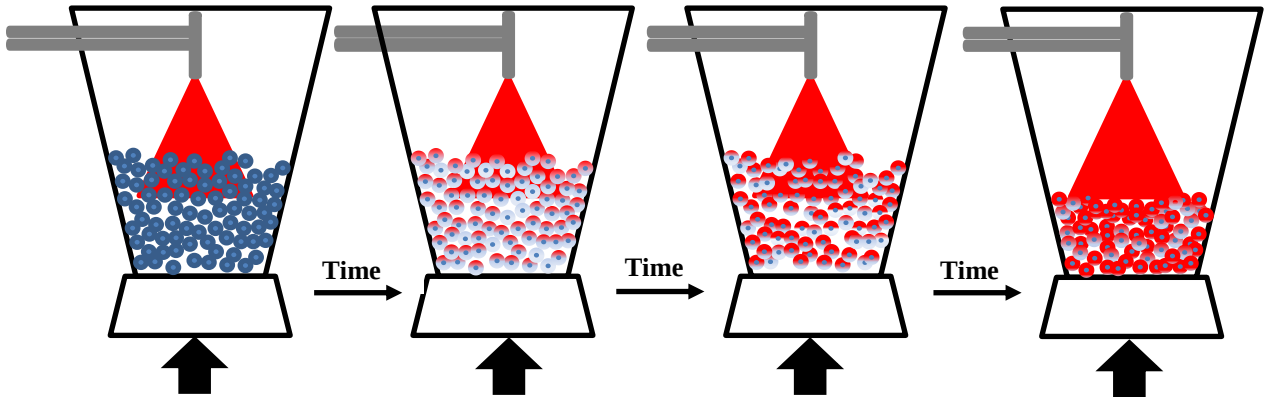

Potential Unwanted Fluidized Bed Coating Pathway: Excessive Spray Drying Resulting From Combination of Low Liquid Coating Solution Flow Rate and High Fluidization Flow Rate/Low Relative Humidity/High Temperature Leading to Lower Particle Coating Thickness Distribution

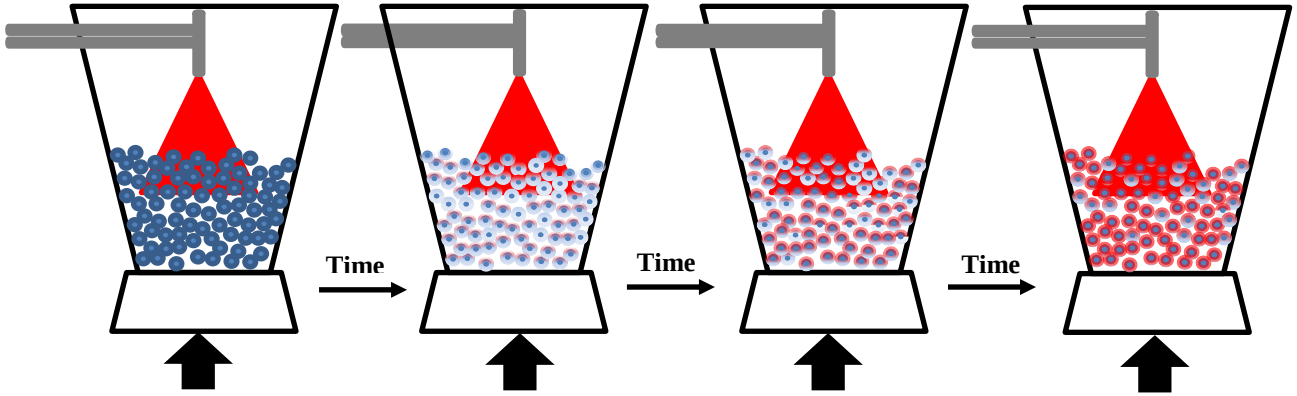

Figure 1.4 Continued

If the agglomeration phenomenon continues, a maximum particle size may be attained within the fluidized bed followed by defluidization of the particles. Defluidization occurs when the particle weight is higher in magnitude than the buoyant force provided by the fluidizing gas. Another way defluidization occurs is by saturating the particle bed with the liquid coating solution such that the heat and mass transfer rates are significantly lower in magnitude relative to the liquid coating solution flow rate. This form of defluidization is termed wet quenching [33]. Particle agglomeration may or may not occur in wet quenching, depending on the liquid coating flow rate.

The challenges discussed and illustrated in this section and Table 1.3 for the fluidized bed particle coating method can be minimized or avoided completely with careful planning and control of the experiment coating conditions. One such solid compound where this element of experiment control would be beneficial is the coating of ammonium nitrate. The properties of ammonium nitrate, of which 7 million tons were produced in 2012 in the US alone [34], will be discussed in the next section.

1.3 Ammonium Nitrate

Ammonium nitrate, NH_4NO_3, is a white synthetic compound made commercially by reacting ammonia with nitric acid, shown as Equation 1.1, as a secondary part of the ammonia producing Haber process:

$$NH_3(g) + HNO_3(aq) \rightarrow NH_4NO_3(s) \quad \Delta H_{rxn} = -146 \ \frac{kJ}{mol} \tag{1.1}$$

Ammonium nitrate is highly soluble in water and has an endothermic heat of mixing, +25.69 kJ/mol, when dissolved in water [35]. Table 1.4 shows some pertinent thermo-physical properties of ammonium nitrate [36].

Table 1.4 Ammonium Nitrate Properties

Property	**Value**
Molecular Weight [g/mol]	80.052
Solubility in Water [g/g H_2O]	0^oC 1.18 60^oC 4.21 10^oC 1.50 70^oC 4.99 20^oC 1.92 80^oC 5.80 30^oC 2.42 90^oC 7.40 40^oC 2.97 100^oC 8.71 50^oC 3.44
Density [kg/m^3] @ 20^oC	1.725
Melting Point [^oC]	169.6
Heat of Combustion [J/g]	1447.7
Heat of Formation [J/g]	4594.0
Heat of Fusion [J/g]	76.3
Heat of Sublimation [J/g] @ 20^oC	2179.8
pH [0.1M Solution]	5.43
Coefficient of Thermal Expansion @ 20^oC [$\%/^oC$]	$9.82e^{-4}$
Detonation Velocity [m/s]	1250-4650

Ammonium nitrate is used in several technologies including fertilizers and explosives [36]. As a fertilizer, ammonium nitrate represents 15% of the global nitrogen supply, whereas 24% of the globally produced ammonium nitrate is utilized as explosives. As recently as 2010, the United States of America, Russia, and Europe accounted for 67% of the global consumption of ammonium nitrate and 73% of the global production of ammonium nitrate [37].

The nitrogen in ammonium nitrate accounts for 35% of its mass. As a fertilizer, ammonium nitrate provides nitrogen in two forms, the nitrate form (NO_3-) and the ammonium form (NH_4+). The nitrate anion is readily absorbed by soil and the plant roots but must be converted to ammonia via reduction before it can be assimilated by the plants. The ammonium cation does not get absorbed by the plant roots until it gets oxidized to the nitrate form. Once the oxidation to the nitrate form is complete, the plants absorb the newly formed nitrate. This is one pathway of the nitrogen cycle necessary for plant growth [38].

Another use for ammonium nitrate in addition to fertilizer is as an explosive. The first investigation into ammonium nitrate as an explosive was done in the early 1800's in an attempt to supplant the potassium nitrate component of black powder. Ammonium nitrate is an ingredient in several explosive materials including: ammonium nitrate fuel oil (ANFO), amatol (ammonium nitrate and trinitrotoluene), ammonal (ammonium nitrate, aluminum powder and trinitrotoluene), minols (ammonium nitrate, aluminum powder, and trinitrotoluene), and tannerite (ammonium nitrate and aluminum powder), water-oil emulsions, and slurries [36]. Even as late as 2000, 67% of the ammonium nitrate purchased for the purpose of explosives was used for coal mining. The rest of the ammonium nitrate explosives were used in quarries, metal mining, or construction [39].

In addition to being utilized as a fertilizer and an explosive, ammonium nitrate has been found to function as a solid rocket propellant [4, 40-43]. Frequently, the ammonium nitrate propellant is phase stabilized to maintain the energetics integrity [44-46] due to problems with agglomeration brought on by high relative humidity, temperature cycling, or a combination of the two. The issues regarding phase stability due to relative humidity or temperature cycling will be discussed in the next sections. Ammonium nitrate as a rocket fuel has limitations for a couple reasons: issues regarding unwanted agglomeration before use due to humidity or temperature fluctuations during storage, low burn rates combined with a low flame temperature, and a low specific impulse compared to other rocket propellants such as ammonium perchlorate, ammonium dinitrimide, or hexanitrohexaazaisowurtzitane (CL-20) [4].

Finally, the high solubility values shown in Table 1.4 along with the previously mentioned endothermic heat of mixing with water make ammonium nitrate an attractive candidate for self-cooling applications. In U.S. patent 4,993,237 Bond and Murray (1991)

ammonium nitrate is used as part of a mixture of chemicals in a self-cooling beverage container [47]. Maxim (1999) used ammonium nitrate as part of a self-adhering cold pack in U.S. patent 5,887,437 [48]. Sabin (2000) used ammonium nitrate as part of a mixture of chemicals in a gelling cold pack in U.S. patent 6,099,555 [49].

While ammonium nitrate is a compound that has many important uses, there are challenges stemming from its crystalline structures and interactions with water (both liquid and vapor) that must be accounted for to yield a product with satisfactory handling or performance properties. The crystalline structures of ammonium nitrate will be discussed next.

1.3.1 Ammonium Nitrate Crystal Structures

One of the biggest challenges in employing ammonium nitrate in industrial or consumer products lies in intermediate storage temperature fluctuations. Ammonium nitrate is hygroscopic in nature and has a critical relative humidity of 59.4% [50]. In an environment above 59.4% relative humidity, ammonium nitrate will absorb water vapor from the air and deliquesce [50]. Ammonium nitrate has five crystalline structures at atmospheric conditions as shown in Table 1.5 which are determined through techniques such as: X-ray diffraction, dilatometry, thermomechanical analysis, dielectric constant measurements, neutron diffraction, differential scanning calorimetry (DSC), differential thermal analysis (DTA), birefringement, optical measurements, density, grain size measurements, and ionic conductivity [36].

Table 1.5 Ammonium Nitrate Crystal Structures

Phase	**Stability Range [K]**	**CS**	**Lattice Parameters**	**Unit Cell**	**Group Space**	**Unit Cell Volume [$10^{-28}m^3$]**	**Density [kg/m^3]**
V	Humid < 255 Dry < 255	O	A: 7.943 B: 7.972 C: 9.832	8	Pccn	6.2258	1707.65

Table 1.5 Continued

IV	Humid 255 - 305 Dry 255 - 328	O	A: 5.745 B: 5.438 C: 4.942	2	Pmmm	1.5439	1721.47
III	Humid 305 - 357 Dry ---	O	A: 7.7184 B: 5.8447 C: 7.1620	4	Pnma	3.2309	1645.27
II	Humid 357 - 398 Dry 328 - 398	T	A: 5.7193 C: 4.9320	2	P4/mbm	1.6132	1647.49
I	>398 >398	C	A: 4.366	1	Pm3m	0.8322	1596.80

CS: Crystal Structure O: Orthorhombic T: Tetragonal C: Cubic

A phase transition has also been chronicled at high pressures (>9000 bar) above 160^{o}C. Furthermore, two more phase transitions have been reported at -170^{o}C and -200^{o}C but the lattice parameters are unknown at this time [36].

In phase I, the nitrate anions can rotate freely while the ammonium cations can diffuse through the lattice structure [51-53]. In the phase II tetragonal orientation, the nitrate anions rotate in their own plane rather than freely [54, 55]. In the phase III orthorhombic orientation, ammonium cations are displaced by an angle of 42^{o}, parallel to the c axis, in two disordered patterns. Seven nitrate groups surround one ammonium group in an unsymmetrical assembly [56-59]. In the phase IV orthorhombic orientation, the structure is similar to that of phase II and is symmetric. The ammonium cations are surrounded by eight nitrate anions [60]. In the phase V orthorhombic orientation, half of the nitrate anions are orthogonally oriented against the other half of the nitrate anions. Two sets of hydrogen bonds hold the ammonium nitrate molecule in a cesium chloride type assembly in a disordered manner [61]. Table 1.6 summarizes the ordering of the ammonium and nitrate groups of ammonium nitrate according to the crystalline structure.

Table 1.6 Ordering of Ammonium Nitrate Groups

Phase	**NH_4+ Order**	**NO_3- Order**
V	Ordered	Ordered
IV	Ordered	Ordered

Table 1.6 Continued

III	Disordered	Ordered
II	Disordered	Disordered
I	Rotating	Rotating

In addition to the phase transitions, there is also a change in ammonium nitrate density as shown in Table 1.5. Table 1.7 shows the magnitude the density change of ammonium nitrate based on the crystalline structure. The negative sign indicates a volumetric expansion of the ammonium nitrate crystal.

Table 1.7 Percent Change in Density

Phase Transition	**Percent Change in Density**
V to IV	+0.81%
IV to III	-4.42%
III to II	+0.13%
IV to II	+4.30%
II to I	-3.08%

As seen in Table 1.7 the biggest changes in density are in the IV to III phase transition and the IV to II transition. The temperatures that these transitions occur at are well within fluidized bed operating temperatures, meaning these changes in particle density will have to be accounted for properly to avoid unwanted agglomeration for a particle coating operation.

With the temperature dependent crystalline structures of ammonium nitrate now identified, the pathways for transitions must be characterized as well. The pathways for the crystalline phase transitions will be discussed next.

1.3.2 Ammonium Nitrate Crystalline Phase Transitions

The crystal structure transitions of ammonium nitrate occur at specific temperatures but do not necessarily progress in a linear fashion. Figure 1.5 shows the potential pathways the ammonium nitrate crystal structure can change according to temperature.

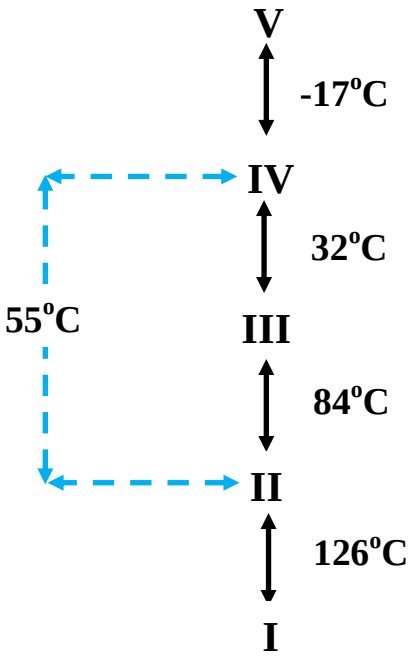

Figure 1.5 Potential Pathways for Ammonium Nitrate Phase Transitions

In the transition from phase I to phase II the NH_4+ ions undergo an ordering regarding space while the NO_3- anions undergo an ordering regarding orientation. Half of the NH_4+ ions are displaced during the crystal structure rearrangement [62-64]. For the phase IV to phase II transition, the NO^3- anions are set in a fixed placement parallel to the [0 1 0] plane, inhibiting the NH_4+ ions from diffusing across the structure [63, 65-67]. The transition from phase IV to phase III can occur simultaneously with the transition of phase IV to phase II. For the transition from phase IV to phase III to phase II smaller crystals transform first then aid in the transformation of larger crystals. Cracked or twinned crystals also go through the IV-III-II transitions quickly (roughly a few minutes) especially if the temperature is at the higher end of the crystal structure temperature range [68-72].

With the pathways for the crystalline structure changes mapped out in Figure 1.5, research work was done to ascertain what factors impact the ammonium nitrate phase transitions. The factors that impact the ammonium nitrate phase transitions will be discussed next.

1.3.2.1 Factors Impacting Ammonium Nitrate Phase Transitions

Research has shown that several factors have an impact on the phase transitions that ammonium nitrate goes through with changes in temperature including: molecular and particle properties, the presence of water, the sample thermal history, and the heating/cooling rates. Changes in these factors can speed up or slow down the phase transitions or alter the order of phase transitions.

The phase transitions occur in part due to the mobility of the NO_3- anion through and around the crystal lattice structures. An increase in temperature increases the mobility of the NO_3- anion thereby providing a driving force for the phase change. Adding an additional component such as potassium nitrate can reduce the NO_3- anion mobility, henceforth creating a stable crystalline phase.

The particle properties also have an impact on the phase transitions. Phase transitions can be initiated on a particle surface with the presence of one or more of the following traits that function as an active site: grain boundaries, corners, edges, cracks, twinning or slipping planes, or a misaligned lattice layer.

The presence of water (0.2-0.5%) increases the rate at which ammonium nitrate switches from phase IV to phase III. A transition to phase III from phase IV does not occur if there is no water present in the system and the ammonium nitrate goes from phase IV to phase II. The presence of water allows for the unstable phase to dissolve, saturate the water, then precipitate as the stable phase. Another way the presence of water impacts the phase transitions of ammonium

nitrate is by changing how much ammonium nitrate of a particle phase changes to a different phase. For example, 5-10% of a sample changes from phase IV to phase II in anhydrous form, but 60-70% of a sample changes from phase IV to phase II when the ammonium nitrate particles are wet [73-77]. This means it is possible to have two different phases of ammonium nitrate present at the same time. This fact can lead to difficulties again when being processed in a fluidized bed environment with too much water present (either in the fluidization air or as the coating solution solvent).

The presence of water vapor can also impact the transitions of ammonium nitrate phases. At low relative humidity (< 30%RH) the transition temperature range from phase IV to II is 45-55^{o}C. At elevated relative humidity, (> 30% RH) the transition temperature range for phase IV to III is about 32-40^{o}C and for phase III to phase II is about 60-84^{o}C [78-80].

The temperature ranges, like those mentioned in the preceding paragraph at which the phase transitions occur are dependent on the thermal history of the ammonium nitrate sample. If the ammonium nitrate is moisture free, upon cooling from 150^{o}C, the phase transitions observed is I to II to IV to V; phase III is not part of the sequence. Transitions from phase IV to phase III vary according to the thermal history of the sample. Moreover transitions from phase IV to phase III and phase IV to phase II occur simultaneously. This is due to the distribution of water molecules within the crystal structure, water may be present in one part of the sample (phase IV to phase III) and not the other (phase IV to phase II). It has also been observed that ammonium nitrate that undergoes a phase IV to phase III transition after cycling undergoes a phase IV to phase II transition only. This is because water that was present for the phase IV to phase III transition has evaporated from the sample, so the transition through phase III does not happen [67].

In addition to the thermal history impacting the phase transitions ammonium undergoes, the rate at which the ammonium nitrate sample is heated/cooled also has an impact on the phase transitions. Superheating or subcooling the ammonium nitrate may delay phase transitions to a temperature range where a different phase is stable. A transition from phase IV to phase III that occurs around 40^{o}C when heated may go from phase III to phase IV at 30^{o}C upon cooling.

An additional component to the phase transitions of ammonium nitrate besides the thermal history, presence of water, and the molecular and particle properties is the energy requirement to complete the phase transitions. The heat of phase transitions and the kinetics of the phase transitions will be discussed in the next section.

1.3.3 Ammonium Nitrate Heat of Phase Transitions and Kinetics

The last aspects of the phase changes of ammonium nitrate that must be accounted for when processing ammonium nitrate are the heat of the phase transition and the rate at which the phase changes occur. The heat of the phase transition can have an impact on the overall energy balances for a process while the rate of change of the phase transition can impact processing times.

The phase transitions of ammonium nitrate are accompanied by an additional energy requirement. All of the phase transitions are endothermic as shown in Table 1.8 [36].

Table 1.8 Heat of Phase Transitions

Phase Transition	Heat of Transition [J/g]
I to II	44.3
II to I	49.7
II to IV	20.4
IV to III	15.4
III to II	16.5
IV to V	5.7
V to IV	3.7

However the addition of other salts or metal oxides can suppress phase transitions or change the temperature at which they occur, in particular potassium salts [36, 83]. On the macroscopic level, the crystalline structure changes translate to particle cracking, decreased mechanical strength, and increased caking [36]. Depending on the type of product the ammonium nitrate is intended for, these properties may be undesirable.

The same factors discussed in section 1.3.2.1 impact the phase transition kinetics. A wet sample of ammonium nitrate moves through the phase transitions IV to III to II faster than a dry sample. The phase transition kinetics for the phase IV to III transition are well characterized by the Avrami-Erofeyev equation for solid state transitions. For example, at 44^{o}C, 50% transition from phase IV to phase III occurs within four minutes, whereas a complete transition from phase IV to phase III happens in 10 minutes [71, 81, 82].

The previous five sections have presented an in-depth look at the thermo-physical properties of ammonium nitrate. Due to the complexity of the ammonium nitrate crystal structures and the factors that impact which phase or phases are present works published regarding the phase transitions can be contradictory [36]. A brief summary of the thermo-phyiscal properties of ammonium nitrate will be presented in the next section.

1.3.4 Summary of Ammonium Nitrate Thermo-Physical Properties

Ammonium nitrate has five temperature dependent crystalline structures called phases at atmospheric pressure. The phase transitions are endothermic and are also accompanied by a change in volume, and therefore density. The transition from phase IV to phase III does not happen if the ammonium nitrate is anhydrous. Otherwise, even in the presence of a small amount of water (< 0.1%) the phase transition progression will go from IV to III to II upon heating. It is also possible to have multiple phases present at the same time within one sample. It

is also possible to avoid the phase transitions completely if the correct component is added to ammonium nitrate, e.g. potassium nitrate, and with the correct amount.

All of the aforementioned thermo-physical properties make ammonium nitrate a difficult candidate to work with in a fluidized bed environment. It is very likely that more than one phase of ammonium nitrate will be present during a coating operation because of the presence of moisture in the fluidization air. Moreover, if water is the solvent for the coating material, this will also increase the likelihood of phase III being present in the processed sample. There will also be a temperature cycling during the fluidized bed coating operation as well. The fluidization gas will heat the particle up, possibly initiating a phase and volume change. Next, the coating droplets will cool the surface as heat is transferred to the droplet for solvent evaporation. If a high liquid coating solution flow rate or a large droplet size distribution is used a significant temperature gradient between the fluidization gas and the particle-droplet conglomerate may evolve. If this temperature gradient is large enough, a phase and volume change may again be initiated. Transitions between phases may also be initiated more easily because of plastic collisions between particles or between particles and the fluidized bed wall at high fluidization flow rates creating more active sites on the particle surface.

As the previous discussion regarding the thermo-physical properties of ammonium nitrate has shown, ammonium nitrate presents a unique set of challenges for processing and proper storage without any surface alterations. One potential way to minimize or eliminate the crystal structure changes and subsequent thermo-physical and thermo-mechanical properties is by applying a coating material to act as a barrier between the surface of the ammonium nitrate particle and moisture in the air and temperature. The choice of coating material is important as the coating material must satisfy several conditions including: being compatible with

ammonium nitrate, having a higher critical relative humidity than ammonium nitrate, having a somewhat flexible structure to handle the volumetric changes brought on by temperature fluctuations without cracking, and be soluble in water. One class of coating materials that satisfies the aforementioned conditions is water soluble polymers which will be discussed in the next section.

1.4 Water Soluble Polymers

Water soluble polymers represent an important segment of the polymer industry in part due to the extensive assortment of applications including: coatings, construction, food additives, paint, paper, pharmaceuticals, and water treatment [84]. Table 1.9 shows a listing of synthetic and natural water soluble polymers [84].

Table 1.9 Synthetic and Natural Water Soluble Polymers

Synthetic Polymers	Natural Polymers
Divinyl Ether Maleic Anhydride (DIVEMA)	Albumin
N-(2-Hydroxypropyl) Methacrylamide (HPMA)	Carrageenan
Polyacrylamides	Cellulose Ethers
Polyethylene Glycol (PEG)	Chitosan/Chitosan Derivatives
Polyoxazoline	Dextran
Polyphosphates	Guar Gum
Polyphosphazenes	Pectins
Polyvinyl Acrylic Acid (PAA)	Starch/Starch Derivatives
Polyvinyl Alcohol (PVA)	Xanthum Gum
Polyvinyl Pyrrolidone (PVP)	

Among the water soluble polymers listed in Table 1.9, polyethylene glycol stands out because of various thermo-physical properties which will be discussed in the next section.

1.4.1 Polyethylene Glycol Thermo-Physical Properties

Polyethylene glycol (PEG), $C_{2n}H_{4n+1}O_{n+1}$ is a water soluble polymer that is available as a solid or liquid depending on the molecular weight. PEG with a molecular weight below 600 g mol^{-1} is liquid at room temperature. PEG has found many uses in various industries including: cosmetics – as ointments and creams in liquid form, soaps, pharmaceuticals – as particle coatings

and fillers for tablets or capsules in solid form [85], ceramics, adhesives, textiles, lubricants, and as a phase change material in solid form [86-88]. Polyethylene glycol is made commercially by reacting ethylene oxide with water or ethylene glycol/ethylene glycol oligomers with an acid or base catalyst. In particular, the reaction between ethylene oxide and ethylene glycol, shown as Equation 1.2, gives a lower polydispersity (molecular weight distribution) compared to using water as a reactant:

$$n(CH_2CH_2O) + HOCH_2CH_2OH \rightarrow HO(CH_2CH_2O)_{n+1}H \qquad (1.2)$$

The length of the polymer chain is a function of the ratio of the initial reactants. Above a molecular weight of 20,000 $gmol^{-1}$ polyethylene glycols are called polyethylene oxides (PEO).

The thermo-physical properties of PEG are dependent on molecular weight which makes the PEG family an attractive candidate for particle coating. The thermo-physical properties of interest for particle coating include: melting point, degree of crystallinity (X_{crys}), heat of fusion (ΔH_{fus}), and the solubility, viscosity, and heat of mixing with the particular solvent of interest (water in this case). Table 1.7 shows how the melting point, degree of crystallinity, and heat of fusion change as a function of molecular weight (MW) [87].

Table 1.10 Melting Point, Degree of Crystallinity, and Heat of Fusion as a Function of Molecular Weight

MW [$gmol^{-1}$]	**Melting Point [^oC]**	**X_{crys} [%]**	**ΔH_{fus} [J/g]**
1000	40.0	85.7	168.6
3400	56.4	87.2	171.6
10000	66.2	91.8	180.6
20000	67.7	83.8	165.0
35000	68.3	96.4	183.4

With the exception of PEG 20,000 the degree of crystallinity and heat of fusion increase with increasing molecular weight as shown in Table 1.10. PEG solubility in water decreases with increasing molecular weight, but 50% (w/w) solutions of PEG 35000-water can be made at

room temperature [89]. PEG is also soluble in others solvents including: acetone, acetonitrile, benzene, carbon tetrachloride, chloroform, dichloromethane, dimethylformamide (DMF), ethanol, and methanol.

Even with the high degree of crystallinity, local regions of amorphous structural matrices can offer flexibility as a coating material for ammonium nitrate. The viscoelastic properties of lower molecular weight solid PEG's like PEG 3400 make it a good candidate to manage density fluctuations brought about by temperature changes. In addition the critical relative humidity for PEG 3400 at room temperature is about 80% [85], much higher than ammonium nitrate alone.

1.5 Objectives of Research

The particle coating methods listed in Table 1.1 are just one part of the overall global scheme of particle design which is depicted in Figure 1.6. As Figure 1.6 shows, the life cycle of particle design involves many factors in addition to the coating method chosen, including predictive modeling, for both the final coated particle and the methodology used for particle coating, and economic feasibility. Furthermore, the global market for encapsulated food products in 2014 is projected to be $35.4 billion USD [90] while the global pharmaceutical market in 2014 is projected to be $1.033 trillion USD [91]. The flow of particle design lifecycle shown in Figure 1.6 combined with the economic impact of particle coatings warrant a comprehensive model describing all quantitative aspects of the coated particle evolution. Multivariate optimization can then be applied to the comprehensive model to determine the coating thickness needed for a particular application that satisfies the desired time profile while minimizing cost. This model can be developed in one of two ways: top to bottom or bottom to top. In the top to bottom approach, the coating thickness distribution is determined from the desired time profile. Then the desired coating thickness distribution is used an input in a coating

growth kinetics model to determine the length of time needed for a given set of experimental conditions. In the bottom to top approach, a coating thickness distribution is calculated from a coating growth kinetics model and used as an input for a diffusion, dissolution, or reaction kinetics model. This time profile would then be compared to a desired time to determine if the coating thickness distribution is satisfactory.

To this end, one purpose of this dissertation research is to develop an a-priori stochastic coating growth kinetics model that will yield the coating thickness distribution of a fluidized bed coating experiment. Among the predictive capabilities of the coating growth kinetics model are: the coating growth rate and the final particle size distribution based on the operating parameters and the initial particle size distribution.

The solid core particle used for this work is ammonium nitrate. The second objective of this dissertation research is to determine the experimental feasibility of coating ammonium nitrate with a water soluble polymer. As discussed previously in sections 1.3-1.34, the temperature dependent crystal structure phase transitions present a challenge for the application of a smooth, even coating that can handle fluctuations in volume without cracking in a fluidized bed environment. Moreover, the use of water as a solvent for the polymer coating will increase the probability that two different crystalline phases will be present simultaneously during the fluidized bed coating operation.

The coating material used for this work is the water soluble polymer PEG 3400. As noted previously, PEG 3400 has a higher critical relative humidity than ammonium nitrate (~80% compared to 59.4%) and also has a slightly amorphous structure that is elastic. These properties, in addition to being soluble in water and having an endothermic heat of mixing with water, make PEG 3400 an attractive candidate as a coating for ammonium nitrate.

The solvent used for PEG 3400 in this work is water. As noted previously in section 1.4.1, PEG is soluble in other solvents, but these solvents were not used due to environmental toxicity or solvent volatility. Water as the solvent for this work presents a challenge in a few areas regarding fluidized bed processing. Water has a high enthalpy of vaporization (2260 $kJkg^{-1}$ at 100^{o}C) in addition to a high specific heat capacity (4184 $Jkg^{-1}K^{-1}$). This translates to energy intensive fluidized bed operating conditions (i.e. high fluidization air temperatures or flow rates to remove the water at a satisfactory rate). The impact of water on the crystalline structures of ammonium nitrate has been addressed as well.

1.6 Dissertation Outline

This dissertation is organized into seven chapters. Chapter two presents background on fluidized bed and fluidized bed coating principles. The discussion includes atomization principles, dimensionless numbers, and heat and mass transfer characteristics. The impact of operational variables on the overall performance of fluidized bed coating operations will also be discussed.

Chapter three presents background on the different modeling approaches taken to fluidized bed coating operations. The modeling approaches to fluidized bed coating operations are classified as empirical and mechanistic, with the mechanistic models having deterministic or stochastic attributes.

Chapter four presents the transient mass and energy balances applied to the fluidized bed coating process. The coating growth kinetics model developed with this work will also be presented. Assumptions for both the mass and energy balances and the coating growth kinetics model will be discussed.

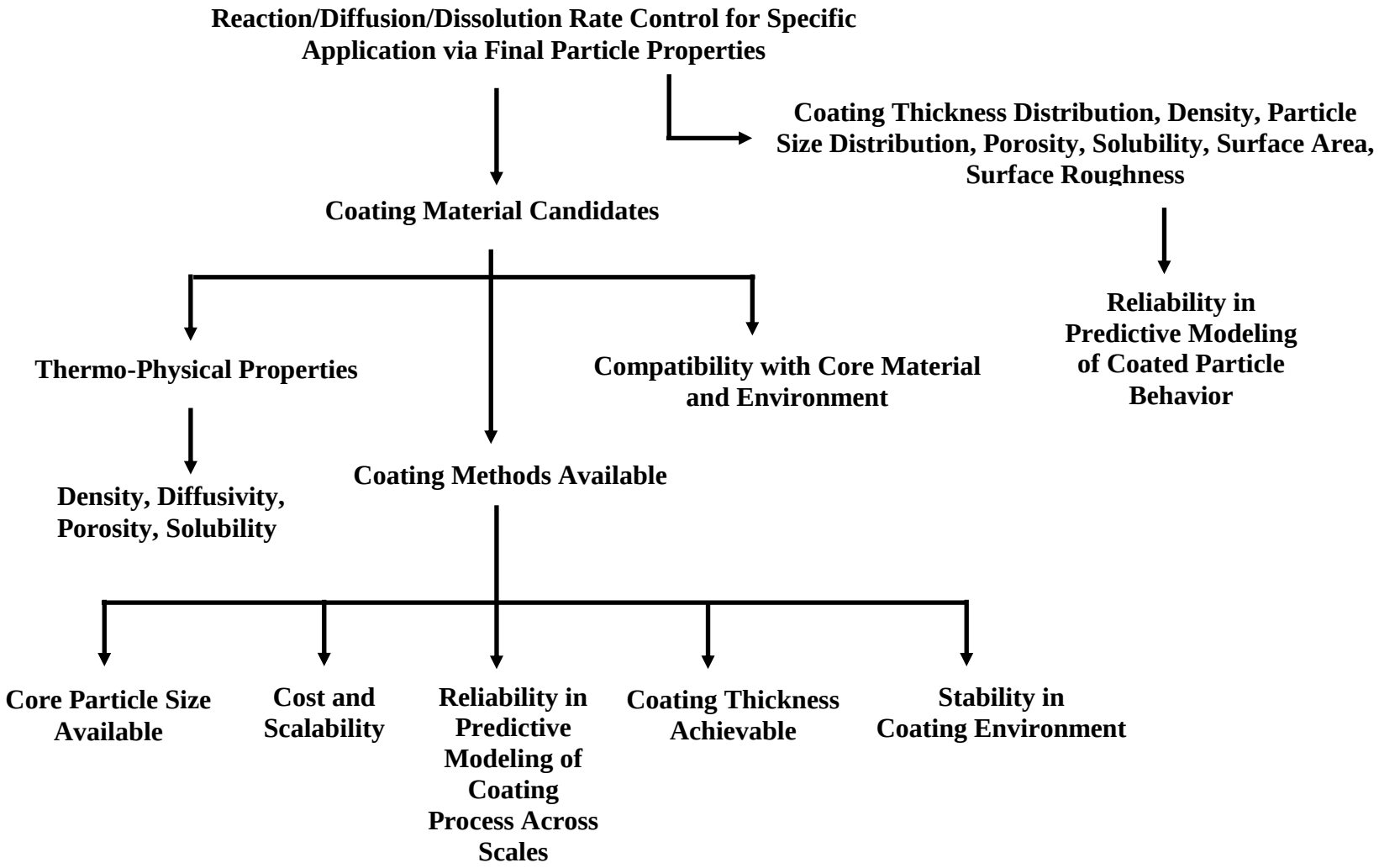

Figure 1.6 Global Scheme of Particle Design

Chapter five discusses the equipment used and the experimental procedures for this research.

Chapter six presents the experimental results of this research and provides a discussion as well.

Chapter seven presents the modeling results and a discussion that will include: thermo-physical properties of fluidization air, dimensionless numbers, time-temperature profiles, coating growth distributions, and sources of error – both experimental and modeling.

Chapter eight presents the conclusions of this research and possible future directions that may be explored.

1.7 References

[1] Dewettinck, K. & Huyghebaert, A. (1999) Fluidized Bed Coating in Food Technology, Trends in Food Science & Technology, 10, 163-168.

[2] Teunou, E. & Poncelet, D. (2002) Batch and Continuous Fluid Bed Coating – Review and State of the Art, Journal of Food Engineering, 53, 325-340.

[3] Zuidam, N.J. & Shimoni, E. (2010) Overview of Microencapsulates for Use in Food Products or Processes and the Methods to Make Them. In Zuidam, N.J. & Nedovic, V. (Eds.) Encapsulation Technologies for Active Food Ingredients and Food Processing. (pp. 3-29). New York: Springer.

[4] Kosky, J.P., Sunol, A.K., & Herren, N. (2010) Nano-Structured Propellants and Launch Systems, Proceedings of the Aerospace Systems Conference, Los Angeles, CA. Feb. 5-10, 157-162.

[5] Gouin, S. (2004) Microencapsulation: Industrial Appraisal of Existing Technologies and Trends, Trends in Food Technology, 15, 330-347.

[6] Carvallo, Raquel (2011) Ph.D. Dissertation, University of South Florida.

[7] Paques, J.P., van der Linden, E., van Rijn, C.J.M., & Sagis, L.M.C. (2013) Alginate Submicron Beads Prepared Through W/O Emulsification and Gelation With $CaCl_2$ Nanoparticles, Food Hydrocolloids, 31, 428-434.

[8] Whitehead, A.B. (1971) Some Problems in Large-Scale Fluidized Beds. In Davidson, J.F. & Harrison, D. (Eds) Fluidization. (pp. 781-814), London: Academic Press Inc.

[9] Kunii, D. & Levenspiel O. (1991) Fluidization Engineering. 2nd Edition, Massachusetts: Butterworth-Heinemann.

[10] Werther, J. (1999) Measurement Techniques in Fluidized Beds, Powder Technology, 102, 15-36.

[11] Prata, A.S., Maudhuit, A., Boillereaux, L., & Poncelet, D. (2012) Development of a Control System to Anticipate Agglomeration in Fluidized Bed Coating, Powder Technology, 224, 168-174.

[12] da Silva, C.A., Butzge, J.J., Nitz, M., & Taranto, O.P. (2013) Monitoring and Control of Coating and Granulation Processes in Fluidized Beds – A Review, Advanced Powder Technology, http://dx.doi.org/10.1016/j.apt.2013.04.008.

[13] Mostoufi, N. & Chaouki, J. (2001) Local Solids Mixing in Gas-Solid Fluidized Beds Powder Technology, 114, 23-31.

[14] Sahoo, A. & Roy, G.K. (2005) Mixing Characteristics of Homogeneous Binary Mixture of Regular Particles in a Gas-Solid Fluidized Bed, Powder Technology, 159, 150-154.

[15] Godlieb, W., Gorter, S., Deen, N.G., & Kuipers, J.A.M. (2009) DEM and TFM Simulations of Solids Mixing in a Gas-Solid Fluidized Bed, Seventh International Conference on CFD in the Minerals and Process Industries, CSIRO, Melbourne, Australia, December 9-11, 1-7.

[16] Boerefijn, R., Poletto, M., & Salatino, P. (1999) Analysis of the Dynamics of Heat Transfer Between a Hot Wire Probe and Gas Fluidized Beds, Powder Technology, 102, 53-63.

[17] Sundaresan, R. & Kolar, A.K. (2002) Core Heat Transfer Studies in a Circulatory Fluidized Bed, Powder Technology, 124, 138-151.

[18] Donsi, G. & Ferrari, G. (1995) Heat Transfer Coefficients Between Gas Fluidized Beds and Immersed Spheres: Dependence on the Sphere Size, Powder Technology, 82, 293-299.

[19] Rüdisüli, M., Schildhauer, T.J., Biollaz, S.M.A. & Ruud van Ommen, J. (2012*)* Scale up of Bubbling Fluidized Bed Reactors – A Review, Powder Technology, 217, 21-38.

[20] Hede, P.D., Bach, P., & Jensen, A.D. (2009) Batch Top-Spray Fluid Bed Coating: Scale Up Insight Using Dynamic Heat and Mass Transfer Modelling, Chemical Engineering Science, 64, 1293-1317.

[21] Rambali, B., Baert, L., & Massart, D.L. (2003) Scaleup of the Fluidized Bed Granulation Process, International Journal of Pharmaceutics, 252, 197-202.

[22] Abba, I. (2001) Ph.D. Dissertation, University of British Columbia.

[23] Chan, C.W., Seville, J.P.K., Parker, D.J., & Baeyens, J. (2010) Particle Velocities and Their Residence Time Distribution in the Riser of a CFB, Powder Technology, 203, 187-197.

[24] Cronin, K., Çatak, M., Tellez-Medina, D., Cregan, V., O'Brien, S. (2010) Modeling of Particle Motion in an Internal Re-Circulatory Fluidized Bed, Chemical Engineering Journal, 164, 403-409.

[25] Finnie, I. (1960) Erosion of Surfaces by Solid Particles, Wear, 3, 87-103.

[26] Achim, D.D., Easton, A.K., Perry, J.H., & Schwartz, P.M. (1995) Modeling Erosion in a Fluidized Bed, 12th Australian Fluid Mechanics Conference, The University of Sydney, Australia, 489-492.

[27] Santana, D., Rodriguez, J.M., Macias-Machin, A. (1999) Modeling Fluidized Bed Elutriation of Particles, Powder Technology, 106, 110-118.

[28] Milioli, F.E. & Foster, P.J. (1995) Entrainment and Elutriation Modeling in Bubbling Fluidized Beds, Powder Technology, 83, 233-245.

[29] Matsen, J.M. (1996) Scale-Up of Fluidized Bed Processes: Principles and Practice, Powder Technology, 88, 237-244.

[30] Rüdisüli, M., Schildhauer, T.J., Biollaz, S.M.A., Ruud van Oommen, J. (2012) Scale Up of Bubbling Fluidized Bed Reactors – A Review, Powder Technology, 217, 21-38.

[31] Ronsse, F., Pieters, J.G., & Dewettinck, K. (2008) Modeling Side-Effect Spray Drying in Top-Spray Fluidized Bed Coating Processes, Journal of Food Engineering, 86(4), 529-541.

[32] Ennis, B.J., Tardos, G., & Pfeffer, R. (1991) A Micro-Level Based Characterization of Granulation Phenomena, Powder Technology, 65, 257-272.

[33] Smith, P.G. & Nienow, A.W. (1983) Particle Growth Mechanisms in Fluidised Bed Granulation – I, Chemical Engineering Science, 38, No. 8, 1223-1231.

[34] IDFC (2013) North American Fertilizer Capacity Report.

[35] Weast, R. & Astle M. (Eds.) CRC Handbook of Chemistry and Physics (1978) West Palm Beach: CRC Press.

[36] Oommen, C. & Jain, S.R. (1999) Ammonium Nitrate: A Promising Rocket Propellant Oxidizer, Journal of Hazardous Materials, A67, 253-281.

[37] IHS Chemical (2010) Ammonium Nitrate Report.

[38] Andrews, G. (1998) Gardening and Water Quality Protection: Understanding Nitrogen Fertilizers, EC 1492, Oregon State University.

[39] Kramer, D.A. (2000) Explosives, US Geological Survey Minerals Yearbook, 26.1-26.7.

[40] Frosch, R.A. & Anderson, F.A. (1979) U.S. Patent 4,158,583 High Performance Ammonium Nitrate Propellant.

[41] Fleming, W.C. (1996) U.S. Patent 5,583,315 Ammonium Nitrate Propellants.

[42] Fleming, W.C., McSpadden, H.J. & Olander, D.E. (2002) U.S. Patent 6,364,975 Ammonium Nitrate Propellants.

[43] Fleming, W.C., McSpadden, H.J. & Olander, D.E. (2004) U.S. Patent 6,726,788 Preparation of Strengthened Ammonium Nitrate Propellants.

[44] Oberth, A.E. (1991) U.S. Patent 5,071,630 Phase Stabilization of Ammonium Nitrate by Zinc Diammine Complexes.

[45] Highsmith, T.K., Hinshaw, C.J., & Wardle, R.B. (1994) U.S. Patent 5,292,387 Phase-Stabilized Ammonium Nitrate and Method of Making Same.

[46] Menke, K., Bohnlein-Mauss, J., Schmid, H., Bucerius, K.M., & Engel, W. (1997) U.S. Patent 5,596,168 Solid Propellant Based on Phase-Stabilized Ammonium Nitrate.

[47] Bond, J.R. & Murray, S.V. (1991) U.S. Patent 4,993,237 Self-Cooling Containers.

[48] Maxim, R. S. (1999) U.S. Patent 5,887,437 Self-Adhering Cold Pack.

[49] Sabin, M. W. (2000) U.S. Patent 6,099,555 Gelling Cold Pack.

[50] European Fertilizer Manufacuturers Association (2006) Guidance For the Compatibility of Fertilizer Blending Materials, Belgium.

[51] Shinnaka, Y. (1959a) Study on the Molecular Rotation of Cubic Ammonium Nitrate, Journal of Physical Society of Japan, 14, 1073-1083.

[52] Riggin, M.T., Knispel, R.R., & Pintar, M.M. (1972) Cation Diffusion Study in NH_4NO_3 by Proton Spin Relaxation, Journal of Chemical Physics, 56, 2911-2918.

[53] Yamamoto, S. & Shinnaka, Y. (1974) X-Ray Studies of Polyorientational Disorder in Cubic NH_4NO_3, Journal of Physical Society of Japan, 37, 732-734.

[54] Shinnaka, Y. (1959b) X-Ray Study on Molecular Rotation in Tetragonal Ammonium Nitrate, Journal Chemical Society of Japan, 14, 1707-1716.

[55] Brooker, M.H. (1978) Raman Evidence for Thermally Disordered Energy States in Various Phases of Ionic Nitrates, Journal of Chemical Physics, 68, 67-73.

[56] Goodwin, T.H. & Whetstone, J. (1947) The Crystal Scattering of Ammonium Nitrate III and Atomic Scattering Factors in Ionic Crystals, Journal of Chemical Society, 1455-1461.

[57] Kearly, G.J. & Kettle, S.F.A. (1982) Raman Spectroscopic Evidence for Heteroionic Vibrational Coupling in Ammonium Nitrate III, Journal of Physical Chemistry, 86, 4007-4011.

[58] Choi, C.S. & Prask, H.J. (1982) Single Crystal Neutron Diffraction Study of Ammonium Nitrate Phase III, Acta Crystallographica Section B, 38, 2324-2328.

[59] Lucas, B.W., Ahtee, M., & Hewat, A.W. (1979) The Crystal Structure of Phase II Ammonium Nitrate, Acta Crystallographica Section B, 35, 1038-1041.

[60] Choi, C.S. & Mapes, J.E. (1972) The Structure of Ammonium Nitrate IV, Acta Crystallographica Section B, 28, 1357-1361.

[61] Choi C.S. & Prask, H.J. (1983) The Structure of NH_4NO_3 Phase V by Neutron Diffraction, Acta Crystallographica Section B, 39, 414-420.

[62] Hendricks et al. (1933) The Refractive Indices of Ammonium Nitrate, Z. Krist., 85, 143-155.

[63] Brown, R.N. & McLaren, A.C. (1962) On the Mechanism of the Thermal Transformations in Solid Ammonium Nitrate, Proceedings of Royal Society of London Series A, 266, 329-343.

[64] Langfelderova, H. & Ambrovic, R. (1982) Study of the Influence of Experimental Conditions on the Course of the DSC Curve of Ammonium Nitrate (20-140^{o}C), Thermochimica Acta, 56, 385-389.

[65] Tang, H.C. & Torrie, B.H. (1977) Raman Scattering of Low Temperature Phase of Ammonium Nitrate, Journal of Physics and Chemistry of Solids, 38, 125-138.

[66] Dellien, I. (1982) A DSC Study of the Phase Transformations of Ammonium Nitrate, Thermochimica Acta, 55, 181-191.

[67] Engel,E. & Eisenreich, N. (1983) The Phase Transition IV-II of Ammonium Nitrate Investigated by X-Ray Diffraction, Z Krist., 164, 211-217.

[68] Davey, R.J., Guy, P.D. & Ruddick, A.J. (1985) The IV-III Polymorphic Phase Transition in Aqueous Slurries of NH4NO3, Journal of Colloid & Interface Science, 108, 189-192.

[69] Davey, R.J. & Ruddick, A.J. (1991) The IV-III Polymorphic Phase Transition in Ammonium Nitrate: A Unique Example of Solvent Mediation, Journal of Physics D Applied Physics, 24, 176-185.

[70] Harju, M., Valkonen, J. & Jayasooriya, U. (1991) Simultaneous Application of Fourier Transform Raman Spectroscopy and Differential Scanning Calorimetry for the In-Situ Investigation of Phase Transitions in Condensed Matter, Specrochimica Acta Part A, 47, 1375.

[71] Harju, M., Minkkinen, P. & Valkonen, J. (1994a) Transition Paths Between Phases IV, III, and II of Ammonium Nitrate Predicted by X-Ray Powder Diffractometer and Differential Scanning Calorimeter Data by Partial Least Squares Regression, Chemometrics and Intelligent Laboratory Systems, 23, 341-350.

[72] Harju, M. (1994b) Transition Path Selection Between Ammonium Nitrate Solid Phases IV, III, and II, Annales Academiae Scientiarum Fennicae, Series A, Chemica, 253.

[73] Griffith, E.J. (1963) Phase Transitions of the Ammonium Nitrate-Magnesium Nitrate Systems, Journal of Chemical & Engineering Data, 8, 22-25.

[74] Yamazoe, N., Miohara, M. & Selyama, T. (1968) Phase Transitions of Ammonium Nitrate and Its Solidification Due to Moisture Adsorption. X. Kinetic Study of Phase Transitions IV-III in Ammonium Nitrate, Kogyo Kagasu Zasshi, 71, 1813-1820.

[75] Sjölin, C. (1971) The Influence of Moisture on the Structure and Quality of NH_4NO_3 Prills, Journal of Agricultural and Food Chemistry, 19, 83-85.

[76] Sjölin, C. (1973) The Influence of Additives on the Structure and Quality of NH_4NO_3 Prills, Doktorsavhandling, Tekniska Högskolan i Stockholm, KTR 73-15.

[77] Rasulic, G., Milanovich, L.J., & Jovanovich, S. (1988) Influence of Frequent Rhombicmonocyclic Crystal Transformation and of Moisture Content on Ammonium Nitrate Crystal Transformation Energies, Journal of Thermal Analysis, 34, 1195-1205.

[78] Davey, R.J., Guy, P.D., Mitchell, B., Ruddick, A.J., & Black, S.N. (1989) The Growth of Phase IV Ammonium Nitrate Crystals and Their Transformation to Phase III Structure, Journal of Chemical Society Faraday Transactions, 85, 1795-1800.

[79] Konkoly-Thege, I. (1977) Phase Transformation of Ammonium Nitrate Crystal by Thermal Factors and Inoculation, Journal of Thermal Analysis, 12, 197-205.

[80] Tsekhanskaya, Y.V., Sorina, G.A., & Mushkina, E.V. (1981) The Effect of the Concentration of Moisture and of Inorganic Salts of the Kinetics of the Modification Conversions of Ammonium Nitrate, The Soviet Chemical Industry, 13, 68-75.

[81] Mauras, H.C.R. (1973) Kinetic Study of the Polymorphic Transformations, Direct and Inverse, of Ammonium Nitrate, Academy of Sciences, 276, 285.

[82] Buscall, R. & McGowan, I.J. (1986) European Patent 190,819 Suspension Fertilizers.

[83] Rao, C. N. R., Prakash, B., & Natarajan, M. (1975) Crystal Structure Transformations in Inorganic Nitrites, Nitrates, and Carbonates, U.S. Department of Commerce, NSRDS-NBS 53.

[84] Kadajji, V.G. & Betageri, G.V. (2011) Water Soluble Polymers for Pharmaceutical Applications, Polymers, 3, 1972-2009.

[85] Baird, J.A., Olayo-Valles, R., Rinaldi, C. & Taylor, L.S. (2010) Effect of Molecular Weight, Temperature, and Additives on the Moisture Sorption Properties of Polyethylene Glycol, Journal of Pharmaceutical Sciences, 99 (1), 154-168.

[86] Han, S., Kim, C., & Kwon, D. (1995) Thermal Degradation of Poly(ethyleneglycol), Polymer Degradation and Stability, 47, 203-208.

[87] Pielichowski, K. & Flejtuch, K. (2002) Differential Scanning Calorimetry Studies on Poly(ethylene Glycol) with Different Molecular Weights for Thermal Energy Storage Materials, Polymers for Advanced Technologies, 13, 690-696.

[88] Shi, Q. & Liu, T. (2009) Study on Transition Characteristics of Poly(Ethylene Glycol)/Selected Fatty Acids Phase Change Material, Materials Science Forum, Eco-Materials Processing and Design X, 620-622, 49-52.

[89] Henning, T. (2002) Polyethylene Glycols (PEGs) and the Pharmaceutical Industry, Fine, Specialty and Performance Chemicals, June, 57-59.

[90] Global Food Encapsulation Market (2012-2017) – By Types, Functions, Applications, Ingredients, Shell Materials, Packaging, and Geography: Trends and Forecasts (June 2012) Market and Markets Research, Dallas: MarketsandMarkets.com

[91] Seget, S. (October 2010). Pharmaceutical Market Trends 2010 – 2014 Report, Isle of Man: URCH Publishing, 1-142.

CHAPTER 2

FLUIDIZED BED AND FLUIDIZED BED COATING PRINCIPLES

The purpose of this chapter is to provide a background on fluidized bed and fluidized bed coating principles. A general explanation of a fluidized bed coating operation will be presented followed by a description of the orientations used for coating operations. A discussion of liquid atomization principles will be presented next. Finally, fundamentals of particle fluidization and fluidized bed coating will be described, including dimensionless numbers, heat and mass transfer, and the impact of numerous operational and theoretical variables.

2.1 An Explanation of Fluidized Bed Coating Operation

Fluidized bed coating operations are typically carried out in tapered bowl geometries, with the largest diameter at the top of the bowl. Particles are suspended and bulk mixing occurs with the introduction of an upward vertical flowing stream of hot gas (usually air). The particles gain enthalpy and kinetic energy from the gas, heat up, and travel up the height of the tapered bowl. Gravity becomes the dominant force acting upon the particle overtaking drag and buoyancy, bringing the particle to a zero velocity at a certain height within the fluidized bed bowl. When this occurs, the particle falls back into the fluidizing gas stream. This pattern of cyclic particle transport creates a working environment suitable for coating particles.

A coating solution is pumped into a two-fluid nozzle and atomized into droplets with a small amount of gas. The droplets are introduced into the fluidized bed in one of two ways: a countercurrent flow pattern in the top spray orientation, and a concurrent flow pattern in the bottom spray orientation. Due to the cyclic particle transport pattern created by the fluidization

gas, usually only a small portion of the particles are exposed to the coating solution droplets at any given time. Once the coating solution spraying begins, the fluidized bed can be viewed as connected segments. The segment where particles become wetted after collisions with the coating solution droplets is the wetting/coating/spray zone. Outside the spray zone segment (usually below) the droplets dry on the particle surface, evaporating the volatile solvent and precipitating the coating material onto the core particle surface in the drying zone [1]. Figure 2.1 shows the general scheme of particle coating in a fluidized bed.

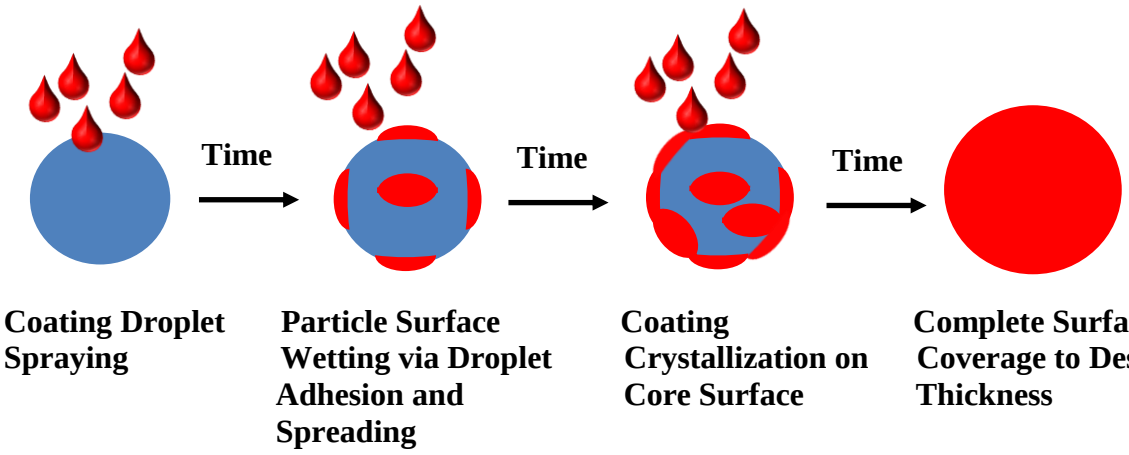

Figure 2.1 Fluidized Bed Particle Coating Scheme

A competing process that can occur within the fluidized bed in addition to particle coating is particle agglomeration. Particle agglomeration occurs because kinetic energy, shown as Equation 2.1, provided by the fluidization gas cannot overcome the cohesive binding forces evolved by the droplet properties (i.e. van der Waals and viscous and capillary forces as a function of droplet diameter shown as Equations 2.2 and 2.3) on the particle surface when a particle-particle collision occurs.

$$E_{kin} = \frac{1}{2} M_p U_p^2 \tag{2.1}$$

$$F_{vdw} = \frac{A}{12l^2}\left(\frac{d_{p1}d_{p2}}{d_{p1}+d_{p2}}\right) \tag{2.2}$$

$$F_{vis} + F_{cap} = \frac{3\pi U_0 a^2}{4h} + (\pi\gamma a)\sin^2\left[\phi\left(\gamma\left(\frac{1}{R_1}+\frac{1}{R_2}\right)+2\right)\right] \quad (2.3)$$

where U_0 is the relative velocity between particles, h is the liquid layer thickness, a is the particle radius, ϕ is filling angle, and C_0 is the pressure deficiency resulting from the liquid curvature over the surface and R_1 and R_2 are the particle radii in the liquid solid bridge.

A liquid bridge can form either when two or more wetted particles collide or wetted particles collide with non-wetted particles and the particles adhere to each other. This liquid bridge between particles will evolve into a mechanically strong solid bridge upon heating and solvent evaporation when particle-particle and particle-wall collision forces cannot break the liquid-solid cohesion. Figure 2.2 shows the general scheme of particle agglomeration in a fluidized bed.

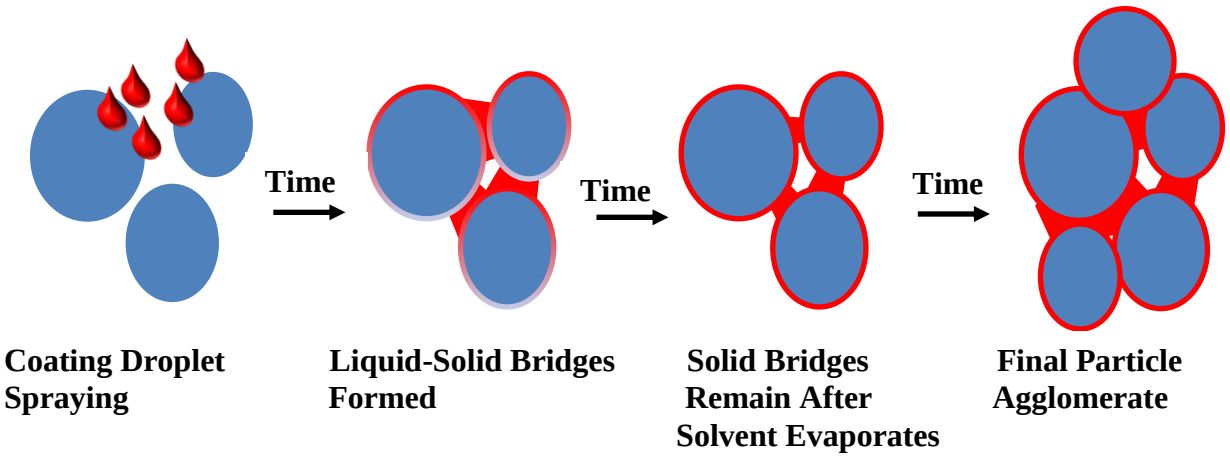

Figure 2.2 Fluidized Bed Particle Agglomeration Scheme

Particle agglomeration will typically continue inside the fluidized bed until the liquid bridge cohesion forces are counteracted by breakage forces generated from particle-particle and particle-wall collisions [2]. When particle coating is the desired outcome of the fluidization operation, agglomeration is an unwanted side effect that must be minimized.

Premature droplet evaporation, spray drying is another unwanted phenomenon that can occur with the top spray orientation. Spray drying occurs when droplets heat up and evaporate before colliding with a particle within the fluidized bed. The freely moving precipitated coating material can then leave the fluidized bed due to its small size or act as a seed within the fluidized bed. Proper operating condition selection (i.e. fluidization gas flow rate and temperature, along with liquid spray rate and atomization air flow rate) will minimize the spray drying probability for a fluidized bed coating operation.

A different approach taken to fluidized bed coating involves the introduction of coating solution droplets in a concurrent manner with the fluidization gas by placing the spray nozzle in the middle of the distributor plate. The Wurster process, a bottom spray orientation, also involves the use of a draft tube and a specially designed distributor plate. In the Wurster process, the particle velocity within the draft tube is much higher than outside the tube. With the spray nozzle in the center of the draft tube, the droplets travel a much shorter distance before colliding with particles. The high particle velocity within the draft tube promotes rapid drying on the particle surface, such that the particles are completely dry at the top exit point of the draft tube. Another important difference between the top spray orientation and the Wurster orientation is the probability of particle-particle collisions. The high velocity within the draft tube is accompanied by a high void fraction as well. The high void fraction within the draft tube means there are fewer particles adjacent to one another. With fewer adjacent particles to one another, the likelihood of two particles colliding decreases [3]. The agglomeration and spray drying probabilities of a coating operation with the Wurster orientation are different from that of the top spray orientation because the balance of the forces involved is different. The task of maintaining the proper balance of forces involved in fluidized bed coating operation requires an

understanding of the underlying variables concerning all the phenomenon occurring and the interactions.

2.2 Fluidized Bed Equipment and Design

Fluidized bed coating operations can be carried out in a variety of orientations within the same bed geometry. The fluidized bed orientation is dependent on the type of distributor plate used and the positioning of the nozzle within the bed. In the top spray orientation the nozzle is positioned above the distributor plate and subsequently above the particle bed. In the bottom spray orientation the nozzle is positioned at the bottom of the particle bed in the middle of the distributor plate. In the tangential spray orientation the nozzle is positioned on the side of the particle bed. Additionally, in the tangential spray orientation, a rotor spins the particles around the bed while fluidization occurs. Small scale fluidized bed coating operations are typically run with one nozzle. In large scale operations, several nozzles are used simultaneously for distributing the coating solution [4]. Figure 2.3 shows the three nozzle orientations used for fluidized bed coating operations.

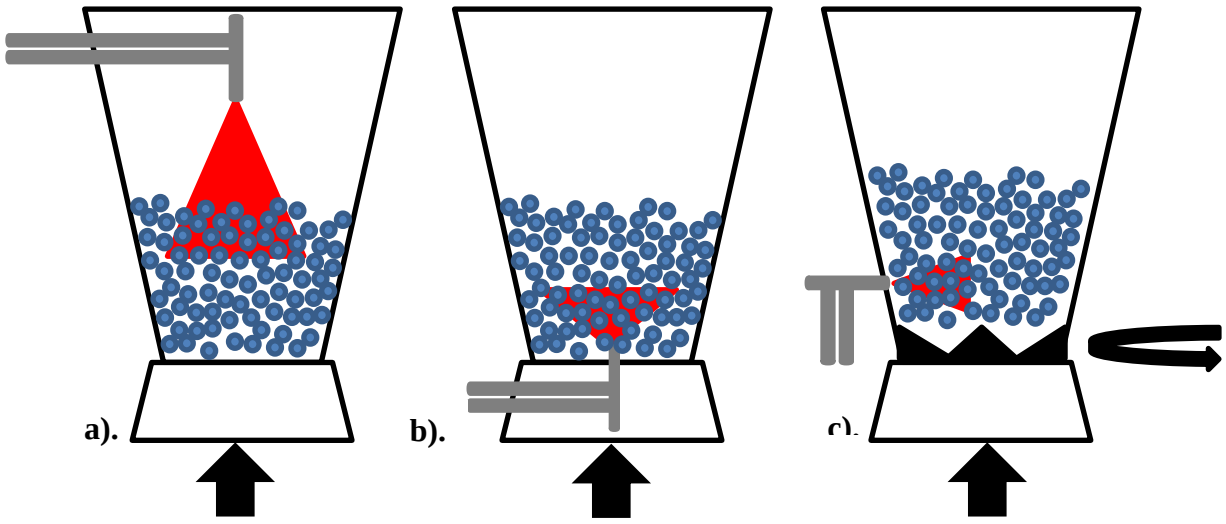

Figure 2.3 Fluidized Bed Orientations Used in Coating Particles: a). Top Spray b). Bottom Spray c). Tangential Spray

A variation of the bottom spray orientation was developed and patented by D.E. Wurster starting in 1959. A draft tube or spout is placed over the distributor plate. The distributor plate is modified such that air flow through the draft tube is substantially higher compared to the air flow outside of the draft tube [5-11]. A fluidized bed coating operation with this kind of setup is called a Wurster process. The Wurster orientation has superior drying capabilities due to the air distributor design with the majority of the perforations being in the middle of the distributor and also can also handle particles of various shapes [12]. Figure 2.4 shows the Wurster orientation.

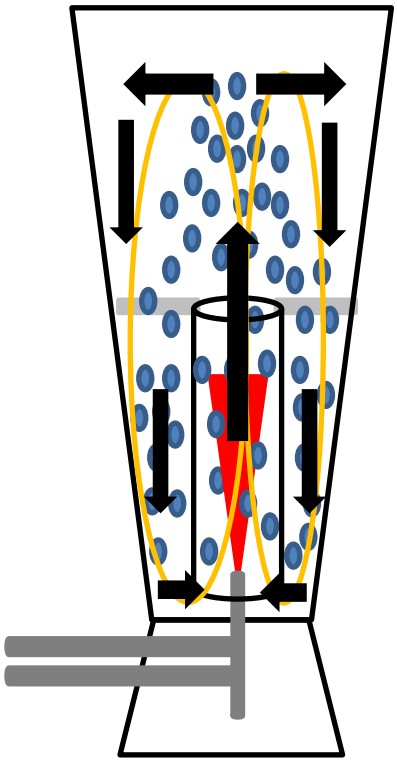

Figure 2.4 Wurster Orientation for Fluidized Bed Coating Operation

The black arrows above the tube in Figure 2.4 represent the cyclic flow pattern of the particles within the fluidized bed.

Several zones have been identified for the top spray orientation and the Wurster orientation. For a top spray fluidized bed four zones have been classified: the heat transfer zone, spray zone, non-active zone, and the drying zone [1]. The zone volume distribution inside the fluidized bed is not evenly divided. The spray zone accounts for a very small percentage of the fluidized bed volume depending on the scale of operation. In small scale fluidized bed coating operations, the spray zone can take up the entire fluidized bed volume. Temperature and relative humidity gradients accompany the zone demarcations of the fluidized bed. In the top spray orientation, the temperature decreases with increasing height. The three temperature regions for a top spray fluidized bed are at the distributor plate with the fluidizing gas, the nozzle exit, and the bulk of the bed [13]. Figure 2.5 shows the general zone scheme and the temperature and gradient of a fluidized bed coating operation.

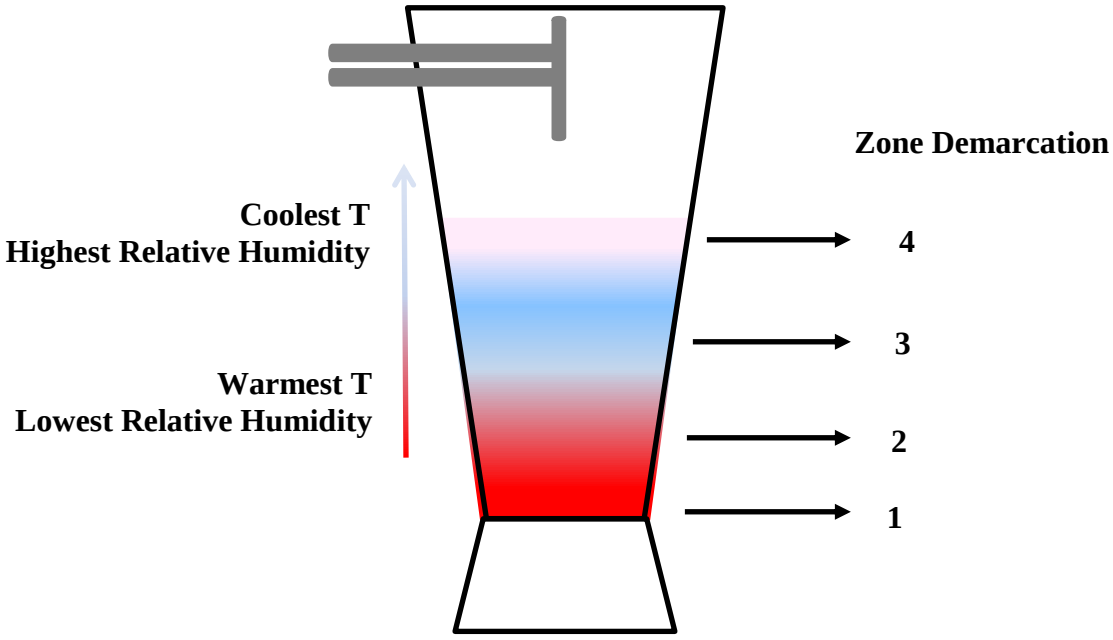

Figure 2.5 General Top Spray Orientation Zone Distinction (1) Heat Transfer Zone (2) Non-Active Zone (3) Drying Zone (4) Spray Zone and Temperature Gradient

A Wurster orientation fluidized bed is divided into the following regions: horizontal transport, down-bed, up-bed, mist, and the deceleration/expansion region [3]. Figure 2.6 shows the various regions of a fluidized bed with the Wurster orientation.

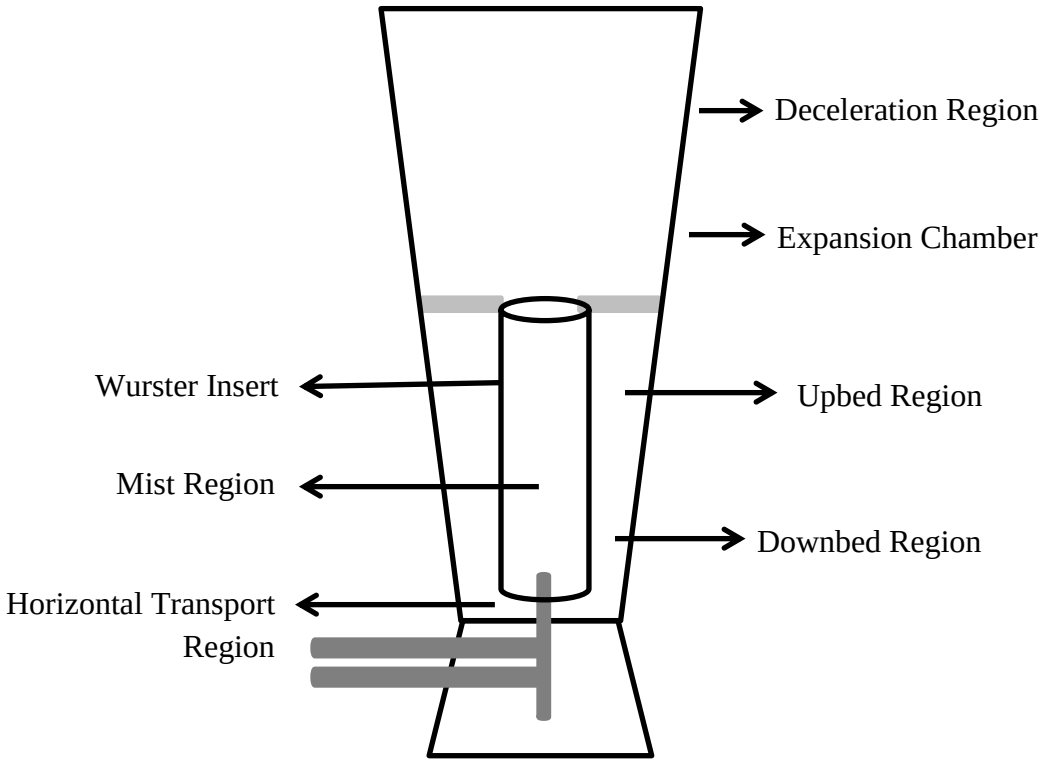

Figure 2.6 General Wurster Orientation Zone Distinction

The temperature and relative humidity gradients within a Wurster orientation fluidized bed are opposite that of the top spray orientation within the draft tube. The temperature and relative humidity gradients outside of the draft tube remain relatively constant because no coating solution is introduced in this area and the particles are generally dry when they exit the top of the draft tube. Figure 2.7 shows the general temperature and relative humidity gradients within a Wurster orientation fluidized bed.

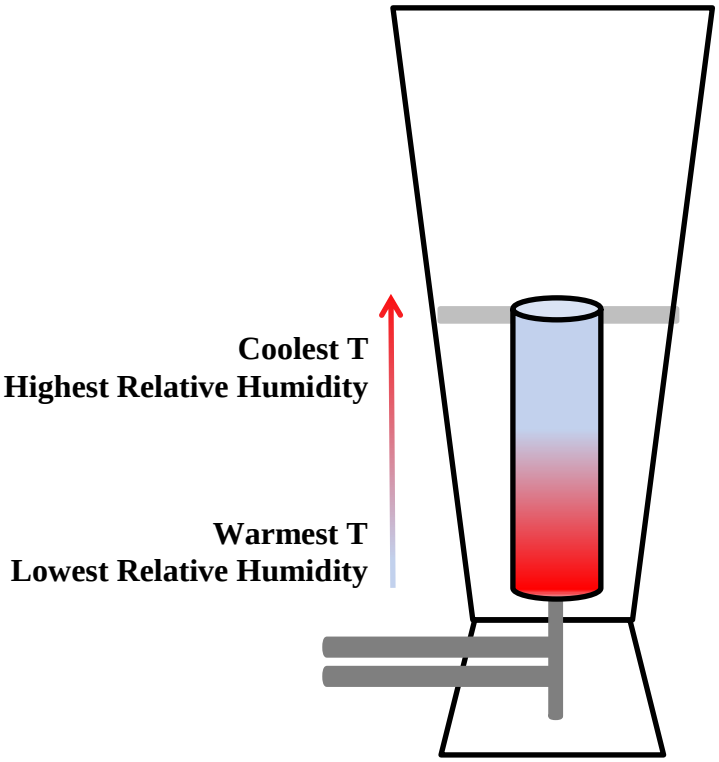

Figure 2.7 General Trend of Temperature and Relative Humidity Gradients in a Wurster Orientation Fluidized Bed

2.2.1 Distributor Plate Design

The distributor plate is a multi-functional part of the fluidized bed. When no fluidizing gas is present, the distributor plate provides structural support to maintain a stable static particle bed. With the addition of fluidization gas, the characteristics of the distributor plate dictate the bubbling pattern that consequently develops [14].

Some of the typical design arrangements of fluidized bed distributor plates include: porous plates, pipe grids, bubble caps, and tuyeres. Ideally, the distributor plate should have many small orifices to provide a smooth, even distribution of the fluidization gas. Botterill (1975) identified four central requirements a distributor plate should do: stimulate a steady and uniform fluidization pattern, minimize both particle attrition and bed erosion, and prevent

particle backflow [14]. Figure 2.8 shows two different types of distributor plates. The distributor plate shown in Figure 2.8 a) is a porous plate design used for the top spray orientation, usually a very fine mesh fused atop a coarser mesh. The distributor plate shown in Figure 2.8 b) is a typical design for the Wurster orientation. The large holes at the center of distributor plate allow for a higher velocity of air to flow through the draft tube promoting rapid coating solution evaporation and particle drying. The small holes outside the draft tube promote horizontal particle transport and minimize the potential for particle movement dead zones.

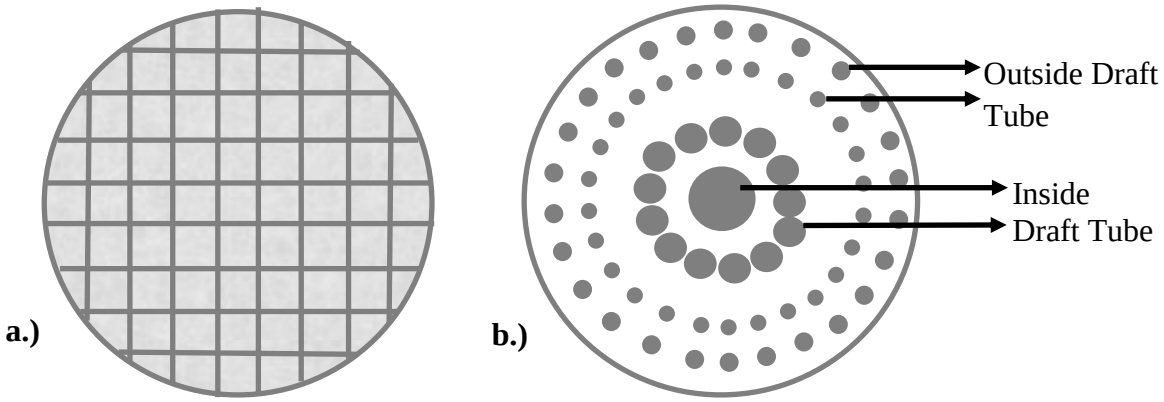

Figure 2.8 Typical Distributor Plate Designs for a Fluidized Bed a). Top Spray Orientation b). Wurster Orientation

An additional factor that has an impact on the fluidization pattern is the pressure drop across the distributor plate. An even flow distribution over the cross sectional area of the distributor plate is obtained when the pressure drop across the distributor plate is roughly 20-40% of the pressure drop within the fluidized bed [15]. For porous plates the pressure drop across the distributor plate is proportional to the superficial velocity of the fluidization gas. For perforated plates and tuyere distributor plates the pressure drop across the distributor plate is proportional to the square of the superficial velocity [15].

2.3 Atomization Principles

The even distribution of a liquid coating solution onto fluidized particles can be achieved by atomizing the liquid into droplets. Atomization is a mechanical process whereby a bulk liquid flow is subjected to external forces that cause instabilities to develop. In two-fluid atomization for example, the external forces acting upon the bulk liquid are due to a concurrent fast flowing gas stream. The instabilities cause the bulk liquid subsequently to breakup into smaller droplets, increasing the surface area to volume ratio significantly. The droplet shape evolved is a complex function of nozzle type and geometry as well as gas and liquid properties [16].

2.3.1 Types of Atomizers

Atomization can be achieved multiple ways: pressure differential, rotational friction, electrostatic pressure, sonic and ultrasonic vibration, and air assistance. The droplet size distribution produced will vary according to the method of atomization. Therefore, the choice of atomization method is an important decision partially dependent on the process for which it is required [16].

Pressure atomizers, also called airless atomizers, produce a high liquid exit velocity by forcing the liquid through a small opening in the nozzle, increasing the pressure. Friction developed with the pressure increase causes the bulk liquid flow to become unstable. The final droplet size distribution is highly dependent on three main factors: the orifice diameter, the ambient pressure of the environment the liquid is introduced into, and the relative velocity of the liquid stream to the ambient environment [17]. Some examples of pressure atomizers include: plain orifice, dual orifice, pressure swirl (also called simplex), square spray, duplex, spill return, and fan spray [16].

Rotary atomizers, also called centrifugal atomizers, liquid flows into the center of the nozzle where a rotating disk or cup resides. Centrifugal force then distributes the liquid radially along the rotating disk or cup where it is then ejected at a high velocity. Liquid sheets and/or ligaments form first on the periphery of the rotating disk or cup. Next, the liquid sheets and/or ligaments break down into droplets [17]. Rotary atomizers offer two forms of control over droplet size: the liquid flow rate and the rotational speed of the disk [16].

Electrostatic atomization is another method atomization available industrially. Electrostatic atomization involves subjecting the liquid to a strong electromagnetic field. The electromagnetic field causes the surface of the liquid to expand, counteracting the surface minimization forces evolved from the liquid surface tension. Droplets form when the electromagnetic forces surpass the surface tensional forces of the liquid [17]. Droplet size is a function of three parameters with electrostatic atomization: the magnitude of the electromagnetic field, the liquid flow rate, and the liquid physical and electrical properties. Electrostatic atomization has limited practical use due to the low liquid throughput [16].

An alternative method to applying an electromagnetic field to induce liquid droplet formation involves providing a high frequency vibration to a liquid flowing through a transducer. In sonic and ultrasonic atomization, after the fluid passes through the vibration absorbing transducer, surface instabilities cause the liquid to break up into droplets. The droplet size generated from a sonic or ultrasonic atomizer is very small, with low droplet size values ranging from 1-5 μm. However, the liquid throughput for a sonic or ultrasonic atomizer is very low, with maximum flow rates around 7 liters per hour at 55 KHz, again limiting practical applications [16].

Unlike the previous types of atomizers discussed air assisted atomizers involve an additional phase of matter to provide the mechanical stresses to generate droplets. Air assisted atomizers are also called two-fluid or pneumatic nozzles. In this arrangement, a high velocity stream of air causes surface instabilities on the bulk liquid flow, resulting in droplet formation.

There are three types of assemblies for the pneumatic nozzle, pneumatic cup atomizer, external mixing and internal mixing arrangements. The pneumatic cup atomizer involves mixing the air stream and the liquid stream at the rim of a nozzle that contains a rotating heat [18]. In the external mixing orientation, the air stream and the liquid stream do not come in contact with one another until they both exit the nozzle. The air stream and the liquid stream mix together just prior to exiting the nozzle in the internal mixing orientation [16]. Figure 2.9 shows a pneumatic nozzle with the external and internal mixing orientations.

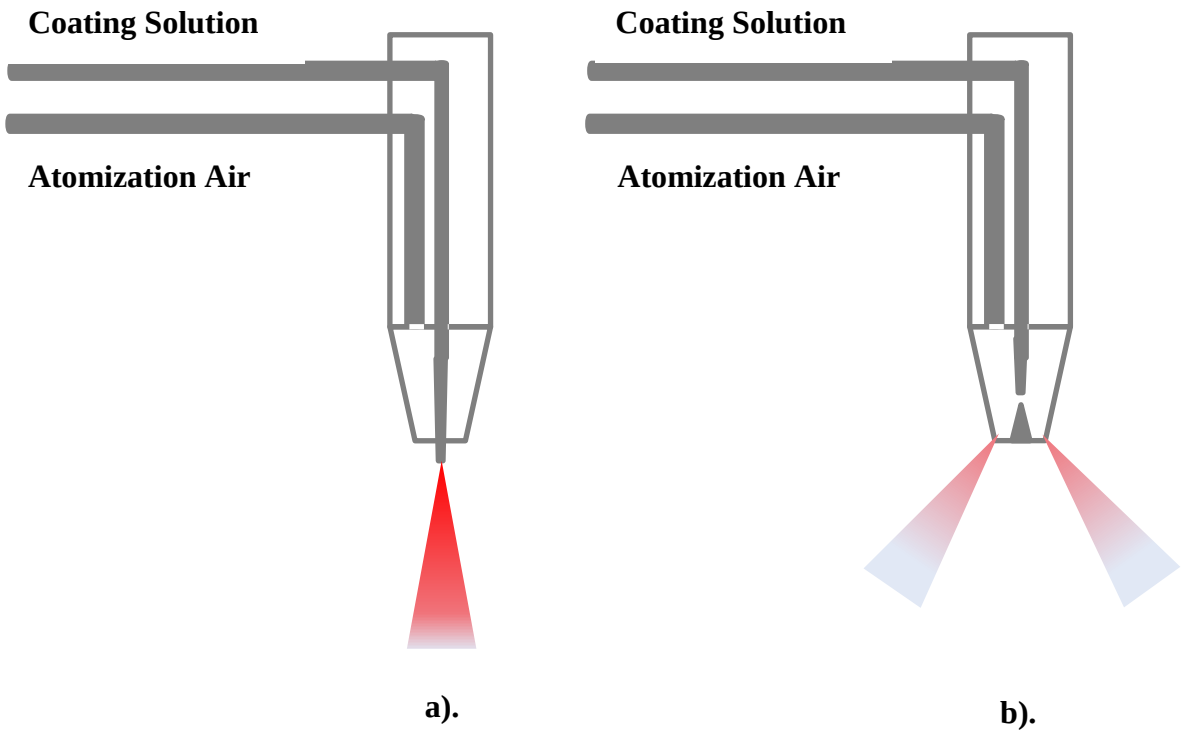

Figure 2.9 Pneumatic Nozzle Orientations: a) External Mixing b) Internal Mixing

The driving force for producing the instabilities within the liquid is the pressure of the air. The internal mixing orientation is more energy efficient than the external mixing orientation because less air is needed for the same droplet size formation. However, the internal mixing orientation can be subject to back pressure buildup that prevents acceptable droplet formation [16]. The probability of nozzle clogging is also reduced with the external mixing orientation compared to the internal mixing orientation because there is no interaction between the air and the liquid until the nozzle exit [16].

The choice for an internal or external mixing orientation is dependent on several factors since identical nozzle performance can be achieved with both orientations. Scaling up liquid flow rates from lab scale to production scale tends to favor the use of an internal mixing orientation because of energy efficiency, particularly when liquid flow rates are greater than 30 kg/hr with a droplet size requirement of 10μm or less. However, internal mixing nozzles can have a shorter lifetime due to erosion if solid impurities are present in the liquid [18].

External mixing nozzles also offer a degree of flexibility regarding placement within the fluidized bed equipment. An external mixing nozzle can be used to spray liquid above, below or within the fluidized bed because back pressure buildup can easily be avoided. The droplet size can be controlled by altering the liquid or the air flow rate independently. Additionally, there is an opportunity for premature liquid evaporation within the mixing chamber of an internal mixing orientation [18].

2.3.2 Spray Patterns

Another aspect of nozzle design in addition to the nozzle mixing orientation is the spray pattern. The spray pattern is a function of the nozzle orifice design and the spray angle of the nozzle. The spray angle of a nozzle is an inherent design property however, it is not constant.

The spray angle diminishes as the liquid moves away from the nozzle due to gravitational effects [19]. Figure 2.10 shows the spray angle and theoretical coverage of a nozzle.

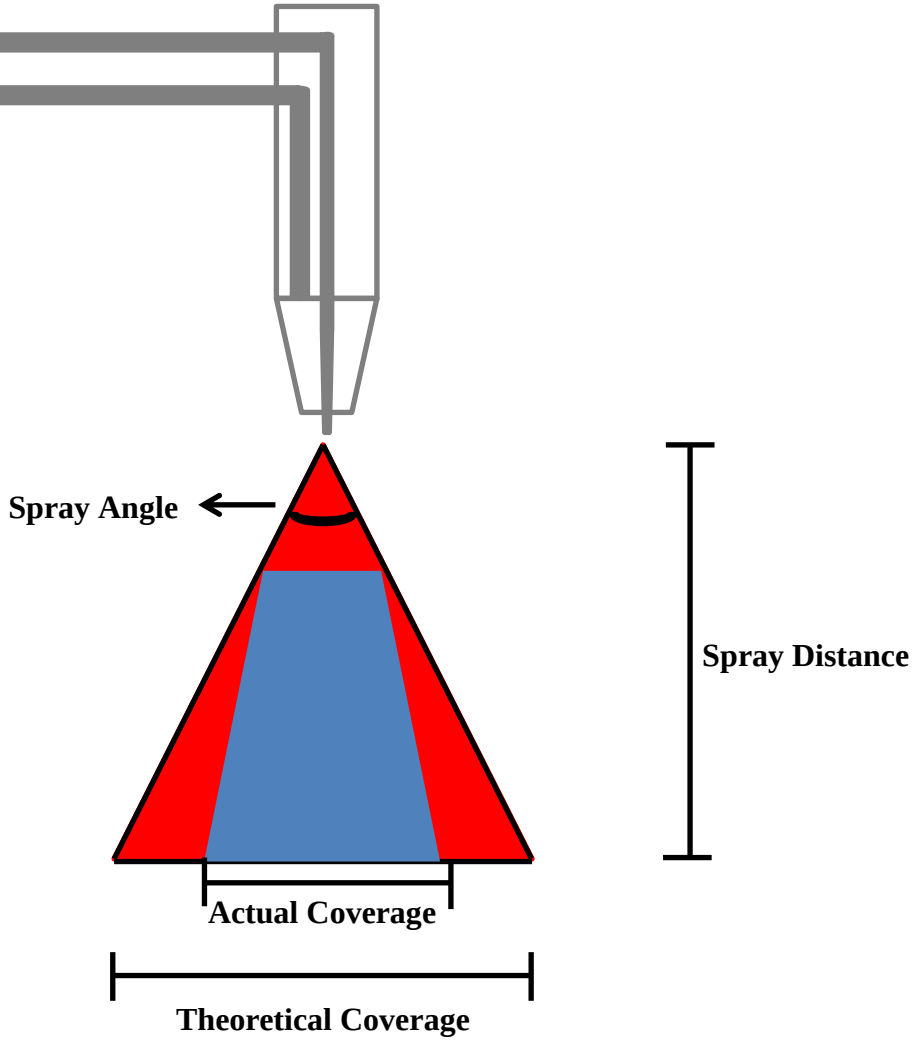

Figure 2.10 Spray Angle of a Nozzle

Common spray patterns seen in nozzle design are: full cone, hollow cone, and flat spray. The full cone spray pattern has droplets that expand outward into a cone pattern, with droplets evenly distributed across the entire diameter and inside the cone. The hollow cone spray pattern has droplets concentrated only on the outer diameter of the expanded cone pattern. The internal diameter of the hollow cone spray pattern is void of droplets until a certain diameter is reached.

In the flat spray pattern, all the droplets are concentrated in a narrow ovular pattern. Figure 2.11 shows the full cone, hollow cone and flat spray patterns [20].

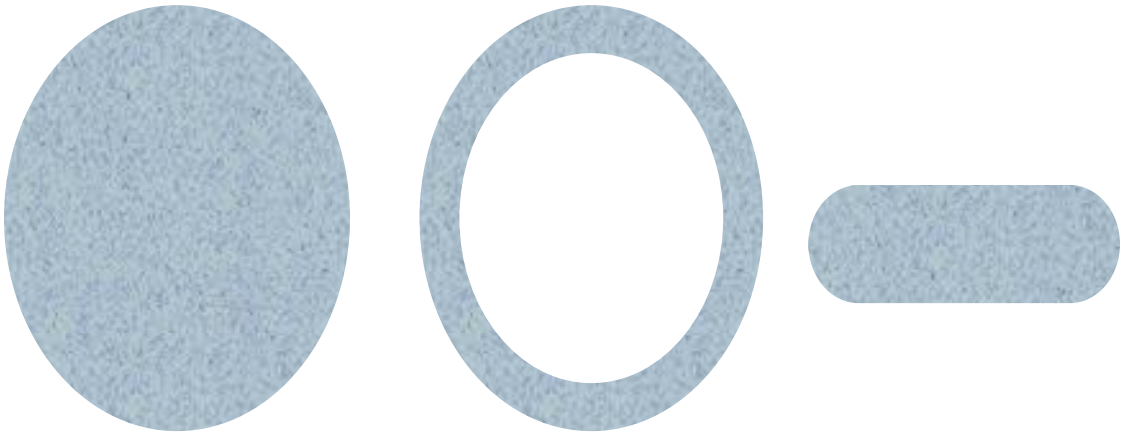

a). **b).** **c).**

Figure 2.11 Examples of External Mixing Nozzle Spray Patterns: a) Full Cone b) Hollow Cone c) Flat Spray

2.3.3 Two-Fluid Atomization Principles

Two-fluid atomization is the result of numerous disintegration mechanisms. Frictional forces develop when a high velocity gas stream passes over the surface of a liquid stream. When the frictional forces cannot be damped out and sufficiently absorbed by the viscous and surface tensional forces holding the liquid together, the liquid fragments into droplets. The first part of the liquid fragmentation involves aerodynamic pressure breaking the liquid sheet into thin ligaments or very large droplets. The ligaments or large droplets are subsequently broken up to smaller droplets until pressure equilibrium is reached between the droplet and the surrounding air stream [16, 20]. The physical properties of the liquid (i.e. density, surface tension, viscosity) and

the properties of the gas stream (i.e. density, superficial velocity) determine the droplet size distribution generated [20].

Frictional forces strong enough to create liquid droplets can be generated by passing a high velocity gas over the liquid surface. A high velocity (sonic or supersonic) gas stream can be evolved in a nozzle by minimizing the cross-sectional area through which the gas flows prior to contact with the liquid. Low velocity liquid jets can be effectively penetrated by a high velocity gas stream. Kinetic energy is transferred to the liquid jet causing surface instabilities and subsequent droplet formation. This initial droplet formation is called primary atomization. If the droplets have a diameter larger than a critical diameter, the droplets will continue to disintegrate to a smaller diameter. This is called secondary atomization. If the liquid jet flow rate is too high, complete atomization will not commence because the high velocity gas jet will not be able to penetrate the liquid jet. For large scale operations where a high liquid atomization flow rate is required, breaking the liquid jet into thin ligaments (called pre-filming) is necessary [16, 20].

Mathematical model development of droplet formation has proven very difficult. Droplet formation studies typically concern one individual phenomenon or a small grouping of phenomena. As a result, there is no complete model describing liquid atomization processes [16]. Nevertheless, the studies conducted on liquid atomization phenomena have revealed many important underlying fundamentals.

2.3.3.1 Droplet Disintegration Mechanisms

The first studies concerning droplet fragmentation were done by Lenard (1904) and Hocschwender (1949). The experiments studied involved free falling droplets in still air and droplets falling in a constant flow of air. Later Hinze (1955) categorized three types of droplet disintegration that occur which are contingent on the air flow pattern to which the liquid is

subjected: droplet flattening to an oblate ellipsoid shape (lenticular deformation), droplet elongation to a cylindrical shape (cigar-shaped deformation), and a bulged or protuberant shape due to local surface deformations. Parallel or rotating flows generate the oblate ellipsoid shape. Plane hyperbolic flows generate the cigar shaped deformation. Irregular flow patterns will yield the bulged droplet deformation [16].

A force balance on a liquid shows that for any liquid, breakup from bulk flow is attained when the surface tension is balanced with the aerodynamic drag of the gas applied as shown in Equation 2.4:

$$C_d\left(\frac{\pi D^2}{4}\right)(0.5)\rho_g U_{rel}^2 = \pi D\sigma \tag{2.4}$$

Rearranging Equation 2.4 into a dimensionless form yields:

$$\left(\frac{\rho_g U_{rel}^2 D}{\sigma}\right)_{crit} = \frac{8}{C_d} \tag{2.5}$$

Here the subscript crit denotes that surface tension force has been balanced by the aerodynamic drag force. The U_{rel} term represents the relative velocity of the gas stream. The left hand term of Equation 2.5, called the Weber number after Moritz Weber is the ratio of inertial forces to surface tensional forces is [16]:

$$We = \frac{\rho_g U_{rel}^2 D}{\sigma} \tag{2.6}$$

Liquid jet disintegration in fast flowing air occurs by different mechanisms compared to slow flowing air described above. Plateau (1945) is acknowledged as the first investigator of liquid jet instability [16]. Haenlein (1932) categorized four distinctive liquid jet breakup regimes: droplet formation in the absence of air, droplet formation with air, droplet formation

resulting from jet waviness, full disintegration of liquid jet. There is no clear distinction between the regimes listed above [16].

Ohnesorge (1936) categorized the liquid jet breakup regimes by the forces involved: surface tension, gravity, viscosity, and inertia. Using dimensional analysis, Ohnesorge developed a dimensionless quantity called the stability number. The stability number is sometimes called the viscosity group but is more commonly known as the Ohnesorge number. The Ohnesorge number, as shown in Equation 2.7, is the ratio of liquid viscous force to the square root of the product of the liquid inertia and surface tensional force [16]:

$$Oh = \frac{\mu_l}{\sqrt{\rho_l \sigma_l d_0}} = \frac{\sqrt{We}}{Re} \tag{2.7}$$

The Bond number is used to assess whether gravity or surface tension dominates the droplet formation. If the Bond number is less than 1 surface tension dominates over gravity. If the Bond number is greater than 1, gravity dominates over surface tension. The Bond number is shown in Equation 2.8 [21]:

$$Bo = \frac{\rho g r_{drop}^2}{\sigma_l} \tag{2.8}$$

Ohnesorge determined three distinct jet breakup regimes when the Ohnesorge number plotted against the Reynolds number, another dimensionless quantity. The Reynolds number, shown in Equation 2.9 is a ratio of inertial force to viscous forces [22]:

$$Re = \frac{\rho_l U_l d_0}{\mu_l} \tag{2.9}$$

Fluid flow is classified as laminar, turbulent or transition based on the magnitude of the Reynolds number. Table 2.1 shows the flow regime classification based on the Reynolds number magnitude [22].

Table 2.1 Flow Regime Classification

Flow Regime	**Reynolds Number**
Laminar	> 2100
Transition	2100 < Re < 4300
Turbulent	> 4300

The liquid jet breakup mechanisms identified by Ohnesorge are: large uniform droplets at low Reynolds numbers (called Rayleigh jet breakup after Lord Rayleigh (1878), who first studied this regime), sinuous wave breakup where a wide assortment of droplet sizes form due to jet oscillations that increase due to increasing air resistance at intermediate Reynolds numbers, and complete atomization at high Reynolds numbers shortly after exiting the nozzle [16].

The work on liquid jet stability was expanded upon by Reitz (1978) by increasing the liquid jet velocity: Rayleigh jet breakup, first wind induced breakup, second wind induced breakup and atomization. In the Rayleigh jet breakup regime surface tension dominates the droplet formation mechanism and the droplets formed are larger than the liquid jet. The first wind induced breakup is characterized by a static pressure distributed across the jet that acts to counterbalance the surface tension of the liquid. Droplets formed in this regime are typically the same size as the jet diameter. In the second wind induced breakup regime unstable short waves impinge on the jet surface causing droplets formed to be smaller than the jet diameter. In the atomization regime, droplets form a very short distance from the nozzle exit as the liquid jet completely disintegrates. The droplet size is much smaller than the jet diameter. Figure 2.12 shows the jet disintegration mechanisms identified by Ohnesorge and Reitz [16].

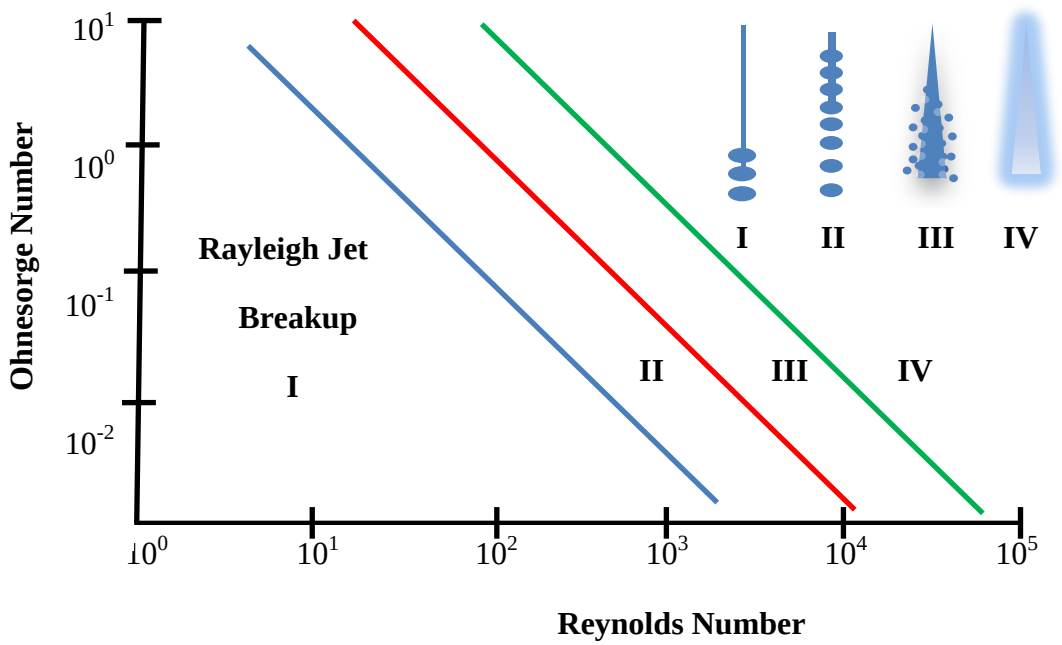

Figure 2.12 Classification of Disintegration Mechanisms: I. Rayleigh Jet Breakup II. First Wind Induced (Sinuous Wave Breakup) III. Second Wind Induced (Wave-Like with Air Friction) IV. Atomization

2.3.4 Factors Impacting Droplet Size

The droplets produced during the atomization process are not all the same size. Typically a distribution of droplet sizes is generated. This distribution can be wide or sharp, depending on several factors. The factors that play a role in determining droplet size and the droplet size uniformity are: the nozzle type, thermophysical properties of the liquid solution, the thermophysical properties of the gas, the flow rates of air and liquid, the air pressure, and the spray angle [20].

The nozzle type used for a process has an influence on the droplet size. Full cone nozzles generally produce the largest droplet size. Hollow cones generally produce the smallest droplet size. Flat spray nozzles produce droplet sizes between that of full and hollow cones. In addition, the liquid flow rate through the nozzle effects the droplet size as well. Increasing the liquid flow

rate will increase the droplet size. The liquid jet velocity increases making high velocity gas jet penetration less effective, resulting in larger droplet formation [20].

The thermo-physical properties of the liquid and air also influence the droplet size produced. The liquid thermo-physical properties of interest are: density, surface tension and viscosity. Higher the magnitudes of density, surface tension, and viscosity translate to higher minimum required pressures for atomization, higher resistance to flow, and lower spray angles. The higher values for liquid thermo-physical properties result in larger droplet formation [20].

The air thermo-physical properties of interest are: density, relative humidity, and viscosity. A higher density helps generate more turbulence on the surface of the liquid jet resulting in smaller droplet formation. Droplet size increases with relative humidity and viscosity on the other hand. In addition to the thermo-physical properties of air, another variable that impacts droplet size is the air pressure. As the air pressure increases, the droplet size decreases [20].

The spray angle also has an effect on the droplet size produced from a nozzle. As the spray angle decreases, the droplet size increases [20]. Table 2.2 summarizes the factors that impact the droplet size and the general qualitative direction of impact on the droplet size.

Table 2.2 Factors That Impact Droplet Size and General Direction of Impact

Property	**Increase Property**	**Impact on Droplet Size**
Liquid		
Density	+	+
Surface Tension	+++	+
Viscosity	+	+
Air		
Density	+	-
Pressure	+++	-
Relative Humidity	+	+
Viscosity	+	+
Nozzle		
Spray Angle	+	-

+++: Strong Impact ++: Medium Impact +: Minimal Impact

The thermo-physical properties of air and liquid mentioned above are all functions of temperature. Typically density decreases with temperature due to volumetric expansion that occurs. Surface tension and viscosity also tend to decrease with an increase in temperature [22].

2.3.5 Droplet Size Correlations and Droplet Size Distribution

Droplet size correlations have been developed for internal and external mixing nozzles. Since nozzles produce a range of droplet sizes that depend on physical properties, geometry, and process parameters, the droplet size correlations have been developed to predict one or two representative sizes: the Sauter mean diameter and the mass median diameter. The mean diameter most often used to describe liquid atomization is the Sauter mean diameter (SMD). The SMD is the diameter of a droplet that has the same volume to surface area ratio as the total liquid being sprayed. The mass median diameter (MMD) is the drop diameter equivalent to 50% of the liquid volume is in drops smaller than this value [16]. The MMD and SMD are related as shown in Equation 2.10 [23]:

$$d_{SMD} = 0.83 d_{MMD} \tag{2.10}$$

2.3.5.1 Droplet Size Correlations for Internal Mixing Nozzles

The earliest published work on droplet size correlation with internal mixing nozzles was by Nukiyama and Tanasawa [24, 25]. The SMD, determined by relating it to the thermophysical properties of the liquid (density, surface tension, and viscosity) and the operation conditions (liquid flow rate, air flow rate, and relative velocity of the air and liquid is shown as Equation 2.11:

$$d_{SMD} = \frac{585000}{v_{rel}} \sqrt{\frac{\sigma_{liq}}{\rho_{liq}}} + 597 \left(\frac{\mu_{liq}^2}{\sigma_{liq} \rho_{liq}} \right)^{0.45} \left(\frac{1000 q_{liq}}{q_{air}} \right)^{1.5} \tag{2.11}$$

The orifice dimensions of the nozzle are not included because the authors concluded there was no effect on the droplet size produced. A drawback to the correlation developed by Nukiyama and Tanasawa is that the air density was constant for their experiments. Interestingly, this correlation has been shown to be valid for external mixing nozzles operating under pressure with low liquid flow rates [26].

Lefebvre has developed many correlations for internal mixing nozzles including one developed with Rizk (1984) for plain jet nozzles, shown as Equation 2.12:

$$d_{SMD} = L_c \left[0.48We^{-0.4} \left(1+\frac{m_{liq}}{m_{air}} \right)^{0.4} + 0.15Oh \left(1+\frac{m_{liq}}{m_{air}} \right) \right] \quad (2.12)$$

where L_c is the nozzle characteristic length, often set equal to the liquid orifice diameter. Nguyen and Rhodes developed a correlation for the MMD of an internal mixing nozzle shown in Equation 2.13 [16]:

$$d_{MMD} = d_{orifice} \left(\frac{\rho_{liq}}{\rho_{air}} \right)^{0.39} \left[0.01We^{0.5} + 1.22Oh \right] \left(1 + \frac{m_{liq}}{m_{air}} \right)^{0.28} \quad (2.13)$$

The length of time necessary for atomization to occur is not factored into any of the above listed correlations.

2.3.5.2 Droplet Size Correlations for External Mixing Nozzles

Several droplet correlations for external mixing nozzle have been published due to their wide spread usage. Gretzinger and Marshall [27] developed a correlation for the MMD shown in Equation 2.14:

$$d_{MMD} = 2600 \left[\left(\frac{m_{liq}}{m_{air}} \right) \left(\frac{\mu_{air}}{G_{air} L_c} \right) \right]^{0.4} \quad (2.14)$$

where G_a is the mass flux of air per gas jet orifice at the nozzle exit and L_c is the characteristic length of the nozzle, often the liquid orifice diameter. Kim and Marshall published a correlation for the MMD shown in Equation 2.15 [23]:

$$d_{MMD} = \left[\frac{249\sigma_{liq}^{0.41}\mu_{liq}^{0.32}}{\left(v_{rel}^2\rho_{air}\right)^{0.57}A_{ann}^{0.36}\rho_{liq}^{0.16}}\right] + 1260\left[\left(\frac{\mu_{liq}}{\sigma_{liq}\rho_{liq}}\right)^{0.17}\left(\frac{1}{v_{rel}^{0.54}}\right)\left(\frac{m_{liq}}{m_{air}}\right)^{m}\right] \quad (2.15)$$

where m = -1 when the liquid to air ratio term is less than 3 and m = -0.5 when the liquid to air ratio is greater than 3. The discontinuity has a significant impact on the calculated MMD but Equation 2.15 is valid for Newtonian fluids.

For pre-filming nozzles Lefebvre has published a few correlations for the SMD. Rizkalla and Lefebvre (1975) developed Equation 2.16 [16]:

$$d_{SMD} = \left[3.3^{-3}\left(\frac{\sqrt{\sigma_{liq}\rho_{liq}d_{prefilm}}}{v_{air}\rho_{air}}\right) + 13.1^{-3}\left(\frac{\mu_{liq}^2}{\sigma_{liq}\rho_{liq}}\right)^{0.425} d_{prefilm}^{0.575}\left(1 + \left(\frac{m_{liq}}{m_{air}}\right)\right)\right]\left(1 + \left(\frac{m_{liq}}{m_{air}}\right)\right) \quad (2.16)$$

El-Shanawany and Lefebvre (1980) developed a slightly different correlation for pre-filming nozzles as shown in Equation 2.17 [16]:

$$d_{SMD} = d_{prefilm}\left[0.33\left(\frac{\sigma_{liq}}{v_{air}\rho_{air}d_{prefilm}}\right)^{0.6}\left(\frac{\rho_{liq}}{\rho_{air}}\right)^{0.1} + 0.068\left(\frac{\mu_{liq}^2}{\sigma_{liq}\rho_{liq}d_{prefilm}}\right)^{0.5}\right]\left(1+\left(\frac{m_{liq}}{m_{air}}\right)\right) \quad (2.17)$$

Wazel (1993) and Groom et al. (2004) developed an equation for the SMD as shown in Equation 2.18 [28, 29]:

$$d_{SMD} = 0.35d_{orifice}\left[\frac{\Delta p(d_{orifice})}{\sigma_{liq}\left(1+\left(\frac{m_{liq}}{m_{air}}\right)\right)^2}\right]^{-0.4}(1 + 2.5Oh) \quad (2.18)$$

Mulhem et al. developed a correlation for the droplet SMD for cases where the coating solution is delivered to the nozzle as a suspension rather than completely dissolved. Equation 2.19 shows the SMD Mulhem et al. developed [30, 31]:

$$d_{SMD} = 0.21 d_{orifice} (Oh)^{0.0622} \left(We_{air} \left(\frac{m_{air}}{m_{liq}} \right) \right)^{-0.4} \tag{2.19}$$

2.3.5.3 Droplet Size Distributions

Atomizers produce a range of droplet sizes based on the characteristics of the nozzle, the liquid being atomized, and the atomizing gas. Due to this fact, representative mean diameters are determined and used to describe the droplet size distribution. Table 2.3 shows some representative mean diameters used to describe drop sizes in a distribution [16].

Table 2.3 Representative Mean Diameters for Drop Sizes in a Distribution

Name	Symbol	Expression
Length	D_{10}	$\frac{\sum N_i D_i}{\sum N_i}$
Surface Area	D_{20}	$\left(\frac{\sum N_i D_i^2}{\sum N_i} \right)^{0.5}$
Volume	D_{30}	$\left(\frac{\sum N_i D_i^3}{\sum N_i} \right)^{0.333}$
Surface Area-Length	D_{21}	$\frac{\sum N_i D_i^2}{\sum N_i D_i}$
Volume-Length	D_{31}	$\left(\frac{\sum N_i D_i^3}{\sum N_i D_i} \right)^{0.5}$
Sauter (SMD)	D_{32}	$\frac{\sum N_i D_i^3}{\sum N_i D_i^2}$

Table 2.3 Continued

DeBrouckere/Herdan	D_{43}	$\frac{\sum N_i D_i^4}{\sum N_i D_i^3}$

In addition to the SMD there are other diameters used to characterize the droplet distribution that are shown in Table 2.4 [16].

Table 2.4 Droplet Diameters Used to Characterize Droplet Distribution

Droplet Size	**Description**
$D_{0.1}$	Droplet diameter where 10% total volume is a smaller diameter
$D_{0.5}$	Droplet diameter where 50% total volume is a smaller diameter Also called Mass Median Diameter (MMD)
$D_{0.632}$	Droplet diameter where 63.2% total volume is a smaller diameter
$D_{0.9}$	Droplet diameter where 90% total volume is a smaller diameter
$D_{0.999}$	Droplet diameter where 99.9% total volume is a smaller diameter
D_{Peak}	Droplet diameter coinciding with peak of droplet size frequency distribution

Figure 2.13 shows the droplet diameters described in Table 2.4 [16].

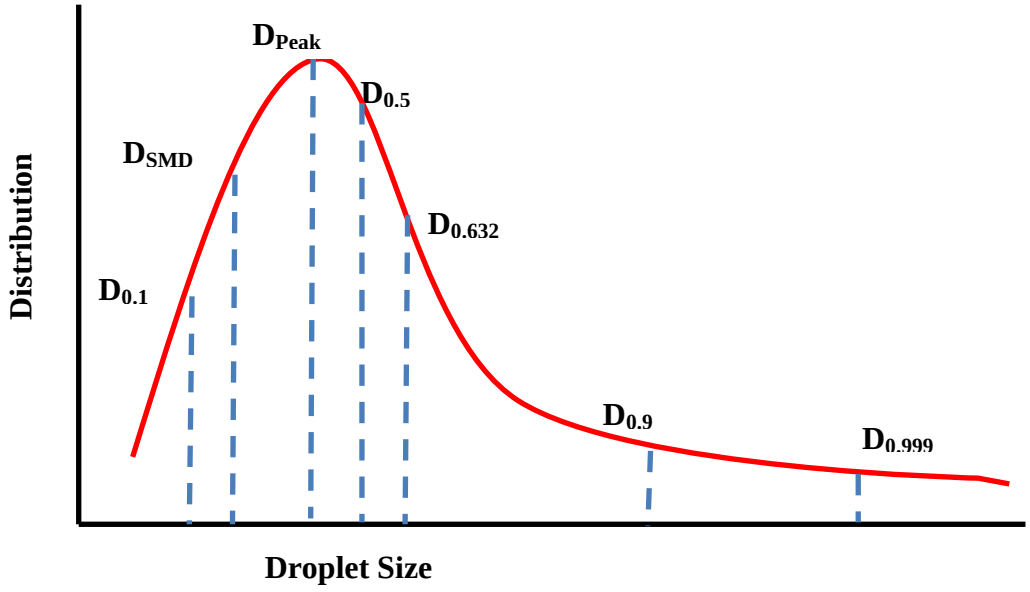

Figure 2.13 Droplet Diameter Positions on Droplet Size Distribution

Several functions have been suggested to depict the droplet size distribution including: Nukiyama-Tanasawa distribution, upper-limit distribution, normal distribution, lognormal distribution, and Rosin-Rammler distribution. The Rosin-Rammler distribution, the most widely used equation to characterize droplet size distribution, is given as Equation 2.20:

$$1 - Q = \exp\left(-\frac{d_d}{X}\right)^q \tag{2.20}$$

where Q is the fraction of total volume contained in droplets diameters less than d_d. Parameters X and q are constants, with q ranging in value from 1.5-2.9 [16].

Many of the droplet sizes listed in Table 2.4 can be calculated once q and the MMD are known. Equations 2.21– 2.25 show the relationships to determine $d_{0.1}$, d_{32}, $d_{0.5}$, $d_{0.9}$, and $d_{0.999}$ (Lefebvre 1989).

$$\frac{d_{0.1}}{d_{MMD}} = (0.152)^{\frac{1}{q}} \tag{2.21}$$

$$\frac{d_{MMD}}{d_{SMD}} = (0.693)^{\frac{1}{q}}\left(1-\frac{1}{q}\right) \tag{2.22}$$

$$\frac{d_{0.5}}{d_{MMD}} = 1 \tag{2.23}$$

$$\frac{d_{0.9}}{d_{MMD}} = (3.322)^{\frac{1}{q}} \tag{2.24}$$

$$\frac{d_{0.999}}{d_{MMD}} = (9.968)^{\frac{1}{q}} \tag{2.25}$$

2.4 Fluidization Principles

Fluidized bed technology involves passing an upward flowing gas through a bed of particles at a velocity high enough that all the particles are held in suspension [15]. Initially fluidized bed coating operations start out as packed beds with gas flowing between the particles.

The pressure drop across the packed bed increases when the superficial gas velocity increases and can be described sufficiently by the Ergun equation, Equation 2.26 [32]:

$$\frac{d_p^3 \rho_g \left(\rho_s - \rho_g\right) g}{\mu^2} = \frac{1.75(1-\varepsilon)}{\varepsilon_{mf}^3 \phi_s} \left(\frac{d_p U_{mf} \rho_g}{\mu}\right)^2 + \frac{150(1-\varepsilon_{mf})}{\varepsilon_{mf}^3 \phi_s^2} \left(\frac{d_p U_{mf} \rho_g}{\mu}\right) \qquad (2.26)$$

where the terms ε_{mf} and U_{mf} represent the void fraction at minimum fluidization and the minimum fluidization velocity. The term ϕ represents the particle sphericity.

The superficial gas velocity at which the pressure drop in the bed is equivalent to the weight of the particles is termed the incipient velocity or the minimum fluidizing velocity, U_{mf} [33]. Figure 2.14 shows the general trend of pressure drop for a packed bed through a fluidized bed.

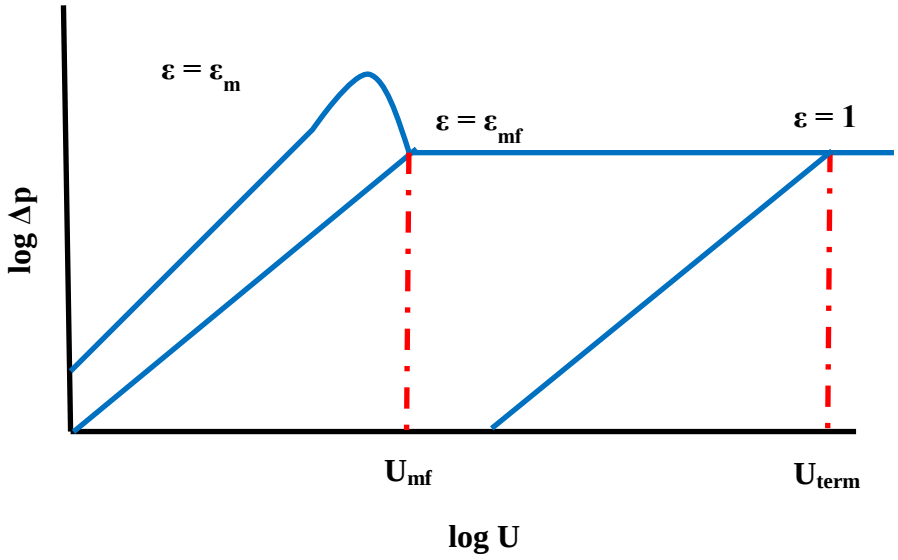

Figure 2.14 Pressure Drop Behavior From a Packed Bed to Fluidized Bed

2.4.1 Minimum Fluidization Velocity

Several gas velocities that are important in fluidized bed operations are defined in Table 2.5. However depending on the type of process the fluidized bed will be used for: particle coating, reactions, or transport, not all the velocities will need to be calculated.

Table 2.5 Velocities of Fluidized Bed Operations

Velocity	Designation	Definition
Minimum Fluidizing[a]	U_{mf}	Lowest velocity of gas needed to go from fixed to fluidized state
Minimum Bubbling[a]	U_{mb}	Lowest velocity at which gas bubbles will form in the bed
Choking[b]	U_{ch}	Velocity at which particles in dilute transport shift to slug flow (vertical transport)
Complete Fluidization[c]	U_{cf}	Velocity where all particle sizes are fluidized
Saltation[b]	U_{salt}	Velocity at which particles in dilute transport cannot be supported by gas flow (horizontal transport)
Slip[c]	U_{slip}	Average velocity of particle in the bed
Slug[d]	U_{slug}	Velocity where gas bubble diameter becomes highly dependent on bed diameter
Superficial	U	Nominal velocity
Terminal[a]	U_t	Velocity at which particle will escape bed entrainment
Transition[e]	U_c, U_k	Velocity at which bed regime changes from bubbling to turbulent, U_k Pressure fluctuations max out at U_c
Transport[e]	U_{tr}	Velocity at which bed regime changes from turbulent to fast fluidized

[a] [15] [b] [34] [c] [35] [d] [36] [e][37].

The minimum fluidizing velocity and the terminal velocity are perhaps the most important velocities in terms of particle coating calculations. Substantial research efforts have been put forth in obtaining accurate correlations involving dimensionless numbers to calculate the minimum fluidizing and terminal velocities. Table 2.6 shows a list of dimensionless numbers used in the determination of the minimum fluidizing velocity [38].

Table 2.6 Dimensionless Numbers Used in Minimum Fluidization Velocity

Dimensionless Number	Ratio	Ratio Meaning
Archimedes (Ar)	$\frac{gD^3\rho_g\left(\rho_p-\rho_g\right)}{\mu^2}$	Buoyant Force to Viscous Force
Galileo (Ga)	$\frac{D^3\rho_f^2 g}{\mu^2}$	Gravity Force to Viscous Force
Mass Ratio (Mv)	$\frac{\rho_p-\rho_g}{\rho_g}$	Density Difference of Particle and Fluid to the Fluid

Table 2.6 Continued

Reynolds (Re)	$\frac{\rho_f U_f d_0}{\mu_f}$	Inertial Force to Viscous Force

As Table 2.6 shows, the important factors in determining fluidizing velocity are gas and particle density, gas viscosity, and gravity. It should also be noted that density and viscosity are also functions of temperature and pressure. Couderc [40] has a summary of several dimensionless number correlations used to calculate the minimum fluidizing velocity with comments on applicability. Sangeetha et al. [41] also present a comparison of correlations for minimum fluidizing velocity. Table 2.7 shows correlations for the minimum fluidizing velocity represented as the Reynolds Number unless otherwise noted.

Table 2.7 Correlations for Minimum Fluidizing Velocity

Reference	Correlation	Comments
[42]	$\left(25.25^2 + 0.0651\mathrm{Ar}\right)^{0.5} - 25.25$	
[43]	$0.00138\mathrm{Ar}/(\mathrm{Ar}+19)^{0.11}$	Spherical particles $Re < 39 \quad Ar < 10^5$
[44]	$U_{mf} = \frac{0.0009125\left(\rho_p - \rho_g\right)^{0.934} g^{0.934} d^{1.8}}{\mu^{0.87}\rho_g^{0.066}}$	
[45]	$\left(25.46^2 + 0.03824\mathrm{Ar}\right)^{0.5} - 25.46$	Spherical particles
[46]	$\left(\frac{\mathrm{Ar}}{2.42\left(10^5\right)\left(\frac{\rho_p}{\rho_g}\right)^{0.13} + 37.7}\right)^{0.5}$	
[47]	$\left(28.7^2 + 0.0494\mathrm{Ar}\right)^{0.5} - 28.7$	
[48]	$U_{mf} = K\left[\frac{D_P^2\left(\rho_s - \rho_g\right) g}{\mu}\left(\frac{\rho_s}{\rho_g}\right)^{1.23}\right]^{\alpha}$	K and α are functions of the solid-gas system of interest
[49]	$0.00078\mathrm{Ar}$	
[50]	$\mathrm{Ar}/\left(1040 + 4.86\mathrm{Ar}^{0.5}\right)$	
[51]	$\left(\left[600\varepsilon_{mf}^3(1-\varepsilon_{mf})\right]^2\right) + 0.0408\mathrm{Ar}^{0.5} - 600\varepsilon_{mf}^3(1-\varepsilon_{mf})$	
[52]	$0.00108\mathrm{Ar}^{0.947}$	

Table 2.7 Continued

[53]	$0.001065Ar$	$Re < 32$
[54]	$G = 0.01558\frac{d^2\varepsilon^3\left(\rho_p - \rho_l\right)\rho_l g}{(1-\varepsilon)\mu\gamma}$	G units: $\frac{\text{mass}}{\text{area time}}$ γ: wettability factor
[55]	$\left[445\left(\frac{D}{d_v}\right)^{0.2} + 0.132\left(\frac{D}{d_v}\right)^{-0.5} GaMv\right]^{0.5} - 21.1\left(\frac{D}{d_v}\right)^{0.1}$ $[292 + 0.029GaMv]^{0.5} - 29$	Re: 1-1000 For $6 < \frac{D}{d_v} < 20$ For $\frac{D}{d_v} > 20$
[56]	$\left(27.2^2 + 0.0408Ar\right)^{0.5} - 27.2$	
[57]	$\frac{0.00138Ar}{(Ar+19)^{0.11}}$	
[58]	$U_{mf} = \frac{7.39d^{1.82}\left(\rho_p - \rho_g\right)^{0.94}}{\rho_g^{0.06}}$	$Re < 5$
[59]	$U_{mf} = \frac{0.0007169d^{1.82}\left(\rho_p - \rho_g\right)^{0.94} g}{\mu^{0.88}\rho_g^{0.06}}$	
[60]	$0.1256Ar^{10.523}Mv^{0.66}$	
[61]	$\left[\left(\frac{12}{C_I}\right)^2 + \frac{0.0114Ga_S Mv}{\psi^{3.2}C_I}\right]^{0.5} - \frac{12}{C_I}$	Re: 140-1100 d_s used: diameter of sphere of equal surface C_I is a function of sphericity and the range of Re numbers
[62]	$U_{mf} = \frac{0.00125d^2\left(\rho_p - \rho_g\right)^{0.9}\rho_g^{0.1} g}{\mu^{0.87}\rho_g^{0.066}}$	
[63]	$\left(33.953^2 + 0.0465Ar\right)^{0.5} - 33.953$ $G = \frac{27.83\mu}{d}\left[(1 + .00057Re_t)^{0.5} - 1\right]$ $G = \frac{42.9\mu}{d}\left(0.231\left(log(d)\right) + 1.417\right)\left[\left(1 + .0000212d^{-0.55}Re_t\right)^{0.5} - 1\right]$	Spherical particles Angular particles Valid for particles less than 508 μm
[64]	$U_{mf} = \frac{0.000701d^2\left(\rho_p - \rho_g\right) g}{\mu}$	$Re < 20$
[65]	$0.0154Ga^{0.66}Mv^{0.70}$	Re: 10-1000

Table 2.7 Continued

[66]	$\left(25.7^2 + 0.0365\text{Ar}\right)^{0.5} - 25.7$	
[67, 68]	$\left[\frac{1}{C_D 68.5}\left(\frac{4}{3}\right)\text{Ar}\right]^{0.5}$ $C_D = \frac{24}{\text{Re}}\left(1 + 0.15\text{Re}^{0.687}\right)$	Re: 0.023 – 1030 C_D from Shiller & Naumann (1935)
[69]	$\left(30.1^2 + 0.0417\text{Ar}\right)^{0.5} - 30.1$	
[70]	$\left(25.28^2 + 0.0571\text{Ar}\right)^{0.5} - 25.28$	
[71]	$G\text{aMv}\frac{\varepsilon^3}{1-\varepsilon} = 250\frac{\text{Re}}{1-\varepsilon}$ $\text{GaMv}\frac{\varepsilon^3}{1-\varepsilon} = 19\left[\frac{\text{Re}}{1-\varepsilon}\right]^{1.67}$	For $\frac{\text{Re}}{1-\varepsilon} < 50$ For $\frac{\text{Re}}{1-\varepsilon} \geq 50$
[72]	$.000754(\text{Ar})^{0.98}$ $.0195(\text{Ar})^{0.66}$	Re < 30 30 < Re < 180
[73]	$\left(31.6^2 + 0.0425\text{Ar}\right)^{0.5} - 31.6$	
[74]	$\text{Ar}/\left(1400 + 5.22\text{Ar}^{0.5}\right)$	
[75]	$\left(33.7^2 + 0.0408\text{Ar}\right)^{0.5} - 33.7$	
[76]	$\left(18.75^2 + 0.03125\text{Ar}\right)^{0.5} - 18.75$	

The effects of tapered bed geometry on minimum fluidization velocity were also investigated by a few authors. A fluidized bed bowl that has a diameter that increases with height is called a tapered fluidized bed. Figure 2.15 shows a tapered fluidized bed and the angle of the taper, α.

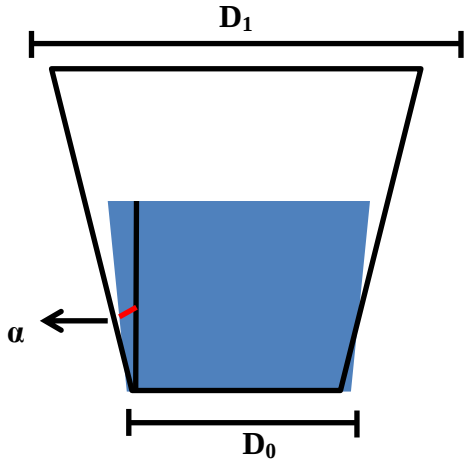

Figure 2.15 Tapered Fluidized Bed and Angle of Taper

Sau et al. [77] developed a correlation for the minimum fluidization velocity in the form of the Froude number. The Sau correlation accounts for the taper angle of the fluidized bed bowl, the particle sphericity and void fraction. The taper angle of the fluidized bed bowl is the angle formed between the The Froude number is the ratio of inertial force to gravitational force is shown in Equation 2.27 [38]:

$$Fr = \frac{U}{\sqrt{gd_p}} \tag{2.27}$$

Table 2.8 shows correlations for minimum fluidization velocity for tapered bowl geometries.

Table 2.8 Minimum Fluidization Velocity Correlations in Tapered Bowl Geometries

Author	**Correlation**
[77]	$Fr = 0.2714Ar^{0.3197}(\sin\alpha)^{0.6092}\left(\frac{\varepsilon_0}{\varphi}\right)^{-0.6108}$
[78]	$Re_{mf} = 0.0302Ar^{0.6467}\left(\frac{d_p}{D_0}\right)^{0.238}\left(\frac{\varepsilon_0}{\varphi}\right)^{-0.833}(\cos\alpha)^{-10.544}$
[79]	$C_1U_{mf} + C_2\left(\frac{D_0}{D_1}\right)U_{mf}^2 - (1-\varepsilon_0)\left(\rho_s - \rho_g\right)g\left(\frac{D_0^2+D_0D_1+D_1^2}{3D_0^2}\right) = 0$

The terms C_1 and C_2 are constants derived from the Ergun equation for pressure drop, previously shown as Equation 2.26.

The minimum fluidizing velocity can be determined by a few different experimental methods: pressure drop, bed voidage, and heat transfer [80]. Using the pressure drop method, the minimum fluidizing velocity can be found by plotting the pressure drop across the bed versus the superficial gas velocity. In a fixed bed the pressure drop increases with superficial velocity, however at the onset of fluidization the pressure drop across the bed becomes constant [80]. The bed voidage method for determining the minimum fluidizing velocity involves measuring the bed voidage as a packed bed is brought to the onset of fluidization. When the bed voidage starts

to increase with increasing superficial gas velocity, the minimum fluidizing velocity has been found. This method for establishing the minimum fluidizing velocity can be difficult as visual inspection of bed voidage cannot be done with a high degree of accuracy [80]. The heat transfer method for minimum fluidizing velocity involves tracking the wall heat transfer coefficient against the superficial gas velocity. In a packed bed the bed heat transfer coefficient increases steadily. The minimum fluidizing velocity is characterized by a sharp increase in the wall heat transfer coefficient. The heat transfer method also gives an optimal superficial gas velocity which corresponds to the upper limit for the wall heat transfer coefficient. The heat transfer method is not used as often as the pressure drop or bed voidage methods for minimum fluidizing velocity [80].

2.4.2 Terminal Velocity Correlations

In addition to the minimum fluidizing velocity, the terminal velocity of a particle is also an important velocity of which to be aware. Recall from Table 3 that the terminal velocity is the velocity at which a particle will escape entrainment in the bed. The Navier-Stokes correlation can be used to determine the terminal velocity of a particle. However, the Navier-Stokes correlation does not take into account turbulence. Table 2.9 shows the Stokes Equation for terminal velocity and some variations as well [15].

Table 2.9 Stokes Equations for Terminal Velocity

Equation	Comments
$\frac{g\left(\rho_p - \rho_g\right) d_p^2}{18\mu}$	$Re < 0.4$
$\frac{4}{225}\left[\frac{\left(\rho_p - \rho_g\right)^2 g^2}{\rho_g \mu}\right]^{1/3} d_p$	$0.4 < Re < 500$
$\left[\frac{3.1 g\left(\rho_p - \rho_g\right) d_p}{\rho_g}\right]^{1/2}$	$500 < Re < 200{,}000$

One of the keys to calculating the correct terminal velocity is the understanding the drag force on a particle. Several authors have developed correlations to calculate the drag coefficient on a particle. The correlations involve factors like: sphericity, weight, buoyancy and gravity (Archimedes Number), inertia and viscosity (Reynolds Number), and bed voidage [80].

Kunii and Levenspiel propose Equation 2.28 for determining particle terminal velocity [15]:

$$U_{term} = \left[\frac{4d_p\left(\rho_s - \rho_g\right)g}{3\rho_g C_d}\right]^{\frac{1}{3}} \tag{2.28}$$

The drag coefficient C_d can be calculated by Equation 2.29:

$$C_d = \frac{24}{Re_{term}} + 3.3643Re_{term}^{-0.3471} + \frac{0.4607Re_{term}}{Re_{term} + 2682.5} \tag{2.29}$$

For non-spherical particles Kunii and Levenspiel recommend a dimensionless approach to determining the terminal velocity as shown in Equation 2.30 [15]:

$$U_{term} = U_{term}^{*}\left[\frac{\mu_g\left(\rho_s - \rho_g\right)g}{\rho_g^2}\right]^{\frac{1}{3}} \tag{2.30}$$

where

$$U_{term}^{*} = \left[\frac{18}{\left(d_p^{*}\right)^2} + \frac{2.335 - 1.744\varphi}{\left(d_p^{*}\right)^{0.5}}\right]^{-1} \tag{2.31}$$

The parameter φ is the particle porosity. The parameter d_p^{*} is also a dimensionless quantity that is represented as Equation 2.32:

$$d_p^{*} = Ar^{\frac{1}{3}} \tag{2.32}$$

Above a Reynolds Number of 0.2, turbulence is no longer negligible so another approach is needed in order to account for the additional drag force. A logarithmic scale developed by Heywood includes this additional drag force in the calculation of the particle terminal velocity. The parameters P_H and Q_H for terminal velocity are shown as Equations 2.33 and 2.34:

$$P_H = \left[\frac{4\left(\rho_s - \rho_g\right)\rho_g g}{3\mu^2}\right]^{\frac{1}{3}} \tag{2.33}$$

$$Q_H = \left[\frac{4\left(\rho_s - \rho_g\right)\mu g}{3\rho_g^2}\right]^{\frac{1}{3}} \tag{2.34}$$

The dimensionless Heywood Tables are applicable for all Reynolds Numbers [81].

The same methods used to determine the minimum fluidization velocity are also used to determine the terminal velocity of a particle. At the terminal velocity the pressure drop across the bed will be zero. However, when the particles are polydisperse the pressure drop across the bed will decrease gradually versus a rapid pressure drop seen with monodisperse particles [80]. Using the bed voidage method, the bed voidage is extrapolated to unity. The value of the superficial velocity at which the bed voidage is unity is then taken as the terminal velocity. However, this extrapolation procedure may lead to terminal velocities several orders of magnitude higher then experimental observation [80]. The heat transfer method will show that the heat transfer coefficient will start to decrease when the bed is empty. The heat transfer method for terminal velocity determination is more tedious then the pressure drop method or the bed voidage method due to the need for accurate temperature measurements and the need to be at steady state operation [80].

The ratio of the terminal velocity to minimum fluidizing velocity can give a rough estimate for the height of the bed. Particle size has the biggest impact on this ratio. Smaller

particles mean a larger bed because the ratio is larger. This ratio gives an indication as to the degree of freedom with which the fluidized bed can be operated [15].

2.4.3 Fluidization Regimes

Fluidized beds are classified into six regimes based on a few factors: the gas flow rate, the bed geometry, and the solid-gas properties. The regimes in order of increasing superficial velocity and void fraction are: fixed bed, bubbling, slug flow, turbulent, fast fluidization, and pneumatic conveying [82]. Figure 2.16 illustrates the regimes.

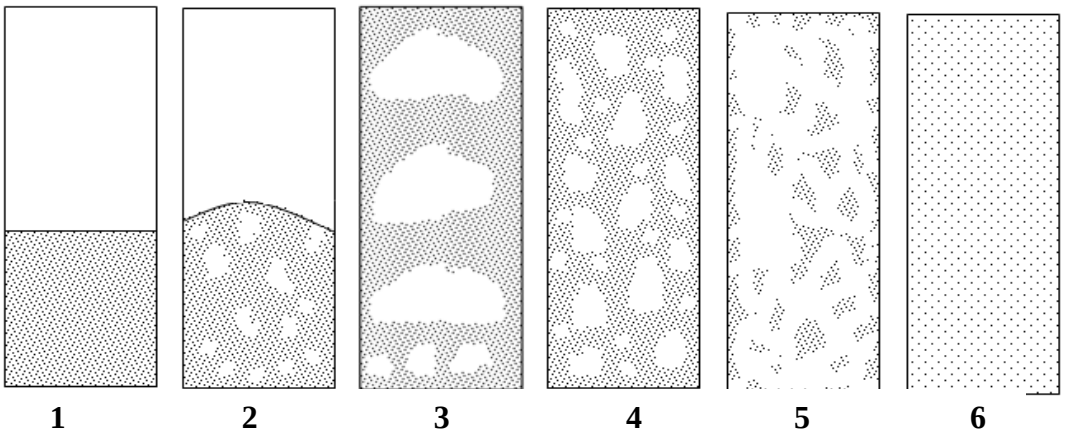

Figure 2.16 Fluidized Bed Regimes: 1). Packed Bed 2). Bubbling 3). Slugging 4). Turbulent 5). Fast 6). Pneumatic Transport

A bubble-less regime between a fixed bed and a bubbling bed is termed homogenous or particulate fluidization. The bubbling regime is also termed heterogeneous or aggregative fluidization [83]. Not all particle systems go through every one of the six regimes of fluidization. The regime path of a particular system is highly dependent on the particle density, size, and size distribution [15]. Figure 2.17 shows the regime classifications for a gas-solid system.

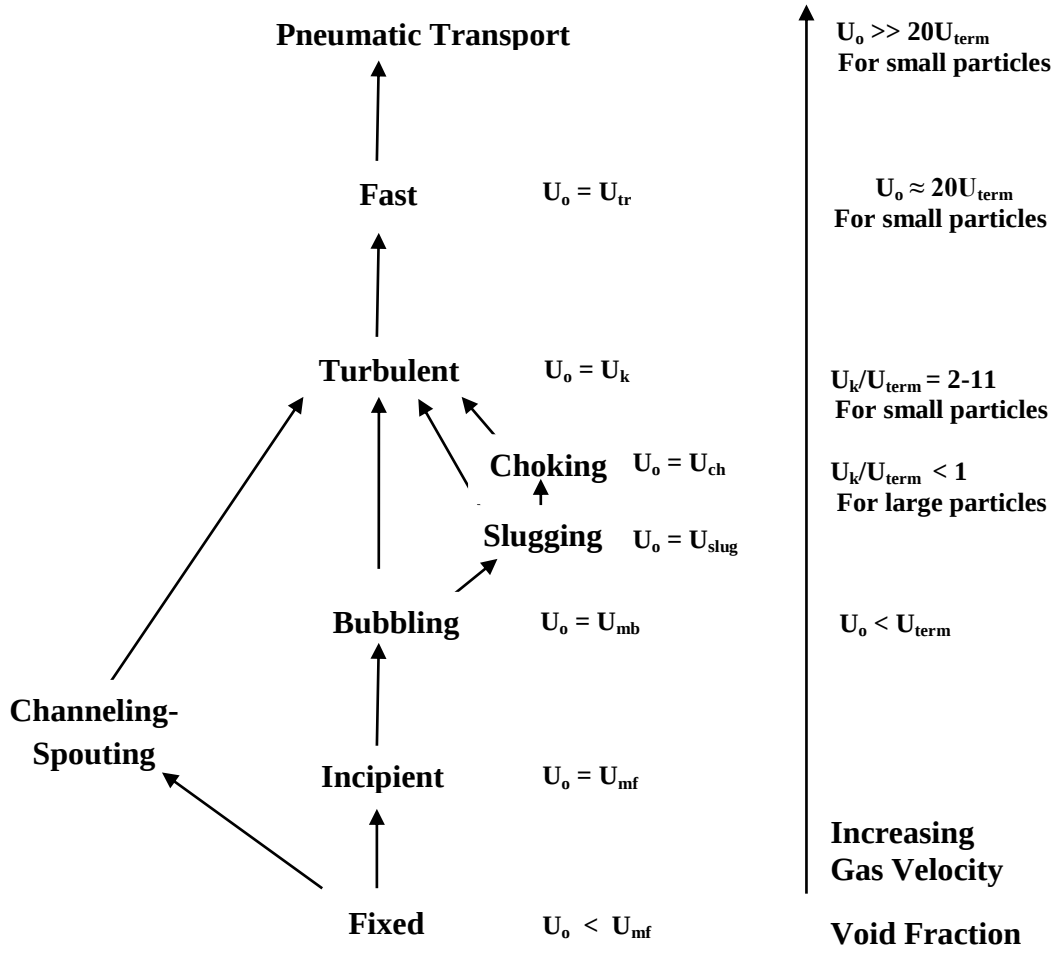

Figure 2.17 Fluidization Regime Pathways

2.4.4 Powder Classification

Materials fluidize differently based on their physical properties as well as the fluidizing gas density. Powders are classified into four groups as shown in Table 2.10 [84].

Table 2.10 Powder Classification

Group	Particle Density (g/cc)	Particle Size (microns)	Description
A	< 1.4	20 – 100	Aeratable
B	1.4 - 4.0	40 – 500	Sand-like
C	Any	< 30	Cohesive
D	Varies	> 600	Spoutable

The powder classification system developed by Geldart is for air at ambient conditions. Figure 2.18 shows the Geldart powder classification with examples [84].

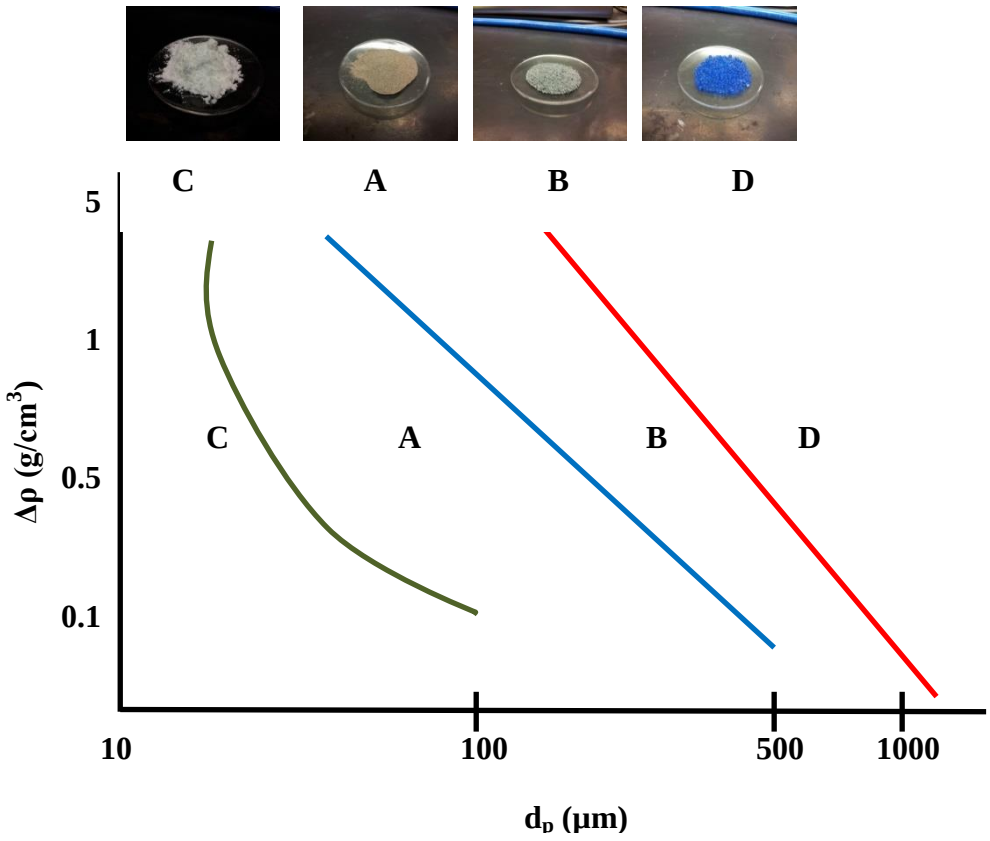

Figure 2.18 Graphical Representation of Geldart Powder Classification

Powders in Group C are the most difficult to fluidize. The difficulty regarding fluidization of Group C powders is due to the presence of stronger inter-particle (van der Waals) forces brought on by the smaller particle size, irregular shaped particles or an electrostatic charge [83]. Group A powders undergo a large bed expansion, again due to high inter-particle forces, before gas bubbling begins whereas, Group B powders experience gas bubbling almost simultaneously with minimum fluidization. Particle mixing is very fast with Group A powders, but a little slower with Group B powders. Group D powders do not mix very well in comparison to Group A or B. Group D powders have a tendency to spout because the combination of large

particle size, high density and horizontal gas bubble coalescence create channels for the fluidizing gas to move through [83].

A great deal of attention has been given to determining where the boundaries between the powder classifications lie. If the ratio of the minimum bubbling velocity to the minimum fluidizing velocity is greater than one, the powder will fall into Group A or C classification. Correlations to differentiate between Group A and C involve ratios between the hydrodynamic and cohesive forces on the particle. Distinguishing between Groups B and D are also important. If the bubble velocity is less than the ratio of the minimum fluidizing velocity to the void fraction at minimum fluidization, the powder belongs to Group D [35]. Other criteria for group identification include: 1). the boundary for Group A or Group B – Group A if the particle diameter times the difference between the particle and gas densities is less than or equal to 225 and 2). the boundary between Group B and Group D – Group D if the square of the particle diameter times the difference between the particle and gas densities is greater than or equal to one million [80].

Correlations for minimum fluidizing velocity based on the Geldart powder classification system have also been looked into by Sangeetha et al. [41]. For Group B powders Sangeetha et al. recommend the equation developed by Babu et al. [42]. Table 16 shows the correlations for the Reynolds Number of Group A and D powders [41].

Table 2.11 Minimum Fluidization Velocity by Powder Classification

Group	**Equation**
A	$\left(60.407^2 + 0.1536\mathrm{Ar}\right)^{0.5} - 60.407$
D	$\left(17.612^2 + 0.02613\mathrm{Ar}\right)^{0.5} - 17.612$

Other researchers have taken the Geldart powder classification and modified it somewhat. Molerus [85] accounted for the interparticle force and the drag force applied to the particle by the

fluidizing gas. Molerus also developed numerical criteria to distinguish between Groups A and B, Groups A and C, and Groups B and D [85]. However, Molerus does not account for a few factors: humidity effects, the electrostatic effect, and gravitational loading effects on particle consolidation prior to operation [80]. Another attempt was made by Clark et al. [86] for powder classification through the development of a dimensionless number called the Powder Number (PN). Table 2.12 shows the ranges and classification of powders based on the Powder Number [86].

Table 2.12 Powder Number Range and Powder Classification

Powder Number	**Powder Classification**
PN < 1.5	C
1.5 < PN < 2.5	A
2.5 < PN < 3.5	B
3.5 < PN < 4.5	D

The equations to calculate the powder number in accordance with the Geldart and Molerus classifications are problematic, particularly for the Geldart classifications due to poor agreement [80].

Saxena and Ganzha [87] classified powders by both hydrodynamic and thermal properties in part by bringing attention to the concept that a large particle by hydrodynamic standards can be small in terms of thermal properties. Saxena and Ganzha classified powders into three groups: I, IIA, IIB, and III. The classification system developed is used in determining settling conditions but it does not have the same association with the Geldart classification [80].

It is worth noting that the Geldart powder classification system has been shown to be unsuitable when fluidizing mediums other than air are used as well as elevated operating pressures and temperatures. The classification system developed by Geldart is based on data at ambient pressures and temperatures [88]. Yang goes on to propose an adaptation to the Geldart

classification by comparing dimensionless density ratio to the Archimedes number. This slight adjustment allows for a graphical comparison of any operating conditions and proper classification between Group A and B powders for scaled up operations. In addition, the adjustment shows that Group D powders can exhibit Group A fluidization behavior at elevated pressure and temperature as reported by others [88].

2.4.5 Bubbling Fluidized Beds

The hydrodynamic properties of bubbles (shape, size, velocity, and occurrence frequency) strongly influence the performance of a fluidized bed operation. Gas bubble presence inside the fluidized bed plays a significant role in several simultaneous processes including: gas-particle contact, particle-particle contact, droplet-particle contact, particle circulation and elutriation, reaction rate conversion, and heat and mass transfer [89]. In part because gas bubble properties have been identified as a key component of the aforementioned processes, accurate correlations for bubble size, shape, velocity, and frequency are crucial to modeling fluidized bed processes.

2.4.5.1 Modeling Approaches to Bubbling Fluidized Beds

There are two approaches to modeling bubble hydrodynamic properties in a fluidized bed, the single bubble approach and the bubbling behavior of the entire bed. The single bubble approach treats each bubble as a single unit and has equations that describe the interactions between single bubble units. The single bubble approach involves correlations to predict bubble diameter and bubble velocity. The entire bubbling bed approach, also called the two-phase model treats the solid and gas phase as an emulsion packet. The two-phase model yields hydrodynamic characteristics like bubble void fraction and the fluidized bed void fraction [15].

2.4.5.2 Bubble Diameter

Among the first postulates of bubbling fluidized beds is that all gas entering the fluidized bed above U_{mf}, (i.e. $U_0 - U_{mf}$), passes in the form of bubbles. Davidson and Harrison [90] proposed the first substantial model to describe bubble movement in a fluidized bed based on work done by Toomey and Johnstone [91] and Davidson [90]. The model accounts for gas movement, solids movement, and pressure distributions around bubbles. The Davidson and Harrison model has three built in assumptions: the bubbles are free of solids and circular, particles move aside as the bubble rises, and Darcy's law is satisfied for any direction [15]. The boundary conditions that apply to the Davidson and Harrison model are: constant pressure inside the gas bubble and an undisturbed pressure gradient exists far from the bubble.

Bubbles formed in a fluidized bed are not spherical in shape and not uniform in size. Bubbles formed actually have a hemispherical shape and form in a distribution of sizes [15, 90, 96]. Even though a distribution of bubble diameters exists, a characteristic bubble diameter is used to describe the hydrodynamic properties of the fluidized bed. Mori & Wen [92] developed a correlation for bubble diameter as a function of height above the distributor plate, Equation 2.35, for Geldart Group B and D particles for a fluidized bed whose height is lower than its diameter [15]:

$$d_{bub} = d_{bub,max} - \left(d_{bub,max} - d_{b0}\right)\exp\left(\frac{-0.3h_{bed}}{d_{bed}}\right) \tag{2.35}$$

Equation 2.35 is valid for fluidized for the following conditions: $d_{bed} \leq 1.3$ m, $0.05 \leq U_{mf} \leq 0.2$ m/s, $60\mu m \leq d_p \leq 450\mu m$, and $U_0\text{-}U_{mf} \leq 0.5$ m/s. The term d_{b0} is the initial bubble size formed at the distributor plate can be calculated using Equation 2.36 [15]:

$$d_{b0} = \frac{2.78}{g^{0.2}}\left(U_0 - U_{mf}\right)^2 \tag{2.36}$$

The term $d_{bub,max}$ is the maximum size bubble that forms after bubble coalescence and can be estimated with Equation 2.37 [15]:

$$d_{bub,max} = 0.65\left[\frac{\pi}{4}d_{bed}^2(U_0 - U_{mf})^2\right]^{0.4} \quad (2.37)$$

A correlation for Geldart Group B particles was developed by Darton et al. [93] which incorporates the distributor plate design is given as Equation 35:

$$d_{bu} = \frac{0.54}{g^{0.2}}(U_0 - U_{mf})^{0.4}\left(h_{bed} + 4\left(\frac{\pi(d_{bed}/2)^2}{N_{or}}\right)^{0.5}\right)^{0.8} \quad (2.38)$$

The N_{or} term represents the number of orifices in the distributor plate. In addition, for porous plate distributor plates, the term $4\left(\frac{\pi(d_{bed}/2)^2}{N_{or}}\right)^{0.5} \approx 0.03$. Karimipour and Pugsley [89] have compiled twenty five different correlations for bubble size in a short review.

2.4.5.3 Bubble Rise Velocity

With correlations to determine bubble size anywhere inside the fluidized bed, the next step is to determine how quickly bubbles travel through a fluidized bed. The correlation for bubble rise velocity developed by Clift and Grace (1985) is given as Equation 2.39:

$$U_{bub} = 0.711(gd_{bub})^{0.5} \quad (2.39)$$

Equation 36 is valid when the bubble diameter is less than 12.5% of the bed diameter. The bubble rise velocity is impeded by wall effects when the bubble diameter is greater than 12.5%. Wallis [94] developed a bubble rise velocity correlation that incorporated wall effects which is given as Equation 2.40 [15]:

$$U_{bub} = (0.711(gd_{bub})^{0.5})(1.2)\exp\left(-\frac{d_{bub}}{d_{bed}}\right) \quad (2.40)$$

When the ratio of bubble diameter to the bed diameter is greater than 0.6, the bed is not classified as bubbling, rather now it is termed a slugging bed [15].

The drag force exerted on a bubble by the bed decreases when several bubbles are present. Equation 2.41 is then modified to reflect the reduction in drag force:

$$U_{bub} = (U_0 - U_{mf}) + 0.711(gd_{bub})^{0.5} \quad (2.41)$$

However, Equation 2.41 is not valid for all particle sizes in the Geldart powder classification. A modified form of Equation 2.41 has been suggested by Kunii & Levenspiel [15] for Geldart Group B particles and is shown as Equation 2.42:

$$U_{bub} = 1.6\left((U_0 - U_{mf}) + 1.13d_{bub}^{0.5}\right)\left(d_{bed}^{1.35}\right) + 0.711(gd_{bub})^{0.5} \quad (2.42)$$

Equation 2.42 is valid for fluidized beds with a diameter smaller than one meter. Karimipour and Pugsley [89] have compiled seven different correlations for bubble rise velocity in a short review.

While the Davidson and Harrison model assumes bubbles to be spherical, bubbles formed in a fluidized bed are not spherical in shape and not uniform in size. Bubbles formed actually have a hemispherical shape and form in a distribution of sizes. In addition, bubbles coalesce when they are small in diameter and split if they are large in diameter. Several approaches have been taken to describe bubble coalescence and bubble splitting at an accurate level mathematically. Bubble coalescence occurs for a couple reasons: larger bubbles moving past smaller ones and absorbing them and bubble acceleration caused by the wake of a higher positioned bubble [15]. Bubble splitting occurs when a downward cusp forms at the top of the bubble, causing the vertical separation of the initial bubble. Figure 2.19 shows the typical hemispherical shape bubbles take in a fluidized bed.

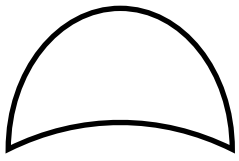

Figure 2.19 Hemispherical Bubble Shape Inside a Fluidized Bed

2.4.5.4 Void Fraction and Expansion

The two-phase approach to modeling bubble phenomena inside a fluidized bed yields information just as valuable as the single bubble approach previously described. The two-phase model treats the bubble and solid phases as an emulsion. The shape of the bubble and the speed at which it moves through the fluidized bed creates a wake in which a slight vacuum draws up to a certain extent the solid phase within the bed. The wake angle, associated with the bubble wake decreases with smaller particles. Figure 2.20 shows the characteristics of a bubble.

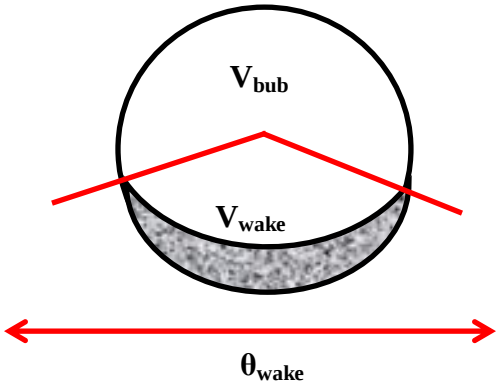

Figure 2.20 Bubble Characteristics

Figure 2.21 shows the bubble wake along with the solid entrainment relative to the fluidized bed.

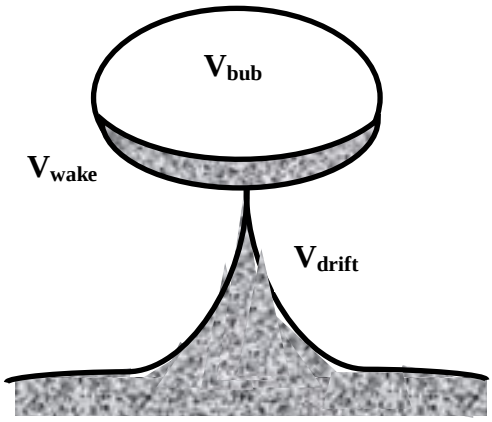

Figure 2.21 Bubble Wake and Solid Entrainment

The bubble wake volume is about 25% of the bubble volume, but varies depending on the Geldart grouping. The drift volume is about 35% of the bubble volume. However, the bubble wake volume may range from 25% to 45% of the bubble volume depending on the Geldart powder classification. Likewise the drift volume may range from 25% to 100% of the bubble volume depending on the Geldart powder classification [95, 96]. These phenomena combined promote excellent solids mixing, the degree to which can be calculated [15].

The two-phase defines a parameter ε, the void fraction, as the volume of fluidized bed occupied by fluidizing gas over the total volume of the fluidized bed. Consequently, there is a void fraction associated with the minimum fluidizing velocity, in addition to the void fraction at the operating conditions. The void fraction at operating conditions is related to the void fraction at minimum fluidization. Broadhurst and Becker [46] developed a correlation for the void fraction at the minimum fluidization velocity that is shown as Equation 2.43:

$$\varepsilon_{mf} = 0.586\varphi^{-0.72}\left(\frac{1}{Ar}\right)^{0.029}\left(\frac{\rho_g}{\rho_s}\right)^{0.021} \tag{2.43}$$

Equation 2.43 is valid for the following conditions:

$$\text{for } \begin{cases} 0.85 < \varphi < 1 \\ Ar < 10^5 \\ 500 < \dfrac{\rho_g}{\rho_s} < 50000 \end{cases}$$

Toomey and Johnstone [91] defined the bubble voidage, ε_{bu}, as a ratio of the excess velocity to the bubble rise velocity. The bubble voidage is shown as Equation 2.44:

$$\varepsilon_{bu} = \begin{cases} \dfrac{\dot{V}_{bu}}{A_{bed}U_{bu}} = \dfrac{U_0 - U_{mf}}{U_{bu}} \cong \dfrac{U_0 - U_{mf}}{U_0 - U_{mf} + 0.711(gd_{bub})^{0.5}} & \text{for } U_{bu} \cong \dfrac{U_{mf}}{\varepsilon_{mf}} \\ \dfrac{\dot{V}_{bu}}{A_{bed}U_{bu}} = \dfrac{U_0 - U_{mf}}{U_{bu} + U_{mf}} \cong \dfrac{U_0 - U_{mf}}{U_0 + 0.711(gd_{bub})^{0.5}} & \text{for } U_{bu} \cong 5\dfrac{U_{mf}}{\varepsilon_{mf}} \end{cases} \tag{2.44}$$

Once the void fraction at minimum fluidization and the void fraction of the bubble have been determined, the void fraction of the bed can be calculated. The void fraction of the bed is given by Equation 2.45 [91]:

$$\varepsilon_{bed} = \varepsilon_{bu} + (1 - \varepsilon_{bu})\varepsilon_{mf} \tag{2.45}$$

Another hydrodynamic property of the bed that has ramifications on fluidized bed performance is the expansion of the fluidized bed. The height of the fluidized bed at operating conditions, h_{bed} is related to the fluidized bed void fraction and the height of the bed at minimum fluidization, h_{mf}. The fluidized bed expands in part because space occupied by the bulk volume of the solid phase is now displaced by moving bubbles. For a constant cross-sectional area the height at minimum fluidization can be determined from Equation 2.46 [97]:

$$h_{mf} = \frac{\Delta p}{(1-\varepsilon_{mf})\left(\rho_s - \rho_g\right) g} \tag{2.46}$$

The height of the expanded bed can be determined with Equation 43 as well, by replacing ε_{mf} with ε_{bed}. However, the cross-sectional area for a tapered bed increases with height. The increase in cross-sectional area with increasing bed height makes the calculation for h_{mf} and h_{bed} an iterative procedure. Couderc [40] has listed several correlations developed for fluidized bed expansion of spherical and non-spherical particles.

Fluidized bed expansion in tapered bed geometries has been studied in literature. Sau et al. [98] have developed correlations for fluidized bed expansion of spherical and non-spherical particles. For spherical particles in tapered bed geometries, Sau et al. report the fluidized bed expansion ratio, R, a ratio of expanded bed volume to static bed volume, as Equation 2.47 [98]:

$$R = 2.811 \left(\frac{D_0}{D_1}\right)^{0.05} \left(\frac{h_{stat}}{D_0}\right)^{-0.027} \left(\frac{d_p}{D_0}\right)^{-0.463} \left(\frac{\rho_s}{\rho_g}\right)^{-0.236} \left(\frac{U_0 - U_{mf}}{U_{mf}}\right)^{0.157} \tag{2.47}$$

The fluidized bed expansion ratio for non-spherical particles is given as Equation 2.48:

$$R = 10.967\left(\frac{D_0}{D_1}\right)^{0.119}\left(\frac{h_{stat}}{D_0}\right)^{-0.233}\left(\frac{d_p}{D_0}\right)^{-0.091}\left(\frac{\rho_s}{\rho_g}\right)^{-0.225}\left(\frac{U_0 - U_{mf}}{U_{mf}}\right)^{0.261} \quad (2.48)$$

where h_{stat} is the static bed height in Equations 2.47 and 2.48.

2.4.5.5 Particle Circulation Time

Particle circulation in a fluidized bed is achieved with the introduction of gas bubbles into the fluidized bed in the top spray orientation. As shown previously in Figure 2.21, a small amount of solids (~1% of the bubble volume) is transported vertically in the bubble and the subsequent bubble wake. The consistent bubble forming pattern evolved by fluidization allows for excellent solids mixing characteristics [15].

Rowe [96] investigated particle circulation time and developed a widely used correlation for particle circulation time. The equation Rowe developed for particle circulation time is shown as Equation 2.49:

$$\tau_c = \frac{h_{mf}}{0.6(U_0 - U_{mf})\left(1 - \frac{U_0 - U_{mf}}{U_{bu}}\right)} \quad (2.49)$$

The average circulation time, τ_c, represents the total time for upward and downward motion.

Determination of the particle circulation time in the Wurster orientation is different compared the top spray orientation. Recall the distributor plate design for the Wurster orientation is such that the superficial velocity within the draft tube is much higher than outside the draft tube. The fluidizing gas is introduced as a long jet through a few large openings compared to the numerous small diameter orifices of a porous plate. Bubble formation is eliminated for the Wurster orientation. Cronin et al. [99] developed a mathematical model describing particle circulation time as the sum of three segmented times. Figure 2.22 shows how the particle circulation time is segmented according to the approach by Cronin et al. [99].

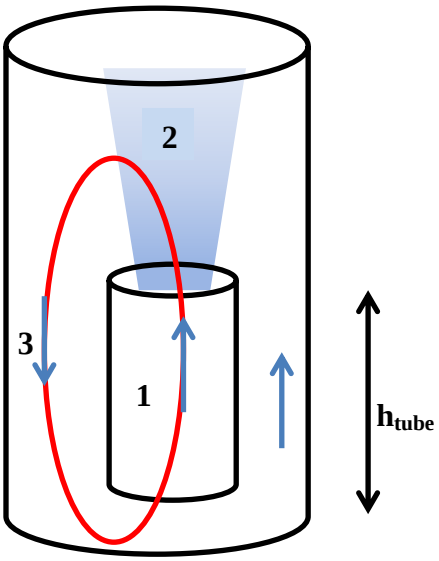

Figure 2.22 Segments for Particle Circulation Time Calculation for Wurster Orientation

The first segment the circulation time calculation is the time spent inside the draft tube. The majority of the time spent inside the draft tube goes toward the acceleration of the particle to just below the operating superficial gas velocity. The time spent inside the draft tube is given by Equation 2.50 [99]:

$$y = U_{g1}t + \frac{U_{term1}^2}{g}\left\{-\ln\left[\sinh\left\{\frac{gt}{U_{term,1}} + \coth^{-1}\left(\frac{U_{g,1}}{U_{term,1}}\right)\right\}\right]\right\} + \ln\left[\sinh\left\{\coth^{-1}\left(\frac{U_{g,1}}{U_{term,1}}\right)\right\}\right] \quad (2.50)$$

where y is the height of the draft tube, $U_{g,1}$ is the velocity of the fluidizing gas in the draft tube and $U_{term,1}$ is the particle terminal velocity within the draft tube. The particle velocity approaches the gas velocity asymptotically. The particle velocity within the draft tube as a function of time is given as Equation 2.51 [99]:

$$U_{part,1} = -U_{term,1}\coth\left(\frac{gt}{U_{term,1}} + \coth^{-1}\left(\frac{U_{g,1}}{U_{term,1}}\right)\right) + U_{g,1} \quad (2.51)$$

The second segment of the circulation time calculation is the time required to reach a zero superficial velocity once the particle has exited the draft tube. There is a switchover time defined by Cronin et al. [99] which is the time it takes for the particle drag force to reverse direction. The switchover time is given as Equation 2.52 [99]:

$$t_{switch} = \frac{U_{term,2}}{g} \tan^{-1}\left(\frac{U_{g,2} - U_{part,1}(t)}{U_{term,2}}\right) \tag{2.52}$$

where $U_{term,2}$ represents the particle terminal velocity in the second section of the bed, $U_{g,2}$ represents the gas superficial velocity in the second section of the bed, and $U_{part,1}(t)$ is the particle velocity at the time it exits the draft tube. For times below the switchover time, the particle displacement is given as Equation 2.53 [99]:

$$y = U_{g,2}t + \frac{U_{term,2}^2}{g}\left\{\ln\left[\cos\left\{\frac{gt}{U_{term,2}} + \tan^{-1}\left(\frac{U_{g,2} - U_{part,1}(t)}{U_{term,2}}\right)\right\}\right]\right\} + 0.5\ln\left\{1 + \frac{U_{g,2} - U_{part,1}(t)}{U_{term,2}}\right\} \tag{2.53}$$

The particle velocity in second section of the bed is given by Equation 2.54 [99]:

$$U_{part,2} = -U_{g,2} \tan\left[\frac{gt}{U_{term,2}} + \tan^{-1}\left(\frac{U_{g,2} - U_{part,1}(t)}{U_{term,2}}\right)\right] + U_{g,2} \tag{2.54}$$

After the switchover time, the particle displacement can be calculated with Equation 2.55 [99]:

$$y = U_{g,2}\left[t + \frac{U_{term,2}^2}{g}\tan^{-1}\left(\frac{U_{g,2} - U_{part,1}(t)}{U_{term,2}}\right)\right] - \frac{U_{term,2}^2}{g}\left\{\ln\left[\cosh\left\{\frac{gt}{U_{term,2}} + \frac{U_{term,2}}{g}\tan^{-1}\left(\frac{U_{g,2} - U_{part,1}(t)}{U_{term,2}}\right)\right\}\right]\right\} + \frac{U_{term,2}^2}{g}\left\{-\frac{U_{g,2}}{U_{term,2}}\tanh^{-1}\left(\frac{U_{g,2} - U_{part,1}(t)}{U_{term,2}}\right) + 0.5\ln\left(1 + \left(\frac{U_{g,2} - U_{part,1}(t)}{U_{term,2}}\right)^2\right)\right\} \tag{2.55}$$

The particle velocity after the switchover time is given by Equation 2.56 [99]:

$$U_{part,2} = -U_{term,2} \tanh\left[\frac{gt}{U_{term,2}} + \tan^{-1}\left(\frac{U_{g,2} - U_{part,1}(t)}{U_{term,2}}\right)\right] + U_{g,2} \quad (2.56)$$

The time for the particle to reach a zero velocity can be found using Equation 2.56. The particle displacement calculated from Equation 2.55 is denoted as h_{max}, the maximum height the particle achieves.

The third segment of the circulation time calculation is the time required to return to the initial position at the bottom of the draft tube from height h_{max}. Equation 2.57 shows the relationship for particle displacement in third segment of the bed [99]:

$$y = U_{g3}t + \frac{U_{term3}^2}{g}\left\{-\ln\left[\cosh\left\{\frac{gt}{U_{term,3}} + \tanh^{-1}\left(\frac{U_{g,3}}{U_{term,3}}\right)\right\}\right]\right\} + \ln\left[\cosh\left\{\tanh^{-1}\left(\frac{U_{g,3}}{U_{term,3}}\right)\right\}\right] \quad (2.57)$$

where y is the maximum height achieved by the particle, $U_{g,3}$ is the fluidizing gas velocity in third section of the fluidized bed, and $U_{term,3}$ is the terminal velocity in the third section of the fluidized bed.

The particle velocity in the third section of the fluidized bed is given by Equation 2.58 [99]:

$$U_{part,3} = -U_{term,3} \tanh\left(\frac{gt}{U_{term,3}} + \tanh^{-1}\left(\frac{U_{g,3}}{U_{term,3}}\right)\right) + U_{g,3} \quad (2.58)$$

Summing up the times for all three segments calculated from Equations 2.50, 2.56, and 2.58 yields the particle circulation time in the Wurster orientation.

2.5 Heat Transfer in Fluidized Beds

Heat transfer is a driving force for many types of operations involving fluidized beds. Fluidized beds are known to exhibit excellent heat transfer rates in part because of the gas-particle contact brought about by the presence of bubbles or fast flowing gas and the large

particle surface available for heat transfer [15]. Heat transfer occurs by three mechanisms which can all be applied to fluidized bed operations: conduction, convection, and radiation [15]. This discussion should be regarded as a general treatise on heat transfer. The actual equations used in modeling the fluidized bed will be presented in a later chapter.

2.5.1 Conduction

Conduction is a process through which energy is transferred via a temperature gradient within a body or between two or more bodies. Heat conduction in gases and liquids is the result of collisions and diffusion on the molecular level. In solids, heat conduction is the result of lattice vibrations and free electron transport [22].

Fourier's law can be used to express the rate of heat transfer by conduction as shown in Equation 2.59:

$$Q_{cond} = -\lambda A \frac{dT}{dx} \tag{2.59}$$

where λ is the material thermal conductivity, A is the area where heat is conducted, dT is the change in temperature and dx is the thickness of the material. The negative sign notation is used because heat flows from hot to cold bodies. Fourier's law of heat transfer can be applied to objects with rectangular, spherical, or cylindrical coordinates [100].

2.5.2 Convection

Convection is the main mechanism of heat transfer in a fluidized bed operation. Convection is a process whereby energy is transferred between a solid surface and a mobile fluid. The mobile fluid can be a gas, liquid, or supercritical fluid [22]. The thermophysical properties of the fluid and the fluid flow parameters determine the rate of heat transfer via convection in a fluidized bed operation [26].

A thermal boundary layer forms when a fluid at a specific temperature flows over a surface that is at a different temperature. The thickness of the boundary layer, δ_t, is the distance at which the temperature difference between the surface and mobile fluid is equal to about 1% of the maximum temperature difference between the mobile fluid and the solid surface. Figure 2.23 shows the thermal boundary layer that forms normal to the surface [22].

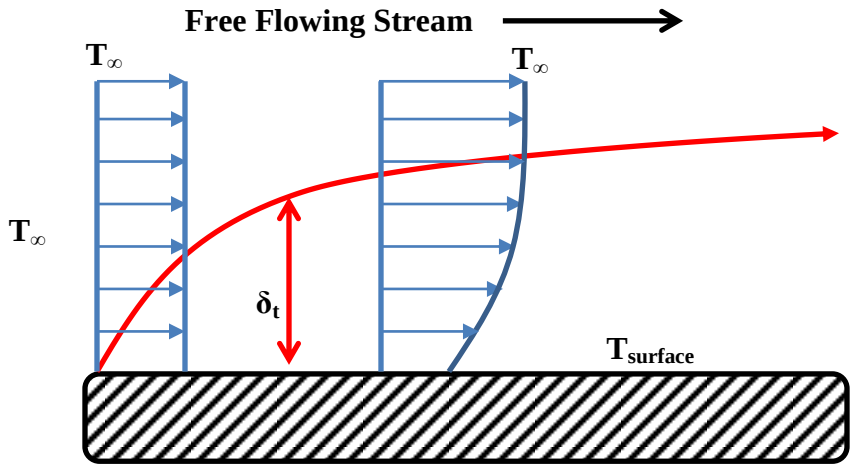

Figure 2.23 Thermal Boundary Layer Normal to Solid Surface

In convective heat transfer, a thermal boundary layer and a velocity boundary layer form at the same time on the surface. The velocity boundary layer has a significant impact on the thermal boundary layer development. Figure 2.24 shows the simultaneous velocity and thermal boundary layer that form normal to the solid surface [22].

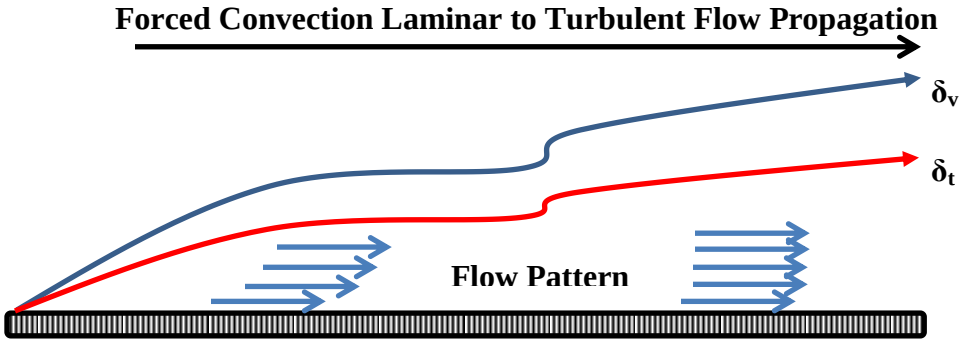

Figure 2.24 Simultaneous Velocity and Thermal Boundary Layer on a Solid Surface

In 1904, Ludwig Prandtl presented the concept of thermal boundary layer to the scientific community. The Prandtl number, shown as Equation 2.60 is a dimensionless quantity that compares the thickness of the thermal boundary layer relative to the velocity boundary layer [22]:

$$Pr = \frac{C_p \mu}{k} \tag{2.60}$$

The Prandtl number for liquids ranges from 0.01 to 100000, whereas for gases, the Prandtl number is close to 1. Conceptually, this means that heat and momentum diffuse through a gas at nearly the same rate [22].

2.5.2.1 Forced Convection

Convective heat transfer occurs inside the fluidized bed from the gas to the particles and from the gas to the walls. The heat loss by convective heat transfer can be written as Equation 2.61 [100]:

$$Q_{conv} = h_{conv} A (T_{bulk} - T_{surf}) \tag{2.61}$$

where h_{conv} is the convective heat transfer coefficient, A is the surface area, T_{bulk} is the temperature of the flowing fluid and T_{surf} represents the surface temperature of interest. The convective heat transfer coefficient is determined by the thermophysical and flow properties of the fluid. The convective heat transfer coefficient, shown as Equation 2.62, is calculated as a dimensionless quantity called the Nusselt Number, after Wilhelm Nusselt [22]:

$$Nu = \frac{h_{conv} d}{k} \tag{2.62}$$

The Nusselt number for forced convection is a function of the interaction between fluid flow and momentum and heat diffusivity. The general form for the forced convection Nusselt number is given as Equation 2.63:

$$Nu = f(Re,Pr) \tag{2.63}$$

Table 2.13 shows particle Nusselt number correlations developed from investigations into fluidized bed heat transfer from the fluidizing gas to the particles.

Table 2.13 Particle Nusselt Number Correlations

Reference	Nusselt Number Correlation	Comments
[101]	$2 + \left(\frac{1}{4}Re + 3e^{-4}Re^{1.6}\right)$	$100 < Re < 200{,}000$
[102]	$2 + 0.6\varepsilon_f^{-1.23}Re^{0.5}Pr^{0.333}$	Incorporates voidage into Ranz Marshall correlation
[103]	$\left(7 - 10\varepsilon_f + 5\varepsilon_f^2\right)\left(1 + 0.7Re^{0.2}Pr^{0.333}\right) + \left(1.33 - 2.4\varepsilon_f + 1.2\varepsilon_f^2\right)Re^{0.7}Pr^{0.333}$	
[104]	$2 + 0.6\varepsilon_f^{3.5}Re^{0.5}Pr^{0.3333}$ $2 + \varepsilon_f^{3.5}\left(0.5Re^{0.5} + 0.02Re^{0.8}\right)Pr^{0.3333}$ $2 + 0.000045\varepsilon_f^{3.5}Re^{1.8}$	$Re < 200$ $200 < Re < 1500$ $Re > 1500$
[105	$0.02469Ar^{0.43}Pr^{0.33}$	$10e5 < Ar < 10e8$
[106]	$2 + 0.6Re^{0.5}Pr^{0.333}$	$10 < Re < 10000$ $Pr > 0.7$
[107]	$2 + \left(0.43Re^{0.5} + 0.06Re^{0.67}\right)Pr^{0.4}$	$3.5 < Re < 76000$ $0.7 < Pr < 380$

Particles in a fluidized bed absorb heat from the fluidizing gas via convection. The heat absorbed on the particle surface is then transferred through the particle to its center by conduction. The convective heat transfer rate and the conductive heat transfer rate are not equal to each other. In order to determine which mechanism of heat transfer is the dominate process, the Biot number is used. The Biot number, shown as Equation 2.64, is the ratio of convection heat transfer to conduction heat transfer [22]:

$$Bi = \frac{h_{conv}d_p}{\lambda_p} \tag{2.64}$$

where λ_p is the particle thermal conductivity. When Bi < 0.1, heat transfer resistance within the particle is considered negligible compared to convective heat transfer resistance at the surface [22].

In addition to the forced convection heat transfer to the particles there is also forced convection heat transfer to the walls of the fluidized bed. For forced convection with laminar flow (Re < 2100) the Nusselt number is given by Equation 2.65 [100]:

$$Nu = 1.86Gz^{0.333}\left(\frac{\mu_{bulk}}{\mu_{wall}}\right)^{0.14} \tag{2.65}$$

where Gz is the Graetz number. The Graetz number, a dimensionless number that is used to describe heat transfer in laminar flow is given as Equation 2.66 [100]:

$$Gz = \left(\frac{D}{H}\right)(RePr) \tag{2.66}$$

The product of the Reynolds number and the Prandtl number is called the Peclet number, Pe [100]. The Nusselt number for transitional flow (2100 < Re < 10,000) in a circular pipe is given by Equation 2.67 [100]:

$$Nu = 0.116\left[Re^{0.667} - 125\right]Pr^{0.333}\left[1 + \left(\frac{d}{L}\right)^{0.667}\right]\left(\frac{\mu_{bulk}}{\mu_{wall}}\right)^{0.14} \tag{2.67}$$

The Nusselt number for turbulent flow (Re > 10,000) in a circular pipe is given by Equation 2.68 [22]:

$$Nu = 0.023Re^{0.8}Pr^{0.667}\left(\frac{\mu_{bulk}}{\mu_{wall}}\right)^{0.14} \tag{2.68}$$

The viscosity term in Equations 2.65, 2.67, and 2.68 for air is ~ 1 [100].

2.5.2.2 Natural (Free) Convection

In addition to forced convective heat transfer from the fluidizing gas to the particles and the fluidized bed walls, there is another form of convection that occurs. Natural convection (also

called free convection) occurs from the outer fluidized bed walls to the ambient environment. The driving force for natural convection is a density gradient that is the result of heat conduction from the surface of a solid to the surrounding gas environment. The heat energy absorbed by the surrounding gas environment lowers the gas density. A natural convection current is created when the lower density warm gas rises creating a small void for cooler air to fill [22].

The Nusselt number for natural convection is determined by the following dimensionless number relationship, Equation 2.69 [100]:

$$Nu = a(GrPr)^b \tag{2.69}$$

where a and b are constants determined by the geometry and type of flow. The term Gr is the dimensionless number called the Grashof number. The Grashof number, a ratio of buoyancy forces to viscous forces is shown as Equation 2.70:

$$Gr = \frac{g\beta\rho_{film}^2(T_{wall}-T_e)}{\mu_{film}^2} \tag{2.70}$$

The term β is volume expansion coefficient, which for an ideal gas is 1/T. The Grashof number and the Prandtl number are evaluated at the film temperature which is an average of the ambient environment temperature, T_e, and the temperature of the surface being heated or cooled, T_s [100]. The values of a and b in Table 2.19 are given as a function of the product of the Grashof number and the Prandtl number [100].

Table 2.14 Parameters for Free Convection Nusselt Number

GrPr	**a**	**b**
GrPr < 10,000	1.36	0.20
10,000 < GrPr < 10^9	0.59	0.25
GrPr > 10^9	0.13	0.33

The product of the Grashof number and the Prandtl number is also called the Rayleigh number [100].

2.5.3 Radiation

Radiation is the third mechanism of heat transfer. Radiation heat transfer occurs when energy in the form of electromagnetic waves are emitted by one surface and adsorbed by another. No medium is required for heat transfer for radiation to occur as compared with conduction and convection. Radiation heat transfer occurs at the speed of light because light is an electromagnetic wave [22].

The Stefan-Boltzmann law, Equation 2.71, can be used to determine the amount of internal energy emitted by a surface via radiation:

$$Q_{rad} = \sigma A \epsilon T^4 \tag{2.71}$$

where σ is the Stefan-Boltzmann constant, $5.669e^{-8}$ $Wm^{-2}K^{-4}$, A is the surface area of the emissive surface, and ϵ is the emissivity of the body. For a perfect black body, the emissivity is equal to one, otherwise the emissivity is between 0 and 1. When radiation is emitted to the environment, the Stefan-Boltzmann law is modified to Equation 2.72 [22].

$$Q_{rad} = \sigma A \epsilon (T_{wall} - T_e)^4 \tag{2.72}$$

Radiation is not a significant source of heat transfer in fluidized bed operations until operating temperatures are above 400^oC [15].

2.6 Mass Transfer in Fluidized Beds

Mass transfer in fluidized beds has been a topic that has garnered as much research interest as heat transfer. Modeling efforts have shown little to no significant difference between the forces of heat and mass flow [33]. Dimensionless numbers developed to describe mass transfer characteristics closely resemble those developed for heat transfer. The mass transfer equivalent to the Prandtl number is the Schmidt number, Sc. The Schmidt number, a ratio of viscous diffusion to molecular diffusion, is shown as Equation 2.73 [108]:

$$Sc = \frac{\mu}{\rho_g D_{ab}} \tag{2.73}$$

where D_{ab} is the diffusion coefficient. The mass transfer equivalent to the Nusselt number is the Sherwood number, Sh. The Sherwood number, shown as Equation 2.74, is a function of the interaction between fluid flow and momentum and mass diffusivity [108]:

$$Sh = \frac{k_m d}{D_{ab}} \tag{2.74}$$

where k_m is the mass transfer coefficient. The general form for the forced convection Sherwood number is given as Equation 2.75:

$$Sh = f(Re,Sc) \tag{2.75}$$

Mass transfer coefficients are also important in determining the drying time necessary for a coating operation. The mass transfer coefficient plays a direct role in constant rate and falling rate periods of the drying time. Table 2.15 shows Sherwood number correlations developed as a result of mass transfer studies in fluidized beds.

Table 2.15 Sherwood Number Correlations

Reference	Sherwood Number Correlation	Comments
[109]	$2\varepsilon_g + 0.89Re^{0.5}Sc^{0.33}$	$54e^{-6} < d < 640e^{-6}$
[110]	$2 + 0.55Re^{0.5}Sc^{0.33}$	$0 < Re < 1200$
[111]	$\left(7 - 10\varepsilon_f + 5\varepsilon_f^2\right)\left(1 + 0.7Re^{0.2}Sc^{0.333}\right) + \left(1.33 - 2.4\varepsilon_f + 1.2\varepsilon_f^2\right)Re^{0.7}Sc^{0.333}$	
[112]	$2\varepsilon_g + 0.61Re^{0.46}Sc^{0.33}$	$0.6 < Re < 500$
[113]	$\left(0.04Re_{mf} + 2.12Re_{mf}^{0.41} + 0.62/Re_{mf}^{0.51}\right)Sc^{0.33}$	
[114]	$0.455\varepsilon_g Re^{0.593}Sc^{0.33}$	$500 < Re < 10000$
[115]	$1.06 + 0.796Re^{0.6}Sc^{0.33}$	$0.01 < Re < 10000$
[116]	$2 + 0.69Re^{0.5}Sc^{0.33}$	$30 < Re < 2000$
[117]	$(0.105 + 1.505(d_a/d_i)^{-1.505})(d_a/d_i)\frac{(1 - \varepsilon_{mf})}{\varepsilon_{mf}}Re_{mf}^{1-m}Sc^{0.33}$	$m = 0.35 + 0.29(d_a/d_i)^{-0.5}$
[118]	$8.314e^{-5}\left(\frac{U\rho_s}{G_s}\right)1.43$	$G_s = 15 - 60\ \frac{kg}{m^2 s}$ $U = 4 - 6\ \frac{m}{s}$

Table 2.15 Continued

[107]	$2 + \left(0.43\mathrm{Re}^{0.5} + 0.06\mathrm{Re}^{0.67}\right)\mathrm{Pr}^{0.4}$	

2.7 Forces Involved in Fluidized Bed Coating

A fluidized bed coating process involves a complex and variable balance of several forces because several phenomena occur simultaneously. An efficient way to classify the forces involved with fluidized bed operations and subsequently obtain a fundamental understanding of dominant mechanisms is by making use of dimensionless numbers. Some of the forces involved in fluidized bed coating operations are listed in Table 2.16.

Table 2.16 Some Forces Involved In Fluidized Bed Operations

Adhesion	Drag	Sintering
Bonding	Elasticity/Inelasticity	Surface Tension
Buoyancy	Electrostatic	Van der Waals
Capillary	Gravity	Viscous
Chemical Bonding	Inertia	
Cohesion	Magnetic	

Dimensionless numbers are quantities used in various engineering fields to evaluate physical phenomena occurring during a process. The use of dimensionless numbers can allow for scale up from pilot plants to industrial operations with reasonable success. Dimensionless numbers that apply to fluidized beds fall into five categories: fluid flow, heat transfer, mass transfer, electromagnetic field, and reactions. The dimensionless numbers in each of the categories are not necessarily mutually exclusive; some dimensionless numbers can be tabulated based on knowledge of relationships with others.

Fluid flow dimensionless numbers give an idea of the dominant forces in a process. Fluid flow is dependent on properties such as: density, gravity, surface tension, viscosity. All of the

aforementioned properties excluding gravity are functions to an extent of pressure and temperature. Table 2.17 shows fluid flow dimensionless numbers that can be applied to fluidized bed processes [38, 39].

Table 2.17 Fluid Flow Dimensionless Numbers

Dimensionless Number	Ratio	Equation
Archimedes	Gravitational Force to Viscous Force	$\frac{gD^3\rho_g\left(\rho_p-\rho_f\right)}{\mu^2}$
Blake	Inertial Forces to Viscous Forces	$\frac{\rho UD}{\mu(1-e)}$
Bond	Gravitational Forces to Surface Tension	$\frac{\rho gD^2}{\gamma}$
Bubble Reynolds	Inertial Forces to Viscous Forces for a Bubble	$\left(\frac{d_b}{\mu}\right)\left(\frac{\pi}{6}d_b^3\rho_v fn\right)$
Capillary	Viscous Forces to Surface Tension	$\frac{\mu U_f}{\gamma}$
Deryagin	Film Thickness to Capillary Length	$d\left(\frac{\rho_f g}{\sigma}\right)^{0.5}$
Eotvos	Buoyancy Force to Surface Tension	$\frac{\Delta\rho gD^2}{\gamma}$
Fedorov	Gravitational Forces to Viscous Forces De equivalent diameter	$d_e\left(\frac{4g\rho_f^2}{3\mu_f^2\left(\frac{\rho_s}{\rho_f}-1\right)}\right)^{\left(\frac{1}{3}\right)}$
Froude	Inertial Forces to Gravitational Forces	$\frac{U}{\sqrt{gh}}$
Galileo	Gravitational Forces to Viscous Forces	$\frac{D^3\rho_f^2 g}{\mu^2}$
Laplace	Surface Tension to Momentum Transport	$\frac{\gamma\rho D}{\mu^2}$
Lyashchenko	Inertial Forces to Gravitational Forces	$\frac{Re^3}{Ar}$
Mass Ratio	Density Difference of Solid and Gas to the Density of Gas	$\frac{\rho_s-\rho_g}{\rho_g}$
Morton	Bubble Shape in a Fluid	$\frac{g\mu_l^4\Delta\rho}{\rho_l^2\gamma^3}$
No Name	Viscous Force to Capillary Force k: permeability	$\frac{U\mu D}{k^{0.5}\sigma\cos\theta}$

Table 2.17 Continued

No Name	Viscous Force to Surface Tension	$\frac{\mu U}{\sigma}$
Ohnesorge	Viscous Force to Surface Tension Force	$\frac{\mu}{\sqrt{\rho\gamma D}}$
Reynolds	Inertial Forces to Viscous Forces	$\frac{\rho U D}{\mu}$
Richardson	Potential Energy to Kinetic Energy	$\frac{gh}{U^2}$
Stokes	Viscous Force to Gravitational Force	$\frac{\mu_f U}{\rho_f g d_p^2}$
Weber	Fluid Inertia to Surface Tension	$\frac{\rho D U^2}{\gamma}$

Fluidized beds are well known for the excellent heat transfer characteristics they exhibit as already noted [15]. The dimensionless numbers for heat transfer can give an idea of the dominant mechanism of heat transfer for given operating conditions. Table 2.18 shows heat transfer dimensionless numbers that can be used with fluidized bed operations [38, 39].

Table 2.18 Heat Transfer Dimensionless Numbers

Dimensionless Number	**Ratio**	**Equation**
Biot	Heat Transfer Resistance Inside to Outside	$\frac{hL_c}{k_b}$
Brinkman	Viscous Flow Conductive Heat Transfer to Surface Conductive Heat Transfer	$\frac{\mu_f U^2}{kT}$
Bubble Nusselt	Convective Heat Transfer to Conduction Heat Transfer for a Bubble	$\frac{Qd_b}{k\Delta T}$
Bulygin	Heat Needed to Vaporize Liquid to Heat Needed to Boil Liquid	$\frac{\lambda}{mC_pT}$
Clausius	Viscous Heat Dissipation to Conductive Heat Transfer	$\frac{U^3 D\rho_f}{k\Delta T}$
Evaporation	Heat Needed to Raise Temperature to Heat Needed for Evaporation	$\frac{C_p}{\lambda\beta}$

Table 2.18 Continued

Fourier	Heat Conduction to Thermal Energy Storage	$\frac{\alpha t}{L^2}$
Graetz	Fluid Thermal Capacity to Conductive Heat Transfer	$\frac{MC_p}{h_c L}$
Grashof	Buoyancy Forces to Viscous Forces	$\frac{g\beta(T_s-T_\infty)D^3}{\nu^2}$
J-Factor		$\frac{h}{mC_p}\left(\frac{C_p\mu}{k}\right)^{2/3}$
Kirpichev	Heat Flux to Heat Conduction	$\frac{Q^*D}{k\Delta T}$
Kossovich	Heat Required to Evaporate Liquid to Heat Required to Heat Liquid from T_o to T	$\frac{\lambda M^*}{C_p\Delta T}$
McAdams	Viscous Heat Convective Heat Transfer to Conduction During Evaporation	$\frac{h^4 D\mu_f \Delta T}{k^3\rho_f^2 g\lambda}$
Nusselt	Convective Heat Transfer to Conduction Heat Transfer	$\frac{hD}{k}$
Peclet	Advection to Thermal Diffusion	$\frac{DU}{\alpha}$
Posnov	Thermal Moisture Diffusivity to Isothermal Moisture Diffusivity in a Porous Material	$\frac{D_{tw}}{D}\frac{T_{ref}}{e}$
Prandtl	Viscosity to Thermal Diffusion	$\frac{C_p\mu}{k}$
Predvoditeiev	Rate of Change of Fluid Medium to Product Medium	$\frac{dT}{dt}\frac{A}{\alpha(T_0-T)}$
Rayleigh	Heat Transfer Mechanism	$\frac{g\beta}{\nu\alpha}(T_s-T_\infty)x^3$
Rebinder	Sensible Heat to Evaporative Heat(*M moisture content)	$\frac{dT^*}{dM^*}\frac{C_p}{\lambda}$
Romanov	Dry Bulb Temperature to Product Temperature	$\frac{T_{db}}{T_{prod}}$
Semenov	Mass Diffusivity to Thermal Diffusivity	$\frac{D_{ab}\rho_f C_p}{k}$
Stanton	Heat Transfer to Fluid to Thermal Capacity	$\frac{h}{C_p\rho U}$

In addition to fluid flow and heat transfer dimensionless numbers, mass transfer dimensionless numbers can also be applied to fluidized bed operations. Table 2.19 shows mass transfer dimensionless numbers [38, 39].

Table 2.19 Mass Transfer Dimensionless Numbers

Dimensionless Number	Ratio	Equation
Biot Mass Transfer	Mass Transfer at Interface to Mass Transfer at Wall Interior	$\frac{h_m L}{D_{ab}}$
Bodenstein	Bulk Mass Transfer to Diffusive Mass Transfer	$\frac{UL}{D}$
J-Factor		$\frac{K_c \rho}{m}\left(\frac{\mu}{\rho D}\right)^{2/3}$
Lewis	Mass Diffusivity to Thermal Diffusivity	$\frac{D_{ab}\rho_f C_p}{k}$
Luikov	Thermal Diffusivity to Mass Diffusivity	$\frac{k}{D_{ab}\rho_f C_p}$
Mass Transfer Nusselt	Mass Diffusivity to Molecular Diffusivity	$\frac{K_c L}{D_{mol}}$
Mass Transfer Peclet	Bulk Mass Transfer to Diffusive Mass Transfer	$\frac{UL}{D}$
Schmidt	Viscosity to Mass Diffusivity	$\frac{\nu}{D}$
Sherwood	Lengthscale to Diffusive Boundary Layer Thickness	$\frac{K_c L}{D_{ab}}$

The effects of electromagnetic fields on fluidization patterns have also been studied. Hristov wrote a series of reviews concerning magnetic field assisted fluidization [119-122] covering a variety of topics including: hydrodynamics, rheology, heat transfer, and continuous fluidized beds. As with the dimensionless numbers associated with fluid flow, heat transfer, and mass transfer, electromagnetic dimensionless numbers give an indication as to the dominant forces involved with the process. Table 2.20 shows dimensionless numbers associated with electromagnetic fields [38].

Table 2.20 Electromagnetic Field Dimensionless Numbers

Dimensionless Number	Ratio	Equation
Alfven	Flow Speed to Alfven Wave Speed	$\frac{U(\rho\mu_o)^{1/2}}{B}$
Electric Reynolds	Motion Induced by an Electric Field to Applied Electric Field	$\frac{e_P U}{q_s bL}$
Electroviscous	Viscous Forces to Applied Electric Field	$\left(\frac{\rho_c}{2\pi e_{ps}}\right)^{1/2}\frac{\rho L^2}{\mu}\frac{q}{m_p}$
Elsasser	Lorentz Forces to Coriolis Forces	$\frac{\rho}{\mu G\mu_o}$
Hartmann	Magnetic Force to Viscous Force	$\frac{BG^{1/2}L}{\mu^{1/2}}$
Joule	Joule Heating Energy to Magnetic Field Energy	$\frac{2\rho C_p\Delta T}{\mu_o H_m^2}$
Lundquist	Alfven Wave Timescale to Diffusion Timescale	$\frac{GH_mL\mu_o^{1/2}}{\rho^{1/2}}$
Lykoudis	Magnetic Force to Buoyancy Force	$\frac{G}{\rho}(\mu_o H_m)^2\left(\frac{1}{g\beta\Delta T}\right)^{1/2}$
Magnetic Dynamic	Magnetic Pressure to Dynamic Pressure	$\frac{GUB^2L}{\rho U^2}$
Magnetic Force	Magnetic Force to Dynamic Force	$\frac{\mu_o H_m^2 GL}{\rho U}$
Magnetic Interaction	Magnetic Force to Surface Tension	$\frac{\mu_o H_m^2 r}{2\sigma_t}$
Magnetic Prandtl	Viscous Diffusion Rate to Magnetic Diffusion Rate	$\mu_o Gv$
Magnetic Pressure	Magnetic Pressure to Dynamic Pressure	$\frac{\mu_o H_m^2}{\rho U^2}$
Magnetic Reynolds	Motion Induced by Magnetic Field to Applied Magnetic Field	$GUL\mu_o$

Fluidized beds are also used to carry out reactions because isothermal conditions can be maintained, high throughputs and conversions can be achieved, and controllability translates to operator safety. Table 2.21 shows dimensionless numbers used in reactions [38].

Table 2.21 Reaction Dimensionless Numbers

Dimensionless Number	Ratio	Equation
Arrhenius	Activation Energy to Potential Energy	$\frac{\varepsilon_a}{RT}$
Damkohler I	Reaction Rate to Flow Rate	$\frac{t_{react}}{t_{res}}$
Damkohler II	Reaction Rate to Diffusion Rate	$\frac{kC_0L^2}{DC_0}$
Damkohler III	Heat Libertated by Reaction to Heat Exported	$\frac{\Delta H_{rxn}kC_0L}{\rho C_pUT}$
Damkohler IV	Heat Liberated by Reaction to Heat Conducted	$\frac{\Delta H_{rxn}kC_0L}{h_cT}$
Karlovitz	Flow Rate to Reaction Rate	$\frac{t_{res}}{t_{react}}$

The dimensionless numbers will be of different orders of magnitude depending on the media used for fluidization: gas, liquid, or supercritical fluid.

2.8 Establishing Operation in Agglomeration or Coating Regime

One of the biggest challenges of fluidized bed coating operations is maintaining the proper balance of forces such that particle coating is the dominant process rather than particle agglomeration. A great deal of effort has been put toward identifying a distinctive point or operating condition landmark such that a clear division between particle agglomeration and particle coating can be declared. A well-defined distinction between the particle agglomeration regime and particle coating regime has far reaching potential applications for scaling up laboratory or pilot bench scale operations. Research in this area has yielded additional dimensionless numbers that can be used to determine a priori whether certain operating conditions will result in particle agglomeration or coating.

2.8.1 The Viscous Stokes Number

Ennis et al. [123] developed a dimensionless quantity called the Stokes number to determine the probability of particle coalescence (agglomeration) or rebound. The viscous

Stokes number, defined as the ratio of the kinetic collision energy to the viscous dissipation energy, is shown as Equation 2.76:

$$St_v = \frac{8U_{col}\rho_s r_{harm}}{9\mu_{sol}} \tag{2.76}$$

where U_{col} is the collision velocity, r_{harm} is the harmonic particle radius, and μ_{sol} is the viscosity of the coating solution. The collision velocity U_{col} is shown as Equation 2.77 [123]:

$$U_{col} = \frac{12U_{bu}r_{harm}}{d_{bu}\delta^2} \tag{2.77}$$

where U_{bu} is the bubble rise velocity, d_{bu} is the bubble diameter, and δ is the dimensionless bubble spacing which is ratio of axial bubble spacing to the bubble radius [123]. The harmonic radius is shown as Equation 2.78 [123]:

$$r_{harm} = \frac{r_1 r_2}{r_1 + r_2} \tag{2.78}$$

In order for particle rebound to be the dominant phenomenon versus particle agglomeration the viscous Stokes number St_v must be higher than a critical value. The critical viscous Stokes number, St_v^*, arises from a differential equation balancing viscous force evolved from the liquid droplet with kinetic forces of motion on the particles to yield Equation 2.79:

$$St_v^* = \left(1+\frac{1}{e}\right)\ln\left(\frac{h_{liq}}{h_{asp}}\right) \tag{2.79}$$

where e is the coefficient of restitution, h_{liq} is the height of the liquid surface on the particle, and h_{asp} is the height of the particle surface asperity. The coefficient of restitution is determined by momentum and kinetic energy balances. The coefficient of restitution is a ratio of the kinetic energy a body has after a collision to the kinetic energy it has just prior to a collision. Typically for fluidized bed coating operations, the coefficient of restitution is taken as 0.8-0.9. However, some research has found the coefficient of restitution to be a function of the liquid amount

present on the particle surface, resulting in a much lower coefficient of restitution of 0.4 and lower [124]. Work has also been done to relate the coefficient of restitution to the mechanical properties of the solids colliding [125].

The height of a liquid droplet on the surface of a particle, h_{liq}, is determined by the properties of the solid and the liquid droplet, mainly surface tension. The contact angle between the liquid and the particle surface determines how far the droplet will spread on the surface of the particle. Complete droplet spreading occurs with a contact angle of 0^o. Droplet spreading decreases with increasing contact angle up to 180^o. At a contact angle of 180^o, there is no droplet spreading [126]. Figure 2.25 shows the h_{liq} and the contact angle.

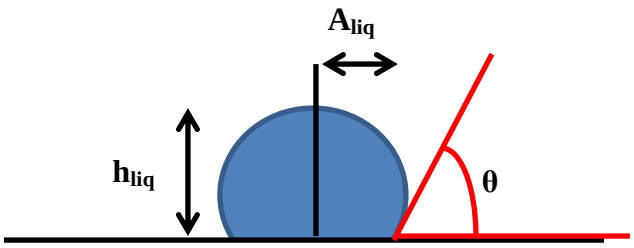

Figure 2.25 H_{liq} and the Contact Angle on the Particle Surface

Clark et al. [127] and Thielman et al. [128] worked out the equations to determine the change in the droplet geometry once adhesion to the particle has occurred. Equations 2.80 and 2.81 show how A_{liq} and subsequently h_{liq} are determined [127, 128]:

$$A_{liq} = \left[\frac{3V_{drop}}{\pi}\frac{\sin^3(\theta)}{2 - 3\cos\theta + \cos^3(\theta)}\right]^{\frac{1}{3}} \tag{2.80}$$

$$h_{liq} = A_{liq}\left(\frac{1 - \cos\theta}{\sin\theta}\right) \tag{2.81}$$

The particle surface asperity, h_{asp}, can be estimated as 1% of the particle radius [129].

There are two simplifications taken by Ennis et al. [123] in the development of the viscous Stokes number. First, capillary forces are neglected. This assumption was made by Ennis et al. [123] with the explanation that energy gained by the liquid droplet coalescence on the particle surface during the particle-particle collision is negated by the rupture forces evolved during the rebound step. No simple analytical solution exists for the real case where capillary forces and viscous forces act together to absorb the kinetic energy of particle-particle collisions [130]. The second assumption made by Ennis et al. [123] is that the particles are non-deformable. Both assumptions simplify the mathematics involved, but still yield valuable information in the discernment between particle agglomeration and coating.

Among the insight gained from the viscous Stokes number and the critical viscous Stokes number is that there are two mechanisms of particle coalescence [131]. Type I particle coalescence occurs when the viscous liquid layer dissipates the particle kinetic energy before the particles actually touch. Figure 2.26 shows type I coalescence [131].

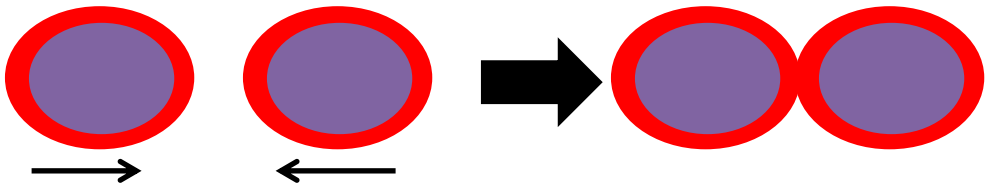

Figure 2.26 Type I Coalescence

Type II coalescence occurs when particle rebound after contact is impeded by viscous dissipation of the particle kinetic energy [131]. Figure 2.27 shows type II coalescence.

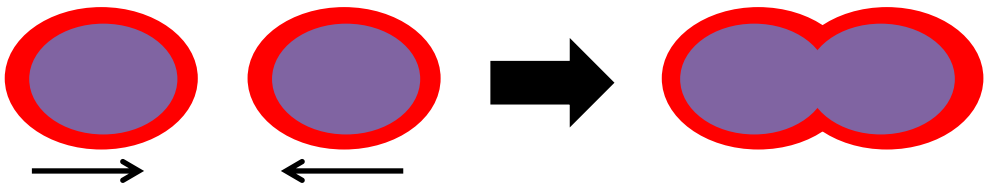

Figure 2.27 Type II Coalescence

The critical viscous Stokes number can also predict the largest stable particle agglomerate formed for a specific fluidized bed operating condition by setting the viscous Stokes number in Equation 2.76 equal to the critical viscous Stokes number in Equation 2.79 [123]. A complete explanation of the derivation of viscous Stokes number can be found in the Ph.D. dissertation of B. Ennis [132].

2.8.2 The Stokes Deformation Number

In an attempt to expand the breadth of the viscous Stokes number Tardos et al. [130] and Iveson and Lister [133] developed the Stokes Deformation number to include the potential for plastic deformation in particle-particle collisions. The original approach by Ennis et al. [123] only treated collisions between non-deformable particles. The approach by Liu et al. [131] incorporates the mechanics of contact, including the mechanical properties of the solid being fluidized such as: Poisson ratio (υ), Young Modulus (E), and Yield Stress (Y_d). The approach by Liu et al. [131] includes calculations for particle rebound velocity, the coefficient of restitution, the amount of plastic deformation and elastic recovery a particle incurs upon collision.

In keeping with the original viscous Stokes number definitions, there are two conditions where particle coalescence will occur with deformable particles. The first condition where particle coalescence will occur is shown as Equation 2.82:

$$St_v < \ln\left(\frac{\upsilon - \epsilon s^*}{6k}\frac{\widetilde{D}}{D_p}\right) \tag{2.82}$$

where υ is the volume fraction of liquid in the granule, ϵ is the granule porosity, s* is the point when a liquid surface appears on top of the granule due saturation, k is a proportionality constant ($k = h_a/D_p$), $\widetilde{D}$ is harmonic diameter, and D_p is the particle diameter.

The second condition where particle coalescence occurs is shown as Equation 2.83:

$$\left(\frac{Y_d}{E^*}\right)^{0.5} (St_{def})^{-1.125} < \frac{0.172}{St_v}\left(\frac{\widetilde{D}}{h_0}\right)^2 \left[1 - \frac{1}{St_v}\ln\left(\frac{h_0}{h_{asp}}\right)\right]^{1.2}$$

$$\left[\left(\frac{h_0^2}{h_{asp}^2} - 1\right) + \frac{2h_0}{\delta''}\left(\frac{h_0}{h_{asp}} - 1\right) + \frac{2h_0^2}{(\delta'')^2}\ln\left(\frac{h_0}{h_{asp}}\right)\right]$$

$$\left\{1 - 7.36\left(\frac{Y_d}{E^*}\right)(St_{def})^{-0.25}\left[1 - \frac{1}{St_v}\ln\left(\frac{h_0}{h_{asp}}\right)\right]^{-0.5}\right\}^2 \quad (2.83)$$

where St_{def} is the Stokes Deformation number and δ" is the permanent elastic deformation.

The Stokes Deformation number, defined as the ratio of particle kinetic energy to the energy required for particle deformation [130], is shown as Equation 2.84 [131]:

$$St_{def} = \frac{\widetilde{m}U_0^2}{2\widetilde{D^3}Y_d} \quad (2.84)$$

The equation for permanent plastic deformation is given as Equation 2.85 [131:

$$\delta'' = \left(\frac{8}{3\pi}\right)^{0.5} (St_{def})^{0.5}\,\widetilde{D}\left[1 - \frac{1}{St_v}\ln\left(\frac{h_0}{h_{asp}}\right)\right] *$$

$$\left\{1 - 7.36\left(\frac{Y_d}{E^*}\right)(St_{def})^{-0.25}\left[1 - \frac{1}{St_v}\ln\left(\frac{h_0}{h_{asp}}\right)\right]^{-0.5}\right\} \quad (2.85)$$

The coefficient of restitution used to calculate the critical viscous Stokes number for coalescence or rebound is not constant and is given as Equation 2.86 [131]:

$$e = 2.46\left(\frac{Y_d}{E^*}\right)^{0.5}\left[1 - \frac{1}{St_v}\ln\left(\frac{h_0}{h_{asp}}\right)\right]^{-0.25} (St_{def})^{-0.125} \quad (2.86)$$

When particle rebound occurs, the particle rebound velocity is estimated by Equation 2.87 [131:

$$U_{reb} \approx 2.46U_0\left(\frac{Y_d}{E^*}\right)^{0.5}\left[1 - \frac{1}{St_v}\ln\left(\frac{h_0}{h_{asp}}\right)\right]^{0.75} (St_{def})^{-0.125} \quad (2.87)$$

As shown by Equations 2.84-2.87, when the mechanics of particle collisions are included into the framework set forth by Ennis et al. [123], the mathematics becomes much more rigorous in nature. However, more information about particle mechanical integrity can be ascertained.

2.8.3 The Flux Number

A different attempt to map out the boundary of the agglomeration regime and the coating regime was done by Akkermanns et al. in an effort to make detergent granules [134]. A dimensionless number was developed in an attempt to balance the particle flux inside the fluidized bed with the liquid, expressed as a flux, introduced into the fluidized bed. The flux number (FN) is given as Equation 2.88:

$$FN = \log\left[\frac{\rho_p U_E}{\dot{q}_{mliq}}\right] \tag{2.88}$$

where ρ_p is the particle density, U_E is the excess velocity, and q_{mliq} is the liquid mass flux rate. The particle density is calculated according to Equation 2.89 [134]:

$$\rho_p = \frac{\rho_{p,bulk}}{1 - \varepsilon_{bed}} \tag{2.89}$$

The excess velocity is the superficial velocity of the fluidizing gas less the particle minimum fluidizing velocity. The liquid mass flux is given as Equation 2.90:

$$\dot{q}_{mliq} = \frac{\dot{Q}_{mliq}}{A_{bed}} \tag{2.90}$$

Akkermans et al. [134] state that the flux number should never be above 6, preferably between 4.5-5, because processing times will be impracticable economically or below 2.5. Boerefijn & Hounslow [135] mapped out the agglomeration and coating regimes for a range of superficial gas velocities and liquid flow rates. Flux numbers below 2 result in liquid flooding of the particles and eventual bed collapse. Flux numbers between 2 and 3.5 result in particle agglomeration. A

Flux number greater than 3.5 will yield particle coating instead of particle agglomeration. It should be noted the superficial gas velocities studied ranged from 0-1 ms^{-1}, while the liquid coating flow rates ranged from 0-11 $kghr^{-1}$ [135].

Wasserman et al. in a patent for Proctor and Gamble [136] confirmed the flux number recommendations by Akkermans et al. but also included a specification for the viscous Stokes number as well. Wasserman et al. [136] recommend viscous Stokes number should have a value of at least 10, but preferably between 100-1000. Another Proctor and Gamble patent by Achanta and Beimesch [137] states that for particle agglomeration to begin the viscous Stokes number should be less than 1.

2.8.4 The Dimensionless Spray Flux

The dimensionless spray flux (DSF) was initially developed for fluidized bed agglomeration operations but has also proven helpful in fluidized bed coating operations as well. The dimensionless spray flux, a measure of the binder flux on the powder surface, is shown as Equation 2.91 [138]:

$$\Psi_a = \frac{3\dot{V}_{drop}}{2\dot{A}d_{drop}} \tag{2.91}$$

where V_{drop} is the volume of the droplet and A is the spray zone area. As the parameter Ψ_a increases, the likelihood of droplets overlapping increases as well. If Ψ_a is too high, droplets will tend to overlap one another and particle agglomeration will occur rather than particle coating. Hapgood et al. [139] extended the DSF to develop a nucleation regime map with some success. Hapgood et al. [139] concluded further work would need to be done with different fluidized bed geometries and particle/binder combinations to distinguish if limitations to the regime mapping are of a general nature or specific to the fluidized bed geometries and particle/binder combination.

2.8.5 The Tack Stokes Number

Hede et al. [142] extended the viscous Stokes number to situations where tacky (sticky) coatings are applied to a core particle to develop the Tack Stokes Number shown as Equation 2.92:

$$St_{tack} = \frac{2m_{harm}U_0^2}{F_{max,tack}\kappa(h_{liq} - h_{asp})\phi} \tag{2.92}$$

where m_{harm} is the harmonic mass, $F_{max,tack}$ is the maximum tack force, κ is a factor accounting for the fact that the tack force does not act across the entire distance of h_{liq}-h_{asp}. The term ϕ, is a correction factor given by Equation 2.93:

$$\phi = \left(\frac{U_0}{U_{test}}\right)\left(\frac{A_{liq}}{A_{con}}\right) \tag{2.93}$$

where A_{con} is the contact area of the particles.

Hede et al. [140, 141] assert that coating solution stickiness in addition to coating solution viscosity influences the agglomeration tendency of particles at a specific operating condition. Moreover, the maximum stickiness value and the length of time the stickiness lasts are more instrumental in determining agglomeration tendency versus viscosity effects. Hede et al. [140] showed that stickiness is a function of the dry matter content in the solvent. The units for stickiness are Nmm^{-2}.

Following the work of Ennis et al. [123], Hede et al. [142] defined a critical Stokes Tack number equal to 1. Below the critical value of the Tack Stokes number, agglomeration will occur, while a Tack Stokes number greater than one will result in particle coating. Unfortunately tack measurements are not a standard technique used in fluidized bed processing, so no further testing of the Tack Stokes number has been undertaken.

2.8.6 Additional Parameters

In addition to the development of dimensionless numbers for determining if specified operating conditions will result in particle agglomeration or particle coating, some parameters concentrate on scale up reproducibility. Maintaining particle coating integrity (coating thickness, morphology, and mechanical properties) with minimal variation across operation scale is paramount.

Hede et al. [143] developed a parameter called the Drying Force in their fluidized bed coating scale up operations. The Drying Force (DF), shown as Equation 2.94, is the difference between the vapor pressure at fluidized bed temperature and the actual partial pressure of the evaporated solvent:

$$DF = P_{sat,T_{bed}} - P_{actual} \tag{2.94}$$

P_{actual} is measured as the outlet relative humidity. However a relationship between the degree of particle agglomeration and the magnitude of the Drying Force was not identified other than the acknowledgement is not linear [143].

Another parameter developed for scale up purposes is the Relative Droplet Size, R_d [144]. The Relative Droplet Size, a ratio of the mass flow rates of liquid and air flowing through a pneumatic nozzle, is shown as Equation 2.95:

$$R_d = \frac{\dot{m}_{liq}}{(\dot{m}_{air})^2} \tag{2.95}$$

The R_d parameter was used in a design of experiments (DOE) approach to fluidized bed coating scale up experiments with success [144]. No further explanation for the development of the relative droplet size parameter is provided. Hede et al. [143] used the relative droplet size as a scaling factor along with their DF parameter and reported across scale successful reproducibility.

2.9 Collisions in a Fluidized Bed

There are three types of collisions that occur during a fluidized bed coating operation: particle-particle, particle-wall, and droplet-particle collisions. The aforementioned collisions introduce small yet noteworthy fluctuations in the particle velocity that can alter which mechanisms dominate a fluidized bed coating operation. The frequency and magnitude of these collisions determine several characteristics: particle breakage and attrition, particle agglomeration tendency, and coating efficiency via droplet impingement efficiency.

2.9.1 Particle-Particle Collisions

Particle-particle collisions occur in a top spray oriented fluidized bed at different rates depending on the axial position within the fluidized bed. In the first attempt to determine the particle collision rate, the kinetic theory of gases was adapted and modified by Bagnold (1954) [145]. The adaptation of the kinetic theory of gases to particulate flow is called kinetic theory of granular flow (KTGF) [146]. In the kinetic theory of granular flow, particle velocities follow a Maxwellian-Boltzmann distribution with velocity fluctuations in each direction producing Gaussian distributions. Particle velocity is described by two terms in this approach as shown in Equation 2.96 [145]:

$$\bar{c} = \bar{U} + \bar{C} \tag{2.96}$$

where $\bar{c}$ is the individual particle velocity, $\bar{U}$ is the local mean velocity, and $\bar{C}$ is the random fluctuating velocity.

The granular temperature, θ, defined by Savage [147] as the measure of the random particle motion is given by Equation 2.97 [145]:

$$\theta = \frac{1}{3}\langle \bar{C}, \bar{C} \rangle \tag{2.97}$$

Since there is a velocity fluctuation in the x,y, and z direction, the velocity distribution of particles is given by Equation 2.98 [145]:

$$f(C_i) = \frac{1}{(2\pi\theta_i)^{0.5}} e^{-C_i^2/2\theta_i} \tag{2.98}$$

where i is the direction x,y, or z.

The overall Maxwellian-Boltzmann distribution for particle velocity is given as Equation 2.99 [145]:

$$f(C) = \frac{4\pi C^2}{(2\pi\theta)^{1.5}} e^{-C^2/2\theta} \tag{2.99}$$

Figure 2.28 shows an example of the Gaussian distribution for C_i and the Maxwell-Boltzmann distribution for C.

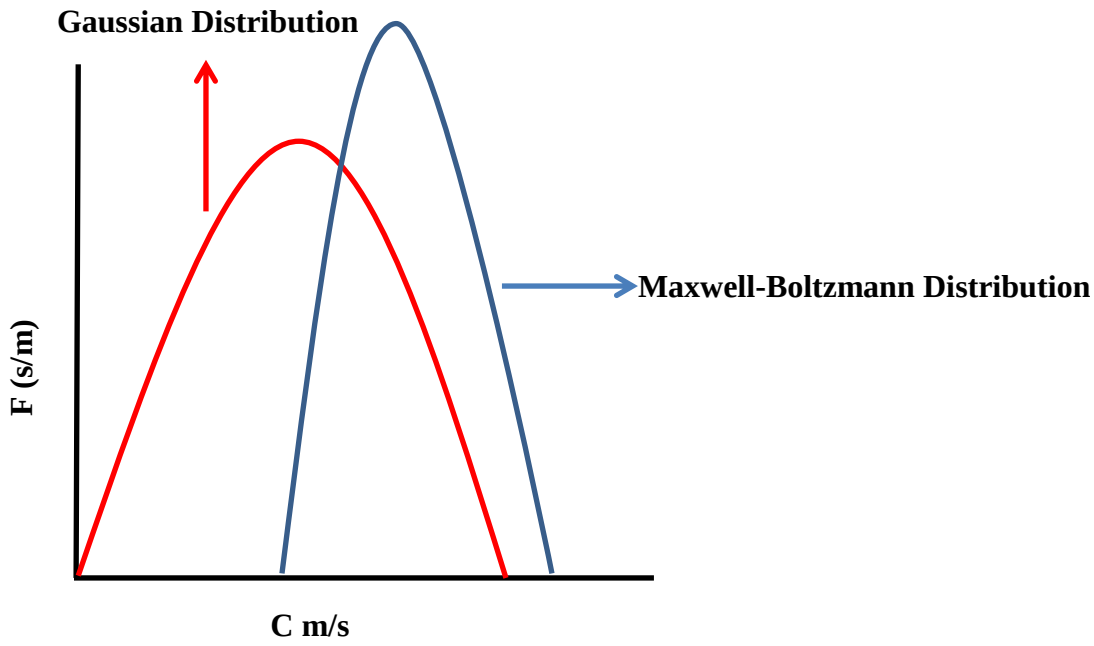

Figure 2.28 Typical Plot of Particle Velocity Fluctuation (C_i) and the Overall Particle Velocity Fluctuation (C)

Huang and Liu [148] developed a model to incorporate the effects of gas bubbling on the granular temperature inside a fluidized bed. The Huang-Liu model is a pseudo-thermal energy

balance between energy generated by rising bubbles (N_{gen}) and energy lost by both viscous dissipation (N_{vis}) and particle-particle collisions (N_{col}), is shown as Equation 2.100:

$$N_{gen} = N_{vis} + N_{col} \tag{2.100}$$

where

$$N_{gen} = \Delta\varepsilon_s \left(\rho_s - \rho_g\right) g\sqrt{3\theta} \tag{2.101}$$

$$N_{vis} = 3\beta_a \theta \tag{2.102}$$

$$N_{col} = \frac{12\left(1 - e^2\right)\varepsilon_s^2 \rho_s g_0 \theta}{d_p}\sqrt{\frac{\theta}{\pi}} \tag{2.103}$$

The $\Delta\varepsilon_s$ term in Equation 2.101 represents the solids volume fraction fluctuation and can be described by Equation 2.104:

$$\Delta\varepsilon_s = \sqrt{(\varepsilon_{bub} - \varepsilon_s)^2 f_b + (\varepsilon_{mf} - \varepsilon_s)^2 (1 - f_b)} \tag{2.104}$$

where ε_{bub} is the bubble void fraction, ε_s is the mean solid volume fraction, and f_b is the bubble fraction. The β_a term is the drag coefficient given by Equation 2.105:

$$\beta_a = \frac{\varepsilon_s (1 - \varepsilon_s)\left(\rho_s - \rho_g\right) g}{\left(\frac{U_0}{1 - \varepsilon_s}\right)} \tag{2.105}$$

The term e is the coefficient of restitution. The term g_0 in Equation 2.103 is the radial distribution function which is given as Equation 2.106:

$$g_0 = \left[1 - \left(\varepsilon_s / \varepsilon_{s,max}\right)^{0.333}\right]^{-1} \tag{2.106}$$

where the term $\varepsilon_{s,max}$ is equal to 0.64.

Plugging Equations 2.98-2.100 into Equation 2.97 will result in a cubic equation that gives the granular temperature, θ, for a bubbling fluidized bed. Only the positive root will have meaning, as the other two roots will be zero and negative [148]. The granular temperature

calculated for this procedure is for the x and y direction. The particle fluctuation velocity in the z direction is $\sqrt{3\theta}$ [148].

The granular temperature can be applied to determine other properties in accordance with the kinetic theory of gases including: collision frequency, mean free path, and viscosity. The collision frequency was obtained by including the radial distribution function (Equation 2.106) in the derivation of dense gas collision frequency by Chapman and Cowling [149]. When two particles collide, the number of binary collision per unit time per unit volume is given by Equation 2.107 [145]:

$$N_{ij} = 4n_1 n_2 d_{12}^2 g_0 \sqrt{\pi\theta} \tag{2.107}$$

where n_1 and n_2 are the number of particles size 1 and number of particles size 2 and d_{12} is harmonic diameter. In the case of uniform particle size, the collision frequency can be described by Equation 2.108:

$$CF = \frac{1}{2}\frac{N_{ii}}{n_i} = \frac{12\varepsilon_s g_0}{\sqrt{\pi} d_p}\sqrt{\theta} \tag{2.108}$$

When Equations 2.107 and 2.108 are expanded to incorporate two different particles with different granular temperatures, they can be represented by Taylor series expansions [150].

The mean free path (MFP), λ, is the average distance a particle traverses before colliding with another particle. Figure 2.29 shows an example of the mean free path of a particle.

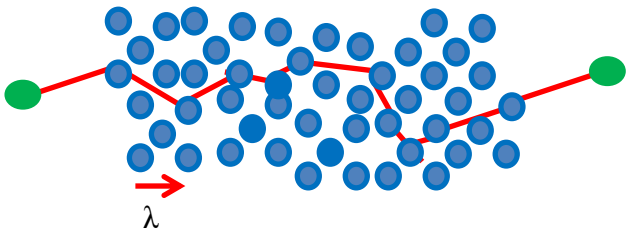

Figure 2.29 Mean Free Path Example

The mean free path of a particle is dependent on the fluidizing gas flow. At the minimum fluidization condition the mean free path will be shorter compared to a fluidized bed closer to pneumatic transport. The mean free path is a product of the collision time τ_{col}, and the average particle velocity. The collision time is given by Equation 2.109 [145]:

$$\tau_{col} = \frac{n_i}{N_{ij}} \tag{2.109}$$

For granular flow, the mean free path is given as Equation 2.110:

$$\lambda_i = \langle c_i \rangle \tau_{col} \tag{2.110}$$

where $\langle c_i \rangle$ is given by Equation 2.111:

$$\langle c_i \rangle = \sqrt{\frac{8\theta}{\pi}} \tag{2.111}$$

With some rearrangement of Equation 2.111, and the use of Equations 2.107 and 2.109, Equation 2.110 is modified to Equation 2.112:

$$\lambda_i = \frac{1}{\pi\sqrt{2} n_1 d_p^2} = \frac{0.707}{\pi n d_p^2 g_0} \tag{2.112}$$

Using Equation 2.113 shown below, for solids volume fraction:

$$\varepsilon_s = \frac{1}{6}\pi d_p^3 n \tag{2.113}$$

Equation 107 (MFP) is then shown to be independent of the granular temperature in Equation 2.114 [145]:

$$\lambda_i = \frac{1}{6\sqrt{2}} \frac{d_p}{\varepsilon_s} \tag{2.114}$$

In addition to the collision frequency and mean free path, the particulate viscosity can also be calculated with the kinetic theory of granular flow. Again following the work of

Chapman and Cowling [149], Gidaspow [145] developed an equation for the particulate viscosity, which is shown as Equation 2.115:

$$\mu_i = \frac{24\varepsilon_{si}\theta_i\rho_i}{\pi^2 d_i^3 \sum_i N_i} \tag{2.115}$$

When two particles collide there is also a pressure that develops upon impact. This pressure is called the collisional pressure and is given as Equation 2.116 [151]:

$$p_0 = \frac{3}{2\pi}\left(\frac{16}{9}F_z\frac{E^{*2}}{a^{*2}}\right)^{0.333} \tag{2.116}$$

where F_z is the force of collision. Equation 2.117 assumes a Hertz pressure distribution.

There is also a granular pressure associated with the granular temperature. The granular pressure is given by Equation 2.117 [148]:

$$p_0 = \varepsilon_s\rho_s\left[1 + 2(1+e)g_0\varepsilon_s\right]\theta \tag{2.117}$$

The kinetic theory of granular flow is used extensively in computational fluid dynamics (CFD) calculations. While the kinetic theory of granular flow allows for the quantification of many important parameters there are also drawbacks. Gantt and Gatzke [146] applied the KTGF to a high shear mixing process. Gantt and Gatzke [146] concluded that the KTGF may not be a good candidate to describe the behavior observed in a high shear mixer because observed velocity distribution profiles did not match theoretical velocity distribution profiles. This may result from idealized conditions of KTGF, including same particle diameter and shape rather than a distribution.

In addition to the kinetic theory of granular flow approach, some research has focused on empirical correlations to determine collision frequency. Experimental work has shown that particle-particle collision frequency decreases when the solids volume fraction is above a certain threshold, the packed bed limit. Above the packed bed limit, particles simply cannot attain a

high velocity because they are blocked by other particles in close proximity [152]. Buffière & Moletta [153] developed an empirical correlation for particle collision frequency in a fluidized bed which is shown as Equation 2.118:

$$f_{col} = 56400\left[1 - \left(\frac{\Phi_{exp}}{\Phi_{fix}}\right)\right]\left(\frac{\Phi_{exp}}{\Phi_{fix}}\right)^2 U_0 \qquad (2.118)$$

where ϕ_{exp} and ϕ_{fix} are the solids fraction at the experiment conditions and fixed conditions. The term ϕ_{fix} was assumed constant at 0.61 [153].

2.9.2 Particle-Wall Collisions

The second type of collision that occurs inside a fluidized bed is a particle-wall collision. In order to calculate the collisional force evolved from a particle-wall collision, the wall is considered a large sphere with an infinite radius [151] as shown in Figure 2.30.

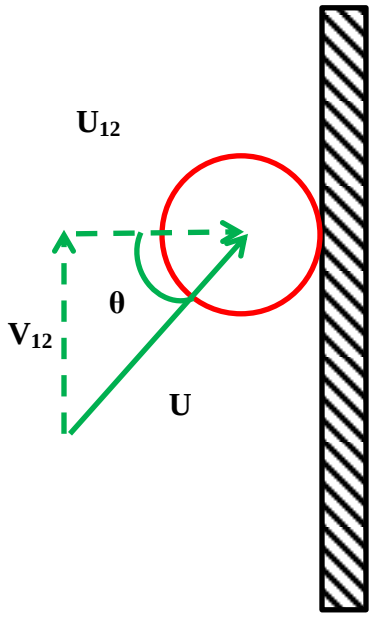

Figure 2.30 Schematic of Particle-Wall Collision

When considered as a collision between two elastic spheres, the collision time is given as Equation 2.119 [151]:

$$t_{col} = \frac{2.94}{U_{12}}\left(\frac{15}{16}\frac{m^*}{E^*}\frac{U_{12}^2}{\sqrt{a^*}}\right)^{0.4} \tag{2.119}$$

where U_{12} is the normal velocity, m* is the relative mass, E* is the relative Young's Modulus, and a* is the relative radius. The normal velocity is given as Equation 2.120 [151:

$$U_{12} = U_0 \cos\theta \tag{2.120}$$

The relative mass is given as Equation 2.121:

$$m^* = \frac{\pi}{6} d_p^3 \rho_p \tag{2.121}$$

The relative Young's Modulus is given as Equation 2.122:

$$E^* = \left(\frac{1-\upsilon_1^2}{E_1} + \frac{1-\upsilon_2^2}{E_2}\right)^{-1} \tag{2.122}$$

where υ is the Poisson Ratio. The relative radius is given by Equation 2.123:

$$a^* = \frac{d_p}{2} \tag{2.123}$$

The typical collision time for a particle-wall collision is 10^{-4} seconds [151].

When collisions occur between inelastic surfaces there is a critical velocity above which plastic deformation occurs. The critical normal velocity for plastic deformation is given by Equation 2.124:

$$U_{12Y} = 10.3\sqrt{\frac{a^* Y^5}{m^* E^{*4}}} \tag{2.124}$$

where Y is the yield strength of the particle. The coefficient of restitution for particle-wall collisions is determined from an elastic-plastic model.

The coefficient of restitution is given as Equation 2.125:

$$e = 2.29\left(\frac{U_{12Y}}{U_{12}}\right)^{0.25} \tag{2.125}$$

However Equation 122 is only valid for the following condition shown in Equation 2.126 [151]:

$$U_{12} < 0.53\sqrt{\frac{Y}{\rho_p}} \tag{2.126}$$

2.9.3 Particle-Droplet Collisions

In order for particle coating to occur, particle-droplet collisions must occur at a controlled rate such that agglomeration is minimal at best. One approach to modeling droplet-particle collisions is a two part process: impingement and adhesion [154]. Figure 2.31 shows how droplet impingement and adhesion occur.

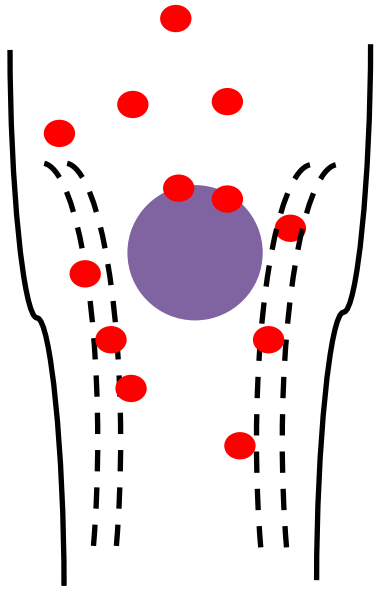

Figure 2.31 Droplet Impingement and Adhesion

Droplet impingement efficiency, defined as a ratio of the number of droplets that collide with a particle to the number of droplets within the vicinity of a particle, is usually represented as a function of the Stokes number as in Equation 2.127:

$$\varphi_{eff} = \left(\frac{St}{St + a}\right)^{b} \tag{2.127}$$

where a and b are constants dependent on the particle Reynolds number. The constants a and b for Equation 2.127 are shown in Table 2.22 [154].

Table 2.22 Constants a and b For Droplet Impingement Efficiency

Reynolds Number	**A**	**b**
Re < 1	0.65	3.7
1 < Re < 30	1.24	1.95
30 < Re < 50	1.03	2.07
50 < Re < 90	1.84	0.506
Re > 90	2.00	0.25

Droplet adhesion on the particle surface occurs after impingement. A droplet may adhere to the particle surface or it may rebound depending on the thermo-physical properties of the liquid (density, surface tension, viscosity) and the hydrodynamic properties of the particle. Mundo et al. [155] developed a dimensionless correlation to determine if a droplet will adhere to the particle surface or rebound called the K-factor. A critical impingement velocity, v_{crit}, shown as Equation 2.128 can be calculated from the K-factor [156]:

$$v_{crit} = \left(\frac{57.7}{Oh}\right)^{0.8} \left(\frac{\mu_{drop}}{d_{drop}\rho_{drop}}\right) \tag{2.128}$$

Above this critical impingement velocity, the droplet will rebound. Below this critical impingement velocity, the droplet will adhere to the particle surface. Ronsse et al. [157] calculate the critical impingement velocity, shown in Equation 2.129, by assuming the particle is a flat surface in part because the droplet size is usually at least one order of magnitude smaller than the particle size in the same manner as Zank et al. [158]:

$$v_{crit} = \frac{4\mu_{drop}(3\tan(\theta/2) + \tan^3(\theta/2))^{\frac{2}{3}}}{d_{drop}\rho_{drop}\tan^2(\theta/2)} \tag{2.129}$$

where θ is the angle of initial contact between the particle and droplet. The adhesion probability, h, can then be calculated by Equation 2.130 [156]:

$$h = \left(\frac{v_{crit}}{v_{rel}}\right)^2 \tag{2.130}$$

The overall deposition efficiency of the droplets onto the particle surfaces is then given by Equation 2.131 [156]:

$$\eta = \varphi_{eff} h \tag{2.131}$$

The droplets that do not hit a particle while traveling through the fluidized bed evaporate. The coating material within the droplet will precipitate and either act as a seed inside the fluidized bed or it will elutriate the bed.

2.10 Droplet Evaporation Kinetics

Droplet evaporation inside a fluidized bed is a combination of heat and mass transfer that has a significant impact on the overall force balance between particle agglomeration and particle coating. Liquid droplets gain enthalpy via heat transfer by conduction from the particle and convection from the fluidizing gas. The liquid droplets undergo a phase change to vapor and then transfer to the gas phase via convection and diffusion. The rate at which the droplets evaporate has a direct effect on particle coalescence probability at the fluidized bed operating conditions. If the droplets evaporate too slowly, the probability of particle agglomeration increases. If the droplets evaporate too quickly spray drying may occur decreasing the particle coating efficiency.

One approach to modeling droplet evaporation kinetics is the D^2 law of droplet evaporation, given as Equation 2.132 [16]:

$$D_0^2 - D^2 = \lambda t \tag{2.132}$$

where λ is the evaporation constant. The assumption behind Equation 2.132 is that there is no evaporation at transient temperatures, only at steady state.

A modified form of the D^2 law of evaporation involves setting a mass transfer number, B_m and a heat transfer number, B_t equal to each other. The mass transfer number and the heat transfer number are shown as Equations 2.133 and 2.134 [16]:

$$B_m = \frac{1}{1-Y_f} \tag{2.133}$$

$$B_m = \frac{C_{p,liq}(T_\infty - T_{surf})}{L} \tag{2.134}$$

where Y_f is the mass fraction of liquid in the air and L is the heat of vaporization. The equilibrium B calculated is then used to calculate the evaporation constant as shown in Equation 2.135:

$$\lambda = \frac{8k_g(1+B)}{C_{p,g}\rho_g} \tag{2.135}$$

Buchanan [159] developed a droplet evaporation kinetic model that incorporated the presence of particles in the kinetic expression. The heat up time to the steady state temperature where the droplet evaporates is given by Equation 2.136:

$$t = \tau \ln\left[\frac{T_a - T}{T_a - T_0}\right] \tag{2.136}$$

where T_a is the air temperature, T_0 is the initial temperature of the droplet and T is the temperature at which evaporation occurs.

The term τ is a heat transfer time given by Equation 2.137 [159]:

$$\tau = \frac{\rho_{liq} C_{p,liq} d_{drop}}{6h} \tag{2.137}$$

The convective heat transfer coefficient, h, can be calculated from correlations for the Nusselt number.

Incorporating the presence of particles in Equation 133, the heat up time becomes Equation 2.138 [159]:

$$T_a - T = \frac{2\rho_{liq} C_{p,liq} d_{drop}}{3U_0 \rho_p (1 - \varepsilon_{bed}) C_{p,p}} \frac{dT}{dt} \tag{2.138}$$

The droplet evaporation rate is then given as Equation 2.139 [159]:

$$\frac{dd_{drop}}{dt} = \frac{-U_0 \rho_p (1 - \varepsilon_{bed}) C_{p,p} (T_a - T)}{2\rho_{liq} L} \tag{2.139}$$

The models presented in Lefebvre [16] and by Buchanan [159] only consider droplets falling in air. Erbil et al. [160] studied droplet evaporation surfaces and classified two modes of evaporation, constant contact angle and constant contact area. Constant contact area was identified as the dominating evaporation mode for water and several other liquids with surface contact angles below 90^o. The approach taken by Erbil et al. [160] assumes that droplet radius and droplet height change simultaneously thereby keeping the contact angle constant. In the constant contact area mode of evaporation, the droplet evaporation rate is given by Equation 2.140 [160]:

$$V_c^{\frac{2}{3}} = V_{c0}^{\frac{2}{3}} - \frac{2}{3} K f(\theta) t \tag{2.140}$$

where V_c and V_{c0} are the droplet volume and the initial droplet volume respectively, K is a constant, $f(\theta)$ is the contact angle, and t is time.

The constant K is given by Equation 2.141:

$$K = \frac{4\pi^{\frac{2}{3}} 3^{\frac{1}{3}} D(C_{surf} - C_\infty)}{\rho_{liq} \beta^{\frac{1}{3}}} \tag{2.141}$$

where D is the diffusion coefficient, C_{surf} is the vapor concentration at the surface of the droplet and C_∞ is the vapor concentration at an infinite distance. The term β is given by Equation 2.142 [160]:

$$\beta = 2 - 3\cos\theta + \cos^3\theta \tag{2.142}$$

For a constant contact angle (θ) evaporation mode, the droplet evaporation rate is given by Equation 2.143 [160]:

$$R_b^2 = R_{bi}^2 - \frac{4D(C_{surf} - C_\infty)\sin^2\theta}{\rho_{liq}(1 - \cos\theta)(2 + \cos\theta)}t \tag{2.143}$$

where R_b and R_{bi} are the droplet radius of contact and the initial droplet radius of contact.

The derivation of Erbil et al. [160] is for spherical cap droplets on a surface. A further rearrangement of Equation 2.143 (constant contact angle mode) yields the change in droplet height with time given as Equation 2.144 [152]:

$$h = h_0 - \frac{2}{3}\frac{\rho_g}{\rho_{liq}}\frac{M_{liq}}{M_g}\frac{\beta}{1 - \cos\theta}\frac{P^{sat}}{P}\left[\frac{1}{1 - \cos\theta} - \frac{1}{3}\right]^{-1} t \tag{2.144}$$

where h and h_0 are the droplet height and initial droplet height, M_{liq} and M_g are the molecular weights of the liquid and the gas, β is the mass transfer coefficient, and P^{sat} is the vapor pressure of the liquid.

Roy et al. [161] took a lumped sum approach to droplet evaporation by looking at moisture content of the fluidized bed. They defined granulation time as the heat required to evaporate excess moisture content in the bed to the heat transfer from the fluidizing gas to the bed.

Mathematically, the granulation time is given as Equation 2.145:

$$t_{gran} = k\frac{\left(\frac{MC}{100}\right)AL(1 - \varepsilon_{bed})\rho_p\lambda}{AU_0\rho_g C_{p,g}(T_{gi} - T_{bed})} \tag{2.145}$$

where k is a correction factor, MC is the moisture content of the bed, and λ is the heat of evaporation. Roy et al. [161] acknowledge that Equation 2.145 is an oversimplification of fluidized bed drying because the fluidized bed temperature and the correction factor are a complex function of heat and mass transfer.

2.11 Investigations on the Impact of Various Factors on Fluidized Bed Coating

A fluidized bed coating process involves the interaction of several parameters. Some of the parameters can be specified by the engineer, while others are determined by the physical nature of the particles, coating-solvent system, and fluidized bed geometry. A thorough knowledge of these interactions and the phenomena that cause them can lead to improved fluidized bed design and operation. Tables 2.23 and 2.24 show the discrete and continuous variables involved in a fluidized bed coating process.

Table 2.23 Discrete Variables of a Fluidized Bed Coating Process

Batch Size	Nozzle Height From Distributor Plate
Bed Geometry	Nozzle Type
Bed Set Up – Top Spray or Wurster Spray	Particle Density
Coating Solution Concentration	Particle Size Distribution
Contact Angle	Spray Angle
Distributor Design	

Table 2.24 Continuous Variables of a Fluidized Bed Coating Process

Air Humidity	Particle Porosity
Atomization Air Density	Particle Size Distribution
Atomization Air Flow Rate	Pressure Drop
Atomization Air Pressure	Relative Humidity
Atomization Air Temperature	Run Time
Average Particle Size	Solution Spray Pressure
Bulk Bed Temperature	Solution Spray Rate
Contact Angle	Solution Surface Tension
Droplet Size	Solution Temperature
Fluidizing Gas Density	Solution Viscosity
Fluidizing Gas Pressure	Superficial Velocity
Fluidizing Gas Temperature	

Several researchers have examined the impact of variables listed in Tables 2.23 and 2.24 on fluidized bed coating operations. Table 2.25 presents a look at the influence of various operating factors on fluidized bed coating operations.

Table 2.25 Factors Investigated in Fluidized Bed Coating Operations

Reference	Factors Investigated	Outcome
[162]	Atomization Pressure Inlet Air Temperature Average Particle Diameter (Volume Weighted)	Nozzle Atomization Pressure Influences More Then Droplet Size
[1]	Temperature Profiles Humidity Profiles	Zones Identified Inside Fluidized Bed and Their Respective Roles in Coating Operation
[163]	Fluidizing Gas Velocity Atomizing Air Particle Size Liquid Flowrate Liquid Concentration Initial Bed Mass	Most Important Variable for a Given Particle Size Coating Deposition Quality Increases with Atomization Pressure Smaller Particle Size (Initial) Shifts Regime From Coating to Inertial (Increases Agglomeration Tendency) No Effect No Effect No Effect
[164]	Wurster Spray Partition Height Wurster Spray Partition Diameter Wurster Spray Partition Gap Fluidizing Air Rate (Inner & Outer)	Increasing Inner & Outer Velocities, Partition Gap, Partition Diameter all Increase Particle Circulation Rates Increasing Partition Height Decreases Particle Circulation Rate Particle Circulation Rate Most Sensitive to Partition Gap Strong Interaction Between Partition Gap and Partition Height
[165]	Particle Circulation Particle-to-Particle Mass Coating Distribution in a Wurster Process	Particle Sheltering Limits the Amount of Coating Material Deposited onto Bed Charge. Only about 2-6% of Particles Passing Through Spray Zone Get Coating Material

Table 2.25 Continued

[165]	Gas Velocity Atomizer Location Liquid Flow Rate Liquid Concentration Atomizing Air Flow Rate Solution Viscosity Initial Particle Mean Size Particle Porosity Wettability	Increasing Gas Velocity Increases Evaporation Promoting Coating Growth versus Agglomeration Nozzle Height Increase Decreases Coating Efficiency- Leads to Spray Drying, Wall Wetting Increasing Atomizing Air Decreases Droplet Size and Improves Distribution Over Particle Surface Smaller Mean Particle Size Increased Coating Growth Rate versus Large Particles Increasing Porosity Increases "No Growth" Period Where Pores Are Filled In or Blocked, Then Coating Begins Smaller Contact Angle Increases Agglomeration Tendency
[166]	Gas Velocity Wurster Gap Height Spray Shape	Cylindrical Spray versus Conical Spray Has Impact on Coating Efficiency – Cylindrical Spray Pattern Deposits More Coating versus Conical Spray Pattern

2.12 Sequential Mapping of Coating Operation Phenomena

Several phenomena occur simultaneously during a fluidized bed coating operation. The thermo-physical properties of the coating-solvent system, core particles, and fluidizing gas as well as the fluidized bed geometry determine performance characteristics of a fluidized bed coating operation. The droplet size distribution is determined by the density, surface tension, and viscosity of the coating-solvent system in addition to the atomization air pressure. Heat and mass transfer properties are determined by hydrodynamic properties of the fluidized bed. The hydrodynamic properties of the bed and the atomization properties also determine collision rates

(particle-particle, particle-wall, and particle-droplet) and collision frequencies. Combined properly, all the aforementioned properties will yield a process that will result in particle coating.

Figures 2.32-2.36 show a general flow to the calculations that must be done to determine atomization properties, fluidized bed hydrodynamic properties, heat and mass transfer properties and a combined calculation map.

As Figures 2.32-2.36 show, there are several calculations that go into determining the various performance characteristics of a fluidized bed coating operation. Most notably, Figures 2.32-2.36 reveal the essential driving forces for fluidized bed coating operations: pressure, temperature, and flow rates, both liquid and air (for fluidization and atomization).

2.13 References

[1] Maronga, S.J. (1998) On the Optimization of the Fluidized Bed Particulate Coating Process, Ph.D. Dissertation, Royal Institute of Technology, Stockholm.

[2] Iveson, S.M., Litster, J.D., Hapgood, K., & Ennis, B.J. (2001) Nucleation, Growth, and Breakage Phenomena in Agitated Wet Granulation Processes: A Review, Powder Technology, 117, 3-39.

[3] Christensen, F.N. & Bertelsen, P. (1997) Qualitative Description of the Wurster-Based Fluid-Bed Coating Process, Drug Development and Industrial Pharmacy, 23, 451-463.

[4] Teunou, E. & Poncelet, D. (2002) Batch and Continuous Fluid Bed Coating – Review and State of the Art, Journal of Food Engineering, 53, 325-340.

[5] Wurster, D.E. (1953) U.S. Patent 2,648,609. Method of Applying Coatings to Edible Tablets or the Like.

[6] Wurster, D.E. (1957) U.S. Patent 2,799,241. Means for Applying Coatings to Tablets or the Like.

[7] Wurster, D.E. (1963) U.S. Patent 3,089,824. Granulation and Coating Process for Uniform Granules.

[8] Lindlof, J. & Wurster, D.E. (1964) U.S. Patent 3,117,027. Apparatus for Coating Particles in Fluidized Bed.

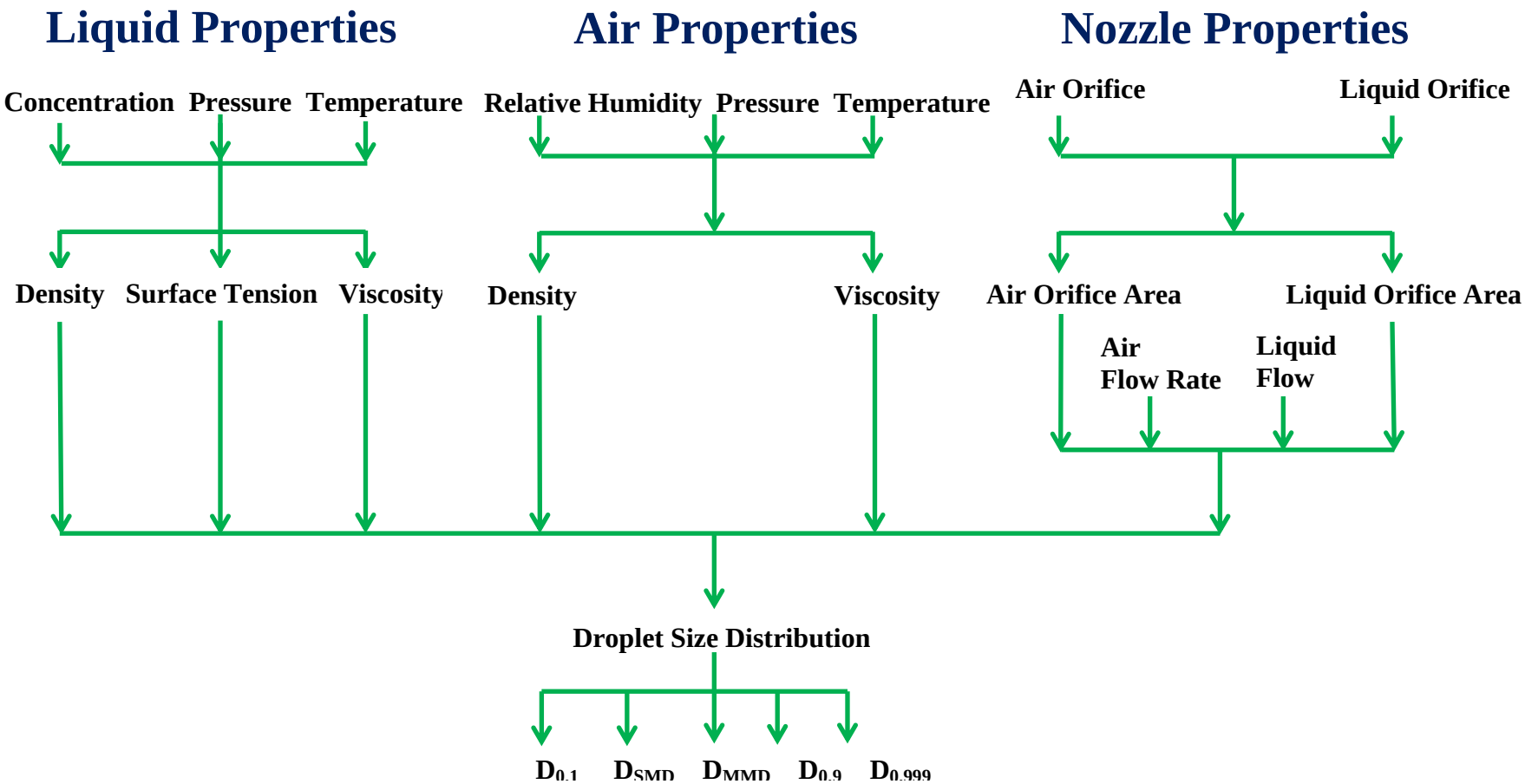

Figure 2.32 Atomization Calculation Map

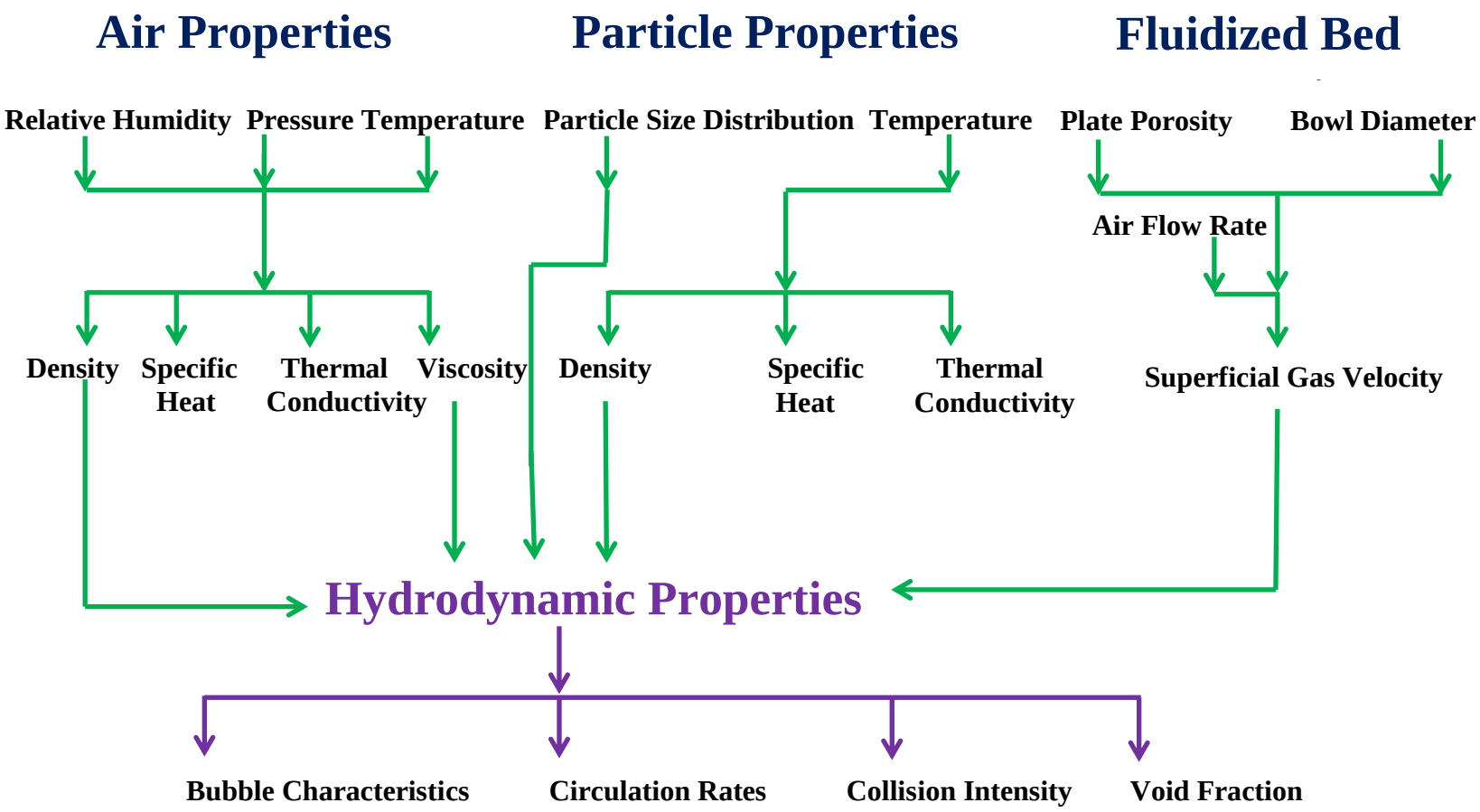

Figure 2.33 Fluidized Bed Hydrodynamics Calculation Map

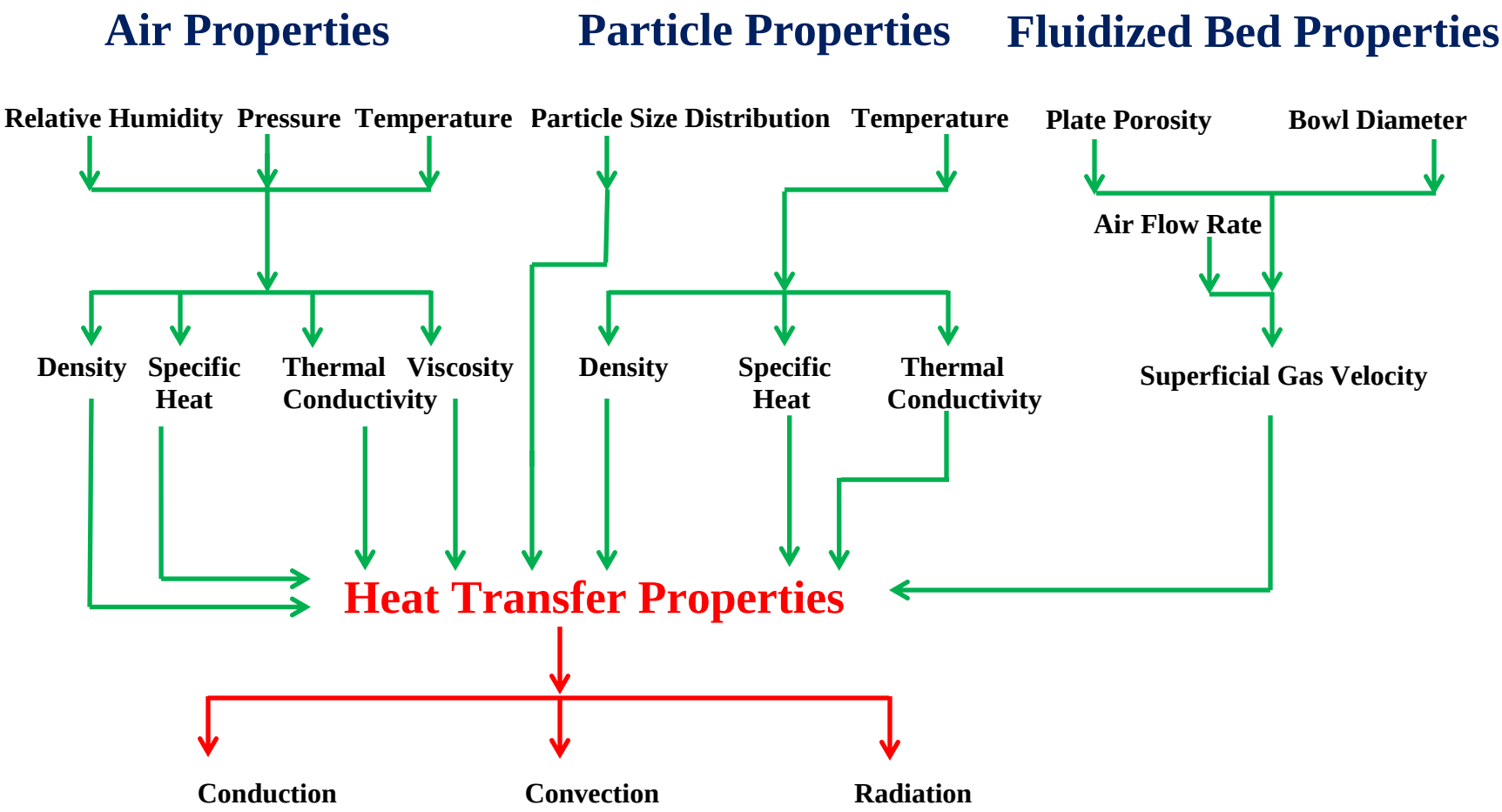

Figure 2.34 Heat Transfer Calculation Map

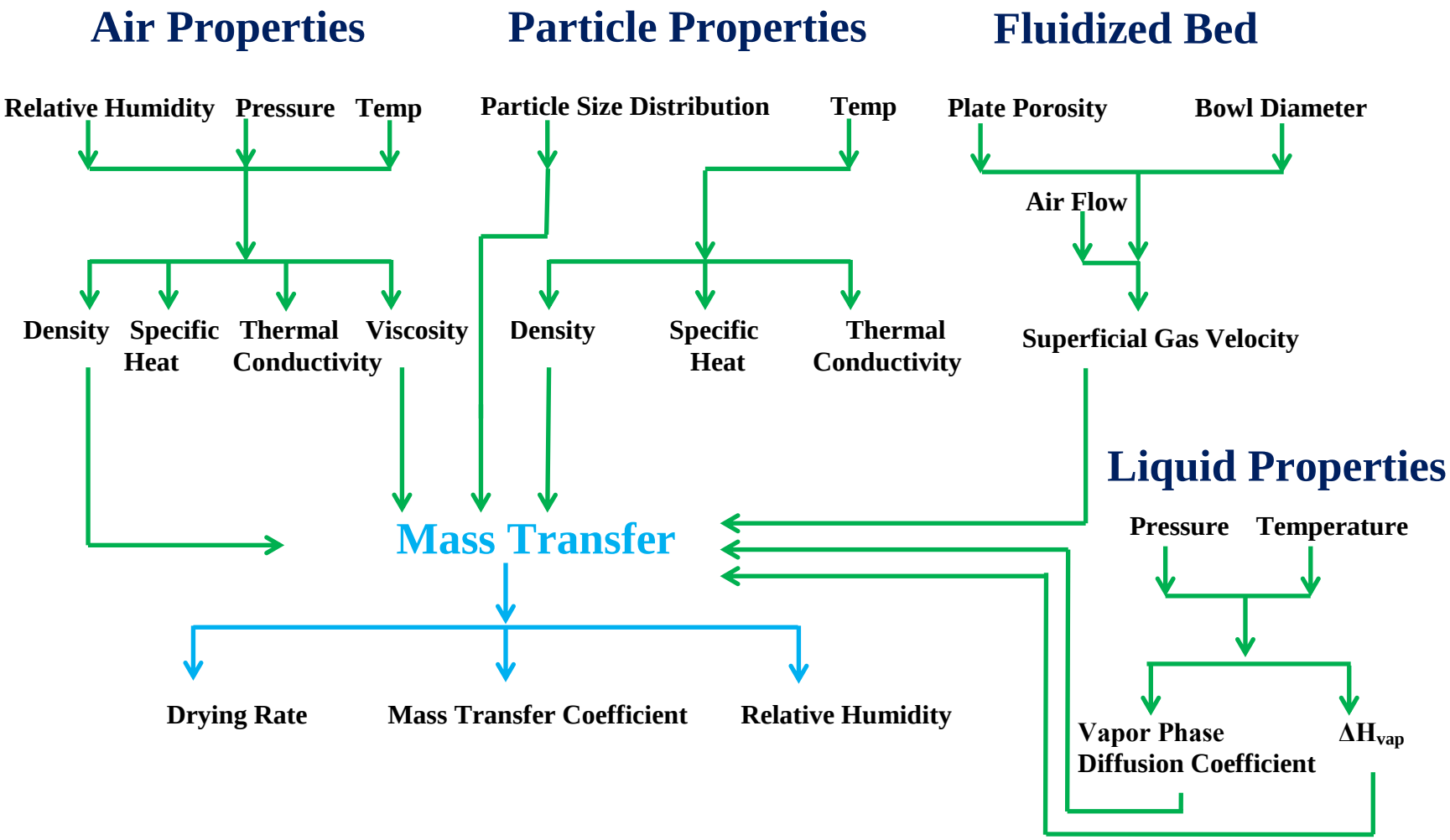

Figure 2.35 Mass Transfer Calculation Map

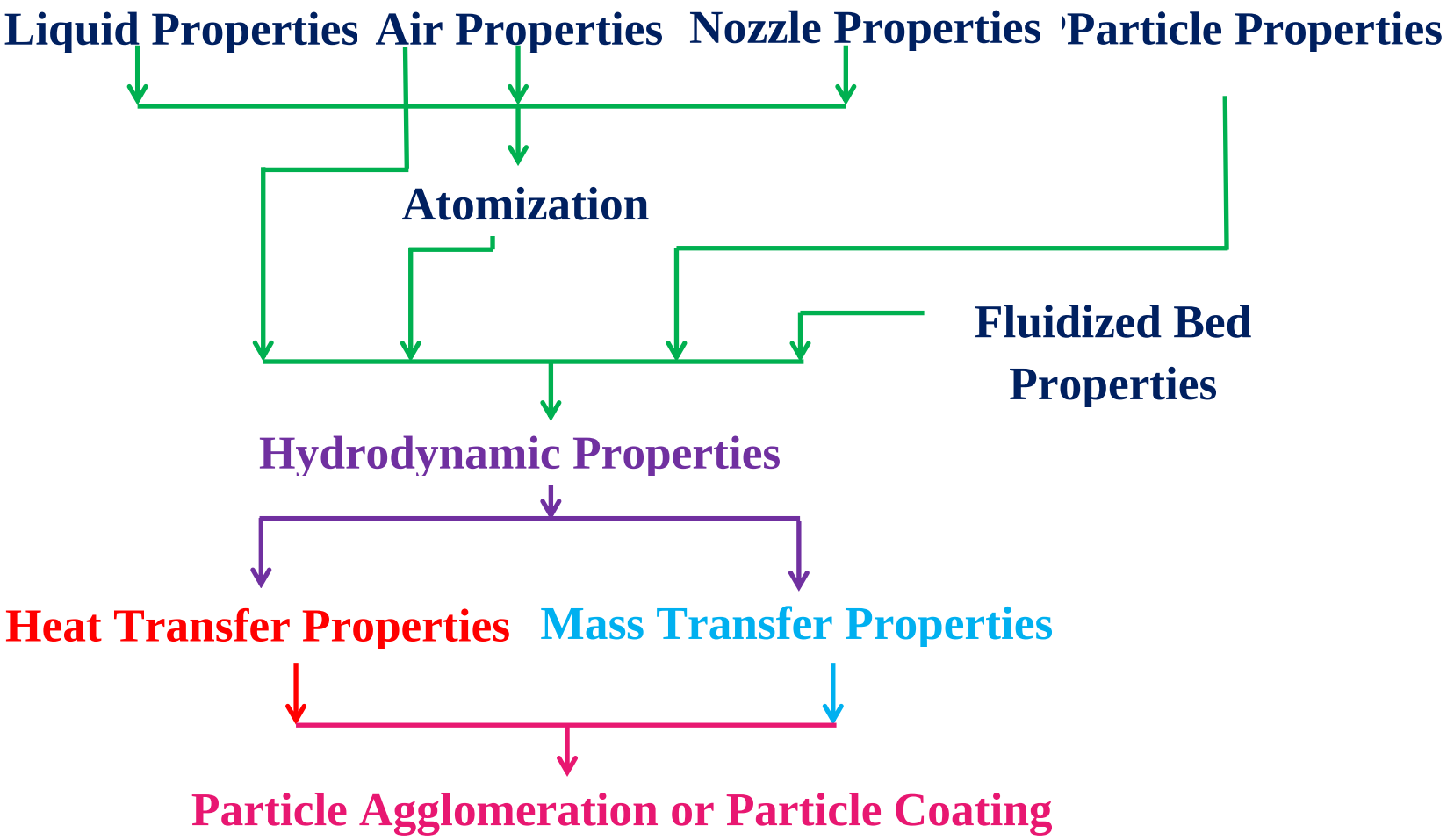

Figure 2.36 Combined Calculation Map

[9] Wurster, D.E. & Lindlof, J. (1965) U.S. Patent 3,196,827. Apparatus for the Encapsulation of Discrete Particles.

[10] Wurster, D.E., Lindlof, J., & Batlibla, J. (1965) U.S. Patent 3,207,824. Process for Preparing Agglomerates.

[11] Wurster, D.E. & Lindlof, J. (1966) U.S. Patent 3,241,520. Particle Coating Apparatus.

[12] Hall, H.S. & Pondell, R.E. (1980) Chapter 7: The Wurster Process. In Kydonis, A.F. (Ed) Controlled Release Technologies: Methods, Theory, and Applications Vol. 2 pp 133-154, Boca Raton: CRC Press.

[13] Maronga, S.J. & Wnukowski, P. (1998) The Use of Humidity and Temperature Profiles in Optimizing the Size of a Fluidized Bed in a Coating Process, Chemical Engineering and Processing: Process Intensification, 37 (5), 423-432.

[14] Smith, P.G. (2007) Applications of Fluidization to Food Processing, London: John Wiley & Sons.

[15] Kunii, D. & Levenspiel O. (1991) Fluidization Engineering. 2nd Edition, Massachusetts: Butterworth-Heinemann.

[16] Lefebvre, A. (1989) Atomization and Sprays, New York: CRC Press.

[17] Graco, Inc. (1995) Atomization: Concept and Theory Training, Minneapolis, MN.

[18] Hede, P., Boch, P., & Jensen, A.D. (2008) Two-Fluid Spray Atomization and Pneumatic Nozzles for Fluid Bed Coating/Agglomeration Purposes: A Review, Chemical Engineering Science, 63 (14), 3821-3842.

[19] Bete Fog Nozzles Inc. (2012) Spray Coverage Pamphlet, Greenfield, MA.

[20] Schick, R.J. (2008) Spray Technology Reference Guide: Understanding Drop Size. Spray Systems Co.

[21] Ashgriz, N. & Yarin, A.L. (2011) Chapter 1: Capillary Instability in Free Liquid Jets. In Ashgriz, N. (Ed.) Handbook of Atomization and Sprays: Theories and Applications, 1st Edition 3-54. New York: Springer.

[22] Çengel, Y.A. & Turner, R.H. (2001) Fundamentals of Thermal Fluid Sciences, Boston: MacGraw Hill.

[23] Kim, K.Y. & Marshall, W.R. (1971) Drop-Size Distributions From Pneumatic Atomizers, AIChE Journal, 17(3), 575-584.

[24] Nukiyama, S. & Tanasawa, Y. (1939) An Experiment on Atomization of Liquid – The Effect of the Properties of Liquid on the Size of Drops, Transactions of the Society of Mechanical Engineers, Japan, (JSME Journal), 18(5), 68-75.

[25] Nukiyama, S. & Tanasawa, Y. (1940) An Experiment on Atomization of Liquid – The Atomization Pattern of Liquid by Means of Air Stream, Transactions of the Society of Mechanical Engineers, Japan, (JSME Journal), 22(6), 7-15.

[26] Dewettinck, K. (1997) Fluidized Bed Coating in Food Technology: Process and Product Quality, Ph.D. Thesis, University of Ghent.

[27] Gretzinger, J., Marshall, W.R. (1961) Characteristics of Pneumatic Atomization, AIChE Journal, 7(2), 312-318.

[28] Wazel, P. (1993) Liquid Atomization, International Chemical Engineering, 33(1), 46-60.

[29] Groom, S., Schaldach, G., Ulmer, M., Wazel, P., Berndt, H. (2004) Adaptation of a New Pneumatic Nebulizer for Sample Introduction in ICP Spectrometry, Journal of Analytical Atomic Spectrometry, 20, 419-447.

[30] Mulhem, B., Fritsching, U., Schulte, G., Bauckhage, B. (2003) Effect of Solid Particle Characteristics on Suspension Atomization, Atomization and Sprays, 133, 321-343.

[31] Mulhem, B., Schulte, G., Bauckhage, B. (2006) Solid Liquid Separation in Suspension Atomization, Chemical Engineering Science, 61, 2582-2589.

[32] Ergun, S. (1952) Fluid Flow Through Packed Columns, Chemical Engineering Progress, 48, 89-94.

[33] Zenz, F.A. & Othmer, D.F. (1960) Fluidization and Fluid-Particle Systems, New York: Reinhold Publishing Corporation.

[34] Knowlton, T.M. (1986) Solids Transfer in Fluidized Systems. In Geldart, D. (Ed) Gas Fluidization Technology, (pp.341-414) Chichester: John Wiley & Sons.

[35] Geldart, D. (1986) Single Particles, Fixed and Quiescent Beds. In Geldart, D. (Ed) Gas Fluidization Technology, (pp.11-32) Chichester: John Wiley & Sons.

[36] Clift, R. & Grace, J.R. (1985) Continuous Bubbling and Slugging. In Davidson, J.F., Clift, R. & Harrison, D. (Eds.) Fluidization 2nd Edition. (pp. 73-132) Academic Press: London.

[37] Yerushalmi, J. & Avidan, A. (1986) High-Velocity Fluidization. In Geldart, D. (Ed) Gas Fluidization Technology. (pp.155-196) Chichester: John Wiley & Sons.

[38] Land, N.S. (1972) A Compilation of Nondimensional Numbers, NASA SP-274 (NASA Science Technology Information Office, Washington, D.C., USA.)

[39] Hall, C.W. (1992) Dimensionless Numbers and Groups for Drying, Drying Technology, 10(4), 1081-1095.

[40] Couderc, J.P. (1985) Incipient Fluidization and Particulate Systems. In Davidson, J.F. Clift, R. & Harrison, D. (Eds.) Fluidization 2nd Edition. (pp. 73-132) London: Academic Press.

[41] Sangeetha, V., Swathy, R., Narayanamurthy, N., Lakshmanan, C.M., & Miranda, L.R. (2000) Minimum Fluidization Velocity at High Temperatures Based on Geldart Powder Classification, Chemical and Engineering Technology, 23, 713-719.

[42] Babu, S.P., Shah, B., & Talwalkar, A. (1978) Fluidization Correlations for Coal Gasification Materials – Minimum Fluidization Velocity and Fluidized Bed Expansion Ratio, AIChE Symposium Series, 74, no. 176, 176-186.

[43] Bena, J. (1960) Vypocet Prahovej Rychlosti Fluidizacie, Chemchy Prumsyl, 10, 285-290.

[44] Baeyens, J. & Geldart, D. (1973) Proceedings of International Symposium on Fluidization, 263

[45] Bourgeois, P., & Grenier, P. (1968) The Ratio of Terminal Velocity to Minimum Fluidizing Velocity for Spherical Particles, Canadian Journal of Chemical Engineering, 46, 325-328.

[46] Broadhurst, T.E. & Becker, H.A. (1975) Onset of Fluidization and Slugging in Beds of Uniform Particles, AIChE Journal, 21, 238-247.

[47] Chitester, D.C., Kornosky, R.M., Fan, L.S., & Danko, J.P. (1984) Characteristics of Fluidization at High Pressure, Chemical Engineering Science, 39 (2), 253-261.

[48] Coltters, R. & Rivas, A.L. (2004) Minimum Fluidization Velocity Correlations in Particulate Systems, Powder Technology, 147, 34-48.

[49] Davies, L. & Richardson, J.F. (1966) Gas Interchange Between Bubbles and the Continuous Phase in a Fluidized Bed, Transactions of the Institute of Chemical Engineers, 44, T293-T305

[50] Davtyan, G.A., Ainshtein, V.G., Grigoran, R.V. & Amamchyeen, M.G. (1976) Izv. Akd. Nauk, Arm. SSR. Ser. Tekh. Nauk, 26, 36.

[51] Delebarre, A. (2004) Revisiting the Wen and Yu Equations for Minimum Fluidization Velocity Prediction, Chemical Engineering Research and Design, 82, 587-590.

[52] Doichev, K. & Akhmanov, N.S. (1979) Fluidisation of Polydisperse Systems, Chemical Engineering Science, 34, 1357-1359.

[53] Franz, J.F. (1966) Minimum Fluidization Velocities and Pressure Drop in Fluidized Beds, Chemical Engineering Progress Symposium Series, 62, 21-31.

[54] Ghosal, S.K. & Dutt, D.K. (1966) Indian Chemical Engineer Transactions, 3, 58.

[55] Ghosal, S.K. & Mukherjea, R.N. (1972) British Chemical Engineering, 17, 248.

[56] Grace, J.R. (1986) In Hetsroni, G. (Ed) Handbook of Multiphase Systems. Hemisphere Publishing Corp: Washington D.C.

[57] Ilavsky, J. & Bena, J. (1967) Determination of Minimum Fluidization Velocity of Polydispersed Systems, Chemicke Zvesti, 21, 877

[58] Leva, M., Shirai, T., & Wen, C.Y. (1956) Prediction of the Onset of Fluidization in Beds of Granular Solids, Genie Chim, 75, 33-42.

[59] Limas-Ballesteros, R. (1980) Ph.D. Dissertation, Institute National Polytechnique, Toulouse.

[60] Limas-Ballesteros, R., Riba, J.P., Couderc, J.P. (1982) Expansion de Couches de Particules Non Spheriques Fluidisees Par un Liquide, Entropie, 106, 37-45.

[61] Miller, C.O. & Logwinuk, A.K. (1961*)* Fluidization Studies of Solid Particles, Industrial & Engineering Chemistry Research, 43, 1220-1226.

[62] Nakamura, M., Hamada, Y., Toyama, S., Fouda, A.E., & Capes, C.E. (1985) Experimental Investigation of Minimum Fluidization Velocity at Elevated Temperatures, Canadian Journal of Chemical Engineering, 63, 8-13.

[63] Narsimhan, G. (1965) On a Generalized Expression for Prediction of Minimum Fluidizing Velocity, AIChE Journal, 11, 550-554.

[64] Pillai, B.C. & Raja Rao, M. (1971) Pressure Drop and Minimum Fluidization Velocities in Air-Fluidized Beds, Indian Journal of Technology, 9, 77-86.

[65] Riba, J.P. (1978) Ph.D. Dissertation. Institute National Polytechnique, Toulouse.

[66] Richardson, J.F. & Jeronimo, M.A.S. (1979) Velocity-Voidage Relations for Sedimentation and Fluidisation, Chemical Engineering Science, 34, 1419-1422.

[67] Rowe, P.N. & Henwood, G.A. (1961) Drag Forces in a Hydralic Model of a Fluidized Bed Part I, Transactions of the Institute of Chemical Engineers, 39, 43-54.

[68] Rowe, P.N. (1961) Drag Forces in a Hydralic Model of a Fluidized Bed Part II, Transactions of the Institute of Chemical Engineers, 39, 175.

[69] Sathyanarayana, K. & Rao, P.G. (1989) Minimum Fluidization Velocity at Elevated Temperatures, Indian Chemical Engineer, 31, 79-81.

[70] Saxena, S.C. & Vogel, G.J. (1977) The Measurement of Incipient Fluidisation Velocities in a Bed of Coarse Dolomite at Temperature and Pressure, Transactions of the Institute of Chemical Engineering, 55, 184-189.

[71] Subbaraju & Rao (1964) Indian Journal of Technology, 7, 222.

[72] Thonglimp (1981) Ph.D. Dissertation, Institue National Polytechnique, Toulouse.

[73] Thonglimp, V., Hiquily, N., & LaGuerie, C. (1984) Vitesse Minimale de Fluidisation et Expansion des Couches Fluidisees par un Gaz, Powder Technology, 38, 233-239.

[74] Todes, O.M., Goroshkov, V.D., & Rozenbaum, R.B. (1958) Approximate Hydralic Dependencies for Fluidized Bed and for Hindered Settling, Izvestilia Vysshikh Uchebnykh Zavedenil Neft' I Gaz, 1, 125-131.

[75] Wen, C.Y. & Yu, Y.H. (1966) A Generalized Method for Predicting the Mimimum Fluidizing Velocity, AIChE Journal, 12(3), 610-612.

[76] Zheng, Z.X., Yamazaki, R., & Jimbo, G. (1985) Minimum Fluidizing Velocity of Large Particles at Elevated Temperatures, Kagaku Kogaku Rombunsha, 11, 115.

[77] Sau, D.C., Mohanty, S., Biswal, K.C. (2007) Minimum Fluidization Velocities and Maximum Pressure Drops for Gas-Solid Tapered Fluidized Beds, Chemical Engineering Journal, 132, 151-157.

[78] Khani, M.H. (2011) Models for Prediction of Hydrodynamic Characteristics of Gas-Solid Tapered and Mini-Tapered Fluidized Beds, Powder Technology, 205 (1-3), 224-230.

[79] Peng, Y. & Fan L.T. (1997) Hydrodynamic Characteristics of Fluidization in Liquid-Solid Fluidized Beds, Chemical Engineering Science, 52 (14), 2277-2290.

[80] Gupta, C.K. & Sathiyamoorthy, D. (1999) Fluid Bed Technology in Materials Processing. Boca Raton: CRC Press.

[81] Holdich, R. (2002) Fundamentals of Particle Technology, United Kingdom: Midland Information Technology and Publishing.

[82] Smolders, K. & Baeyens, J. (2001) Gas Fluidized Bed Operating at High Velocities: A Critical Review of Occurring Regimes. Powder Technology, 119, 269-291.

[83] Hartman, M., Beran, Z., Svoboda, K. & Vesely, V. (1995) Operation Regimes of Fluidized Beds, Collection of Czechoslovakia Chemical Communications. 60, 1-33.

[84] Geldart, D. (1972) The Effect of Particle Size and Size Distribution on the Behavior of Gas-Fluidized Beds, Powder Technology, 6, 201-215.

[85] Molerus, O. (1982) Interpretation of Geldart's Type A, B, C, and D Powders by Taking Into Account Interparticle Cohesion Forces, Powder Technology, 33, 81-87.

[86] Clark, N.N., Van Egmond, J.W., & Turton, R. (1988) A Numerical Representation of Geldart's Classification, Powder Technology, 225-226.

[87] Saxena, S.C. & Ganzha, V.L. (1984) Heat Transfer to Immersed Surfaces in Gas-Fluidized Beds of Large Particles and Powder Characterization, Powder Technology, 39, 199-208.

[88] Yang, W.C. (2007) Modification and Re-Interpretation of Geldart's Classification of Powders, Powder Technology, 171, 69-74.

[89] Karimipour, S. & Pugsley, T. (2011) A Critical Evaulation of Literature Correlations for Predicting Bubble Size and Velocity in Gas-Solid Fluidized Beds, Powder Technology, 205, 1-14.

[90] Davidson, J.F. & Harrison, D. (1963) Fluidized Particles, Cambridge University Press: New York.

[91] Toomey, R.J. & Johnstone, H.F. (1952). Gaseous Fluidization of Solid Particles. Chemical Engineering Progress, 48, 220-226.

[92] Mori, S. & Wen, C.Y. (1975) Estimation of Bubble Size in Gaseous Fluidized Beds, AIChE Journal, 21, 109-115.

[93] Darton, R.C., LaNauze, D.C., Davidson, J.F., & Harrison, D (1977) Bubble Growth Due to Coalescence in Fluidized Beds, Transactions of the Institute of Chemical Engineers, No. 55, 274-280.

[94] Wallis, G.B. (1969) One-Dimensional Two-Phase Flow, McGraw-Hill: New York.

[95] Baeyens, J. & Geldart, D. (1986) Chapter 5: Solids Mixing in D. Geldart (Ed) Gas Fluidization Technology, 97-122, John Wiley & Sons: New York.

[96] Rowe, P.N. (1972) Estimation of Solids Circulation Rate In Bubbling Fluidized Bed, Chemical Engineering Science, 28, 979-980.

[97] Rhodes, M. (2001) Educational Resources for Particle Technology, Monash University: Melbourne Australia.

[98] Sau, D.C., Mohanty, S., Biswal, K.C. (2010) Experimental Studies and Empirical Models for the Prediction of Bed Expansion in Gas-Solid Tapered Fluidized Beds, Chemical Engineering and Processing: Process Intensification, 49(4), 418-424.

[99] Cronin, K., Çatak, M., Tellez-Medina, D., Cregan, V., O'Brien, S. (2010) Modeling of Particle Motion in an Internal Re-Circulatory Fluidized Bed, Chemical Engineering Journal, 164, 403-409.

[100] Holman, J.P. (1976) Heat Transfer 4th Edition. New York: McGraw Hill

[101] Achenbach, E. (1978) Heat Transfer From Spheres Up to Re = 6 x 106, Proceedings of 6th International Heat Transfer Conference, 5, Washington D.C.: Hemisphere.

[102] Agarwal, P. (1988) Transport Phenomena in Multi-Particle Systems II: Particle-Fluid Heat and Mass Transfer, Chemical Engineering Science, 43 (9), 2501-2510.

[103] Gunn, D.J. (1978) Transfer of Heat or Mass to Particles in Fixed and Fluidized Beds, International Journal of Heat Transfer, 21 (4), 467-476.

[104] Li, J. & Mason, D.J. (2000) A Computational Investigation of Transient Heat Transfer in Pneumatic Transport of Granular Particles, Powder Technology, 112 (3), 273-282.

[105] Molerus, O. (1992) Heat Transfer in Gas Fluidized Beds I, Powder Technology, 70 (1), 1-14.

[106] Ranz, W.E. & Marshall, W.R. (1952) Evaporation From Drops, Chemical Engineering Progress, p173.

[107] Whitaker, S. (1972) Forced Convection Heat Transfer Correlations for Flow in Pipes, Past Flat Plates, Single Cylinders, Single Spheres, and For Flow in Packed Beds and Tube Bundles, AIChE Journal, 18, 361-371.

[108] Hines, A.L. & Maddox, R.N. (1985) Mass Transfer: Fundamentals and Applications, Prentice Hall: New Jersey.

[109] Basu, P. & Halder, P.K. (1988) Mass Transfer From a Coarse Particle to a Fast Bed of Fine Solids, AIChE Symposium, 84, 58-67.

[110] Frosling, N. (1938) The Evaporation of Falling Drops, Gerlands Beitr. Geophys, 170-216.

[111] Gunn, D.J. (1978) Transfer of Heat or Mass to Particles in Fixed or Fluidized Beds, International Journal of Heat and Mass Transfer, 21, 467-476.

[112] Hayhurst, A.N. & Parmar, M.S. (2002) Measurement of the Mass Transfer Coefficient and Sherwood Number for Carbon Spheres Burning in a Bubbling Fluidized Bed, Combustion and Flame, 130 (4), 361-375.

[113] Hsiung, T.H. & Thodos, G. (1977) Mass Transfer in Gas Fluidized Beds: Measurement of Driving Forces, Chemical Engineering Science, 32, 581-592.

[114] Kumar, H.B. & Sublette, K.L. (1993) Effect of High Voidage on Mass Transfer Coefficient in a Fluidized Bed, Chemical Engineering Communication, 121, 157-163.

[115] Romkes, S.J.P., Dautzenberg, F.M., van der Bleek, C.M., & Calis, H.P.A. (1993) CFD Modelling and Experimental Validation of Particle to Fluid Mass and Heat Transfer in a Packed Bed at Very Low Channel to Particle Diameter Ratio, Chemical Engineering Journal, 96 (1-3), 3-13.

[116] Rowe, P.N., Klaxton, K.T., & Lewis, J.B. (1965) Heat and Mass Transfer From a Single Sphere in an Extensive Flowing Fluid, Transactions of the Institute of Chemical Engineers, 43, 14-31.

[117] Scala, F. (2007) Mass Transfer Around Freely Moving Active Particles in the Dense Phase of a Gas Fluidized Bed of Inert Particles, Chemical Engineering Science, 62 (16), 4159-4176.

[118] Subbarao, D. & Gambhir, S. (2002) Gas to Particle Mass Transfer in Risers, Proceedings of 7th International Circulating Fluidized Beds Conference, Canadian Society for Chemical Engineering, Niagara Falls, 97-104.

[119] Hristov, J. (2002) Magnetic Field Assisted Fluidization – A Unified Approach: Part 1. Fundamentals and Relevant Hydrodynamics of Gas-Fluidized Beds (Batch Solids Mode), Reviews in Chemical Engineering, 18, 295-509.

[120] Hristov, J. (2003) Magnetic Field Assisted Fluidization – A Unified Approach: Part 2. Solids Batch Gas-Fluidized Beds: Versions and Rheology, Reviews in Chemical Engineering, 19, 1-132.

[121] Hristov, J. (2003) Magnetic Field Assisted Fluidization – A Unified Approach: Part 3. Heat Transfer in Gas-Solid Fluidized Beds – A Critical Re-evaluation of the Results, Reviews in Chemical Engineering, 19, 229-355.

[122] Hristov, J. (2004) Magnetic Field Assisted Fluidization – A Unified Approach: Part 4. Moving Gas-Fluidized Beds, Reviews in Chemical Engineering, 20, 377-550.

[123] Ennis, B.J., Tardos, G. & Pfeffer R. (1991) A Microlevel-Based Characterization of Granulation Phenomena, Powder Technology, 65, 257-272.

[124] Darabi, P., Pougatch, K., & Salcudean, D. (2011) DEM Investigations of Fluidized Beds in the Presence of Liquid Coating, Powder Technology, 214, 365-374.

[125] Mangwandi, C., Cheong, Y.S., Adams, M.J., Hounslow, M.J., & Salman, A.D. (2007) The Coefficient of Restitution of Different Representative Types of Granules, Chemical Engineering Science, 62, 437-450.

[126] Lazghab, M., Saleh, K., Pezron, I., Guigon, P. & Komunjer, L. (2005) Wettability Assessment of Finely Divided Solids, Powder Technology, 157, 79-91.

[127] Clarke, A., Blake, T.D., Carruthers, K., & Woodward, A. (2002*)* Spreading and Imbibition of Liquid Droplets on Porous Surfaces, Langmuir, 18, 2980-2984.

[128] Thielmann, F., Naderi, M., Ansari, M.A., & Stepanek, F. (2008) The Effect of Primary Particle Surface Energy on Agglomeration Rate in Fluidized Bed Wet Granulation, Powder Technology, 181, 160-168.

[129] Barnocky, G. & Davis, R.H. (1988) Elastohydrodynamic Collision and Rebound of Spheres: Experimental Verification, Physics of Fluids, 31 (6), 1324-1329.

[130] Tardos, G., Irfan Khan, M., Mort, P.R. (1997) Critical Parameters and Limiting Conditions in Binder Granulation of Fine Powders, Powder Technology, 94(3) 245-258.

[131] Liu, L.X., Lister, J.D., Iveson, S.M., & Ennis, B.J. (2000*)* Coalescence of Deformable Granules in Wet Granulation Processes, AIChE Journal, 46 (3), 529-539.

[132] Ennis, B.J. (1991) Ph.D. Dissertation, On the Mechanics of Granulation, City College New York.

[133] Iveson, S., & Lister, J.D. (1998) Growth Regime Map for Liquid-Bound Granules, AIChE Journal, 44 (7), 1510-1518.

[134] Akkermans, J.H.M., Edwards, M.F., Groot, A.T.J., Montanus, C.P.M., Van Pomeren, R.W.J., & Yuregir, K.R. (1998) Production of Detergent Granules, Patent WO98/58046.

[135] Boerefijn, R. & Hounslow, M.J. (2005) Studies of Fluidized Bed Granulation in an Industrial R&D Context, Chemical Engineering Science, 60, 3879-3890.

[136] Wasserman, M.I., Ridyard, M.W., Capeci, S.W., Beimesch, W.E., & Mort, P.R. (2000) Process For Coating Detergent Granules in a Fluidized Bed, Patent WO00/78912A1.

[137] Achanta, S. & Beimesch, W.E. (1999) Process For Making a Low Density Detergent Composition by Controlled Agglomeration in a Fluidized Bed Dryer. Patent WO99/03964.

[138] Lister, J.D., Hapgood, K.P., Michaels, J.N., Sims, A., Roberts, M., Kameneni, S.K., & Hsu, T. (2001) Liquid Distribution in Wet Granulation: Dimensionless Spray Flux, Powder Technology, 114, 32-39.

[139] Hapgood, K.P., Lister, J.D., & Smith, R. (2003) Nucleation Regime Map for Liquid Bound Granules, AIChE Journal, 49 (2), 350-361.

[140] Hede, P.D., Boch, P., Jensen, A.D. (2009a) Fluidized Bed Coating With Sodium Sulfate and PVA-TiO2, 1: Review and Agglomeration Regime Maps, Industrial Engineering and Chemistry Research, 48 (4), 1893-1904.

[141] Hede, P.D., Boch, P., Jensen, A.D. (2009b) Fluidized Bed Coating With Sodium Sulfate and PVA-TiO2, 2: Influence of Coating Solution Viscosity, Stickiness, pH, and Droplet Diameter on Particle Agglomeration, Industrial Engineering and Chemistry Research, 48 (4), 1905-1913.

[142] Hede, P.D., Boch, P., Jensen, A.D. (2009c) Fluidized Bed Coating With Sodium Sulfate and PVA-TiO2, 3: The Role of Tackiness and the Tack Stokes Number, Industrial Engineering and Chemistry Research, 48 (4), 1914-1920.

[143] Hede, P.D., Boch, P., Jensen, A.D. (2008) Top Spray Fluid Bed Coating Scale Up in Terms of Relative Drop Size and Drying Force, Powder Technology, 184, 318-332.

[144] Rambali, B., Baert, L., & Massart, D.L. (2003) Scaling Up of the Fluidized Bed Granulation Process, International Journal of Pharmaceutics, 252, 197-206.

[145] Gidaspow, D. (1994) Multiphase Flow and Fluidization: Continuum and Kinetic Theory Descriptions, Boston: Academic Press.

[146] Gantt, J.A. & Gatzke, E.P. (2006) Kinetic Theory of Granular Flow Limitations for Modeling High-Shear Mixing, Industrial Engineering and Chemistry Research, 45, 6721-6727.

[147] Savage, S.B. (1983) Granular Flows at High Shear Rates in R.E. Meyer (Ed.) Theory of Disperse Multiphase Flow. New York: Academic Press.

[148] Huang, X. & Liu, Z. (2008) Granular Temperature in Bubbling Fluidized Beds, Chemical Engineering Technology, 31 (9), 1358-1361.

[149] Chapman, S. & Cowling, T.G. (1970) The Mathematical Theory of Non-Uniform Gases, London: Cambridge University Press.

[150] Rahaman, M.F. & Naser, J. (2001) Effect of Unequal Granular Temperature on Number of Collision and Dilute Viscosity of Kinetic Theory, 14th Australasian Fluid Mechanics Conference, Adelaide University.

[151] Fan, L.S. & Zhu, C. (2005) Principles of Gas-Solid Flows. London: CambridgeUniversity Press.

[152] Terrazas-Velarde, K., Peglow, M. & Tsotsas, E. (2009) Stochastic Simulation of Agglomerate Formation in Fluidized Bed Spray Drying: A Micro-Scale Approach. Chemical Engineering Science, 64, 2631-2643.

[153] Buffière, P. & Moletta, R. (2000) Collision Frequency and Collisional Particle Pressure in Three-Phase Fluidized Beds, Chemical Engineering Science, 55, 5555-5563.

[154] Loeffler, F. (1988) Staubabscheiden, Thieme Verlag, Stuttgart & New York.

[155] Mundo, C., Sommerfield, M. & Tropea, C. (1995) Droplet-Wall Collisions: Experimental Studies of the Deformation and Breakup Process, International Journal of Multiphase Flow, 21 (2), 151-173.

[156] Li, Z., Kind, M., & Gruenewald, G. (2009) Modeling the Fluid Dynamics and the Growth Dynamics of Fluid Bed Spray Granulation, Seventh International Conference on CFD in the Minerals and Process Industries. Melbourne, Austrailia.

[157] Ronsse, F., Pieters, J.G., & Dewettinck, K. (2008) Modeling Side-Effect Spray Drying in Top Spray Fluidized Bed Coating Processes, Journal of Food Engineering, 86, 529-541.

[158] Zank, J., Kind, M. & Schlünder, E.-U., (2001) Particle Growth and Droplet Deposition in Fluidized Bed Granulation, Powder Technology, 120 (1), 76-81.

[159] Buchanan, J.S. (1994) Analysis of Heating and Vaporization of Feed Droplets in Fluidized Catalytic Cracking Risers, Industrial Engineering and Chemistry Research, 33, 3104-3111.

[160] Erbil, H.Y., McHale, G., & Newton, M.I. (2002) Drop Evaporation on Solid Surfaces: Constant Contact Angle Mode, Langmuir, 18, 2636-2641.

[161] Roy, P., Khanna, R., & Subbarao, D. (2010) Granulation Time in Fluidized Bed Granulators, Powder Technology, 199, 95-99.

[162] Dewettinck, K. & Huyghebaert, A. (1998) Top-Spray Fluidized Bed Coating: Effect of Process Variables on Coating Efficiency, Lebensm.-Wiss. u.-Technol., 31 568-575.

[163] Saleh, K., Cherif, R., & Hemati, M. (1999) An Experimental Study of Fluidized Bed Coating: Influence of Operating Conditions on Growth Rate and Mechanism, Advanced Powder Technology, 10 (3), 255-277.

[164] Cheng, X. X. & Turton, R. (2000a) The Prediction of Variability Occuring in Fluidized Bed Coating Equipment. I. The Measurement of Particle Circulation Rates in a Bottom-Spray Fluidized Bed Coater, Pharmaceutical Development and Technology, 5, No. 3, 311-322.

[165] Cheng, X. X. & Turton, R. (2000b) The Prediction of Variability Occuring in Fluidized Bed Coating Equipment. II. The Role of Nonuniform Particle Coverage as Particles Pass Through the Spray Zone, Pharmaceutical Development and Technology, 5, No. 3, 323-332.

[166] Hemati, M., Cherif, R., Saleh, K., & Pont, V. (2003) Fluidized Bed Coating and Granulation: Influence of Process Related Variables and Physicochemical Properties on the Growth Kinetics, Powder Technology, 130, 18-34.

[167] KuShaari, K., Pandey, P., Song, Y., & Turton, R. (2006) Monte Carlo Simulations to Determine Coating Uniformity in a Wurster Fluidized Bed Coating Process, Powder Technology, 166 (2), 81-90.

CHAPTER 3

MODELING APPROACHES TO FLUIDIZED BED COATING

The purpose of this chapter is to provide a description of the different approaches applied to modeling fluidized bed coating processes. The different classifications of models – empirical and mechanistic will be presented. Previous coating growth kinetic models will also be given. The strengths and limitations of the empirical and mechanistic approaches will be discussed.

3.1 Model Classification

Modeling approaches to fluidized bed coating can be classified into two categories, empirical and mechanistic. Empirical models involve fitting experimental data (recorded parameters) and the response variable together in the form of a mathematical equation through linear or non-linear regression with a design of experiments approach (DOE). However, despite providing quantitative analysis, empirical models often have no physical meaning, i.e. little to no information can be ascertained from the model regarding how or why the model parameters impact the response variable [1]. The typical procedure to developing an empirical model is as follows: 1). Collect data 2). Specify response variable relationship with recorded parameters 3). Regress data and develop fitted equation 4). Validate the model. If the model is not validated with the parameters chosen, then a new relationship should be specified and regressed between model parameters and the response variable until a valid or acceptable fit is found [2].

Mechanistic models on the other hand involve the application of fundamental laws (e.g. Newton's law of gravitation, the ideal gas law, the four laws of thermodynamics) mass, energy,

and momentum balances, and simplifying assumptions (e.g. isothermal/adiabatic temperature, incompressible flow, ideal gas, perfect spherical shape, etc.) within a modeling framework [2]. The procedure to developing a mechanistic model is similar to the empirical model development, except prior to collecting data, the fundamental laws are applied to the situation of interest a priori [2].

3.1.1 Further Classification of Mechanistic Models

Mechanistic models can be further classified as deterministic or stochastic. Deterministic models have mathematical equations to determine the values of interest. There is no randomness involved in a deterministic model. A deterministic approach can be used to model particle level phenomena -e.g. particle coalescence (agglomeration) or particle rebound (coating), computational fluid dynamics (CFD) simulations, and particle coating growth.

A stochastic model on the other hand describes a phenomenon in terms of a probability distribution, thus allowing for randomness to be present in the modeling description. The stochastic modeling approach involves using population balance equations when distributions are known and Monte Carlo analysis when distributions are not necessarily known. Figure 3.1 shows the calculation flow and general result trend of mechanistic models.

3.2 Empirical Models

Empirical models represent the simplest approach to fluidized bed coating in part because the modeling involves regressing independent variables to a response parameter of interest. The empirical model approach is often called the “black box” approach because there are no equations that describe the actual physical phenomena (see Figures 2.32-2.36 in Chapter 2) that occur during the fluidized bed coating operation [3].

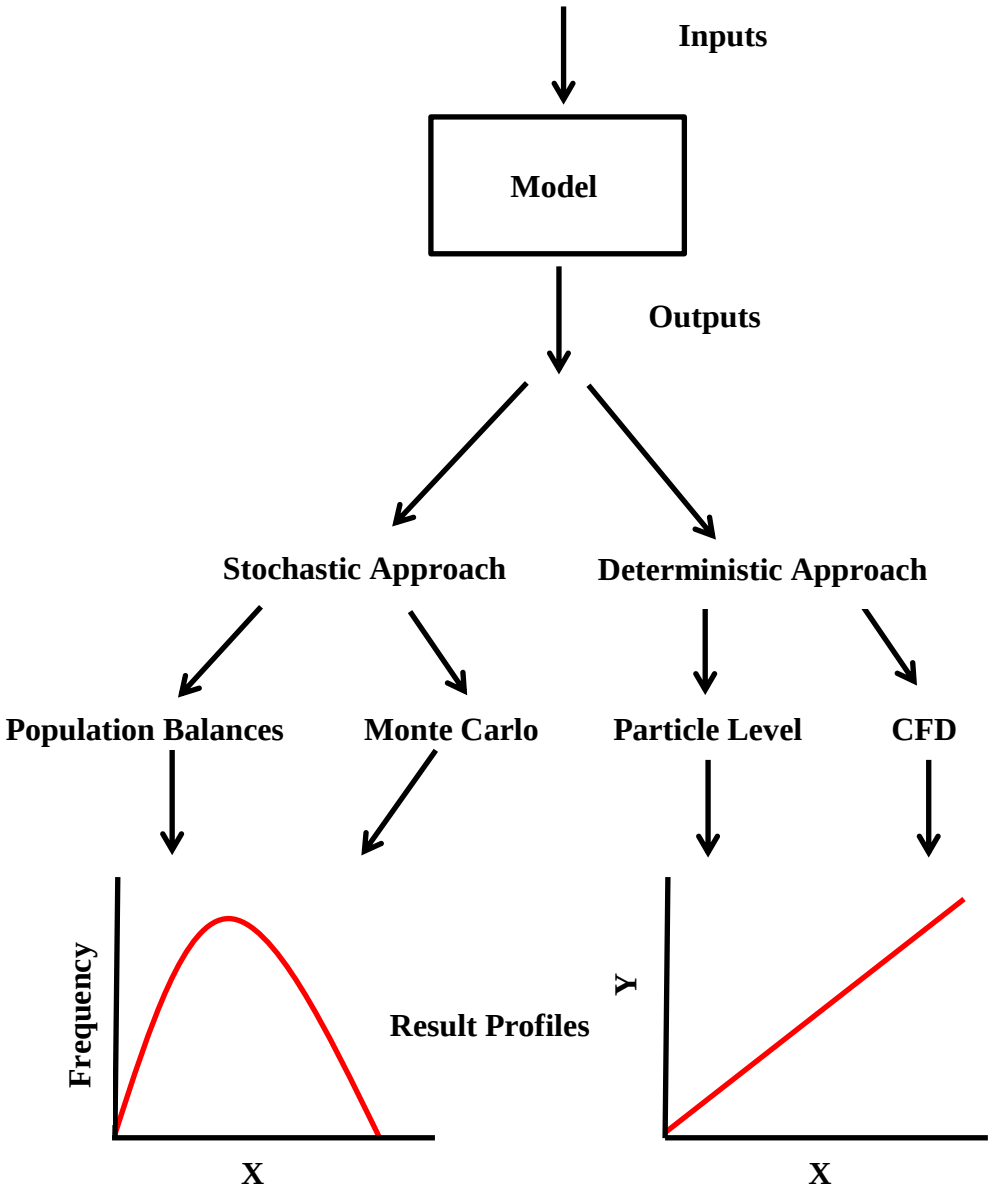

Figure 3.1 Mechanistic Model Calculation Flow

There are a few different approaches to empirical modeling including: factorial design, artificial neuron networks (ANN), and evolutionary algorithms. As noted previously, there is flexibility in the choice of independent and response variables for modeling purposes when using an empirical approach. In the case of fluidized bed coating or fluidized bed agglomeration

operations there are several choices for independent (or measurable) variables, shown in Table 3.1, and response parameters, shown as Table 3.2.

Table 3.1 Potential Independent Measureable Variables for Empirical Fluidized Bed Models

Fluidization Air	
Flow Rate	Inlet Temperature
Inlet Relative Humidity	Velocity
Atomization Air	
Flow Rate	Pressure
Inlet Relative Humidity	Velocity
Inlet Temperature	
Liquid Coating Solution	
Concentration	Temperature
Flow Rate	Velocity
Particles	
Batch Size	Initial Surface Area
Initial Particle Size Distribution	Initial Surface Roughness
Initial Porosity	
Nozzle	
Distance From Distributor Plate	
Fluidized Bed	
Geometry	Height During Operation
Pressure Drop	
Wurster Orientation Additional Parameters	
Partition Gap Height	

Table 3.2 Potential Response Parameters for Empirical Fluidized Bed Models

Agglomeration Percentage/Tendency	Fluidized Bed Temperature
Angle of Repose	Particle Flowability
Breakage Percentage/Tendency	Particle Friability
Bulk Density	Particle Porosity
Coating Efficiency	Particle Shape
Coating Thickness/Relative Particle Growth	Particle Size Distribution
Coating Uniformity/Concentration	Particle Surface Area
Dissolution/Reaction Rate	Particle Surface Roughness
Fluidized Bed Relative Humidity	pH

Tables 3.1 and 3.2 reiterate the flexibility of choice regarding which measureable variables can be tracked and the response parameters that can be potentially modeled.

3.2.1 Factorial Design Empirical Modeling

One approach to empirical modeling is factorial design. Factorial design is typically employed to quantify the impact of two or more factors (x_1, x_2, …x_n) on a response parameter (y). Factorial design involves performing a series of experiments where the independent variables are varied simultaneously versus individually. When several factors are of interest, a 2^k or 3^k factorial experimental design can be used, depending on the number of levels-value magnitude (high and low or high, medium, and low) of the independent variables (Montgomery 2005). The result of a factorial analysis is a regressed equation relating the response parameter to the factors of interest (x_1, x_2, …x_n) as shown in Equation 3.1:

$$y = \beta_0 + \beta_1 x_1 + \beta_2 x_2 + \beta_3 x_1 x_2 + \beta_n x_n^a \qquad (3.1)$$

A 3-D plot of Equation 3.1 is called a response surface plot. A 2-D plot Equation 3.1 plotted at constant y values is called a contour plot [1]. Figure 3.2 shows an example of response surface plot and a contour plot that can be generated from a factorial experimental design.

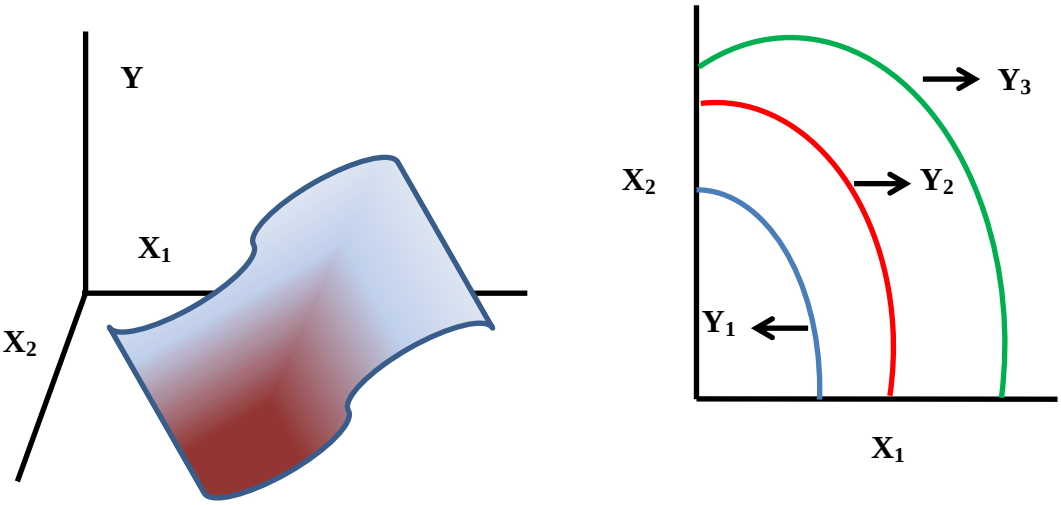

a). b).

Figure 3.2 Examples of a) Response Surface Plot and b) Contour Plot

While factorial experimental design offers insight into which factors have an impact on fluidized bed particle coating there are a few drawbacks of which to be aware. The number of experiments needed for statistical analysis increases exponentially with the number of factors to be tested. Each factor is tested at two (2^k) or three (3^k) levels which increases the total number of experiments that must be done. For example, if there are four factors of interest, at two levels 16 (2^4) experiments must be done, while at three levels 81 (3^4) experiments must be done. Orthogonal analysis or center point analysis allows for a minimization of the necessary number of experiments needed. However, in exchange for minimizing the number of experiments needed, very specific conditions must be implemented in the experiment design [1].

In addition to the exponential increase in the number of experiments, no fundamental explanation for why which factors are or are not significant in fluidized bed particle coating can be ascertained from the regressed equation. This fact limits the predictive power of the regressed equation to just the range of conditions tested with the factorial experiment design.

3.2.1.1 Fluidized Bed Factorial Design Empirical Models

Several researchers have published factorial design empirical models for fluidized bed particle coating, particle granulation, or spray drying as shown in Table 3.3. Factorial design empirical models offer great flexibility with the choice of dependent and independent variables. Furthermore, empirical models can be amended quickly and easily with the advent of additional data.

Table 3.3 Previously Published Fluidized Bed Factorial Design Empirical Models

Reference	Independent Variables	Response Variable(s)	Empirical Relationship
Particle Coating			
[4]	Coating Solution Concentration Fluidization Air Pressure Inlet Air Temperature Spray Rate Talc Filler Addition	Dissolution Time for 50% Dissolved (T50) Mean Particle Diameter	Not Reported
[5]	Fluidization Air Velocity Inlet Air Temperature Nozzle Distance From Bed Spray Rate	Yield Percentage Agglomeration Percentage	Presented as Significant or Not Significant
[6]	Atomization Air Pressure Atomization Air/Coating Temperature Coating Flow Rate	Bulk Density (BD) Content Uniformity (CU) Dissolution Percentage Acidic pH (DP_1) Dissolution Percentage Neutral pH (DP_2) Drug Percentage (DP_3) Flowability (F) Particle Size (PS) Tapped Density (TD)	$BD = 0.635+0.016P_{at}$ $CU = 1.38 - 0.19T_{at} + 0.18V + 0.34P_{at} -0.3T_{at}V - 0.25T_{at}P_{at} + 0.23VP_{at} - 0.27T_{at}$ $DP_1 = 51.5 - 7.5V + 8.5P_{at} -9T_{at}P_{at}V$ $DP_2 = 53.1 - 7.4V + 8.3P_{at} -7.1T_{at}P_{at}V$ $DP_3 = 13.45 + 0.1V - 0.18P_{at} + 0.1T_{at}P_{at} - 0.35P_{at}^2$ $F = 13.1 + 1.6P_{at}^2$ $PS = 104.1 + 4.23V - 10.64P_{at} + 4.13T_{at}P$ $TD = 0.735 - 0.1V + 0.27P_{at} - 0.05T_{at}P_{at}V - 0.009P_{at}^2$

Table 3.3 Continued

[7]	Atomization Pressure Inlet Air Temperature Volume Weighed Particle Diameter	Fluidized Bed Temperature (TB) Deposited Coating Mass (WC)	$TB = -1.07 - 1.1552P_{at} + 0.62281T_{in}$ $WC = -56.68 - 0.012d_p + 1.24P_{at} + 2.05T_{in} - 0.014T_{in}^2$
[8]	Fluidization Velocity Outlet Air Temperature Plasticizer Level Spray Rate	First Order Rate Constant Coating Efficiency	Not Reported
[9]	Air Temperature Atomization Air Pressure Coating Flow Rate Fluidization Air Pressure Particle Diameter	Coating Efficiency (CE) Relative Particle Growth (RPG)	$CE = 77.8 - 7P_{at} - 1.8T_{air} + 2.9d_p + 22d_pP_{at} - 2.8W_sT_{air} + 3.6P_{air}W_sT_{air} + 2P_{at}W_sd_p$ $RPG = 11.8 - 0.8P_{at} + 0.3W_s - 0.3T_{air} + 0.5d_p + 0.3P_{at}T_{air} + 0.3P_{air}d_p + 0.4P_{at}W_sd_p$
[10]	Batch Load Coating Solution Viscosity Coating Spray Time	Coating Efficiency (CE)	$CE = 76.35 - 544\left(\frac{L - 140}{40}\right)$
[11]	Atomization Air Pressure Coating Concentration Fluidized Bed Temperature Fluidization Velocity	Agglomeration Tendency (AG) Particle Breakage Percentage (Br)	$AG = 245.5 - 81.1P_{at} - 7.4C + 2.5P_{at}C$ $Br = 35.7 - 1.7P_{at} - 0.2C - 0.3T_{bed}$
[12]	Frequency (rpm) Particle Diameter Coating Flow Rate	Drug Dissolution Percentage at 4 hours and 8 hours	$L_4 = 37.2 - 7.35V - 13.3d_p - 1.67Vf$ $L_8 = 59.0 - 7.50V - 14.2d_p - 1.59Vf$

Table 3.3 Continued

[13]	Drug-Polymer Ratio (DPR) Coating Flow Rate	Encapsulation Efficiency (EE) Particle Size (PS) Percent Yield (PY)	$EE = 84.96 + 8.05(DPR) - 2V - 0.67(DPR)^2 + 3.341V^2 + 0.64(DPR)(V)$ $PS = 25.58 + 2.83(DPR) + 4.79V - 0.32(DPR)^2 + 1.33V^2 - 2.2(DPR)(V)$ $PY = 36.79 + 12.79(DPR) - 2.4V + 0.65(DPR)^2 + 3.75V^2 - 0.25(DPR)(V)$
[14]	Fluidization Air Temperature Coating Solution Volumetric Flow Rate	Coating Efficiency Percent Agglomeration	Not Given
Particle Agglomeration/Granulation			
[15]	Povidone Concentration Dry Binder Addition Rate Atomization Pressure Inlet Fluidization Air Temperature Solution Spray Rate	Particle Size Crushing Strength	Multiple Factors and Interactions Found to be Significant
[16]	Inlet Fluidization Air Temperature Atomization Air Pressure Fluidization Air Volumetric Flow Rate Binder Solution Spray Rate	Bulk Density Tapped Density Particle Size Distribution for Dried, Milled, and Unlubricated Granulation Particle Compressibility Tablet Disintegration Time and Dissolution	Atomization Air Pressure and Binder Solution Spray Rate Determined to be Most Significant Factors

Table 3.3 Continued

[17]	Microcrystalline Cellulose Concentration Fluidization Air Inlet Temperature Binder Spray Rate	Particle Roundness Particle Elongation Particle Eccentricity	All Individual Factors and Interactions Between All Three Factors Determined to be Significant
[18]	HPMC Concentration Tween 20 Concentration Inlet Air Temperature During Spraying Inlet Air Temperature During Drying	Tapped Density Hausner Ratio	Tapped Density: HPMC Concentration, Spraying Temperature, Drying Temperature, and Interaction Between HPMC Concentration and Spraying Temperature Significant Hausner Ratio: HPMC Concentration and Interaction Between HPMC Concentration and Spraying Temperature Significant
[19]	Pulse Frequency (X_1) Binder Spray Rate (X_2) Atomization Air Pressure (X_3)	Mean Final Particle Size (Y_1) Yield (Y_2) Relative Width of Final Particle Size Distribution (Y_3) Hausner Ratio (Y_4) Moisture Content 30% Binder Added (Y_5) Moisture Content 70% Binder Added (Y_6) Moisture Content 100% Binder Added(Y_7)	$Y_1 = 403.67 – 66.13X_1 + 37.37X_2 - 91.75X_3 + 97.92X_1^2$ $Y_2 = 85.28 – 7.92X_1X_2$ $Y_3 = 1.07 - 0.10X_3 + 0.20X_1X_2 – 0.17X_1X_3 – 0.10X_3^2$ Y_4 Reported as Abnormal $Y_5 = 22.19 – 2.84X_1X_3$ $Y_6 = 32.92 + 2.93X_1X_2 – 4.73X_1X_3 – 3.34X_3^2$ $Y_7 = 36.4 + 4.57X_1X_2 - 6.60X_1X_3 – 5.69X_3^2$

Table 3.3 Continued

Spray Drying			
[20]	Feed Concentration Suspension pH Inlet Air Temperature Suspension Flow Rate Atomization Air Flow Rate	Geometric Particle Size Aerodynamic Particle Size Particle Shape Degree of Hollowness	Multiple Factors and Interactions Determined to be Significant
[21]	Inlet Air Temperature Atomization Air Flow Rate Pump Setting Aspirator Setting Feed Concentration	Angle of Repose Compressibility Index Moisture Content Hygroscopicity Outlet Air Temperature Yield Sauter Mean Particle Diameter	Multiple Factors and Interactions Determined to be Significant

The coefficient of determination values for the regressed equations listed in Table 3.3 are all higher than 0.9. In addition, Table 3.3 shows factorial design allows for flexibility in the choice of independent and dependent variables. Factorial design also shows the presence of interactions between the independent variables – e.g. Jozwiakowski et al. [6] report an interaction between the atomization air pressure and atomization air temperature.

Factorial design represents a simple form of empirical modeling which mainly focuses on linear regression of the response variable with the tracked independent variables. Artificial neural networks (ANN) represent another type of empirical modeling approach. ANN, which can handle non-linear relationships, will be discussed in the next section.

3.2.2 Artificial Neural Networks

Artificial neural networks represent an empirical modeling approach that is based on the neuron network of the human brain. Biologically, a neuron (first postulated by Santiago Ramón y Cajal for which he would win the 1906 Nobel Prize in Medicine with Camillo Golgi) is a cell within the brain composed of three parts: the axon, the cell body, and the dendrites [22]. A chemical or electrical signal is received by the dendrites. The signal is then transported across the cell body to the axon where the signal is transferred to another neuron via a synapse [23]. It is estimated that the human brain contains around 10 billion neurons, each of which are around 100 μm long [24]. Figure 3.3 shows a simplified illustration of the information pathway experienced by the brain.

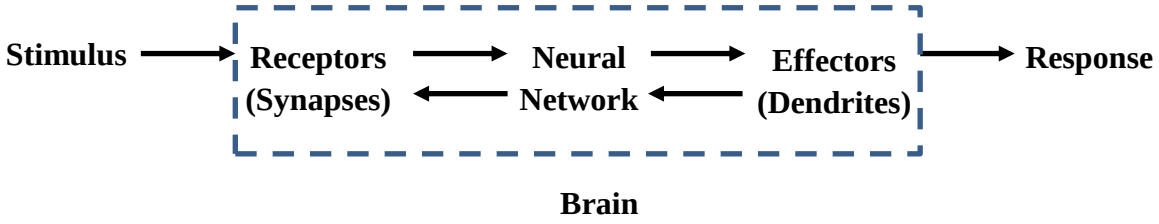

Figure 3.3 Information Pathways Experienced by Brain

In 1943, the first ANN was created when the information pathway shown in Figure 3.3 was transformed into a computational algorithm by McCulloch, a neuroscientist, and Pitts, a mathematician. The next advancement in neural network understanding was the explanation of how the brain learns [25]. Hebb [25], as a follow up to Cajal's work, postulated that physiological learning in the brain involves a transformation of the neuron at the synaptic level where new neuron pathways are generated after repeated stimulation between two or more neurons. The generation of these new neuron pathways signifies that the brain neuron connectivity changes when new information has been learned.

Rosenblatt [26] is credited with designing the first ANN, called the perceptron, for pattern recognition. The perceptron was a computer algorithm that summed values, then subtracted a threshold value, and finally produces one value out of two choices as an output. However, Minsky and Papert [27] showed that the perceptron had limited capabilities and in doing so, stalled the development of ANN's until the processing power of computers began to increase in the early 1980's. Work done by Hopfield [28], Kohonen [29] and Rumelhart, Hinton, and Williams [30] is mainly responsible for reviving interest in the applicability of ANN's to interdisciplinary sciences. Since the 1980's several types of ANN's have been developed successfully and will be discussed in the next section.

3.2.2.1 Types of Artificial Neural Networks and Network Architecture

Several types of ANN's have been developed since interest in their applicability was renewed in the 1980's. Table 3.4 shows the ANN's that have been developed along with its characteristics [24].

Table 3.4 Types of ANN's

Type of ANN	Characteristics
Feed Forward	Information Moves Only One Direction, No Loops, No Cycles
Radial Basis Function (RBF)	Has a Built in Distance From a Center Criterion
Kohonen Self-Organizing Map (SOM)	Produces a Lower Dimensional Space From a Larger Multi-Dimensional Space
Learning Vector Quantization (LVQ)	Precursor to SOM
Recurrent Neural Network (RNN)	Multidirectional Information Flow Includes: Fully Recurrent, Hopfield Network, Boltzmann Machine, Simple, Echo State Network, Long Short Term Memory, Bi-Directional, Hierarchical,
Modular Neural Network (MNN)	A Collection of Smaller Neural Networks to Function as One Large Neural Network

In addition to the different types of ANN's, there are different structures or architectures to the design of an ANN. There are single layer networks as shown in Figure 3.4.

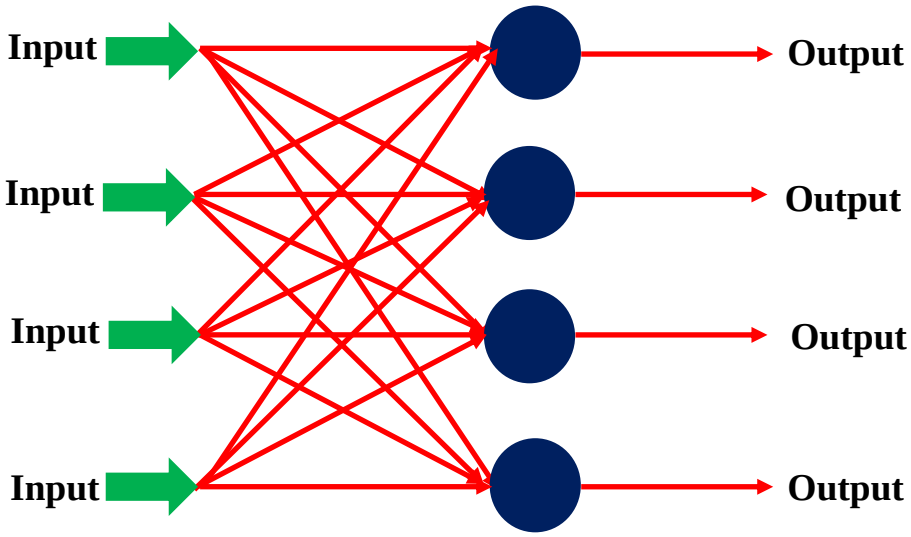

Figure 3.4 Single Layer Feed Forward Neural Network

Figure 3.4 is denoted as a single layer neural network because calculations only take place at one node inside the network.

There are also multilayer neural networks as shown in Figure 3.5.

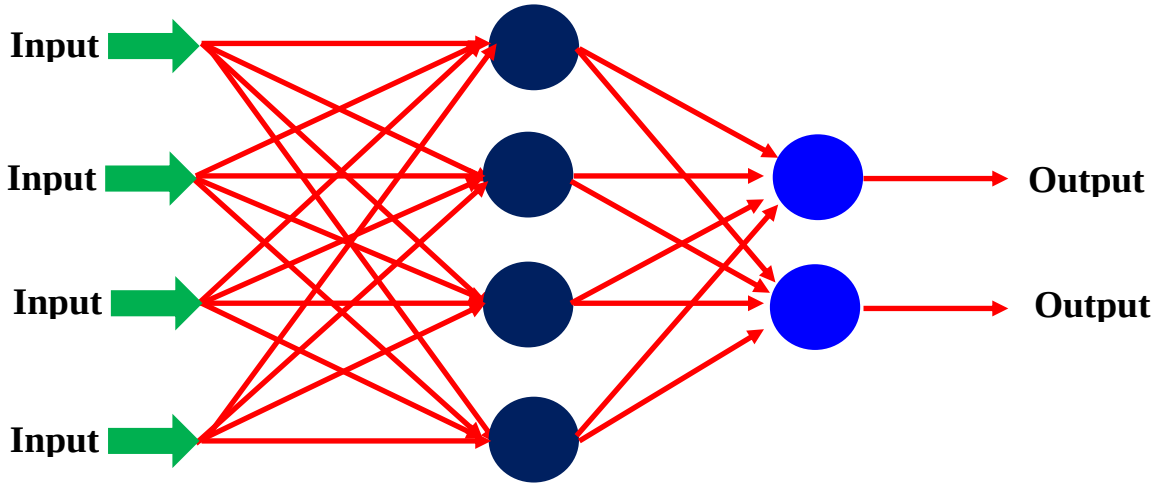

Figure 3.5 Multilayer Feed Forward Neural Network

In the multilayer architecture, there is a hidden layer (the dark blue nodes in Figure 3.5) of calculations before the model outputs are calculated.

An additional ANN architectural arrangement involves loops or cycles in the calculation sequence, as shown in Figure 3.6. ANN structures with this type of arrangement are called recurrent neural networks.

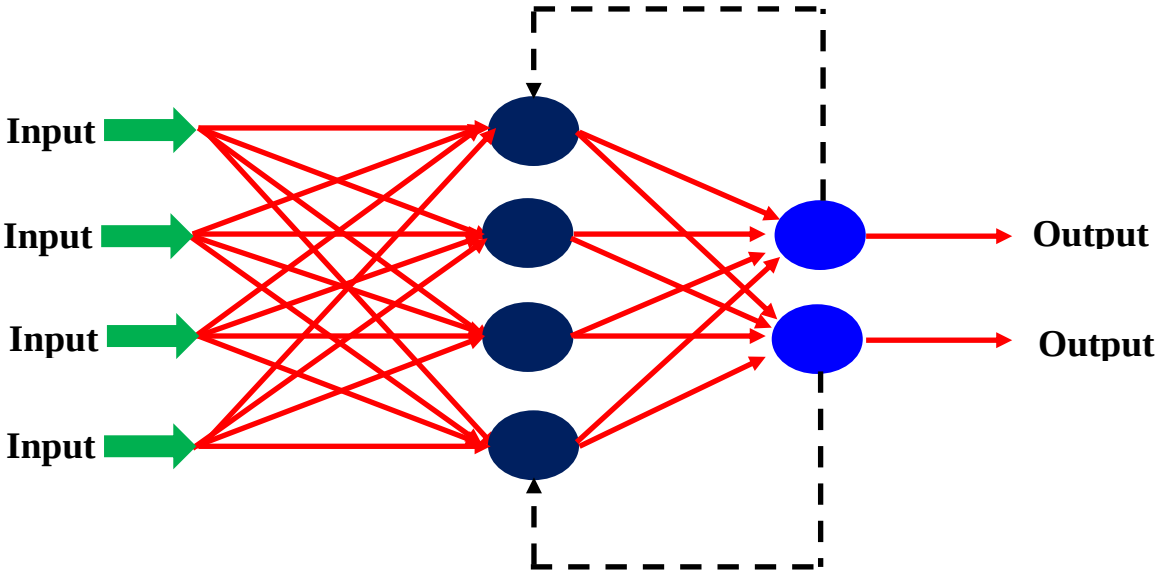

Figure 3.6 Multilayer Recurrent Neural Network with Two Feedback Loops

As the discussion in this section has shown, there are many different forms of the ANN that can be applied to a process. In the next section, published applications of ANN's will be presented.

3.2.2.2 Fluidized Bed Artificial Neural Network Empirical Models

Since the resurgence of interest in the ANN in the 1980's, ANN's have been applied to many areas of scientific research, including fluidized bed operations. Table 3.5 presents a listing of published ANN models concerning fluidized bed operations.

Table 3.5 Published Fluidized Bed ANN Models

Reference	Application
[31-38]	Granulation
[39-41]	Combustion/Gasification
[42-44]	Circulating Fluidized Bed
[45-46]	Particle Segregation
[47-52]	Drying
[53-54]	Electrostatic Coating
[55]	Review

As Table 3.5 shows, ANN's have been successfully applied to many different types of fluidized bed operations. ANN's represent a stronger empirical modeling approach for fluidized bed modeling compared to linear regression approaches such as factorial design because ANN's can handle non-linear relationships between inputs and outputs [56]. However, there is another empirical modeling approach, called evolutionary algorithm, which is often used in conjunction with ANN's to improve the accuracy of empirical models. Evolutionary algorithms will be discussed in the next section.

3.2.3 Evolutionary Algorithms

The evolutionary algorithm approach to modeling is based on the principle of natural selection, originally put forth by Charles Darwin in 1859, for process optimization [57]. Evolutionary algorithms were developed in the 1960's and 1970's as an expansion of work done

by Barricelli [58, 59] regarding modeling evolution with a computer, with the work done by Rechenberg [60], Schwefel [61, 62], Fogel et al. [63], and Holland [64].

Evolutionary algorithms are typically classified into four groups: genetic algorithms, genetic programming, evolutionary strategies, and evolutionary programming [65]. The main difference between the four groups lies in the perturbation methods used to generate new populations for model development [65]. The general flow of evolutionary algorithms is shown in Figure 3.7.

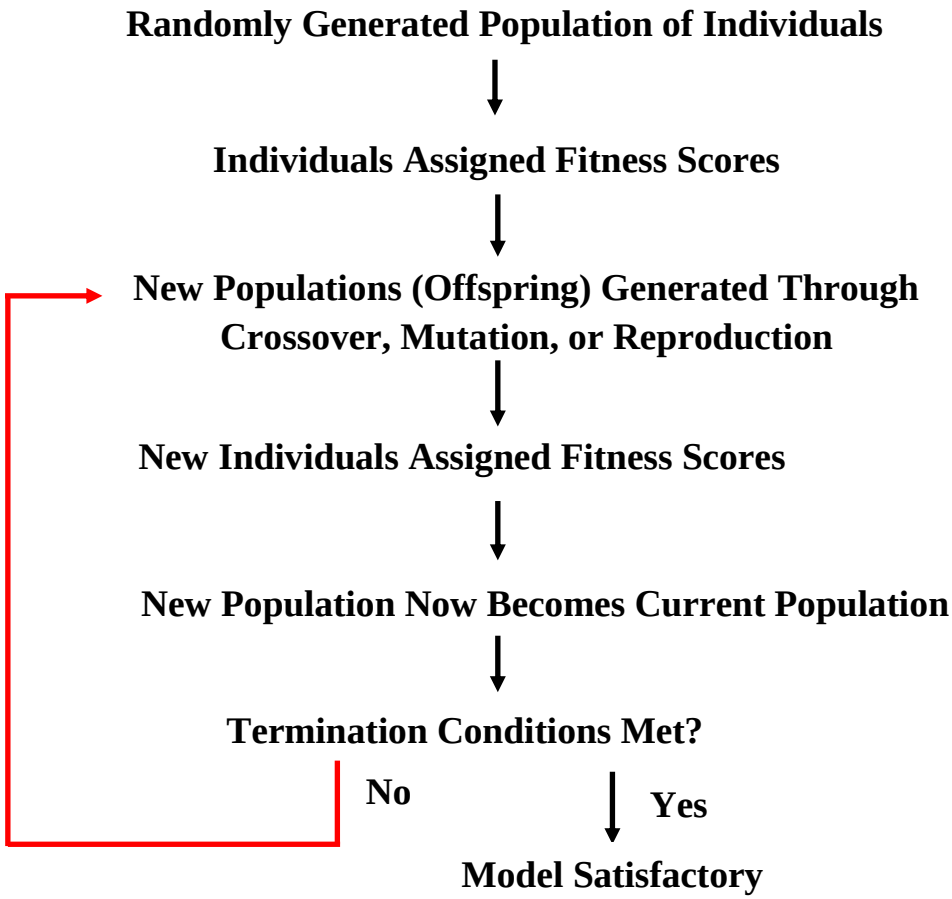

Figure 3.7 General Flow of Evolutionary Algorithms

Initially a population of individuals (mathematical functions, e.g. linear, power law, exponential, logarithmic, polynomial, etc.) is generated to solve a particular problem. Each

individual is given a fitness based on how well it solves the problem. Next, the iterative part of the evolutionary algorithm begins when a new population, called the offspring, is generated through crossover, mutation, or reproduction. The mechanism that occurs, crossover, mutation, or reproduction for the offspring production is dependent on the previously allotted fitness score, i.e. the higher the individual fitness score, the higher the probability is for being selected. The three mechanisms for new population generation will be discussed in the next paragraph. A new fitness score is assigned for the new population based on how well it solves the problem, as it now called the current population. If the current population describes the problem in a satisfactory manner the evolutionary algorithm is terminated and the model has been created. Otherwise, new populations are generated and fitness scores are assigned until a satisfactory model has been created.

In evolutionary algorithms, functions can be represented as tree structures as shown in Figure 3.8.

$$P^{vap} = A + A_1(T) + A_2(T)^2 + A_3(T)^3$$

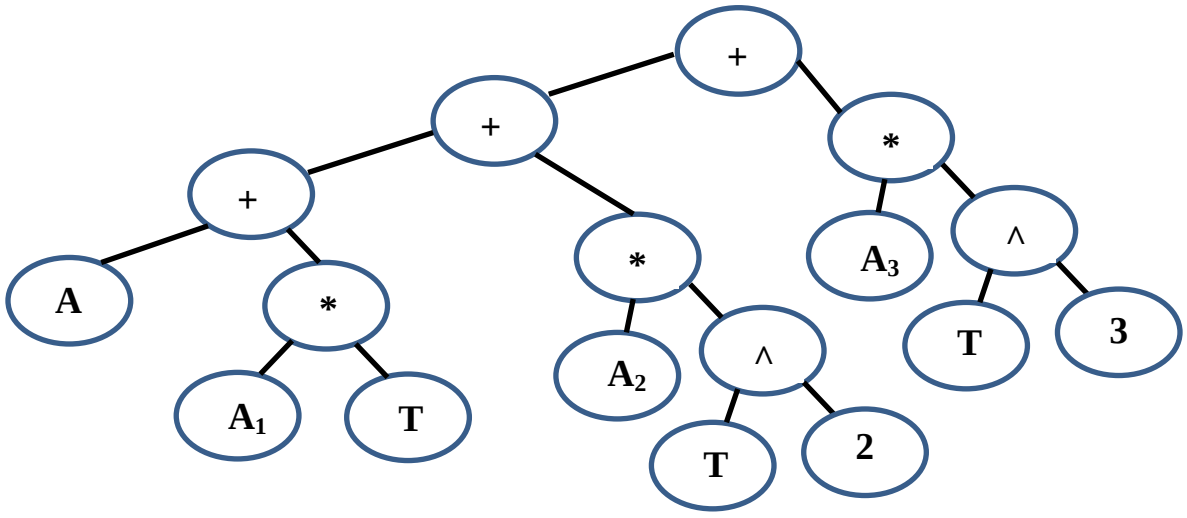

Figure 3.8 Tree Structure of Vapor Pressure Function

The mathematical operators in Figure 3.8, +, *, and ^ represent nodes within the tree structure, while parameters A, A_1, A_2, and A_3, input variable T, and the exponents "2" and "3" represent leaves within the tree structure.

There are three mechanisms for new population generation in the evolutionary algorithm: crossover, mutation, and reproduction. Crossover, as shown in Figure 3.9, involves the recombination of random parts of two existing individuals. Two new individuals (offspring) result from crossover operations [64].

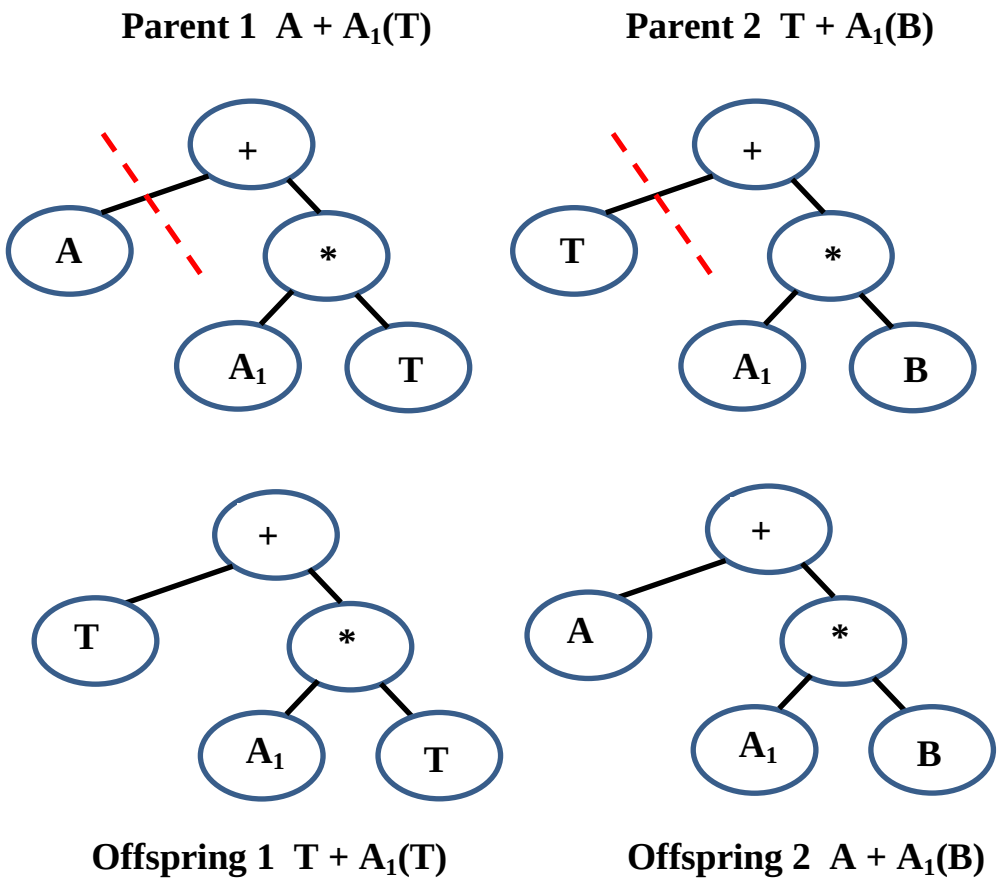

Figure 3.9 Evolutionary Algorithm Crossover Example

Mutation, shown as Figure 3.10, is the random modification of an existing individual and produces only one individual. Mutation can occur two ways. One mutation is a function

replacing a function or a terminal replacing a terminal. The second mutation is an entire model structure replacing an entire model structure [64].

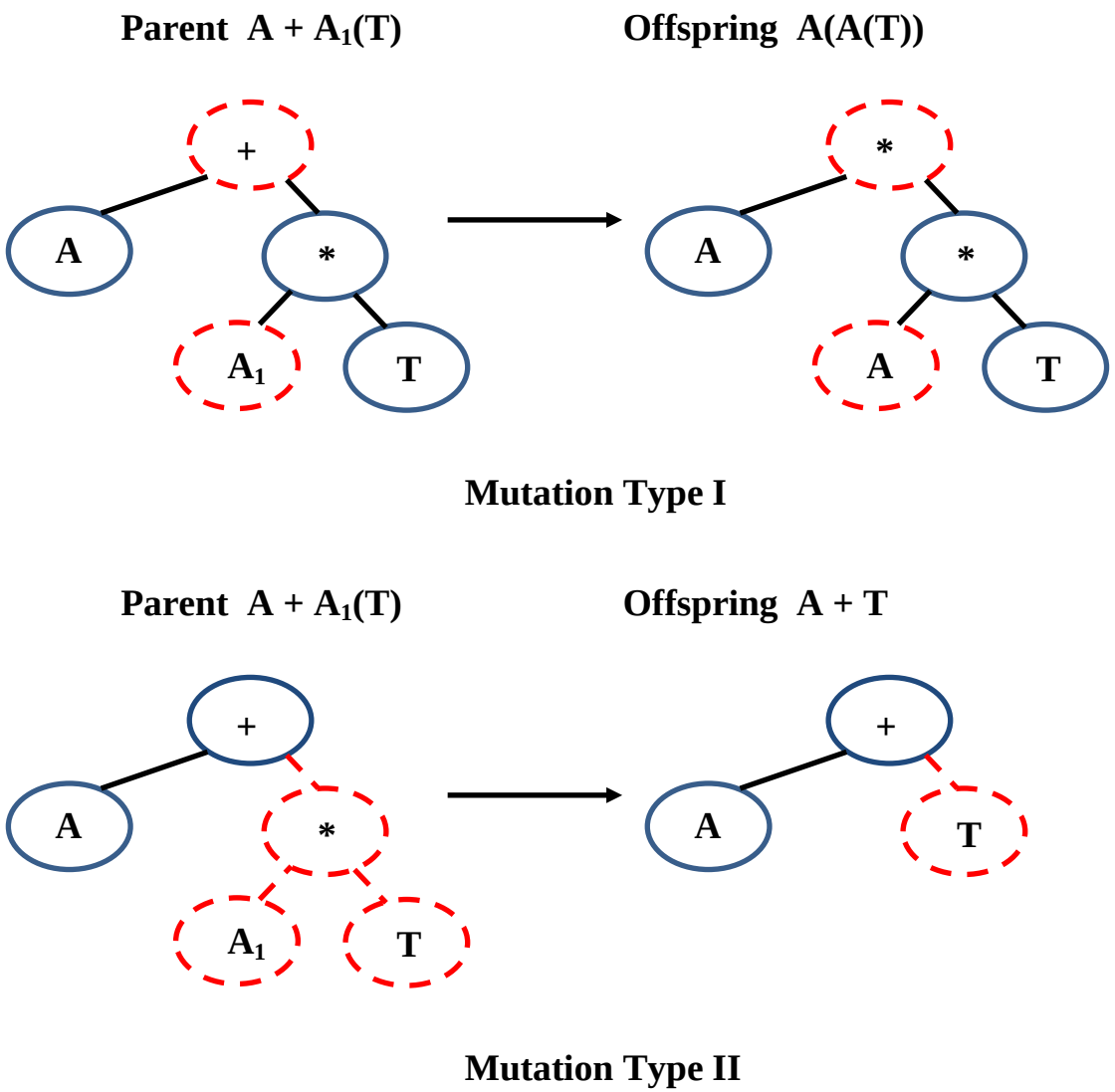

Figure 3.10 Evolutionary Algorithm Mutation Examples

Reproduction, shown as Figure 3.11 involves copying an individual into the new population [64]. Fitness scores are determined by sum of squares error, absolute error, or normalized error.

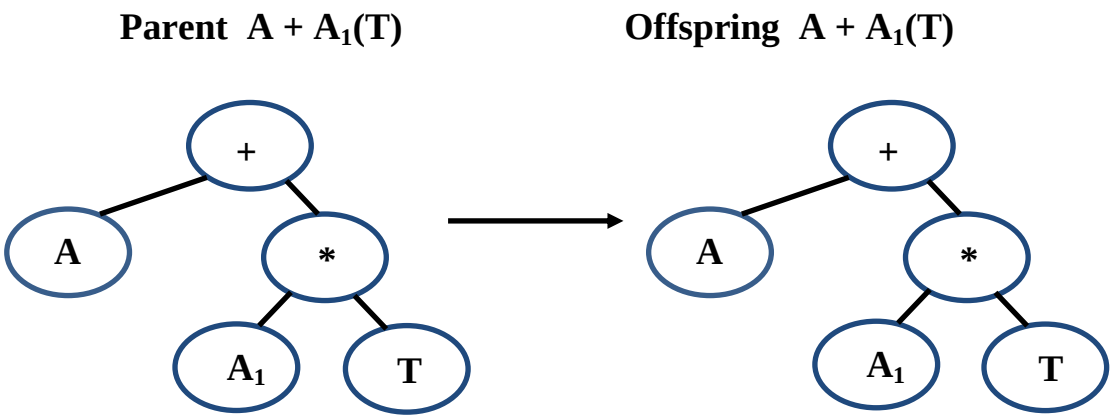

3.11 Evolutionary Algorithm Reproduction Example

The power of using an evolutionary algorithm to develop an empirical model lies in the fact that it is a data driven process, i.e. the data develops the model. Similarly to ANN's, non-linear processes like fluidized bed operations, can be handled quite well using evolutionary algorithms in the modeling approach. Fluidized bed models utilizing the evolutionary algorithm approach will be presented in the next section.

3.2.3.1 Fluidized Bed Models Utilizing Evolutionary Algorithms

The evolutionary algorithm approach has been applied to fluidized bed operations as a route to developing accurate empirical models. Table 3.6 shows published works regarding fluidized bed modeling using evolutionary algorithms.

Table 3.6 Published Fluidized Bed Models Utilizing Evolutionary Algorithms

Reference	Application
[66, 67]	FCC Unit
[68, 69]	CFB Boiler
[53]	Electrostatic Coating
[70]	Biomass Gasification
[71]	Combustion
[72]	Phenol Biodegradation
[73]	Gas Holdup
[51]	Drying

Table 3.6 Continued

[74]	Pressure Drop
[38]	Granulation

As Table 3.6 shows, evolutionary algorithms have been applied to various modes of fluidized bed operations with success. Evolutionary algorithms allow for process data to influence the kind of model it develops. Similarly to the factorial design and artificial neural network approach it does not give information regarding underlying mechanisms for why the independent variables and their interactions (if any) have an impact on the response variable(s) of interest.

3.2.4 Summary of Empirical Modeling

Empirical modeling represents the simplest modeling approach to fluidized bed operations, whether the operation is gasification, granulation, particle coating or drying. Three types of empirical modeling approaches include: experimental design (factorial design), artificial neural networks (ANN's), and evolutionary algorithms. Empirical models yield what variables and variable interactions are statistically significant to a fluidized bed process.

However, despite having the capacity to reveal parameter interactions and flexibility with regard to variable regression choice, there are issues that limit empirical models. Empirical models for fluidized bed coating tend to be specific to the equipment used, i.e. they cannot be applied to operations with larger fluidized beds when scaling up [75]. New empirical models often have to be developed during scale up because of different fluidized bed geometries and/or a shift in the parameters investigated. In addition, while empirical models give insight into which factors have an impact on the parameter of interest as shown in Table 3.1, no additional information regarding the underlying fundamental mechanisms that make the independent variables significant can be ascertained from the regression.

Drawbacks with regard to ANN's and evolutionary algorithm models lie mainly in computation time and the choice of model. The larger the neural network, the longer the computation time. Moreover, the ANN model developed by data driven evolutionary algorithms may only represent locally optimized solutions and not globally optimized solutions.

Empirical models ar the least complex modeling approach to fluidized beds. Mechanistic models represent the next level up in modeling complexity for fluidized beds and will be discussed in the next section.

3.3 Mechanistic Models

The next level up in modeling complexity from empirical models is mechanistic models. Compared to empirical models, mechanistic models incorporate governing laws of various phenomena including: momentum, motion, and transport. Mechanistic model results provide insight in two areas – elementary technical comprehension of a process and the optimization potential for a process with newly acquired knowledge [76].

As noted in Section 3.1.1 there are two different methodologies within mechanistic modeling, deterministic and stochastic. Mechanistic models which are deterministic in nature that are applied to describe fluidized bed phenomena include: particle level modeling, population balance modeling, computational fluid dynamics (CFD) modeling, and lumped region modeling [3, 76, 77]. Each of the aforementioned approaches yields valuable information for fluidized bed process characteristics but also has drawbacks which must be taken into account as well.

3.3.1 Particle Level Modeling

Particle level modeling is an approach used in fluidized bed modeling where force balances concerning various phenomena (e.g. gravity, surface tension, viscosity) are carried out on a single particle or a small number of particles (e.g. less than 5). Particle level modeling, also

referred to as micro-level modeling covers several different processes that occur during fluidized bed particle coating including: particle wetting, particle coalescence and coating, and particle attrition and breakage [78, 79]. A direct and valuable result of particle level modeling is the development of new additional dimensionless numbers, discussed previously in Section 2.8, that are used to identify if fluidized bed conditions lead to particle coating or agglomeration. However, while providing greater insight into fluidized bed coating phenomena versus empirical models discussed in Section 3.2, particle level modeling alone is not robust enough to be the only modeling approach used for fluidized bed coating.

3.3.1.1 Particle Wetting and Adsorption Into Pores

One area where particle level modeling has aided the understanding of fluidized bed coating is the particle wetting process. Particle wetting is the capacity of a liquid to maintain contact with a solid surface, resulting from a balance between liquid-solid, liquid-vapor, and vapor-solid interactions [80]. The parameter θ, called the contact angle, represents the angle at which the liquid-vapor boundary meets the liquid-solid boundary [81] and is shown as Figure 3.12 [80].

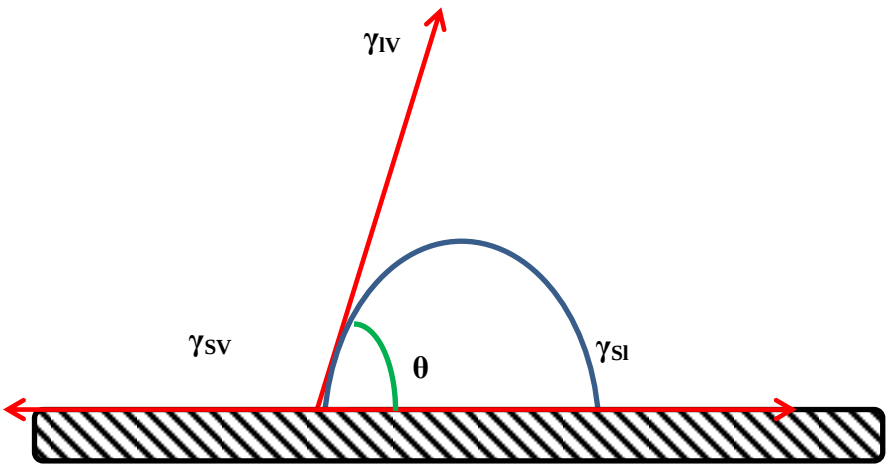

Figure 3.12 Solid-Liquid Contact Angle

Large contact angle values indicate cohesion forces (the tendency to avoid spreading over a surface) dominating over adhesion forces (the tendency to spread over a surface). Table 3.7 shows contact angle values, degree of wetting, and which interactions dominate. The contact angle is directly influenced by particle surface characteristics (i.e. roughness) and solubility in the solvent and liquid surface tension [82]. However, since solubility and surface tension are both functions of temperature as well, the contact angle is also an indirect function of temperature.

Table 3.7 Contact Angle Values, Degree of Wetting, and Interaction Strength

Contact Angle	**Degree of Wetting**	**Strength**	
		Liquid-Solid	**Liquid-Vapor**
0^o	Perfect Wetting	Strong	Weak
$0^o < \theta < 90^o$	High Wettability	Strong	Strong
		Weak	Weak
$90^o < \theta < 180^o$	Low Wettability	Weak	Strong
180^o	Poor Wettability	Weak	Strong

Three phases of particle wetting have been identified: adhesional (onset of liquid-solid-vapor contacting), spreading (liquid spreading on particle surface), and imersional (complete spreading of liquid over particle surface) [80]. A particle can undergo all three phases of wetting (only in sequential order), if the process is thermodynamically favorable. The Gibbs free energy per unit area associated with adhesion, spreading, and immersion are shown as Equations 3.2-3.4 [80]:

$$\Delta G_{adh} = \gamma_{sl} - \gamma_{sv} - \gamma_{lv} \quad (3.2)$$

$$\Delta G_{spr} = \gamma_{sl} - \gamma_{sv} + \gamma_{lv} \quad (3.3)$$

$$\Delta G_{imm} = \gamma_{sl} - \gamma_{sv} \quad (3.4)$$

Equations 3.2 and 3.3 are typically reported in terms of adhesion work and spreading coefficient and are rearranged into Equations 3.5 and 3.6:

$$W_{adh} = -\Delta G_{adh} \quad (3.5)$$

$$S_{ls} = -\Delta G_{spr} \quad (3.6)$$

When Equations 3.5 and 3.6 are combined with Young's equation for three-phase equilibrium (shown as Equation 3.7), the Gibbs free energy of adhesion can be simplified to two variables as shown in Equations 3.8-3.10 [80]:

$$\gamma_{sv} = \gamma_{sl} + \gamma_{lv} \cos\theta \quad (3.8)$$

$$\Delta G_{adh} = -\gamma_{lv}(1+\cos\theta) \quad (3.9)$$

$$\Delta G_{spr} = \gamma_{lv}(1-\cos\theta) \quad (3.10)$$

$$\Delta G_{sl} = -\gamma_{lv} \cos\theta \quad (3.11)$$

Equations 3.8-3.11 are valid only if $\frac{\gamma_{sv} - \gamma_{sl}}{\gamma_{lv}}$ falls between -1 and 1 [80]. Measurement of the contact angle between the powder and liquid can be done on a single particle basis using techniques like AFM, ESEM, or floating particle methods. The contact angle can also be measured on the bulk powder using techniques like capillary rise, adsorption, powder compaction, crystallization kinetics, or immersional wetting [82].

In addition to wetting occurring on the particle surface, there is also the possibility of liquid adsorption occurring within the particle pore structure. Factors such as pore diameter, liquid surface tension and viscosity, and wetting thermodynamics play a role in determining if a liquid droplet will be adsorbed into the pores before spreading can commence or the droplet evaporates.

Capillary forces, shown as Equation 3.12, can develop when working with porous particles that can aid or disrupt liquid spreading on the particle surface:

$$F_{cap} = 2\pi R_{pore}\gamma_{lv}\cos\theta \tag{3.12}$$

Capillary action draws the liquid into the porous structure resulting in a capillary pressure gradient between the particle surface and the internal pore, shown as Equation 3.13:

$$P_{cap} = \frac{2\gamma_{lv}\cos\theta}{R_{pore}} \tag{3.13}$$

The depth to which the pore is filled with liquid is given by Equation 3.14 [83]:

$$h = \frac{2\gamma_{lv}\cos\theta}{\rho_{liq} g\, R_{pore}} \tag{3.14}$$

The maximum volume of liquid that can fill the pore (assuming cylindrical geometry) is given by Equation 3.15:

$$V_{liq,\,pore} = \frac{2\pi\gamma_{lv}R_{pore}\cos\theta}{\rho_{liq}g} \tag{3.15}$$

The length of time needed for a droplet to be adsorbed by the porous particle is given as Equation 3.16 [84, 85]:

$$\tau_{ads} = \frac{2V_{drop}^2}{\pi^2\varepsilon_{sp}^2 r_{drop}^4 R_{pore}} \frac{\mu_{liq}}{\gamma_{lv}\cos\theta} \tag{3.16}$$

where ε_{sp} is the particle surface porosity and the pore radius is given as Equation 3.17 with the Kozeny approach in the absence of experimental data (Denesuk 1993):

$$R_{pore} = \frac{2\varepsilon_{sp}}{(1-\varepsilon_{sp})s_o\rho_{part}} \tag{3.17}$$

with s_o representing the specific surface area (m^2/kg) of the particles. However, Equation 3.17 has been shown to be valid only for low porosity solids that have a narrow pore size distribution [79, 86].

3.3.1.2 Liquid Droplet and Wet Particle Drying

A brief discussion regarding liquid droplet evaporation has been presented previously in Chapter 2. This discussion has been expanded here to include drying of wet particles.

A potentially competitive process to the droplet spreading is droplet drying. If liquid droplets evaporate before impacting the fluidized particles, the overall coating efficiency drops and processing time may have to be increased to compensate. On the other hand, if the drying process is too slow, the particle bed may become too saturated with liquid to fluidize sufficiently (Nienow 1995). Therefore, an understanding of the phenomena and mechanisms involved with drying is imperative.

Three stages of drying have been identified for drying of wet porous particles: the constant rate, the first falling rate period, and the second falling rate period. Figure 3.13 shows how the segments progress [88].

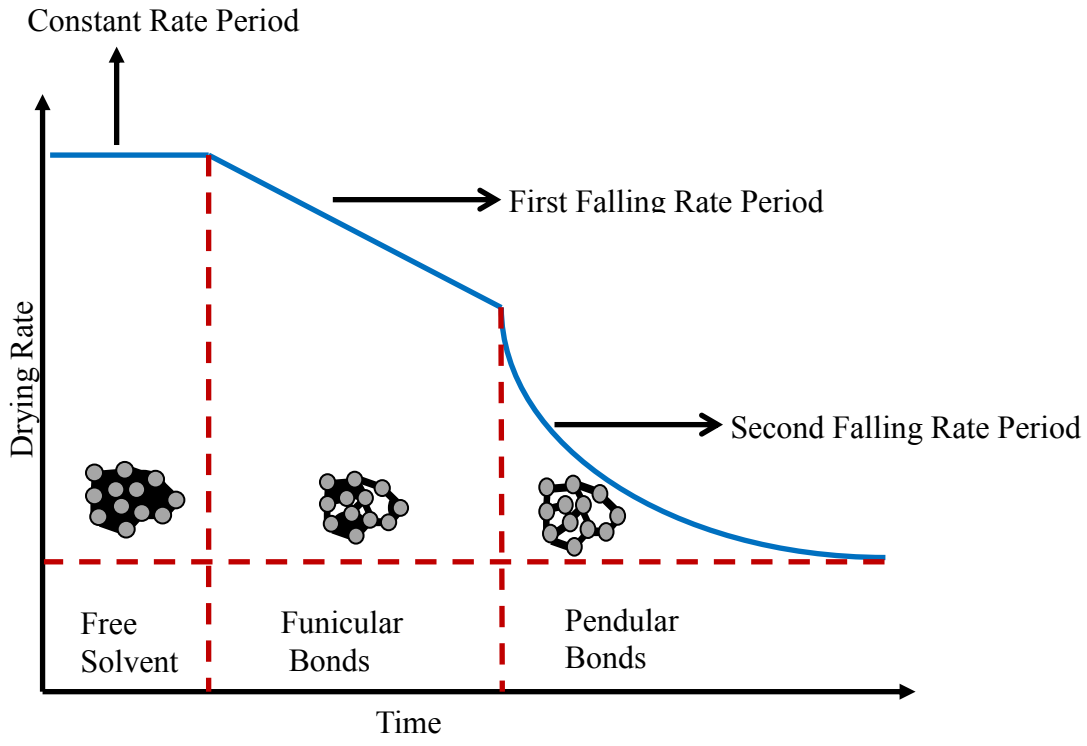

Figure 3.13 Wet Particle Drying Segments

During the constant drying rate period, free solvent evaporates first. Capillary forces are not too significant during this segment, but they increase as the amount of free solvent decreases. Particle shrinking can begin during the constant rate period as the capillary forces begin to increase in magnitude. At a critical liquid content, the second segment of the drying phase, the first falling rate period begins. During the first falling rate period capillary forces increase, leading to a greater potential for particle shrinkage if the solid how weak mechanical properties. Liquid available for evaporation recedes such that it is only present in the particle pores. At this point liquid within the pores is driven to the particle surface via a vapor pressure gradient between the particle surface and the particle pore. The second falling rate period onset is characterized by an increase in particle temperature. The remaining liquid within the particle pores during this phase is transported to the surface via diffusion [88].

Drying wet particles in a fluidized bed is slightly different however. In fluidized bed coating, complete saturation of the particle surface with liquid is not desired. In addition, high diffusion rates transport solvent to the particle surface quickly such that a constant rate period is seldom observed [89].

3.3.1.3 Particle Morphology

The coated particle morphology, a direct result of the fluidized bed wetting and drying characteristics, is a factor for product quality. Product quality in terms of fluidized bed coating has multiple definitions including: the incidence of spray drying loss, particle attrition, or particle agglomeration, or coating homogeneity or coating shell thickness [90]. In addition, particle morphology also establishes other potential measures of quality such as dissolution rate, mechanical strength (sometimes called friability), color or flavor preservation and flowability [89].

Walton and Mumford [91] sorted spray dried particles into three groupings according to morphology: agglomerate, skin forming, and crystalline. The agglomerate category refers to a particle made up of two or more core particles bridged together with a binder material. The skin-forming category refers to particles that have a continuous non-liquid phase with an appearance similar to skin or a polymer and typically have low melting points. Examples of skin-forming morphology include: spray dried milk products, spray dried coffee, and spray dried flavors. The crystalline category applies to crystalline particles bound together via a continuous microcrystalline phase.

Several types of defects can occur changing the particle morphology during fluidized bed processing. Capillary pressure within particle pores during the constant drying rate period of Figure 3.13, reaching a maximum during the first falling rate period – up to 200 MPa [88, 92]. If the capillary pressure exceeds the tensile strength of the particle, the pores will collapse and internal surface area will be lost. An additional factor that can influence the capillary pressure is capillary condensation. Capillary condensation, represented mathematically as Equation 3.18, occurs when solvent vapor condenses on the particle pore walls and the vapor-liquid meniscus reforms [93]:

$$\ln\left(\frac{P_{ev}}{P_{sat}}\right) = \frac{2H\gamma_{lv}V_M}{RT} \tag{3.18}$$

where P_{ev} is the equilibrium vapor pressure, H is the curvature of the meniscus, and V_M is the molar liquid volume. Some of the defects that may occur include: particle blowholes, particle craters, cracking of the coating material, and shrinkage [91].

Walton and Mumford [94] also investigated the impact of process variables on final particle morphology. The process variables manipulated include: air temperature (one below the solvent boiling point and one above the solvent boiling point), the feed concentration, and the

atomization quality. Qualitative relationships were reported regarding final particle morphology and the manipulated variables. The liquid viscosity has been shown to have an impact on particle morphology as well. Increasing the liquid viscosity increases the probability of droplet adhesion after particle impact because the energy of impact is dampened by the viscous droplet [95].

Due to the complexity of multiple processes occurring simultaneously in fluidized bed coating along with property specific particle-liquid coating solution parameters, developing predictive models yielding morphology characteristics is still a difficult challenge [96, 97]. However, general guidelines for good coating quality have been outlined [98]: using low coating concentrations in liquid solvent (this will generally keep the surface tension and viscosity low allowing for smaller droplets to form during atomization process), and having a liquid-solid contact angle favorable to spreading (this will increase surface coverage and therefore coating thickness).

3.3.1.4 Particle Collision Phenomena: Coalescence and Rebound, Breakage and Attrition

Another branch of particle level modeling involves particle collision phenomena. The particle collision phenomena that lead to coalescence an rebound have been discussed previously in Chapter 2, sections 2.8.1, 2.8.2, and 2.9.1-3 so the discussion here will focus on particle breakage and attrition. Particle breakage is classified as two different phenomena – either wet or dry. Dry particle breakage is also called attrition [79]. Wet and dry particle breakage studies are typically associated with granulation studies, but they also provide valuable insight for particle coating operations as well.

Particle breakage and attrition rates have been identified as the third rate process of particle granulation, after wetting and nucleation, and consolidation and growth [79]. The

fluidized bed operating conditions dictate the extent of wet particle breakage due to the frequency of particle-particle collisions and the impact energy sustained by the solid-liquid bridges that form during granulation. The particle mechanical properties (e.g. shear, tensile, and yield strength, modulus of elasticity, and hardness) tend to be the focus of understanding dry particle breakage [99]. Fundamental understanding of mechanisms that cause wet and dry particle breakage provides a gateway to enhanced fluidized bed equipment and particle design as well [99].

Five different types of liquid-solid bridges, shown as Figure 3.14, have been identified in literature: pendular, funicular, and capillary [100], droplet [101], and pseudo-droplet [102].

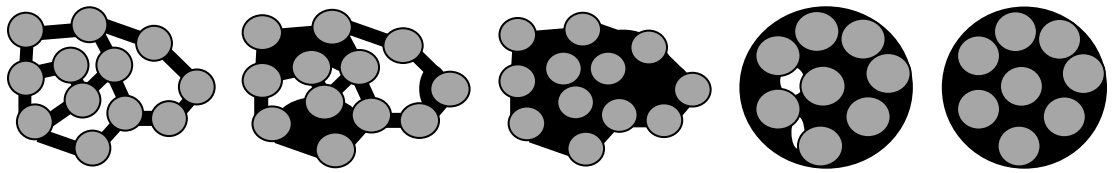

A B C D E

Figure 3.14 Liquid-Solid Bridges: A) Pendular B) Funicular C) Capillary D) Pseudo-Droplet E) Droplet

The type of liquid-solid bridge present in a fluidized bed operation is dependent on the particle porosity and amount of liquid in the particle pores. As the pores become saturated with liquid a transition from one type of liquid-solid bridge to another occurs. Table 3.8 shows the pore saturation range associated with the liquid-solid bridge [103].

Table 3.8 Pore Saturation Range Associated with Liquid-Solid Bridge

Liquid-Solid Bridge	**Pore Saturation Percentage**
Pendular	< 25%
Funicular	25% < S < 80%
Capillary	80% < S < 100%
Pseudo-Droplet	>100 %
Droplet	>100 %

In the case of fluidized bed coating, formation of all the aforementioned liquid-solid bridges is undesired. If the liquid-solid bridges do form after a particle-particle collision, having the predictive capability to determine if the bridge will survive the processing conditions can help salvage particle coating operations and improve a priori particle design.

One of the difficulties surrounding particle breakage in fluidized bed operations is the inability to predict the circumstances necessary for wet or dry particle breakage [79, 99]. Several factors have been investigated regarding their impact on particle breakage including: 1). liquid-solid properties - liquid surface tension and viscosity, the liquid-particle contact angle, particle shape and size, 2). equipment properties - mixer construction, impeller and chopper size and speed, 3). process characteristics – run time, amount of liquid added, and the liquid addition method [99].

In an attempt to quantify particle breakage conditions the Stokes deformation number, previously discussed in Chapter 2 was developed [104]. Keningley et al. [105] used the viscous Stokes number (discussed previously in Chapter 2) to determine the minimum amount of binder necessary for a granulation process with an order of magnitude prediction. However, a fully descriptive model for particle breakage is unrealized at the present time [79, 99, 106].

Dry granule breakage studies focus on classifying particle breakup via impact tests. One approach for particle breakage impact testing is the multi-particle impact test [99]. Multi-particle impact tests provide results that mirror real conditions inside a fluidized bed, but do not provide detail regarding the mechanism(s) behind the particle breakage [107]. Single particle impact tests involve colliding single particles/agglomerates with a target at multiple angles at high velocities while filming with a high speed camera. The results are analyzed to determine the

breakage mechanism. A free fall arrangement is used to determine the breakage mechanism(s) at low velocity impacts [99, 108].

Four particle breakage modes have been identified in literature [109]: fracture, shattering, disintegration, and total disintegration. The fracture mode of particle breakage is characterized by evident fissures and the presence of fines or daughter particles. The shattering mode of particle breakage refers to daughter particle segments breaking into smaller pieces (usually occurring at high impact velocities). The disintegration mode of particle breakage refers to agglomerated particles breaking up into primary particles, whereas the total disintegration mode of particle breakage is defined as having no primary particles left after impact.

With particle breakage modes defined as above, impact velocity regimes were examined to ascertain which particle breakage modes were duly associated. In low velocity experiments (< 8 m/s), wet granules (5-6 mm) underwent plastic deformation at the impact area without any crack formation. Increasing the impact velocity to the intermediate region, particle cracking begins. Cracks were observed in dry binder less granules at a lower velocity with fracture occurring as the impact velocity was increased [110].

At intermediate impact velocities (> 12 m/s), fracture was observed in wet granules, while the dry binder less particles had fragmented into several equivalent sized bits. At high impact velocities (> 20 m/s), the wet granules underwent a high degree of disintegration, while the dry binder less particles completely disintegrated [110]. The angle of impact was not found to be significant to the particle breakage mode other than providing a source for asymmetry in the crack patterning. Particle size was determined to have an effect on the breakage mode for wet granules, as significant plastic deformation occurs before breakage occurs [110]. There are still no quantitative studies relating impact velocity to breakage mechanism or extent of breakage

despite research showing similar modes of particle breakage occur within each impact velocity regime.

3.3.2 Computational Fluid Dynamics Approach

Computational fluid dynamics (CFD) represents a different mechanistic modeling approach for fluidized bed behavior. CFD was developed initially in the 1950's and 1960's with the arrival of the computer in an effort to solve sub and supersonic fluid flow over a blunt body [111]. Since that time, multiple modeling approaches have been incorporated within CFD framework to solve a variety of scenarios including flow in a gas-solid fluidized bed [112].

CFD calculations center around conservation of mass, energy, and Newton's second law of motion (F = ma). In the case of two-phase flow (i.e. a fluidized bed), the Navier-Stokes equations for continuity and momentum are shown as Equations 3.19-3.22 [113]:

$$\frac{\partial}{\partial t}\left(\varepsilon_g \rho_g\right) + \nabla\cdot\left(\varepsilon_g \varepsilon_g \bar{u}_g\right) = 0 \tag{3.19}$$

$$\frac{\partial}{\partial t}\left(\varepsilon_s \rho_s\right) + \nabla\cdot\left(\varepsilon_s \varepsilon_s \bar{u}_s\right) = 0 \tag{3.20}$$

$$\frac{\partial}{\partial t}\left(\varepsilon_g \rho_g\right) + \nabla\cdot\left(\varepsilon_g \varepsilon_g \bar{u}_g \bar{u}_g\right) = -\varepsilon_g \nabla P_g - \nabla\cdot\left(\varepsilon_g \bar{\tau}_g\right) - \beta\left(\bar{U}_g - \bar{U}_s\right) + \varepsilon_g \rho_g \bar{g} \tag{3.21}$$

$$\frac{\partial}{\partial t}\left(\varepsilon_s \rho_s\right) + \nabla\cdot\left(\varepsilon_s \varepsilon_s \bar{u}_s \bar{u}_s\right) = -\varepsilon_s \nabla P_s - \nabla\cdot\left(\varepsilon_s \bar{\tau}_s\right) - \beta\left(\bar{U}_g - \bar{U}_s\right) + \varepsilon_s \rho_s \bar{g} \tag{3.22}$$

As noted by Goldschmidt [113] the origins to Equations 3.19-3.22 can be found in literature [114-118].

The general setup for solving a problem via the CFD technique follows as such: 1) Definition of geometry 2) Discretization of geometry into a mesh grid 3) Definition of model equations - mass, energy, and momentum balances 4) Definition of boundary conditions 5) Iterative solution of equations 6) Visual representation of results [119].

3.3.2.1 Discretization Methods Used in CFD

CFD calculations involve simultaneous and iterative solution of many partial differential equations (PDE) to describe the fluid flow characteristics of a particular scenario. Analytical solutions for the Navier Stokes equations rarely exist, so the Navier Stokes PDE's are converted to algebraic equations and subsequently solved at discrete positions within the area of interest [120]. There are several discretization methods available for CFD calculations but the three methods used most often are: the finite volume method (FVM), the finite element method (FEM), and the finite difference method (FDM).

The finite element method, which has roots in mechanical engineering, involves segmenting the system of interest into units called elements. The element can be triangle or rectangular shaped and linear or curved [121]. Combining all the elements together creates a mesh of PDE's to solve. Boundary conditions are applied to the PDE's and the algebraic transformed PDE's are solved. Boundary conditions used in the finite element method take differential form as well, thus leading to higher solution accuracy. An underlying assumption with the finite element method is that the mathematical form of the solution is already known [121].

The finite difference method is another method used for discretization in CFD calculations. The finite difference method is similar to the finite element method but it can only handle simple geometries (i.e. rectangles) compared to the finite element method – grids must be uniform [121].

The finite volume method involves separating the system of interest into multiple control volumes and then applying the model equations to the central point of the control volumes. The finite volume method is an attractive solution method for CFD computation for a few reasons:

structured and unstructured meshes, shown as Figure 3.15, can be implemented (i.e. control volume shape/size is not restricted), the laws of conservation hold for surface and volume integrals, and body fitted coordinate systems are not needed [120].

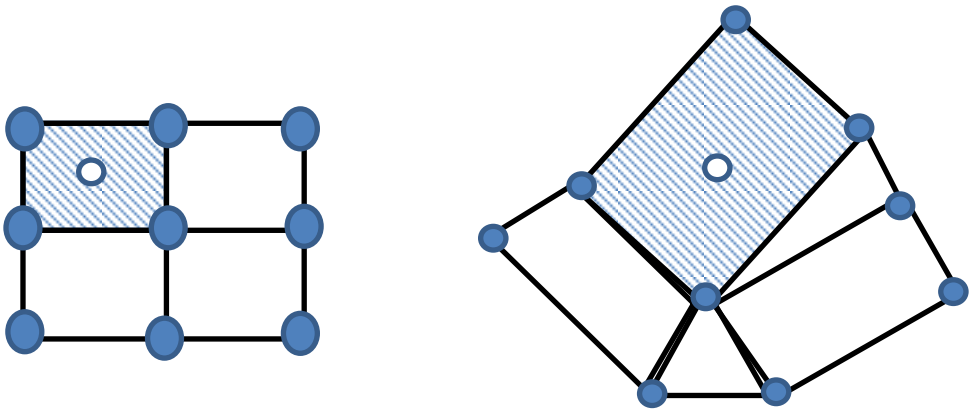

Figure 3.15 FVM Structured and Unstructured Mesh Example

3.3.2.2 Turbulence Models Used in CFD

The turbulent flow regime has garnered a great deal of attention regarding CFD computations in part because of the difficulty of representing turbulence properly in a theoretical framework. The turbulent flow regime is exemplified by irregular fluctuations (small or large) which cause deviations in the pressure and velocity of a fluid. These pressure and velocity oscillations in turn help to enhance other properties such as diffusion, heat transfer, mass transfer, mixing, drag, etc. [122].

Several approaches to modeling turbulence, shown in Table 3.9 have been developed for CFD calculations. Reynolds stress tensors are introduced as additional variables to account for the fluctuations in flow. Table 3.9 shows the turbulence models that are incorporated into CFD computations [122].

Table 3.9 Turbulence Models Used in CFD Computations

Model Group	Model	Comments
Reynolds-Averaged Navier Stokes (RANS)	Zero Equation	Widely Used Short Computation Time Stable Results Reasonable Results
	One Equation	
	Two Equation κ-ε κ-ω	
Reynolds Stress Model (RSM)		Good Estimate for Many Types of Flows Longer Computation Time than RANS
Large Eddy Simulation (LES)	Smagorinsky-Lilly	Good Results for All Kinds of Flows Solves Large Scale Motions of Flow Models Only Small Scale Motions of Flow
	Dynamic Subgrid-Scale	
	RNG-LES	
	WALLE	
Detached Eddy Simulation		Combination of RANS and LES Model
Direct Numerical Simulation		Most Rigorous Approach

3.3.2.3 Multi-Phase Multi-Scale Models Used in CFD

Several models, with various levels of complexity, have been developed to describe multi-phase (e.g. fluidized bed) flow behavior via CFD. The length scale used for modeling purposes serves as the driving force for the creation of multiple multi-phase models, as one all-encompassing CFD framework is yet to be developed. Different kinds of fluid-particle interactions occur depending on the length scale chosen for observation [123, 124].

The level of interaction between the phases must be determined before a simulation can be run. The three types of phase interactions, also called coupling, regarding multi-phase flow in CFD are shown in Table 3.10 [125].

Table 3.10 Types of Phase Interaction Coupling

Type of Coupling	Comments
One Way	Primary phase influences secondary phase, but secondary phase does not impact primary phase
Two Way	Primary phase influences secondary phase and secondary phase influences primary phase, but no interaction between particles
Four Way	Primary phase influences secondary phase and secondary phase influences primary phase, and there is interaction between particles

Once the level of interaction has been established the modeling scale can be addressed. There are three scales for models in CFD (listed by increasing geometry): lattice Boltzmann model (LBM), discrete particle model (DPM), the continuum model, and the discrete bubble model - a combination of DPM and continuum models [112, 123]. The LBM focuses on interactions between the fluid and particle. The DPM focuses on interactions between particles. The continuum model incorporates bubble phenomena with the DPM particle-particle interactions [112, 123]. The computation time increases as the scale length used for calculation decreases. In addition, the number of particles that can be included in the simulation decreases with decreasing scale length [123]. van der Hoef et al. [112] incorporated the LBM and DPM into a continuum model in an attempt to model a fluidized bed. Quantitative data from the LBM was found to improve agreement between DPM simulations and experiment results, yet only qualitative results could be ascertained from DPM simulations.

Due in part to the large size of industrial fluidized bed equipment (for coating, combustion, reactions, etc.) the two different approaches primarily used to model behavior are Eulerian (continuum) models and Lagrangian (discrete element) models [3, 113, 126]. Both the Eulerian and Lagrangian models handle the gas phase as a continuum, but differ in the treatment of the particulate phase [3].

3.3.2.4 Eulerian (Continuum) Modeling

In Eulerian (continuum) modeling the particulate phase is treated as a continuum just like the gas phase and both phases are completely interpenetrative. The kinetic theory of granular flow (KTGF) – discussed briefly in Chapter 2, an expansion of the kinetic theory of gases, is used to represent dense particulate flow non-idealities (e.g. drag forces on a particle body, the coefficient of restitution for particle-particle collisions). Eulerian models have been reported to be highly sensitive to the magnitude of the coefficient of restitution in part for a few reasons: limitations regarding modeling inelastic particle-particle collisions or particle-wall collisions and the absence of gas phase turbulence [113].

The particulate phase in a Eulerian model is typically taken as a uniform distribution of one particle diameter with uniform properties (i.e. porosity, sphericity, surface area, volume etc.) The particulate phase also has no equation of state, so averaging techniques are used to help solve momentum balances [3].

The Eulerian approach has been successfully implemented for modeling general hydrodynamics of fluidized bed reactors [127, 128]. In addition to collision dynamics, other interactions in fluidized bed coating such as gas-liquid-solid interactions have yet to be incorporated into a standard modeling framework [129]. However, Duangkhamchang et al. [129] demonstrated fluidized bed coater could be modeled to some degree of accuracy. The gas superficial velocity was found to have a significant impact on the bed hydrodynamic behavior. A particle sub-model has also been successfully developed to predict the particle bed height, voidage distribution, and solids volume fraction [130].

3.3.2.5 Lagrangian (Discrete) Modeling

In Lagrangian modeling, the particulate phase is discretized such that the equations governing particle motion (including particle-particle collisions and drag) shown as Equations 3.23 and 3.24 are solved for individual particles [131]:

$$m_i \frac{dv_i}{dt} = f_{ci} + f_{fpi} + m_i g \tag{3.23}$$

$$I_i \frac{d\omega_i}{dt} = T_i \tag{3.24}$$

where f_{ci} represents the particle-particle collision force, f_{fpi} is the fluid-particle interaction force (drag), I_i is the moment of inertia and T_i is torque resulting from the tangential components of the contact forces. Equation 3.23 represents the translational motion of the particle, while Equation 3.24 represents the rotational particle motion. Since the particulate phase is discretized and the motion for each particle is calculated, the supplemental closure equations of the Eulerian approach are not needed [113]. However, the number of particles that can be tracked via discretization is limited. Lagrangian models can generally track the movement of 10^6 particles, but an industrial size fluidized bed coating operation will have several orders of magnitude more particles [113].

There are two classes of Lagrangian models in literature, the hard-particle model and the soft-particle model. The main difference between the two models lies in the particle-particle interactions [113]. Furthermore, the hard particle approach is classified as event driven while the soft particle approach is classified as time driven [123].

In the hard sphere approach, developed by Alder and Wainwright [132, 133], instantaneous binary collisions allow for interaction between particles. A series of collisions is evaluated individually (numerous particle-particle collisions cannot be treated yet) and an

inventory of future collisions is created for evaluation at the next event stage [77, 123]. Collision laws describe energy dissipation with the introduction of three coefficients: coefficient of normal restitution, coefficient of tangential restitution, and coefficient of friction [113]. The coefficient of tangential restitution arises from two different possibilities that can occur after contact between particles, sliding or sticking. Sliding occurs when there is a high impact velocity between particles adequate enough that the particles slide across one another during the entire course of impact. Sticking occurs after an initial sliding phase, but in this case one of the particles has no tangential velocity post impact [113]. Since the hard sphere approach focuses on the energy dissipation of particle-particle collisions, to keep the particles in a consistent state of motion an external source of energy must be provided to the particles. The energy source for particle motion can be supplied via a few different paths: the boundary conditions imposed on the system, gravitational force, or the drag force resulting from the gas phase [123].

The hard sphere approach has been used to model several aspects of fluidized bed operation: particle segregation, gas bubble formation, spouted fluidized beds, circulating fluidized beds, and flow through contracting pipes [77]. Hard sphere models have also been used to develop granulation models [123, 134]. All kinds of collisions – wet and dry particle-particle, droplet-droplet, and droplet-particle collisions are considered hard sphere collisions. New particles are formed if boundary conditions for agglomeration are met [134].

The soft sphere approach, developed by Cundall and Strack [135], involves calculation of collision dynamics (i.e. collision forces, energy dissipation, etc.) based on deformation profiles from a linear spring/dashpot model, after fixed time steps have occurred [77, 123]. The soft sphere approach allows for a small degree of overlapping between particles compared to the hard sphere approach [123].

The soft sphere approach has been used to model several aspects of fluidized bed operation: particle segregation, 2-D fluidized bed behavior, cohesive powder fluidization, Geldart A particulate fluidization, and decomposition of ozone in a fluidized bed reactor [77].

The soft sphere approach requires higher computation cost compared to the hard sphere approach, but does provide additional insight. The soft sphere approach yields information regarding particle: force and energy distributions, velocities, and positions. In the case of granulation, agglomerates are modeled as primary particle clusters and an inherent assumption of spherical shape and elastic in nature is taken [136]. Another perk of the soft sphere approach is that particle/agglomerate morphology can be ascertained from the CFD simulation [137].

CFD modeling approaches have been applied to fluidized bed granulation operations with variety of parameters investigated. Table 3.11 shows a list of published works regarding CFD modeling of fluidized bed granulation.

Table 3.11 CFD Modeling of Granulation

Reference	**Comments**
[113]	Eulerian
[134]	Lagrangian-Eulerian
[138, 139, 143]	Lagrangian
[140, 142, 144, 145]	Eulerian-Eulerian
[141]	Lagrangian-Lagrangian
[146, 147]	Lagrangian-Eulerian

CFD modeling of fluidized bed coating is still in the introductory phase of becoming a mainstream computation. Part of the reason for this is because most models used for spraying in CFD computation until recently accounted for all the spray droplets rather than a portion [90]. Table 3.12 shows a list of published works for CFD modeling of fluidized bed coating operations.

Table 3.12 CFD Modeling of Particle Coating

Reference	Comments
[148]	Atomization Air Pressure Combined with Fluidization Air Flow Rate Impact on Particle Circulation Pattern in Spray Area
[149]	Eulerian-Eulerian, Particle Moisture Content Specified
[128]	Merged Nozzle Air Flow Hydrodynamics (No Liquid) into Fluidized Bed Model
[130]	Bubbling Fluidized Bed Hydrodynamics Introduced (Bed Height and Particle Distribution)

Computational fluid dynamics overall has provided a great deal of insight into various details of fluidized bed operation [150, 151]. However, DEM/CFD has yet to reach the point where coating uniformity can be predicted a priori [152].

3.4 Stochastic Models

Stochastic models represent the other class of mechanistic models that have been used to describe fluidized bed coating performance. In this approach distributions for certain parameters (e.g. particle size, droplet size, etc.) are used rather than singular values as in the deterministic model approach. The end result of a stochastic model is a distribution of values rather than a single point. There are two different methodologies within the stochastic model approach that are used - population balances and Monte Carlo methods. Moreover, Monte Carlo methods are often used as solution techniques in the population balance approach, depending on the model complexity [153].

3.4.1 Population Balance Modeling

The origins to the population balance equation (PBE) can be traced to work done Smoluchowski [154] in an effort to describe the coagulation of a particle size distribution as a function of time. The PBE developed by Smoluchowski was written in a discrete form. The general form of the PBE was later published independently by Hulbert and Katz [155] and

Randolph [156] with a great deal of mathematical work following in the 1970's and 1980's to provide a solid basis for the PBE as a statistical tool for modeling [157]. PBE's have since been applied to many chemical processes containing a particulate phase (particulate in this case can mean a solid or liquid droplet), including: agglomeration (aerosol technology or particles in a fluidized bed), polymerization, combustion, flocculation, mixing, crystallization, comminution, and microbial cell growth [158-160].

Population balances have internal and external coordinate systems. The internal coordinate system reflects properties of the system (i.e. volume, particle size, surface area, porosity, etc.) written out in a vector form, while the external coordinate system identifies the particle position within the fluidized bed (in rectangular, spherical, or cylindrical coordinates) [137]. The general form of the 1-D population balance equation is shown as Equation 3.25 [153]:

$$\underbrace{\frac{\partial f(x,t)}{\partial t}}_{\substack{\text{Number Density}\\ \text{Function}}} + \underbrace{\frac{\partial}{\partial x}\left(G(x,t)\cdot n(x,t)\right)}_{\text{Growth by Coating}} = \underbrace{B(x,t)}_{\text{Birth Term}} - \underbrace{D(x,t)}_{\text{Death Term}} \qquad (3.25)$$

The number density function in Equation 3.25 accounts for the accumulation term of a material balance, while the growth term represents the convective movement of the particles in the fluidized bed. The birth and death terms of Equation 3.25 represent the appearance and disappearance of particles due to agglomeration and breakage (there are birth and death terms for each phenomenon) and are given as Equations 3.26-3.29 [161]:

$$B_{agg}(x,t) = \frac{1}{2}\int_0^x \beta(x-\epsilon,t)n(x-\epsilon,t)n(\epsilon,t)d\epsilon \qquad (3.26)$$

$$B_{break}(x,t) = \int_0^\infty b(x,\epsilon)S(\epsilon)n(\epsilon,t)d\epsilon \qquad (3.27)$$

$$D_{agg}(x,t) = n(x,t)\int_0^x \beta(x,\epsilon,t)n(\epsilon,t)d\epsilon \tag{3.28}$$

$$D_{break}(x,t) = S(x)n(x,t) \tag{3.29}$$

where β is the coalescence kernel (rate constant), n(ε,t) represents the probability of coalescence success, b(x,ε) represents the breakage probability density function and the selection function S(x), is the rate particles are selected to break.

The coalescence kernel is an empirical or semi-empirical parameter because it is regressed from experiment data. Several different models have been proposed in literature to describe the coalescence kernel based on colliding particle volumes. Table 3.13 shows some previously published coalescence kernel models where u and v represent particle volumes [137, 162, 163].

Table 3.13 Previously Published Coalescence Kernel Models

Model	**Reference**
$\beta = \beta_o$	Kapur & Fuerstenau (1969)
$\beta = \beta_o \frac{(u+v)^a}{(uv)^b}$	Kapur (1972)
$\beta = \beta_o \frac{\left(u^{\frac{2}{3}} + v^{\frac{2}{3}}\right)}{\left(\frac{1}{u}+\frac{1}{v}\right)}$	Sastry (1975)
$\beta = a(u+v)$	Golovin (1963)
$\beta = a\frac{(u-v)^2}{(u+v)}$	Golovin (1963)
$\beta = \begin{cases} k, t < t_1 \\ \text{Golovin Kernel, } t > t_1 \end{cases}$ k, t, constant, t1 is transition time determined by experiment observations	Adetayo et al. (1995)
$\beta = \begin{cases} k, w < w^* \\ 0, w > w^* \end{cases}$ k = constant $w = \frac{(uv)^a}{(u+v)^b}$ w* is a critical granule volume	Adetayo & Ennis (1997)
$\beta = \beta_o(1/u + 1/v)^{0.5}\left(u^{\frac{1}{3}} + v^{\frac{1}{3}}\right)^2$ $\beta = \beta_o\left(u^{-\frac{1}{3}} + v^{-\frac{1}{3}}\right)\left(u^{\frac{1}{3}} + v^{\frac{1}{3}}\right)$	Friedlander (1977, 2000)

Table 3.13 Continued

$\beta_{lu,v} = \begin{cases} \beta_1 & \text{Types I \& II Coalescence} \\ \beta_2 & \text{Type II Coalescence} \\ 0 & \text{Rebound} \end{cases}$	Liu & Lister (2002)

Currently, there is no methodology behind choosing a kernel model for the PDE birth and death terms. Two assumptions behind the PBE (Equation 3.25) that may have negative implications are that particle size is the only independent variable that plays a role in granulation and that there is special uniformity within the fluidized bed [163]. While the particle property most often tracked using a 1-D population balance is volume (via the diameter/radius), Iveson [163] proposed a 4-D population balance incorporating the following variables: granule porosity, binder to solid weight ratio (kg binder/kg solid), solid mass, and solid phase mass fraction (component a, b, etc.). One drawback to developing a 4-D population balance is that the solution method for the multidimensional differential equations can be challenging [153, 163].

3.4.1.1 Solution Methods for Population Balance Models

Analytical solutions for PBE's rarely exist due to the complexity of the system of equations used to describe the particulate phase. Therefore, numerical techniques must be used to transform the equation set into something that can be solved. The numerical techniques employed to solve PBE's include [153]: discrete formulations, method of Laplace transforms, the method of moments and weighted residuals, the method of successive generations, and Monte Carlo methods.

The method of moments numerical solution method was the first solution method for PBE's [164]. Population parameters of interest are estimated at various "moments" during the

simulation and then set equal to the intangible population moments. There are several different techniques that fall under the method of moments classification as shown in Table 3.14.

Table 3.14 Method of Moments Techniques

Technique	Reference
Quadrature Method of Moments (QMOM)	[165]
Direct Quadrature Method of Moments (DQMOM)	[166]
Modified Quadrature Method of Moments (M-QMOM)	[167]
Adaptive Direct Quadrature Method of Moments (ADQMOM)	[168]
Fixed Pivot Quadrature Method of Moments (FPQMOM)	[169]
Moving Particle Ensemble Method (MPEM)	[170]
Local Fixed Pivot Quadrature Method of Moments (LFPQMOM)	[171]

While the method of moments techniques offer a path to the solution of the PBE, it is not without issues. Most of the method of moments techniques cannot give a particle size distribution because of function overlap, with the exceptions being MPEM and LFPQMOM [171].

Monte Carlo methods can be event based or time based [172]. The Monte Carlo method can be utilized as a tool for solving PBE's when three criteria are fulfilled: the process behavior dynamics follow in accordance with the probabilities outlined by system boundary conditions, the time step within which events (e.g. coalescence, rebound, coating, deformation) occur can be defined rigorously, and all the events are independent of one another [173]. Additionally, Monte Carlo methods can be categorized according to particle dynamics - i.e. constant number of particles during a simulation or a changing number of particles during a simulation [172].

There are several Monte Carlo methods that can be used to solve PBE's as shown in Table 3.15. While the Monte Carlo methods have slightly different approaches to solving a problem, they all yield similar results with respect to particle size distribution. Computation time is the only advantage for choosing one Monte Carlo method over. Event driven Monte Carlo

simulations tend to be less computationally demanding than time driven Monte Carlo simulations, because event occurrence serves as the driving force for the advancement of time in a simulation, but a time step forward does not guarantee the occurrence of an event [172].

Table 3.15 Monte Carlo Methods Used to Solve PBE's

Monte Carlo Method	Event or Time Driven	Reference
Constant Number	Event	[174]
Constant Volume	Event	[175]
Direct Simulation	Time	[176]
Multi	Time	[177]

Constant Number refers to the number of particles remaining constant for the entire simulation. Constant Volume refers to the particle volume remaining constant during the simulation, but the number of particles can change. In Direct Simulation Monte Carlo, the simulation moves forward via a time step with occasional adjustments for the number of particles. Multi-Monte Carlo simulations work in a similar manner to Direct Simulation but in addition it keeps track of weighting factors for the particles (each particle represents a cluster of particles) [172].

3.4.1.2 Previously Published Population Balance Models for Fluidized Bed Granulation and Coating

PBE's have been used successfully in modeling fluidized bed granulation operations. Table 3.16 provides a listing of some published works regarding fluidized bed granulation modeled by PBE's.

Table 3.16 Fluidized Bed Granulation Population Balance Published Works

Reference	Comments
[178]	Random Coalescence in Granulation
[179]	Random Coalescence Model with a Non-Random Coalescence Kernel
[180]	Transformation of PBE into ODE's and Solved for Nucleation, Growth, and Aggregation
[159]	Two Stage Granulation Kernel PBE Developed
[162]	Coalescence Kernel Model Incorporating Stokes Viscous Number
[181]	PBE's for Tracers, Generalized Method to Calculate Rate Constants from PBE's
[182]	Start Up Process of Continuous Fluidized Bed Granulation
[183]	Different Rate Constants Assigned to Type I and II Coalescence
[184]	Separation of Growth Kernel into 3 Segments for PBE
[185]	Process Stability of a Continuous Fluidized Bed Granulation
[186]	2-D PBE Fluidized Bed Melt Granulation
[187]	3-D PBE for Wet Granulation (Liquid Volume, Solid Volume, Liquid in Solid Pores)
[188]	Need for Higher Dimension PBE to Model Granulation
[189]	CFD-PBE Combination for Wurster Fluidized Bed Granulation
[190, 191]	3-D (Particle Size, Binder Amount, Particle Porosity) Population Balance for Granulation
[192]	New Breakage Kernel for PBE Model for Granulation
[193]	PBE Accounting for Pre-Drying of Spray Droplets
[194]	Process Stability of Large Scale Granulation
[195]	CFD and PBE Combination for Continuous Granulation Modeling
[196]	PBE for Flow Induced Phase Inversion Granulation
[197]	3-D PBE for Design and Control of a Continuous Granulation Process
[198]	Need for Particle Surface Moisture Content to be Included in PBE for Granulation
[199]	Multidimensional PBE Coupled with Mass and Energy Balance for Granulation
[200]	Multidimensional PBE Incorporating Particle Morphology into Granule Growth

In the case of particle coating, ideally no agglomeration or particle breakage occurs so that the population balance equation presented in Equation 3.25 is simplified to Equation 3.30:

$$\underbrace{\frac{\partial f(x,t)}{\partial t}}_{\substack{\text{Number Density}\\ \text{Function}}} = -\underbrace{\frac{\partial}{\partial x}\left(G(x,t)\cdot n(x,t)\right)}_{\text{Growth by Coating}} \tag{3.30}$$

Table 3.17 shows a list of some published works regarding fluidized bed coating modeled by PBE's.

Table 3.17 Fluidized Bed Coating Population Balance Published Works

Reference	Comments
[201]	PBE for Three Different Zones in Top Spray Orientation
[202]	PBE Accounting for Coating and Agglomeration
[203]	PBE Developed for Two Different Zones in Bottom Spray Orientation
[204, 205]	Combined Thermodynamic Behavior with PBE
[206]	PBE with Incorporation of Spray Drying Loss Estimate
[207]	2-D PBE to Model Coating Growth
[208]	PBE for Continuous Wurster Orientation Fluidized Bed Coating Process

Typical assumptions that accompany particle growth models include: only spherical non-porous particles are present, particle growth only occurs by coating deposition, no particle breakage, no particle elutriation, the particle attrition rate and spray drying rate are constant, the fluidization gas exhibits ideal plug flow behavior, spray dried material elutriates the bed [201, 206].

3.4.2 Monte Carlo Methods

The Monte Carlo method of analysis, developed in 1944 to estimate the value of π, is a technique where deterministic relationships are transformed into probability distributions because a range of values is put in place of single inputs. The resulting distribution shows the sensitivity of a process to parametric uncertainties [209]. Figure 3.16 maps the flow of data for Monte Carlo simulations.

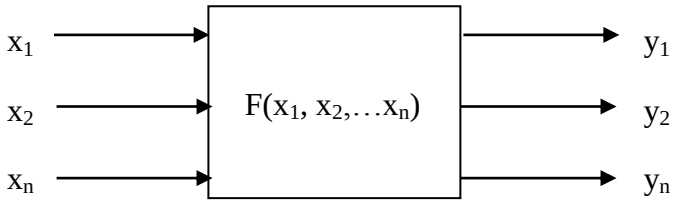

Figure 3.16 General Data Flow for Monte Carlo Simulations

Monte Carlo analysis has been applied to many areas of fluidization as shown in Table 3.18.

Table 3.18 Published Fluidized Bed Stochastic Models

Aspects Modeled	Reference
Attrition	[210]
Bubble Motion, Population, Size	[211-213]
Fluidized Bed Void Fraction	[214]
Gas Residence Time	[215]
Mixing	[216, 217]
Particle Convective Heat Transfer	[218]
Particle Motion	[219, 220]
Particle Residence Time	[221-223]
Particle Velocity Distribution	[224]
Pressure Fluctuations	[225]
Reactions	[226]

Monte Carlo analysis has also been applied to fluidized bed granulation and fluidized bed coating operations as shown in Table 3.19.

Table 3.19 Stochastic Models for Fluidized Bed Granulation and Fluidized Bed Coating

Aspects Modeled	Reference	Comments
Granulation	[227-228]	Validation of Dimensionless Spray Flux Validation of Incorporation of Particle-Level Modeling into Overall Balance
Coating	[229-234]	Coating Mass Distribution Coating Mass Distribution Coating Thickness Distribution Coating Efficiency Coating Uniformity

Similarly to the assumptions made for coating growth models using PBE's, additional assumptions are sometimes made regarding various attributes– spray drying losses and spray geometry [234].

3.5 Lumped Modeling

One final approach to modeling fluidized beds was initially developed by Overturf & Reklaitis [235, 236] for atmospheric coal combustion. Here the gas-solid behavior is combined (or "lumped") with the two-phase bubbling bed behavior into a series of grids. The grids are then iteratively solved for temperature profiles. The lumped approach to fluidized bed modeling can provide a bridge between the relatively simplistic fluidized bed modeling approaches (particle level models) and computationally demanding fluidized bed modeling approaches (i.e. CFD, PBE's).

This approach has subsequently been used by many others in research to model fluidized bed various aspects of granulation and particle coating as shown in Table 3.20.

Table 3.20 Variables Investigated with Lumped Fluidized Bed Models

Reference	Variables Investigated
[237]	Temperature and Relative Humidity as a Function of Height and Radial Distance
[238]	Particle Wetting and Temperature Distribution
[204, 205]	Fluid Bed Thermodynamic Behavior
[3]	Viscous Stokes Number, Drying Force

The work by Maronga and Wnukowski [237] identified different regions within the fluidized bed noted previously in Chapter 2 and provided the groundwork for work done by Ronsse [204, 205] and Hede [3].

3.6 Summary of Fluidized Bed Coating Modeling Approaches

As shown throughout this chapter, there has been a great deal of effort put forth to understanding and replicating two phase behavior in a fluidized bed. Several different approaches, with varying levels of complexity, have been used to model fluidized beds with success. Table 3.21 provides a short summary of the modeling approaches to fluidized bed behavior.

Table 3.21 Summary of Fluidized Bed Modeling Approaches

Model Approach	Advantages	Drawbacks
Empirical	Easy to Implement Flexibility with Choice of Dependent/Independent Variable Combinations	Usually Equipment/Experiment Condition Specific No Knowledge Regarding Elemental Phenomena/Mechanisms
Deterministic Models		
Particle Level	Gives Insight into Phenomena/Mechanisms That Occur During Coating/Granulation Operations	Not Robust Enough to Use Alone for Modeling
Computational Fluid Dynamics	Can Be Used to Model Fluid Flow at Any Scale Individual Particle Motions Calculated Particle Morphology Can Be Ascertained Using Soft Particle Model	Particle Equation of State Needed for Eulerian Models Limited Number of Particles Can Be Tracked Because of Computation Intensity Particle Morphology Cannot Be Ascertained From Hard Particle Model
Stochastic Models		
Population Balance	Particles/Particle Properties Are Characterized as Distributions Can Be Used for Dynamic Modeling	1-D PBE Not Deemed Rigorous Enough for Modeling Still Somewhat Empirical Nature of Breakage/Death Terms Higher Order PBE Solutions Techniques Not Available

Table 3.21 Continued

Monte Carlo	Parameters of Interest Are Characterized as Distributions Can Be Used for Dynamic Modeling	Can Be Computationally Intensive
Combined		
Lumped	Flexible Approach Allows Incorporation of Multiple Approaches	Particle Level Information Not Immediately Evident

3.7 References

[1] Montgomery, D.C. (2005) Design and Analysis of Experiments, John Wiley & Sons:New York.

[2] Tham, M. (2000) Overview of Mechanistic Modeling Techniques, University of New Castle upon Tyne, Department of Chemical and Process Engineering, United Kingdom.

[3] Hede, P.D. (2008) Ph.D. Dissertation,Technical University of Denmark.

[4] Spitael, J., Kinget, R., & Naessens, K. (1979) Application of a Factorial Design Study to the Coating of Four Drug Substances in Fluidized Bed, Pharmacy World & Science, 1(1), 1438-1443.

[5] Johansson, M.E., Ringberg, A., & Nichlasson, M. (1987) Optimization of a Fluid Bed Coating Process Using Reduced Factorial Design, Journal of Microencapsulation, 4(3), 217-222.

[6] Jozwiakowski, M.J., Jones, D.M., & Franz, R.M. (1990*)* Characterization of a Hot Melt Fluid Bed Coating Process for Fine Granules, Pharmaceutical Research, 7(11), 1119-1126.

[7] Dewettinck, K. & Huyghebaert, A. (1998) Top Spray Fluidized Bed Coating: Effect of Process Variables on Coating Efficiency, Food Science and Technology, 31(6), 568-575.

[8] Williams, R.O. & Liu, J. (2000) Influence of Processing and Curing Conditions on Beads Coated with an Aqueous Dispersion of Cellulose Acetate Phthalate, European Journal of Pharmaceutics and Biopharmaceutics, 49(3), 243-252.

[9] da Silva, O. & Rocha, S.C.S. (2004) Prediction of Efficiency and Particles Growth in the Granules Coating and Drying Process by Statistical Experimental Design, Drying – Proceedings of the 14th International Drying Symposium, Vol. B, 860-867.

[10] Oliveira, H.V.A., Peixoto, M.P.G., & Freitas, L.A.P. (2005*)* Study on the Efficiency of Hard Gelatin Capsules Coating in a Spouted Fluidized Bed, Drying Technology, 23, 2039-2053.

[11] Hede, P.D., Boch, P., & Jensen, A.D. (2007) Small Scale Top Spray Fluidized Bed Coating: Granule Impact Strength, Agglomeration Tendency, and Coating Layer Morphology, Powder Technology, 176, 156-167.

[12] Nitz, M. & Taranto, O.P. (2008) Film Coating of Theophylline Pellets in a Pulsed Fluidized Bed Coater, Chemical Engineering and Processing, Process Intensification, 47(8), 1412-1419.

[13] Shah, V.A., Shinde, M.L., Patil, S.B., Nikam, M.B., Ghodke, D.S., & Shah, R.R. (2011). Impact of Selected Variables on the Preparation of Aceclofenac Microspheres by Spray Drying Using Full Factorial Design, International Journal of PharmTech Research, 3 (2), 1066-1072.

[14] Albanez, R., Nitz, M. & Taranto, O.P. (2013) Enteric Coating Process of Diclofenac Sodium Pellets in a Fluid Bed Coater with a Wurster Insert: Influence of Process Variables on Coating Performance and Release Profile, Advanced Powder Technology, 24, 659-666.

[15] Menon, A., Dhodi, N., Mandella, W., & Chakrabarti, S. (1996) Identifying Fluid-Bed Parameters Affecting Product Variability, International Journal of Pharmaceutics, 140, 207-218.

[16] Gao, J.Z.H., Jain, A., Motheram, R., Gray, D.B., & Hussein, M.A. (2002) Fluid Bed Granulation of a Poorly Water Soluble, Low Density, Micronized Drug: Comparison With High Shear Granulation, International Journal of Pharmaceutics, 237,1-14.

[17] Paterakis, P.G., Korakianiti, E.S., Dallas, P.P., & Rekkas, D.M. (2002) Evaluation and Simultaneous Optimization of Some Pellets Characteristics Using a 3^3 Factorial Design and the Desirability Function, International Journal of Pharmaceutics, 248, 51-60.

[18] Burggraeve, Van Den Kerkof, T., Hellings, M., Remon, J.P., Vervaet, C., & De Beer, T. (2010) Evaluation of In-Line Spatial Filter Velocimetry as PAT Monitoring Tool for Particle Growth During Granulation, European Journal of Pharmaceutics and Biopharmaceutics, 76, 138-146.

[19] Liu, H., Wang, K., Schlindwein, W., & Li, M. (2013) Using the Box-Behnken Experimental Design to Optimize Operating Parameters in Pulsed Spray Fluidized Bed Granulation, International Journal of Pharmaceutics, 448, 329-338.

[20] Cheow, W.S., Li, S., & Hadinoto, K. (2010) Spray Drying Formulation of Hollow Spherical Aggregates of Silica Nanoparticles by Experimental Design, Chemical Engineering Research and Design, 88, 673-685.

[21] Gallo, L., Llabot, J.M., Allemandi, D., Bucalá, V., & Piña, J. (2011) Influence of Spray Drying Operating Conditions on Rhamnus Purshiana (Cáscara Sagrada) Extract Powder Physical Properties, Powder Technology, 208, 205-214.

[22] López-Muñoz, F., Boya, J. & Alamo, C. (2006) Neuron Theory, the Cornerstone of Neuroscience, on the Centenary of the Nobel Prize Award to Santiago Ramón y Cajal, Brain Research Bulletin, 70, 391-405.

[23] Basheer, I.A., & Hamjeer, M. (2000) Artificial Neural Networks: Fundamentals, Computing, Design, and Application, Journal of Microbiological Methods, 43, 3-31.

[24] Haykin, S. (1999) Neural Networks: A Comprehensive Foundation, Prentice Hall: New York.

[25] Hebb, D.O. (1949) The Organization of Behavior: A Neuropsychological Theory, Wiley: New York.

[26] Rosenblatt, F. (1958) The Perceptron: A Probabilistic Model for Information Storage and Organization in the Brain, Psychological Review, 65, 386-408.

[27] Minsky, M.L. & Papert, S.A. (1969) Perceptrons, Cambridge: MIT Press.

[28] Hopfield, J.J. (1982) Neural Networks and Physical Systems with Emergent Collective Computational Abilities, Proceedings of the National Academy of Sciences, USA, 79, 2554-2558.

[29] Kohonen, T. (1982) Self-Organized Formation of Topologically Correct Feature Maps, Biological Cybernetics, 43, 59-69.

[30] Rumelhart, D.E., Hinton, G.E., & Williams, R.J. (1986) Learning Representations of Back-Propagation Errors, Nature, 323, 533-536.

[31] Murtoniemi, E., Yliruusi, J., Kinnunen, P., & Leiviskä, K. (1994a) The Advantages By the Use of Neural Networks in Modeling the Fluidized Bed Granulation Process, International Journal of Pharmaceutics, 108, 155-164.

[32] Murtoniemi, E., Merkku, P., Kinnunen, P., Leiviskä, K. & Yliruusi, J. (1994b) Effect of Neural Network Topology and Training End Point in Modeling the Fluidized Bed Granulation Process, International Journal of Pharmaceutics, 110, 101-108.

[33] Watano, S., Sato, Y., & Miyanami, K. (1997) Application of Neural Network to Granulation Scaleup, Powder Technology, 90, 153-159.

[34] Rantanen, J., Räsänen, E., Antikainen, O., Mannerma, J.P., & Yliruusi, J. (2001) In-Line Moisture Measurement During Granulation with a Four-Wavelength Near-Infrared Sensor: An Evaluation of Process-Related Variables and a Development of Non-Linear Calibration Model, Chemometrics and Intelligent Laboratory Systems, 56, 51-58.

[35] Laitinen, N., Rantanen, J., Laine, S., Antikainen, O., Räsänen, E., Airaksinen, S., & Yliruusi, J. (2002) Visualization of Particle Size and Shape Distributions Using Self-Organizing Maps, Chemometrics and Intelligent Laboratory Systems, 62, 47-60.

[36] Behzadi, S.S., Klocker, J., Hüttlin, H., Wolschann, P., & Vierstein, H. (2005) Validation of Fluid Bed Granulation Utilizing Artificial Neural Network, International Journal of Pharmaceutics, 291, 139-148.

[37] Behzadi, S.S., Prakasvudhisarn, C., Klocker, J., Wolschann, P., & Vierstein, H. (2009) Comparison Between Two Types of Artificial Neural Networks for Validation of Pharmaceutical Processes, Powder Technology, 195, 150-157.

[38] Petrović, J., Chansanroj, K., Meier, B., Ibrić, S., & Betz, G. (2011) Analysis of Fluidized Bed Granulation Process Using Conventional and Novel Modeling Techniques, European Journal of Pharmaceutical Sciences, 44, 227-234.

[39] Liukkonen, M., Heikkinen, M., Hiltunen, T., Hälikkä, E., Kuivalainen, R., & Hiltunen, Y. (2011) Artificial Neural Networks for Analysis of Process States in Fluidized Bed Combustion, Energy, 36, 339-347.

[40] Chavan, P.D., Sharma, T., Mall, B.K., Rajukar, B.D., Tambe, S.S., Sharma, B.K., & Kulkarni, B.D. (2012) Development of Data Driven Models for Fluidized Bed Coal Gasification, Fuel, 93, 44-51.

[41] Puig-Arnavat, M., Hernandez, J.A., Bruno, J.C., & Coronas, A. (2013) Artificial Neural Network Models for Biomass Gasification in Fluidized Bed Gasifiers, Biomass and Bioenergy, 49, 279-289.

[42] Chen, W., Tsutsumi, A., Lin, H., & Otawara, K. (2005) Modeling Nonlinear Dynamics of Circulating Fluidized Beds Using Neural Networks, China Particuology, 3, 84-89.

[43] Razzak, S.A., Rahman, S.M., Hossain, M. M. & Zhu, J. (2012) Investigation of Artificial Neural Network Methodology for Modeling of a Liquid-Solid Circulating Fluidized Bed Riser, Powder Technology, 229, 71-77.

[44] Krzywanski, J. & Nowak, W. (2012) Modeling of Heat Transfer Coefficient in the Furnace of CFB Boilers by Artificial Neural Network Approach, International Journal of Heat and Mass Transfer, 55, 4246-4253.

[45] Sahoo, A. & Roy, G.K. (2007) Artificial Neural Network Approach to Segregation Characteristic of Binary Homogeneous Mixtures in Promoted Gas-Solid Fluidized Beds, Powder Technology, 171, 54-62.

[46] Sahoo, A. & Roy, G.K. (2008) Segregation Characteristics of Irregular Binaries in Gas Solid Fluidized Beds – an ANN Approach, Particuology, 6, 199-206.

[47] Zbiciński, I., Strumillo, P., & Kamiński, W. (1996) Hybrid Neural Model of Thermal Drying in a Fluidized Bed, Computers & Chemical Engineering, 20, S695-S700.

[48] Cubillos, F.A., Alvarez, P.E., Pinto, J.C., & Lima, E.L. (1996) Hybrid-Neural Modeling for Particulate Solid Drying Processes, Powder Technology, 87, 153-160.

[49] Topuz, A. (2010) Predicting Moisture Content of Agricultural Products Using Artificial Neural Networks, Advances in Engineering Software, 41, 464-470.

[50] Neshat, N., Mahlooji, H., & Kazemi, A. (2011) An Enhanced Neural Network Model for Predictive Control of Granule Quality Characteristics, Scientia Iranica, 18, 722-730.

[51] Nazghelichi, T., Aghbashlo, M., & Kianmehr, M.H. (2011) Optimization of an Artificial Neural Network Topology Using Coupled Response Surface Methodology and Genetic Algorithm for Fluidized Bed Drying, Computers and Electronics in Agriculture, 75, 84-91.

[52] Aghbashlo, M., Mobli, H., Rafiee, S., & Madadlou, A. (2012) The Use of Artificial Neural Network to Predict Exergetic Performance of Spray Drying Process, Computers and Electronics in Agriculture, 88, 32-43.

[53] Barletta, M., Gisario, A., & Guarino, S. (2007) Modeling Electostatic Fluidized Bed (EFB) Coating Process Using Artificial Neural Networks, Engineering Applications of Artificial Intelligence, 20, 721-733.

[54] Barletta, M., Gisario, A., Guarino, S. & Tagliaferri, V. (2008) Fluidized Bed Coating of Metal Substrates by Using High Performance Thermoplastic Powders: Statistical Approach and Neural Network Modeling, Engineering Applications of Artificial Intelligence, 21, 1130-1143.

[55] Burggraeve, A., Monteyne, T., Vervaet, C., Remon, J.P., & De Beer, T. (2013) Process Analytical Tools for Monitoring, Understanding, and Control of Pharmaceutical Fluidized Bed Granulation: A Review, European Journal of Pharmaceutics and Biopharmaceutics, 83, 2-15.

[56] Arumugasamy, S.K. & Ahmad, Z. (2009) Elevating Model Predictive Control Using Feedforward Artificial Neural Networks: A Review, Chemical Product and Process Modeling, 4, Article 45.

[57] Fogel, D.B. (1998) Evolutionary Computation: The Fossil Record, IEEE Press: New York.

[58] Barricelli, N.A. (1954) Esempi Numerici di Processi di Evoluzione, Methodos, 45-68.

[59] Barricelli, N.A. (1957) Symbiogenetic Evolution Processes Realized by Artificial Methods, Methodos, 143-182.

[60] Rechenberg, I. (1973) Evolutionsstrategie, Holzmann-Froboog: Stuttgart.

[61] Schwefel, H.P. (1974) Ph.D. Dissertation, Technical University of Berlin.

[62] Schwefel, H.P. (1977) Numerische Optimierung von Computor-Modellen Mittels der Evolutionsstrategie: Mit Einer Vergleichenden Einführung in die Hill-Climbing-und-Zufallsstrategie, Basel, Birkhaüser: Stuttgart.

[63] Fogel, L.J., Owens, A.J., & Walsh, M.J. (1965) Artificial Intelligence Through a Simulation of Evolution, Biophysics and Cybernetic Systems, 131-165.

[64] Holland, J.H. (1975) Adaptation in Natural and Artificial Systems, University of Michigan: Ann Arbor.

[65] Cordón, O., Herrera-Viedma, E., López-Pujalte, C., Luque, M., & Zarco, C. (2003) A Review on the Application of Evolutionary Computation to Information Retrieval, International Journal of Approximate Reasoning, 34, 241-264.

[66] Kasat, R.B. & Gupta, S.K. (2003) Multi-Objective Optimization of an Industrial Fluidized Bed Catalytic Cracking Unit (FCCU) Using Genetic Algorithm (GA) with Jumping Genes Operator, Computers & Chemical Engineering, 27, 1785-1800.

[67] Sankararao, B., & Gupta, S.K. (2007) Multi-Objective Optimization of an Industrial Fluidized Bed Catalytic Cracking Unit (FCCU) Using Two Jumping Genes Adaptations of Simulated Annealing, Computers & Chemical Engineering, 31, 1496-1515.

[68] Wang, D.F. Han, P., Liu, N., Dong, Z., & Jiao, S.M. (2002) Modeling the Circulating Fluidized Bed Boiler Using RBF-NN Based on Immune Genetic Algorithm, 2002 International Conference on Machine Learning and Cybernetics, 4, 2121-2125.

[69] Hengyan, X., Lingmei, W., Huahua, C. (2011) The Study of Optimizing Circulating Fluidized Bed Boiler Operational Parameters Based on Neural Network and Genetic Algorithm, Proceedings of 2011 4th International Conference on Intelligent Computation Technology and Automation, 1, 287-290.

[70] Fakhimghanbarzadeh, B., Farhanieh, B., Marzi, H., & Javadzadegan, A. (2009) Evolutionary Algorithm for Multi-Objective Exergoeconomic Optimization of Biomass Waste Gasification Combined Heat and Power System, 7th IEEE International Conference on Industrial Informatics, 361-366.

[71] Ćojabšić, Z., Nikolić, V.D., Ćirić, I.T., & Ćojabšić, L.R. (2011) Computationally Intelligent Modeling and Control of Fluidized Bed Combustion Process, Thermal Science, 15, 321-338.

[72] Vinod, A.V., Kumar, K.A., & Reddy, G.V. (2009) Simulation of Biodegradation Process in a Fluidized Bed Bioreactor Using Genetic Algorithm Trained Feedforward Neural Network, Biochemical Engineering Journal, 46, 12-20.

[73] Jena, H.M., Roy, G.K., & Mahapatra, S.S. (2010) Determination of Optimum Gas Holdup Conditions in a Three Phase Fluidized Bed by Genetic Algorithm, Computers & Chemical Engineering, 34, 476-484.

[74] Alwan, G. (2012) Optimization of Pressure Drop in a Spouted Bed Via Genetic Algorithm, Innovative Systems Design and Engineering, 3, 12-26.

[75] Faure, A., York, P., & Rowe, R.C. (2001) Process Control and Scale-Up of Pharmaceutical Wet Granulation Processes: A Review, European Journal of Pharmaceutics and Biopharmaceutics. 52, 269-277.

[76] Mortier, S.T.F.C., De Beer, T., Gernaey, K.V., Remon, J.P., Vervaet, C., & Nopens, I. (2011) Mechanistic Modelling of Fluidized Bed Drying Processes of Wet Porous Granules: A Review, European Journal of Pharmaceutics and Biopharmaceutics, 79, 205-225.

[77] Deen, N.G., Van Sint Annaland, M., Van der Hoef, M.A., & Kuipers, J.A.M. (2007) Review of Discrete Particle Modeling of Fluidized Beds. Chemical Engineering Science, 62, 28-44.

[78] Ennis, B.J., Tardos, G. & Pfeffer R. (1991) A Microlevel-Based Characterization of Granulation Phenomena, Powder Technology, 65, 257-272.

[79] Iveson, S.M., Litster, J.D., Hapgood, K., & Ennis, B.J. (2001) Nucleation, Growth, and Breakage Phenomena in Agitated Wet Granulation Processes: A Review, Powder Technology, 117, 3-39.

[80] Chander, S., Hogg, R. & Fuerstenau D.W. (2007) Characterization of the Wetting and Dewetting Behavior of Powders. Kona, No. 25, 56-75.

[81] Sharfrin, E. & Zisman, W.A. (1960) Constitutive Relations in the Wetting of Low Energy Surfaces and the Theory of the Retraction Method of Preparing Monolayers. Journal of Physical Chemistry, 64(5), 519-524.

[82] Lazghab, M. Saleh, K., Pezron, I., Guigon, P. & Komunjer, L. (2005) Wettability Assessment of Finely Divided Solids. Powder Technology, 157, 79-91.

[83] Batchelor, G.K. (1967) An Introduction to Fluid Dynamics, Cambridge University: London.

[84] Denesuk, M., Smith, G.L., Zelinski, B.J.J., Kreidl, N.J., & Uhlmann, D.R. (1993) Capillary Penetration of Liquid Droplets into Porous Materials, Journal of Colloid Interface Science, 158, 114-120.

[85] Denesuk, M., Smith, G.L., Zelinski, B.J.J., Kreidl, N.J., & Uhlmann, D.R. (1993) Dynamics of Incomplete Wetting on Porous Materials, Journal of Colloid Interface Science, 168, 141-151.

[86] Hapgood, K., Lister, J.D., Biggs, S.R., & Howes, T. (2002) Drop Penetration into Porous Powder Beds, Journal of Colloid Interface Science, 253, 353-366.

[87] Nienow, A.W. (1995) Fluidised Bed Granulation and Coating: Applications to Materials, Agriculture, and Biotechnology, Chemical Engineering Communications, 139, 233-253.

[88] Sunol, A.K. & Sunol, S.G. (2004*)* Templating Aerogels for Tunable Nanoporosity, Dekker Encyclopedia of Nanoscience and Nanotechnology, 3843-3851.

[89] Sloth, J. (2007) Formation of Enzyme Containing Particles by Spray Drying, Ph.D. Thesis Technical University of Denmark.

[90] Vanderroost, M., Ronsse, F., Dewettinck, K., & Pieters, J. (2011) Modelling Coating Quality in Fluidized Bed Coating: Spray Sub-Model, Journal of Food Engineering, 106, 220-227.

[91] Walton, D.E. & Mumford, C.J. (1999) Spray Dried Products – Characterization of Particle Morphology, Transactions of the Institute of Chemical Engineers, 77, 21-38.

[92] C.A. Garcia-Gonzalex, M.C. Camino-Rey, M. Alnaief, C. Zetzl, I. Smirnova (2012) Supercritical Drying of Aerogels Using CO_2: Effect of Extraction Time on the End Material Textural Properties, Journal of Supercritical Fluids, 66, 297-306.

[93] Hunter, R.J. (2001) Foundations of Colloid Science 2nd Edition, Oxford University Press: London.

[94] Walton, D.E. & Mumford, C.J. (1999). Spray Dried Products – the Effect of Process Variables upon Particle Morphology of Spray Dried Particles,Transactions of the Institute of Chemical Engineers, 77, 442-460.

[95] Link, K.C., & Schlunder, E.U. (1997) Fluidized Bed Spray Granulation – Investigation of the Coating Process on a Single Sphere, Chemical Engineering and Processing, 36, 443-457.

[96] Guignon, B., Duquenoy, A., & Dumoulin, E. (2002*)* Fluid Bed Encapsulation of Particles: Principles and Practice. Drying Technology, 20(2), 419-447.

[97] Werner, S.R.L., Jones, J.R., Paterson, A.H.J., Archer, R.H., & Pearce, D.L. (2007) Air Suspension Particle Coating in the Food Industry: Part I – State of the Art, Powder Technology, 171, 25-33.

[98] Kleinbach, E. & Riede, T. (1995) Coating of Solids, Chemical Engineering and Processing, 34(3), 329-337.

[99] Reynolds, G.K., Fu, J.S., Cheong, Y.S., Hounslow, M.J., & Salman, A.D. (2005) Breakage in Granulation: A Review, Chemical Engineering Science, 60, 3969-3992.

[100] Newitt, D.M. & Conway-Jones, J.M. (1958) A Contribution to the Theory and Practice of Granulation, Transactions of the Institute of Chemical Engineers, 36, 422-442.

[101] Rumpf, H. (1958) *Zerkleinern und Sichten*, Chemie-Ingeniur Technik, 30(12), 814-819.

[102] York, P. & Rowe, R.C. (1994) Monitoring Granulation Size Enlargement Processings Using Mixer Torque Rheology, First International Particle Technology Forum, Denver CO.

[103] Sherrington, P.J. & Oliver, O. (1981) Granulation, Heyden: London.

[104] Tardos, G., Irfan Khan, M., Mort, P.R. (1997) Critical Parameters and Limiting Conditions in Binder Granulation of Fine Powders, Powder Technology, 94(3) 245-258.

[105] Keningley, S.T., Knight, P.C., & Marson, A.D. (1997) An Investigation into the Effects of Binder Viscosity on Agglomeration Behavior, Powder Technology, 91, 95-103.

[106] Pitchumani, R., Meesters, G.M.H., & Scarlett, B. (2003) Breakage Behavior of Enzyme Granules in a Repeated Impact Test, Powder Technology, 130, 421-427.

[107] Bemrose, C.R., & Bridgwater, J. (1987) A Review of Attrition and Attrition Test Methods, Powder Technology, 49, 97-126.

[108] Salman, A.D., Reynolds, G.K., & Hounslow, M.J. (2003) Particle Impact Breakage in Particulate Processing, Kona, 21, 88-99.

[109] Mishra, B., & Thornton, C. (2001) Impact Breakage of Particle Agglomerates, International Journal of Mineral Processing, 61, 225-239.

[110] Salman, A.D., Reynolds, G.K., Fu, J.S., Cheong, Y.S., Biggs, C.A., Adams, M.J., Gorham, D.A., Lukenics, J., & Hounslow, M.J. (2004) Descriptive Classification of the Impact Failure Modes of Spherical Particles, Powder Technology, 143-144, 19-30.

[111] Anderson Jr., J.D. (2009). Chapter 1. The Basic Philosophy of CFD. In Wendt, J.F. (Ed.) Computational Fluid Dynamics 3rd Edition, 3-14. Springer: Verlag Berlin Heidelburg.

[112] van der Hoef, M.A., van Sint Annaland, M., & Kuipers, J.A.M. (2005) Comuptational Fluid Dynamics for Dense Gas-Solid Fluidized Beds: A Multi-Scale Modeling Strategy, China Particuology, 3, 69-77.

[113] Goldschmidt, M. (2001) Ph.D. Thesis University of Twente.

[114] Anderson, T. & Jackson, R. (1967) A Fluid Mechanical Description of Fluidized Beds, Industrial and Engineering Chemistry Fundamentals, 6, 527-539.

[115] Ishii, M. (1975) Thermo-Fluid Dynamic Theory of Two Phase Flow, Eyrolles: Paris.

[116] Gidaspow, D. (1994) Multiphase Flow and Fluidization: Continuum and Kinetic Theory Descriptions, Academic Press: Boston.

[117] Enwald, H., Peirano, E., & Almstedt, A.E. (1996) Eulerian Two-Phase Flow Theory Applied to Fluidization, International Journal of Multiphase Flow, 22, Supplement, 21-66.

[118] Jackson, R. (1997) Locally Averages Equations of Motion for a Mixture of Identical Spherical Particles and a Newtonian Fluid, Chemical Engineering Science, 52, 2457-2469.

[119] Davidson, D.L. (2002) The Role of Computational Fluid Dynamics in Process Industries, Expanding Frontiers of Engineering, 32(4).

[120] Tu, J., Yeoh, G.H., & Liu, C. (2007) Computational Fluid Dynamics: A Practical Approach, Burlington: Elsevier.

[121] Dick, E. (2009). Chapter 10. Introduction to Finite Element Methods in Computational Fluid Dynamics. In Wendt, J.F. (Ed.) Computational Fluid Dynamics 3rd Edition, 235-274. Springer: Verlag Berlin Heidelburg.

[122] Gonzalez Silva, G., Jimenez, N.P., & Salazar, O.F. (2012) Fluid Dynamics of Gas-Solid Fluidized Beds In Oh, H.W. (Ed.) Advanced Fluid Dynamics, InTech: Shanghai.

[123] Hoomans, B.P.B. (2000) Ph.D. Thesis, University of Twente.

[124] Delnoij, E., Kuipers, J.A.M., van Swaaij, W.P.M. (1997) Computational Fluid Dynamics Applied to Gas-Liquid Contactors, Chemical Engineering Science, 52, 3623-3638.

[125] Andersson, B., Andersson, R., Hakansson, L., Mortensen, M., Sudiyo, R., & van Wachem, B. (2012). Chapter 6. Multiphase Flow Modeling In Andersson, B., Andersson, R., Hakansson, L., Mortensen, M., Sudiyo, R., & van Wachem, B. (Ed.) Computational Fluid Dynamics for Engineers, 143-173, New York: Cambridge University Press.

[126] Taghipour, F., Ellis, N., & Wong, C. (2005) Experimental and Computational Study of Gas-Solid Fluidized Bed Hydrodynamics, Chemical Engineering Science, 60, 6857-6867.

[127] Panneerselvam, R., Savithri, S., & Surender, G.D. (2009). CFD Simulation of Hydrodynamics of Gas-Liquid-Solid Fluidized Bed Reactor, Chemical Engineering Science, 64, 1119-1135.

[128] Duangkhamchang, W., Ronsse, F., Depypere, F., Dewettinck, K., & Pieters, J.G. (2010) Comparison and Evaluation of Interphase Momemtum Exchange Models for Simulation of the Solids Volume Fraction in Tapered Fluidized Beds, Chemical Engineering Science, 65, 3100-3112.

[129] Duangkhamchang, W., Ronsse, F., Depypere, F., Dewettinck, K., & Pieters, J.G. (2011) CFD Study of Solids Concentration in a Fluidized Bed Coater with Variation of Atomization Air Pressure, Powder Technology, 212, 103-114.

[130] Vanderroost, M., Ronsse, F., Dewettinck, K., & Pieters, J.G. (2012) Modelling the Bed Characteristics in Fluidized Bed for Top Spray Coating Processes, Particulology, 10, 649-662.

[131] Kafui, K.D., Thornton, C., & Adams, M.J. (2002) Discrete Particle-Continuum Fluid Modelling of Gas-Solid Fluidized Beds, Chemical Engineering Science, 57, 2395-2410.

[132] Alder, B.J., & Wainwright, T.E. (1957) Phase Transition for a Hard-Sphere System, Journal of Chemical Physics, 27, 1208-1209.

[133] Alder, B.J., & Wainwright, T.E. (1959) Studies in Molecular Dynamics I. General Method, Journal of Chemical Physics, 31, 459-4.

[134] Goldschmidt, M.J.V., Weijers, G.G.C., Boerefijn, R., & Kuipers, J.A.M. (2003) Discrete Element Modeling of Fluidized Bed Spray Granulation, Powder Technology, 138, 39-45.

[135] Cundall, P.A., & Strack, O.D.L. (1979) A Discrete Numerical Model for Granular Assemblies, Geotechnique, 29, 47-65.

[136] Lian, G., Thornton, C. & Adams, M.J. (1998) Discrete Particle Simulation of Agglomerate Impact Coalescence, Chemical Engineering Science, 19, 3381-3391.

[137] Cameron, I.T., Wang, F.Y., Immanuel, C.D., & Stepanek, F. (2005) Process System Modelling and Applications in Granulation: A Review, Chemical Engineering Science, 60, 3723-3750.

[138] Gantt, J.A. & Gatzke, E.P. (2005) High-Shear Granulation Modeling Using a Discrete Element Simulation Approach, Powder Technology, 156, 195-212.

[139] Link, J.M., Godlieb, W., Deen, N.G, & Kuipers, J.A.M. (2007) Discrete Element Study of Granulation in a Spout-Fluidized Bed, Chemical Engineering Science, 62, 195-207.

[140] Darelius, A., Rasmuson, A., van Wachem, B., Bjorn, I.N., & Folestad, S. (2008) CFD Simulation of the High Shear Mixing Process of Granular Flow and Frictional Stress Models, Chemical Engineering Science, 63, 2188-2197.

[141] Kafui, D.K., Johnson, S., Thornton, C., & Seville, J.P.K. (2008) Parallelization of a Lagrangian-Eulerian DEM/CFD Code for Application to Fluidized Beds, Powder Technology, 207, 270-278.

[142] Ng, B.H., Ding, Y.L., & Ghadiri, M. (2009*)* Modeling of Dense and Complex Granular Flow in High Shear Mixer Granulator – A CFD Approach, Chemical Engineering Science, 64, 3622-3632.

[143] van Buijtenen, M., Deen, N., Heinrich, S., Antonyuk, S., & Kuipers, J.A.M. (2009) A Discrete Element Study of Wet Particle-Particle Interaction During Granulation in a Spout Fluidized Bed, Canadian Journal of Chemical Engineering, 87, 308-317.

[144] Chau, K.W., Makkawi, Y.T., & Hounslow, M.J. (2011) Time Scale Analysis for Fluidized Bed Melt Granulation I: Granule-Granule and Granule-Droplet Collision Rates, Chemical Engineering Science, 66, 318-326.

[145] Chau, K.W., Makkawi, Y.T., & Hounslow, M.J. (2011) Time Scale Analysis for Fluidized Bed Melt Granulation II: Binder Spreading Rates, Chemical Engineering Science, 66, 327-335.

[146] Fries, L., Antonyuk, S., Heinrich, S., & Palzer, S. (2011) DEM-CFD Modeling of a Fluidized Bed Spray Granulator, Chemical Engineering Science, 66, 2340-2355.

[147] Fries, L., Antonyuk, S., Heinrich, S., Dopfer, D. & Palzer, S. (2013) Collision Dynamics in Fluidized Bed Granulators: A DEM-CFD Study, Chemical Engineering Science, 86, 108-123.

[148] Duangkhamchan, W., Ronsse, F., Depypere, F., Dewettinck, K., & Pieters, J.G. (2007) A CFD Model Based on Optimization of Fluidized Bed Coating Process for Food Ingredients, Communications in Agriculture and Applied Biological Sciences, 72, 183-187.

[149] Karlsson, S., Rasmuson, A., van Wachem, B., & Bjorn, I.N. (2009) CFD Modeling of the Wurster Bed Coater, AIChE Journal, 55, 2578-2590.

[150] Zhu, H.P., Zhou, R.Y., Yang, R.Y. & Yu, A.B. (2007) Discrete Particle Simulation of Particulate Systems: Theoretical Developments, Chemical Engineering Science, 62, 3378-3392.

[151] Zhu, H.P., Zhou, R.Y., Yang, R.Y. & Yu, A.B. (2008) Discrete Particle Simulation of Particulate Systems: A Review of Major Applications and Findings, Chemical Engineering Science, 63, 5728-5770.

[152] Turton, R. (2008) Challenges in the Modeling and Prediction of Coating Pharmaceutical Dosage Forms, Powder Technology, 181, 186-194.

[153] Ramkrishna, D. (2000) Population Balances: Theory and Applications to Particulate System Engineering, New York: Academic Press.

[154] Smoluchowski, M. (1916) Drei Vortrage Uber Diffusion, Brownsche Molekularbewegung und Koagulation von Kolloidteilchen, Z. Angew Physik, 17, 557-571.

[155] Hulbert, H.M. & Katz, S. (1964) Some Problems in Particle Technology – A Statistical Mechanical Formulation, Chemical Engineering Science, 19, 555-574.

[156] Randolph, A.D. (1964) A Population Balance for Countable Entities, Canadian Journal of Chemical Engineering, 42, 280-281.

[157] Sporleder, F., Borka, Z., Solsvik, J., & Jakobsen, H.A. (2012) On the Population Balance Equation, Reviews in Chemical Engineering, 28, 149-169.

[158] Verkoeijen, D., Pouw, G.A., Meesters, G.M.H., & Scarlett, B. (2002) Population Balances for Particulate Processes, Chemical Engineering Science, 57, 2287-2303.

[159] Adetayo, A.A., Lister, J.D., Pratsinis, S.E., & Ennis, B.J. (1995) Population Balance Modeling of Drum Granulation of Materials with Wide Size Distribution, Powder Technology, 82, 37-49.

[160] Vikhansky, A. & Kraft, M. (2006) Two Methods for Sensitivity Analysis of Coagulation Processes in Population Balances by a Monte Carlo Method, Chemical Engineering Science, 61, 4966-4972.

[161] Kumar, J., Peglow, Warnecke, G. & Heinrich, S. (2008). An Efficient Numerical Technique for Solving Population Balance Equation Involving Aggregation, Breakage, Growth, and Nucleation, Powder Technology, 182, 81-104.

[162] Cryer, S.A. (1999) Modeling Agglomeration Processes in Fluid-Bed Granulation, AIChE Journal, 45, 2069-2078.

[163] Iveson, S.M. (2002) Limitations of One Dimensional Population Balance Models of Wet Granulation Processes, Powder Technology, 219-229.

[164] Su, J.W., Gu, Z.L., & Xu, X.Y. (2009) Advances in Numerical Methods for the Solution of Population Balance Equations for Disperse Phase Systems, Science in China Series B: Chemistry, 52, 1063-1079.

[165] McGraw, R. (1997) Description of Aerosol Dynamics by Quadrature Method of Moments, Aerosol Science and Technology, 27, 255-265.

[166] Rong, F., Marchisio, D., & Fox R O. (2004) Application of the Direct Quadrature Method of Moments to Polydisperse Gas Solid Fluidized Beds, Powder Technology, 139, 7-20.

[167] Su, J.W., Gu, Z.L., Li,Y., Feng, S.Y., & Xu, X.Y. (2007) Solution of Population Balance Equation Using Quadrature Method of Moments with an Adjustable Factor, Chemical Engineering Science, 62 5897-5911.

[168] Su, J.W., Gu, Z.L., Li,Y., Feng, S.Y., & Xu, X.Y. (2008) An Adaptive Direct Quadrature Method of Moment for Population Balance Equation, AIChE Journal, 54, 2872-2887.

[169] Alopaeus, V., Laakkone, N.M., & Aittamaa, J. (2006) Numerical Solution of Moment Transformed Population Balance Equation with Fixed Quadrature Points, Chemical Engineering Science, 61, 4919-4929.

[170] Su, J.W., Gu, Z.L., & Xu, X.Y. (2008) Solution of the Population Balance Equation for Growth Using the Moving Particle Ensemble Method. AIChE Journal.

[171] Su, J.W., Gu, Z.L., Jiao, J.Y., & Xu, X.Y. (2009) Local Fixed Pivot quadrature Method of Moment for Bubble Population Balance Equation Including Coalescence and Breakage, In 6th International Symposium on Multiphase Flow, Heat Mass Transfer and Energy Conversion Xi'an,China, 11-15 July 2009.

[172] Zhao, H., Maisels, A., Matsoukas, T., & Zheng, C. (2007) Analysis of Four Monte Carlo Methods for the Solution of Population Balances in Dispersed Systems, Powder Technology, 173, 38-50.

[173] Fichthom, K.A. & Weinburg, W.H. (1991) Theoretical Foundations of Dynamical Monte Carlo Simulations, Journal of Chemical Physics, 95, 1090-1096.

[174] Smith, M. & Matsoukas, T. (1998) Constant-Number Monte Carlo Simulation of Population Balances, Chemical Engineering Science, 53, 1777-1786.

[175] Maisels, A., Kruis, F.E., & Fissan, H. (2004) Direct Simulation Monte Carlo for Simultaneous Nucleation, Coagulation, and Surface Growth in Disperse Systems, Chemical Engineering Science, 59, 2231-2239.

[176] Liffman, K. (1992) A Direct Simulation Monte-Carlo Method for Cluster Coagulation, Journal of Computational Physics, 100, 116-127.

[177] Haibo, Z., Chuguang, Z., & Minghou, Z. (2005) Multi-Monte Carlo Approach for General Dynamic Equation Considering Simultaneous Particle Coagulation and Breakage, Powder Technology, 154, 164-178.

[178] Kapur, P.C. & Fuerstenau, D.W. (1969) Coalescence Model for Granulation, Industrial and Engineering Chemistry Process Design and Development, 8, 56-62.

[179] Sastry, K.V.S. (1975) Similarity Size Distribution of Agglomerates During Their Growth by Coalescence in Granulation or Green Pelletization, International Journal of Mineral Processing, 2, 187-203.

[180] Hounslow, M.J., Ryall, R.L., & Marshall, V.R. (1988) A Discretized Population Balance for Nucleation, Growth, and Aggregation, AIChE Journal, 34, 1821-1832.

[181] Hounslow, M.J., Pearson, J.M.K., & Instone, T. (2001) Tracer Studies of High Shear Granulation II: Population Balance Modeling, AIChE Journal, 47, 1984-1999.

[182] Heinrich, S., Peglow, M., Ihlow, M., Henneberg, M., & Morl, L. (2002) Analysis of the Start-Up Process in Continuous Fluidized Bed Granulation by Population Balance Modelling, Chemical Engineering Science, 57, 4369-4390.

[183] Liu, L.X., & Lister, J.D. (2002) Population Balance Modelling of Granulation with a Physically Based Coalescence Kernel, Chemical Engineering Science, 57, 2183-2191.

[184] Wauters, P.A.U., Scarlett, B., Liu, L.X., & Lister, J.D. (2003) A Population Balance for High Shear Granulation, Chemical Engineering Communications, 190, 1309-1324.

[185] Drechsler, J., Peglow, M., Heinrich, S., Ihlow, M., & Morl, L. (2005) Investigating the Dynamic Behavior of Fluidized Bed Spray Granulation Processes Applying Numerical Tools,Chemical Engineering Science, 60, 3817-3833.

[186] Tan, H.S., Goldschmidt, M.J.V., Boerefijn, R., Hounslow, M.J., Salman, A.D., & Kuipers, J.A.M. (2005) Population Balance Modeling of Fluidized Bed Melt Granulation, Chemical Engineering Research and Design, 83, 871-880.

[187] Darelius, A., Brage, H., Rasmuson, A., Bjorn, I.N., & Folestad, S. (2006) A Volume Based Multi-Dimensional Population Balance Approach for Modelling High Shear Granulation, Chemical Engineering Science, 61, 2482-2493.

[188] Gantt, J., Palathra, T., & Gatzke, E.P. (2007) Analysis of Multidimensional Behavior of Granulation, Journal of Materials Processing Technology, 183, 140-147.

[189] Rajniak, P., Stepanek, F., Dhanasekharan, K., Fan, R., Mancinelli, C. & Chern, R.T. (2009) A Combined Experimental and Computational Study of Wet Granulation in a Wurster Fluid Bed Granulator, Powder Technology, 189, 190-201.

[190] Poon, J.M.H., Immanuel, C.D., Doyle III, F.J., & Lister, J.D. (2008) A Three-Dimensional Population Balance Model of Granulation with a Mechanistic Representation of Nucleation and Aggregation Phenomena, Chemical Engineering Science, 63, 1315-1329.

[191] Poon, J.M.H., Ramachandran, R., Sanders, C.F.W., Glaser, T., Immanuel, C.D., Doyle III, F.J., Lister, J.D., Stepanek, F., Wang, F.Y., & Cameron, I.T. (2009) Experimental Validation Studies on a Multi-Dimensional and Multi-Scale Population Balance Model of Batch Granulation, Chemical Engineering Science, 64, 775-786.

[192] Ramachandran, R., Immanuel, C.D., Stepanek, F., Lister, J.D., & Doyle III, F.J. (2009) A Mechanistic Model for Breakage in Population Balances of Granulation: Theoretical Kernel Development and Experimental Validation, Chemical Engineering Research and Design, 87, 598-614.

[193] Dernedde, M., Peglow, M., & Tsotsas, E. (2011) Stochastic Modeling of Fluidized Bed Granulation: Influence of Droplet Pre-Drying, Chemical Engineering & Technology, 34, 1177-1184.

[194] Vreman, A.W., van Lare, C.E., & Hounslow, M.J. (2009) A Basic Population Balance Model for Granulation, Chemical Engineering Science, 64, 4389-4398.

[195] Li, Z., Kind, M., Gruenewald, G. (2011) Modeling the Growth Kinetics of Fluidized Bed Spray Granulation, Chemical Engineering and Technology, 34, 1067-1075.

[196] Liu, L., Akay, G., & Tong, L. (2011) Population Balance Modelling for a Flow Induced Phase Inversion Based Granulation in a Two-Dimensional Rotating Agglomerator, Chemical Engineering Research and Design, 89, 39-47.

[197] Ramachandran, R. & Chaudhury, A. (2012) Model-Based Design and Control of a Continuous Drum Granulation Process, Chemical Engineering Research and Design, 90, 1063-1073.

[198] Ronsse, F., Depelchin, J., & Dewettinck, K. (2012) Particle Surface Moisture Content Estimation Using Population Balance Modelling in Fluidized Bed Granulation, Journal of Food Engineering, 109, 347-357.

[199] Chaudhury, A., Niziolek, A., & Ramachandran, R. (2013) Multidimensional Mechanistic Modeling of Fluid Bed Granulation Processes: An Integrated Approach, Advanced Powder Technology, 24, 113-131.

[200] Marshall, C.J., Rajniak, P., & Matsoukas, T. (2013). Multi-Component Population Balance Modeling of Granulation with Continuous Addition of Binder, Powder Technology, 236, 211-220.

[201] Maronga, S.J. & Wnukowski, P. (1997) Modelling of the Three Domain Fluidized Bed Particulate Coating Process, Chemical Engineering Science, 52, 2915-2925.

[202] Saleh, K., Steinmetz, D., & Hemati, M. (2003) Experimental Study and Modeling of Fluidized Bed Coating and Agglomeration, Powder Technology, 130, 116-123.

[203] Alavi, S.M., Mirmomen, L., and Saleh, K. (2007) Experimental Study and Population Balance Modeling of Coating in a Jet Fluidized Bed, Advanced Powder Technology, 18, 311-327.

[204] Ronsse, F., Pieters, J.G., & Dewettinck, K. (2007a) Combined Population Balance and Thermodynamic Modelling of Top Spray Fluidized Bed Coating Process Part I – Model Development and Validation, Journal of Food Engineering, 78, 296-307.

[205] Ronsse, F., Pieters, J.G., & Dewettinck, K. (2007b) Combined Population Balance and Thermodynamic Modelling of Top Spray Fluidized Bed Coating Process Part II – Model and Process Analysis, Journal of Food Engineering, 78, 308-322.

[206] Ronsse, F., Pieters, J.G., & Dewettinck, K. (2008) Modelling Side-Effect Spray Drying in Top Spray Fluidized Bed Coating Processes, Journal of Food Engineering, 86, 529-541.

[207] Li, J., Freireich, B., Wassgren, C., & Lister, J.D. (2012) A General Compartment Based Population Balance Model for Coating and Layered Granulation, AIChE Journal, 58, 1397-1408.

[208] Hampel, N., Buck, A., Peglow, M., & Tsotsas, E. (2013) Continuous Pellet Coating in a Wurster Fluidized Bed Process, Chemical Engineering Science, 86, 87-98.

[209] Hammersley, J.M. & Handscomb, D.C. (1964) Monte Carlo Methods, New York: John Wiley & Sons.

[210] Duggirala, S.K. & Fan, L.T. (1989) Stochastic Analysis of Attrition - A General Cell Model, Powder Technology, 57, 1-20.

[211] Ligon, J.R. & Amundson, N.R. (1981) Modeling of Fluidized Bed Reactors- VI(a) An Isothermal Bed with Stochastic Bubbles, Chemical Engineering Science, 36, 661-671.

[212] Ligon, J.R. & Amundson, N.R. (1981) Modeling of Fluidized Bed Reactors- VI(b) The Non-Isothermal Bed with Stochastic Bubbles, Chemical Engineering Science, 36, 673-685.

[213] Ho, T.C., Yutani, N., Fan, L.T., & Walawender, W.P. (1983) Stochastic Modeling of Bubble Formation on the Grid in a Gas-Solid Fluidized Bed, Canadian Journal of Chemical Engineering, 61, 654-659.

[214] Yutani, N., Ototake, N., & Fan, L.T. (1986) Stochastic Analysis of Fluctuations in Local Void Fractions of a Gas-Solid Fluidized Bed, Powder Technology, 48, 31-38.

[215] Raghuraman, J. & Varma, Y.B.G. (1974) A Stochastic Model for Residence Time and Contact Time Distributions of the Gas in Multistage Fluidized Beds, Chemical Engineering Science, 29, 697-703.

[216] Larachi, F., Grandjean, B.P.A., & Chaouki, J. (2003) Mixing and Circulation of Solids in Spouted Beds: Particle Tracking and Monte Carlo Emulation of the Gross Flow Pattern, Chemical Engineering Science, 58, 1497-1507.

[217] Dehling, H.G., Dechsiri, C., Gottschalk, T., Wright, P.C. & Hoffman, A.C. (2007) A Stochastic Model for Mixing and Segregation in Slugging Fluidized Beds, Powder Technology, 171, 118-125.

[218] Mathur, A. (1990) A Stochastic Model for Particle Convective Heat Transfer in Gas Solid Fluidized Beds, International Journal of Heat and Mass Transfer, 33, 1929-1936.

[219] Gottschalk, T., Dehling, H.G., & Hoffman, A.C. (2008) Multiphase Stochastic Model for Fluidized Beds, Physical Review E, 77, 0313061-03130611

[220] Cronin, K., Catak, M., Bour, J., Collins, A., & Smee, J. (2011) Stochastic Modeling of Particle Motion Along a Rotary Drum, Powder Technology, 213, 79-91.

[221] Harris, A.T., Thorpe, R.B., & Davidson, J.F. (2002) Stochastic Modeling of Particle Residence Time Distribution in Circulating Fluidized Bed Risers, Chemical Engineering Science, 57, 4779-4796.

[222] Guo, Q., Liang, Q., Ni, J., Xu, S., Yu, G., & Yu, Z. (2008) Markov Chain Model of Residence Time Distribution in a New Type Entrained-Flow Gasifier, Chemical Engineering and Processing, 47, 2061-2065.

[223] Gao, H. & Fu, Y. (2011) Mean Residence Time of Markov Processes for Particle Transport in Fluidized Bed Reactors, Journal of Mathematical Chemistry, 49, 444-456.

[224] Leszczynski, J.S., Bis, Z., & Gajewski, W. (2002) Evaluation of Structure and Particle Velocity Distribution in Circulating Fluidized Beds, Powder Technology, 128, 22-35.

[225] Yashima, M., Nassar, R., Fan, L.T. & Kang, Y. (1992) Stochastic Modeling of Pressure Fluctuations in a Three Phase Fluidized Bed, AIChE Journal, 38, 629-634.

[226] Too, J.R., Fox, R.O., Fan, L.T., & Nassar, R. (1985) Stochastic Modeling of a Fluidized Bed Reactor, AIChE Journal, 31, 992-998.

[227] Hapgood, K., Lister, J.D., White, E.T., Mort, P.R. & Jones, D.G. (2004) Dimensionless Spray Flux in Wet Granulation: Monte-Carlo Simulations and Experimental Validations, Powder Technology, 141, 20-30.

[228] Terrazas-Velarde, K., Peglow, M., & Tsotsas, E. (2009) Stochastic Simulation of Agglomerate Formation in Fluidized Bed Spray Drying: A Microscale Approach, Chemical Engineering Science, 64, 2631-2643.

[229] Nakamura, H., Abe, E., & Yamada, N. (1998) Coating Mass Distribution of Seed Particles in a Tumbling Fluidized Bed Coater Part II: Monte Carlo Simulation of Particle Coating, Powder Technology, 99, 140-146.

[230] Cheng, X. X. & Turton, R. (2000) The Prediction of Variability Occuring in Fluidized Bed Coating Equipment. I. The Measurement of Particle Circulation Rates in a Bottom-Spray Fluidized Bed Coater, Pharmaceutical Development and Technology, 5, No. 3, 311-322.

[231] Cheng, X. X. & Turton, R. (2000) The Prediction of Variability Occuring in Fluidized Bed Coating Equipment. II. The Role of Nonuniform Particle Coverage as Particles Pass Through the Spray Zone, Pharmaceutical Development and Technology, 5, No. 3, 323-332.

[232] Haddish-Berhane, N., Jeong, S.H., Haghighi, K., & Park, K. (2006) Modeling Film Coat-Thickness Non-Uniformity in Polymer Coated Pellets: A Stochastic Approach, International Journal of Pharmaceutics, 323, 64-71.

[233] KuShaari, K., Pandey, P., Song, Y., & Turton, R. (2006) Monte Carlo Simulations to Determine Coating Uniformity in a Wurster Fluidized Bed Coating Process, Powder Technology, 166, 81-90.

[234] Kandela, B., Sheorey, U., Banerjee, A. & Bellare, J. (2010) Study of Tablet-Coating Parameters for a Pan Coater Through Video Imaging and Monte Carlo Simulation, Powder Technology, 204, 103-112.

[235] Overturf, B.W. & Reklaitis, G.V. (1983) Fluidized Bed Reactor Model with Generalized Particle Balances Part I: Formulation and Solution, AIChE Journal, 29, 813-820.

[236] Overturf, B.W. & Reklaitis, G.V. (1983) Fluidized Bed Reactor Model with Generalized Particle Balances Part II: Coal Combustion Application, AIChE Journal, 29, 820-829.

[237] Maronga, S.J. & Wnuknowski, P. (1998) The Use of Humidity and Temperature Profiles in Optimizing the Size of Fluidized Bed in a Coating Process, Chemical Engineering and Processing, 37, 423-432.

[238] Heinrich, S. & Morl, L. (1999) Fluidized Bed Spray Granulation – A New Model for the Distribution of Particle Wetting and of Temperature and Concentration Distribution, Chemical Engineering and Processing, 38, 635-663.

CHAPTER 4

FLUIDIZED BED COATING GROWTH KINETICS MODEL DEVELOPMENT

This chapter will present a detailed description of the equations used to model particle coating growth kinetics in a fluidized bed. Transient mass and energy balances will be presented first followed by a short explanation of the assumptions made for them. Next, equations will be presented for determining coating deposition and particle growth for a particle size distribution. Assumptions made for the coating deposition and particle growth will also be given.

4.1 Transient Mass and Energy Balances

The model used in this work to describe the mass and energy balances of a fluidized bed coating operation is the same model used by Hede et al.[1]. The Hede et al. model is an expansion of the mass and energy balance model developed by Ronsse [2, 3] such that it is scalable to any size fluidized bed. The Ronsse model is an extension of an earlier mass and energy balance developed by Dewettinck [4]. The Dewettinck model considers the fluidized bed as one element, whereas the Ronsse model has the fluidized bed discretized into smaller axial segments.

The mass and energy balance shown here is a one-dimensional (1-D) balance in the vertical direction that separates the fluidized bed into several well mixed vertical segments (called control volumes) with the same height. The model is dynamic in nature, accounting for all modes of heat transfer: gas-particle, gas-wall, particle-particle, particle-wall, wall to the environment, and radiation, the addition of coating liquid to the fluidized bed, the moisture

content of the particles and fluidizing gas. The model can be modified to incorporate a radial distribution. Figure 4.1 shows how the fluidized bed is discretized into smaller 1-D control volumes.

The first phase of building a time dependent model for fluidized bed particle coating growth is creating an accurate representation of the dynamic heat and mass transfer characteristics at the specified operating conditions. The fluidized bed is represented as a series of control volumes in order to depict the changes in hydrodynamics, heat, and mass transfer. Furthermore, the control volumes are identified as coating control volumes and non-coating control volumes. This division of control volumes is necessary because depending on the scale of operation, the coating solution does not cross the threshold of each control volume. The coupled transient mass and energy balances for a fluidized bed coating operation involve the simultaneous solution of six ordinary differential equations. The balances are slightly different depending on the type of control volume specified. The total number of control volumes is denoted by n, while the total number of coating control volumes is denoted by c. The equations for the dynamic mass and energy balances presented here are the same as those published by Hede et al. [1].

The particle balance of a single control volume is given as Equation 4.1 [1]:

$$\underbrace{\frac{dN_i}{dt}}_{\substack{\text{Rate of Change in}\\ \text{Number of Particles}\\ \text{In Control Volume } S_i}} = \underbrace{r_{i-1}N_{bed}}_{\substack{\text{Particles From}\\ \text{Control Volume } S_{i-1}}} + \underbrace{r_{i+1}N_{bed}}_{\substack{\text{Particles From}\\ \text{Control Volume } S_{i+1}}} - \underbrace{r_iN_{bed}}_{\substack{\text{Particles Going to}\\ \text{Control Volume } S_{i+1}}} - \underbrace{r_iN_{bed}}_{\substack{\text{Particles Going}\\ \text{Control Volume } S_{i-1}}} = 0 \qquad (4.1)$$

where r_i is the particle exchange rate with units of s^{-1}.

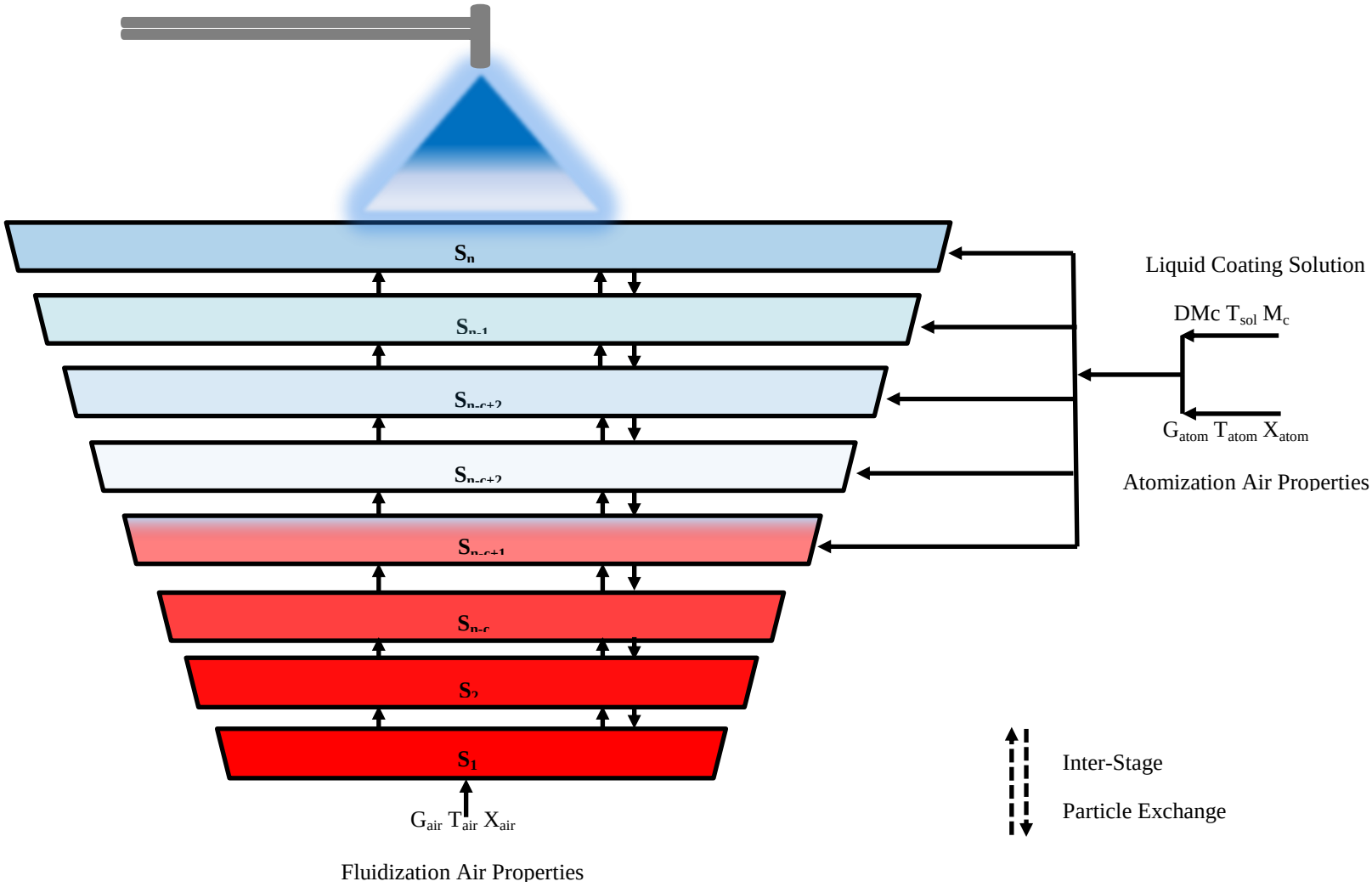

Figure 4.1 Discretization of Fluidized Bed into Control Volumes for Dynamic Mass and Energy Balances

Moisture is added to the fluidized bed both in the liquid phase and with evaporation as the vapor phase. The moisture (water) balance (W_p - kg H_2O per kg Particles) of the particles for a non-coating control volume is given as Equation 4.2 [1]:

$$\underbrace{M_p N_i \frac{dW_{p,i}}{dt}}_{\substack{\text{Rate of Change in Water Content on Particle Surface in Control Volume } S_i}} = \underbrace{M_p N_i W_{p,i-1} r_{i-1}}_{\substack{\text{Mass of Water From Wet Particles Entering From Control Volume } S_{i-1}}} + \underbrace{M_p N_i W_{p,i+1} r_{i+1}}_{\substack{\text{Mass of Water From Wet Particles Entering From Control Volume } S_{i+1}}} - \underbrace{M_p N_i W_{p,i} r_i}_{\substack{\text{Mass of Water From Wet Particles Going to Control Volume } S_{i+1}}} - \underbrace{M_p N_i W_{p,i} r_i}_{\substack{\text{Mass of Water From Wet Particles Going to Control Volume } S_{i-1}}} - \underbrace{R_{D,i} M_p N_i}_{\substack{\text{Mass of Water Evaporating From Wet Particles}}} \quad (4.2)$$

where R_d is the drying rate (kg H_2O per kg Particles). The moisture (water) balance of the particles for a coating control volume is given as Equation 4.3 [1]:

$$\underbrace{M_p N_i \frac{dW_{p,i}}{dt}}_{\substack{\text{Rate of Change in Water Content on Particle Surface in Control Volume } S_i}} = \underbrace{M_p N_i W_{p,i-1} r_{i-1}}_{\substack{\text{Mass of Water From Wet Particles Entering From Control Volume } S_{i-1}}} + \underbrace{M_p N_i W_{p,i+1} r_{i+1}}_{\substack{\text{Mass of Water From Wet Particles Entering From Control Volume } S_{i+1}}} - \underbrace{M_p N_i W_{p,i} r_i}_{\substack{\text{Mass of Water From Wet Particles Going to Control Volume } S_{i+1}}} - \underbrace{M_p N_i W_{p,i} r_i}_{\substack{\text{Mass of Water From Wet Particles Going to Control Volume } S_{i-1}}} - \underbrace{R_{D,i} M_p N_i}_{\substack{\text{Mass of Water Evaporating From Wet Particles}}} + \underbrace{\frac{1}{c}(1 - C_{coat}) M_c}_{\substack{\text{Mass of Water From Coating Solution Droplets}}} \quad (4.3)$$

The moisture (water) balance in the gas phase in a non-coating control volume represented as absolute humidity (X_a) is given as Equation 4.4 [1]:

$$\underbrace{M_{a,i}\frac{dX_{a,i}}{dt}}_{\substack{\text{Rate of Change of}\\ \text{Water in Gas Phase}\\ \text{in Control Volume } S_i}} = \underbrace{G_a X_{a,i-1}}_{\substack{\text{Mass of Water in}\\ \text{Fluidization Air Entering}\\ \text{Control Volume } S_i}} - \underbrace{G_a X_{a,i}}_{\substack{\text{Mass of Water in}\\ \text{Fluidization Air Entering}\\ \text{Control Volume } S_{i+1}}} + \underbrace{R_{D,i} M_p N_i}_{\substack{\text{Mass of Water Evaporating}\\ \text{From Wet Particles}\\ \text{to Gas Phase}}} \tag{4.4}$$

The moisture (water) balance in the gas phase in a coating control volume is given as Equation 4.5 [1]:

$$\underbrace{M_{a,i}\frac{dX_{a,i}}{dt}}_{\substack{\text{Rate of Change of}\\ \text{Water in Gas Phase}\\ \text{in Control Volume } S_i}} = \underbrace{\left(G_a + \frac{i-(n-c)}{c} G_{at}\right) X_{a,i-1}}_{\substack{\text{Mass of Water in}\\ \text{Fluidization Air and}\\ \text{Atomization Air Entering}\\ \text{Control Volume } S_i}} - \underbrace{\left(G_a + \frac{i-(n-c)}{c} G_{at}\right) X_{a,i}}_{\substack{\text{Mass of Water in}\\ \text{Fluidization Air and}\\ \text{Atomization Air Entering}\\ \text{Control Volume } S_{i+1}}} + \underbrace{\frac{1}{c} G_{at} X_{at}}_{\substack{\text{Mass of Water in}\\ \text{Atomization Air Entering}\\ \text{Control Volume } S_i}} + \underbrace{R_{D,i} M_p N_i}_{\substack{\text{Mass of Water Evaporating}\\ \text{From Wet Particles}\\ \text{to Gas Phase}}} \tag{4.5}$$

The coating balance in a non-coating control volume is given as Equation 4.6 [1]:

$$\underbrace{M_p N_i \frac{dY_i}{dt}}_{\substack{\text{Rate of Change of}\\ \text{Coating Mass in}\\ \text{Control Volume } S_i}} = 0 \tag{4.6}$$

where Y is the coating mass in kg coating per kg particles.

The coating balance in a coating control volume is given as Equation 4.7 [1]

$$\underbrace{M_p N_i \frac{dY_i}{dt}}_{\substack{\text{Rate of Change of}\\ \text{Coating Mass in}\\ \text{Control Volume } S_i}} = \underbrace{\frac{1}{c}(C_{coat}) M_c}_{\substack{\text{Mass of Coating}\\ \text{Solution Entering}\\ \text{Control Volume } S_i}} \tag{4.7}$$

where C_{coat} is the dry matter content of the coating solution M_c.

The energy balances for the fluidized bed operation will be presented next. There are three temperatures of interest with fluidized bed operation: fluidization gas temperature, particle

temperature, and the fluidized bed wall temperature. The energy balances must incorporate all the components present in order to obtain an accurate estimation of each respective temperature. The energy balance of the gas phase in a non-coating control volume is given as Equation 4.8 [1]:

$$\underbrace{M_{a,i}C_{p,a,i}\frac{dT_{a,i}}{dt}}_{\substack{\text{Rate of Change of}\\ \text{Fluidization Gas Enthalpy}\\ \text{in Control Volume } S_i}} = \underbrace{G_aC_{pa,i-1}\left(T_{a,i-1}-T_{ref}\right)}_{\substack{\text{Fluidization Gas Enthalpy}\\ \text{Entering From}\\ \text{Control Volume } S_{i-1}}} - \underbrace{G_{a,i}C_{pa,i}\left(T_{a,i}-T_{ref}\right)}_{\substack{\text{Fluidization Gas Enthalpy}\\ \text{Leaving From}\\ \text{Control Volume } S_i}}$$
$$- \underbrace{\alpha_pN_pA_p\left(T_{a,i}-T_{p,i}\right)}_{\substack{\text{Convective Heat Transfer}\\ \text{From Fluidization Gas}\\ \text{to Particles in}\\ \text{Control Volume } S_i}} - \underbrace{R_{D,i}M_pN_iC_{pv,i}\left(T_{a,i}-T_{ref}\right)}_{\substack{\text{Enthalpy Necessary to}\\ \text{Heat Up Moisture Vapor}\\ \text{to Fluidization Gas Temperature}\\ \text{in Control Volume } S_i}}$$
$$+ \underbrace{R_{D,i}M_pN_iC_{pv,i}\left(T_{p,i}-T_{ref}\right)}_{\substack{\text{Enthalpy Gained by Steam}\\ \text{Generation in Control Volume } S_i}} - \underbrace{\Phi_{loss,a,i}}_{\substack{\text{Heat Loss to Surroundings}\\ \text{Gas to Wall Heat Transfer}\\ \text{in Control Volume } S_i}} \quad (4.8)$$

Equation 4.8 simplifies to Equation 4.9 [1]:

$$\underbrace{M_{a,i}C_{p,a,i}\frac{dT_{a,i}}{dt}}_{\substack{\text{Rate of Change of}\\ \text{Fluidization Gas Enthalpy}\\ \text{in Control Volume } S_i}} = \underbrace{G_aC_{p,a,i-1}\left(T_{a,i-1}-T_{a,i}\right)}_{\substack{\text{Fluidization and Atomization Gas Enthalpy}\\ \text{Entering From}\\ \text{Control Volume } S_{i-1}}} - \underbrace{\alpha_pN_pA_p\left(T_{a,i}-T_{p,i}\right)}_{\substack{\text{Convective Heat Transfer}\\ \text{From Fluidization Gas}\\ \text{to Particles in}\\ \text{Control Volume } S_i}}$$
$$- \underbrace{R_{D,i}M_pN_iC_{pv,i}\left(T_{a,i}-T_{pi}\right)}_{\substack{\text{Enthalpy Necessary to}\\ \text{Heat Up Moisture Vapor}\\ \text{to Fluidization Gas Temperature}\\ \text{in Control Volume } S_i}} - \underbrace{\Phi_{loss,a,i}}_{\substack{\text{Heat Loss to Surroundings}\\ \text{Gas to Wall Heat Transfer}\\ \text{in Control Volume } S_i}} \quad (4.9)$$

In the coating control volume an additional term must be included into the gas phase energy balance to account for the presence of the atomization gas. In addition an adjustment must be done to ensure the proper amount of atomization gas is correctly assigned to each coating control volume. The gas phase energy balance in a coating control volume is given as Equation 4.10 [1]:

$$\underbrace{M_{a,i}C_{p,a,i}\frac{dT_{a,i}}{dt}}_{\substack{\text{Rate of Change of}\\ \text{Fluidization Gas Enthalpy}\\ \text{in Control Volume } S_i}} = \underbrace{\left(G_a + \frac{i-(n-c)+1}{c}G_{at}\right)C_{pa,i-1}\left(T_{a,i-1}-T_{ref}\right)}_{\substack{\text{Fluidization and Atomization Gas Enthalpy}\\ \text{Entering From}\\ \text{Control Volume } S_{i-1}}}$$

$$- \underbrace{\left(G_a + \frac{i-(n-c)}{c}G_{at}\right)C_{pa,i}\left(T_{a,i}-T_{ref}\right)}_{\substack{\text{Fluidization and Atomization Gas Enthalpy}\\ \text{Leaving From}\\ \text{Control Volume } S_i}} + \underbrace{\frac{1}{c}G_{at}C_{pa,i}\left(T_{at,i}-T_{ref}\right)}_{\substack{\text{Atomization Gas Enthalpy}\\ \text{Entering From Control Volume } S_i}}$$

$$- \underbrace{\alpha_p N_p A_p\left(T_{a,i}-T_{p,i}\right)}_{\substack{\text{Convective Heat Transfer}\\ \text{From Fluidization Gas}\\ \text{to Particles in}\\ \text{Control Volume } S_i}} - \underbrace{R_{D,i}M_pN_iC_{pv,i}\left(T_{a,i}-T_{ref}\right)}_{\substack{\text{Enthalpy Necessary to}\\ \text{Heat Up Moisture Vapor}\\ \text{to Fluidization Gas Temperature}\\ \text{in Control Volume } S_i}}$$

$$+ \underbrace{R_{D,i}M_pN_iC_{pv,i}\left(T_{p,i}-T_{ref}\right)}_{\substack{\text{Enthalpy Gained by Steam}\\ \text{Generation in Control Volume } S_i}} - \underbrace{\Phi_{loss,a,i}}_{\substack{\text{Heat Loss to Surroundings}\\ \text{Gas to Wall Heat Transfer}\\ \text{in Control Volume } S_i}} \qquad (4.10)$$

Equation 4.10 simplifies to Equation 4.11 [1]:

$$\underbrace{M_{a,i}C_{p,a,i}\frac{dT_{a,i}}{dt}}_{\substack{\text{Rate of Change of}\\ \text{Fluidization Gas Enthalpy}\\ \text{in Control Volume } S_i}} = \underbrace{G_aC_{pa,i-1}\left(T_{a,i-1}-T_{a,i}\right)}_{\substack{\text{Fluidization Gas Enthalpy}\\ \text{Entering From}\\ \text{Control Volume } S_{i-1}}} + \underbrace{\left(\frac{i-(n-c)}{c}G_{at}\right)C_{pa,i}\left(T_{a,i-1}-T_{a,i}\right)}_{\substack{\text{Atomization Gas Enthalpy}\\ \text{Leaving From}\\ \text{Control Volume } S_i}}$$

$$+ \underbrace{\frac{1}{c}G_{at}C_{pa,i}\left(T_{at,i}-T_{a,i-1}\right)}_{\substack{\text{Atomization Gas Enthalpy}\\ \text{Entering From Control Volume } S_i}} - \underbrace{\alpha_pN_pA_p\left(T_{a,i}-T_{p,i}\right)}_{\substack{\text{Convective Heat Transfer}\\ \text{From Fluidization Gas}\\ \text{to Particles in}\\ \text{Control Volume } S_i}}$$

$$- \underbrace{R_{D,i}M_pN_iC_{pv,i}\left(T_{a,i}-T_{p,i}\right)}_{\substack{\text{Enthalpy Necessary to}\\ \text{Heat Up Moisture Vapor}\\ \text{to Fluidization Gas Temperature}\\ \text{in Control Volume } S_i}} - \underbrace{\Phi_{loss,a,i}}_{\substack{\text{Heat Loss to Surroundings}\\ \text{Gas to Wall Heat Transfer}\\ \text{in Control Volume } S_i}} \qquad (4.11)$$

The energy balance for particles in a non-coating control volume is given as Equation 4.12 [1]:

$$\underbrace{N_i M_p C_{pp,i} \frac{dT_{p,i}}{dt}}_{\substack{\text{Rate of Change of}\\ \text{Particle Enthalpy}\\ \text{in Control Volume } S_i}} = \underbrace{M_p N_{bed} C_{pp,i} r_{i+1} \left(T_{p,i+1} - T_{ref}\right)}_{\substack{\text{Particle Enthalpy Entering}\\ \text{From Control Volume } S_{i+1}}} + \underbrace{M_p N_{bed} C_{pp,i} r_{i-1} \left(T_{p,i-1} - T_{ref}\right)}_{\substack{\text{Particle Enthalpy Entering}\\ \text{From Control Volume } S_{i-1}}}$$

$$- \underbrace{M_p N_{bed} C_{pp,i} r_i \left(T_{p,i} - T_{ref}\right)}_{\substack{\text{Particle Enthalpy Leaving}\\ \text{To Control Volume } S_{i-1}}} + \underbrace{\alpha_p N_p A_p \left(T_{a,i} - T_{p,i}\right)}_{\substack{\text{Convective Heat Transfer}\\ \text{From Fluidization Gas}\\ \text{to Particles in}\\ \text{Control Volume } S_i}}$$

$$- \underbrace{R_{D,i} M_p N_i Q_{lat,i}}_{\substack{\text{Latent Heat Needed}\\ \text{to Evaporate Moisture}\\ \text{in Control Volume } S_i}} - \underbrace{\Phi_{lossp,i}}_{\substack{\text{Heat Loss To Surroundings}\\ \text{(Particle to Wall Heat Transfer)}}} \tag{4.12}$$

Equation 4.12 simplifies to Equation 4.13 [1]:

$$\underbrace{N_i M_p C_{pp,i} \frac{dT_{p,i}}{dt}}_{\substack{\text{Rate of Change of}\\ \text{Particle Enthalpy}\\ \text{in Control Volume } S_i}} = \underbrace{M_p N_{bed} C_{pp,i} r_{i+1} \left(T_{p,i+1} - T_{p,i}\right)}_{\substack{\text{Particle Enthalpy Entering}\\ \text{From Control Volume } S_{i+1}}} + \underbrace{M_p N_{bed} C_{pp,i} r_{i-1} \left(T_{p,i-1} - T_{p,i}\right)}_{\substack{\text{Particle Enthalpy Leaving}\\ \text{To Control Volume } S_{i+1}}}$$

$$+ \underbrace{\alpha_p N_p A_p \left(T_{a,i} - T_{p,i}\right)}_{\substack{\text{Convective Heat Transfer}\\ \text{From Fluidization Gas}\\ \text{to Particles in}\\ \text{Control Volume } S_i}} - \underbrace{R_{D,i} M_p N_i Q_{lat,i}}_{\substack{\text{Latent Heat Needed}\\ \text{to Evaporate Moisture}\\ \text{in Control Volume } S_i}}$$

$$- \underbrace{\Phi_{lossp,i}}_{\substack{\text{Heat Loss To Surroundings}\\ \text{(Particle to Wall Heat Transfer)}}} \tag{4.13}$$

In the coating control volume an additional term must be included into the particle energy balance to account for the presence of the coating solution. In addition an adjustment must be done to ensure the proper amount of coating solution is correctly assigned to each coating control volume In a coating control volume the energy balance for the particles is given as Equation 4.14 [1]:

$$\underbrace{N_i M_p C_{pp,i} \frac{dT_{p,i}}{dt}}_{\substack{\text{Rate of Change of}\\ \text{Particle Enthalpy}\\ \text{in Control Volume } S_i}} = \underbrace{M_p N_{bed} C_{pp,i} r_{i+1} \left(T_{p,i+1} - T_{ref}\right)}_{\substack{\text{Particle Enthalpy Entering}\\ \text{From Control Volume } S_{i+1}}} + \underbrace{M_p N_{bed} C_{pp,i} r_{i-1} \left(T_{p,i-1} - T_{ref}\right)}_{\substack{\text{Particle Enthalpy Entering}\\ \text{From Control Volume } S_{i-1}}}$$

$$- \underbrace{M_p N_{bed} C_{pp,i} r_i \left(T_{p,i} - T_{ref}\right)}_{\substack{\text{Particle Enthalpy Leaving}\\ \text{To Control Volume } S_{i+1}}} - \underbrace{M_p N_{bed} C_{pp,i} r_i \left(T_{p,i} - T_{ref}\right)}_{\substack{\text{Particle Enthalpy Leaving}\\ \text{To Control Volume } S_{i-1}}}$$

$$+ \underbrace{\alpha_p N_p A_p \left(T_{a,i} - T_{p,i}\right)}_{\substack{\text{Convective Heat Transfer}\\ \text{From Fluidization Gas}\\ \text{to Particles in}\\ \text{Control Volume } S_i}} - \underbrace{R_{D,i} M_p N_i Q_{lat,i}}_{\substack{\text{Latent Heat Needed}\\ \text{to Evaporate Moisture}\\ \text{in Control Volume } S_i}} + \underbrace{\frac{1}{c} M_c C_{psol} \left(T_{wb,i} - T_{ref}\right)}_{\substack{\text{Enthalpy From Liquid}\\ \text{Droplets Entering}\\ \text{Control Volume } S_i}}$$

$$- \underbrace{\frac{1}{c} M_c C_{psol} \left(T_{p,i} - T_{ref}\right)}_{\substack{\text{Enthalpy Needed to Heat}\\ \text{Droplets to Particle Temperature}\\ \text{in Control Volume } S_i}} - \underbrace{\Phi_{lossp,i}}_{\substack{\text{Heat Loss To Surroundings}\\ \text{(Particle to Wall Heat Transfer)}}} \tag{4.14}$$

Equation 4.14 simplifies to Equation 4.15 [1]:

$$\underbrace{N_i M_p C_{pp,i} \frac{dT_{p,i}}{dt}}_{\substack{\text{Rate of Change of}\\ \text{Particle Enthalpy}\\ \text{in Control Volume } S_i}} = \underbrace{M_p N_{bed} C_{pp,i} r_{i+1} \left(T_{p,i+1} - T_{p,i}\right)}_{\substack{\text{Particle Enthalpy Entering}\\ \text{From Control Volume } S_{i+1}}} - \underbrace{M_p N_{bed} C_{pp,i} r_{i-1} \left(T_{p,i-1} - T_{p,i}\right)}_{\substack{\text{Particle Enthalpy Leaving}\\ \text{To Control Volume } S_{i+1}}}$$

$$+ \underbrace{\alpha_p N_p A_p \left(T_{a,i} - T_{p,i}\right)}_{\substack{\text{Convective Heat Transfer}\\ \text{From Fluidization Gas}\\ \text{to Particles in}\\ \text{Control Volume } S_i}} - \underbrace{R_{D,i} M_p N_i Q_{lat,i}}_{\substack{\text{Latent Heat Needed}\\ \text{to Evaporate Moisture}\\ \text{in Control Volume } S_i}} + \underbrace{\frac{1}{c} M_c C_{psol} \left(T_{p,i} - T_{wb,i}\right)}_{\substack{\text{Enthalpy From Liquid}\\ \text{Droplets Entering}\\ \text{Control Volume } S_i}}$$

$$- \underbrace{\Phi_{lossp,i}}_{\substack{\text{Heat Loss To Surroundings}\\ \text{(Particle to Wall Heat Transfer)}}} \tag{4.15}$$

Next the energy balance for the fluidized bed wall will be presented. The fluidized bed wall energy balance has all three modes of heat transfer incorporated into it. The energy balance for the fluidized bed wall is given as Equation 4.16 [1]:

$$\underbrace{C_{pwall,i}\rho_{wall}A_{wall,i}d_{wall,i}\frac{dT_{wall,i}}{dt}}_{\substack{\text{Rate of Change of Wall}\\ \text{Enthalpy in Control Volume } S_i}} = \underbrace{\frac{A_{wall,i}\delta_{wall}(T_{a,i}- T_{wall,i})}{R_{conv,i}}}_{\substack{\text{Convective Heat Transfer}\\ \text{From Gas Bubbles in}\\ \text{Control Volume } S_i}} + \underbrace{\frac{A_{wall,i}(1 - \delta_{wall})(T_{a,i}- T_{wall,i})}{R_{p,i}}}_{\substack{\text{Convective Heat Transfer}\\ \text{From Particles in}\\ \text{Control Volume } S_i}}$$

$$- \underbrace{\sigma\theta_{wall}A_{wall,i}(T^4_{wall,i}- T^4_e)}_{\substack{\text{Radiative Heat Transfer}\\ \text{From Wall to Surrounding in}\\ \text{Control Volume } S_i}} - \underbrace{\frac{A_{wall,i}(T_{wall,i}- T_e)}{R_{wall,i}}}_{\substack{\text{Convetive Heat Transfer}\\ \text{From Wall to Surrounding in}\\ \text{Control Volume } S_i}}$$

$$+ \underbrace{\frac{\pi d_{s,i}d_{wall,i}(T_{wall,i-1}- T_{wall,i})}{R_{cond,i-1}}}_{\substack{\text{Conductive Heat Transfer}\\ \text{From Control Volume } S_{i-1}}} - \underbrace{\frac{\pi d_{s,i}d_{wall,i}(T_{wall,i}- T_{wall,i+1})}{R_{cond,i}}}_{\substack{\text{Conductive Heat Transfer}\\ \text{From Control Volume } S_i}} \tag{4.16}$$

4.1.1 Thermo-Physical Properties of Humid Air

In order to solve the mass and energy balances presented in section 4.1 simultaneously, the thermo-physical properties of air must be determined as a function of temperature and relative humidity (RH). The thermo-physical properties of interest for air include: density, viscosity, thermal conductivity, and specific heat capacity. The thermo-physical properties of air as a function of temperature and relative humidity were calculated based on empirical equations developed by Tsilingiris [5] for 0°C to 100°C and 0% RH to 100% RH. The combination of air and water vapor is treated as a binary ideal gas mixture in the Tsilingiris approach. Due to ideal gas approach an additional factor, called the enhancement factor, is included in the relative humidity calculation and henceforth all thermo-physical property calculations as well. The enhancement factor is given as Equation 4.17 [5]:

$$f(P,T) = \exp\left[\xi_1\left(1 - \frac{P_{sat}}{P_0}\right) + \xi_2\left(\frac{P_{sat}}{P_0} - 1\right)\right] \tag{4.17}$$

where

$$\xi_1 = A_0 + A_1T + A_2T^2 + A_3T^3 + A_4T^4 \tag{4.18}$$

$$\xi_2 = B_0 + B_1T + B_2T^2 + B_3T^3 + B_4T^4 \tag{4.19}$$

The term P_0 is atmospheric pressure and is taken as 101.325 kPa. The temperature scale in Equations 4.18 and 4.19 is Kelvin. The constants for A and B are shown in Table 4.1.

Table 4.1 Constants A and B for Enhancement Factor Parameters

Subscript	A	B
0	$3.53624e^{-4}$	$-1.07588e^{1}$
1	$2.93228e^{-5}$	$6.32529e^{-2}$
2	$2.61474e^{-7}$	$-2.53591e^{-4}$
3	$8.57538e^{-9}$	$6.33784e^{-7}$

The vapor pressure of water (kPa) is given as Equation 4.20 [5]

$$P_{sat} = E_0 + E_1 t + E_2 t^2 + E_3 t^3 + E_4 t^4 \tag{4.20}$$

The temperature scale for vapor pressure equation is Celsius. The constants for E are shown in the Table 4.2:

Table 4.2 Constants for Water Vapor Pressure in Equation 4.20

Constant	Value
E_0	0.7073034146
E_1	$-2.703615165e^{-2}$
E_2	$4.36088211e^{-3}$
E_3	$-4.662575642e^{-5}$
E_4	$1.034693708e^{-6}$

The density of air (kg/m^3) is given as Equation 4.21 [5]:

$$\rho_m = \frac{1}{Z_v(RH,T)}\left(\frac{P_0}{RT}\right)28.9635\frac{kg}{kmol\ Air}\left[1 - f(P,T)(RH)\left(1 - \frac{18.02\frac{kg}{kmol\ H_2O}}{28.9635\frac{kg}{kmol\ Air}}\right)\left(\frac{P_{sat}}{P_0}\right)\right] \tag{4.21}$$

where 28.9635 kg $kmol^{-1}$ is the molecular weight of air and 18.02 kg $kmol^{-1}$ is the molecular weight of water vapor.

The compressibility factor Z_v is given as Equation 4.22 [5]:

$$Z_v(RH,T) = 1 + A(P_{sat}) + B(P_{sat})^2 \tag{4.22}$$

The constants A and B in Equation 4.22 are given as Equations 4.23 and 4.24:

$$A = C_1 + C_2 \exp\left(\frac{C_3}{T}\right) \tag{4.23}$$

$$B = K_1 + K_2 \exp\left(\frac{K_3}{T}\right) \tag{4.23}$$

The temperature scale for Equations 4.23 and 4.24 is Kelvin. The constants for A and B are given in the Table 4.3.

Table 4.3 Constants for A and B Parameters of Compressibility Factor

Subscript	C	K
1	$0.7e^{-8}$ Pa^{-1}	$0.104e^{-14}$ Pa^{-2}
2	$-0.147184e^{-8}$ Pa^{-1}	$-0.335297e^{-17}$ Pa^{-2}
3	1734.29 K^{-1}	3645.09 K^{-1}

Figure 4.2 shows the density of air as a function of relative humidity from 0-100°C.

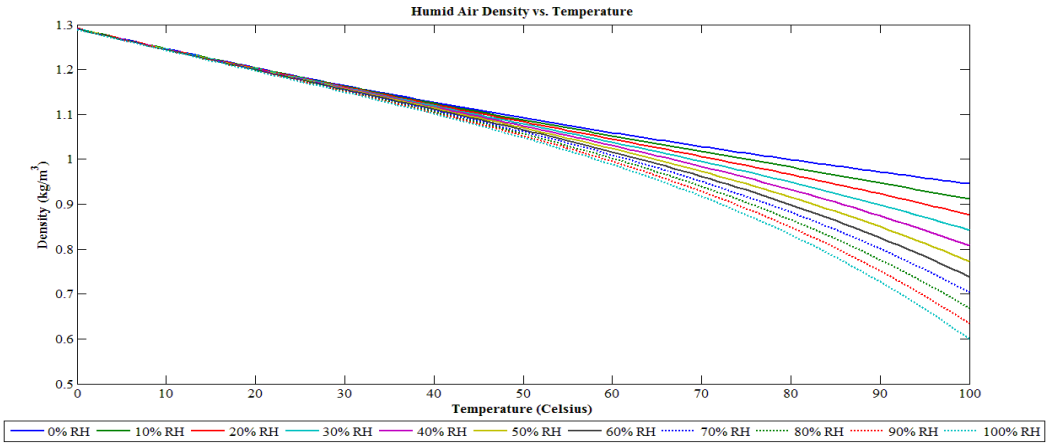

Figure 4.2 Humid Air Density

As Figure 4.2 shows, the density of air decreases with increasing temperature and increasing relative humidity. Water vapor has a lower density than air and as the water vapor displaces air molecules, the resulting humid air mixture is less dense then air alone.

The viscosity (Pa s) of air as a function of temperature and relative humidity is given as Equation 4.25 [5]:

$$\mu_m = \frac{\left[1 - f(P,T)(RH)\left(\frac{P_{sat}}{P_0}\right)\right]\mu_a}{\left[1 - f(P,T)(RH)\left(\frac{P_{sat}}{P_0}\right)\right] + f(P,T)(RH)\left(\frac{P_{sat}}{P_0}\right)\Phi_{av}} + \frac{f(P,T)(RH)\left(\frac{P_{sat}}{P_0}\right)\mu_v}{f(P,T)(RH)\left(\frac{P_{sat}}{P_0}\right) + \left[1 - f(P,T)(RH)\left(\frac{P_{sat}}{P_0}\right)\right]\Phi_{va}} \quad (4.25)$$

where μ_a is the viscosity of dry air, μ_v is the viscosity of water vapor, and Φ_{av} and Φ_{va} are interaction parameters. The viscosity of dry air is given as Equation 4.26 [5]:

$$\mu_a = MA_0 + MA_1T + MA_2T^2 + MA_3T^3 + MA_4T^4 \quad (4.26)$$

with T in Kelvin. Equation 4.26 for the viscosity of dry air is valid for -23°C to 327°C. The viscosity of water vapor is given as Equation 4.27 [5]:

$$\mu_v = MV_0 + MV_1t \quad (4.27)$$

with t in Celsius. The constants for the viscosity of dry air and water vapor are shown in Table 4.4.

Table 4.4 Constants for Dry Air and Water Vapor Viscosity

Subscript	MA	MV
0	$-9.8601e^{-1}$	$8.058131868e^{1}$
1	$9.080125e^{-2}$	$4.000549451e^{-1}$
2	$-1.17635575e^{-4}$	--
3	$1.2349703e^{-7}$	--
4	$-5.7971299e^{-11}$	--

The interaction parameters Φ_{av} and Φ_{va} are defined by Equations 4.28 and 4.29 [5]:

$$\Phi_{av} = \frac{\sqrt{2}}{4}\left(1 + \frac{28.9635\frac{kg}{kmol\ Air}}{18.02\frac{kg}{kmol\ H_2O}}\right)^{-\frac{1}{2}}\left[1 + \left(\frac{\mu_a}{\mu_v}\right)^{\frac{1}{2}}\left(\frac{18.02\frac{kg}{kmol\ H_2O}}{28.9635\frac{kg}{kmol\ Air}}\right)^{\frac{1}{4}}\right]^2 \quad (4.28)$$

$$\Phi_{va} = \frac{\sqrt{2}}{4}\left(1 + \frac{18.02\frac{kg}{kmol\ H_2O}}{28.9635\frac{kg}{kmol\ Air}}\right)^{-\frac{1}{2}}\left[1 + \left(\frac{\mu_v}{\mu_a}\right)^{\frac{1}{2}}\left(\frac{28.9635\frac{kg}{kmol\ Air}}{18.02\frac{kg}{kmol\ H_2O}}\right)^{\frac{1}{4}}\right]^2 \quad (4.29)$$

Figure 4.3 shows the viscosity of air as a function of relative humidity from 0-100°C.

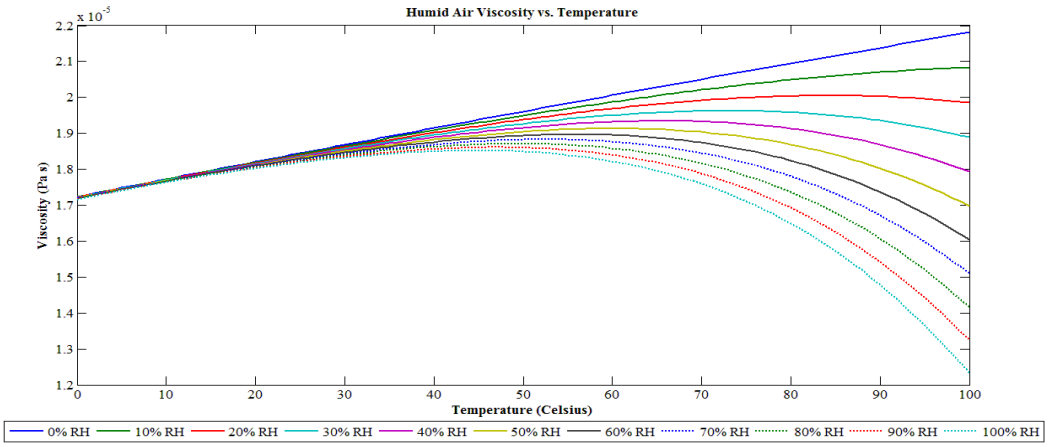

Figure 4.3 Humid Air Viscosity

The trend in Figure 4.3 shows air viscosity decreasing with increasing relative humidity. The viscosity of water vapor is lower than air such that when water vapor displaces air, the viscosity of the humid air mixture lowers.

The thermal conductivity (W/mK) of air as a function of temperature and relative humidity is similar, in form, to the viscosity equation and is given as Equation 4.30 [5]:

$$k_m = \frac{\left[1 - f(P,T)(RH)\left(\frac{P_{sat}}{P_0}\right)\right] k_a}{\left[1 - f(P,T)(RH)\left(\frac{P_{sat}}{P_0}\right)\right] + f(P,T)(RH)\left(\frac{P_{sat}}{P_0}\right)\Phi_{av}} + \frac{f(P,T)(RH)\left(\frac{P_{sat}}{P_0}\right) k_v}{f(P,T)(RH)\left(\frac{P_{sat}}{P_0}\right) + \left[1 - f(P,T)(RH)\left(\frac{P_{sat}}{P_0}\right)\right]\Phi_{va}} \quad (4.30)$$

where k_a is the thermal conductivity of dry air and k_v is the thermal conductivity of water vapor. The thermal conductivity of dry air is given as Equation 4.31 [5]:

$$k_a = KA_0 + KA_1 T + KA_2 T^2 + KA_3 T^3 + KA_4 T^4 + KA_5 T^5 \quad (4.31)$$

with T in Kelvin. Equation 4.31 for the thermal conductivity of dry air is valid for -23°C to 777°C. The viscosity of water vapor is given as Equation 4.32 [5]:

$$k_v = KV_0 + KV_1 t + KV_2 t^2 \quad (4.32)$$

with t in Celsius. The constants for the thermal conductivity of dry air and water vapor are shown in the Table 4.5.

Table 4.5 Constants for Dry Air and Water Vapor Thermal Conductivity

Subscript	KA	KV
0	$-2.276501e^{-3}$	$1.761758242e^{1}$
1	$1.2598485e^{-4}$	$5.558941059e^{-1}$
2	$-1.4815235e^{-7}$	$1.663336663e^{-4}$
3	$1.73550646e^{-10}$	--
4	$-1.066657e^{-13}$	--
5	$2.47663035e^{-17}$	--

Figure 4.4 shows the thermal conductivity of air as a function of relative humidity from 0 to 100°C:

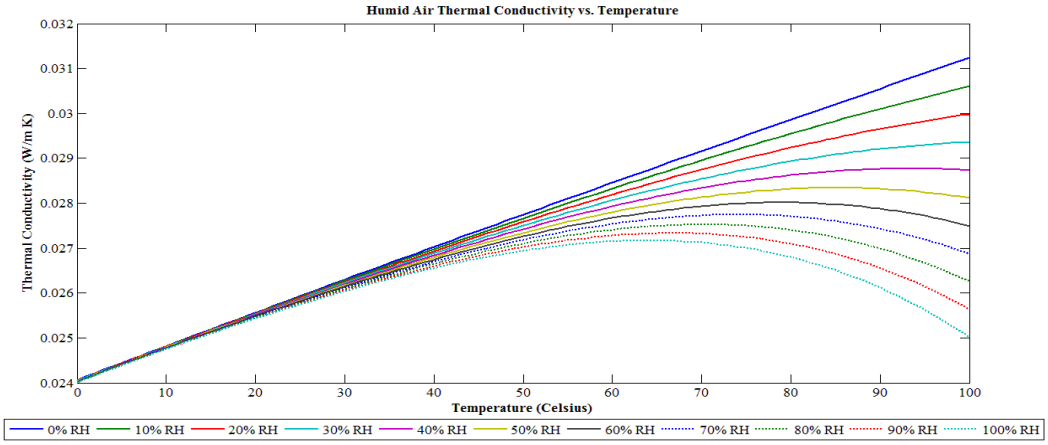

Figure 4.4 Humid Air Thermal Conductivity

The trend for the effect of relative humidity on air thermal conductivity in Figure 4.4 follows the same trend as the viscosity in Figure 4.3, decreasing with increasing relative humidity.

The specific heat capacity (kJ/kg K) of air as a function of temperature and relative humidity is given as Equation 4.33 [5]:

$$C_{p,m}= \frac{C_{p,a}\left[1 - f(P,T)(RH)\left(\frac{P_{sat}}{P_0}\right)\right]28.9635\frac{kg}{kmol\ Air} + C_{p,v}f(P,T)(RH)\left(\frac{P_{sat}}{P_0}\right)18.02\frac{kg}{kmol\ H_2O}}{28.9635\frac{kg}{kmol\ Air}\left[1 - f(P,T)(RH)\left(\frac{P_{sat}}{P_0}\right)\right] + f(P,T)(RH)\left(\frac{P_{sat}}{P_0}\right)18.02\frac{kg}{kmol\ H_2O}} \quad (4.33)$$

where $C_{p,a}$ is the specific heat capacity of dry air and $C_{p,v}$ is the specific heat capacity of water vapor. The specific heat capacity of dry air is given as Equation 4.34 [5]:

$$C_{p,a} = CA_0 + CA_1T + CA_2T^2 + CA_3T^3 + CA_4T^4 \quad (4.34)$$

with T in Kelvin. The equation for the specific heat capacity of dry air is valid for -23°C to 777°C. The specific heat capacity of water vapor is given as Equation 4.35 [5]:

$$C_{p,v} = CV_0 + CV_1t + CV_2t^2 \quad (4.35)$$

with t in Celsius. The constants for the specific heat capacity of dry air and water vapor are shown in the Table 4.6.

Table 4.6 Constants for Dry Air and Water Vapor Specific Heat Capacity

Subscript	CA	CV
0	$0.103409e^{1}$	1.86910989
1	$-0.284887e^{-3}$	$-2.578421578e^{-4}$
2	$0.7816818e^{-6}$	$1.941058941e^{-5}$
3	$-0.4970786e^{-9}$	--
4	$0.1077024e^{-12}$	--

Equations 4.27, 4.32, and 4.35 for pure water vapor properties are valid from 0°C to 120°C. Figure 4.5 shows the specific heat capacity of air as a function of relative humidity from 0-100°C.

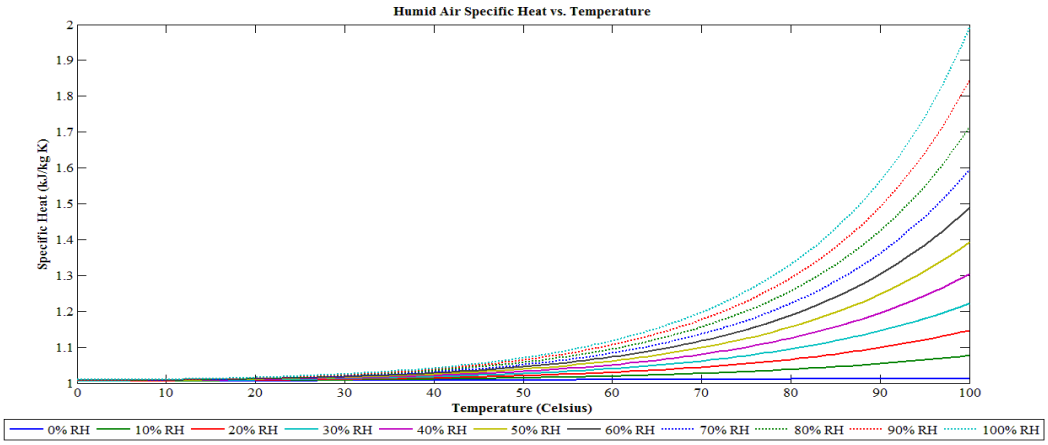

Figure 4.5 Humid Air Specific Heat Capacity (C_p)

As Figure 4.5 shows, the specific heat capacity of air increases with temperature and relative humidity. The increase in the specific heat capacity with relative humidity is due to the specific heat capacity of water vapor being higher than air alone.

With the thermo-physical properties of air now defined as a function of temperature and relative humidity, the hydrodynamic properties of the fluidized bed can now be determined.

4.1.2 Fluidized Bed Hydrodynamic Properties

In order to determine the heat and mass transfer capacity of a fluidized bed, an understanding of the fluid flow characteristics, including bubbles, must be taken into account. One of the first flow properties tabulated in fluidization calculations is the minimum fluidization velocity. The minimum fluidization velocity in dimensionless form as the Reynolds number is given as Equation 4.36 from Table 2.7 [6]:

$$Re_{mf} = \left(33.7^2 + 0.0408Ar\right)^{0.5} - 33.7 \tag{4.36}$$

The Archimedes number is given as Equation 4.37 from Table 2.6:

$$Ar = \frac{gD^3\rho_g\left(\rho_p - \rho_g\right)}{\mu^2} \tag{4.37}$$

The minimum fluidization velocity, U_{mf} is calculated from the Reynolds number at minimum fluidization as Equation 4.38:

$$U_{mf} = \frac{Re_{mf}\mu}{\rho d_p} \tag{4.38}$$

The bed voidage at minimum fluidization is given by Equation 2.43 in Chapter 2 [7]. The superficial gas velocity is given as Equation 4.39:

$$U_{0,i} = \frac{G_{a,i}}{\rho_{a,i}\left(\frac{\pi}{4}\right)d_{s,i}^2} \tag{4.39}$$

where G_a is the mass flow rate of humid air.

The bubble diameter is given as Equation 2.38 in Chapter 2 [8]. Bubble frequency is given as Equation 4.40:

$$f_{bub} = \frac{G_a}{\left(\frac{\pi}{6}\right)d_{bub}^3} \tag{4.40}$$

The bubble rise velocity is given as Equation 2.41 in Chapter 2 [12]. The bubble voidage is given as Equation 2.44 in Chapter 2 [9]. The bed voidage is given as Equation 2.44 in Chapter 2 [9]. The particle exchange rate, r (1/s) is given as the reciprocal of Equation 2.49 in Chapter 2 [1].

4.1.3 Fluidized Bed Heat Transfer Properties

Heat transfer calculations for a fluidized bed are somewhat tedious due to the multiple types of heat transfer occurring simultaneously, including: gas-to-particle, gas-to-inner bed wall, particle-to-inner bed wall, bubble-to-inner bed wall, wall-to-wall, wall-to-external environment. Figure 4.6 shows a representation of all the heat transfer resistances of a control volume in a fluidized bed.

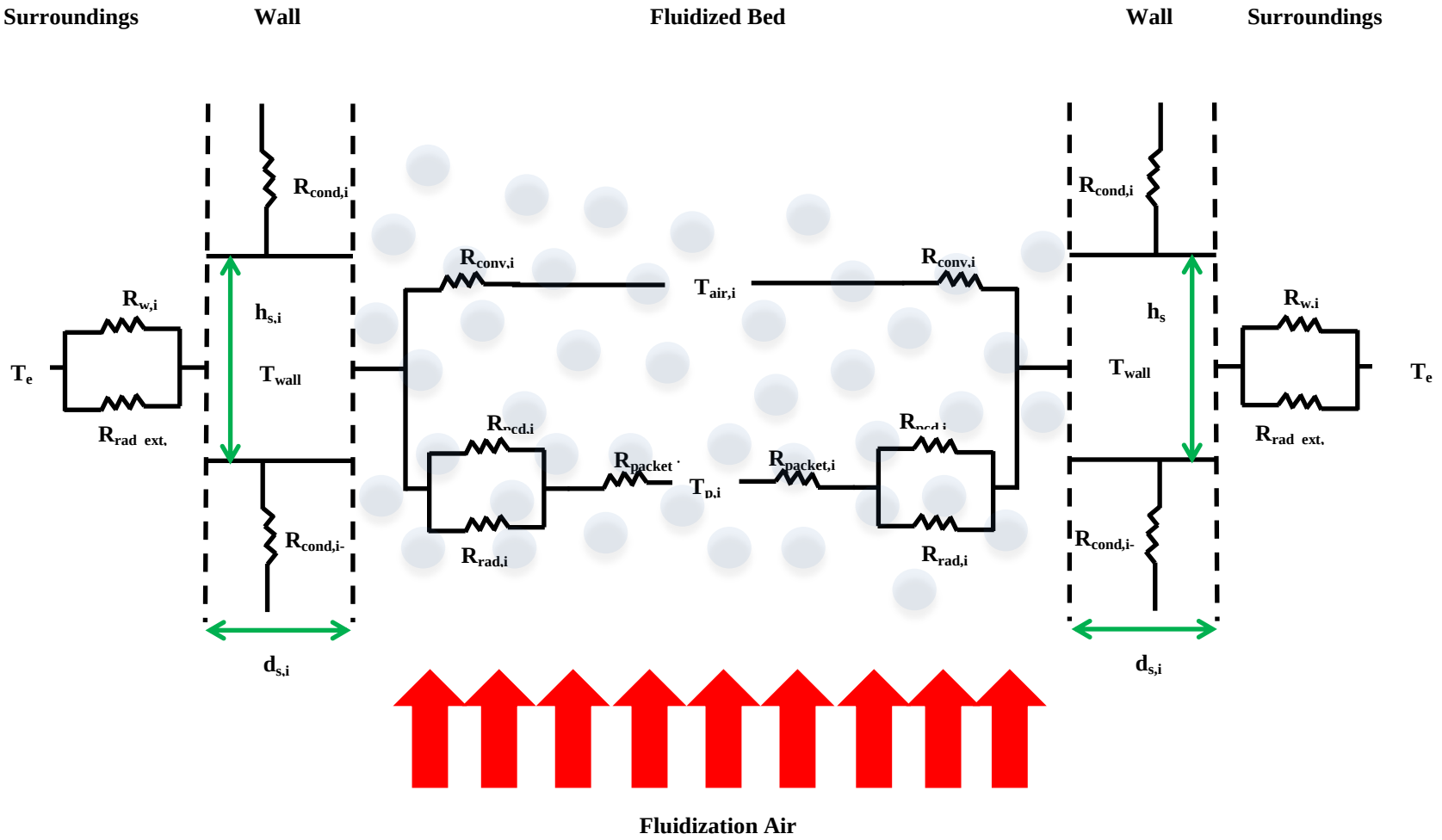

Figure 4.6 Heat Transfer Resistances in a Fluidized Bed Control Volume

The Nusselt Number, used to calculate the convective heat transfer from the fluidization gas to the particle, is given as Equation 4.41 from Table 2.18 in Chapter 2 [10]:

$$Nu_{p,i} = 2 + Pr_i^{0.4}\left(0.43Re_{p,i}^{0.5} + 0.06Re_{p,i}^{0.667}\right) \tag{4.41}$$

where Pr is the Prandtl number. The Prandtl number is given by Equation 4.42 from Table 2.18 in Chapter 2:

$$Pr = \frac{C_p\mu}{k} \tag{4.42}$$

The convective heat transfer coefficient is given as Equation 4.43 [11]:

$$\alpha_{p,i} = \frac{Nu_{p,i}\left(k_{a,i}\right)}{d_p} \tag{4.43}$$

Gas bubbles provide a source for heat transfer within the fluidized bed due to the constant movement of particles within all parts of the bed, including against the inner bed wall. Treating the mixture of solid particles and gas as an emulsion packet, a resistance to heat transfer develops which can be described by Equation 4.44 [1]:

$$\frac{1}{R_i} = \frac{\varepsilon_{bub}}{R_{conv,i}} + \frac{(1 - \varepsilon_{bub})}{R_{p,i}} \tag{4.44}$$

The term $R_{p,i}$ represents particle-to-wall heat transfer resistance and is given as Equation 4.45 [1]:

$$R_{p,i} = \left(\frac{1}{R_{pcd,i}} + \frac{1}{R_{rad,i}}\right)^{-1} + R_{packet,i} \tag{4.45}$$

Radiative heat transfer can be neglected if $T_a < 400^oC$, so Equation 4.45 simplifies to Equation 4.46 [12]:

$$R_{p,i} = R_{pcd,i} + R_{packet,i} \tag{4.46}$$

The $R_{pcd,i}$ term, which represents heat transfer resistance of the particle vertical surface contact point and the surrounding gas layer, is given by Equation 4.47 [1]:

$$\frac{1}{R_{pcd,i}} = \frac{2k_{aw,i}}{d_p} + \kappa_w C_{pa,i}\rho_{a,i}U_{0,i} \tag{4.47}$$

The κ_w term is a mixing constant, suggested to be equal to 0.05 [12]. The $k_{aw,i}$ term, which represents the thermal conductivity of gas around the particle, is given by Equation 4.48 [1]:

$$k_{aw,i} = \varepsilon_{mf}k_{a,i} + (1 - \varepsilon_{mf})k_p\left[\frac{1}{\tau_w\left(k_p/k_{a,i}\right) + 1/3}\right] \tag{4.48}$$

where k_p is the particle thermal conductivity and τ_w is the ratio of effective gas film thickness around a contact point to the particle diameter. The τ_w term is given by Equation 4.49 [12]:

$$\tau_w = 0.3361\left(k_p/k_{a,i}\right)^{-0.1862} \tag{4.49}$$

Equation 4.49 is valid for $1 \le \left(k_p/k_{a,i}\right) \le 10000$.

The $R_{packet,i}$ term in Equation 4.46 represents thermal diffusion through an emulsion packet and is given by Equation 4.50 [1]:

$$\frac{1}{R_{packet,i}} = \frac{2}{\sqrt{\pi}}\left(\frac{k_{amark,i}\rho_p(1 - \varepsilon_{mf})C_{pp,i}f_{bub}}{1 - \varepsilon_{bub}}\right)^{0.5} \tag{4.50}$$

where k_{amark} is the thermal conductivity of stagnant gas in the fluidized bed. The term k_{amark} is given by Equation 4.51 [1]:

$$k_{amark,i} = \varepsilon_{mf}k_{a,i} + (1 - \varepsilon_{mf})k_p\left[\frac{1}{\tau_{mark,i}\left(k_p/k_{a,i}\right) + 2/3}\right] \tag{4.51}$$

The term $\tau_{mark,i}$ represents the gas film thickness around a contact point to a particle diameter for particle-particle contact and is given by Equation 4.52 [12]:

$$\tau_{mark} = 0.3116\left(k_p/k_{a,i}\right)^{-0.2174} \tag{4.52}$$

Equation 4.52 is valid for $1 \le \left(k_p/k_{a,i}\right) \le 10000$.

Next, consideration must be given to heat transfer as a result of bubble movement along the fluidized bed wall. The Dittus-Boelter equation for turbulent fluid flow in a vertical pipe is

used here to estimate the heat transfer resistance between gas bubbles and the inner fluidized bed wall. The Nusselt number according to the Dittus-Boelter equation is given as Equation 4.53 [13]:

$$Nu_{wall,i} = 0.023 Re_{wall,i}^{0.8} Pr_i^{0.4} \tag{4.53}$$

where Re_{wall} is the Reynolds number of the gas flowing through the fluidized bed. The Reynolds number of the wall is given by Equation 4.54 [1]:

$$Re_{wall,i} = \frac{\rho_{a,i} U_{0,i} d_{s,i}}{\mu_{a,i}} \tag{4.54}$$

The term $R_{conv,i}$ which represents convective heat transfer resistance at a submerged surface is estimated as Equation 4.55 [1]:

$$R_{conv,i} = \frac{1}{\alpha_{wall,i}} = \frac{d_{s,i}}{Nu_{wall,i} k_{a,i}} \tag{4.55}$$

The conductive heat transfer resistance through the fluidized bed wall is given as Equation 4.56 [1]:

$$R_{cond,i} = \frac{h_{s,i} + h_{s,i+1}}{2k_{a,i}} \tag{4.56}$$

where h_s is the height of the control volume.

Finally, heat transfer from the outer fluidized bed wall to the environment must be accounted for. The Nusselt Number for natural or free convection, calculated from the Prandtl Number and Grashof Number is given as Equation 4.57 [1]:

$$Nu_e = 0.50(Gr_e Pr_e)^{0.25} \tag{4.57}$$

Equation 4.57 is valid for $10000 \leq (Gr_e Pr_e) \leq 10e^{9.}$ The Grashof number from Table 2.18 in Chapter 2 is given by Equation 4.58 [11]:

$$Gr = \frac{g\beta(T_s - T_\infty)D^3}{\nu^2} \tag{4.58}$$

The environment Prandtl number is the same form as Equation 4.42 but the properties are evaluated at the film temperature. The environmental Nusselt number is given as Equation 4.59 [11]:

$$Nu_{e,i} = \frac{\alpha_{film,i} d_{s,i}}{k_{film,i}} \tag{4.59}$$

The term β in Equation 4.58 represents the thermal expansion coefficient of the fluidization air. For an ideal gas, the thermal expansion coefficient is the reciprocal of the absolute temperature. All of the film properties of air are calculated at the film temperature, which is an average of the environment temperature and the wall temperature. The fluidized bed wall heat transfer resistance to the environment is given as Equation 4.60 [1]:

$$R_{wall,i} = \frac{1}{\alpha_{film,i}} = \frac{d_{s,i}}{Nu_{film,i} k_{film,i}} \tag{4.60}$$

Radiation heat loss from the fluidized bed wall is given as Equation 2.72 in Chapter 2. The θ_w term is the emissivity, taken as 0.28 for stainless steel. The particle to wall heat transfer is given by Equation 4.61 [1]:

$$\Phi_{loss,p,i} = \frac{A_{wall,i}(1- \varepsilon_{bub})(T_{p,i}- T_{wall,i})}{R_{p,i}} \tag{4.61}$$

The gas to wall heat transfer is given by Equation 4.62 [1]:

$$\Phi_{loss,a,i} = \frac{A_{wall,i}\varepsilon_{bub}(T_{a,i}- T_{wall,i})}{R_{conv,i}} \tag{4.62}$$

4.1.4 Fluidized Bed Mass Transfer Properties

In order to calculate the liquid drying rate at operating conditions, the mass transfer coefficient must first be determined from the Sherwood Number, Reynolds Number, and Schmidt Number. The Schmidt Number is given as Equation 2.73 in Chapter 2.

The Diffusion coefficient of water is given as Equation 4.63 [1]:

$$D_{v,i} = 24.2e^{-6}\left(\frac{T_{a,i}}{293.15}\right)^{1.75}\left(\frac{10^5}{P_i}\right) \tag{4.63}$$

where P_i is the pressure inside the fluidized bed. The Sherwood Number is given as Equation 4.64 from Table 2.19 in Chapter 2 [10]:

$$Sh = 2 + \left(0.43Re^{0.5} + 0.06Re^{0.67}\right)Sc^{0.4} \tag{4.64}$$

The mass transfer coefficient then calculated as a rearrangement of Equation 2.74 in Chapter 2. The drying rate, defined as a ratio mass unit of liquid (water) per mass unit particle is given as Equation 4.65 [1]:

$$R_{D,i} = \frac{\alpha'_{p,i}A_p\left(\frac{W_{p,i}}{|W_{p,i}| + a}\right)\left(P_{satp,i} - P_{sata,i}\right)}{M_p\left(R_g/18.02\frac{kg}{kmol\ H_2O}\right)\left(T_{a,i} + T_{p,i}\right)/2} \tag{4.65}$$

where W_p is the water moisture content in kg water per kg particles. The parameter a is added to the drying rate term in order to avoid zero order drying rates which are problematic for Matlab ODE solvers. The parameter a is set to a value of 0.05 and only influences the W_p curve [1].

The addition of liquid (water) to the fluidized bed changes the absolute and relative humidity of the fluidization gas. The absolute humidity, X_a (kg H_2O/kg Dry Air), is given as Equation 4.66 [1]:

$$\frac{P_{actual,i}}{P_{ambient}} = \frac{X_{a,i}}{X_{a,i} + \left(\frac{18.02\frac{kg}{kmol\ H_2O}}{28.96\frac{kg}{kmol\ Air}}\right)} \tag{4.66}$$

The second term in the denominator of Equation 4.66 is the ratio of the molecular weight of water to the molecular weight of air.

The relative humidity is given as Equation 4.67 (Hede et al. 2009):

$$RH\% = \frac{P_{actual,i}(100\%)}{P_{sat,i}} \tag{4.67}$$

4.1.5 Transient Mass and Energy Balance Assumptions

The mass and energy balances presented in Section 4.1 represent a one-dimensional approach to predicting the temperature profiles of the fluidization air, the fluidized bed wall, and the particle bed. There are several assumptions that accompany this approach to make calculations less tedious and time consuming.

The control volumes are divided into coating control volumes and non-coating control volumes. Coating solution droplets can only penetrate the fluidized bed to a certain depth. Droplet-particle collisions only occur in the upper volume of a top spray fluidized bed, so particle coating only occurs in the upper volume of a top spray fluidized bed [14]. Coating control volumes are therefore limited to the upper volume of a top spray fluidized bed. Non-coating control volumes are used for the remaining fluidized bed volume [1].

The mass of coating liquid is assumed to be evenly distributed into each coating control volume, M_c/c, where c is the total number of control volumes for the fluidized bed. Furthermore, no premature droplet evaporation occurs, meaning all the coating liquid is accumulated on the particle surface in each control volume [1].

There are also assumptions made regarding the particles inside the fluidized bed. All the particles in the fluidized bed have the same diameter and are perfectly mixed in each control volume. The postulate regarding perfect mixing also extends to the moisture content and surface temperature being equal for all particles within a control volume. The number of particles within a control volume is considered constant, i.e. the number of particles that enters a control volume equals the number of particles that leave the control volume. There is no particle attrition as the

particles are mechanically strong and there is no particle elutriation, including coating material [1]. Internal heat transfer resistance is considered negligible as the Biot number for particles and droplets is assumed to be less than 0.1; therefore the temperature for droplets and particles is assumed to be isothermal [1].

In addition to assumptions regarding the particles of the fluidized bed, there are also some assumptions regarding the fluidization and atomization air. The exhaust air pressure is taken as atmospheric pressure; therefore the drying process is also at atmospheric pressure. The specific heat capacity of the atomization air is considered equal to that of the fluidization air for a coating control volume [1]. Figure 4.7 shows a typical temperature profile of a control volume during preheating.

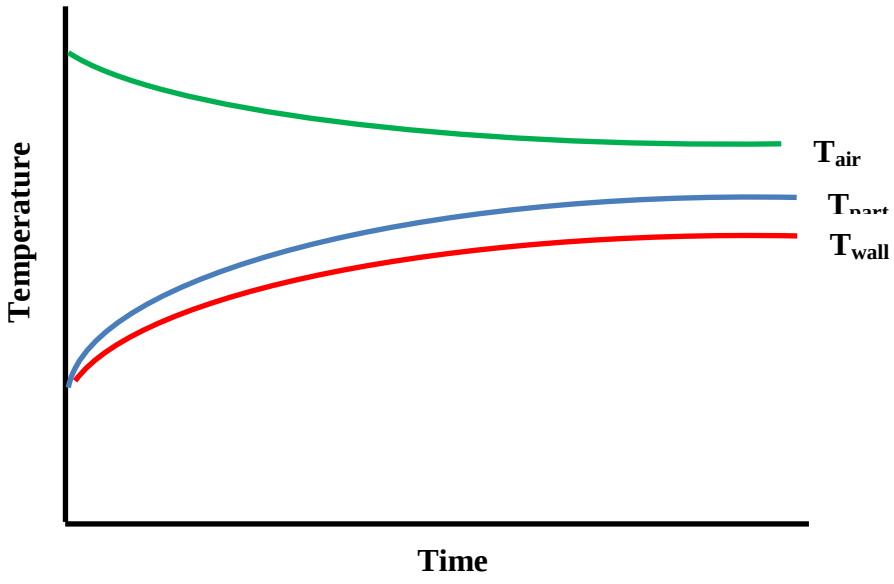

Figure 4.7 Typical Temperature Profile Produced by Transient Mass and Energy Balance for a Control Volume

As Figure 4.7 shows, the fluidization air cools as the particles and wall heat up simultaneously. Eventually, a thermal steady state is reached with all three components.

4.1.6 Drawbacks to 1-D Approach for Transient Mass and Energy Balances

There are some drawbacks to the 1-D approach used for the transient mass and energy balances. The model does not account for temperature or velocity fluctuations in the radial direction. Research has shown that there is a velocity distribution that is dependent on radial location and the flow regime (laminar or turbulent). For laminar flow in a circular tube, the radial velocity can be calculated by Equation 4.68 [15]:

$$\frac{v_z}{v_{z,max}} = 1 - \left(\frac{r}{R}\right)^2 \tag{4.68}$$

where v_z is the velocity at radius r and R is the maximum radius. For turbulent flow, the radial velocity can be calculated by Equation 4.69 [15]:

$$\frac{\bar{v}_z}{v_{z,max}} = \left(1 - \frac{r}{R}\right)^{1/7} \tag{4.69}$$

where $\bar{v}_z$ is the average velocity at radius r. Figure 4.8 gives a qualitative representation of the difference between the velocity distributions of laminar and turbulent flow.

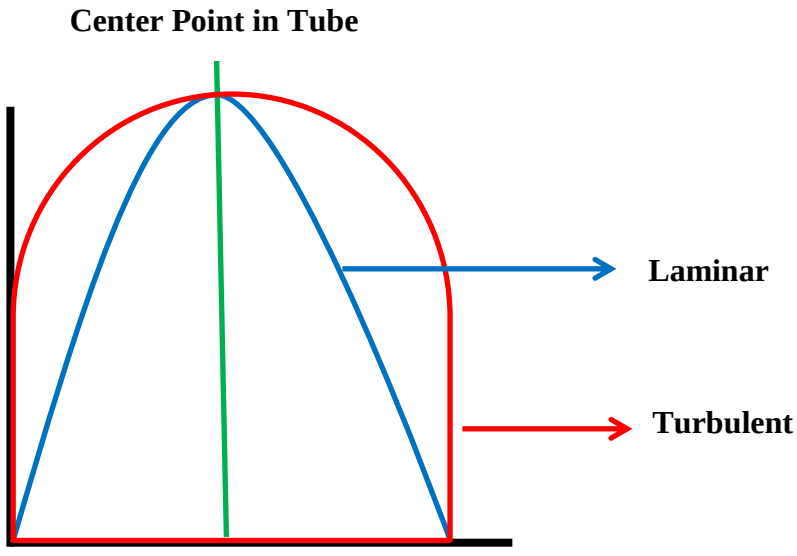

Figure 4.8 Qualitative Difference Between Laminar and Turbulent Velocity Profile Distributions

The coating liquid is assumed to be evenly distributed among the particles in coating control volumes. However, this may not be entirely accurate because the spray area increases as the liquid travels away from the nozzle and the fluidized bed void fraction decreases approaching the spray nozzle. This may lead to different droplet-particle collision rates, an uneven distribution of the liquid coating, and different temperature profiles for the fluidizing gas, particles and fluidized bed wall.

Most notably the transient mass and energy balances do not explicitly give any indication of whether particle agglomeration or particle coating will dominate the fluidized bed operation. Part of the reason for this is because only one particle size is used to represent the entire particle size distribution.

4.1.7 Wurster Orientation Property Estimation

In the Wurster orientation, shown as Figure 4.9, the particles undergo high acceleration rates due to exposure to fluidization velocities above the particle terminal velocities. The particle acceleration rate within the Wurster tube insert occurs at different rates because the terminal velocity has a distribution of values dependent on the particle size distribution. For this reason, particles travel different distances when making a revolution within the fluidized bed and ultimately have a distribution of coating material.

Inside the Wurster tube insert, the bed void fraction and particle velocity change as a function of height. At the bottom of the Wurster tube insert, the bed void fraction is nearly the void fraction at minimum fluidization, while the particle velocity is very nearly zero (Cheng & Turton 2000). When the particles exit the Wurster tube insert, the bed void fraction is much higher and the particle velocity approaches the fluidization velocity asymptotically.

The equations to calculate the flow pattern properties in the Wurster orientation: total cycle time, particle velocities, and distance traveled are given in Chapter 2 as Equations 2.50-2.58.

The last flow pattern property to calculate for the Wurster orientation is the bed void fraction as a function of height. The particle acceleration rate is a force balance involving drag, gravity and friction as shown by Equation 4.70 [17]:

$$dM\frac{dU_p}{dt} = dF_{drag} - dF_{grav} - dF_{fric} \tag{4.70}$$

where dF_{drag}, dF_{grav}, and dF_{fric} are given as Equations 4.71-4.73 [17]:

$$dF_{drag} = \frac{3}{4} C_d \varepsilon^{-4.7} \frac{\rho_f \left(U_f - U_p\right)^2}{\left(\rho_p - \rho_f\right) d_p} dM \tag{4.71}$$

$$dF_{grav} = g\, dM \tag{4.72}$$

$$dF_{fric} = \frac{f_p U_p^2}{2D} dM \tag{4.73}$$

Here f_p is the solid friction factor given by Equation 4.74 [17]:

$$f_p = 0.0206 \frac{(1 - \varepsilon)}{\varepsilon^3} \left[(1 - \varepsilon) \frac{Re_{term}}{Re_{part}}\right]^{-0.869} \tag{4.74}$$

The dM term in Equations 4.71-4.73 is the mass of particles in a discretized section of the Wurster tube insert [17]. Equation 4.70 is simplified in practice by setting the friction term to zero.

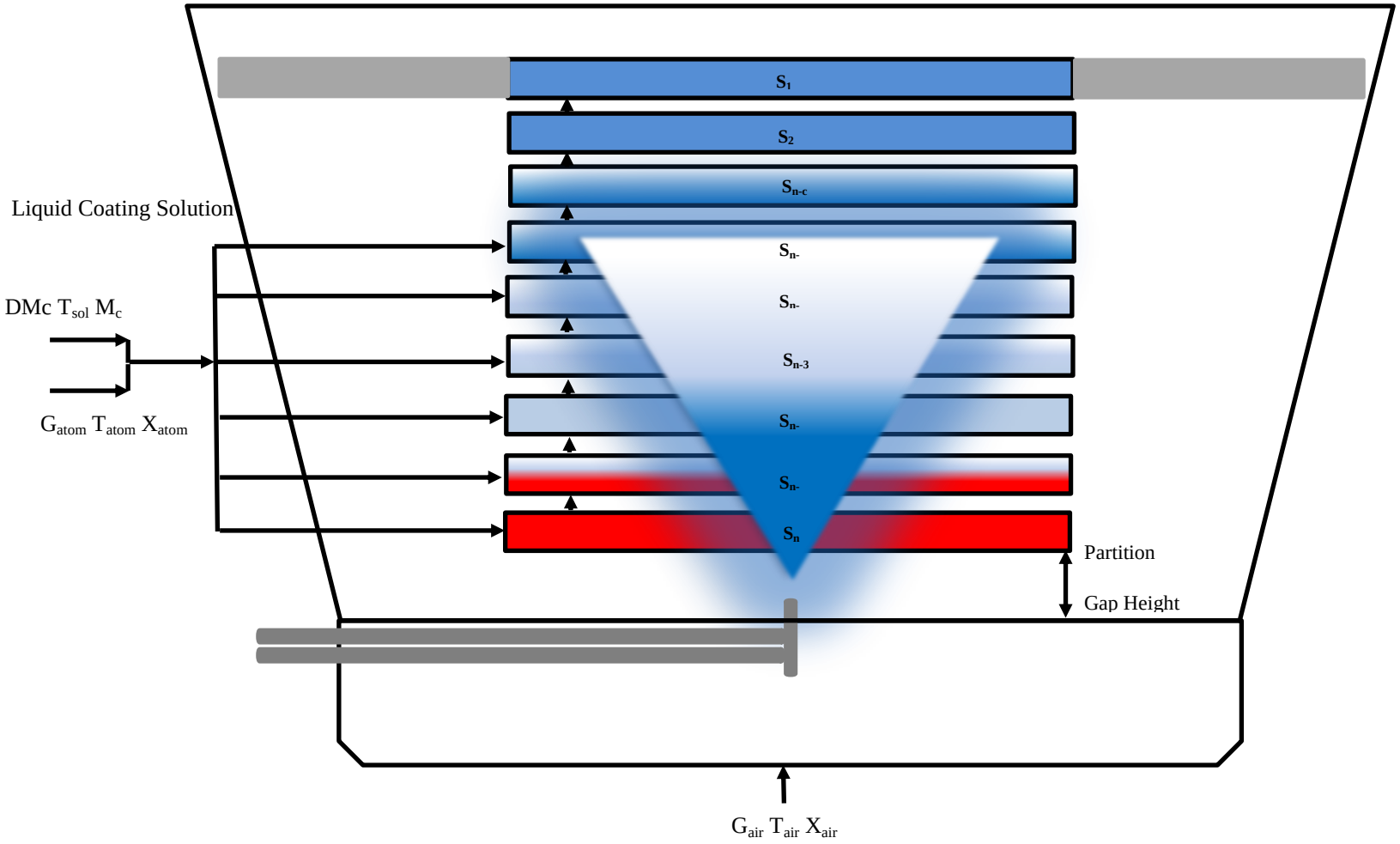

Figure 4.9 Wurster Orientation Discretization

4.1.8 Wurster Spray Orientation Spray Control Volume Determination

In the Wurster spray orientation the length of the nozzle spray cone is crucial to the calculations for coating efficiency and coating growth. Ideally, no liquid coating solution exits the Wurster tube and no liquid coating solution collides with the wall before evaporating into the fluidization air. Additionally, a small droplet size distribution is desirable such that the particle surface is completely dry before exiting the Wurster tube if it collides with a coating solution droplet.

The first step to determining how many spray control volumes there are for a Wurster orientation fluidized bed experiment is to determine the maximum amount of solvent vapor (in this case water) that air can hold without condensing as a function of temperature, this is called specific humidity. As Figure 4.10 shows, the specific humidity of water in air increases with air temperature. A mass balance yields the maximum solvent flow rate that can be adsorbed by the fluidization air.

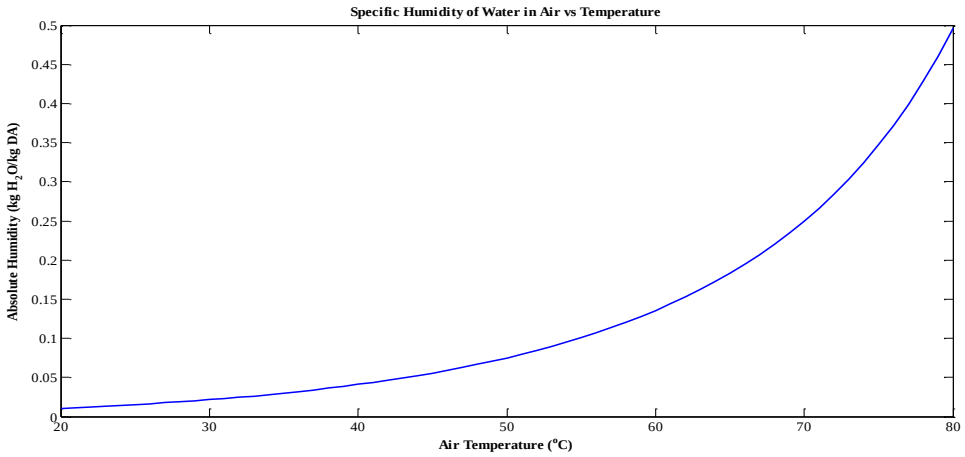

Figure 4.10 Specific Humidity of Water in Air vs. Temperature

For example, for a volumetric flow rate of 8 m^3/hr at an inlet relative humidity of 50% heated to 50°C from room temperture, the mass flow rate of fluidization air-water vapor mixture

is 9.467 kg/hr with an inlet absolute humidity of 0.0153 kg H_2O per kg Dry Air. An energy balance on the fluidization air with a specific liquid coating solution flow rate determines the maximum temperature drop for the fluidization air with complete solvent evaporation. The maximum flow rate of liquid coating solution can then be interpolated from Figure 4.11 which shows the maximum amount of water the fluidization air can hold as a function of temperature. In this case, if no higher than a 10°C drop in the fluidization air temperature is desired, the maximum amount of liquid coating solution that can be adsorbed is 4 grams per minute. The slightly negative values below 25°C in Figure 4.11 indicate that condensation will take place rather than absorption.

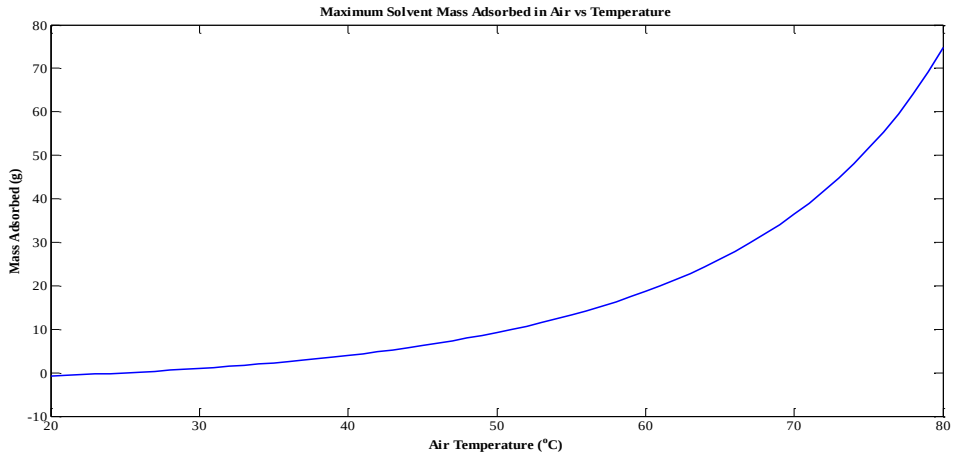

Figure 4.11 Maximum Amount of Solvent Adsorbed vs. Temperature

Once the overall energy balance is completed, a dynamic energy balance is computed with the selected liquid coating solution flow rate in the same fashion as the top spray dynamic energy balance. The number of coating control volumes is calculated using convective heat transfer coefficients and droplet surface areas based on the Sauter mean diameter of the nozzle atomization conditions. For example, based on the energy balance calculations, the liquid

coating solution droplet with a 20 μm diameter will be totally evaporated by the 6th control volume. Therefore, six control volumes are used in the coating growth kinetics model.

With the hydrodynamic properties and proper number of coating control volumes of the Wurster orientation fluidized bed experiments determined, the next step is to calculate the coating growth kinetics for the experiment. The coating growth kinetics model will be discussed next.

4.2 Coating Growth Kinetics Model Development

The 1-D transient mass and energy balances can be extended to incorporate particle growth rates with careful consideration. Further detailed calculations must be carried out to obtain particle growth rates from the mass and energy balances presented in Section 4.1. The extra calculations needed include: droplet properties – size, volume, and surface area as a function of the liquid-particle contact angle and for every coating control volume - spray area, probability of being in the spray area, probability of a droplet-particle collision, dimensionless spray flux (DSF), and viscous Stokes number. The details to the above listed calculations will be presented in the next sections.

4.2.1 Particle Size Distribution

The first step to developing a coating growth kinetics model involves having knowledge of the particle size distribution of the core solid material. In the absence of actual data (mean, standard deviation, etc.) a particle size distribution can still be ascertained via a triangular probability distribution using the maximum, minimum, and mode of a particle size range. Other probability distributions however, (e.g. beta, normal, rectangular, trapezoidal, etc.) can be used in place of the triangular probability distribution. Figure 4.12 shows the probability density and the cumulative distribution function of a general triangular probability distribution.

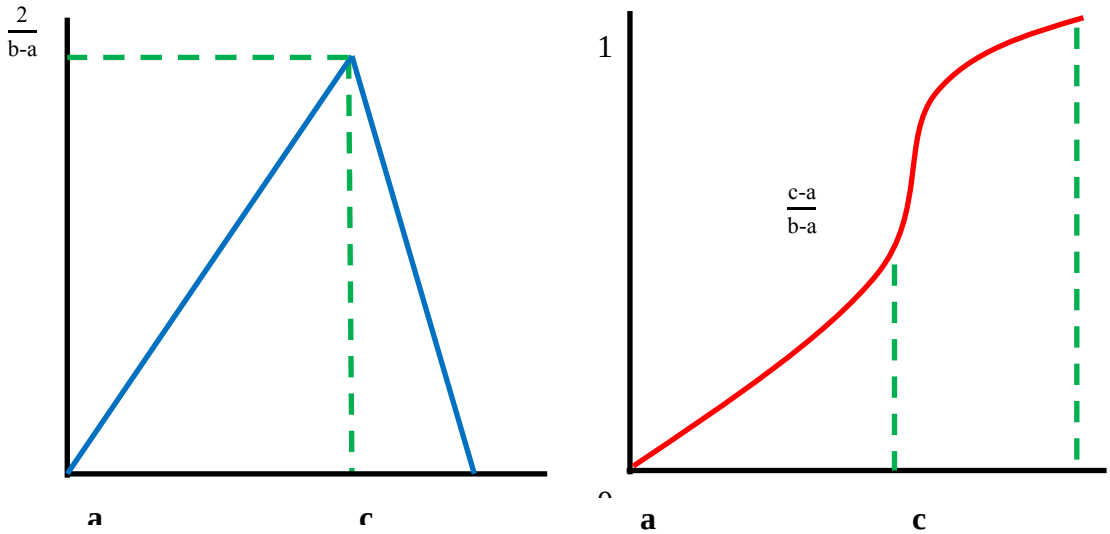

A) Probability Density B) Cumulative Distribution

Figure 4.12 A) Triangular Probability Distribution B) Triangular Cumulative Distribution

The probability density function and the cumulative density function of a triangular distribution are shown as Equations 4.75 and 4.76 [18]:

$$PDF = \begin{cases} 0 & \text{for } x < a \\ \dfrac{2(x-a)}{(b-a)(c-a)} & \text{for } a \le x \le c \\ \dfrac{2(b-x)}{(b-a)(b-c)} & \text{for } c < x \le b \\ 0 & \text{for } x > b \end{cases} \tag{4.75}$$

$$CDF = \begin{cases} 0 & \text{for } x < a \\ \dfrac{(x-a)^2}{(b-a)(c-a)} & \text{for } a \le x \le c \\ 1-\dfrac{(b-x)^2}{(b-a)(b-c)} & \text{for } c < x \le b \\ 1 & \text{for } x > b \end{cases} \tag{4.76}$$

where a is the distribution minimum, b is the distribution maximum, c is the distribution mode, and x is the actual value within the distribution. For this work, maximum and minimum particles sizes are determined based on particle sieve sizes which are used to separate particles of all sizes. A value for the particle distribution mode is selected between the maximum and minimum

values. A random number generator is utilized to generate 10,000 random variates for the CDF defined in Equation 4.76. The actual particle size, x, is calculated from Equation 4.76 as well.

4.2.2 Spray Droplet Characteristics: Droplet Size Distribution, Spray Area, Spray Area Volume, Spray Void Fraction, and Probability of Being in the Spray Area

The next part of the coating growth kinetics model involves the calculation of the droplet spray characteristics within the fluidized bed. First, the Sauter mean diameter of the droplets produced from the nozzle. The proper correlation must be used depending on whether an external or internal mixing pneumatic nozzle is used. For this work, an external nozzle was used and the correlation for the Sauter mean diameter used is given as Equation 2.18 in Chapter 2 [19, 20]. The droplet mass median diameter (MMD) is calculated according to Equation 2.10 in Chapter 2. The droplet size distribution is calculated using the Rosin-Rammler distribution shown in Equation 2.20 in Chapter 2 with the equation constants q and X set to 2.5 [1] and the previously calculated droplet MMD respectively. A random number generator between 0 and 1 (10,000 points) is used for the 1-Q term on the left hand side of Equation 2.20 and the droplet size distribution is calculated. The volume of the droplet size distribution is calculated as Equation 4.77:

$$V_{drop} = \frac{4\pi}{3}\left(\frac{d_{dsd}}{2}\right)^3 \tag{4.77}$$

Once droplet size and volume distribution have been tabulated, next the spray area must be calculated as a function of distance from the spray nozzle. The spray area is a function of the nozzle spray angle and the distance from the nozzle. First the spray diameter is given as Equation 4.78 [21]:

$$d_{spray,\,i} = 2h_i\left(\tan\left(\frac{\theta}{2}\right)\right) \tag{4.78}$$

where h is the distance from the nozzle and θ is the nozzle spray angle. The spray area is then dependent on the type of nozzle used. For a full cone nozzle, the spray area is given as Equation 4.79:

$$A_{spray,\,i} = \pi\left(\frac{d_{spray,\,i}}{2}\right)^2 \tag{4.79}$$

The spray area will increase as long as the nozzle gas velocity is greater than the fluidization velocity, regardless of top-spray or Wurster orientation. However, proper calibration should be done such that the spray area is not larger than the bed diameter or Wurster tube diameter because the spray droplets will hit the fluidized bed wall or Wurster tube wall and thereby increasing processing time. The difference between the nozzle gas velocity and the fluidization velocity is called the nozzle relative velocity and is shown as Equation 4.80:

$$U_{rel} = U_{noz} - U_{super,\,i} \tag{4.80}$$

For the top-spray orientation, a negative U_{rel} value means the gas from the nozzle does not reach that particular segment of the fluidized bed, therefore no liquid droplets will either. Equation 4.80 sets the boundary condition for the number of coating control volumes within the top-spray oriented fluidized bed.

With the proper number of spray areas for the fluidized bed calculated with Equations 4.78-4.80, the amount of space allocated to the spray area of each segment of the fluidized bed can be calculated by multiplying the spray area by the control volume height as shown in Equation 4.81:

$$\text{Spray Area CV Volume}_i = A_{spray,\,i}(\text{CV Height}) \tag{4.81}$$

The volume calculated by Equation 4.81 increases as distance from the nozzle increases in both the top-spray and Wurster orientations.

An additional aspect of the spray droplet characteristics that must be taken into account for the coating growth kinetics model is the void fraction of the atomization air-liquid coating mixture. The void fraction of the atomization air-liquid coating mixture is shown as Equation 4.82:

$$\varepsilon_{spray,\,i} = \frac{\dot{V}_{atom}}{\dot{V}_{atom} + \dot{V}_{liq\ coat,\,i}} \tag{4.82}$$

Finally, with the spray area calculation in Equation 4.79 the probability of a particle being in the spray area in any segment of the fluidized bed is given by Equation 4.83:

$$p_{ISA,\,i} = \frac{A_{spray,\,i}}{A_{bed,\,i}} \tag{4.83}$$

Figure 4.13 shows the side view and top view of a top-spray orientation that physically represents Equation 4.83.

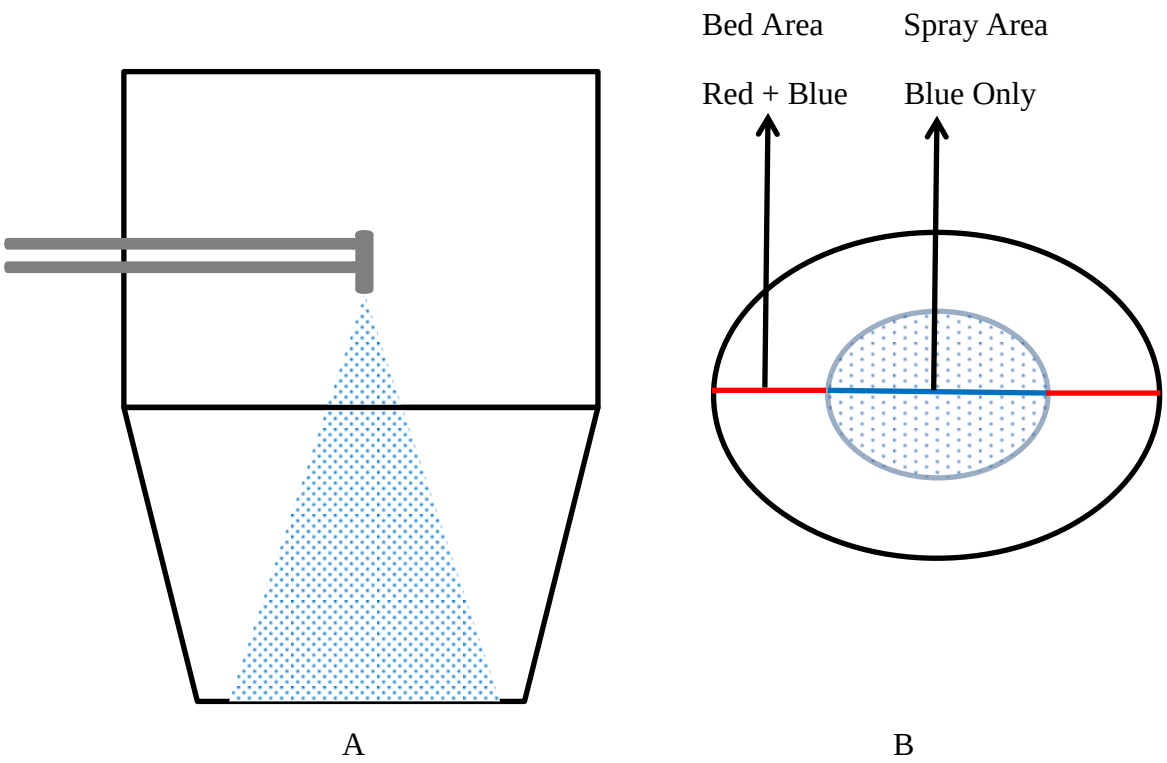

Figure 4.13 A) Side View B) Top View of Top-Spray Oriented Fluidized Bed

For a fluidized bed in the Wurster orientation, top view of Figure 4.13 is the same as for a top-spray orientation. The spray area increases as distance from the nozzle increases in the top-spray orientation, while the bed area decreases. However, in the Wurster orientation, the bed area is constant while the spray area increases with increasing distance from the nozzle.

4.2.3 Fluidized Bed Characteristics: Number of Particles in the Spray Area, Liquid Volume Deposited, Liquid Volume Left, Coating Efficiency, and Probability of Being Coated in the Spray Area

Once the values of Equations 4.78-4.83 have been calculated, they can be combined with the void fraction of the fluidized bed determined by the dynamic mass and energy balances previously determined in Section 4.1 to yield more information regarding the coating growth kinetics. The additional aspects calculated here include: the number of particles in the spray area, the liquid volume deposited in each coating control volume, the remaining liquid volume that travels to the next coating control volume, the coating efficiency, and the probability of being coated in the spray area.

The number of particles in the spray area can be determined once the spray area, fluidized bed void fraction and the particle size distribution are known. First, the particle volume of the control volume is determined by Equation 4.84:

$$V_{part,\,i} = V_{bed,\,i}\left(1 - \varepsilon_{bed,\,i}\right) \tag{4.84}$$

The number of particles in a control volume can then be calculated using the respective particle volume bin percentages from the cumulative particles size distribution. The number of particles in the spray area is then given as Equation 4.85:

$$N_{partISA,\,i} = N_{part,\,total}\left(p_{ISA,\,i}\right) \tag{4.85}$$

The liquid volume deposited in a control volume involves the fluidized bed void fraction, the atomization air-liquid coating void fraction and the spray area CV volume and is shown as Equation 4.86:

$$V_{dep,\,i} = \left(1 - \frac{\varepsilon_{bed,i}}{\varepsilon_{spray,i}}\right)(V_{left})_i \tag{4.86}$$

The liquid volume left that travels to the next control volume is given as Equation 4.87:

$$V_{left,\,i} = V_{sol} - \sum V_{dep,i} \tag{4.87}$$

It should be noted at this point, since the void fraction of the atomization air-liquid coating mixture changes after passing through each control volume because a small amount is deposited on particles within the spray area. Therefore, Equation 4.82 must be recalculated for each coating control volume.

With values tabulated for the liquid volume deposited and the liquid volume left, the coating deposition efficiency of the fluidized bed coating operation can be calculated with Equation 4.88:

$$\text{Efficiency} = \left(1 - \frac{V_{left}}{V_{sol}}\right) \times 100\% \tag{4.88}$$

In addition to the coating efficiency, the probability that a particle is coated in the spray area can also be calculated with knowledge of the liquid volume deposited as shown in Equation 4.89:

$$p_{CISA,\,i} = 1 - \frac{\varepsilon_{bed,\,i}}{\varepsilon_{spray,\,i}} \tag{4.89}$$

4.2.4 Number of Times in the Spray Area and Number of Times Coated in the Spray Area

Now that the probability of being in the spray area and the probability of being coated in the spray area have been calculated by Equations 4.83 and 4.89 respectively, the next step is to

calculate the number of times a particle is in the spray area and the number of times a particle is coated in the spray area for the entire length of time that the liquid coating solution is sprayed.

In order to do this the number of revolutions the particles make inside the fluidized bed must be determined as well, for both the top-spray and Wurster orientation. The number of revolutions the particles make in the top-spray orientation can be determined by dividing the length of time the liquid coating mixture is sprayed by the summation of τ_c values Equation 2.49 in Chapter 2. The magnitude of τ_c will depend on the particle size, so τ_c should be tabulated for the particle size distribution of interest. If a small range is used as the particle size distribution, the values of τ_c will vary slightly, and an average value for τ_c can be used to determine the number of revolutions the particles make.

For the Wurster orientation, the number of revolutions the particles make during the timeframe that the liquid coating mixture is sprayed can be determined by dividing the length of time the liquid coating mixture is sprayed by the summation of Equations 2.50, 2.56, and 2.58 in Chapter 2. Unlike the top-spray orientation, an average value for particle circulation time cannot be used here because the particles travel different distances at different velocities through the Wurster tube and fountain region of the fluidized bed. Therefore, each particle size will have a different number of revolutions associated with it.

The number of times a particle is in the spray area can be determined now using a binomial distribution, shown as Equation 4.90 [22]:

$$P_p = \binom{N}{k} p^k q^{N-k} \tag{4.90}$$

where k is the number of successes within N total trials, p is the probability of success and q is the probability of failure (1-p). The $\binom{N}{k}$ term is the binomial coefficient and is given as Equation 4.91 [22]:

$$\binom{N}{k} = \frac{N!}{k!(N-k)!} \tag{4.91}$$

The function binornd in Matlab is used to generate the number of successful trials (number of times a particle is in the spray area) using the total number of times a particle is in that particular control volume and the probability of success associated with that specific control volume (the probability of being in the spray area). This will generate a distribution of values for each particle used in the simulation.

The number of successes determined for the probability of being in the spray area is in turn used as the value of N in Equations 4.90 and 4.91 for a second round of binomial distribution calculations. In this second round of binomial distribution calculations with the binornd function in Matlab, the probability of being coated in the spray area is used as the probability of success for Equations 4.90 and 4.91. The final result from the binomial distribution calculations is a distribution showing the number of times a particle is in the spray area and subsequently the number of times a particle is coated when it is in the spray area.

4.2.5 Droplet Size, Coating Mass, Volume, and Growth Rate

To this point the time element of the coating growth kinetics has yet to be addressed. The length of time for spraying the liquid coating mixture is established a priori. However, the two calculations in the previous section, the number of times a particle is in the spray area and the number of times a particle is sprayed while in the spray area, only take into account the entire time span that the liquid coating mixture is sprayed. The entire time span the liquid coating mixture is sprayed is divided into twenty equal segments and the same is done with number of times a particle is coated when inside the spray area.

A random sample from the droplet size distribution is then coupled with each successful trial of potential coating deposition while in the spray area. This is done with the randsample

function in Matlab. The rest of the coating growth calculations come directly from this operation, including: droplet volume, coating mass, coating volume, droplet surface area, coating surface area, droplet height, coating height.

The volume of the droplet is given previously as Equation 4.77. The droplet mass is given as Equation 4.92:

$$M_{drop} = \rho_{liq} V_{drop} \tag{4.92}$$

Next, the mass of the coating in the droplet is given by Equation 4.93:

$$M_{coat} = M_{drop} \left(\frac{DM_c}{1 + DM_c} \right) \tag{4.93}$$

The volume of the coating is given by Equation 4.94:

$$V_{coat} = \frac{M_{coat}}{\rho_{coat}} \tag{4.94}$$

Once the coating volume has been calculated, the coating growth rate can then be determined. The coating growth rate is dependent on the number of droplets per particle, the surface area coverage of the droplet on the particle surface, and the height of the droplet on top of the particle surface. The surface area coverage of the droplet on the particle surface is dependent on the contact angle between the liquid droplet and the particle. The height of the droplet, h_{liq}, on the particle surface is dependent on the surface area coverage of the droplet on the particle surface, and therefore the radius of droplet, A_{liq}. Equations 2.80 and 2.81 in Chapter 2 show how A_{liq} and subsequently h_{liq} are determined [23, 24].

A contact angle of 0^o results in complete droplet spreading around the particle surface. Droplet spreading decreases with increasing contact angle up to 180^o. At a contact angle of 180^o, there is no droplet spreading [25]. This has implications on the coating growth rate. For a contact angle of 0^o, the coating growth rate is given by Equation 4.95:

$$CGR = \left[\left(\frac{3}{4\pi}\right)\left(\dot{V}_{coat} + V_{part}\right)\right]^{\frac{1}{3}} - \frac{D_{part}}{2} \quad (4.95)$$

When the contact angle is between 0^o -180^o, the coating growth rate calculation also must incorporate surface area for completeness. Once the droplet hits the particle surface, and spreads accordingly with respect to the contact angle, it will take the shape of a spheroid. The volume and surface area of the newly formed spheroid can be calculated with the A_{liq} and h_{liq} parameters of Equations 2.80 and 2.81 in Chapter 2. Figure 4.14 shows a spheroid and its dimensional parameters.

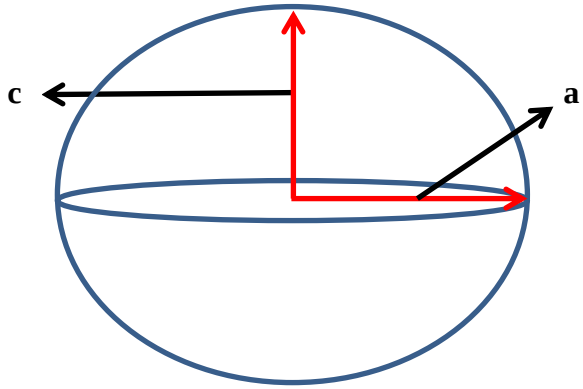

Figure 4.14 Spheroid Geometry

The parameters A_{liq} and h_{liq} replace the parameters a and c respectively in the spheroid geometry. Once the correct orientation is determined, oblate or prolate, the coating growth rate can be determined from surface area calculations.

The coating growth rate for situations where the contact angle is greater than 0^o is given as Equation 4.96:

$$CGR = \left[\frac{\left(SA_{part} + \dot{SA}_{coat}\right)}{4\pi}\right]^{0.5} - \left(\frac{D_{part}}{2}\right) \quad (4.96)$$

4.2.6 Determining the Number of Coating Control Volumes for Wurster Orientation

While the top-spray orientation has the number of control volumes and coating control volumes specified a priori, the number of control volumes and coating control volumes for the Wurster orientation is not. However, the number of coating control volumes for the Wurster orientation can be determined using a small number of coupled mass and energy balances.

The first step for calculating the number of coating control volumes in the Wurster orientation is determining if the liquid coating mixture addition rate can be evaporated without saturating the fluidization gas. Setting the left hand side of Equation 4.66 equal to one and solving for X_{air} will yield the mass ratio of water to air for the fluidizing gas. Because the volumetric flow rate of fluidizing gas is known, the density and mass flow rate of air can be calculated. Multiplying the X_{air} value obtained here by the mass flow rate of air will yield the maximum amount of solvent in the vapor state with air.

Once the saturation capacity of the fluidizing air has been determined and the liquid coating mixture flow rate has been adjusted accordingly, the next step is to determine the evaporation capacity of the fluidizing air. This is done by a coupled mass and energy balance within the Wurster tube in a similar manner to the top-spray orientation. The lowest value for the control volume in which there is no more liquid coating solution present is used as the number of control volumes for the Wurster orientation coating growth kinetics modeling.

4.3 Coating Growth Kinetics Model Boundary Conditions

Since there are two competing mechanisms that occur when a liquid is added to a fluidized bed, proper boundary conditions must be satisfied in order for the coating growth kinetics model to be valid. The boundary conditions for the coating growth kinetics model

revolve around two dimensionless numbers, the dimensionless spray flux more importantly, the viscous Stokes number.

Recall, the dimensionless spray flux is a measure of the binder flux on the powder surface, given as Equation 2.91 in Chapter 2 [26]. As the parameter Ψ_a increases, the likelihood of droplets overlapping increases as well. Hapgood et al. [27] mapped out a nucleation regime classifying a droplet controlled regime for $\Psi_a < 0.1$, an intermediate regimefor $0.1 < \Psi_a < 1$ and a mechanical dispersion controlled regime for $1 < \Psi_a < 10$. High values of the dimensionless spray flux can result in wet quenching of the fluidized bed. Wet quenching occurs when too much liquid is sprayed into the fluidized bed such that the droplet evaporation rate is overcome by the droplet deposition rate. Buoyant and drag forces increase in magnitude such that there is not a sufficient enough pressure drop in the fluidization air to cause the particle bed to fluidize. The result is the liquid saturation causes the entire bed to defluidize [28].

In a tapered fluidized bed the dimensionless spray flux will decrease as the liquid droplets flows away from the nozzle for a couple reasons: the volumetric flow of the droplets will decrease because of droplet-particle collisions in a coating control volume and the spray area increases in each coating control volume as the distance from the spray nozzle increases. High values for the dimensionless spray flux must be avoided in every coating control volume to avoid droplet overlapping and subsequent particle agglomeration after particle-particle collisions. Therefore, the dimensionless spray flux should be kept within the droplet controlled regime where $\Psi_a < 0.1$ for every coating control volume. However, higher values of the dimensionless spray flux may be acceptable if the boundary conditions of the viscous Stokes number are satisfied.

The boundary condition that must be satisfied is the coalescence-rebound postulate of the viscous Stokes number. Recall, the viscous Stokes number, previously defined as the ratio of the kinetic collision energy to the viscous dissipation energy is shown as Equation 2.76 in Chapter 2. The collision velocity U_{col} is shown as Equation 2.77 in Chapter 2 [29].

The viscous Stokes number in Equation 2.79 must be larger than a critical value for particle rebound to occur. Otherwise, if the viscous Stokes number is below the critical value, particle coalescence will occur. The critical value of the viscous Stokes number is given by Equation 2.79 in Chapter 2. Critical viscous Stokes numbers must be calculated for the entire particle size distribution of the fluidized bed coating operation. The viscous Stokes number must be calculated for the entire particle size distribution in every coating control volume as well. The viscous Stokes number must be greater than the critical viscous Stokes number in every coating control volume for the duration of the coating operation in order for particle rebound to be the dominant phenomenon over particle agglomeration.

There are some difficulties with using the viscous Stokes number as a boundary condition for a coating growth kinetic model however. First, there is the question of how much higher in magnitude should the viscous Stokes number be compared to the critical viscous Stokes number. Secondly, there is the difficulty in properly assessing how the coefficient of restitution changes as a function of the liquid coating spray rate. Current trends in research keep the coefficient of restitution constant for the duration of the fluidized bed operation. Thirdly, there is the issue of how much particle agglomeration is acceptable for a particle size distribution. The percentage of particle agglomeration in a batch of product is a quality issue that must be addressed by properly. For this work, the coefficient of restitution used was 0.9. The acceptable percentage of particle agglomeration is no more than 5% of particle size distribution.

4.4 Coating Growth Model Assumptions

There are a few assumptions made in effort to simplify the coating growth kinetics model developed for this work. The assumptions for this particle growth model are the same as those made by Maronga and Wnukowski [30] and Ronsse et al. [31]:

1) All particles have spherical geometries
2) All particles are non-porous
3) Particle growth occurs only by coating deposition (i.e. no agglomeration)
4) No particle breakage occurs during particle-particle collisions or particle-wall collisions
5) There is no particle elutriation from the fluidized bed
6) The particle attrition rate and the spray drying rate are constant
7) The fluidization gas exhibits ideal plug flow behavior
8) Any spray dried material elutriates the bed and cannot therefore act as a seed for coating deposition.

4.5 Calculation Mapping

As shown in Section 4.1 and 4.2 there are several calculations involved in determining the coating growth kinetics of a fluidized bed coating process. Figures 4.15-4.19 show the calculation mapping of all the parameters that go into determining the mass and energy balances of a fluidized bed. The green color designation indicates a starting parameter. The yellow color indicates a constantThe blue color designation indicates an intermediate parameter and a red color designation indicates the final parameter calculation needed for the mass and energy balances. Some parameters that are outputs for one calculation map are inputs for subsequent calculation maps.

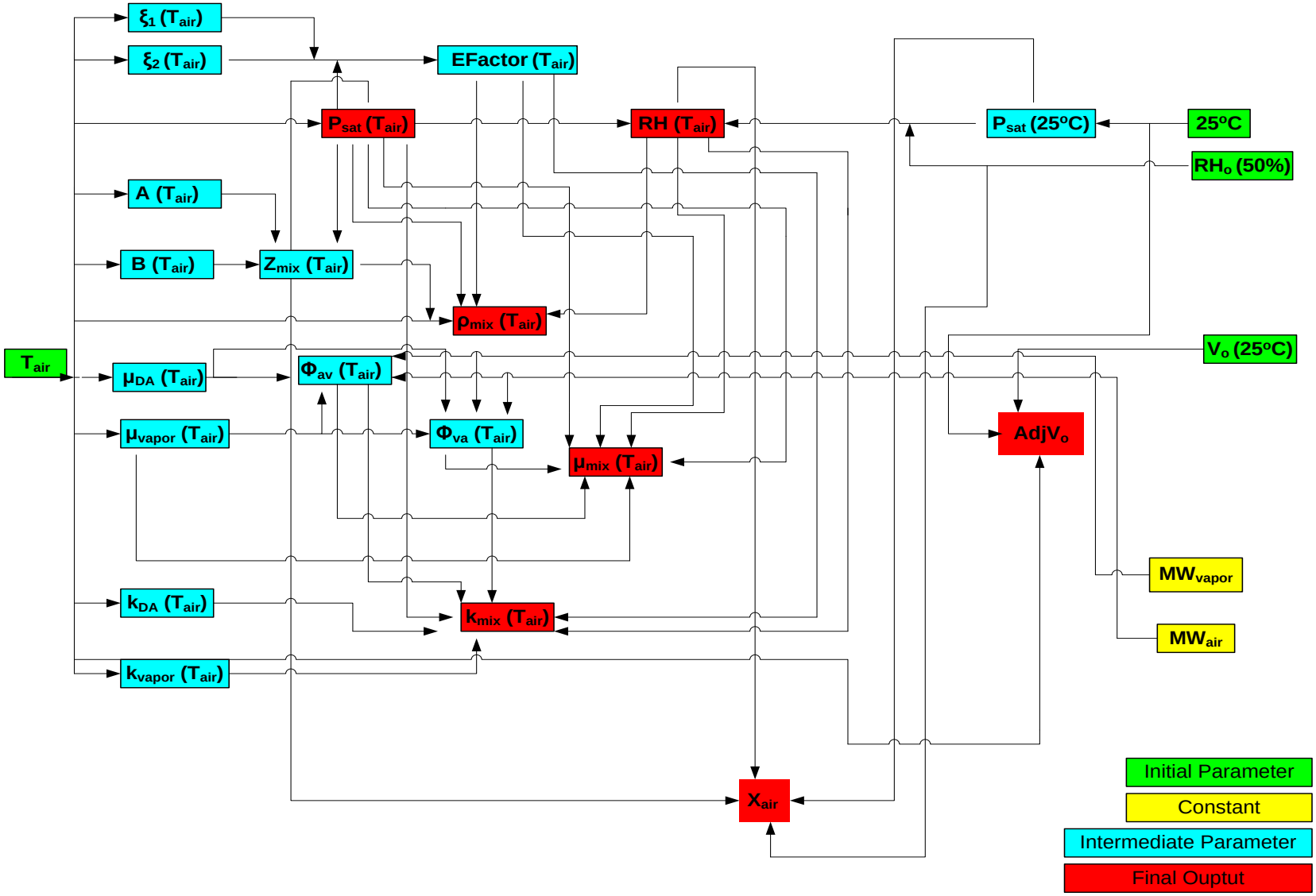

Figure 4.15 Thermo-Physical Properties of Air Calculation Map

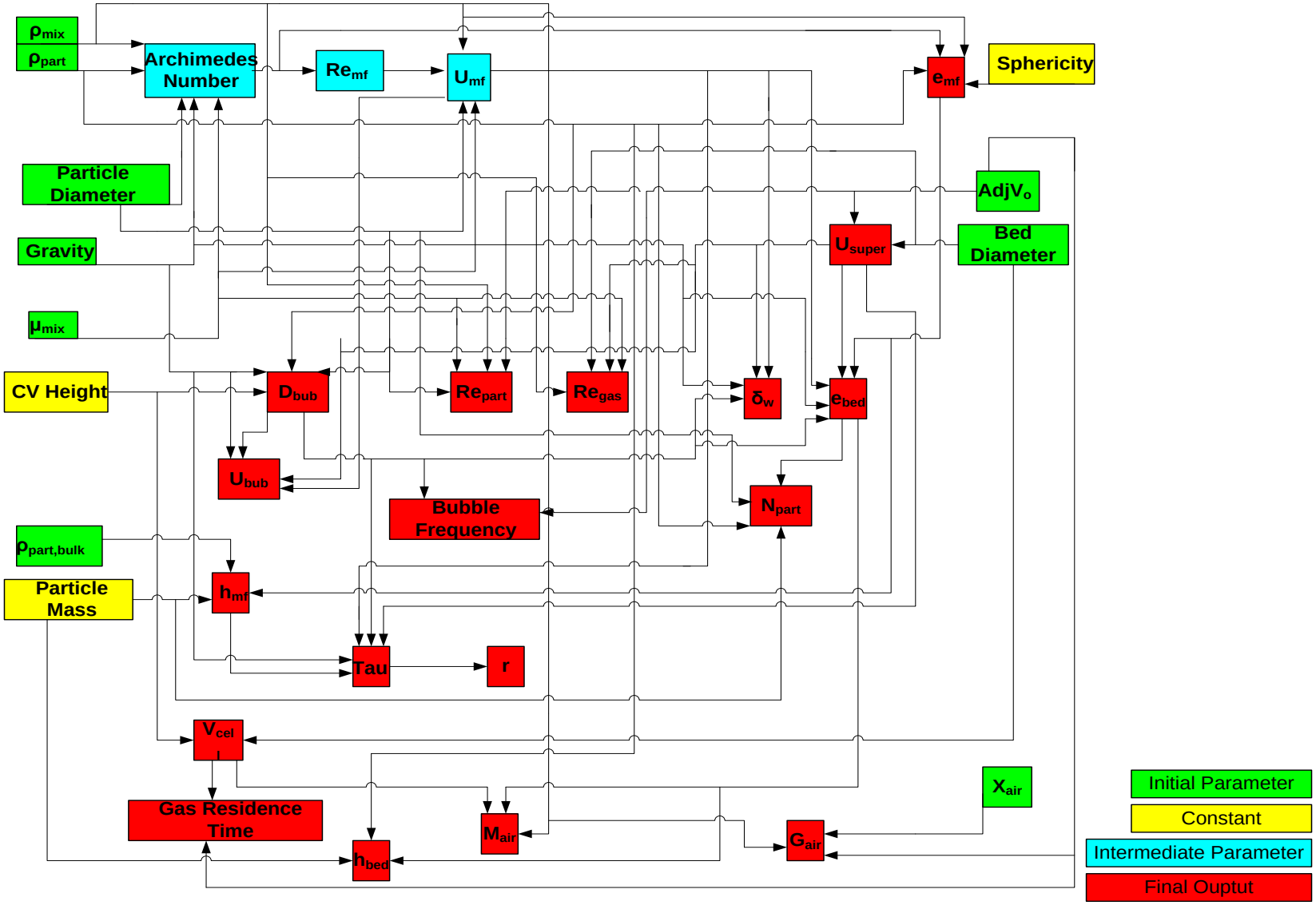

Figure 4.16 Fluidized Bed Hydrodynamics Calculation Map

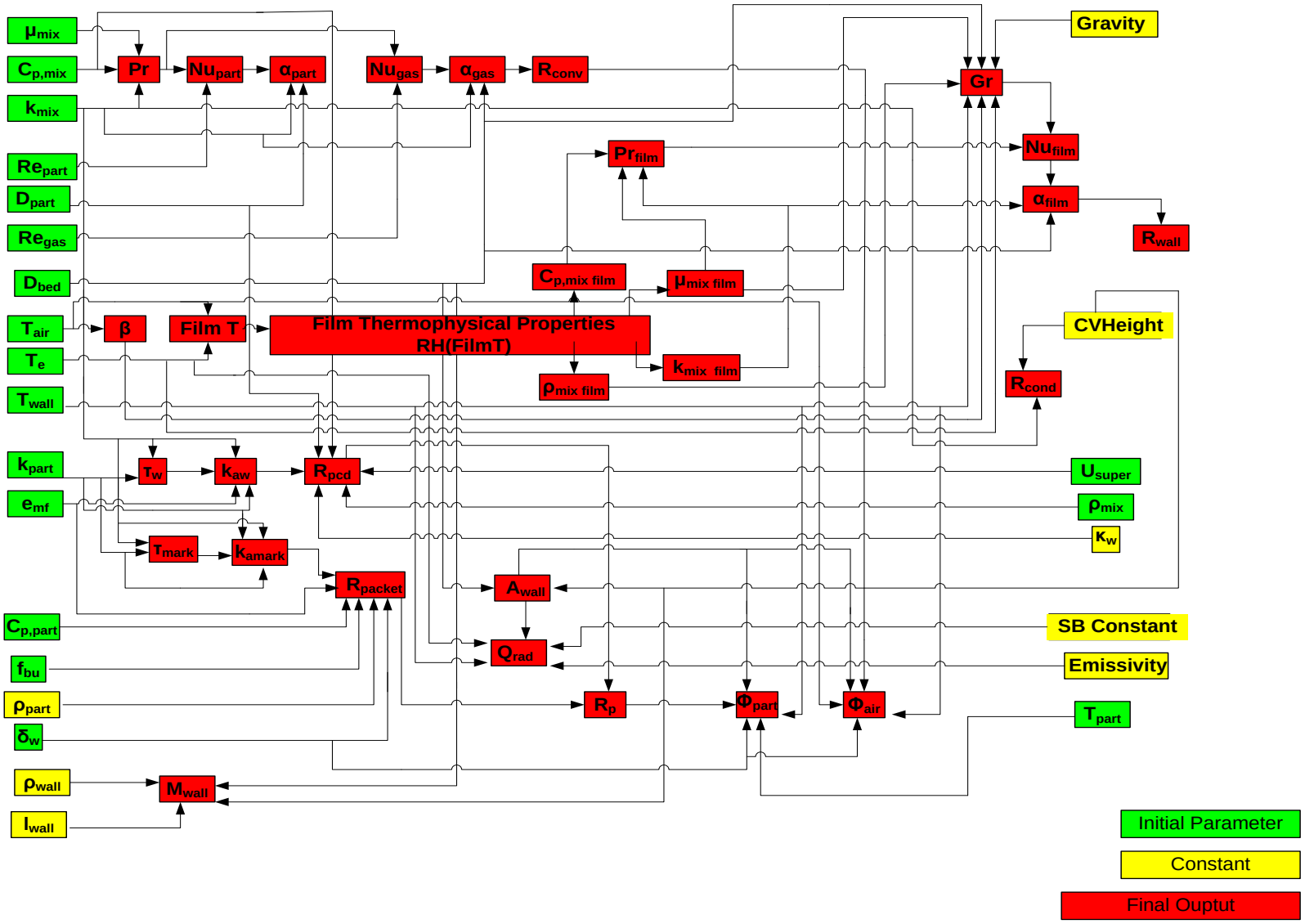

Figure 4.17 Fluidized Bed Heat Transfer Characteristics Calculation Map

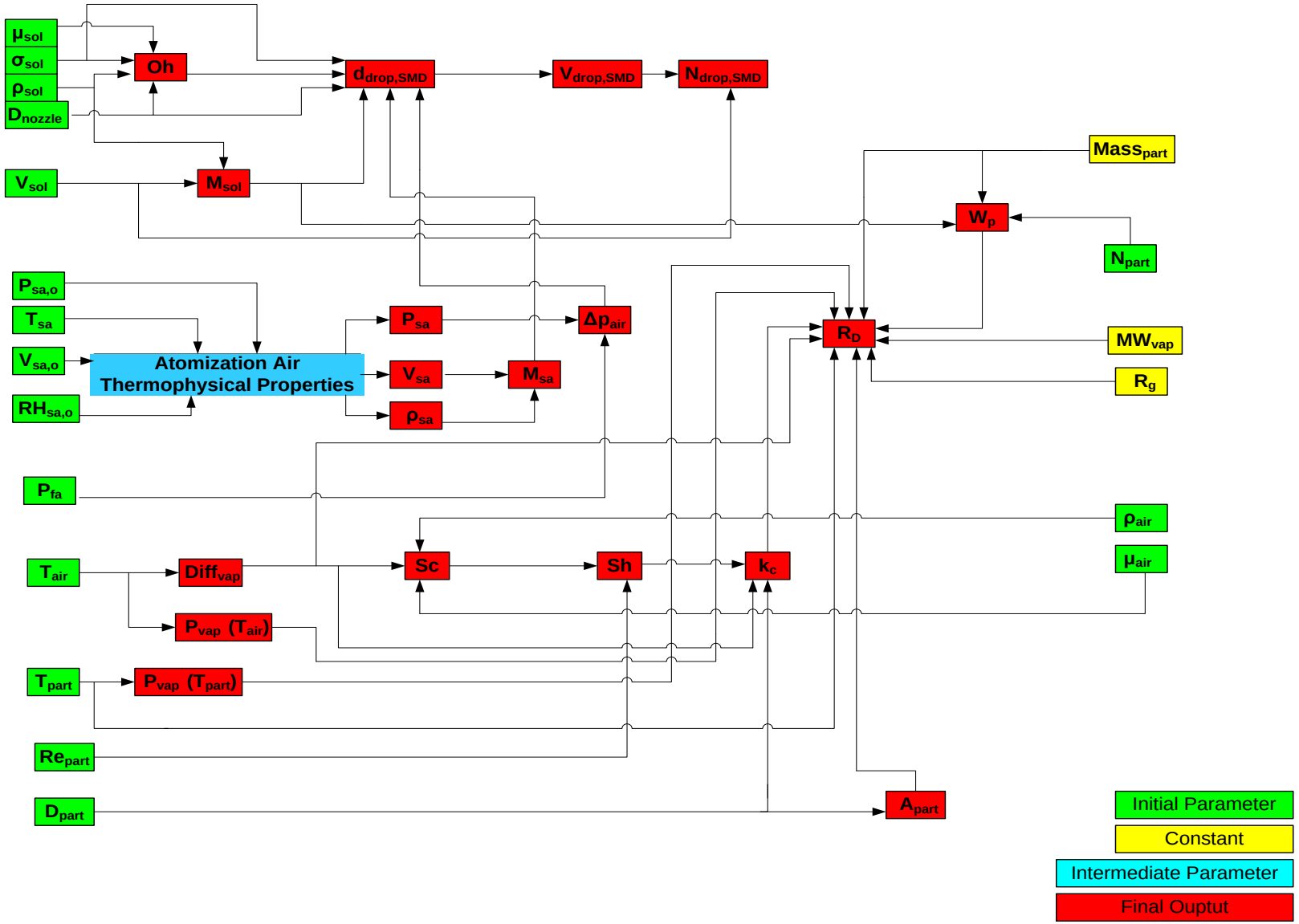

Figure 4.18 Fluidized Bed Mass Transfer Characteristics Calculation Map

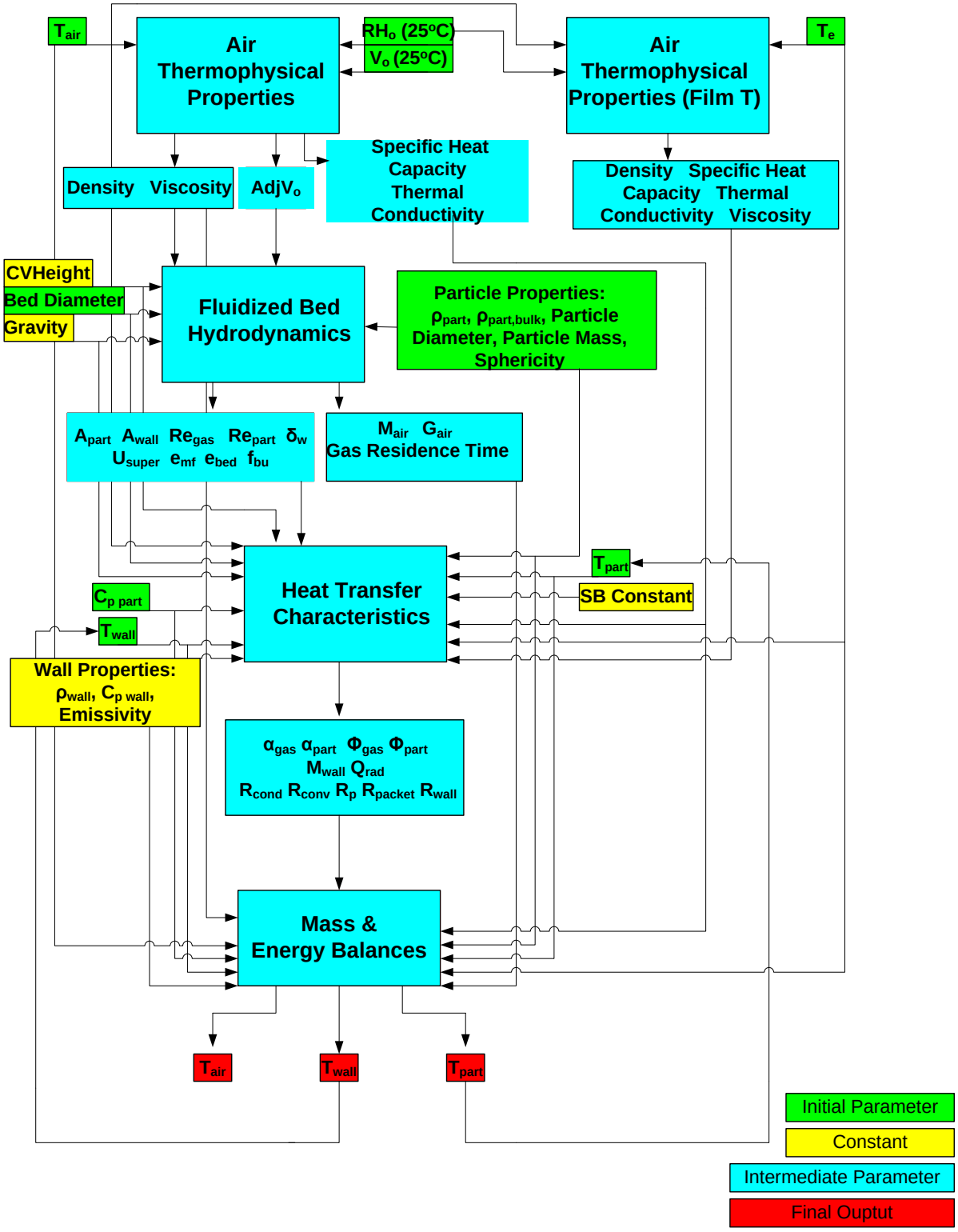

Figure 4.19 Overall Mass and Energy Balance Calculation Map

Table 4.7 shows the number of parameters: initial, intermediate, and final in order to calculate the temperature profiles of the fluidized bed.

Table 4.7 Number of Parameters Needed for Fluidized Bed Mass and Energy Balances

Segment	Initial	Intermediate	Final
Air Thermophyiscal Properties	6	13	7
Fluidized Bed Hydrodynamics	12	3	18
Heat Transfer	26	--	31
Mass Transfer	20	--	19
Overall	19	33	3

The calculation map for thermo-physical properties of the film air is not shown because it is identical to that of Figure 4.13. The sum of all the segments in each column of Table 4.7 do not equal the overall numbers in part because some initial parameters in one segment are also initial parameters needed in other segments as well.

The calculation map for the coating growth model is shown in Figure 4.20.

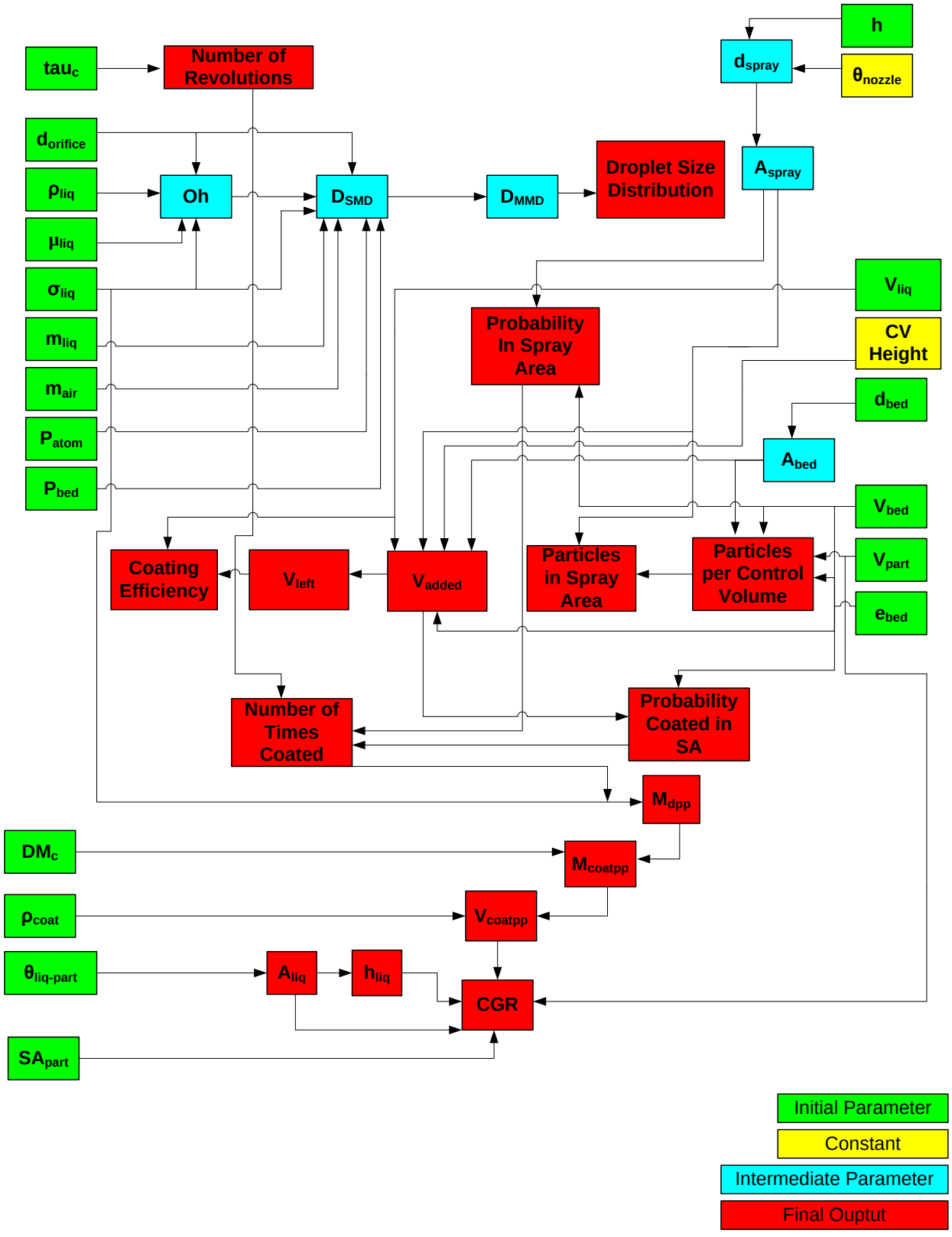

Figure 4.20 Coating Growth Kinetics Calculation Map

4.6 References

[1] Hede, P.D., Bach, P., & Jensen, A.D. (2009). Batch Top-Spray Fluid Bed Coating: Scale Up Insight Using Dynamic Heat and Mass Transfer Modelling, Chemical Engineering Science, 64, 1293-1317.

[2] Ronsse, F.D. (2006) Ph.D. Thesis, Ghent University.

[3] Ronsse, F.D., Pieters, J.G., & Dewettinck, K. (2007) Combined Population Balance and Thermodynamic Modelling of the Batch Top-Spray Fluidized Bed Coating Process Part I: Model Development and Validation, Journal of Food Engineering, 78, 296-307.

[4] Dewettinck, K. (1997) Fluidized Bed Coating in Food Technology: Process and Product Quality, Ph.D. Thesis, University of Ghent.

[5] Tsilingiris, P.T. (2008) Thermophysical and Transport Properties of Humid Air at Temperature Range from 0^{o}C to 100^{o}C. Energy Conversion and Management, 49 (5), 1098-1110.

[6] Wen, C.Y. & Yu, Y.H. (1966) A Generalized Method for Predicting the Minimum Fluidizing Velocity, AIChE Journal, 12(3), 610-612.

[7] Broadhurst, T.E. & Becker, H.A. (1975) Onset of Fluidization and Slugging in Beds of Uniform Particles, AIChE Journal, 21, 238-247.

[8] Darton, R.C., LaNauze, D.C., Davidson, J.F., & Harrison, D (1977) Bubble Growth Due to Coalescence in Fluidized Beds, Transactions Institute Chemical Engineers, 55, 274-280.

[9] Toomey, R.J. & Johnstone, H.F. (1952) Gaseous Fluidization of Solid Particles, Chemical Engineering Progress, 48, 220-226.

[10] Whitaker, S. (1972) Forced Convection Heat Transfer Correlations for Flow in Pipes, Past Flat Plates, Single Cylinders, Single Spheres, and For Flow in Packed Beds and Tube Bundles, AIChE Journal, 18, 361-371.

[11] Land, N.S. (1972) A Compilation of Nondimensional Numbers, NASA SP-274 (NASA Science Technology Information Office, Washington, D.C., USA.)

[12] Kunii, D. & Levenspiel O. (1991) Fluidization Engineering 2^{nd} Edition, Massachusetts: Butterworth-Heinemann.

[13] Holman, J.P. (1976) Heat Transfer 4^{th} Edition, New York: McGraw Hill

[14] Maronga, S.J. & Wnukowski, P. (1998) The Use of Humidity and Temperature Profiles in Optimizing the Size of a Fluidized Bed in a Coating Process, Chemical Engineering and Processing: Process Intensification, 37, 423-432.

[15] Bird, R.B., Stewart, W.E., & Lightfoot, E.N. (2002) Transport Phenomena 2nd Edition, New York: John Wiley & Sons.

[16] Cheng, X. X. & Turton, R. (2000) The Prediction of Variability Occuring in Fluidized Bed Coating Equipment. II. The Role of Nonuniform Particle Coverage as Particles Pass Through the Spray Zone, Pharmaceutical Development and Technology, 5, No. 3, 323-332.

[17] Yang, W. (1977) A Unified Theory on Dilute Phase Pneumatic Transport, Journal of Powder Bulk Solids Technology, 1, 89-95.

[18] Evans, M., Hastings, N., Peacock, B. (2000) Statistical Distributions 3rd Edition, New York: Wiley.

[19] Wazel, P. (1993) Liquid Atomization, International Chemical Engineering, 33, 46-60.

[20] Groom, S., Schaldach, G., Ulmer, M., Wazel, P., Berndt, H. (2004) Adaptation of a New Pneumatic Nebulizer for Sample Introduction in ICP Spectrometry, Journal of Analytical Atomic Spectrometry, 20, 419-447.

[21] T.P.S. Inc. (2012) www.fluidproducts.com. New Jersey.

[22] Papoulis, A. (1984) Probability, Random Variables, and Stochastic Processes, 2nd Ed., New York: MacGraw-Hill.

[23] Clarke, A., Blake, T.D., Carruthers, K., & Woodward, A. (2002) Spreading and Imbibition of Liquid Droplets on Porous Surfaces, Langmuir, 18, 2980-2984.

[24] Thielmann, F., Naderi, M., Ansari, M.A., & Stepanek, F. (2008) The Effect of Primary Particle Surface Energy on Agglomeration Rate in Fluidized Bed Wet Granulation, Powder Technology, 181, 160-168.

[25] Lazghab, M., Saleh, K., Pezron, I., Guigon, P. & Komunjer, L. (2005) Wettability Assessment of Finely Divided Solids, Powder Technology, 157, 79-91.

[26] Lister, J.D., Hapgood, K.P., Michaels, J.N., Sims, A., Roberts, M., Kameneni, S.K., & Hsu, T. (2001) Liquid Distribution in Wet Granulation: Dimensionless Spray Flux, Powder Technology, 114, 32-39.

[27] Hapgood, K.P., Lister, J.D., & Smith, R. (2003) Nucleation Regime Map for Liquid Bound Granule, AIChE Journal, 49, 350-361.

[28] Smith, P.G. & Nienow, A.W. (1983) Particle Growth Mechanisms in Fluidised Bed Granulation – I, Chemical Engineering Science, 38, 1223-1231.

[29] Ennis, B.J., Tardos, G. & Pfeffer R. (1991) A Microlevel-Based Characterization of Granulation Phenomena, Powder Technology, 65, 257-272.

[30] Maronga, S.J. & Wnukowski, P. (1997) Modelling of the Three Domain Fluidized Bed Particulate Coating Process, Chemical Engineering Science, 52, 2915-2925.

[31] Ronsse, F., Pieters, J.G., & Dewettinck, K. (2008) Modelling Side-Effect Spray Drying in Top Spray Fluidized Bed Coating Processes, Journal of Food Engineering, 86, 529-541.

CHAPTER 5

EXPERIMENTAL SYSTEMS AND EXPERIMENTAL DESIGN

This chapter presents all the experimental systems used for fluidized bed coating and post processing. The experimental systems used for this work include a fluidized bed, a micro-calorimeter, and a UV/Vis spectrometer. The purpose of using the microcalorimeter and UV/Vis spectrometer is to determine the coating efficiency for each fluidized bed experiment. To determine particle morphology scanning electron microscopy (SEM) analysis and atomic force microscopy (AFM) analysis was conducted on coated and uncoated particle samples.

5.1 Fluidized Bed Equipment

A Mini-Glatt fluidized bed was purchased from Glatt Air Techniques, Inc. to conduct particle coating experiments. The fluidized bed assembly consists of four separate components held together by adjustable clamps. The plenum, the bottom most component of the fluidized bed, has an opening on the side that functions as a nozzle insert when the Wurster orientation is used. When the top spray orientation is used, the side opening on the plenum is closed with a blind plug, otherwise fluidization gas will leak out of the system.

Figure 5.1 shows the plenum blind plug, otherwise fluidization gas will leak out of the system.

Figure 5.1 Fluidized Bed Plenum

The fluidized bed distributor plate sits on top of the plenum and a silicone o-ring. The next highest component of the fluidized bed is the product bowl. The product bowl is shown in Figure 5.2.

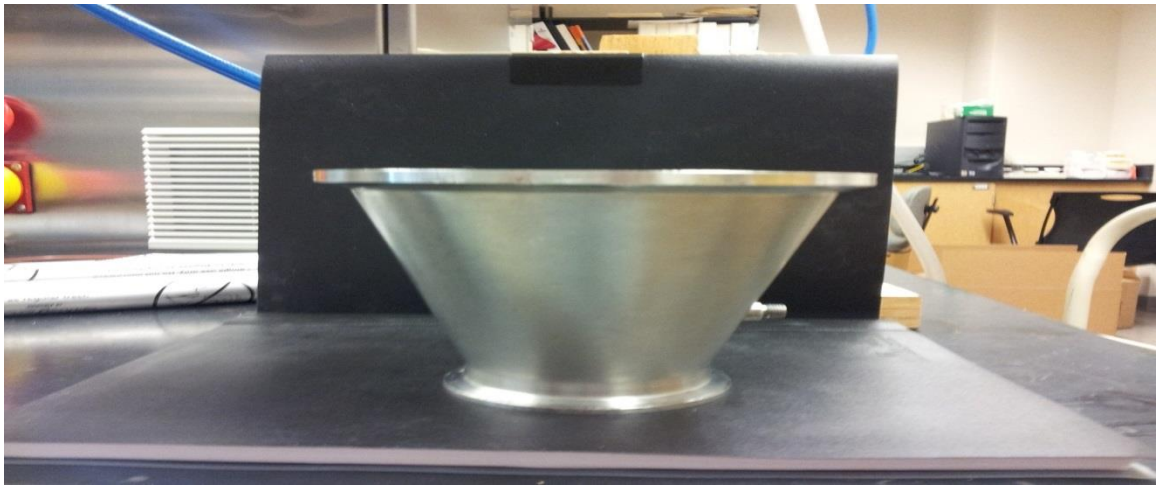

Figure 5.2 Fluidized Bed Product Bowl

The product bowl has a tapered geometry, with a bottom diameter of 6.35 cm and a top diameter of 14.605 cm. The bowl has a height of 11 cm before the diameter becomes constant at

14.605 cm. There is also an opening on the side of the product bowl that is used for measuring the fluidized bed temperature during operation. When the Wurster orientation is used for coating experiments and additional insert is put inside the product bowl. Figure 5.3 shows the additional Wurster insert.

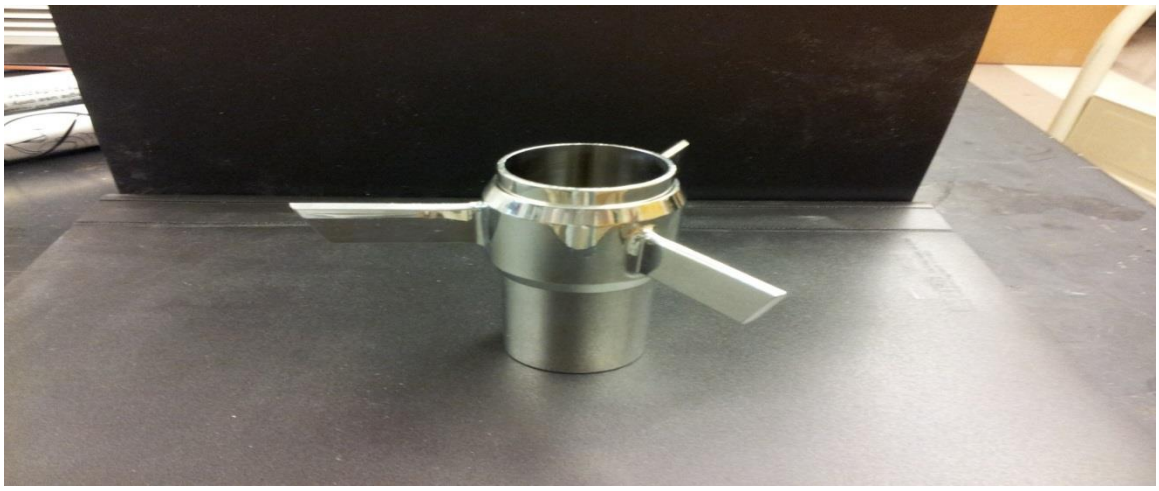

Figure 5.3 Fluidized Bed Wurster Insert

The Wurster insert is 9.5 cm in length with an internal diameter of 3 cm. The insert height from the distributor plate can be adjusted by sliding the three prongs on the insert up or down as desired [1].

Above the product bowl is the fluidized bed expansion chamber. Figure 5.4 shows the fluidized bed expansion chamber. The expansion chamber has an opening on the side that functions as a nozzle insert for the top spray orientation. When the Wurster orientation is used the blind plug shown in Figure 5.2 is inserted in the opening to prevent fluidizing gas from leaking out of the system.

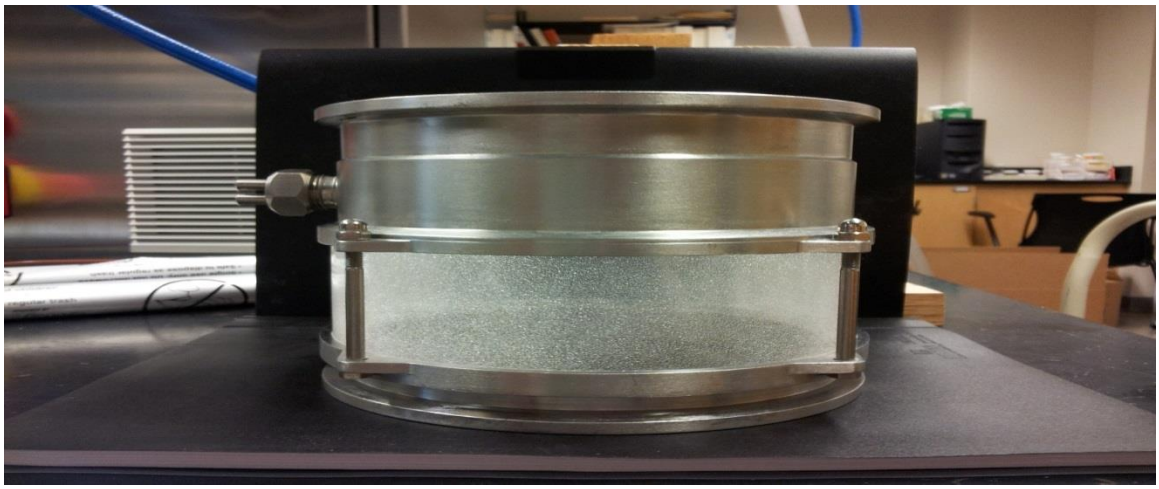

Figure 5.4 Fluidized Bed Expansion Chamber

The expansion chamber has a constant diameter of 14.605 cm and a height of 15.24 cm. Above the fluidized bed expansion chamber, there is the filter house. Figures 5.5 and 5.6 show the filter house with large and small filters respectively. The large filter setup is used in the top spray orientation, while the small filter setup is used for the Wurster setup.

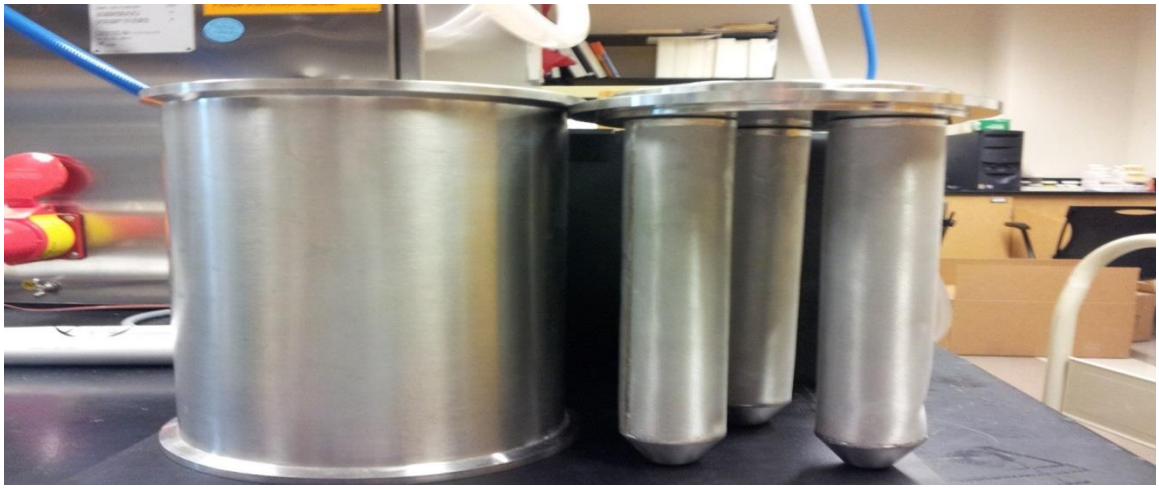

Figure 5.5 Fluidized Bed Filter House with Large Filters

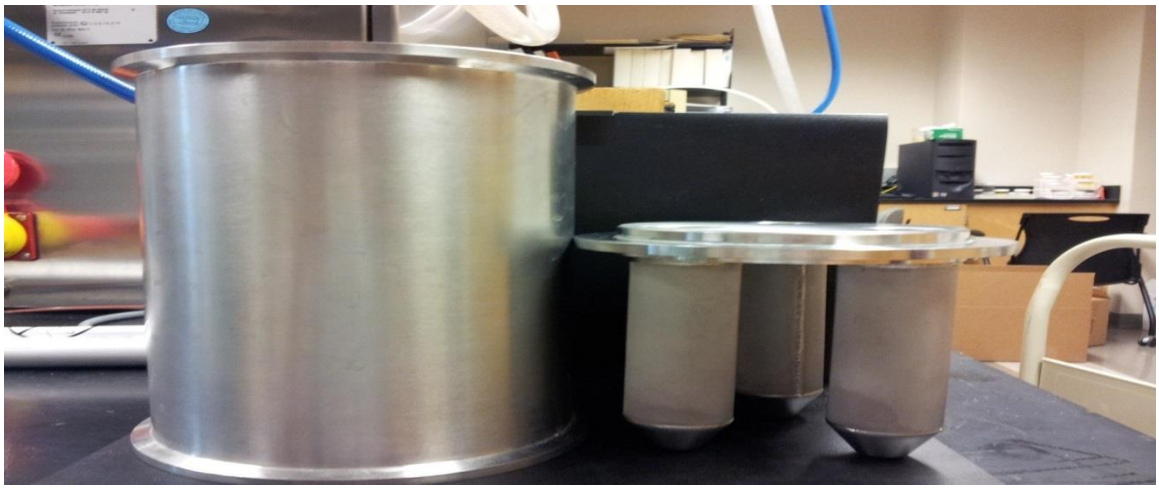

Figure 5.6 Fluidized Bed Filter House with Small Filters

The filter house contains three 4 cm diameter, 22 cm long 10µm filters. Compressed air is cycled through each filter to return any particles that elutriated during the fluidized bed coating experiment at a rate determined by the operator, ranging from 0.5-10 seconds [1].

The nozzle used in the fluidized bed coating experiments is shown in Figure 5.7.

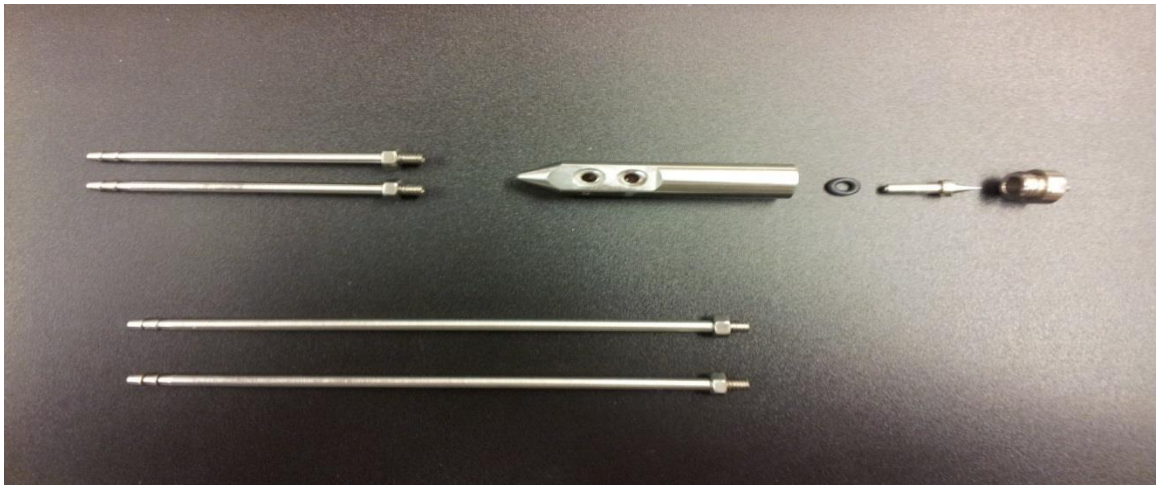

Figure 5.7 Fluidized Bed Nozzle

The nozzle orifice diameter used in the fluidized bed experiments was 0.5 mm. The opening for the gas used to atomize the liquid coating solution is 1 mm. The wall thickness of

the nozzle orifice is 0.002 mm. The orifice openings for the inlets of atomization air and liquid coating solution are 0.8 mm in diameter [1].

The technical cabinet ,shown in Figure 5.8, houses several important components for stream splitting, preheating, and process parameter measurement including: a three-way stream splitter, an air flow meter, a 3 kW air heater, and a 500 mL bomb for filter blowout.

Figure 5.8 Fluidized Bed Technical Cabinet

The flow meter for the fluidizing gas measures the volumetric flow rate of in units of Nm^3hr^{-1}, at intervals of $2m^3hr^{-1}$. The maximum flow rate of air the fluidized bed is rated for is 100 Nm^3hr^{-1} with a maximum pressure of 6 bar. The 3 kW air heater heats the fluidizing air up to a maximum temperature of $80^oC \pm 1^oC$ before it enters the fluidized bed. The maximum pressure for the fluidizing air is 2 bar, while the maximum pressure for the atomizing air is 4 bar. The atomizing air stream is split from the fluidizing air stream prior to any preheating, so the atomization air is always at ambient condition unless it is preheated separately.

The entire fluidized bed is constructed with 316 stainless steel and the view cell in the expansion chamber is acrylic glass. The O-rings between each separate component of the fluidized bed are made of white silicone. The pressure and flow rate of the fluidizing air and

atomization air are controlled by ball valves within the technical cabinet. Vegabar 14 pressure transducers measure the pressure of the fluidizing and atomization air. The variance for the pressure transducers is ± 0.01 bar.To measure the fluidized bed temperature during operation a Testo 925 thermocouple is used [1]. The variance for the thermocouple is ± 0.1^{o}C.

The liquid coating solution is delivered into the nozzle by use of a Series 1000 Model 1B.1003-R/65 peristaltic pump from Petro Gas Ausrüstungen Belin and transparent silicone tubing with and internal diameter 0.5 mm. The pump is a single cage with automatic or manual speed controls. The maximum speed of the pump is 65 rpm (Mini Glatt Operation Manual 2006). The volumetric flow rate of the liquid coating solution is dependent on the density, viscosity, and surface tension of liquid coating solution and the rpm setting of the pump. The rpm setting of the pump is a 0-99 scale, with 99 being 65 rpm. The pump head does not rotate below an rpm setting of 4 [1].

5.2 Fluidized Bed Experimental Setup

The experimental setup for the fluidized bed particle coating experiments is shown in Figure 5.9.

Ambient air is compressed using a 5hp rotary compressor. The compressed air is then sent into an Ingersoll Rand D25IN circulating dryer to remove moisture. The working fluid within the circulating dryer is refrigerant 134a. The dew point of the compressed air as it exits the circulating dryer ranges from 3^{o}C to 10^{o}C depending on the dew point of the incoming air stream. The temperature and relative humidity of the compressed air are measured using a Hanna Instruments HI 9564 thermo hygrometer. The accuracy for the HI 9564 thermo hygrometer is ± 0.1^{o}C and ± 3% RH.

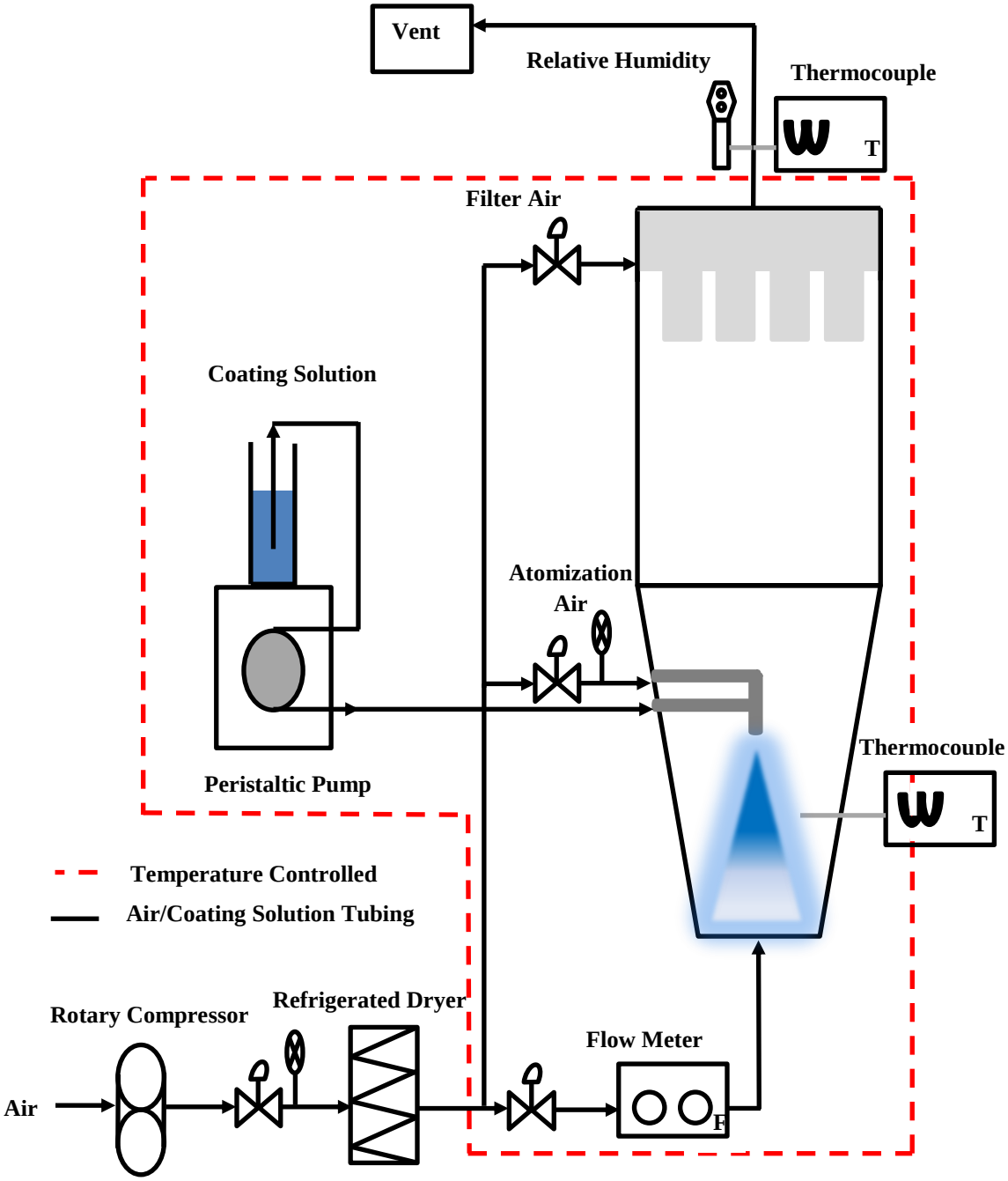

Figure 5.9 Fluidized Bed Experimental Setup

The compressed air then enters the technical cabinet of the fluidized bed equipment where it enters a stream splitter. A small portion of the compressed air travels to a 500 ml bomb to be utilized as filter blow out air. A small portion of the air is used for atomizing the liquid

coating solution. Neither stream of compressed air for filter blow out or atomization is treated any further before use. The remaining portion of air passes through a flow meter in the back of the technical cabinet that is demarked from 6-60 Nm^3hr^{-1}. The demarcations on the flow meter are 2 Nm^3hr^{-1} from 10-60 Nm^3hr^{-1}. After passing through the flow meter, the compressed air is sent through a 3 kW heater which heats the air from ambient temperature to any temperature desired up to 80^oC. The accuracy of the air heater is ± 1^oC. The heater will only function when the air flow is greater than 5 Nm^3hr^{-1}. After preheating, the compressed air is sent into the fluidized bed where heat transfer to the particles, liquid coating solution, the nozzle, and the fluidized bed walls cool it down before it exits the bed and leaves in the exhaust.

5.2.1 Experimental Procedure

Fluidized bed coating experiments were done both with the top spray orientation and the Wurster orientation. The experimental procedure done for both orientations is the same despite the different internal geometries.

The first part of conducting a fluidized bed coating experiment involves sample preparation. Ammonium nitrate (CAS 6484-52-2) was purchased from Fischer Scientific (> 98% purity) and used as is. PEG 3400 (CAS 25322-68-3) was purchased from Sigma Aldrich (99% purity) and used as is. Ammonium nitrate was separated into various particle size distributions by sieving. The particle size ranges typically used for coating experiments are 200-600 µm. PEG 3400 was dissolved in water at various concentrations at room temperature.

Next, proper assembly of the fluidized bed components must be done such that there are no air leaks during operation. First the fluidized bed plenum is attached to the opening extending out from the technical cabinet with an adjustable clamp. An O-ring and a distributor plate are placed on top of the plenum. The meshed porous distributor plate is used for top spray

orientation coating experiments and a segmented distributor plate that has a higher open area for air flow is used for the Wurster orientation. Figure 5.10 shows the top spray and Wurster orientation distributor plates. The orifice openings of the porous plate are 5μm. The plate used for the Wurster orientation has 48 orifices within the Wurster insert with a 2 mm diameter and 72 orifices around the perimeter of the Wurster insert with a 1 mm diameter.

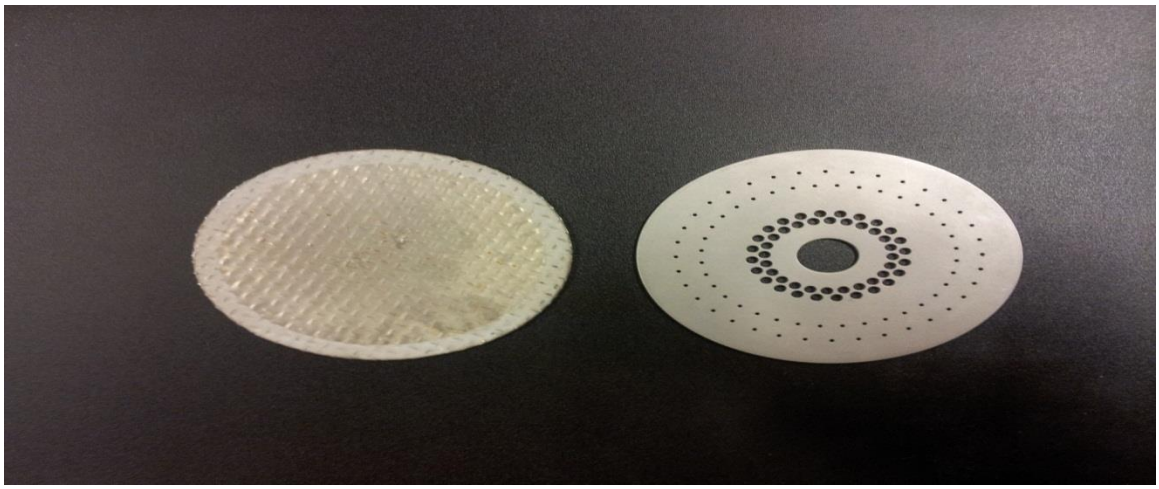

Figure 5.10 Top Spray and Wurster Orientation Distributor Plates

If the top spray orientation is used for the experiment, the side openings are closed off with a blind plug and a k-thermocouple used for measuring the temperature of the inlet fluidizing air. If the Wurster orientation is used, the nozzle is inserted into the plenum such that the nozzle inlets prevent air from leaking out of the side openings.

The fluidized bed product bowl is placed on top of the plenum and secured in place with the adjustable clamp. If the Wurster orientation is used, the Wurster insert is placed inside the product bowl, such that the interior orifices of the Wurster distributor plate are all within the Wurster insert. The Testo 925 thermometer is placed in the side opening of the product bowl to measure the temperature of the fluidized bed during the experiment. The sieved ammonium nitrate is then placed within the product bowl. Figure 5.11 shows the expansion chamber,

product bowl, and plenum in the top spray orientation. Figure 5.12 shows the expansion chamber, product bowl, and plenum in the Wurster orientation.

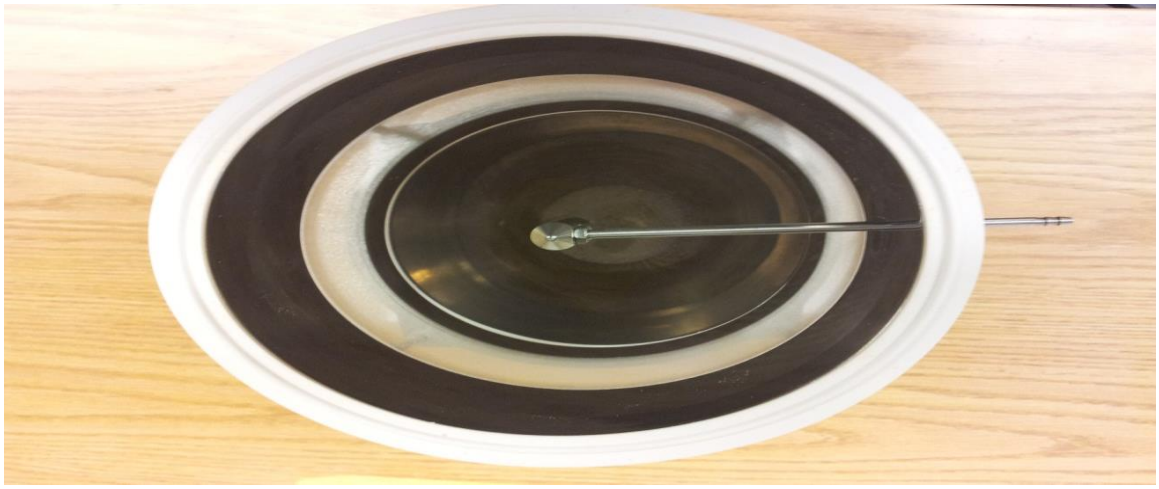

Figure 5.11 Fluidized Bed Assembly Top Spray Orientation

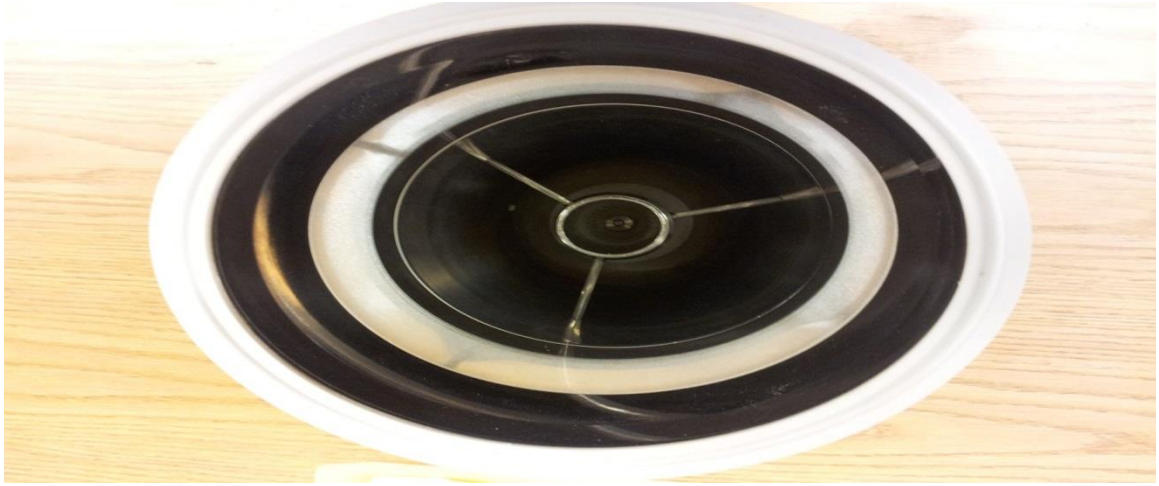

Figure 5.12 Fluidized Bed Assembly Wurster Orientation

Next, the filter house is assembled by attaching each of the three filters into a solid plate that sits atop the filter house. The filter house is then placed at the top of the fluidized bed assembly and secured into place with an adjustable clamp. Finally, the expansion chamber is put secured in between the filter house and the product bowl. In the top spray orientation, the nozzle is inserted into the side openings prior to placement in the fluidized bed assembly. If the Wurster

orientation is used, one opening is closed with a blind plug and a j-thermocouple is placed within the other opening to measure the fluidized bed temperature. The j-thermocouple within the plenum and the expansion chamber are connected to a transducer that reports the temperature with an accuracy of ± 0.1^{o}C.

Once the fluidized bed assembly is properly set up, the atomization air and liquid coating solution must be connected to the nozzle inlets. The atomization air stream is sent from the stream splitter in the technical cabinet to a silicone tube that is situated at the front of the technical cabinet. The silicone tube is then attached to the air inlet of the nozzle. Figure 5.13 shows the fluidized bed completely assembled in the top spray orientation. Figure 5.14 shows the fluidized bed completely assembled in the Wurster orientation.

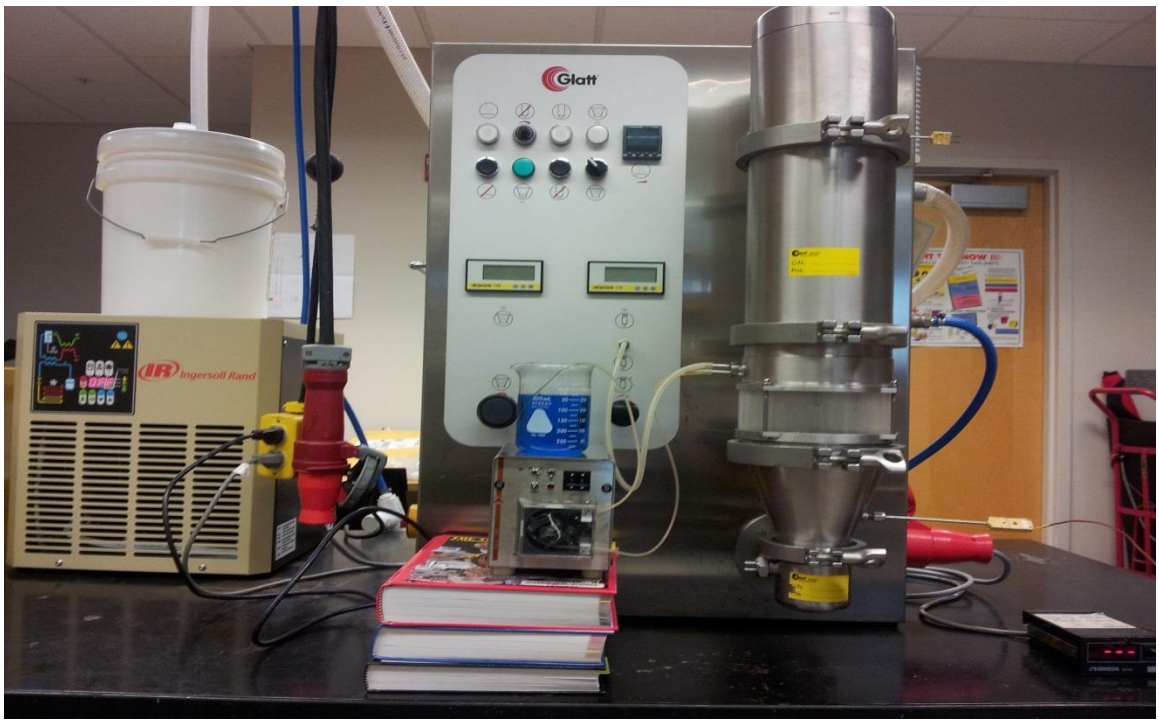

Figure 5.13 Fluidized Bed Completely Assembled in Top Spray Orientation

Figure 5.14 Fluidized Bed Completely Assembled in Wurster Orientation

The liquid coating solution is made by weighing out the desired amount of coating for the experiment in a beaker. The volume of liquid solvent (water) is measured with a 100 ml graduated cylinder and then transferred into the beaker containing the coating material. Five to 10 drops of food coloring dyes are added to the coating-solvent mixtures to aid in visual inspection of coating experiments. The coating material is then dissolved and the dye is distributed within the solvent by stirring. One end of a small silicone tube is put into the beaker containing the coating solution. The other end of the silicone tube is put into the pump head of the peristaltic pump and then attached to the liquid inlet of the nozzle.

When all of the components of the fluidized bed assembly are properly connected and the atomization air and liquid coating solution are attached to the nozzle inlets, a fluidized bed coating experiment can be done. First, the circulating dryer must be turned on to allow for components within to reach normal operating conditions. The circulating dryer should be turned on and allowed to run for at least five minutes prior to the introduction of air. While the circulating dryer is warming up, the fluidized bed electric switch should be turned on to supply power to the heater and pressure transducers within the technical cabinet. The pressure

transducers for the fluidization air and the atomization air will both read zero, meaning there is no flow through the valve.

The first part of a fluidized bed coating experiment is the preheating phase. A ball valve is opened to introduce compressed air into the circulating dryer. After lowering the dew point to between $3^{o}C$ and $10^{o}C$, the air enters the technical cabinet at the right side via a $3/8^{th}$ inch air-line, but bypasses the fluidized bed until a switchover is done. To begin the fluidization process the ball valve on the left should be turned to the right. When the volumetric flow rate is above the minimum amount, a green lamp will come on indicating that the air flow rate is okay. Switch on the heating element by depressing the heating element button on the front control panel of the Mini Glatt. The temperature can be adjusted from $20^{o}C$ to $80^{o}C$ in $1^{o}C$ increments by pressing the up/down buttons on the temperature controller. When the air reaches the desired operating temperature, switch the air flow direction by flipping the turnover valve to allow the air flow to enter the fluidized bed. Turning the left ball valve on the front of the Mini Glatt control panel increases or decreases the fluidization air flow to the desired experimental operating conditions. If the flow is decreased to 6 $Nm^{3}hr^{-1}$ or lower, the air heater will automatically shut off. The inlet air temperature and relative humidity from the circulating dryer are recorded as well as the fluidization air flow rate, pressure, and inlet air temperature. Once the particle bed reaches the desired experiment temperature, the preheating phase of is over and the coating phase commences.

The coating phase begins with turning the smaller ball valve on the right side of the Mini Glatt control panel to the right to introduce air into the nozzle for liquid atomization. Next, the peristaltic pump is turned on at the proper rpm setting to pump the liquid coating solution into the fluidized bed. If the pressure reading for the atomization air is below the pressure reading of

the fluidization air, a back pressure will evolve inside the nozzle and no liquid will flow out. The atomization pressure inside the nozzle must always be higher than the fluidized bed air pressure.

Once all the liquid coating solution has been sprayed, the drying phase of the experiment begins for the top spray orientation. The peristaltic pump can be turned off by turning the switch to the off position. During this phase of the experiment, the air flow rate or heater temperature may be increased to promote faster drying of the particle bed. There is a drying phase with the Wurster orientation, but this orientation promotes instantaneous drying within the Wurster insert such that particles are completely dry upon exiting the top of the Wurster insert.

During each phase of the fluidized bed coating experiment (preheating, coating, and drying) there are several variables recorded at regular intervals: temperature after the circulating dryer, the inlet of the fluidized bed, and the product bowl of the fluidized bed assembly, relative humidity after the circulating air dryer, the level of the liquid coating solution.

Once the coating operation is complete, the fluidization air and atomization air flows are shut off by closing each respective ball valve on the control panel of the Mini Glatt. The heater will shut off automatically once the fluidization flow rate is below 6 Nm^3hr^{-1}. The filter blow out is turned on from the Mini Glatt control panel to return any particles that may have elutriated to the product bowl. After a brief time period for filter blow out, the filter blow out mechanism is turned off from the Mini Glatt control panel. The Ingersoll Rand circulating dryer is shut off by pressing the off button. The ball valve that allows air to flow into the circulating dryer is closed allowing the line to depressurize.

The disassembly of the fluidized bed is done in the following manner, such as to leave the removal of the product bowl for the final step. First, the silicone tubing for the liquid coating solution and atomization air are removed from the nozzle inlet. Then the adjustable clamp

holding the expansion chamber and filter house together is loosened. The adjustable clamp holding the expansion chamber and the product bowl together is loosened. The expansion chamber is then removed from the fluidized bed assembly and set aside for cleaning. Next, the filter house is removed from the fluidized bed assembly by loosening the adjustable clamp at the top of the filter house. The filter house is then set aside for cleaning. Finally, the plenum and product bowl are removed together from the front of the fluidized bed technical cabinet when the adjustable clamp holding the plenum to the front of the technical cabinet is loosened. The coated particles are then poured into a pre-weighed beaker. The coated particles are then weighed and this weight is recorded.

5.2.2 Cleaning

The components of the fluidized bed need to be cleaned properly between experiments to prevent any possible cross contamination between experiments. A thorough cleaning can be done when the fluidized bed is broken down to all of its individual components. Each filter is removed from the filter house and each piece of the nozzle is separated and cleaned individually. Cleaning is done with a comprehensive wash with soap and water. Each component of the fluidized bed assembly is washed: filters, filter house, expansion chamber, product bowl, plenum, air and liquid coating solution nozzle inlets, and the four white silicone O-rings. Each component of the fluidized bed assembly is wiped dry with a towel.

5.2.3 Atomization Air Calibration

There is no flow meter attached to the atomization air stream within the fluidized bed technical cabinet. Therefore a calibration must be done to determine the volumetric flow rate as a function of atomization pressure. A Dwyer 471 Digital Thermo Anemometer was used to determine the velocity of the atomization air. The Dwyer 471 Digital Thermo Anemometer can

register velocities from 0-70 ms^{-1} ± 5% within a temperature range of 15-30^{o}C [2]. The velocity calibration experiments were carried out at ambient temperature (25^{o}C). The atomization air pressure was varied from 0-2 bar and the velocity reported by the Dwyer 471 Digital Thermo Anemometer was recorded. A linear regression was done to relate the atomization pressure to the volumetric flow rate of the atomization air.

5.2.4 Top Spray Distributor Plate Porosity

The distributor plate used in top spray orientation fluidized bed coating experiments is porous, having 5μm orifice openings. Because the orifice openings are small, the distributor plate area open for air flow is much smaller than the total distributor plate area. Plate porosity experiments were done at room temperature (25^{o}C) with known volumetric flow rates of fluidization air. The Dwyer 471 Digital Thermo Anemometer measured velocities at the top of fluidized bed product bowl of different fluidization air flow rates. Velocities were then calculated based on the known volumetric flow rates. The ratio of the measured fluidization air velocity and the calculated fluidization air velocity give the distributor plate porosity.

5.3 Experimental Design for Coating Experiments

The initial fluidized bed experiments conducted were done to determine the operating condition limits for the particle coating mechanism to dominate over the particle agglomeration mechanism. Operating condition variables such as: fluidization air flow rate and temperature, coating solution concentration, temperature, and flow rate, atomization air pressure, flow rate, and temperature, nozzle position and orifice diameter were manipulated to find acceptable ranges for the subsequent particle coating experiments. For the Wurster spray setup the gap between the Wurster tube insert and the nozzle was also investigated.

The maximum fluidization air flow rate used for any top spray experiment was 26 m^3/hr preheated. The rotary compressor supplying the air for experiments had a maximum output of 30 m^3/hr but an allowance was made for atomization air and air for the filters as well. In the case of the Wurster spray setup, the fluidization air flow rate used did not exceed 16 m^3/hr. Otherwise it was observed that particle elutriation from the bed would become a significant issue as the particle fountain developed would be higher than the freeboard available resulting in unwanted adherence to the fluidized bed filters.

The Mini-Glatt has a 3 kW heater that allows for the fluidization air to be heated to 80^{o}C. In the top spray orientation, the air temperature was measured using a thermocouple in the plenum just before the fluidization air passes through the porous distributor plate and was found to be 8-10^{o}C below the operating set point of 80^{o}C. The reason for this loss in temperature is due to convective heat transfer from the air to the tubing in the Mini-Glatt technical cabinet before entering the fluidized bed. Insulation of the tubing in the technical cabinet resulted in air temperature 6-8^{o}C below the set point of 80^{o}C. This difference in temperature from set point to entering the fluidized bed was observed to be constant regardless of the temperature setting, 50-80^{o}C.

Selection of the proper fluidization air temperature for operation is dependent on a few factors including: coating solution flow rate, solvent heat of evaporation, solvent vapor pressure, the droplet size distribution, and the coating thermo-physical properties (melting point, glass transition temperature, etc.). Typically a higher air temperature is preferred (unless heat labile materials are being processed) because it serves as a thrust for fast drying of the particle due to the partial pressure gradient evolved between the fluidization air and the solvent on the particle surface. In addition, the relative humidity of air lowers as temperature increases thus providing

an environment where fast drying will occur. The air temperature set points used for the particle coating experiments ranged between 50-80^{o}C for both the top spray and Wurster setups.

The coating solution properties represent another important set of variables in fluidized bed coating. The coating solution concentration impacts other thermo-physical properties such as density, surface tension, and viscosity. The aforementioned properties then play a role in the droplet size distribution and particle-particle collision coalescence or rebound success. Another area where the coating solution concentration has an impact is the fluidized bed run time. Lower concentrations lead to longer run times because more solvent is needed to introduce the coating into the fluidized bed. The concentrations of PEG in water used for these experiments ranged from 0.02 g/ml H_2O to 0.10 g/ml H_2O so as to keep density and viscosity changes to a minimum without impacting processing time significantly.

One way to overcome the increase in density and viscosity is to increase the temperature of the coating solution prior to introducing it into the fluidized particle bed. Increasing the coating solution temperature can also have the unwanted side effect of evaporating the droplet solvent prior to a droplet-particle collision necessary for particle coating. There are two components to solvent evaporation, heating the solvent up to the wet bulb temperature, and then the phase change from liquid to vapor at the wet bulb temperature. Heating the coating solution can minimize the first component of solvent energy balance such that evaporation can occur immediately upon introduction into the fluidized bed. The coating solution temperatures used for these experiments ranged from 25-60^{o}C.

The coating solution flow rate determination is coupled with the coating solution concentration and the coating solution temperature. Particle agglomeration is undesired when particle coating is the experiment objective, so a coating droplet must dry quickly after impacting

a particle as well as not be able to absorb fully the impact energy evolved during a particle-particle collision anywhere in the fluidized bed. In addition, introducing the coating solution at too high a flow rate can cause wet quenching collapse of the fluidized bed. Coating solution flow rates above 1.5 ml/min at any fluidization air flow rate and temperature combination previously mentioned resulted in a collapse of the fluidized bed.

The coating solution flow rate is controlled by a peristaltic pump. However, because the peristaltic pump produces liquid flow due to the Bernoulli principle and upstream and downstream pressure gradients, producing a pressure inside the tubing for the coating solution that is higher than the fluidized bed pressure can be difficult. In addition, the droplet atomization process can be negatively impacted with low liquid flow rates (i.e. liquid dripping versus droplet formation, or no liquid introduction into fluidized bed at all). For this reason, the peristaltic pump rpm setting is adjusted such that the coating solution flow rate is 1 ml/min. As an additional control for the coating solution flow rate, the peristaltic pump is augmented with a variable on/off timer typically set between 20-40%. For example, a 1 ml/min setting with the peristaltic pump and the variable timer set at 20%, the peristaltic pump would deliver 0.2 ml of the coating solution in one minute, at a rate of 1 ml/min for twelve seconds. This additional control turns the fluidized bed coating process in these experiments into a semi-continuous process, but aids with particle drying, and droplet atomization.

The atomization air pressure and flow rate are directly proportional to each other with the Mini-Glatt setup. The atomization air pressure can be varied from 0 to 4 bar in the Mini-Glatt. Initial experiments showed the flow rate of the atomization air to be 1 liter per minute for every bar of pressure. This relationship was also determined to be independent of the fluidization air flow rate. If the atomization air pressure is lower than the fluidization air pressure no coating

solution will enter the fluidized bed and no particle coating will occur, regardless of spray orientation setup. Another issue encountered with the atomization air pressure involves using a very high atomization air pressure (>1.5 bar, 1.5 liters per minute). In the top spray orientation, a very high atomization air pressure will push particles out of the spray cone and suppress the particle fluidization pattern, lowering coating efficiency. The high atomization air pressure can also lead to wet quenching of the particle fluidization pattern by a couple different mechanisms: a). particles collide with the fluidized bed wall and adhere after the fluidized bed wall has been wetted near the distributor plate due to droplets rebounding from collision with the fluidized bed distributor plate or b). over-wetting of the particles at a lower position in the fluidized bed which will lower the fluidization air temperature, increase the fluidization air humidity, and alter the drying characteristics.

In the Wurster spray orientation, a very high atomization pressure can have unwanted consequences as well. One issue early experiments showed was the high pressure atomization air coupled with the liquid coating solution being sprayed actually increasing the height of the particle fountain after exiting the Wurster tube insert at low fluidization velocities. A subsequent problem of this phenomenon is that the particle surface is still wet when outside the Wurster tube insert, thus increasing the probability of agglomeration during particle-particle collisions or loss of bed mass from the circulation pattern because of adherence to the filters above the freeboard.

In addition to atomization air pressure and flow rate, the impact of the atomization air temperature was also investigated during the initial coating experiments. The atomization fluid density has an important role in determining the characteristic droplet sizes as shown in Chapter 2. The atomization air temperature was varied from room temperature up to the same temperature as the fluidization air for the initial experiments (25-80^{o}C). It was found that the

coating solution was atomized to smaller droplets when using heated air compared room temperature air. However, coating efficiencies were also determined to be slightly lower when the atomization air was heated to the same temperature as the fluidization air, in some cases 10-12% lower. A possible explanation for this trend could be spray drying brought on by convective heat transfer within the spray cone before the droplets reach the particle bed coupled with the reduced relative humidity of the atomization air. In an effort to take advantage of the droplet size reduction due to the temperature impact on the atomization air properties, the atomization air was heated to the fluidized bed temperature before being introduced into the fluidized bed.

The nozzle for the Mini-Glatt can be set in two positions within the fluidized bed in the top spray orientation. The lower position is 13 cm from the distributor plate and the upper position is 18 cm from the distributor plate. The lower nozzle position has the advantage of being closer to the fluidized particle bed helping to minimize any potential spray drying. However, it was observed that even moderate atomization air pressures (1-1.2 bar) depressed the normal particle fluidization pattern. In addition, it was observed that moderate liquid coating solution flow rates (0.5-0.8 ml/min) at the lower nozzle position could lead to wet quenching of the fluidized bed after half to three-fourths of the desired coating amount has been introduced into the fluidized bed.

The upper nozzle position was observed to allow for a little more flexibility with the coating solution flow rate due to having a little more space for the spray cone to develop. A larger spray cone area spreads the liquid solution further across the fluidized bed cross sectional area, thereby increasing the number of particles that get wetted with the coating solution –

preventing particle over-wetting. For the top spray experiments, the upper nozzle position was used because of the observed advantages over the lower nozzle position previously noted.

The nozzle liquid orifice diameter was the last variable examined in the initial coating experiments. Two different nozzle liquid orifices were available for use with the Mini-Glatt, 0.3 mm diameter and 0.5 mm diameter. The larger orifice opening is 1 mm diameter – the atomization air flows between the 1mm opening and the liquid nozzle orifice opening. A higher liquid coating solution velocity can be achieved with the smaller diameter nozzle liquid orifice at a constant flow rate, but a larger atomization air flow rate must be used to achieve an acceptable droplet size distribution because the air has a larger cross sectional area to flow thorough before entering the fluidized bed. For this reason, the 0.5 mm liquid orifice diameter was used for subsequent coating experiments in both the top spray and Wurster orientations.

The gap between the Wurster tube insert and the nozzle was also observed to have an impact in the initial coating experiments. A small gap height (~0.5 cm) decreases the number of particles that can enter the Wurster insert and then get coated. On the other hand, a large gap height allows more particles to enter the Wurster insert, but if the gap height is too large, the spray cone that develops can actually hit the walls of the Wurster insert rather than the particles. Another issue with a gap height that is too large is that the Wurster insert can actually be inside the particle fountain, so unwanted back-mixing may occur leading to agglomeration. Another issue with a gap height that is too large is insufficient drying of the coating solution solvent which may again lead to unwanted agglomeration tendencies. Wet particles may also adhere to the walls of the Wurster insert without having a sufficient opportunity to dry first with a large gap height. This can lead to an altered circulation pattern to the point that the Wurster insert can be totally blocked to particle flow and wet quenching may occur.

One additional variable changed for the initial coating experiments is the particle size range. Different particle size ranges were used in effort to keep fluidized particle characteristics relatively unchanged (i.e. minimum fluidization velocity, circulation rate, convective heat transfer coefficient, etc.) The sieve sizes used were 210 microns, 355 microns, 425 microns, 500 microns, and 600 microns.

As a recap, Table 5.1 shows the operating condition ranges determined from the initial coating experiments.

Table 5.1 Operating Condition Parameter Ranges

Parameter	**Range**
Fluidization Air	
Flow Rate	12-26 m^3/hr Preheated
Temperature	50-80^oC Set Point
Particle Size	
Range	210-600 microns
Coating Solution	
Concentration	0.02 – 0.10 g/ml Solvent
Flow Rate	< 1.5 ml/min
Temperature	25-55^oC
Timer Setting On	20-40%
Atomization Air	
Flow Rate/Pressure	400-600 ml/min 0.4-0.6 bar
Temperature	25-60^oC
Nozzle	
Orifice Diameter	0.5 mm
Position (Top Spray Only)	Upper
Wurster Tube	
Gap Height	1-2 cm

5.4 Microcalorimeter Experiments

An OmniCal Technologies Super CRC 20-305-2.4 Isothermal Mixing and Reaction Calorimeter is used to determine the coating efficiency of the fluidized bed coating experiments. The heat evolved or absorbed by a mixture is measured by the calorimeter via a differential scanning calorimetric technique. The calorimeter can be used to determine the specific heat

capacity at constant pressure of a solid, liquid, or a mixture. The calorimeter can also be used to quantify energy evolved or absorbed during phase changes as well. The calorimeter has two sample ports that hold 16 ml vessels, one port is for the sample of interest and the other port is used as a reference point. The Super CRC 20-305-2.4 calorimeter has an accuracy of 1% of the measured heat. The calorimeter can operate from -50 to 200^{o}C when attached to a circulating heater. In the absence of a circulating heater the calorimeter has an internal heater that can go up to 100^{o}C [4].

5.4.1 Heat of Mixing Experiments

To determine the amount of PEG 3400 coating present in a sample, heat of mixing experiments were conducted with known concentrations of PEG 3400 and ammonium nitrate. Experiments consisted of 0.5g of solid sample ranging in concentration from pure ammonium nitrate to pure PEG 3400 and two milliliters of water. The heat of mixing of each concentration was recorded. A regression of the heat of mixing data gives a calibration for determining the concentration of coated samples. Figure 5.15 shows a heat flow profile of an endothermic system that is expected for this system. The red line in Figure 5.15 represents the heat flow (mW) while the blue line represents the temperature of the calorimeter (constant).

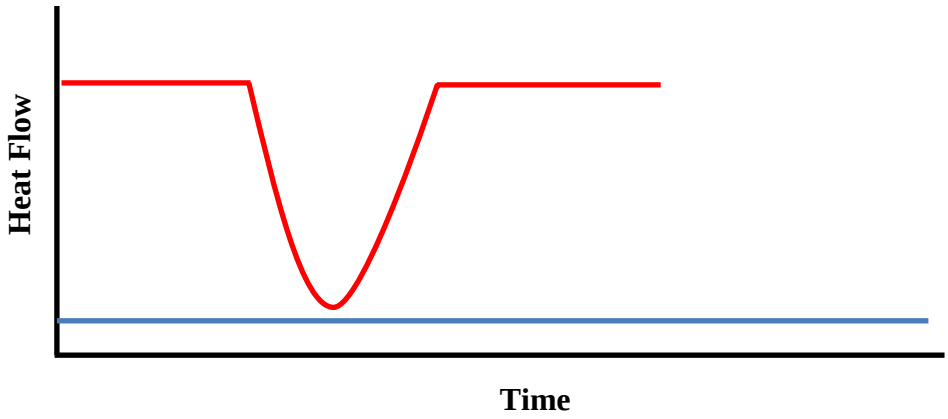

Figure 5.15 Typical Heat Profile Evolved From Endothermic Heat of Mixing Calorimetry Experiments

Integration of the curve represented by the red line will yield the heat of mixing for the sample. The heat of mixing of the coated sample will then be compared with a calibration curve for PEG 3400-ammonium nitrate-water heat of mixing to determine the ratio of PEG 3400 to ammonium nitrate in the coated sample. An overall mass balance with the ratio of PEG 3400 to ammonium nitrate will then yield the coating efficiency of the fluidized bed experiment.

5.4.2 Heat of Mixing Calibration Experiments for Determining Coated Sample Concentration

Among the properties calorimetry can measure is the heat of mixing of a multi-component solution, in this case water-ammonium nitrate-PEG 3400. The heat of mixing is directly proportional to the amount of ammonium nitrate and PEG 3400 present as well as the ratio of ammonium nitrate to PEG 3400. A calibration was carried out at room temperature with 2 ml of water and 0.5g of solid sample, repeated twice and value averaged. The solid concentration was varied from 100% ammonium nitrate to 100% PEG 3400 at 10% intervals. A regression was then done relating the heat of mixing to the concentration of ammonium nitrate and PEG 3400. The heats of mixing were determined for the unknown samples and the concentrations of ammonium nitrate and PEG 3400 were determined. With the concentration of ammonium nitrate and PEG 3400 now known, the coating efficiency of the fluidized bed experiment is then calculated. Table 5.2 shows the heat of mixing for the calibration runs, while Figure 5.16 shows the calibration run heats of mixing and the error for the heat of mixing regression.

Table 5.2 Heat of Mixing Values for Calibration Runs

Concentration		**ΔH_{mix} [J]**
AN	**PEG 3400**	
0%	100%	21.25
5%	95%	22.29
10%	90%	27.31
20%	80%	40.08

Table 5.2 Continued

30%	70%	53.22
40%	60%	65.82
50%	50%	78.08
60%	40%	88.15
70%	30%	100.29
80%	20%	113.20
90%	10%	121.67
95%	5%	128.32
100%	0%	142.64

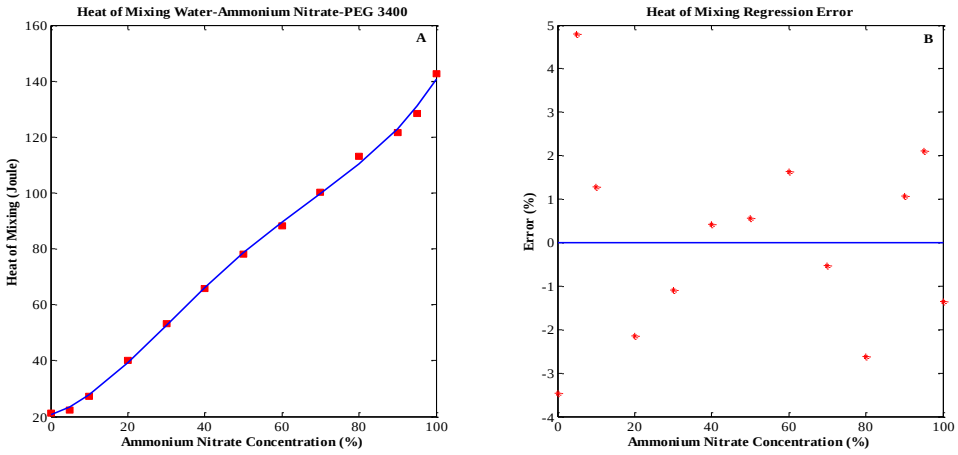

Figure 5.16 A) Calibration Run Heats of Mixing at Room Temperature B) Regression Error

The regressed equation for the heat of mixing of the water-ammonium nitrate- PEG 3400 system at room temperature is shown as Equation 5.1:

$$\Delta H_{mix} = 315.702C^4 - 620.310C^3 + 386.430C^2 + 38.327C + 20.553 \qquad (5.1)$$

where C represents the ammonium nitrate concentration as a percentage. The R^2 value of Equation 5.1 is 0.9987 with an adjusted R^2 value of 0.9978.

As subplot B of Figure 5.1 shows, the largest error of the regressed equation for the heat of mixing at room temperature is about 5%, but this occurs at concentrations that are almost pure PEG 3400. The error at high concentrations of ammonium nitrate is about ±2%.

5.5 UV/Vis Absorbance

An Ocean Optics USB4000 Fiber Optic Spectrometer (200-2000 nm) was used as another method of determining the coating efficiency of the fluidized bed experiments. Compounds absorb light at various wavelengths depending on several factors including: different types of atoms and atomic bonds present, concentration, crystalline structure, temperature, pressure and phase. When solids are dissolved in a solvent, the amount of light absorbed by the mixture can be related to the solid concentration within the solvent by the Beer-Lambert law.

To determine the amount of coating present in a coated sample of ammonium nitrate, concentration experiments were done using the USB4000 Fiber Optic Spectrometer. First the Deuterium-Tungsten UV lamp is turned on to warm up for at least two hours prior to use [5]. While the UV lamp is warming up, a small amount of coated sample (< 0.5 g) is weighed on the Adventurer Pro Balance and the weight is recorded (± 0.001 g) [3]. A known volume of water is measured with a graduated cylinder (~100 ml), recorded, and poured into a beaker. The coated sample is then transferred to the beaker containing the known volume of water. The beaker is briefly stirred to aid in particle dissolution and allowed to sit for the remainder of the UV lamp warm up time (~ 2 hours).

After the UV lamp has had sufficient time to warm up, the visible light halogen lamp is turned on. The dissolved sample solution is quickly stirred to ensure no concentration gradients exist. A small amount of the dissolved sample solution is poured into a cuvette (5-10 ml). A T300-RT-UV-Vis Transmission Dip Probe is then immersed into the cuvette. A previously determined calibration curve profile is then used by the Ocean Optics computer software to determine and report the concentration of the ammonium nitrate in the water (g ml^{-1}). The amount of coating present with the sample is then calculated from an overall mass balance.

5.5.1 UV/Vis Concentration Calibration

In order to determine the unknown amount of coating present in a sample, a concentration calibration curve must be constructed. The first attempt at constructing a concentration calibration curve involved dissolving PEG 3400 in water. However, there was no significant light absorbance within the 200-2000 nm range for PEG 3400 dissolved in water at room temperature. A second attempt at constructing a concentration calibration curve was done with ammonium nitrate dissolved in water. Four concentrations were used to generate the calibration curve. The highest concentration was made by dissolving a half gram of ammonium nitrate in 100 ml of water (5000 ppm). An absorbance measurement was taken and recorded. The 5000 ppm ammonium nitrate solution was subsequently diluted by 50% three times to concentrations of 2500 ppm, 1250 ppm and 625 ppm respectively. Absorbance measurements were taken and recorded at each concentration. A linear regression was done with the four points and pure water to produce the calibration curve.

5.5.2 UV/Vis Calibration Experiments for Determining Coated Sample Concentration

UV/Vis spectroscopy was the other analytical technique used to determine the amount of PEG 3400 present in the solid sample after the fluidized bed experiments. Light absorbance displays a linear relationship with concentration according to the Beer-Lambert law, so unknown sample concentrations can be determined after a calibration is done with known concentrations.

The UV/Vis absorbance of water-PEG 3400 solutions was examined first. However, a 50,000 ppm aqueous PEG 3400 solution barely registered with an absorbance measurement of 0.1 around the 220 nm, with a very narrow range of absorbance, ~220-230 nm. Next, the UV/Vis absorbance of ammonium nitrate-water solutions was examined. A 25,000 ppm aqueous ammonium nitrate solution was found to an absorbance measurement around 0.85 using a

wavelength range from 233-300 nm. Since the aqueous ammonium nitrate solution absorbs light at a higher magnitude and absorbs the light above the spectrum that the aqueous PEG 3400 solution absorbs, the aqueous ammonium nitrate solution was used for calibration. Absorbance measurements were taken for aqueous ammonium nitrate solutions and are shown in Table 5.3.

Table 5.3 Aqueous Ammonium Nitrate Solution Absorbance

Concentration [ppm]	**Absorbance**
0	0
1000	0.208253
2000	0.260970
3000	0.290750
4000	0.319694
5000	0.332910
6250	0.356872
12500	0.539317
25000	0.844957

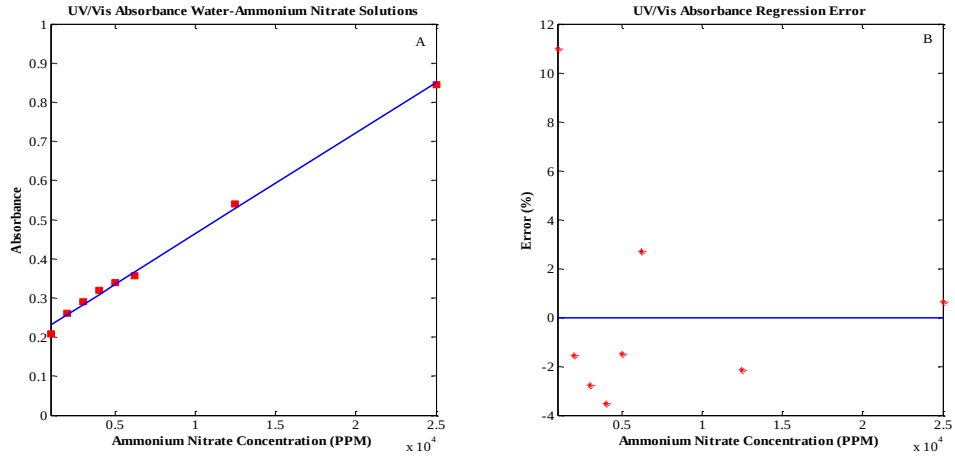

Figure 5.17 A) UV/Vis Absorbance of Aqueous Ammonium Nitrate Solutions B) UV/Vis Regression Error

Figure 5.17 shows the UV/Vis absorbance of aqueous ammonium nitrate solutions and the error associated with the regressed equation for absorbance. The regressed equation for the UV/Vis absorbance of aqueous ammonium nitrate solutions is shown as Equation 5.2:

$$\text{Absorbance} = 0.02583C + 0.2053 \quad (5.2)$$

where C is the ammonium nitrate concentration in ppm divided by 1000. The R^2 value associated with Equation 5.2 is 0.9966.

As subplot B of Figure 5.17 shows the highest error for the regressed absorbance equation is at very low concentrations of ammonium nitrate, around 11%. Therefore, during the concentration determination of the unknown solutions, this low concentration region of ammonium nitrate was avoided by increasing the sample size used.

5.6 Particle Morphology Examination

The particle morphology was examined for before and after experiments with SEM and AFM analysis. SEM analysis is a non-destructive and analysis technique that provides a magnified visualization of the particle sample. AFM analysis is an analysis technique that proves quantification in all three dimensions (length, width, and height) of the particle sample topology.

SEM analysis of the coated and uncoated samples was carried out with a Hitachi S-800 scanning electron microscope. The Hitachi S-800 has a magnification capability of up to 300,000x the actual size. The SEM image is generated by collecting electrons that scatter after hitting the sample surface when an electron beam scans the sample surface. SEM analysis shows many characteristics of the particle sample including: the presence of cracks, particle asperities, particle shape, grain boundaries, particle porosity, and coating imperfections such as pinholes or exposed core particle surfaces. Sample preparation for SEM analysis involves placing a small amount of sample (~1 mg) onto double-sided tape that is then placed in a vacuum environment (10^{-5}-10^{-6} torr). A thin layer (<100 nm) of conductive material (gold) was applied to the samples prior to SEM analysis to avoid a charge buildup and yield high resolution images.

In addition to SEM analysis particle morphology characteristics will also be ascertained from AFM analysis. For this work an Atomic Force Microscope Dimension 3000 was used. AFM analysis involves scanning over the particle sample surface with a very small (~30 μm) cantilever to obtain the particle surface roughness magnitude (for both coated and uncoated samples) with nanometer resolution. Sample preparation for this analysis involves using double-sided tape to hold the loose particles in place on a sample holder. The sample size analyzed for AFM analysis is 100 μm by 100 μm.

5.7 References

[1] Mini Glatt Operation Manual (2006) Berlin, Germany.

[2] Dwyer 471 Digital Thermo Anemometer Bulletin H-17-A (2009) Michigan City, IN.

[3] Ohaus Adventurer Pro Balances Instruction Manual (2011) Parsippany, NJ.

[4] OmniCal Technologies Isothermal Mixing and Reaction Calorimeter Model SuperCRC 20-305-2.4 (2006) Houston, TX.

[5] Ocean Optics USB4000 Fiber Optic Spectrometer Installation and Operation Manual (2006) Dunedin, FL.

CHAPTER 6

EXPERIMENTAL RESULTS AND DISCUSSION

The purpose of this chapter is to present the experimental results of this study and provide a discussion as well. The results and subsequent discussion presented will cover several areas including: the experimental conditions, the experiment coating efficiency, and the particle morphology including SEM analysis and AFM surface roughness quantification.

6.1 Top Spray and Wurster Spray Coating Experiments

The fluidized bed experiment conditions used in this work are shown in Tables 6.1 and 6.2. The run time in the last column of Table 6.1 signifies the length of time the coating solution is added into the fluidized bed semi-continuously as noted in the previous section. An additional drying time of ten minutes followed every top spray coating experiment.

Table 6.1 Top Spray Coating Experiment Conditions

Run	BS	PS	Fluidization Air			Atomization Air			Coating Solution			TS	RT
			FR	T	RH	FR	T	RH	Conc	FR	T		
1	50	210-300	20	80	50	400	25	50	0.05	1	25	20	500
2	75	355-425	22	80	55	500	25	55	0.10	1	25	35	214
3	50	210-300	26	50	50	450	40	50	0.02	1.2	40	40	521
4	100	210-300	26	80	37.5	600	25	37.5	0.075	1.2	25	40	278
5	75	300-355	20	70	37.5	550	55	37.5	0.05	1	50	35	429
6	50	210-300	24	60	37.5	400	40	37.5	0.05	1	35	25	400
7	75	300-355	26	75	43.75	450	55	43.75	0.10	1	50	35	214
8	75	210-300	24	80	35	600	25	35	0.075	1.2	25	40	209
9	100	210-300	22	70	30	400	60	30	0.05	1	50	30	667
10	50	300-355	26	70	40	500	25	40	0.08	1	25	20	313
11	100	355-425	26	70	50	600	50	50	0.10	1	25	25	400
12	50	355-425	26	80	30	550	55	30	0.05	1	55	20	500
13	75	425-500	24	50	43.75	600	25	43.75	0.08	1.2	25	30	261
14	50	425-500	24	70	37.5	550	50	37.5	0.075	1	50	40	167
15	75	355-425	22	60	30	400	40	30	0.05	1	40	35	429

BS: Batch Size [g] PS: Particle Size Range [microns] FR: Flow Rate [m^3/hr for Fluidization Air ml/min for Atomization Air] T: Temperature Set Point [^oC] RH: Preheated Relative Humidity [%] Conc: Coating Solution Concentration [g Coating/ml Solvent] TS: Timer Setting [%] RT: Run Time [minutes]

Table 6.2 Wurster Spray Coating Experiment Conditions

Run	BS	PS	Fluidization Air			Atomization Air			Coating Solution			GH
			FR	T	RH	FR	T	RH	Conc	FR	T	
1	50	210-300	12	50	50	400	25	50	0.05	1	25	1
2	100	210-300	16	80	50	500	60	50	0.10	1.2	60	1
3	100	300-355	14	70	50	400	50	50	0.075	1.2	50	2
4	75	210-300	16	80	37.5	550	55	37.5	0.08	1	40	2
5	75	355-425	12	70	40	450	25	40	0.05	1	25	1.5
6	100	300-355	16	80	37.5	400	25	37.5	0.10	1.2	25	2
7	50	425-500	14	60	43.75	600	45	43.75	0.05	1	30	2
8	100	210-300	14	70	37.5	500	50	37.5	0.075	1	50	2
9	100	300-355	16	70	30	550	30	30	0.10	1.2	30	1.5
10	50	425-500	16	70	50	400	25	50	0.05	1	25	2
11	100	210-300	14	60	40	600	50	40	0.075	1	40	1.5
12	100	500-600	16	80	37.5	500	35	37.5	0.05	1.2	35	2
13	75	210-300	16	50	30	450	45	30	0.08	1	45	1
14	100	355-425	14	80	30	500	40	30	0.10	1.2	40	2
15	100	300-355	16	80	30	400	25	30	0.05	1.2	25	2

BS: Batch Size [g] PS: Particle Size Range [microns] FR: Flow Rate [m^3/hr for Fluidization Air ml/min for Atomization Air] T: Temperature Set Point [^oC] RH: Preheated Relative Humidity [%] Conc: Coating Solution Concentration [g Coating/ml Solvent] GH: Gap Height [cm]

The coating efficiency of each experiment, which will be discussed in the next section, was subsequently determined by two methods outlined in Chapter 5, heat of mixing from isothermal calorimetry and UV/Vis absorbance from UV/Vis spectroscopy.

6.2 Coating Efficiency

Coating efficiency is the ratio of coating material present with the core particles to the total amount of coating material added to the fluidized bed. Coating efficiency is a parameter that can be used to determine if fluidized bed operating conditions are within acceptable tolerances. Visual inspection of the particles after coating experiments as well as Fourier transform infrared spectroscopy (FTIR) can only provide qualitative descriptions of the fluidized bed coating efficiency. To determine the coating efficiency of the top spray and Wurster spray experiments outlined in Table 6.1 and 6.2, calorimetry and UV/Vis spectroscopy were used.

Colored dyes were added to the clear coating solutions of PEG 3400-water for a couple reasons: to establish visual confirmation that the particles are being coated and also to establish visual confirmation that the liquid atomization characteristics are not resulting in overspray hitting and adhering to the fluidized bed walls. Figure 6.1 shows ammonium nitrate before and after a coating experiment. The hue of the orange dye is same everywhere visually indicating that the coating has been distributed evenly.

Figure 6.1 Ammonium Nitrate Particles Before (Left) and After (Right) a Coating Experiment

As an additional means for confirmation that the ammonium nitrate surface had been altered by the addition of PEG 3400, samples were subjected to FTIR. FTIR analysis was carried out on pure ammonium nitrate, pure PEG 3400, and PEG 3400 coated ammonium nitrate with a Bio-Rad Excalibur FTS 3000. Figures 6.2-6.4 show the FTIR spectrums of pure ammonium nitrate, pure PEG 3400, and a PEG 3400 coated ammonium nitrate sample. The spectrum in Figure 6.4 displays characteristic peaks displayed in Figure 6.2 and 6.3 indicating the presence of PEG 3400 in the sample. The peak around 2380 cm^{-1} in Figures 6.2 and 6.3 is the C=O double bond signal from CO_2 as analysis with the Bio-Rad Excalibur FTS 3000 is in open air rather than enclosed.

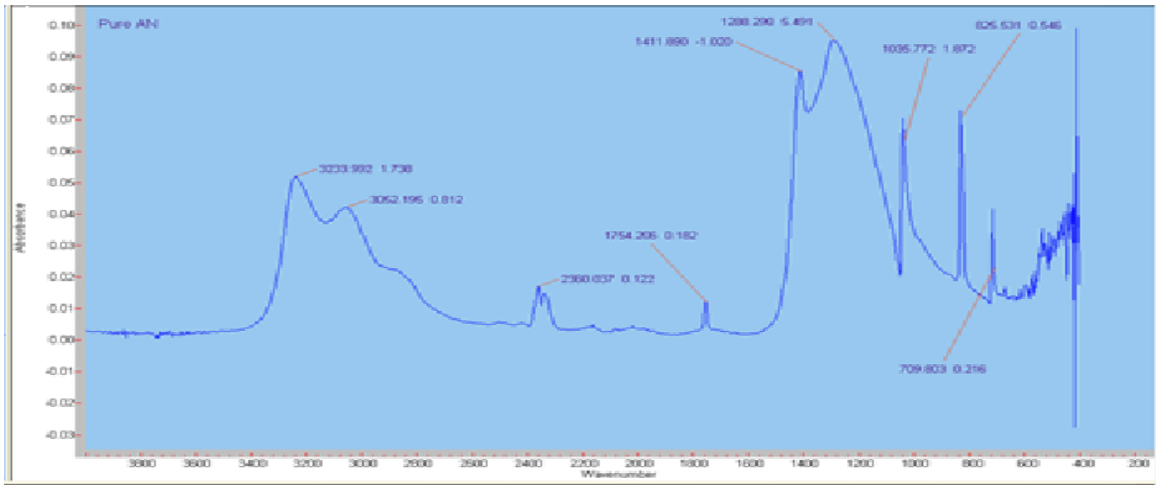

Figure 6.2 Pure Ammonium Nitrate FTIR Spectrum

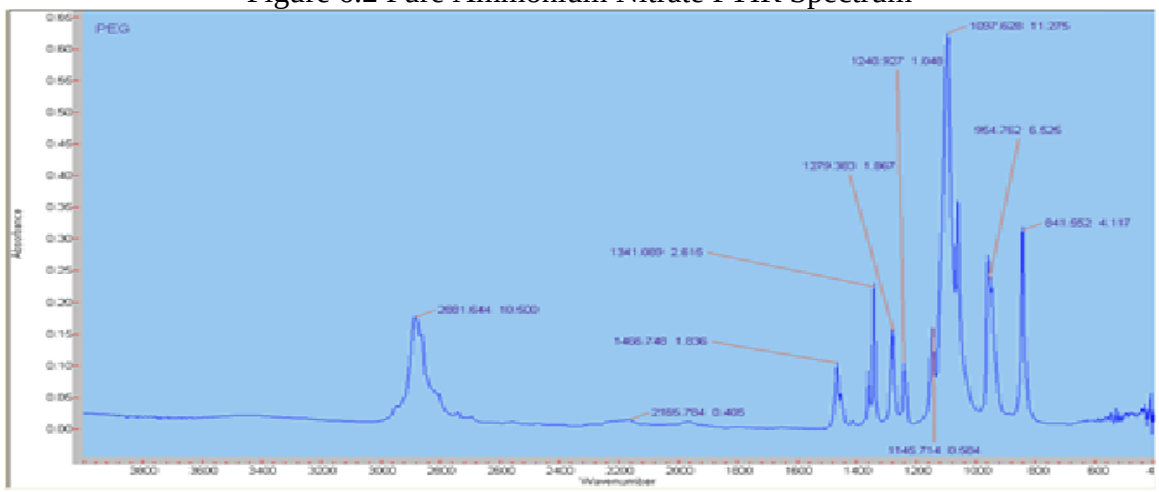

Figure 6.3 Pure PEG 3400 FTIR Spectrum

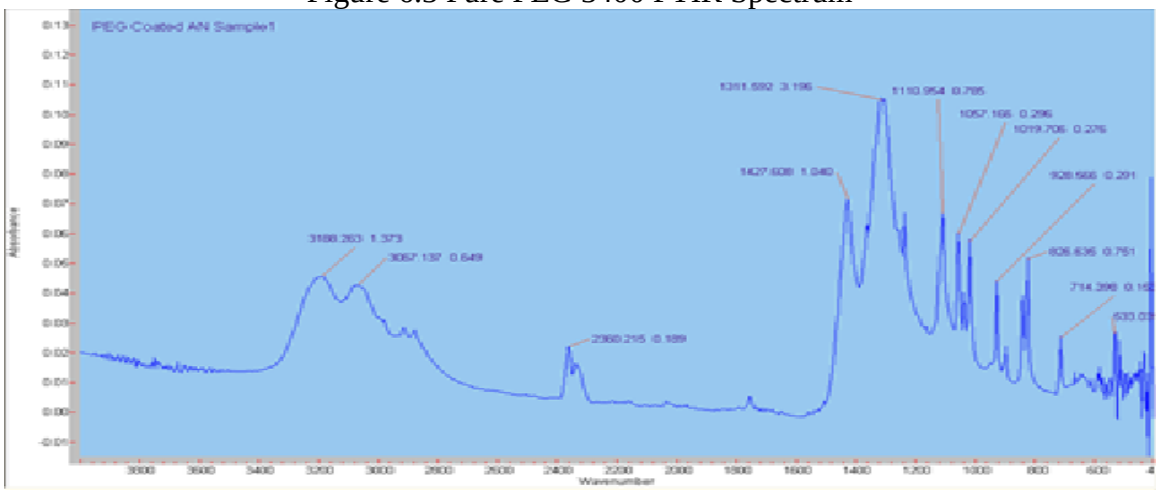

Figure 6.4 PEG 3400 Coated Ammonium Nitrate FTIR Spectrum

While FTIR analysis qualitatively proves that the fluidized bed coating operations were successful, calorimetry and UV/Vis absorbance experiments were done to determine the extent

to which the fluidized bed coating operations were successful. Calibrations for the heat of mixing of the ammonium nitrate-PEG 3400-water system with a constant amount of water can be found in Chapter 5. Calibrations for the UV/Vis absorbance of ammonium nitrate-water system can be found in Chapter 5. With the calorimetry and UV/Vis absorbance calibrations complete, the coating efficiency was tabulated for the top spray and Wurster spray runs and Tables 6.3 and 6.4 show their respective results.

Table 6.3 Top Spray Coating Efficiency

Run	ΔH_{mix} [J]	UV/Vis Absorbance	Coating Efficiency [%]		
			Calorimetry	UV/Vis	Absolute Difference
1	129.45	0.32670	62.4	63.8	1.4
2	128.75	0.32598	67.7	70.2	2.5
3	129.98	0.32730	58.2	58.6	0.4
4	128.43	0.32606	70.4	69.5	0.9
5	129.31	0.32665	63.5	64.3	1.2
6	130.22	0.32765	56.4	55.6	0.8
7	129.65	0.32696	60.8	61.6	0.8
8	129.28	0.32665	63.8	64.3	0.5
9	128.57	0.32582	69.4	71.6	2.2
10	130.08	0.32727	57.4	58.9	1.5
11	128.70	0.32637	68.3	66.7	1.6
12	129.90	0.32736	58.9	58.1	0.8
13	129.07	0.32684	65.4	62.6	2.8
14	129.61	0.32714	61.1	60.0	1.1
15	128.62	0.32572	69.0	72.5	3.5

Table 6.4 Wurster Spray Coating Efficiency

Run	ΔH_{mix} [J]	UV/Vis Absorbance	Coating Efficiency [%]		
			Calorimetry	UV/Vis	Absolute Difference
1	131.69	0.32911	45.0	43.1	1.9
2	132.32	0.32928	40.1	41.7	1.6
3	131.32	0.32842	47.8	49.0	1.2
4	131.90	0.32924	43.4	42.0	1.4
5	130.42	0.32805	54.8	52.1	2.7
6	130.20	0.32772	56.5	55.0	1.5
7	130.33	0.32753	55.5	56.6	1.1
8	132.52	0.32963	38.6	38.8	0.2

Table 6.4 Continued

9	130.18	0.32749	56.7	57.0	0.3
10	128.70	0.32731	57.4	58.5	1.1
11	132.36	0.32972	39.9	38.0	1.9
12	128.32	0.32547	71.3	74.7	3.4
13	133.60	0.33058	30.4	30.9	0.5
14	129.49	0.32721	62.1	59.4	2.7
15	130.29	0.32790	55.8	53.4	2.4

As Tables 6.3 and 6.4 show, there is a small absolute difference between the experimental coating efficiencies determined by calorimetry and UV/Vis absorbance. Calorimetry experiments show the top spray coating experiment efficiencies to range from 56-70%. Whereas, UV/Vis absorbance experiments show the coating experiment efficiencies to vary from 56-73% for the top spray experiments. In with Wurster orientation, calorimetry results show the experimental coating efficiencies to range from 30-71%, while UV/Vis absorbance results show the experimental coating efficiencies to range from 31-75%. This small difference can be attributed to a few potential sources: variation in the amount of coating present in the samples selected for analysis, a non-uniform concentration for UV/Vis absorbance, or selection of the wrong beginning and endpoints for curve integration of calorimetry experiments.

In addition to coating efficiency, another aspect of the fluidized bed coating experiments that is very important is the particle morphology, both before experiment and after the experiment. Particle morphology will be discussed in the next section.

6.3 Particle Morphology

Knowledge of the particle morphology is an important aspect of fluidized bed particle coating as the final particle surface properties (porosity, surface area, surface roughness, etc.) directly impact performance characteristics (e.g. dissolution rate, heat and mass transfer rate, reaction rate). For this work, uncoated ammonium nitrate particles and PEG 3400 coated

ammonium nitrate particles were photographed with a Hitachi S-800 scanning electron microscope (SEM) at various magnifications: 40x, 70x, 300x, and 1000x. Figures 6.5-6.8 show the SEM pictures of each respective magnification listed above of the coated and uncoated ammonium nitrate particles.

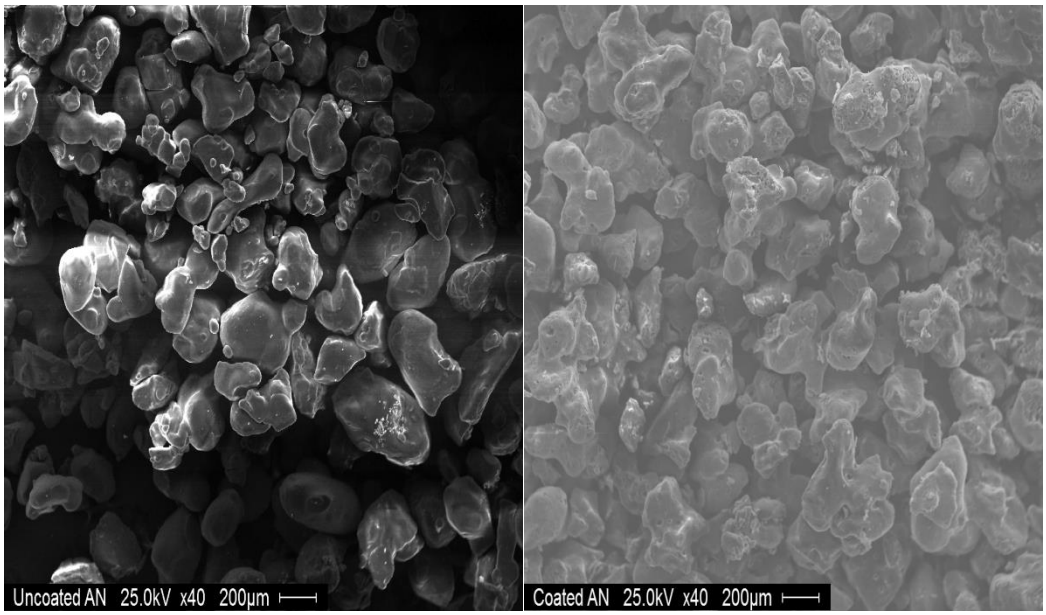

Figure 6.5 SEM Pictures 40x Magnification A) Uncoated Ammonium Nitrate Particles B) PEG 3400 Coated Ammonium Nitrate Particles

As Figure 6.5 shows, the uncoated and coated ammonium nitrate particles are not completely spherical. In addition, the PEG 3400 coating (Picture B) is not completely smooth as small pinholes are visible on several particles at the surface.

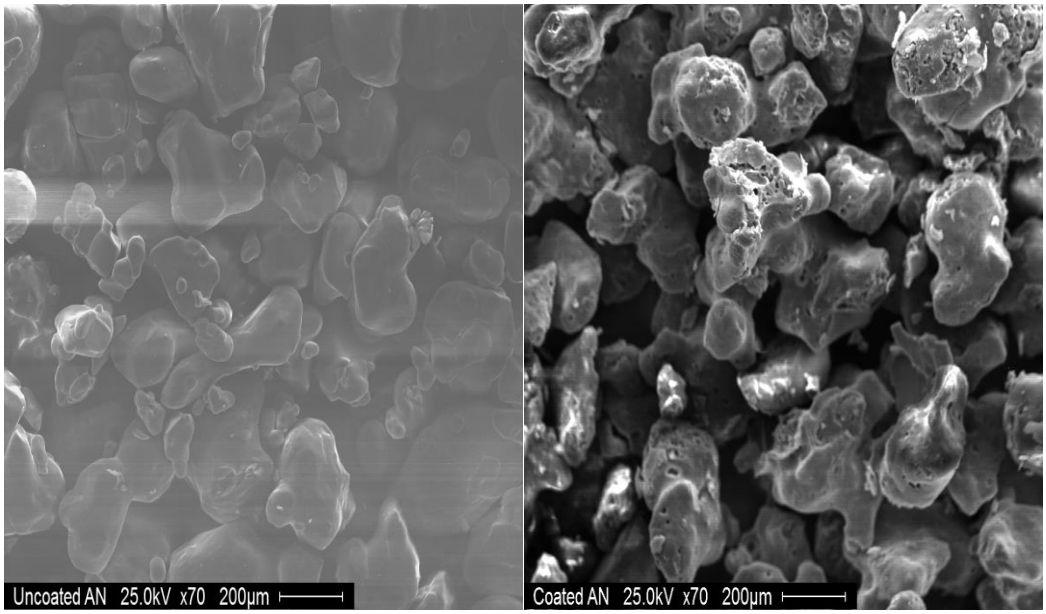

Figure 6.6 SEM Pictures 70x Magnification A) Uncoated Ammonium Nitrate Particles B) PEG 3400 Coated Ammonium Nitrate Particles

The non-spherical nature of the uncoated and coated ammonium nitrate particles is highlighted further at greater magnification as shown in Figure 6.6.

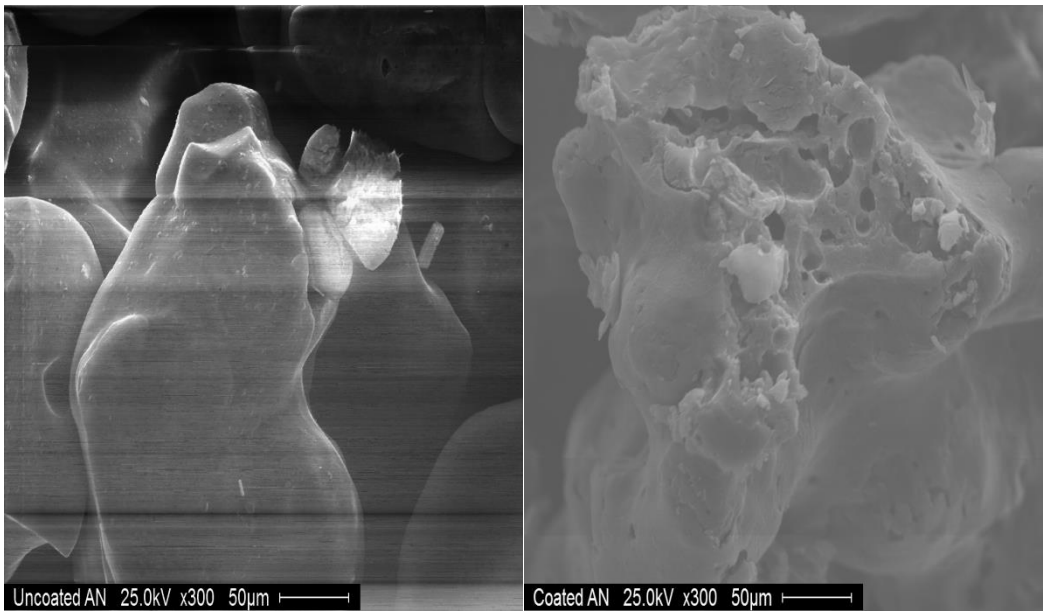

Figure 6.7 SEM Pictures 300x Magnification A) Uncoated Ammonium Nitrate Particles B) PEG 3400 Coated Ammonium Nitrate Particles

At 300x magnification as shown in Figure 6.7, the uncoated ammonium nitrate particles have rounded edges and cracks on the particle surface are faintly visible. The coated ammonium nitrate particles in Figure 6.7 show a combination of rough and smooth surfaces and pinholes randomly distributed around the particles. The alternating surface textures and pinholes are possibly a result of three phenomena: incomplete surface coating of the core ammonium nitrate particle, a capillary pressure gradient in the core particle pore leading to a pore structure collapse, or the ammonium nitrate particle expansion and contraction that accompanies the crystal structure phase transitions that occur during fluidized bed processing.

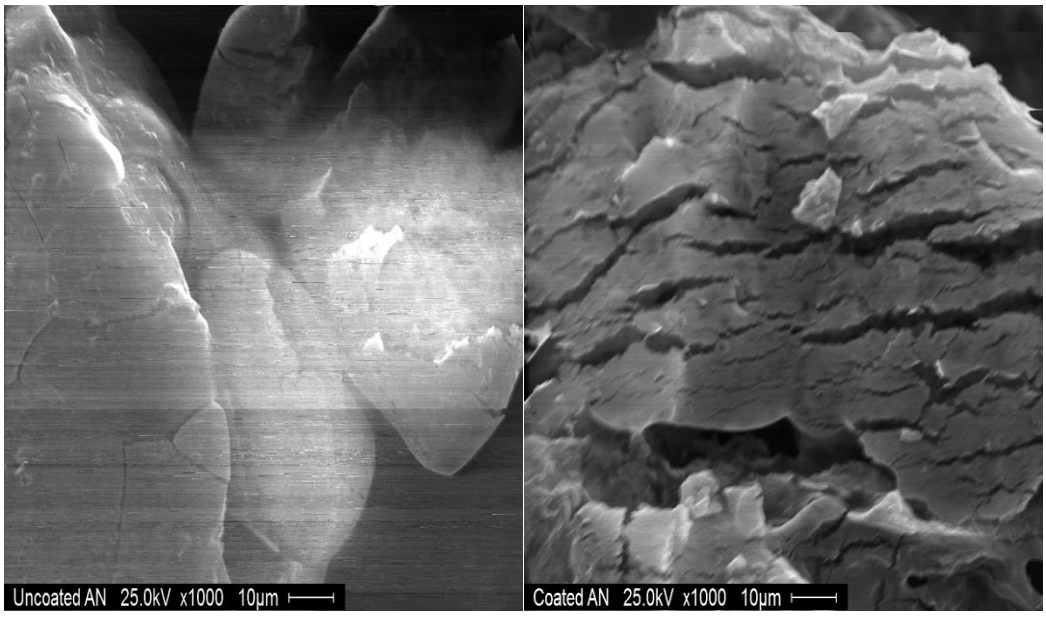

Figure 6.8 SEM Pictures 1000x Magnification A) Uncoated Ammonium Nitrate Particles B) PEG 3400 Coated Ammonium Nitrate Particles

At 1000x magnification several cracks are now visible in the uncoated ammonium nitrate particles in Figure 6.8. In addition, several asperities are visible, particularly with the ammonium nitrate particle on the left. The PEG coated ammonium nitrate particle has several deep cracks again indicating an imperfect or incomplete core particle coating. The cracks in the PEG 3400 coating may also indicate that PEG 3400 is not elastic enough to handle the repetitive

crystal structure phase transitions that ammonium nitrate undergoes during fluidized bed processing.

While SEM analysis yields insight into particle morphology characteristics such as particle shape and coating quality (the presence/absence of cracks, gaps, or pinholes in coating), atomic force microscopy was used to determine an additional surface property, the surface roughness. To determine the surface roughness of the PEG 3400 coated and uncoated ammonium nitrate particles atomic force microscopy (AFM) measurements were done with a VEECO Dimension 3100 Atomic Force Microscope. Five different measurements of the uncoated ammonium nitrate and PEG 3400 coated ammonium nitrate particles were taken.

Figures 6.9 and 6.10 show the 2-D AFM scans of the uncoated and PEG coated ammonium nitrate particles. The scan size for the 2-D AFM measurements was 100 μm^2 or 900 μm^2 depending on the best resolution achievable. The uncoated particles in Figure 6.9 appear smooth with deep crevices or edges. The PEG coated particles by comparison, in Figure 6.10, appear to be cloud-like.

The 3-D scans of the uncoated and PEG coated ammonium nitrate particles are shown as Figures 6.11 and 6.12 respectively. The same trends for the uncoated and PEG coated ammonium nitrate particles in the 2-D scans are evident in the 3-D scans, with the uncoated particles appearing to be smooth, while the coated particles appear cloud-like.

The surface roughness for each of the measured samples is shown in Table 6.5:

Table 6.5 Uncoated Ammonium Nitrate and PEG 3400 Coated Ammonium Nitrate Surface Roughness Measurements

Particle Sample	Uncoated Roughness [nm]	Coated Roughness [nm]
1	449.61	792.27
2	431.99	254.17
3	393.48	160.88
4	280.74	560.63
5	343.22	325.86

The uncoated particles have a smaller range for surface roughness at 168.87 nm compared to the coated particles at 631.39 nm. The disparity in surface roughness values could be the result of many processing factors including: imperfect or incomplete coating of the particle surface, a capillary pressure gradient developed within the core particle pore structure, or particle abrasion/fracture during collisions with other particles or the fluidized bed wall. There is also the potential for the surface roughness measurements being so vastly different due to the actual AFM processing technique itself. If a particle becomes dislodged from the sample holder, the needle recording the surface roughness measurements may move the particle yielding an incorrect assessment.

To date fluidized bed coating models that incorporate changes in particle morphology are not available in literature as previously noted in Chapter 3. A summary of the experimental results will be presented next.

6.4 Summary of Experimental Results

Fluidized bed coating experiments were conducted in the top spray orientation and the Wurster orientation as part of an effort to develop a stochastic coating growth kinetics model that will be presented in the next chapter. Ammonium nitrate was used as the core material, while PEG 3400 was used as the coating material. Colored dyes were incorporated into the coating solution to aid in qualitative visual inspection that particle coating had occurred rather than particle agglomeration. FTIR analysis was also conducted as a qualitative measure to ensure that coating material was present in the sample as shown in Figure 6.4. Calorimetry and UV/Vis absorbance analysis were done to determine the coating efficiency of each experiment. The experimentally determined coating efficiencies were within a few percent of each other.

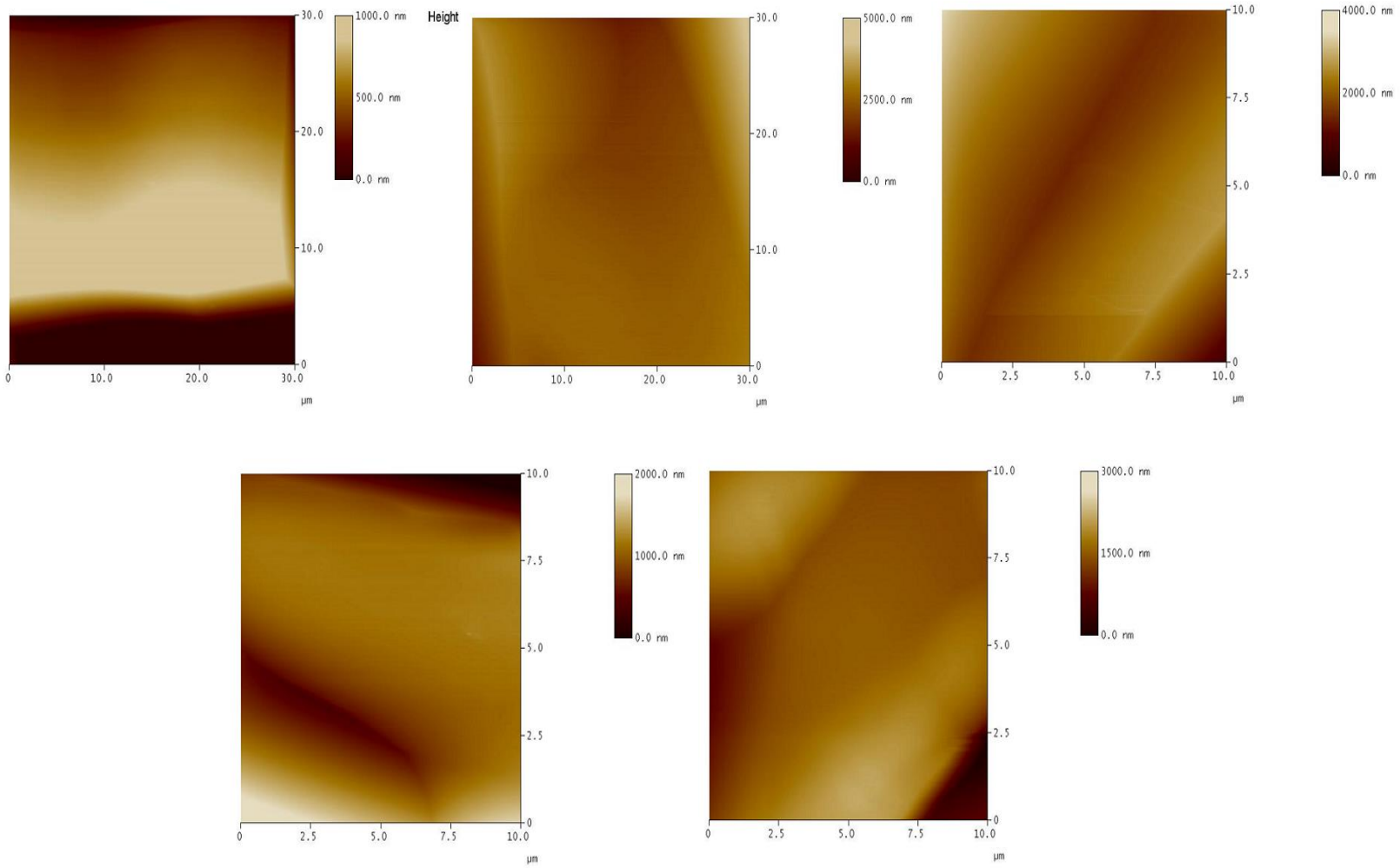

Figure 6.9 2-D AFM Scans of Uncoated Ammonium Nitrate Particles

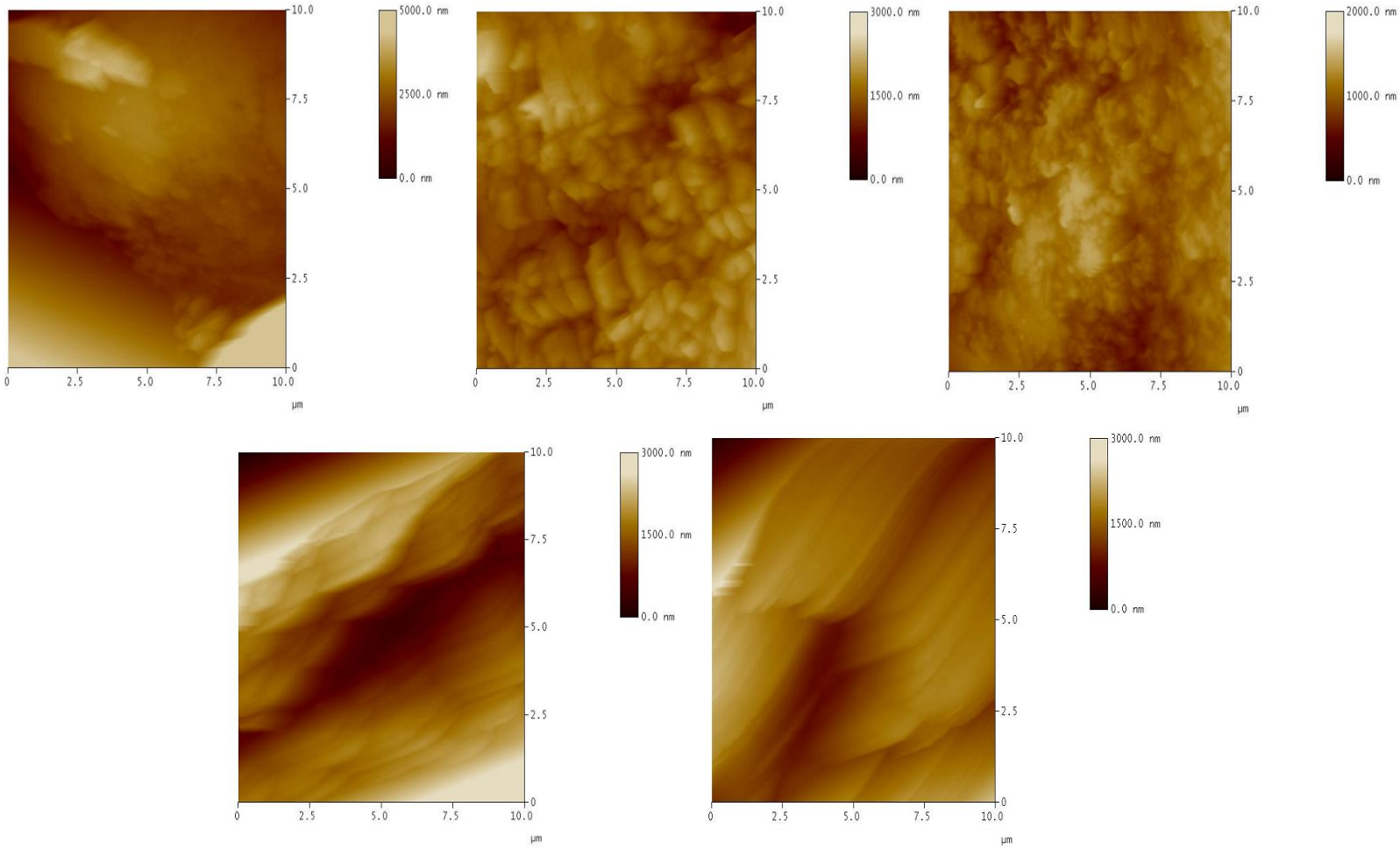

Figure 6.10 2-D AFM Scans of PEG 3400 Coated Ammonium Nitrate Particles

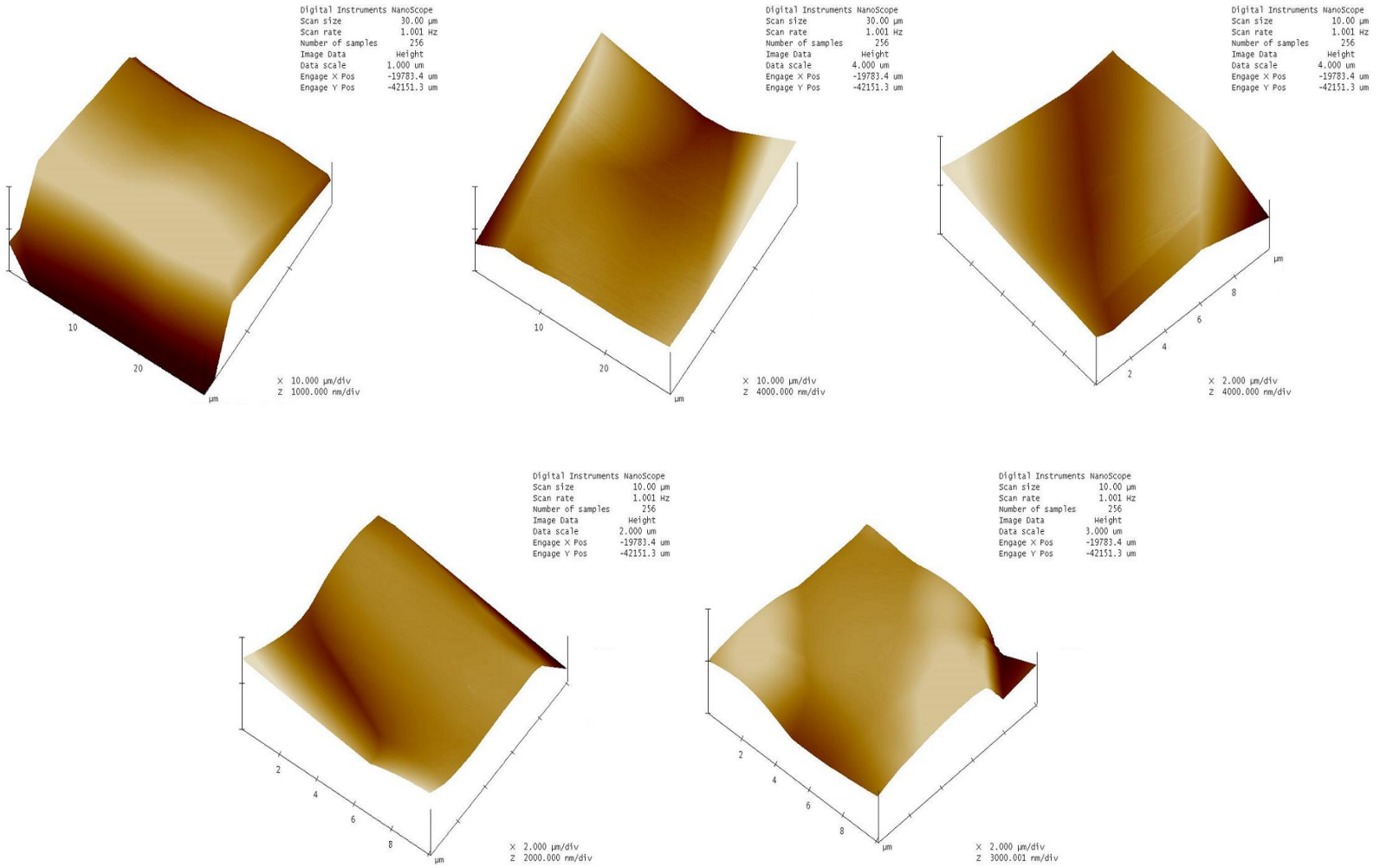

Figure 6.11 3-D AFM Scans of Uncoated Ammonium Nitrate Particles

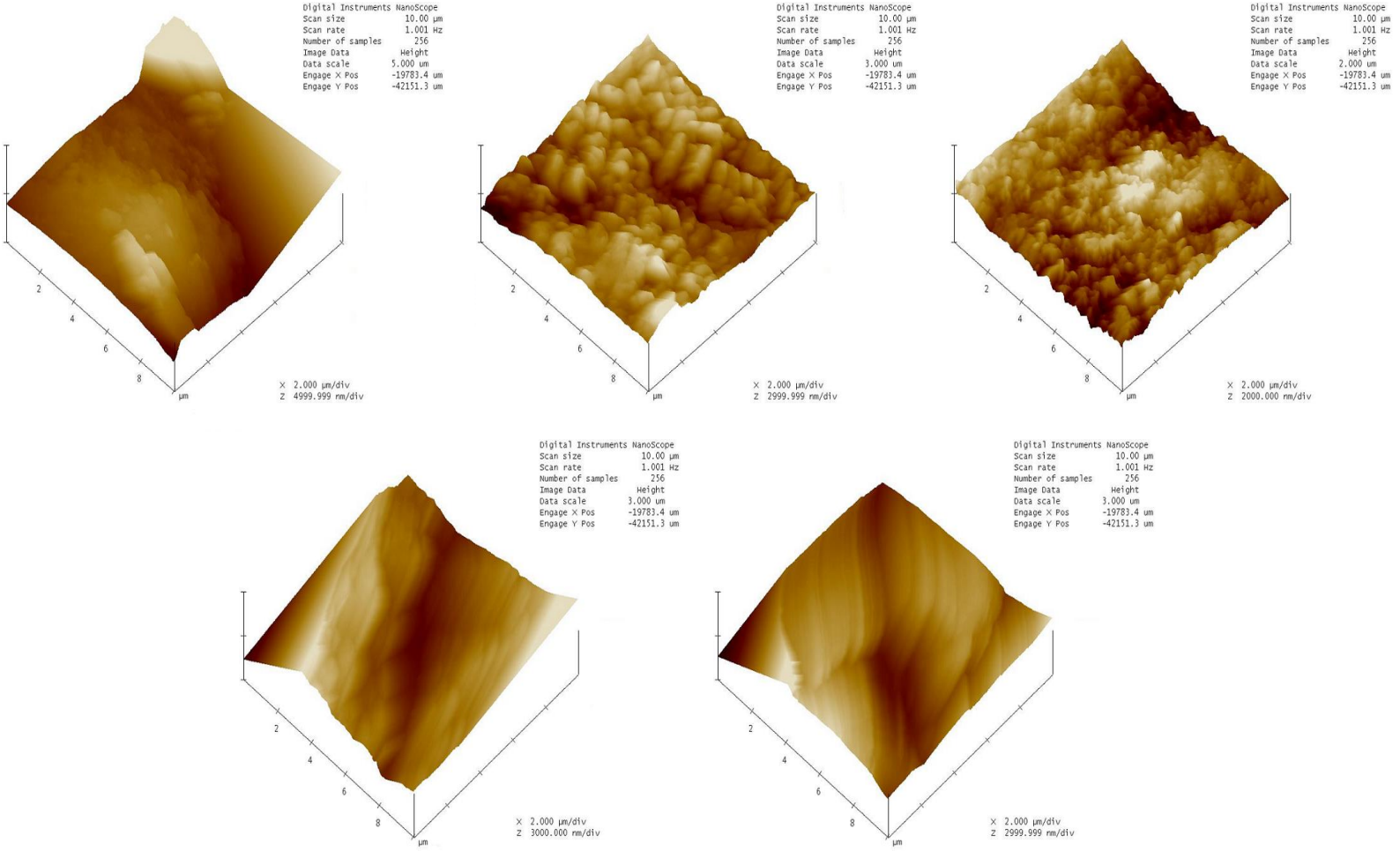

Figure 6.12 3-D AFM Scans of PEG 3400 Coated Ammonium Nitrate Particles

The coated and uncoated ammonium nitrate was investigated with SEM and AFM analysis. SEM analysis showed the uncoated ammonium nitrate particles to have a smooth appearance with asperities and small cracks visible at higher magnification (1000x). In addition, the ammonium nitrate particles were shown by SEM analysis not to be completely spherical in shape. By comparison, SEM analysis showed the PEG 3400 coated ammonium nitrate particles to have an imperfect coating layer. In particular, small pinholes are visible on the coating surface. Upon further magnification (1000x) the coating layer is shown to be imperfect with the presence of several cracks within the coating layer. These cracks in the coating layer may be the result of two phenomena – a potentially high capillary pressure gradient within the particle pores or repeated ammonium nitrate crystalline phase changes brought about by temperature swings and the presence of water. Additional experiments investigating these phenomena would have to be done to determine if both mechanisms are present. Unfortunately, the impact of temperature on the coated ammonium nitrate particle morphology could not be studied with SEM analysis as the Hitachi S-800 scanning electron microscope did not have the capability to take measurements at elevated temperatures.

The surface roughness of the coated and uncoated ammonium nitrate particles was determined by AFM analysis. The uncoated ammonium nitrate surface was shown to be smoother than the coated ammonium nitrate particles. However, the range surface roughness values for the coated ammonium nitrate particles was much larger than the uncoated ammonium nitrate particles. A few possible explanations may provide insight into why the coated particle surface roughness range is larger than the uncoated particle surface roughness: an imperfect PEG 3400 coating on the surface of the ammonium nitrate, a capillary pressure gradient evolution

during evaporation of water from the ammonium nitrate particle surface, or perhaps an unsecured particle was examined for the AFM processing technique.

Now that the coating efficiency has been determined experimentally, modeling efforts to describe the evolution of the particle coating can commence. The first steps to developing a coating growth model involves having an accurate model for the mass and energy balances of a fluidized bed coating operation which will be shown in the next chapter.

CHAPTER 7 MODELING RESULTS AND DISCUSSION

The purpose of this chapter is to present the modeling results for the dynamic mass and energy balances and the coating growth kinetics model developed for this work. The results and subsequent discussion presented will cover several areas including: a comparison between experimental temperature profiles and the predicted temperature profiles from the dynamic mass and energy balances with a sensitivity analysis, the coating growth kinetics model with a sensitivity analysis, and finally a discussion of the sources of error – for experiment design and modeling.

7.1 Modeling Calculation Flow

The main goal of this dissertation is to develop a stochastic coating growth kinetics model for fluidized bed coating operations carried out in the top spray or Wurster orientation. Among the outputs of the aforementioned model are the overall coating efficiency, the coating thickness distribution, and the final particle size distribution. The coating growth kinetics model involves using data calculated from a dynamic mass and energy balance that discretizes the fluidized bed into two types of control volumes, coating control volumes or a non-coating control volumes. Each type of control volume has a specific set of differential equations to solve to obtain the temperature profile with respect to time. The dynamic mass and energy balances are validated via temperature and relative humidity measurements. The fluidized bed hydrodynamic properties are then used as part of the input for the coating growth kinetics model. Figure 7.1 shows the general flow of calculation from the dynamic mass and energy balances through the coating growth kinetics model.

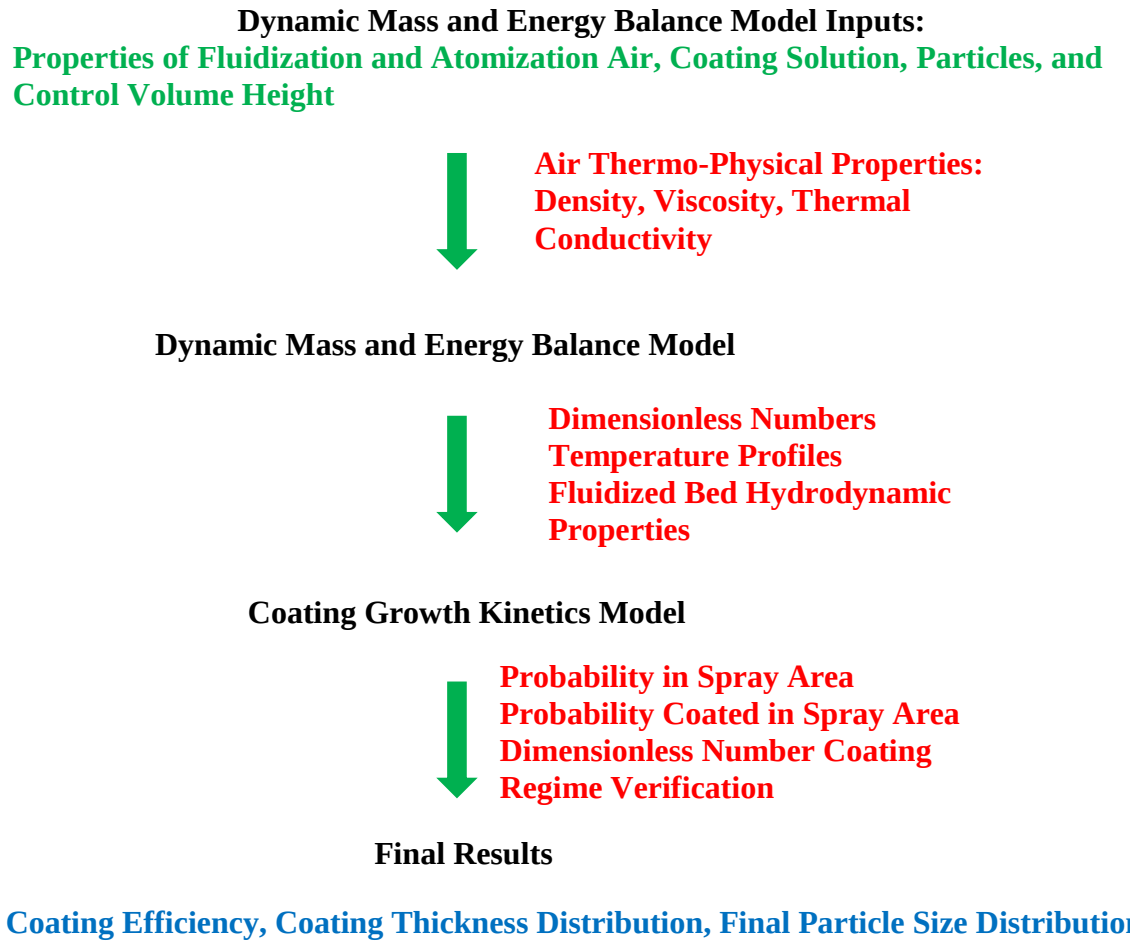

Figure 7.1 General Calculation Flow of Models Used in This Work

As mentioned previously, the first step to developing a model to describe the evolution of a coating thickness distribution in a fluidized bed is the validation of a model used to describe the dynamic (and subsequent steady state) mass and energy balances for a fluidized bed system. The temperature profile validation for the top spray orientation will be discussed in the next section.

7.2 Top Spray Fluidized Bed Temperature Profiles Validation

In order to develop a fluidized bed coating growth kinetics model first the temperature profile of the fluidized bed must be modeled, namely the fluidization air temperature, the particle

temperature, and the fluidized bed wall temperature as a function of time. For any fluidized bed simulation Table 7.1 shows the variables that must be defined a priori.

Table 7.1 Variables to Define Prior to Fluidized Bed Numerical Simulation

Aspect	Variables to Define
Atomization Air	Pressure, Temperature, Flow Rate, Preheat Relative Humidity or Absolute Humidity
Fluidization Air	Preheat Relative Humidity or Absolute Humidity, Fluidized Bed Inlet Temperature, Pressure, Flow Rate
Particles	Density, Particle Size, Bed Mass, Specific Heat Capacity, Initial Temperature
Fluidized Bed Wall	Initial Temperature, Density, Wall Thickness, Specific Heat Capacity, Emissivity
Coating Solution	Density, Surface Tension, Viscosity, Specific Heat Capacity, Latent Heat of Vaporization, Dry Matter Content, Temperature, Flow Rate
Environment	Temperature, Relative Humidity or Absolute Humidity
Experiment	Preheat Time, Coating Solution Addition Time, Drying Time
Simulation	Control Volume Height, Number of Control Volumes, Number of Coating Control Volumes

A validation of the dynamic mass and energy balances for top spray fluidized bed operations presented in Chapter 4 was done and similar results to those presented by Hede et al (2009) were obtained. Two temperatures were measured for each experiment, one two centimeters from the bottom of the fluidized bed product bowl and the other at the fluidization air exhaust before entering the vent. The relative humidity was also measured at the fluidization air exhaust.

The position of the thermocouple within the fluidized bed corresponds to the fourth control volume (using a control volume height of 0.5 cm), so the temperature profile for this control volume is used for validation purposes. The last and highest control volume is used for comparison regarding temperature and relative humidity.

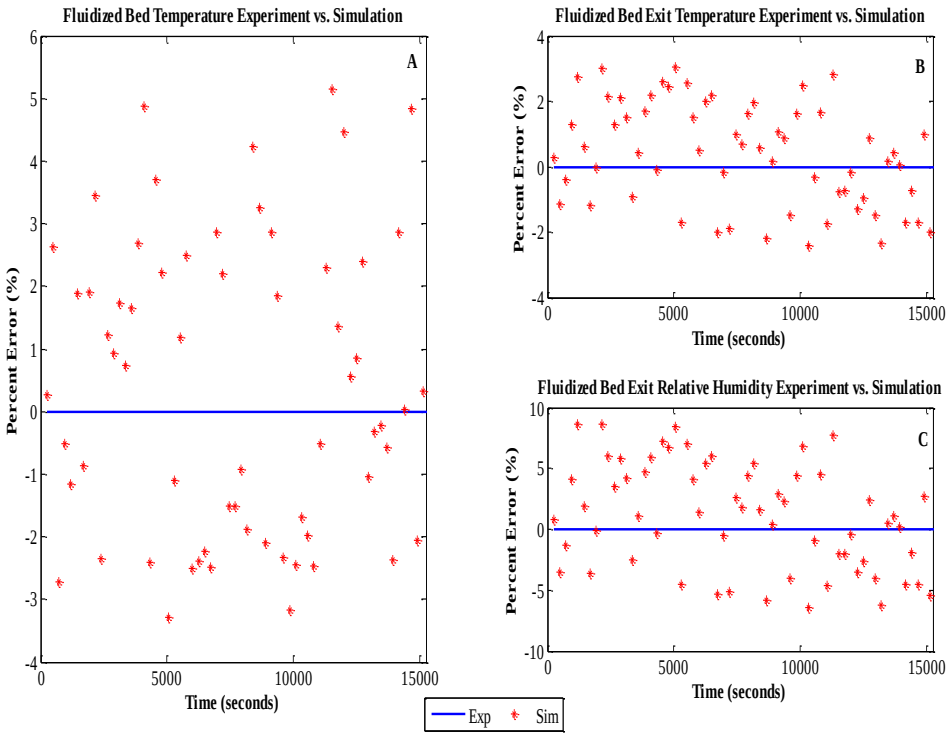

Figure 7.2 Comparison of Fluidized Bed Experiment and Simulation Temperature and Relative Humidity Profiles

As Figure 7.2 shows there is a small variation between experiment and simulation temperatures for the particle temperature and fluidization air (subplots A and B), with deviations on the order of ±6%. The deviation for relative humidity in subplot C is slightly higher however. One possible explanation for the higher deviation between experiment and simulation relative humidity is the response time of the relative humidity probe. The response time for the relative humidity probe is about 30 seconds compared to about 3 seconds for the thermocouples.

With the top spray mass and energy balance validation within an acceptable variation range now the dynamic and steady state behavior of the fluidized bed can be explored.

7.2.1 Top Spray Dynamic and Steady State Behavior

The dynamic and steady state fluidized bed behavior (temperatures and relative humidity) can now be examined since the mass and energy balance validation from the previous section

shows reasonable agreement with experiments. Certain parameters generated from the dynamic mass and energy balances (e.g. void fraction, circulation rate, bubble velocity, etc.) will be used in the development of the coating growth kinetics model, but this will be discussed in further detail later.

Figure 7.3 shows three different profiles for fluidized bed behavior. Subplot A shows the temperature profile for the fluidization air, particles, and the fluidized bed wall as a function of time for the fourth control volume (where the thermocouple is located). For every simulation control volume there is a corresponding temperature profile similar to what is shown in subplot A. The point at which all the temperature profiles start to decrease in subplot A corresponds to the beginning of the coating solution addition into the fluidized bed. As expected the particle temperature is slightly higher than the wall temperature prior to the addition of the coating solution because the convective heat transfer coefficient for the particles is larger compared to the wall.

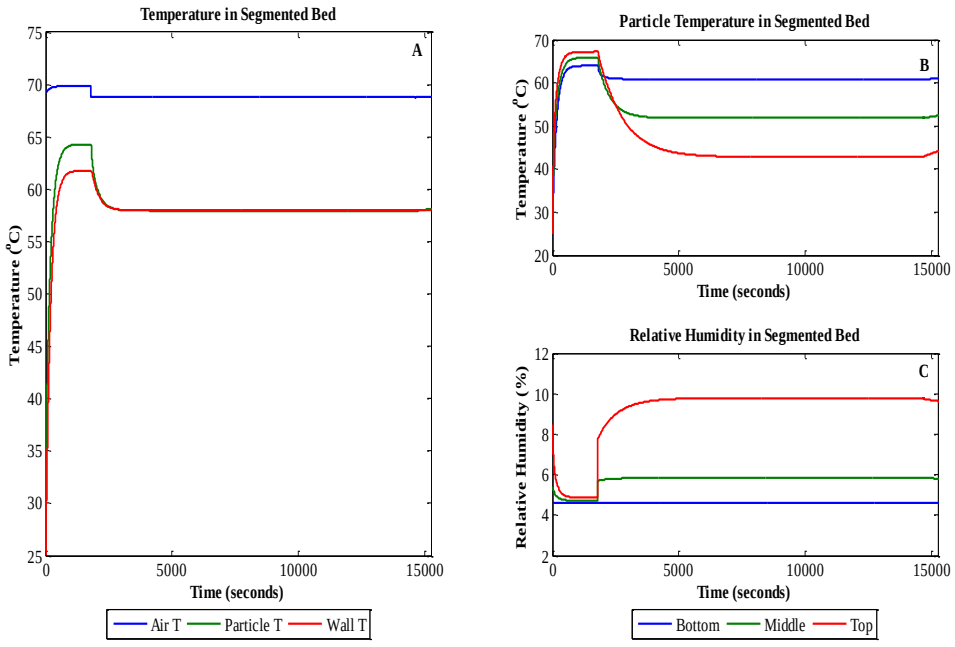

Figure 7.3 A) Control Volume Temperature Profiles B) Particle Temperature Profile in Various Control Volumes C) Relative Humidity Profiles in Various Control Volumes

Subplot B of Figure 7.3 shows the particle temperature at the bottom, middle, and top of the fluidized bed. As expected the particle temperature at the bottom of the fluidized bed is higher than the particle temperature at the top of the bed. This is because the particles at the bottom of the fluidized bed are fluidized by the warmest, driest air. The fluidization air cools slightly as it travels through each control volume which then translates to less heat available for transfer to the particles. The slight upward trend of the temperature profile just before the end of the graph indicates the drying stage of the fluidized bed operation.

Subplot C of Figure 7.3 shows the relative humidity of the fluidization air as it travels through the fluidized bed. As expected, the fluidization air has the lowest relative humidity at the bottom of the fluidized bed and the highest relative humidity at the top of the fluidized bed. The beginning of the relative humidity profiles is marked by a downward trend for the middle and top of the fluidized bed, because the fluidization air reaching the subsequent control volumes is slightly warmer with the progression of time because gas-particle heat transfer reaches a steady state.

During the addition of the coating solution the particle temperature drops because heat that would have elevated or maintained the particle temperature instead is utilized to evaporate the coating solution solvent. However, a steady state temperature is reached after some time has passed (how much time is necessary is a function of the fluidized bed operating conditions, particle and coating solution properties, and fluidized bed geometry) as evident in all three subplots of Figure 7.3.

Figure 7.4 shows the steady state temperature profiles of the fluidized bed operation as a function of normalized fluidized bed height. Subplot A shows the steady state temperature profile of the fluidization air and the particles. In this case, the fluidization air temperature drops

from 70°C at the distributor plate to 55°C at the top of the fluidized bed while the coating solution is introduced into the fluidized bed. The particle temperature also drops as a function of normalized height at steady state from about 60°C at the distributor plate to 45°C at the top of the fluidized bed. A 10°C differential between the fluidization air and the particles is maintained throughout the fluidized bed.

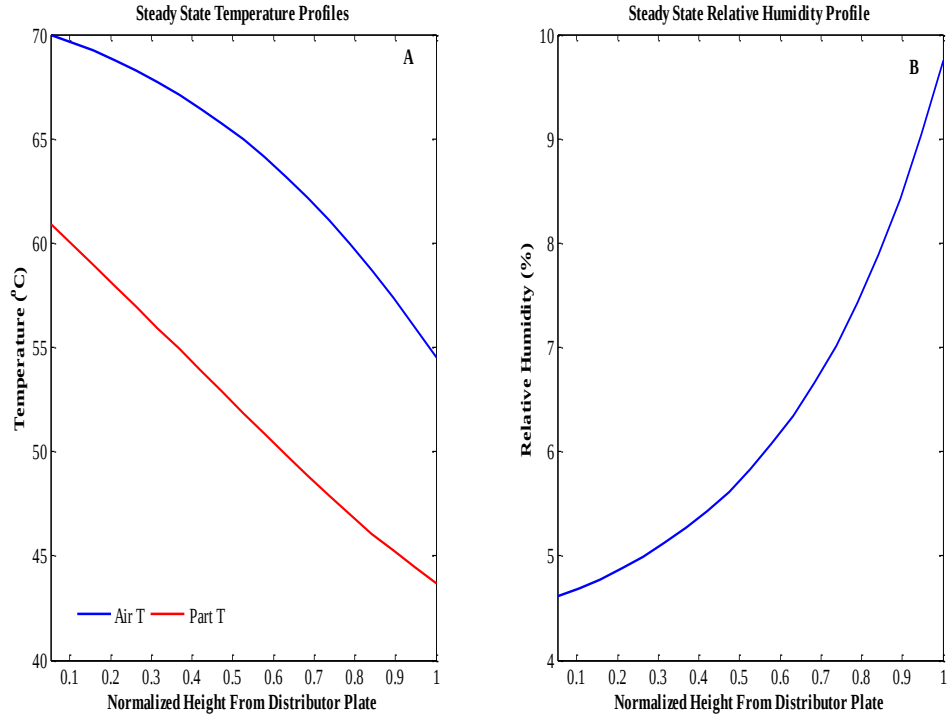

Figure 7.4 A) Steady State Temperature Profiles as a Function of Normalized Fluidized Bed Height B) Steady State Relative Humidity Profile as a Function of Normalized Fluidized Bed Height

Subplot B of Figure 7.4 shows how the fluidization air relative humidity changes as a function of normalized fluidized bed height at steady state. At the distributor plate, the relative humidity is smallest in magnitude at just below 5% RH. In this case, the relative humidity is doubled by the time it reaches the top of the fluidized bed. The reason for this is a combination of the fluidization air cooling as it flows higher through the fluidized bed and the addition of solvent vapor at cooler temperatures, thus saturating the fluidization air.

The normalized fluidized bed height is used as the x axis in Figure 7.4 because the number of control volumes used to simulate the fluidized bed temperature profiles differs experiment to experiment. Normalization of the fluidized bed height can allow for comparison between experiments or between different size scales.

7.2.2 Dynamic Mass and Energy Balance Sensitivity Analysis

A sensitivity analysis was done for the dynamic mass and energy balances to determine the impact of experiment conditions (fluidization air flow rate, temperature, and initial relative humidity, particle size) and simulation conditions (control volume height) on the particle temperature within the fluidized bed, and the fluidized bed hydrodynamic properties, heat transfer properties, and mass transfer properties. Table 7.2 shows the hydrodynamic, heat transfer, and mass transfer properties examined for the sensitivity study.

Table 7.2 Fluidized Bed Hydrodynamic, Heat and Mass Transfer Properties Examined for Sensitivity Study

Properties		
Hydrodynamic	**Heat Transfer**	**Mass Transfer**
Bubble Diameter	Gas-Particle Convective Heat Transfer Coefficient	Mass Transfer Coefficient
Bubble Velocity	Gas-Wall Convective Heat Transfer Coefficient	Drying Rate
Bubble Void Fraction	Natural Convection Heat Transfer Coefficient	
Minimum Fluidization Velocity		
Particle Mass		
Superficial Velocity		
Void Fraction of Fluidized Bed		
Void Fraction at Minimum Fluidization		
Volume of Control Volume		

Table 7.3 shows the variable initial conditions as well as high and low values used for the sensitivity analysis. The same fluidized bed bowl height was used for each sensitivity analysis simulation to remove any bias.

Table 7.3 Sensitivity Analysis Parameters

Variable	**Simulation Condition**	**High Value**	**Low Value**
Relative Humidity	50% (Preheated)	90% (Preheated)	10% (Preheated)
Particle Diameter	250 microns	300 microns	200 microns
Volumetric Flow Rate	20 m^3/hr	25 m^3/hr	15 m^3/hr
Fluidization Air Temperature	70^{o}C	75^{o}C	65^{o}C
CV Height	0.5 cm	1 cm	0.25 cm

The effect of the preheated fluidization air relative humidity was investigated and Figure 7.5 shows the results. As subplot A shows and subplot B confirms, there is virtually no difference between the particle temperature profiles at different preheat relative humidities. The vapor pressure of water increases with increasing temperature, thus the relative humidity of air drops. In this case, when a stream of air at 25^{o}C and 50% relative humidity is heated to 70^{o}C, the relative humidity drops to 5.12%. At 10% and 90% preheat relative humidity, the heated air relative humidity is 1.02% and 9.23% respectively. The deviation in subplot B is due to the change in the amount of water present in the air. Dry air has a lower specific heat capacity compared to air saturated with water, leading to a slightly higher particle temperature.

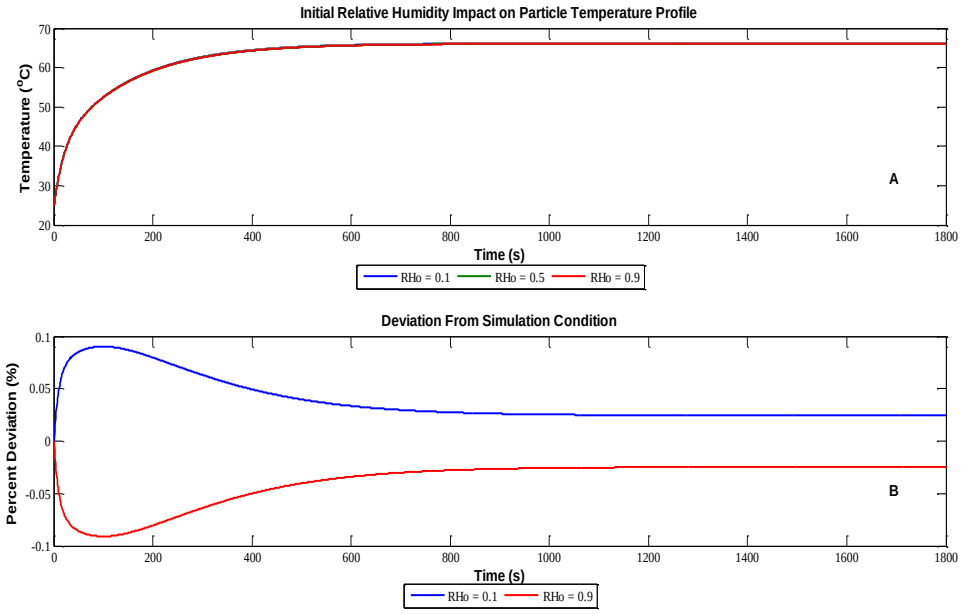

Figure 7.5 A). Particle Temperature Profiles at Different Preheat Fluidization Air Relative Humidities B). Deviation From Simulation Condition

A closer look at the hydrodynamic, heat transfer, and mass transfer characteristics of the simulation in Figure 7.6 show very low parameter sensitivity to a change in the initial preheat air relative humidity.

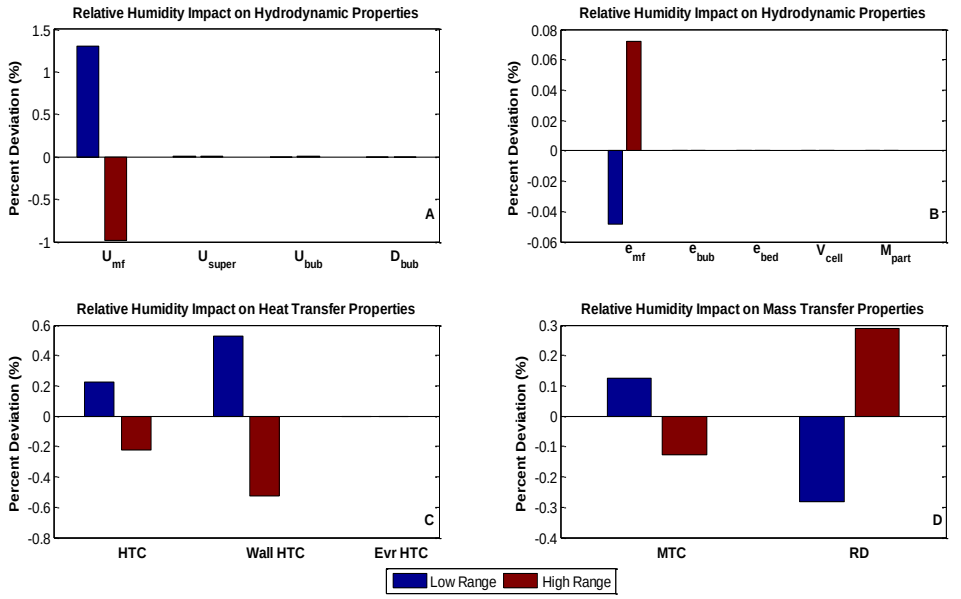

Figure 7.6 Fluidized Bed Hydrodynamics, Heat Transfer, and Mass Transfer Property Sensitivity to Initial Relative Humidity

The minimum fluidization velocity in subplot A shows the highest sensitivity to relative humidity, but only at ±1% difference for 80% swings in preheat relative humidity.

Figure 7.7 shows the effect of the particle size used for the numerical simulations. As expected, subplot A shows some variation in the particle temperature profiles. This is because smaller particles have less mass than larger particles. In this case a 300 micron diameter particle has a mass 3.375 greater then a 200 micron diameter particle. In addition to less mass heating up, there is also a smaller diameter for heat transfer to occur leading to a slightly higher temperature compared to larger particles. As subplot B shows the deviation is very pronounced at the beginning of the simulation before reaching a steady state value.

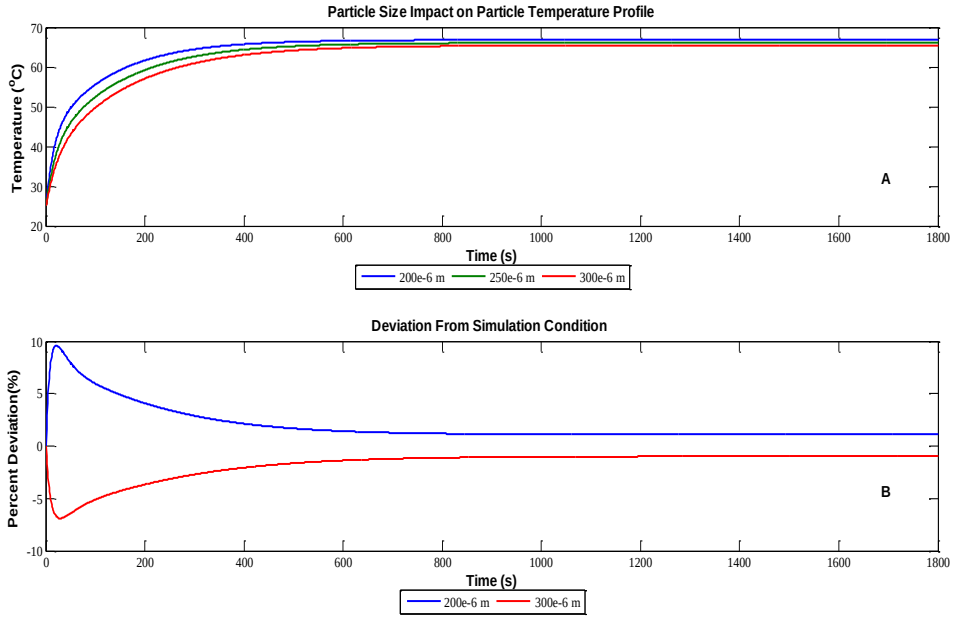

Figure 7.7 A). Particle Temperature Profiles at Different Particle Sizes B). Deviation From Simulation Condition

A closer look at the hydrodynamic, heat transfer, and mass transfer characteristics of the simulation in Figure 7.8 show various levels of parameter sensitivity to a change in the particle diameter. Not surprisingly, the minimum fluidization velocity is very sensitive to the particle

diameter as shown in subplot A, a 20% change in particle diameter results in about a 40% swing in the minimum fluidization velocity. However, the bubble diameter and bubble velocity are practically unchanged. All the hydrodynamic parameters in subplot B show some sensitivity to particle diameter except for the cell volume, but the largest impact here is a 1.5% difference.

The heat and mass transfer parameters in subplots C and D show a stronger sensitivity to particle diameter, close to a 1:1 ratio with the 20% change in particle diameter yielding roughly 20% changes in the particle convective heat transfer coefficient, mass transfer coefficient, and drying rate.

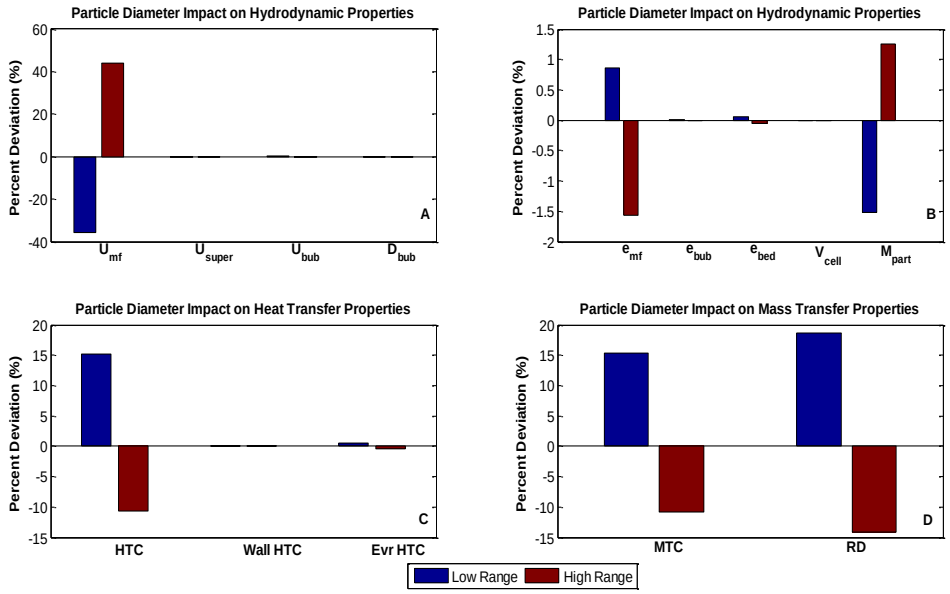

Figure 7.8 Fluidized Bed Hydrodynamics, Heat Transfer, and Mass Transfer Property Sensitivity to Particle Diameter

Figure 7.9 shows the impact of the fluidization air flow rate on the particle temperature profile. The final particle temperatures reach essentially the same temperature at steady state (~900 seconds) with the main variation occurring during the first 200 seconds of operation. The deviation at the beginning shown in subplot B is an order of magnitude lower than the flow rate

swing, 20% swing in fluidization flow rate and roughly a 6% difference in the particle temperature in the first 200 seconds.

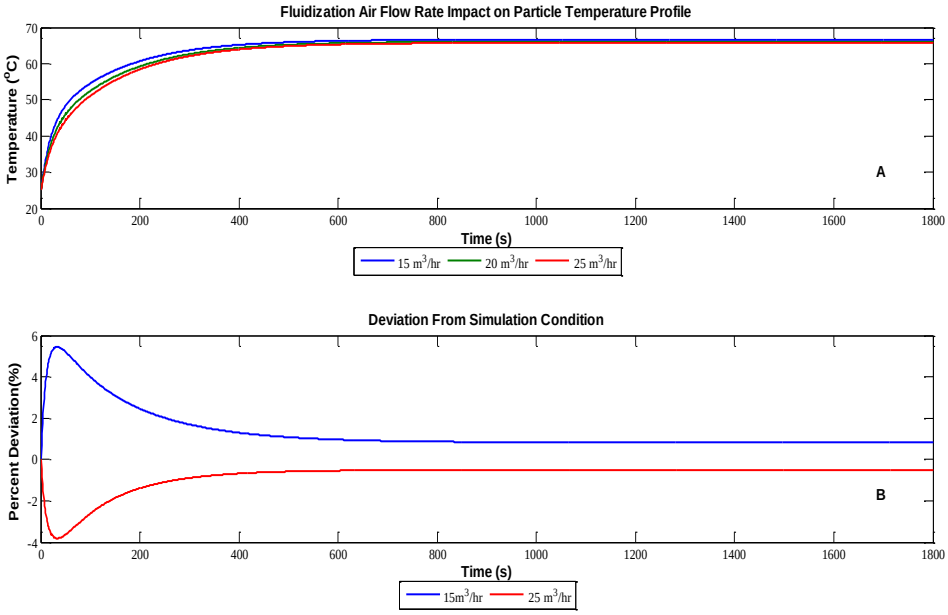

Figure 7.9 A). Particle Temperature Profiles at Different Fluidization Air Flow Rates B). Deviation From Simulation Condition

A closer look at the hydrodynamic, heat transfer, and mass transfer characteristics of the simulation in Figure 7.10 show various levels of parameter sensitivity to a change in the fluidization air flow rate. Subplot A shows that the bubble properties and superficial velocity are strongly influenced by the fluidization air flow rate, whereas the minimum fluidization is not. Subplot B shows that the particle mass in one control volume is strongly influenced by the fluidization air flow rate, with smaller impacts on the magnitudes of the bubble void fraction and overall bed void fraction.

The heat transfer and mass transfer characteristics shown in subplots C and D show again the strong influence changes in the fluidization air flow rate has on parameter magnitudes, with the 20% swings in flow rate yielding 20%-40% changes in heat transfer and mass transfer characteristics.

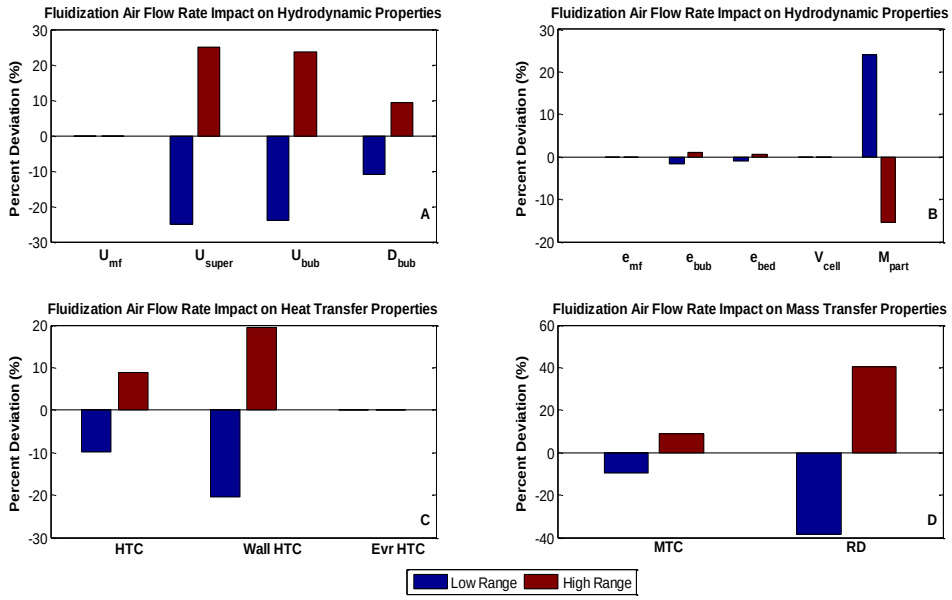

Figure 7.10 Fluidized Bed Hydrodynamics, Heat Transfer, and Mass Transfer Property Sensitivity to Fluidization Air Flow Rate

Figure 7.11 shows the impact of the fluidization air temperature on the particle temperature profile. As expected, with a higher fluidization air temperature a higher particle temperature can be obtained. As shown with subplot B, the deviation in particle temperature (~5%) is the same order of magnitude as the temperature swing (7.14%).

A closer look at the hydrodynamic, heat transfer, and mass transfer characteristics of the simulation in Figure 7.12 show various levels of parameter sensitivity to a change in the fluidization air temperature. The hydrodynamic properties in subplots A and B show very low sensitivity to temperature swings compared to the hydrodynamic property sensitivity to flow rate swings in Figure 7.11. However, the minimum fluidization temperature is a function of temperature, as viscosity and density are both functions of temperature.

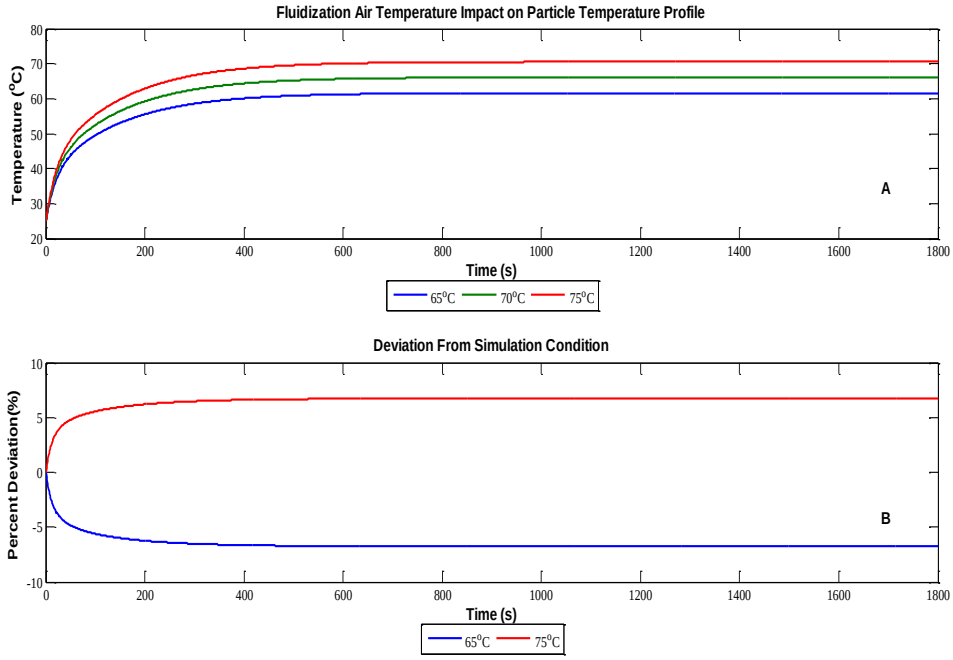

Figure 7.11 A). Particle Temperature Profiles at Different Fluidization Air Temperatures B). Deviation From Simulation Condition

As subplot C shows the fluidization air temperature impacts all three heat transfer coefficients to a certain extent (±~3%). The impact of the fluidization air temperature is low itself, however the impact on the drying rate is much more pronounced. The reason for this is because the drying rate is also a function of the solvent vapor pressure in addition to the mass transfer coefficient. Vapor pressure is an exponential function of temperature, so small increases in temperature when a system is already at an elevated temperature result in significant jumps in solvent vapor pressure (e.g. increasing temperature from 70°C to 72°C is 2.86% increase, whereas water vapor pressure increases 8.97% for the aforementioned temperatures).

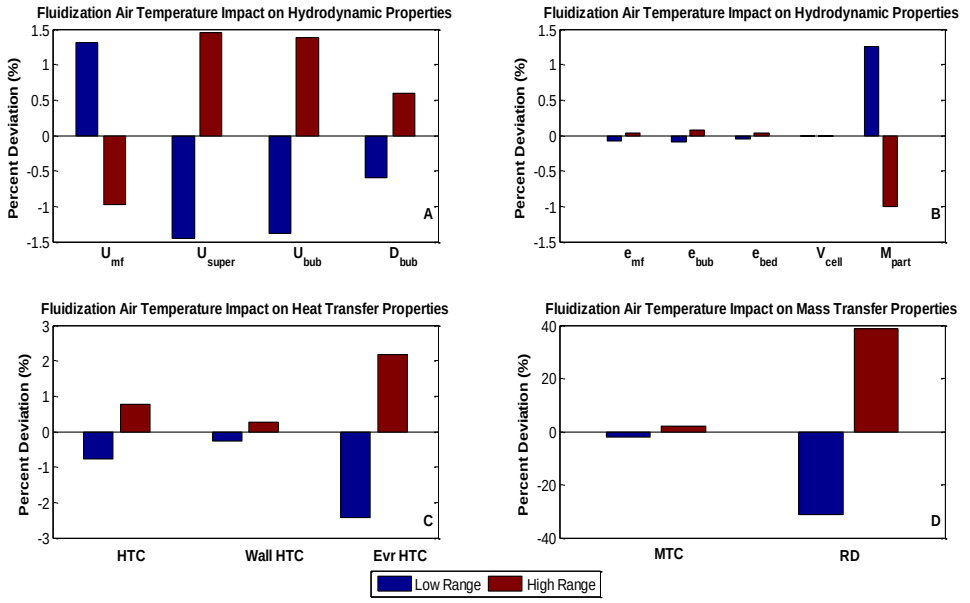

Figure 7.12 Fluidized Bed Hydrodynamics, Heat Transfer, and Mass Transfer Property Sensitivity to Fluidization Air Temperature

Figure 7.13 shows the impact of the control volume height on the particle temperature profile. The difference in particle temperature profiles is due in part to the number of fluidized bed bowl diameters calculated. Different control volume heights mean fluidized bed bowl diameters are calculated at different locations. Thus the hydrodynamic properties used for heat and mass transfer calculations are different as well (e.g. for 0.25 cm control volume height 4 fluidized bed bowl diameters are calculated 1 cm of particle bed height, for 0.5 cm control volume height 2 fluidized bed bowl diameters are calculated 1 cm of particle bed height, and for 1 cm control volume height 1 fluidized bed bowl diameter is calculated 1 cm of particle bed height). As subplot B shows, the deviation is strongest during the initial 200 seconds of operation.

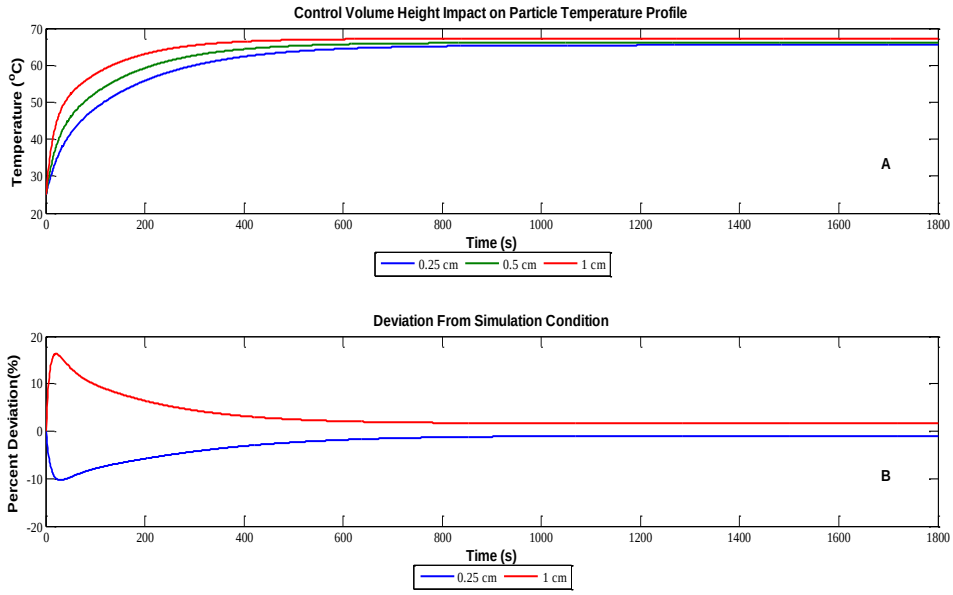

Figure 7.13 A). Particle Temperature Profiles with Different Control Volume Heights B). Deviation From Simulation Condition

A closer look at the hydrodynamic, heat transfer, and mass transfer characteristics of the simulation in Figure 7.14 show various levels of parameter sensitivity to a change in the control volume height. All the fluidized bed hydrodynamic properties in subplots A and B are impacted by a change in the control volume height except the minimum fluidization velocity and the void fraction at minimum fluidization – fluidized bed geometry has no impact on either aforementioned parameter.

The heat and mass transfer characteristics in subplots C and D also show a high sensitivity to the control volume height. The reason for this is because the fluidized bed bowl geometry plays a role in the determination of each parameter in subplots C and D.

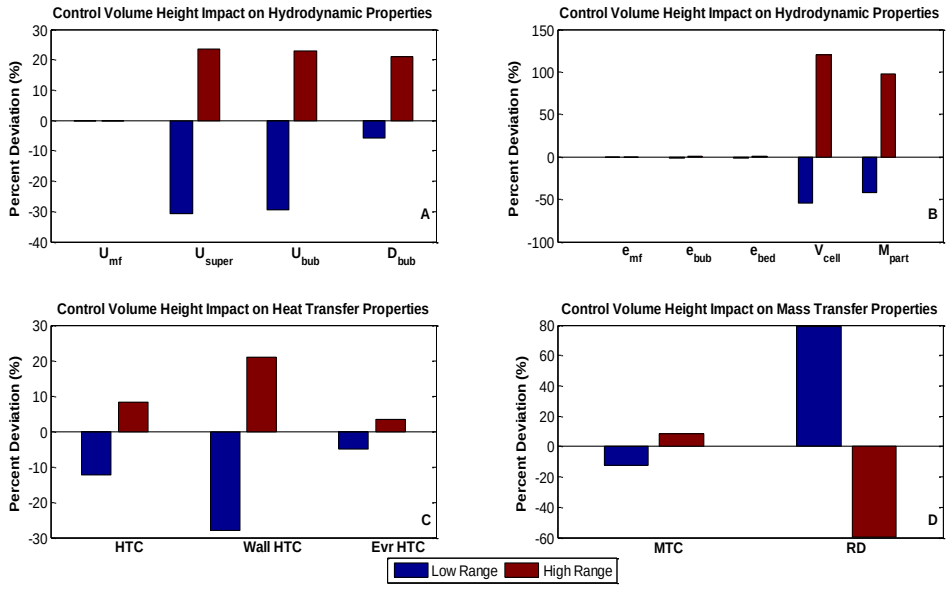

Figure 7.14 Fluidized Bed Hydrodynamics, Heat Transfer, and Mass Transfer Property Sensitivity to Control Volume Height

Among the experimental conditions manipulated the particle temperature sensitivity from highest to least is as follows: fluidization air temperature, fluidization air flow rate, particle diameter, and preheat relative humidity. As Figures 7.13 and 7.14 show, choosing the proper control volume height is an important factor in matching experimental temperature profiles to simulation temperature profiles.

The sensitivity analysis for the dynamic mass and energy balance also provides insight as to what factors may have the largest impact on the coating growth kinetics model. The basis for the coating growth kinetics model is the hydrodynamic properties calculated in the dynamic mass and energy balances along with a few other factors that will be introduced shortly. The coating growth kinetics model, which takes a stochastic form, will be presented next.

7.3 Development of Coating Growth Kinetics Modeling – Event Driven Monte Carlo

In order to develop a coating growth kinetics model, there are several parameters (i.e. distributions) that must be calculated before a Monte Carlo simulation can be attempted. Among

the distributions needed for coating growth calculations are: particle size, droplet size, particle residence time, particle bed revolutions, the number of times a particle is in the spray area, the number of times a particle is coated in the spray area, dimensionless numbers (Stokes Number and others).

As noted in Chapter 4, Monte Carlo simulations can be solely time driven, event driven, or a combination time-event driven numerical approach. The coating growth model developed for this work is an event driven numerical approach. One of the initial distributions needed is the initial particle size distribution.

7.3.1 Initial Particle Size Distribution

In the absence of particle size distribution data (i.e. average, maximum size, minimum size, mode, range, shape, and standard deviation) a triangular distribution can be used to generate an initial particle size distribution. The only data needed for a triangular distribution is maximum size, minimum size, and the mode. The triangular distribution can be used to generate a normal or tailed distribution depending on the mode used for calculation in Equation 4.76 of Chapter 4.

A random number generator (10000 points) is used to generate values for the cumulative distribution function. The particle size is then calculated from the cumulative distribution function. Figure 7.15 shows how a triangular distribution can be manipulated to a represent a normal distribution, a left-tailed distribution, and a right-tailed distribution. The maximum value used in Figure 7.15 is 300 microns, while the minimum value used is 210 microns. The modes used in Figure 6.28 are as follows: A) 255 microns B) 215 microns and C) 285 microns.

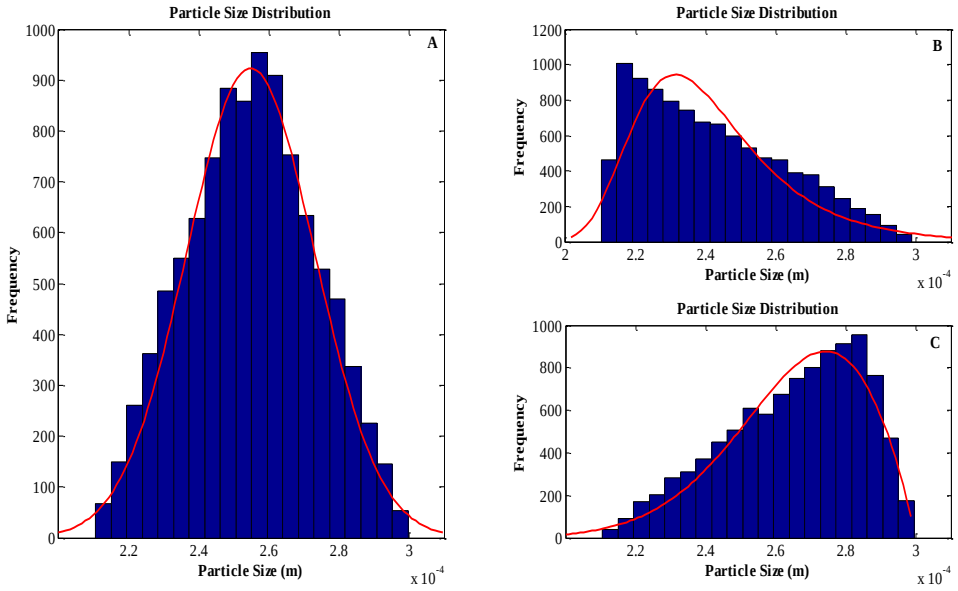

Figure 7.15 Triangular Distribution Representing: A). Normal Distribution B). Left-Tailed Distribution C). Right-Tailed Distribution

Once the particle size distribution is tabulated, other important statistics (i.e. the mean and standard deviation) are calculated and tracked for the duration of the coating growth simulation. The next distribution of interest is the droplet size distribution.

7.3.2 Droplet Size Distribution

The droplet size distribution is modeled as a Rosin-Rammler distribution as described by Equation 2.20 in Chapter 2 with q = 2.5 and X = MMD. The MMD and SMD of a droplet size distribution are dependent on properties of the atomization fluid, coating solution, and nozzle. Figure 7.16 shows a typical droplet size distribution and cumulative frequency distribution.

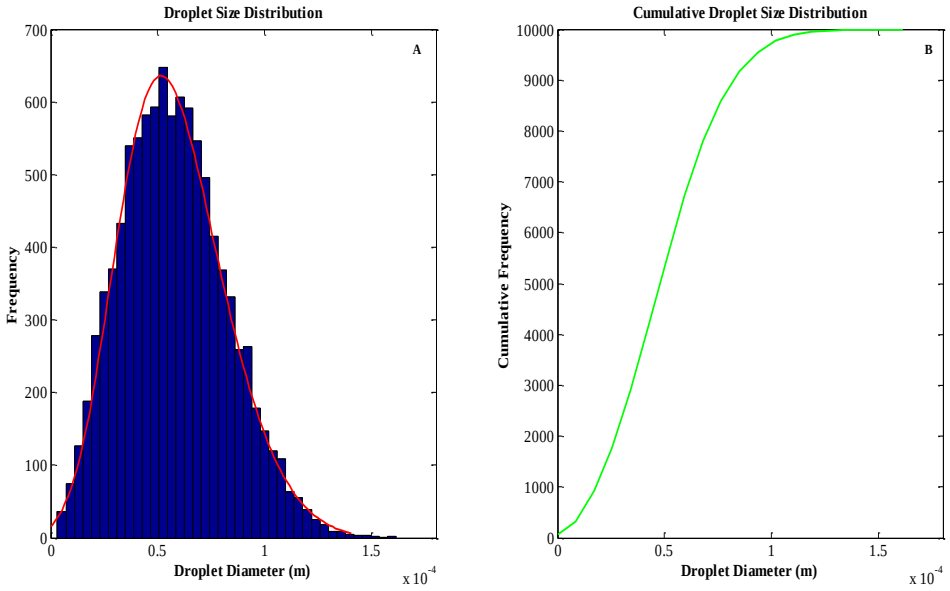

Figure 7.16 Droplet Size Distribution and Cumulative Droplet Size Distribution

With the initial particle size distribution and droplet size distributions now calculated, the particle circulation time distribution and revolution distribution are the next distributions needed for the coating growth model.

7.3.3 Circulation Time Distribution and Revolution Distribution for a Particle Size Distribution

While particle movement inside a fluidized bed is generally considered to be random, there are general characteristics such as circulation time distribution and revolutions within the fluidized bed that can be calculated for a particle size distribution. These two aforementioned characteristics are a necessary component of developing a coating growth kinetics model. The calculation procedure is dependent on the fluidized bed orientation as shown in Chapter 2, section 2.4.5.5.

7.3.3.1 Particle Circulation Time Distribution and Revolution Distribution in Top Spray Orientation

To calculate the particle circulation time distribution and the revolution distribution for a particle size distribution in a top spray oriented fluidized bed, there are several other parameter distributions that must be calculated first. The parameter distributions that must be obtained first include: minimum fluidization velocity, the void fraction at minimum fluidization, the fluidized bed height at minimum fluidization, the bubble diameter, and the bubble velocity.

Using the conditions listed for Experiment 2 in Table 6.2 the distributions listed in the paragraph above were generated. Figure 7.17 shows the distributions for minimum fluidization velocity, void fraction at minimum fluidization, and the fluidized bed height at minimum fluidization.

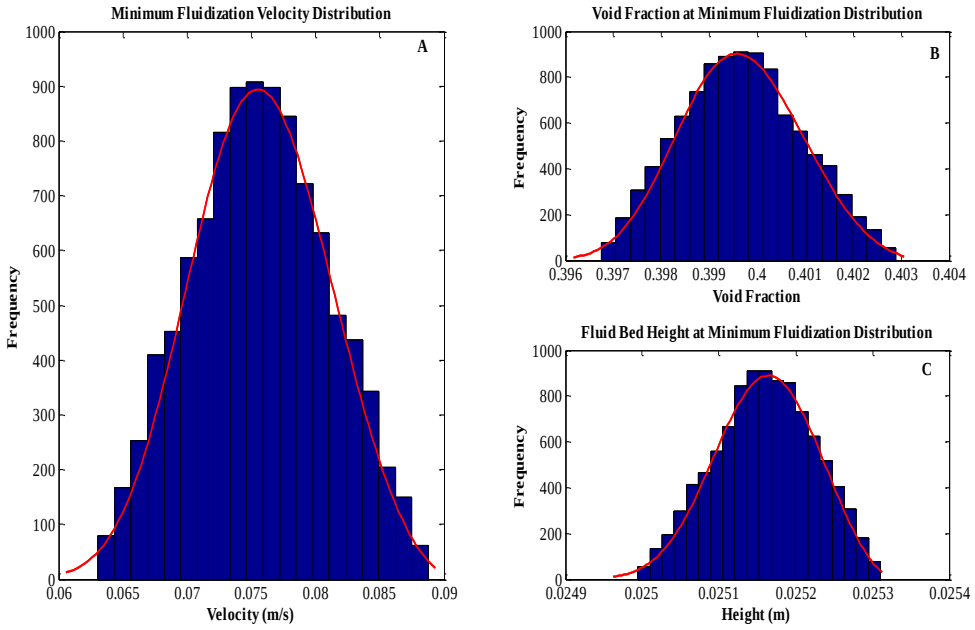

Figure 7.17 A) Minimum Fluidization Velocity Distribution B) Void Fraction at MinimumFluidization C) Fluidized Bed Height at Minimum Fluidization

The parameter with the largest variation in Figure 7.17 is the minimum fluidization velocity – this is a direct result of the particle size distribution range. All three subplots in Figure 7.17 are shown for only one control volume of the simulation, as the shape of the distribution

and magnitude of property value are identical. The void fraction at minimum fluidization and fluidized bed height at minimum fluidization have much narrower ranges because they are less sensitive to particle size fluctuations.

Figure 7.18 shows the bubble diameter, bubble void fraction, and fluidized bed void fraction distributions also needed for the particle cycle time distribution and revolution distribution.

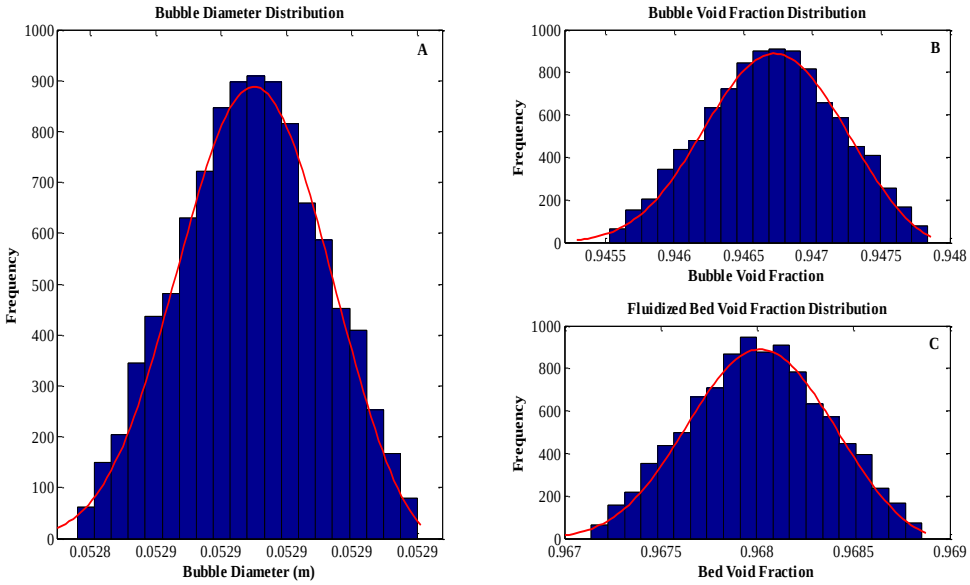

Figure 7.18 A) Bubble Diameter Distribution B) Bubble Void Fraction C) Fluidized Bed Void Fraction

As with Figure 7.17 the distributions shown in Figure 7.18 are shown for only the one of control volumes because combining all the control volume data convolutes the distributions, but the individual distributions will have similar shapes for each control volume. The distributions in Figure 7.18 all have narrow ranges similarly to subplots B and C in Figure 7.17.

With all the distributions in Figure 7.17 and 7.18 now tabulated the particle circulation time and the number of revolutions during the coating solution addition time frame can be calculated. Figure 7.19 shows the particle circulation time and the number of revolutions the particles make during the coating solution addition time (for this simulation 4494 seconds).

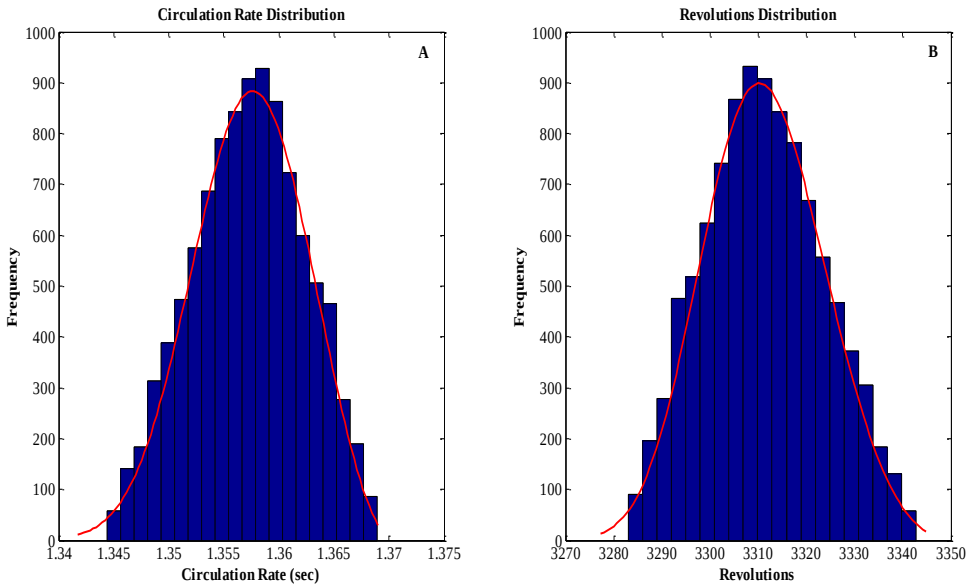

Figure 7.19 A) Particle Circulation Time Distribution B) Particle Bed Revolutions Distribution

As subplots A and B in Figure 7.19 show both the particle circulation time distribution and the particle bed revolutions are very narrow normal distributions. The narrow normal distribution results here stem from the narrow ranges in the previous distributions in Figures 7.17 and 7.18. The impact of particle size on the particle circulation time and revolutions distribution will be discussed later.

Table 7.4 summarizes the calculated particle circulation time and number of revolutions during a top spray coating operation, with minimum, maximum, and average values for a particle size distribution consisting of 10000 values.

Table 7.4 Top Spray Orientation Particle Circulation Time and Revolutions Summary

Run	Circulation Time [sec]			Revolutions		
	Min	Max	Average	Min	Max	Average
1	0.8492	0.8535	0.8526	7030	7066	7037
2	1.3441	1.3688	1.3512	9380	9552	9460
3	0.8084	0.8137	0.8125	15367	15468	15390
4	2.0514	2.0555	2.0548	3234	3241	3235
5	1.3429	1.3572	1.3507	6638	6709	6670
6	0.8196	0.8246	0.8235	7276	7321	7286
7	1.3091	1.3222	1.3163	3399	3433	3414

Table 7.4 Continued

8	1.3478	1.3541	1.3528	3704	3722	3708
9	1.9529	1.9631	1.9609	6116	6148	6122
10	0.8359	0.8446	0.8407	4447	4493	4468
11	2.0329	2.0581	2.0461	2915	2952	2932
12	0.8139	0.8293	0.8220	7235	7372	7299
13	1.2341	1.2675	1.2512	3707	3807	3755
14	0.7672	0.7878	0.7778	5087	5224	5153
15	1.2902	1.3159	1.3036	6846	6983	6911

As Table 7.4 shows, the average particle circulation times range from 0.78 seconds to 2.05 seconds depending on the fluidized bed operating conditions and the particle size listed in Table 6.1. The average number of revolutions has a much larger range due to the length of time the coating solution is sprayed into the fluidized bed.

7.3.3.2 Particle Circulation Time Distribution and Revolution Distribution in Wurster Spray Orientation

The particle circulation time distribution and the revolution distribution in the Wurster spray orientation is dependent on different particle and process parameters than the top spray orientation, namely the particle terminal velocity and the distance traveled after exiting the Wurster tube insert. While all particles are exposed to the same fluidization velocity within the tube, particle acceleration occurs within the Wurster insert at different rates according to particle size. Larger particles have a larger mass and a higher terminal velocity compared to smaller particles, therefore they will have lower velocities when exiting the Wurster tube insert and will not travel as far after exiting the Wurster tube insert. This situation culminates in a lower circulation time and thus a higher number of revolutions inside the fluidized bed.

Figure 7.20 shows the particle terminal velocity distribution, distance traveled distribution, and the particle velocity at the Wurster tube exit distribution for Experiment 1 in Table 6.3.

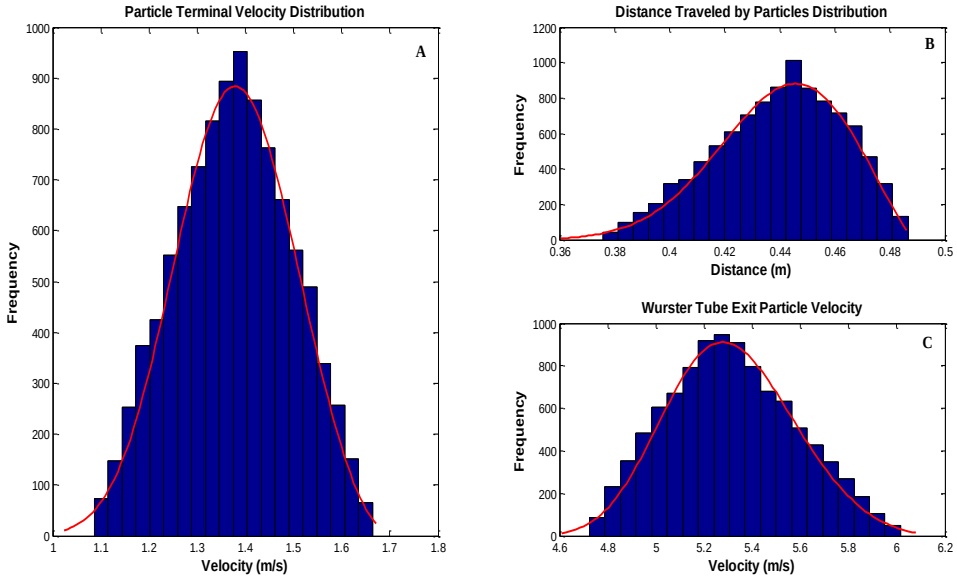

Figure 7.20 A) Particle Terminal Velocity Distribution B) Distance Traveled Distribution C) Particle Velocity at Wurster Tube Exit Distribution

The terminal velocity distribution in subplot A follows a normal distribution because 255μm was taken as the mean particle size. The distance traveled distribution and particle velocity distribution at the Wurster tube exit in subplots B and C are tailed distributions because the smaller particles travel longer distances and have higher velocities at the Wurster tube exit than larger particles.

With the distributions in Figure 7.20 tabulated for terminal velocity, the distance traveled and the Wurster tube exit velocity, the particle cycle time and the number of revolutions made during a coating process are calculated and shown as Figure 7.21. As subplot A shows, the cycle time range for a coating operation in the Wurster orientation is large at 0.12 seconds.

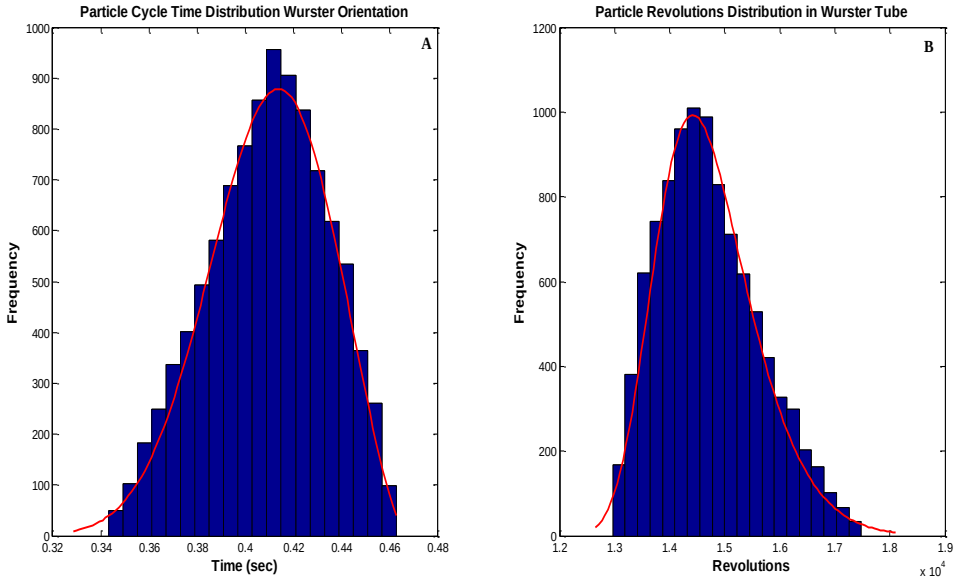

Figure 7.21 A) Total Cycle Time Distribution B) Particle Revolutions Distribution

In addition the number of particle revolutions for a coating operation in the Wurster orientation, shown as subplot B has a large range at 3000 revolutions.

Table 7.5 summarizes the calculated particle circulation time and number of revolutions during a Wurster orientation coating operation, with minimum, maximum, and average values for a particle size distribution consisting of 10000 values.

Table 7.5 Wurster Orientation Particle Circulation Time and Revolutions Summary

Run	Circulation Time [sec]			Revolutions		
	Min	Max	Average	Min	Max	Average
1	0.3432	0.4626	0.4092	12969	17841	14719
2	0.3421	0.4813	0.4169	12465	17539	14463
3	0.4744	0.5263	0.5024	12654	14038	13261
4	0.3427	0.4818	0.4168	12452	17507	14468
5	0.5066	0.5314	0.5221	16937	17767	17239
6	0.4830	0.5421	0.5147	11068	12422	11664
7	0.5630	0.5725	0.5700	10481	10658	10526
8	0.3428	0.4736	0.4133	16977	23452	19540
9	0.4834	0.5428	0.5152	11053	12413	11652
10	0.5894	0.6082	0.6014	9865	10180	9988
11	0.3439	0.4741	0.4147	16833	23205	19328
12	0.5992	0.6092	0.6068	9849	10013	9889
13	0.3467	0.4833	0.4202	12414	17308	14343

Table 7.5 Continued

14	0.5270	0.5631	0.5484	10656	11386	10943
15	0.4832	0.5424	0.5148	11062	12418	11662

As Table 7.5 shows, there is a larger range for the calculated particle circulation times in the Wurster orientation compared to the top spray orientation in Table 7.4. As noted previously, the reason for this is the difference in particle terminal velocities and the subsequent distance the particle travels once exiting the Wurster tube insert. The difference in circulation times translates into each particle having a unique number of revolutions in the same coating operation time span. The range of revolutions varies from about 1000 revolutions to 5000 revolutions.

The most important segment of the total cycle time in the Wurster orientation is the amount of time the particles spend in the Wurster tube insert itself, because this is where the coating solution is sprayed. This segment of the total cycle time is the shortest part because the particle undergoes high acceleration rates to achieve high heat and mass transfer rates at pneumatic transport conditions. Figure 7.22 shows the total cycle time distribution and the Wurster tube insert time segment for Experiment 1 in Table 6.2.

The time spent in the Wurster tube insert represents about 7% of the total cycle time for Experiment 1 as shown in Figure 7.22. Table 7.6 summarizes the calculated Wurster tube time segment of the calculated total cycle time for each experiment listed in Table 6.2. As Table 7.6 shows, the calculated average Wurster tube time segment ranges from 5-8% of the total cycle time for this work.

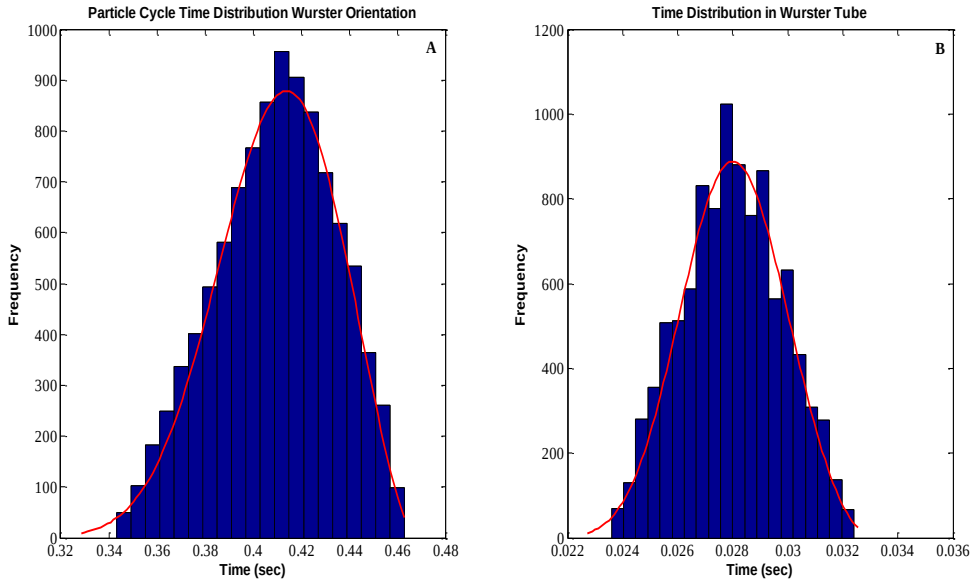

Figure 7.22 Wurster Orientation Particle Cycle Time Distribution and Wurster Tube Time Distribution

Table 7.6 Wurster Tube Time Segment of Total Cycle Time Summary

Run	Wurster Tube Time [sec]			Percent of Total Cycle Time [%]		
	Min	Max	Average	Min	Max	Average
1	0.0236	0.0324	0.0280	6.8765	7.0039	6.8426
2	0.0175	0.0240	0.0207	5.1155	4.9865	4.9652
3	0.0277	0.0323	0.0300	5.8395	6.1372	5.9713
4	0.0175	0.0240	0.0207	5.1065	4.9813	4.9664
5	0.0380	0.0452	0.0416	7.5010	8.5058	7.9678
6	0.0241	0.0284	0.0261	4.9896	5.2389	5.0709
7	0.0383	0.0445	0.0414	6.8028	7.7729	7.2632
8	0.0201	0.0276	0.0238	5.8635	5.8277	5.7585
9	0.0241	0.0282	0.0261	4.9855	5.1953	5.0660
10	0.0333	0.0386	0.0359	5.6498	6.3466	5.9694
11	0.0202	0.0276	0.0239	5.8738	5.8216	5.7632
12	0.0388	0.0459	0.0424	6.4753	7.5344	6.9874
13	0.0177	0.0241	0.0209	5.1053	4.9866	4.9738
14	0.0324	0.0383	0.0354	6.1480	6.8016	6.4551
15	0.0241	0.0281	0.0261	4.9876	5.1807	5.0699

The particle circulation rate and revolutions distributions are the last initial distributions needed for the coating growth models. The next parameters to calculate are the probability of a

particle being in the spray area and the probability a particle is coated in the spray area, along with the number of times each event occurs during the total number of revolutions made during the coating segment of a fluidized bed operation.

7.3.4 Number of Times a Particle is in the Spray Area and the Number of Times a Particle is Coated in the Spray Area

The number of times a particle is in the spray area and the number of times a particle is coated in the spray area is a function of the liquid atomization conditions, the fluidized bed operating conditions, the nozzle geometry, and the fluidized bed geometry. A large spray area in either spray orientation increases the probability that a particle will be hit with coating solution a sufficient number of times to achieve the desired coating thickness.

For this work a full cone nozzle was employed to atomize the coating solutions. Figure 7.23 shows the surface areas of the fluidized bed in the top spray and Wurster orientations as well as the full cone surface area of atomized coating solution. As subplot A of Figure 7.23 shows, the surface area of the top spray orientation fluidized bed increases as the bowl height increases. In this orientation, the spray cone increases in surface area as the atomized droplets travel further from the nozzle, which explains why highest spray cone surface area is at the bottom of the fluidized bed. For the Wurster orientation as shown in subplot B, the Wurster insert has the same diameter at every height, and again the spray cone surface area increases as the atomized droplets travel further away from the nozzle.

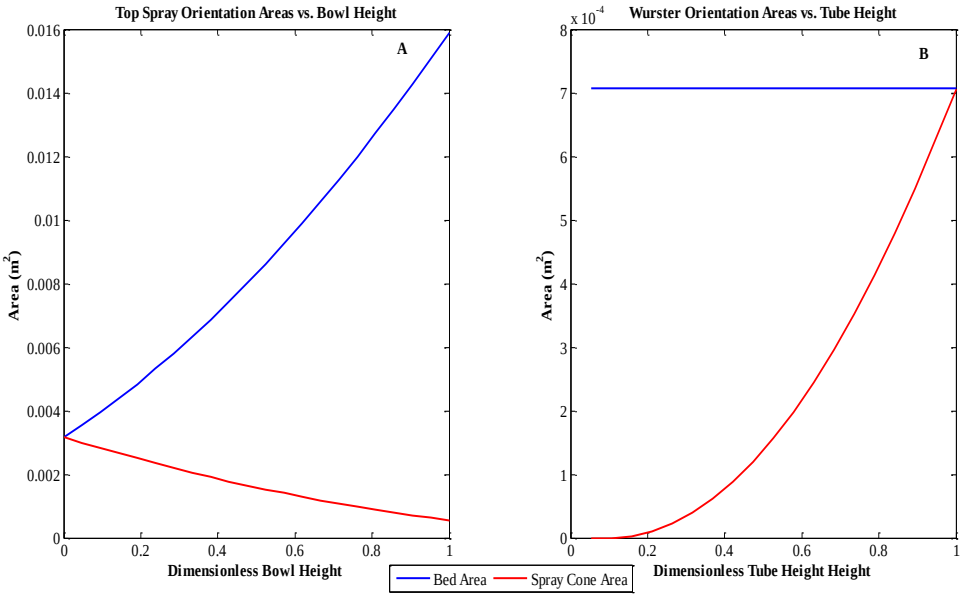

Figure 7.23 Fluidized Bed and Spray Cone Areas of A) Top Spray Orientation B) Wurster Orientation Fluidized Bed

With the data provided for both fluidized bed orientations, the probability a particle is in the spray cone area is the ratio of the spray cone area to the fluidized bed area as shown in Figure 7.24. As subplot A shows, the probability a particle is in the spray cone area decreases with the fluidized bed height, going from almost 100% at the bottom of the fluidized bed to about 3.5% at the top of the fluidized bed. The Wurster orientation in subplot B displays the opposite behavior of the top spray orientation with regards to this probability calculation. The probability a particle is in the spray cone area of a Wurster orientation increases as the distance from the nozzle increases. The reason for a 0% probability until a 0.2 dimensionless tube height is because the nozzle extends this far into the Wurster tube insert – this gap between the nozzle and Wurster tube insert can be and was adjusted for experiments.

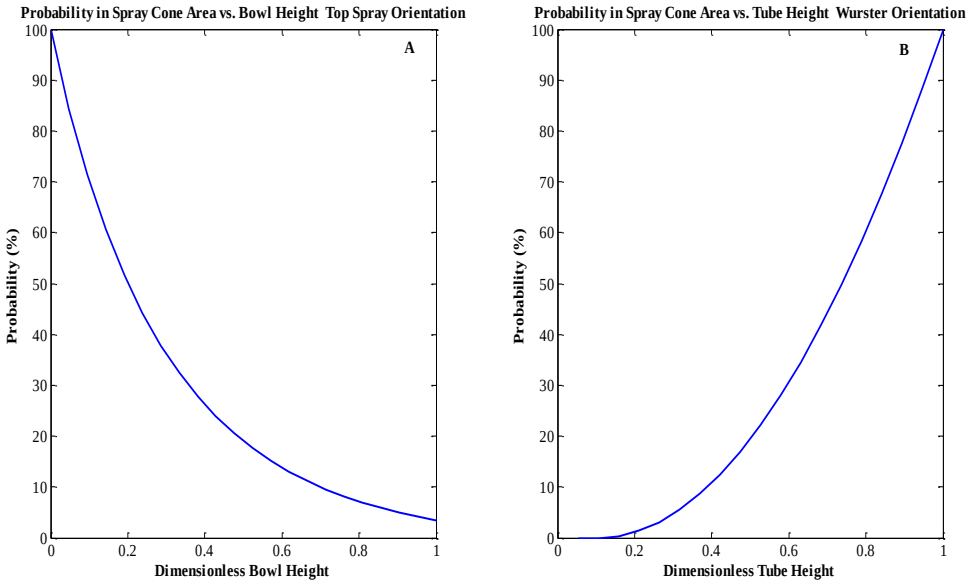

Figure 7.24 Probability a Particle Is In The Spray Cone Area in A) Top Spray Orientation B) Wurster Orientation

One inherent assumption in Figures 7.23 and 7.24 is that the spray cone extends through the entire height of the fluidized bed or the Wurster tube insert. In the case of top spray orientation, the spray cone will only extend to the distance where the nozzle velocity is larger than the fluidization velocity. Maintaining a sufficient positive relative velocity between the atomization nozzle and the fluidization air for the full distance between the nozzle tip and the distributor plate can be problematic because the large velocity differential at the top of the fluidized bed can alter fluidization characteristics and create the potential for over-wetting and wet quenching. To avoid this potential problem, the atomization velocities were kept at no higher than about 1 m/s higher than the inlet fluidization velocity.

In the case of the Wurster orientation, droplets evaporate as they travel co-currently with the fluidization air at a high velocity. The high velocity within the Wurster tube insert promotes high heat and mass transfer rates for evaporation. Typically, all the atomized droplets have evaporated regardless of whether there has been a collision with a particle inside the Wurster

tube before having an opportunity to exit the Wurster tube. The droplet lifetime is a function of the droplet properties (density, diameter, dry matter content, heat of vaporization, specific heat capacity, temperature, vapor pressure, etc.) and the fluidization air properties (absolute humidity, density, specific heat capacity, thermal conductivity, velocity, viscosity, etc.) . Once the droplet lifetime is calculated, the actual size of the spray cone area can be calculated as outlined previously in Section 4.2.2. Another aspect not addressed in Figures 7.23 and 7.24 is gravity. The effects of gravity decreasing the spray cone area will be shown later as part of the sensitivity analysis.

The probability that a particle is coated in the spray cone area is calculated according to Equations 4.83 and 4.89 in Chapter 4. Figure 7.25 shows the probability that a particle is coated in the spray cone area for the top spray and Wurster orientation as a function of dimensionless bed or tube height.

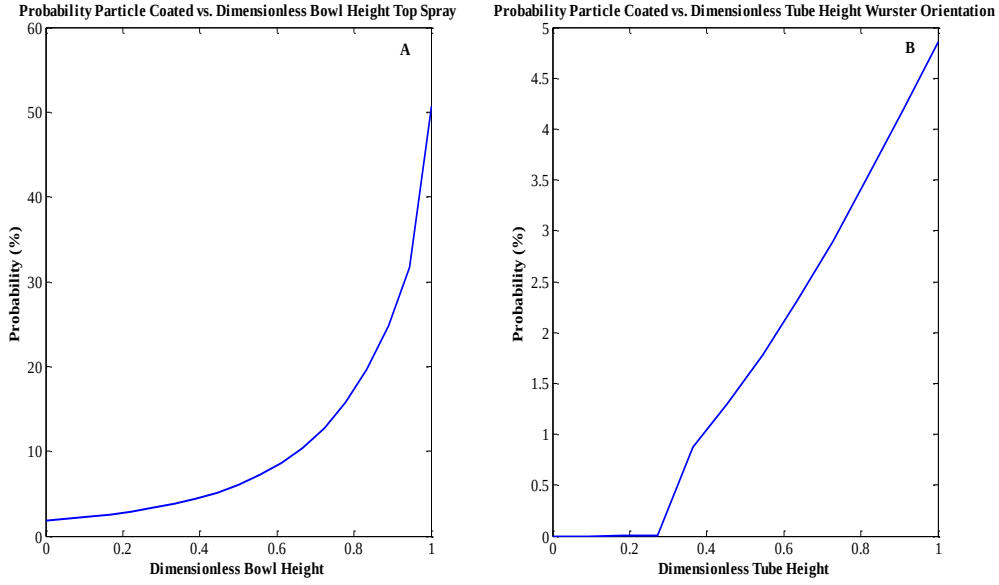

Figure 7.25 Probability a Particle is Coated in Spray Cone Area for A) Top Spray Orientation B) Wurster Orientation

As subplot A in Figure 7.25 shows, the probability a particle is coated in the top spray orientation (Experiment 2) is lowest near the distributor plate at about 2% and highest at its closest point to the atomization nozzle at about 51%. The reasons for this are as follows: 1) the spray cone area is smaller at the top of the fluidized bed compared to the bottom of the fluidized bed 2) there are more atomized liquid droplets available at the top of the fluidized bed compared to the bottom of the fluidized bed because particle-droplet collisions have not occurred yet to remove them from the spray cone area.

The probability that a particle is coated in the Wurster orientation (Experiment 1) shown in subplot B, is a much lower magnitude compared the top spray orientation, with a maximum value of about 5%. There are a couple reasons for this difference: 1) a smaller spray cone area development due to the nozzle placement at the distributor plate and the co-current flow of fluidization air and the atomized droplets translate to a shorter liquid droplet lifetime due to high heat and mass transfer rates. Tables 7.7 and 7.8 summarize the average number of times a particle is in the spray cone area and the number of times a particle is coated in the spray cone area. A sensitivity analysis investigating the impact of parameter choice on the probability a particle is coated will be discussed later.

The next step in the calculation of the coating growth is the determination of whether the fluidized bed operation is in the agglomeration regime or the coating regime via dimensionless number calculations, in particular the viscous Stokes number.

Table 7.7 Top Spray Orientation Calculated Average Number of Times in Spray Cone Area, Coated in Spray Cone Area

Run	CCV	TNTA	Times in Spray Cone Area	PISA [%]	Times Coated in Spray Cone Area	CISA [%]	Overall Percentage [%]
1	16	225184	82639	36.698	3718	4.499	1.651
2	19	125818	38883	30.904	1650	4.243	1.311
3	16	492480	180733	36.699	7074	3.914	1.436
4	22	142340	39557	27.791	1523	3.850	1.070
5	18	240120	79410	33.071	3765	4.741	1.568
6	16	233152	85564	36.699	3475	4.061	1.490
7	19	129732	41003	31.606	1585	3.866	1.222
8	16	118656	44534	37.532	1784	4.006	1.531
9	21	257124	74509	28.978	3309	4.441	1.287
10	17	151912	52638	34.650	2031	3.858	1.337
11	22	129008	35852	27.791	1457	4.064	1.129
12	16	262752	96426	36.699	3730	3.868	1.420
13	18	135180	44705	33.071	1990	4.451	1.472
14	16	164896	60515	36.699	2510	4.148	1.522
15	18	248796	81160	32.621	3750	4.621	1.507

** CCV: Number of Coating Control Volumes TNTA: Total Number of Times Available PISA: Times in Spray Cone Area Divided by TNTA CISA: Times Coated in the Spray Cone Area Divided by Times in Spray Cone Area

Table 7.8 Wurster Orientation Calculated Average Number of Times in Spray Cone Area, Coated in Spray Cone Area

Run	CCV	TNTA	Times in Spray Cone Area	PISA [%]	Times Coated in Spray Cone Area	CISA [%]	Overall Percentage [%]
1	10	141790	18859	13.300	1309	6.941	0.923
2	12	173556	19236	11.083	1311	6.815	0.755
3	14	185654	46498	25.046	4042	8.693	2.177
4	12	173616	32488	18.713	2434	7.492	1.402
5	7	120673	8338	6.910	1537	18.433	1.274
6	10	116640	15513	13.300	1620	10.442	1.389
7	12	126312	23634	18.711	3081	13.036	2.439
8	14	273560	68516	25.046	4770	6.962	1.744
9	14	163128	40855	25.045	3540	8.665	2.170
10	10	99880	13285	13.301	1912	14.392	1.914
11	12	231936	43400	18.713	2992	6.894	1.290
12	10	98890	13152	13.300	2232	16.971	2.257
13	16	229488	74127	32.301	4423	5.967	1.927
14	9	98487	10773	10.938	1426	13.237	1.448
15	13	151606	32995	21.763	2963	8.980	1.954

** CCV: Number of Coating Control Volumes TNTA: Total Number of Times Available PISA: Times in Spray Cone Area Divided by TNTA CISA: Times Coated in the Spray Cone Area Divided by Times in Spray Cone Area

7.3.5 Stokes Number Distribution

The dimensionless viscous Stokes number was used as the primary indicator of whether a fluidized bed operation was in the coating regime or agglomeration regime. If the Stokes number is above a critical value, the fluidized bed operation is said to be in the coating regime. Otherwise, if the Stokes number is below this critical value, the fluidized bed operation is said to be in the agglomeration regime. With the current status of fluidized bed particle coating and agglomeration modeling, there is no dimensionless number formulation that can predict the extent of agglomeration for a set of operating conditions.

The Stokes number for a fluidized bed operation becomes a distribution of values when applied to a particle size distribution. In addition, the Stokes number changes as a function of bed height due to the geometry of the fluidized bed and fluidization gas hydrodynamics. Figure 7.26 shows the Stokes number distribution for top spray experiment 2. The lowest values for the Stokes number occur at the top of the fluidized bed where the bubble velocity is at its lowest magnitude.

While Figure 7.26 shows how the Stokes number has a distribution of values, Figure 7.27 shows how the minimum, maximum, and mean values for the Stokes number change as a function of fluidized bed height for top spray experiment 2. All three values for the Stokes number decrease with increasing fluidized bed height for the reason mentioned previously. One additional factor that can be ascertained from Figure 7.27 is where in the bed agglomeration takes place (if at all) once the critical Stokes number is known and will be shown shortly.

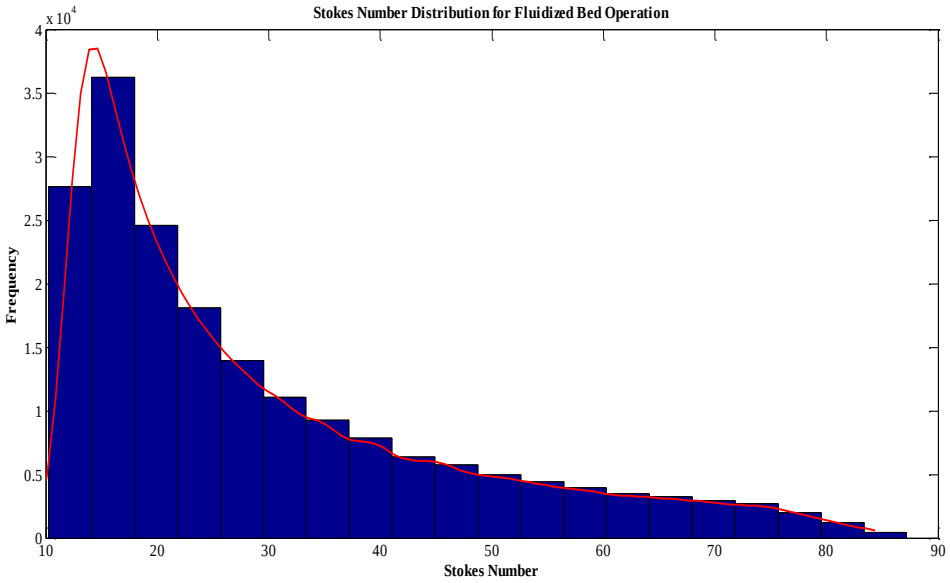

Figure 7.26 Stokes Number Distribution for Top Spray Experiment 2

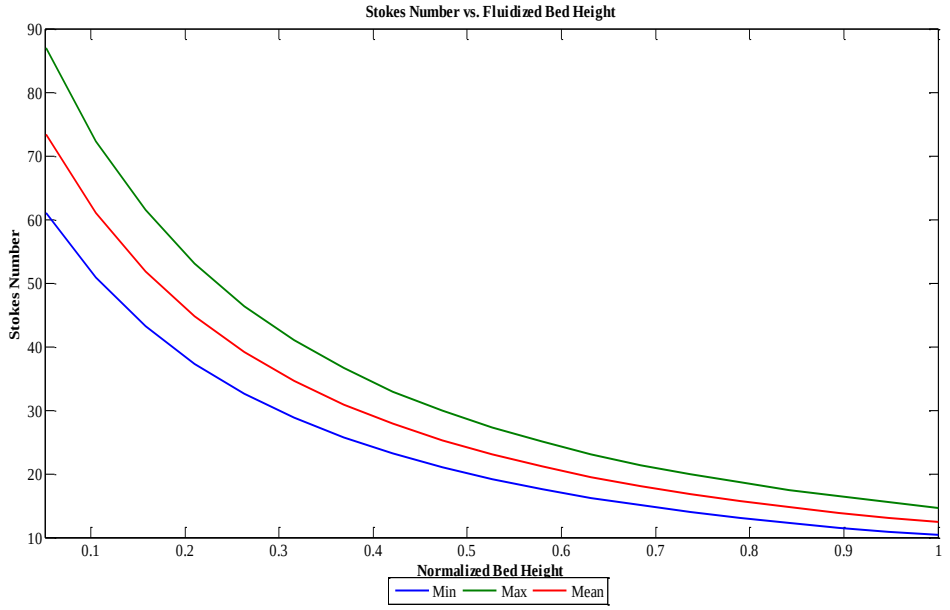

Figure 7.27 Stokes Number as a Function of Fluidized Bed Height for Top Spray Experiment 2

With the Stokes number behavior mapped out in Figure 7.27, next the critical Stokes number is calculated. The critical Stokes number is a function of particle properties (diameter and asperity size), liquid droplet properties (liquid-solid contact angle, surface tension, viscosity, and diameter) and the coefficient of restitution as noted in Chapter 2. The difficulty with this

relationship is the accurate prediction of the coefficient of restitution. For this work a value of 0.9 was used as the coefficient of restitution.

Figure 7.28 shows how the liquid-solid contact angle impacts the critical Stokes number. As the contact angle increases the liquid droplet height from the particle surface increases as well. This increased distance from the particle surface provides a means for a greater damping effect when particles collide, thus leading to particle agglomeration. As Figure 7.28 shows, the critical Stokes number ranges from about 6 to 9. The critical Stokes number does change during the coating operation however, this change is minimal because the critical Stokes number calculation involves the natural logarithm function. For example, let a 200 micron particle have a critical Stokes number of 3.4. A 200 micron particle with a 2.5 micron thick coating has a critical Stokes number of 3.35 using the same droplet diameter and liquid-solid contact angle for a -1.53% difference.

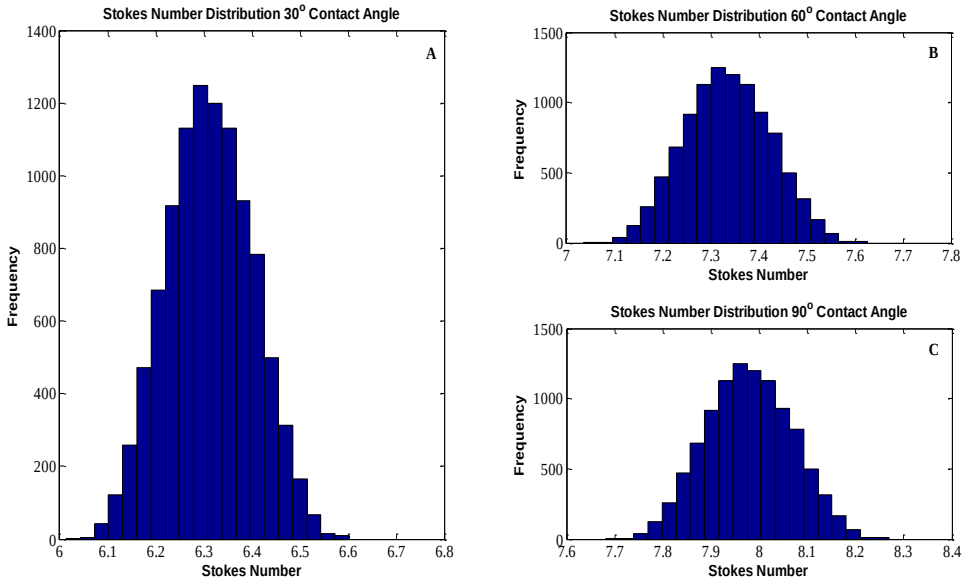

Figure 7.28 Critical Stokes Number Distribution as a Function of Liquid-Solid Contact Angle for Top Spray Experiment 2: A) 30° Contact Angle B) 60° Contact Angle C) 90° Contact Angle

The Stokes number calculation from Figure 7.27 can now be revisited with the critical Stokes number determined. Figure 7.29 shows the Stokes number as a function of fluidized bed height with the addition of the critical Stokes numbers from Figure 7.28 included. As can be seen in Figure 7.29, the only region where the Stokes number and the critical Stokes number are equivalent is at the top of the fluidized bed. Since the bubble velocity is highest at the distributor plate, the Stokes number is also at a maximum at the distributor plate as well. Another important detail from Figure 7.29 is that if any particle agglomeration were to occur, it would occur with particle-particle collisions at the top of the fluidized bed. Similar behavior is observed for the remaining experiments in the top spray orientation.

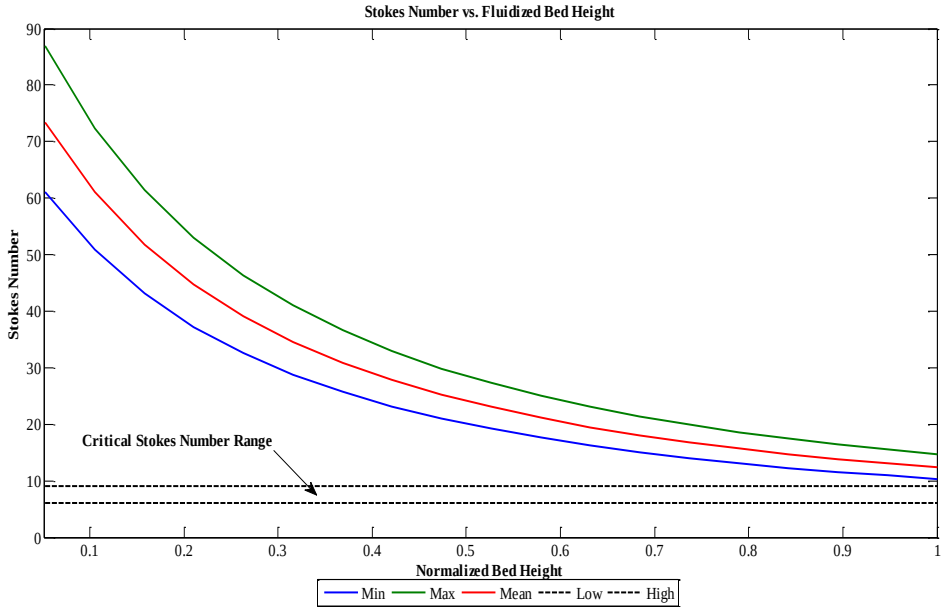

Figure 7.29 Critical Stokes Number Range and Fluidized Bed Stokes Number as a Function of Fluidized Bed Height for Top Spray Experiment 2

In the case of the Wurster orientation, the Stokes number is at a minimum at the bottom of the Wurster insert and increases with height as shown in Figure 7.30. The critical Stokes number distribution for the Wurster orientation is similar to that of the top spray orientation presented in Figure 7.29, ranging from about 6 to 9 in magnitude. Figure 7.31 shows how the

Stokes number for the Wurster orientation is above the critical Stokes number range for the entire length of the Wurster insert. This means that there should be no particle agglomeration present in the final product.

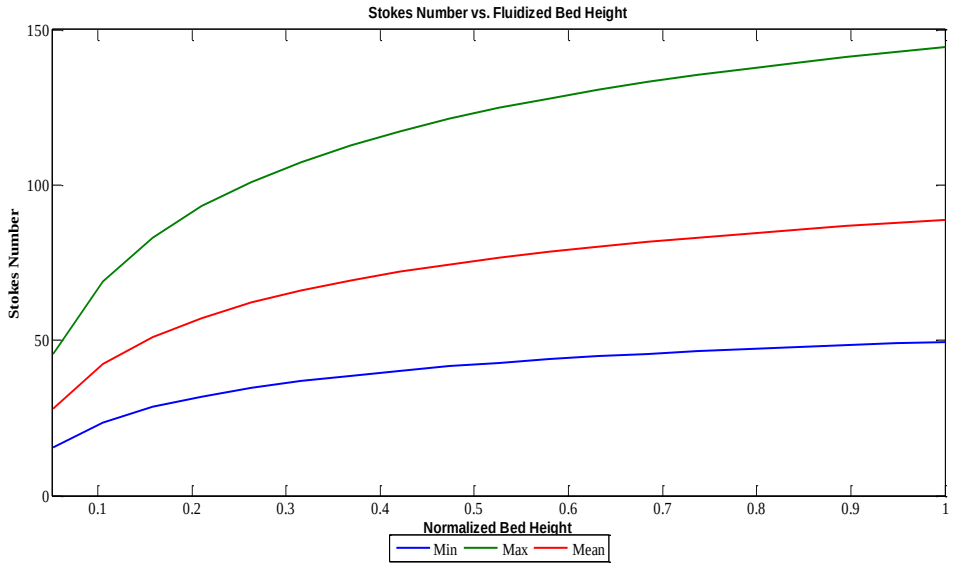

Figure 7.30 Stokes Number as a Function of Fluidized Bed Height for Wurster Orientation Experiment 1

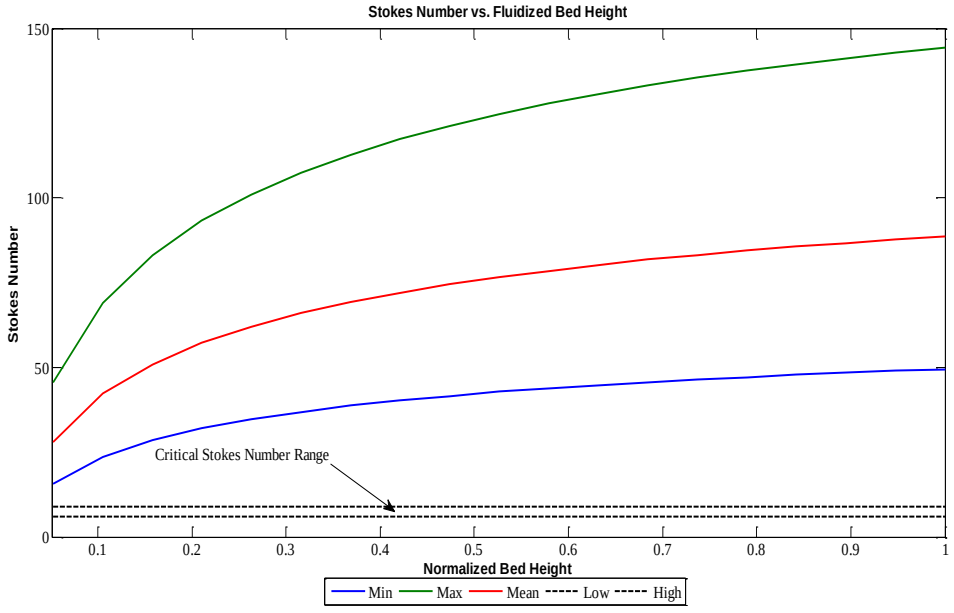

Figure 7.31 Critical Stokes Number Range and Fluidized Bed Stokes Number as a Function of Fluidized Bed Height for Top Spray Experiment 2

The trends presented for the Stokes number and the critical Stokes number presented in Figures 7.26-7.31 are similar for the remaining fluidized bed experiments in the top spray and Wurster orientations respectively.

In addition to the dimensionless Stokes number there are other dimensionless numbers, namely the dimensionless spray flux and the flow number, to aid in the determination of whether a fluidized bed operation is in the coating regime or agglomeration regime. The dimensionless spray flux and the flux number will be discussed next.

7.3.6 Other Dimensionless Number Distributions – Dimensionless Spray Flux and Flux Number

As noted in Chapter 2, a great deal of work has been put forth to find other dimensionless numbers to aid in the determination of whether a fluidized bed operation will result in particle coating or agglomeration. The dimensionless spray flux was initially developed for particle agglomeration operations, but still has merit with regards to describing particle coating operations as well.

Figure 7.32 shows the dimensionless spray flux distribution for experiment 2 of the top spray orientation.

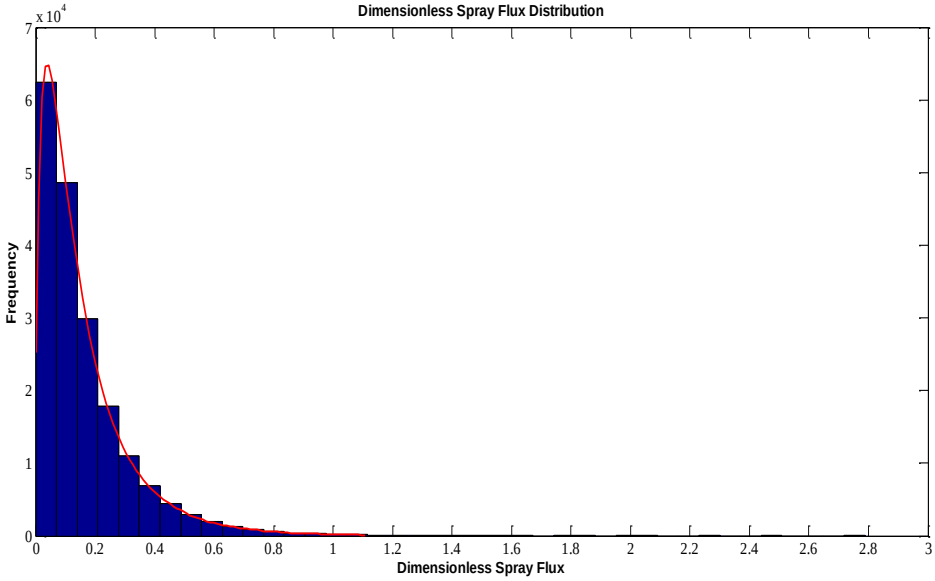

Figure 7.32 Dimensionless Spray Flux Distribution for Top Spray Experiment 2

As Figure 7.32 shows, the majority of the distribution is tailed to values around 0.2. Values below 0.1 translate to fluidized bed operation governed by a droplet controlled regime, meaning there is little to no droplet overlap leading to saturation of the particle surface with coating solution. Values between 0.1 and 1 fall into the intermediate regime, some droplet overlapping may occur, potentially leading to agglomeration. Values above 1, mean there is droplet overlapping, and the particle surface gets saturated with coating solution. Saturation of the particle surface can lead to particle agglomeration and potential defluidization as the particle weight cannot be overcome by drag and the buoyant force provided by the fluidization air. However, as noted before the extent of agglomeration cannot be ascertained from the dimensionless number analysis.

Similarly to the Stokes number, the average dimensionless spray flux changes as a function of fluidized bed height which is shown in Figure 7.33. Unlike the Stokes number, the dimensionless spray flux increases with the height of the fluidized bed. The reason for this trend is because in the top spray orientation, the spray cone area is the smallest at the top of the

fluidized bed. Values for the average dimensionless spray flux range from about 0.08 to 0.32 which falls into the droplet controlled and intermediate regimes respectively.

The dimensionless spray flux for the Wurster orientation is slightly different because the nozzle is placed at the bottom of the fluidized bed. Figure 7.34 shows how the average dimensionless spray flux changes in the Wurster orientation. The average dimensionless spray flux for the Wurster orientation is four orders of magnitude higher than that of the top spray orientation. The average dimensionless spray flux values are at a maximum at the bottom of the bed because the spray area is smallest right after the nozzle exit. Despite the very large values for the average dimensionless spray flux, the Wurster orientation experiments resulted in coated particles with little or no agglomeration at all.

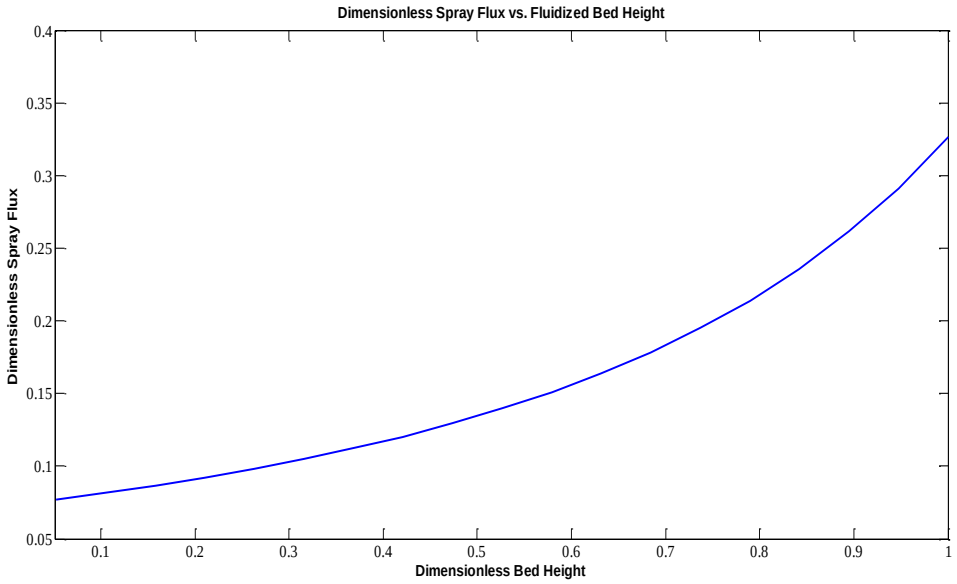

Figure 7.33 Average Dimensionless Spray Flux vs. Dimensionless Fluidized Bed Height for Top Spray Experiment 2

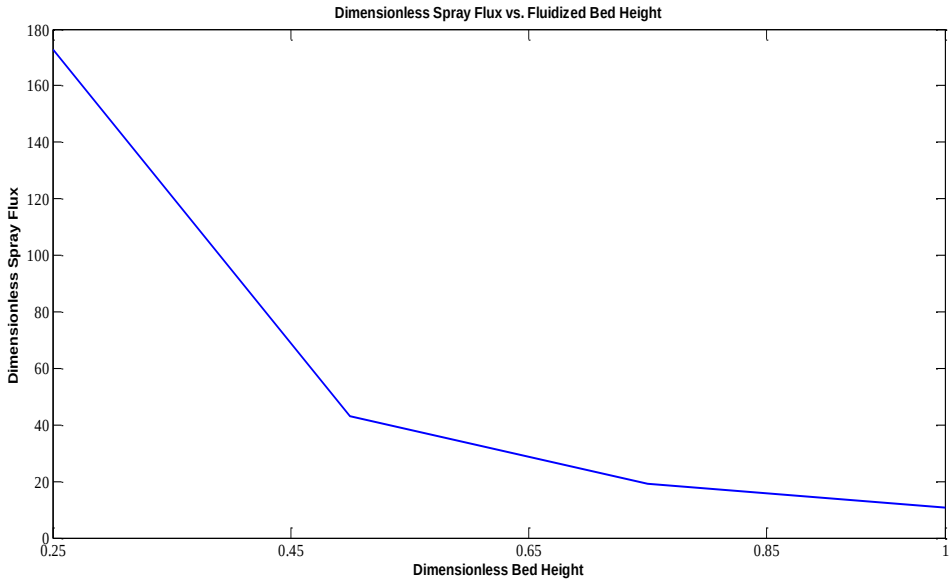

Figure 7.34 Average Dimensionless Spray Flux vs. Dimensionless Fluidized Bed Height for Wurster Experiment 1

While the dimensionless spray flux does provide some insight into whether a set of fluidized bed operating conditions will lead to particle coating or particle agglomeration, there is still fundamental work that needs to be done regarding clear demarcations where the coating and agglomeration regime boundaries are. For this reason, in addition to the calculations done for the top spray and Wurster orientations, the dimensionless spray flux was used as a secondary means of numerical confirmation that operating conditions were in the particle coating regime and not the particle agglomeration regime. The dimensionless spray flux trends for the remaining top spray and Wurster orientation fluidized bed experiments are similar to those shown in Figures 7.33 and 7.34.

In addition to the Stokes number and the dimensionless spray flux, another dimensionless number was used to determine whether the fluidized bed experiment would be in the coating regime or agglomeration regime, the flux number. The flux number takes into account the excess fluidization velocity, the amount of liquid added, the spray area, and the particle density.

Neither the particle size nor particle size distribution are a factor in the flux number calculation. Figure 7.35 shows the flux number for top spray experiment 2 and Wurster orientation experiment 1 as a function of fluidized bed height.

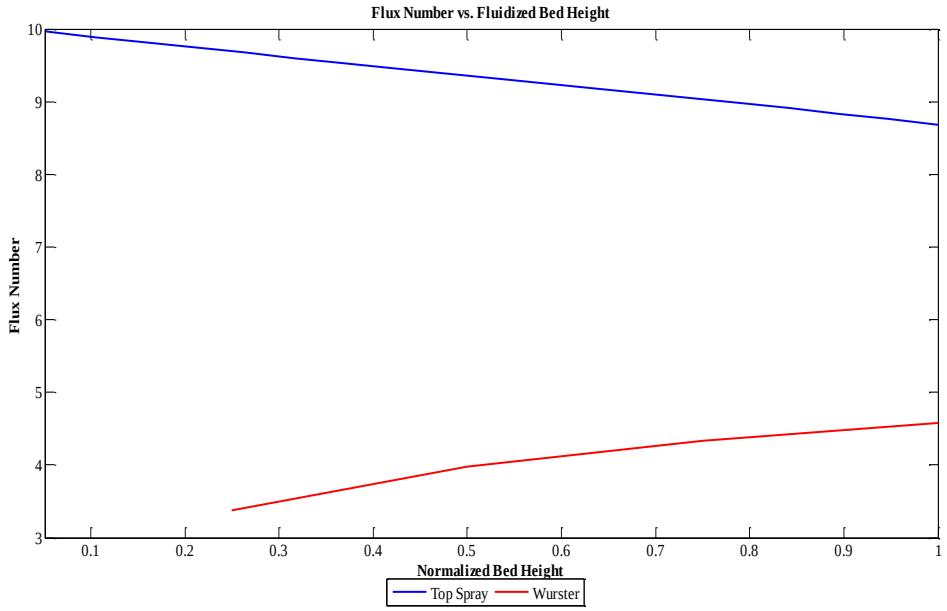

Figure 7.35 Average Flux Number vs. Dimensionless Fluidized Bed Height

In the case of the top spray, the flux number decreases with increasing fluidized bed height due to a reduction in the excess fluidization velocity. Conversely, in the Wurster orientation, the flux number increases with increasing fluidized bed height because of the increasing spray area. Values for each orientation are above those named by Akkermanns to ensure that the fluidized bed operation is in the coating regime and not the agglomeration regime, above 3.5. The trends for the other top spray and Wurster orientation experiments are similar to those presented in Figure 7.35.

As noted previously, the dimensionless number demarcation between the agglomeration regime and the coating regime is not completely mapped out. Multiple dimensionless numbers have been developed in the attempt to make this distinction clear with some promising results. For this reason, the combination of the Stokes number, dimensionless spray flux, and flux

number were used in the calculations to determine that particle coating was the dominant phenomenon for the coating experiments, not agglomeration. The next step, calculating the coating efficiency of the fluidized bed operation, will be discussed next.

7.4 Coating Efficiency as Determined by the Coating Growth Kinetics Model

Recall from Figure 7.1, one of the outputs from the coating growth kinetics model developed for this work is the coating efficiency of the fluidized bed operation. The coating efficiency is determined mathematically by Equation 4.88 in Chapter 4 with the aid of post coating experiment analysis via calorimetry and UV/Vis absorbance. Tables 7.9 and 7.10 show the coating efficiencies for the top spray and Wurster orientation experiments listed in Tables 6.1 and 6.2.

Table 7.9 Top Spray Coating Efficiency

Run	ΔH_{mix} [J]	UV/Vis Absorbance	Coating Efficiency [%]		Model Calculated CE [%]	% Difference	
			Calor	UV/Vis		Calor	UV/Vis
1	129.45	0.32655	62.4	63.8	69.2	10.9	8.5
2	128.75	0.32591	67.9	70.2	80.8	19.0	15.1
3	129.98	0.32718	58.2	58.6	64.6	11.0	10.2
4	128.43	0.32584	70.4	69.5	86.1	22.3	23.9
5	129.31	0.32663	63.5	64.3	78.9	24.2	22.7
6	130.22	0.32788	53.6	55.6	65.9	22.9	18.5
7	129.65	0.32721	60.8	61.6	72.1	18.6	17.0
8	129.28	0.32642	63.8	64.3	71.9	12.7	10.6
9	128.57	0.32630	69.4	71.6	84.3	21.5	17.7
10	130.08	0.32770	57.4	58.9	68.8	19.9	16.8
11	128.70	0.32638	68.3	65.7	88.8	30.0	35.2
12	129.90	0.32728	58.9	58.1	69.5	18.0	19.6
13	129.07	0.32655	65.4	62.6	79.8	22.0	27.4
14	129.61	0.32700	61.1	60.0	70.5	15.4	17.5
15	128.62	0.32623	69.0	72.5	79.4	15.1	9.5

Table 7.10 Wurster Spray Coating Efficiency

Run	ΔH_{mix} [J]	UV/Vis Absorbance	Coating Efficiency [%]		Model Calculated CE [%]	% Difference	
			Calor	UV/Vis		Calor	UV/Vis
1	131.69	0.32912	45.0	43.1	51.7	14.9	20.0
2	132.32	0.32941	40.1	40.6	47.8	19.2	17.7
3	131.32	0.32859	47.8	47.6	53.7	12.3	12.8
4	131.90	0.32883	43.4	45.5	48.1	10.8	5.7
5	130.42	0.32749	54.8	57.0	65.0	18.6	14.0
6	130.20	0.32724	56.5	59.2	63.4	12.2	6.6
7	130.33	0.32791	55.5	53.3	68.0	22.5	27.6
8	132.52	0.32945	38.6	40.3	44.8	16.1	11.1
9	130.18	0.32760	56.7	56.1	66.3	16.9	18.2
10	128.70	0.32597	68.3	70.3	82.8	21.2	17.8
11	132.36	0.32929	39.9	41.6	45.0	12.8	8.2
12	128.32	0.32546	71.3	74.8	84.9	19.1	13.5
13	133.60	0.33045	30.4	32.0	36.6	20.4	14.4
14	129.49	0.32683	62.1	62.7	73.1	17.7	16.6
15	130.29	0.32783	55.8	54.1	68.4	22.6	26.4

As Tables 7.9 and 7.10 show, the 1-D discretized coating growth model developed in Chapter 4 consistently overestimates the coating efficiency of both the top spray (up to 35%) and Wurster orientation (up to 28%) fluidized bed coating operations. There are a few possible reasons for this deviation: 1) the lack of a spray drying term in the model 2) neglecting the impact of gravity on the evolution of the nozzle spray cone, thus overstating the spray area for both spray orientations and 3) the incorporation of too many coating control volumes into the model. Since the coating efficiency is overstated by the coating growth model, the coating thickness distribution for each experiment will be overstated as well. A sensitivity analysis will be presented later in the chapter to quantify the sensitivity of the coating efficiency calculation in the coating growth model, as well as the coating thickness distribution to the aforementioned factors along with other aspects.

In order to match the experimental coating efficiency determined by calorimetry and UV/Vis absorbance, a tunable parameter was incorporated into the calculations for coating efficiency. This tunable parameter will be discussed in the next section.

7.4.1 Tunable Parameter for Coating Efficiency

A tunable parameter was incorporated into the coating efficiency calculations to make the model coating efficiency match the experimental coating efficiency. This was done for both the top spray and Wurster orientations for the calorimetry and UV/Vis absorbance results. This tunable parameter was regressed for each experiment such that there was less than ±1% error between the experimental and model coating efficiencies. Tables 7.11 shows the regressed tunable parameter for the top spray experiments and the error between experimental coating efficiencies presented in Tables 7.9 and model coating efficiencies.

Table 7.11 Top Spray Experiments Coating Efficiency Tunable Parameter

Experiment	Calorimetry Results		UV/Vis Results	
	Tunable Parameter	Coating Efficiency % Difference	Tunable Parameter	Coating Efficiency % Difference
1	0.838621	0.00	0.868126	-0.10
2	0.702004	0.00	0.746610	0.01
3	0.848158	0.2	0.855496	-0.40
4	0.640000	0.09	0.625000	0.21
5	0.662696	0.01	0.676205	0.00
6	0.725425	0.00	0.765060	0.09
7	0.683000	-0.40	0.705000	0.25
8	0.746139	0.01	0.760000	0.34
9	0.653834	-0.01	0.693770	0.01
10	0.745242	0.20	0.773328	0.12
11	0.550000	0.15	0.510000	-0.31
12	0.759662	-0.44	0.745340	-0.41
13	0.689000	0.11	0.640000	0.04
14	0.784465	0.07	0.763453	0.11
15	0.753016	-0.77	0.827199	-0.70

As Table 7.11 shows, the tunable parameters are all below 1. This is because the model calculated coating efficiency is higher than the experimentally determined coating efficiency in every experiment. The addition of the tunable parameter to match the experimental coating efficiency leads to very low errors between the experiment and model coating efficiency, as the largest magnitude error is 0.77% difference.

Table 7.12 shows the tunable parameter for the Wurster orientation experiments and the error between the experimentally determined and model calculated coating efficiencies. Similarly to the top spray experiments the tunable parameter is below 1 for each experiment because the coating growth model calculated coating efficiency is higher than the experimentally determined coating efficiency. The largest magnitude error between experimental and model calculated coating efficiency is 0.32%.

Table 7.12 Wurster Orientation Experiments Coating Efficiency Tunable Parameter

Experiment	Calorimetry Results		UV/Vis Results	
	Tunable Parameter	Coating Efficiency % Difference	Tunable Parameter	Coating Efficiency % Difference
1	0.828222	-0.09	0.782196	-0.10
2	0.795719	-0.10	0.830790	-0.52
3	0.849895	-0.24	0.879341	-0.10
4	0.872935	-0.10	0.835981	-0.29
5	0.768249	0.00	0.715383	-0.01
6	0.837751	0.02	0.803152	-0.09
7	0.728312	-0.06	0.750403	0.07
8	0.826484	-0.32	0.832423	-0.29
9	0.778550	-0.02	0.784283	-0.02
10	0.504558	0.16	0.518330	-0.17
11	0.854431	-0.16	0.808072	-0.06
12	0.680853	-0.13	0.745341	-0.05
13	0.803037	-0.06	0.813416	-0.32
14	0.751029	-0.10	0.701842	-0.02
15	0.720091	-0.18	0.675097	-0.23

A regression analysis was to determine what factors play a role in determining the value of the tunable parameter for coating efficiency. The factors investigated for the tunable parameter regression include: experimental coating efficiency, average fluidized bed void fraction, the average liquid spray void fraction, and the height of the fluidized bed (via the number of control volumes used for the simulation). For the top spray orientation using the calorimetry data for experimental coating efficiency, the tunable parameter was found to be a function of all of the aforementioned variables as shown in Equation 7.1:

$$\text{Tunable Parameter} = \frac{\text{CE} - 0.29029}{77.65236\left(1-\frac{\varepsilon_{\text{bed, avg}}}{\varepsilon_{\text{spray, avg}}}\right)\text{CV}(\text{CV Height})} \tag{7.1}$$

where CE is is the experimental coating efficiency. The R^2 value for Equation 7.1 is 0.97821.

Using the UV/Vis data for top spray experimental coating efficiency, the tunable parameter was found to be a function of all of the aforementioned parameters as shown by Equation 7.2:

$$\text{Tunable Parameter} = \frac{\text{CE} - 0.29375}{76.88983\left(1-\frac{\varepsilon_{\text{bed, avg}}}{\varepsilon_{\text{spray, avg}}}\right)\text{CV}(\text{CV Height})} \tag{7.2}$$

The R^2 value for Equation 7.2 is 0.98432. Figure 7.36 shows the residual error for tunable parameter regression for both the calorimetry and UV/Vis absorbance data for the top spray orientation.

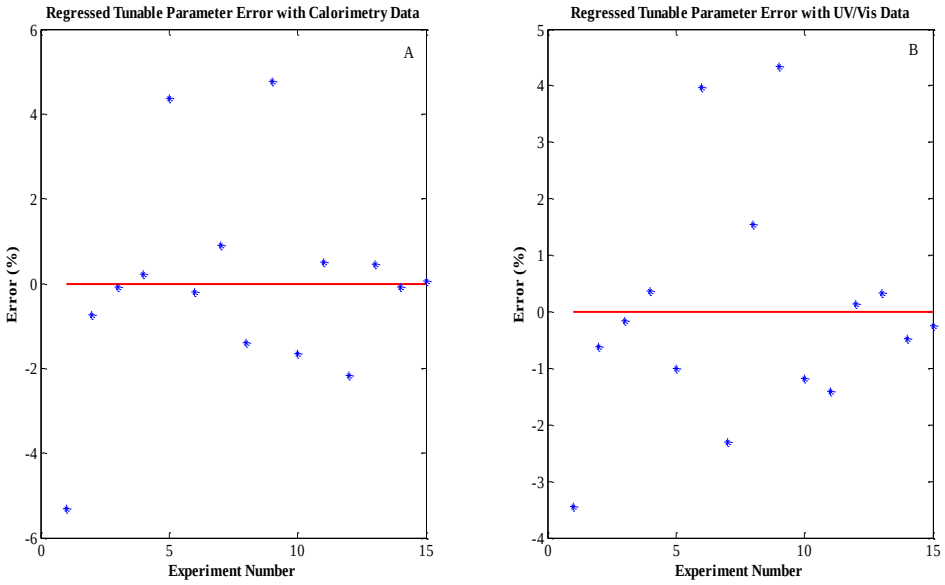

Figure 7.36 Regression Error for Coating Efficiency Tunable Parameter for Top Spray Experiments A) Based on Calorimetry Data B) Based on UV/Vis Data

Similarly for the Wurster orientation, the regressed equations for the tunable parameter using the calorimetry and UV/Vis data respectively are given by Equations 7.3 and 7.4:

$$\text{Tunable Parameter} = \left[\exp\left(\frac{\text{CE} - 2.34585}{0.31822}\right)\right]\left(1 - \frac{\varepsilon_{\text{bed, avg}}}{\varepsilon_{\text{spray, avg}}}\right)\text{CV(CV Height)} \qquad (7.3)$$

$$\text{Tunable Parameter} = \left[\exp\left(\frac{\text{CE} - 2.27258}{0.30503}\right)\right]\left(1 - \frac{\varepsilon_{\text{bed, avg}}}{\varepsilon_{\text{spray, avg}}}\right)\text{CV(CV Height)} \qquad (7.4)$$

The R^2 values for Equations 7.3 and 7.4 are 0.99847 and 0.97398 respectively. Linear regression attempts for the tunable parameter in the Wurster orientation resulted in lower R^2 values of 0.95970 and 0.88982. Figure 7.37 shows the residual error for tunable parameter regression for both the calorimetry and UV/Vis absorbance data for the Wurster orientation.

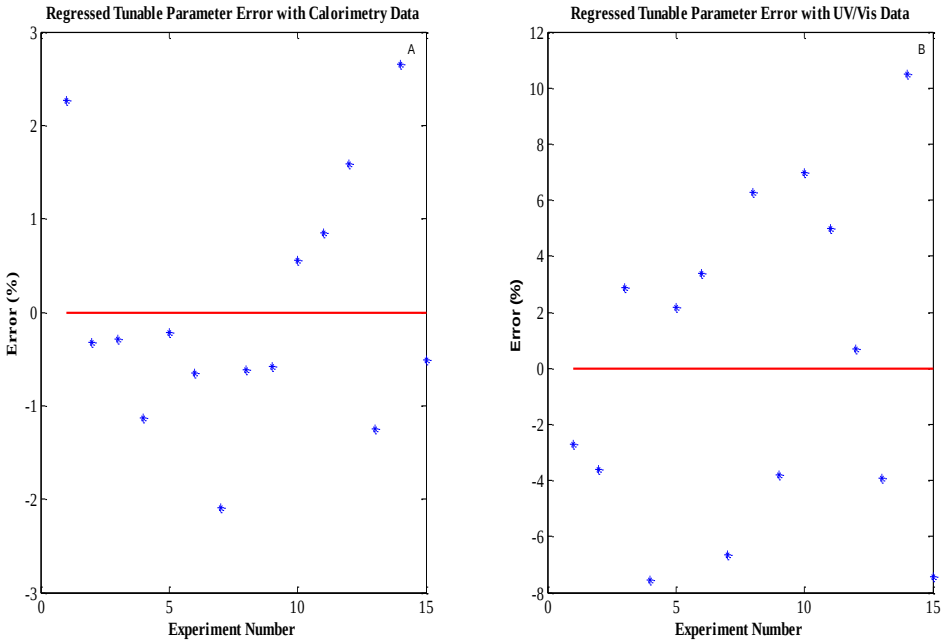

Figure 7.37 Regression Error for Coating Efficiency Tunable Parameter for Wurster Orientation Experiments A) Based on Calorimetry Data B) Based on UV/Vis Data

The highest residual error for the regressed tunable parameter of the top spray experiments is 5%. With regards to the Wurster orientation experiments the highest magnitude regression error is 10% for the UV/Vis data. Using an improper value for the tunable parameter will lead to a misrepresentation of the coating thickness distribution later on. Suggestions for determining the tunable parameter experimentally will be given in the next chapter.

With the tunable parameter tabulated, the coating growth kinetics model now predicts the correct coating efficiency for the fluidized bed operating conditions. The next step in the coating growth kinetics model is the calculation of the coating growth thickness for the particle size distributions of the coating experiments.

7.4.2 Coating Thickness Distribution as Determined by the Coating Growth Kinetics Model

With the confirmation via the Stokes number distribution calculated previously in section 7.3.5 that the coating operation is in the coating regime and not the agglomeration regime and the

tunable parameter from the previous section, calculations for the particle coating growth were carried out with the assumptions listed in Chapter 4.

Figures 7.38 and 7.39 show the calculated particle size distribution and coating thickness distribution for Experiment 2 of the top spray orientation using the calorimetry results. The trends shown in Figures 7.38 and 7.39 are the same for the calorimetry coating efficiency results and the UV/Vis coating efficiency results. As Figure 7.38 shows, the minimum particle size increases from about 360 microns in subplot A to just above 370 microns in subplot D. A Gaussian distribution was used to generate the initial particle size distribution in subplot A of Figure 7.38, and the Gaussian shape was maintained throughout the coating addition time due to the fluidized bed conditions employed for particle coating.

The coating thickness distribution, shown in Figure 7.39, is slightly left tailed early in the coating run, however the tailing effect diminishes with the longer run time for the coating operation. The coating thickness distribution range increases from about 0.5 microns in subplot B to about 1.5 microns in subplot D at the end of the coating run. The reason for this increase in the range of coating thickness values is due to the randomness of being in the spray cone area and being coated in the spray cone area. Another reason for the increased range of coating thickness values is the particle size distribution itself. Smaller particles have a lower surface area to cover with coating than larger particles, so for the same amount of coating material applied to both, the larger particle will have a thinner coating thickness than the smaller particle.

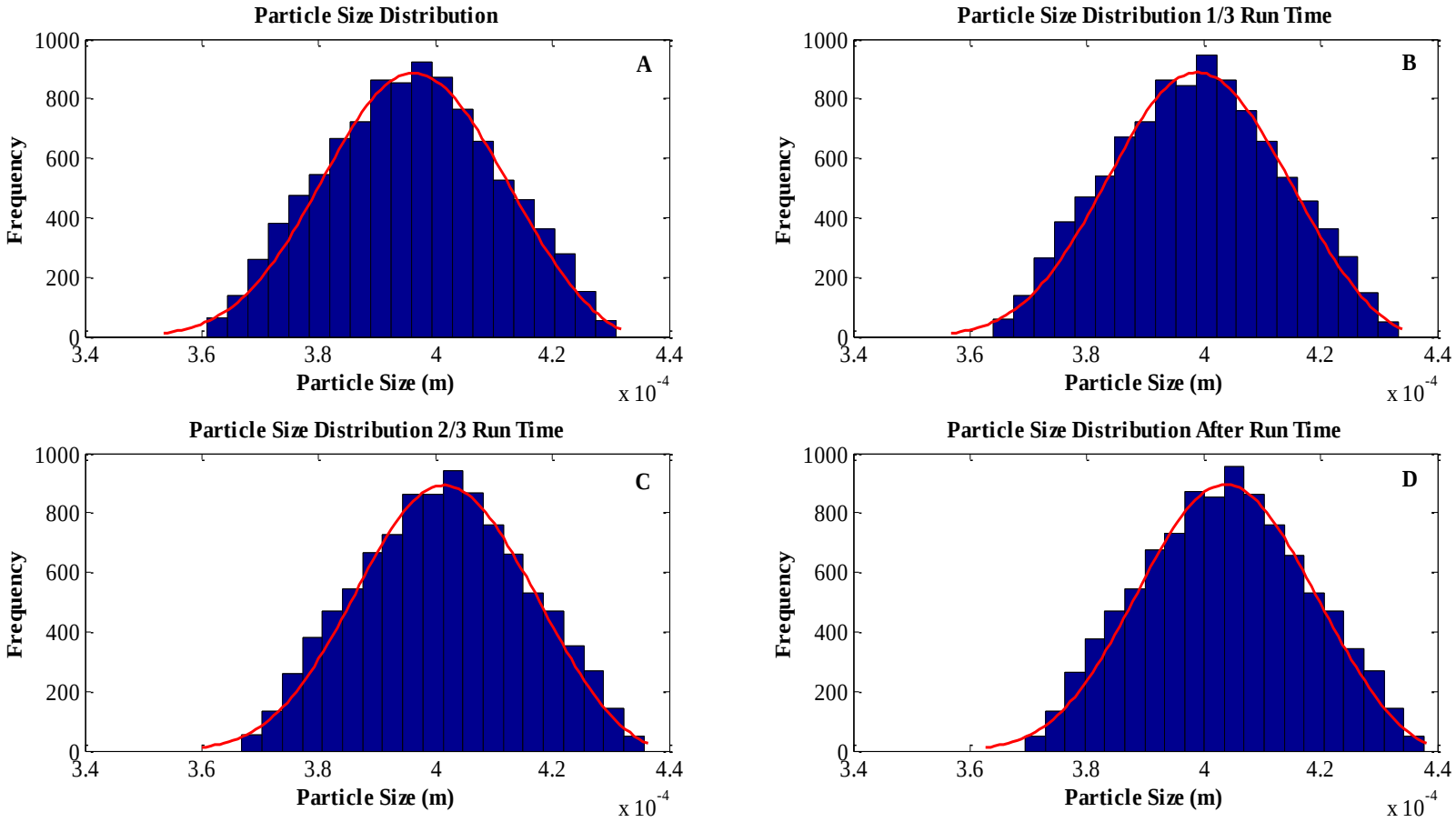

Figure 7.38 Calculated Particle Size Distribution Snapshots for Top Spray Experiment Two with Calorimetry Results: A) Beginning Particle Size Distribution B) Particle Size Distribution After 1/3 Coating Addition Time C) Particle Size Distribution After 2/3 Coating Addition Time D) Particle Size Distribution at End of Coating Addition Time

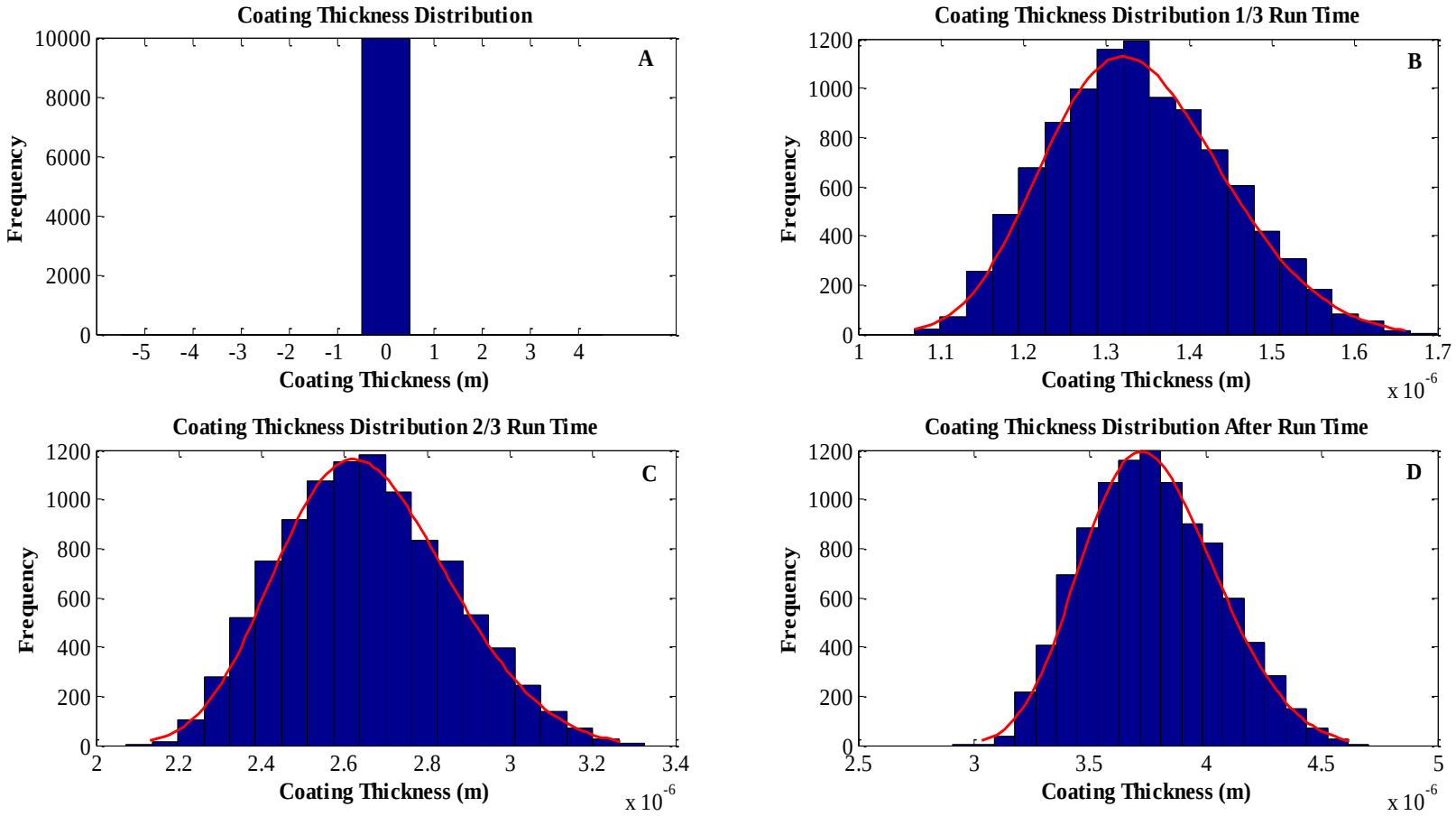

Figure 7.39 Calculated Coating Thickness Distribution Snapshots for Top Spray Experiment Two with Calorimetry Results: A) Beginning Coating Thickness Distribution B) Coating Thickness Distribution After 1/3 Coating Addition Time C) Coating Thickness Distribution After 2/3 Coating Addition Time D) Coating Thickness Distribution at End of Coating Addition Time

While Figure 7.39 shows how the coating thickness distribution changes with the run time, Figure 7.40 shows how the average coating thickness changes with time. The coating growth trend is linear in Figure 7.40 because the fluidization and coating solution atomization conditions are kept constant for the duration of the coating operation.

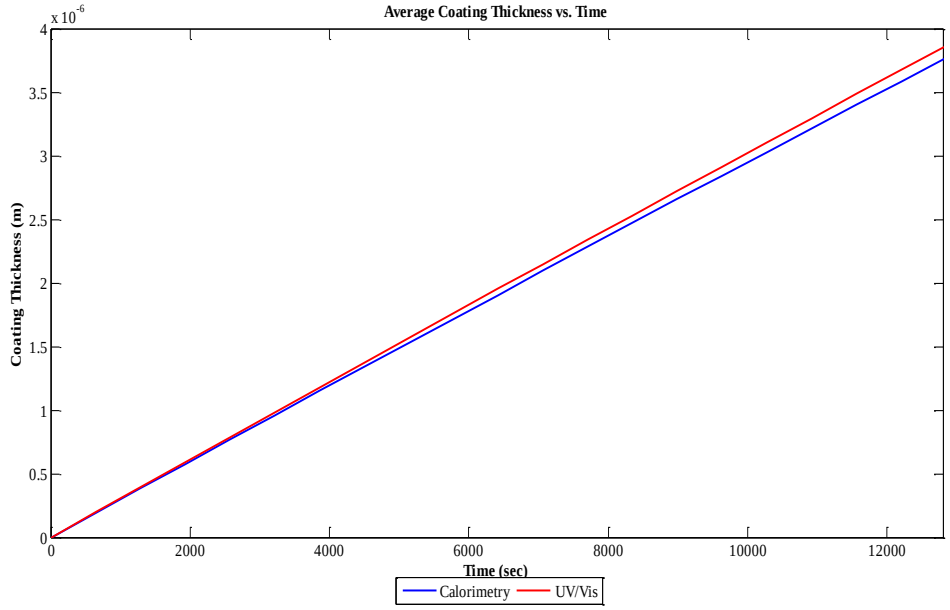

Figure 7.40 Average Coating Thickness vs. Time

Tables 7.13 and 7.14 show the statistics for the coating thickness calculations for the top spray experiments according to the calorimetry and UV/Vis spectroscopy coating efficiency analysis:

Table 7.13 Top Spray Coating Thickness Calculation Statistics According to Coating Efficiency Calorimetry Analysis

Run	Calculated Average Coating Thickness [µm]	Minimum Coating Thickness [µm]	Maximum Coating Thickness [µm]	Coating Thickness Range [µm]
1	2.32 ± 0.34	1.55	3.44	1.89
2	3.67 ± 0.28	2.93	4.63	1.70
3	2.43 ± 0.34	1.71	3.52	1.81
4	2.27 ± 0.34	1.55	3.43	1.88

Table 7.13 Continued

5	3.17 ± 0.22	2.60	3.86	1.26
6	2.16 ± 0.32	1.49	3.20	1.71
7	3.18 ± 0.23	2.52	3.98	1.46
8	2.57 ± 0.38	1.71	3.88	2.17
9	2.62 ± 0.38	1.79	3.92	2.13
10	2.73 ± 0.20	2.18	3.38	1.20
11	3.08 ± 0.24	2.42	3.84	1.42
12	3.20 ± 0.24	2.60	3.95	1.35
13	3.04 ± 0.21	2.49	3.74	1.25
14	4.03 ± 0.28	3.28	4.91	1.63
15	2.74 ± 0.21	2.25	3.42	1.17

Table 7.14 Top Spray Coating Thickness Calculation Statistics According to Coating Efficiency UV/Vis Analysis

Run	**Calculated Average Coating Thickness [μm]**	**Minimum Coating Thickness [μm]**	**Maximum Coating Thickness [μm]**	**Coating Thickness Range [μm]**
1	2.37 ± 0.34	1.64	3.49	1.85
2	3.79 ± 0.28	3.01	4.69	1.68
3	2.43 ± 0.35	1.69	3.59	1.90
4	2.24 ± 0.35	1.47	3.34	1.87
5	3.20 ± 0.22	2.66	3.90	1.24
6	2.24 ± 0.32	1.46	3.38	1.92
7	3.23 ± 0.23	2.61	3.96	1.35
8	2.59 ± 0.38	1.76	3.98	2.22
9	2.70 ± 0.38	1.83	4.07	2.24
10	2.73 ± 0.20	2.18	3.41	1.13
11	2.96 ± 0.24	2.38	3.71	1.33
12	3.16 ± 0.24	2.59	3.90	1.31
13	2.92 ± 0.24	2.41	3.60	1.19
14	3.96 ± 0.28	3.23	4.86	1.63
15	2.88 ± 0.21	2.36	3.59	1.23

As can be seen in Tables 6.15 and 6.16, the slight difference in coating efficiency determined by calorimetry and UV/Vis absorbance results in small differences for the coating thickness statistics. The same trend can be seen for the calculated coating thickness statistics for the Wurster orientation coating experiments in Tables 7.15 and 7.16.

Table 7.15 Wurster Orientation Coating Thickness Calculation Statistics According to Coating Efficiency Calorimetry Analysis

Run	Calculated Average Coating Thickness [µm]	Minimum Coating Thickness [µm]	Maximum Coating Thickness [µm]	Coating Thickness Range [µm]
1	2.57 ± 0.60	1.22	5.14	3.92
2	2.30 ± 0.56	1.04	5.06	4.02
3	3.53 ± 0.53	1.94	5.86	3.92
4	2.41 ± 0.61	1.01	5.17	4.16
5	4.79 ± 0.57	3.26	7.20	3.94
6	4.16 ± 0.57	2.34	7.08	4.74
7	5.76 ± 0.76	3.38	8.90	5.52
8	2.21 ± 0.53	0.99	4.86	3.87
9	4.17 ± 0.55	2.63	6.58	3.95
10	5.96 ± 0.63	4.21	8.44	4.23
11	2.29 ± 0.55	1.02	4.63	3.61
12	8.73 ± 0.98	6.03	13.10	7.07
13	1.75 ± 0.47	0.73	4.86	4.15
14	5.42 ± 0.67	3.37	8.68	5.51
15	4.10 ± 0.52	2.46	6.41	3.95

Table 7.16 Wurster Orientation Coating Thickness Calculation Statistics According to Coating Efficiency UV/Vis Analysis

Run	Calculated Average Coating Thickness [µm]	Minimum Coating Thickness [µm]	Maximum Coating Thickness [µm]	Coating Thickness Range [µm]
1	2.46 ± 0.60	1.07	5.05	3.98
2	2.39 ± 0.56	1.05	5.32	4.27
3	3.61 ± 0.53	2.01	5.92	3.91
4	2.41 ± 0.61	0.99	5.26	4.27
5	4.57 ± 0.58	2.91	6.97	4.06
6	4.05 ± 0.57	2.52	6.62	4.10
7	5.87 ± 0.78	3.59	9.52	5.93
8	2.23 ± 0.53	1.08	4.51	3.43
9	4.19 ± 0.55	2.67	6.79	4.13
10	6.06 ± 0.63	3.98	8.98	5.00
11	2.18 ± 0.55	1.03	4.68	3.65
12	9.13 ± 1.02	5.80	13.67	7.87
13	1.78 ± 0.48	0.50	4.32	3.82
14	5.20 ± 0.68	3.37	8.13	4.76
15	3.93 ± 0.52	2.51	6.02	3.51

The standard deviation of the coating thickness for the top spray experiments ranges from 0.2 microns to 0.4 microns. By contrast, the coating thickness standard deviations for the Wurster experiments range from about 0.5 microns to above 1 micron. The reason for the large range of standard deviations with the Wurster orientation is due to the number of revolutions the particles make during the coating operation. Recall from Table 7.4, in the top spray orientation, the highest range for the number of revolutions made in the fluidized bed is about 200 revolutions. In comparison, the highest range for the number of revolutions a particle makes in the Wurster orientation in Table 7.5 is about 6500 revolutions. A smaller variation in the number of revolutions a particle makes results in smaller standard deviation for the coating thickness.

Figure 7.41 shows a graphical comparison of the data presented in Tables 7.13-7.16 for the calculated average coating thickness with the calorimetry and the UV/Vis results for coating efficiency.

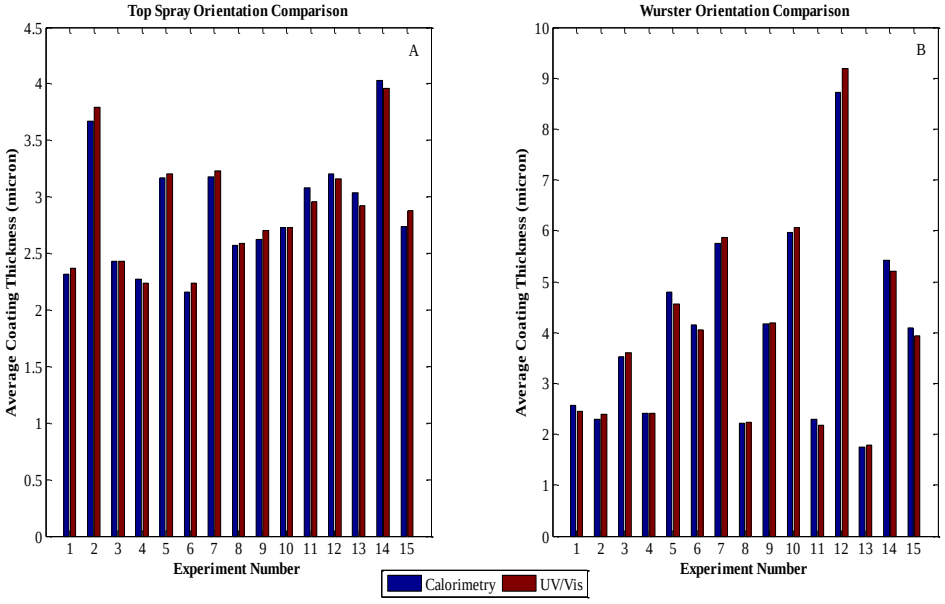

Figure 7.41 Calculated Average Coating Thickness Comparison Between Calorimetry and UV/Vis Results A) Top Spray Orientation B) Wurster Orientation

Since the experimental coating efficiencies determined by calorimetry and UV/Vis absorbance are within a few percentage points of each other, the average coating thickness for each experiment determined by each method is very similar as well.

Further examination of the coating growth kinetics model is warranted as the sensitivity of the coating growth calculations to its model parameters should be assessed. Recall from the dynamic mass and energy balance sensitivity analysis in section 7.2.2, the particle bed temperature was most sensitive to the fluidization air temperature with regards to the experiment parameters and the control volume height for discretization had a significant impact as well. The sensitivity analysis for the coating growth kinetics model will be discussed next.

7.4.3 Coating Growth Kinetics Model Sensitivity Analysis

A sensitivity analysis was done on the coating growth kinetics model to assess how sensitive the coating thickness outputs were to the model parameters. The parameters of interest for this sensitivity analysis are: coating solution concentration, flow rate, and temperature, the droplet size distribution, fluidization air flow rate, fluidization air temperature, the initial particle size distribution, the particle porosity, the solid-liquid contact angle, the spray area cone, the control volume height, and the number of control volumes. The coating growth calculations for top spray experiment 2 were used for the sensitivity analysis. Table 7.17 shows the parameters of interest for this sensitivity analysis including the high and low values tested for each parameter. The variations used for the fluidization air temperature and flow rate are along the same order of potential experimental variation. The model results, not the corrected results for the calorimetry or UV/Vis analysis for the coating thickness calculations were used as the basis for comparison for this sensitivity analysis. A sensitivity analysis was also done for the Wurster

orientation as well examining the impact of the terminal velocity magnitude, the number of revolutions made, and the partition gap height of the Wurster insert.

Table 7.17 Variables of Interest for Sensitivity Analysis of Coating Growth Kinetics Model for Top Spray Experiments

Variable	Initial Condition	Low Value	High Value
Coating Solution Properties			
Concentration	0.1	0.05	0.15
Flow Rate	1 ml/min	0.7 ml/min	1.3 ml/min
Temperature	25^{o}C	27^{o}C	30^{o}C
Droplet Size Distribution	SMD: 17.8 μm	-3% IC*	+3% IC
Spray Cone Area	Varies with height	-3% IC	+3% IC
Fluidization Air			
Flow Rate	22 m^{3}/hr	21 m^{3}/hr	23 m^{3}/hr
Temperature	70^{o}C	69^{o}C	71^{o}C
Particle Revolutions	9460	-5% IC	+5% IC
Particle Properties			
Particle Size Distribution	325-425 μm Mean 390 μm	Mean 325μm	Mean 425 μm
Porosity	Non-Porous	5%	35%
Solid-Liquid Contact Angle	0^{o}	30^{o}	90^{o}
Control Volume			
Height	0.5 cm	0.25 cm	1 cm
Number	19	18	20

*IC: Initial Condition

As Table 7.17 shows, there are many variables that could potentially impact the magnitude of the coating thickness calculations. The sensitivity of the average coating thickness to the coating solution properties listed in Table 7.17 is shown as Figure 7.42. Variations in the solution concentration produce the largest changes in the average coating thickness. However, the average coating thickness is less sensitive to the coating solution concentration compared to the coating solution flow rate. The 30% change in coating solution flow rate produces a 30% change in the average coating thickness. The 500% change in coating solution concentration produces about a 50% change in average coating thickness. The droplet size distribution has the

next largest impact on the average coating thickness, with 3% fluctuations producing about a 10% change in the average coating thickness.

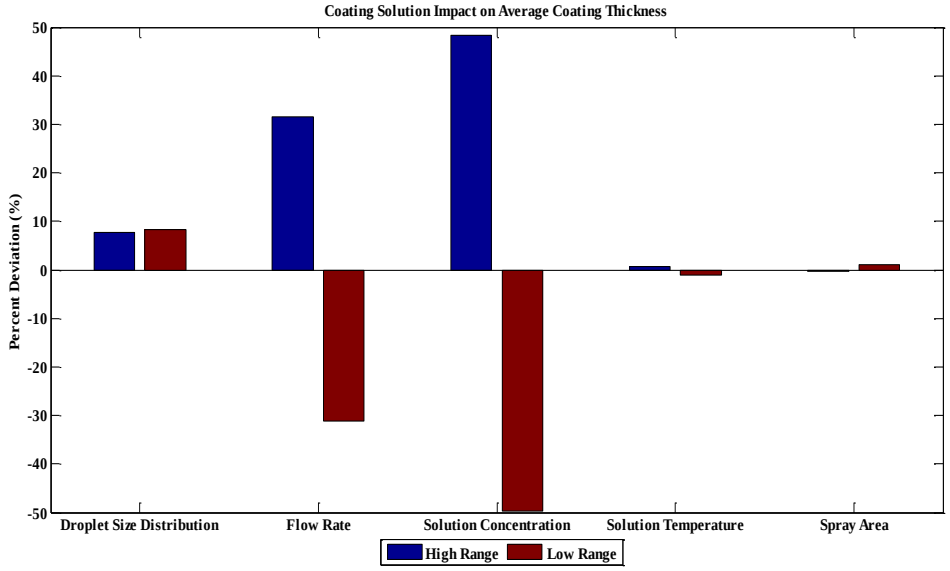

Figure 7.42 Average Coating Thickness Sensitivity to Coating Solution Properties

The spray area and the solution temperature impacts were about equal at around ±2% change in the average coating thickness. The change in the coating solution temperature slightly changes the droplet SMD and subsequent droplet size distribution. This slight change marginally alters the droplet per particle ratio (a parameter to be discussed in the numerical sources of error section 6.6 of this chapter). The small fluctuation in the spray area changes the number of times a particle is in the spray area and the number of times it can be coated in the spray cone area. In the base case, the number of times a particle is in the spray area is 39776. For the 3% increase, this value changes to 40,959 for a 2.97% increase in the number of times being in the spray cone area. For the 3% decrease, this value changes to 38572, for a 3.03% decrease. The new values for being in the spray cone area are not exactly 3% because of the randomness incorporated into the model, specifically the random binomial function. These new values for the number of times

being in the spray cone area leads to new values for the number of times coated, both changes by the same magnitude as the number of times being in the spray area.

The next set of variables examined in the sensitivity analysis was the fluidization air properties. Figure 7.43 shows the average coating thickness sensitivity to the fluidization air properties. Increasing the preheat fluidization air flow rate by 4.5% increases the average coating thickness by roughly the same amount, 4.5%. This happens because the residence time inside each control volume lowers slightly (due to changes in excess fluidization velocity, bubble rise velocity and void fraction), thus increasing the number of revolutions made during a coating operation. Lowering the preheat fluidization air flow rate by 4.5% does not have the same magnitude impact due to the stability of bubble void fraction and the overall fluidized bed void fraction to small fluctuations in the flow rate (see Figure 7.10).

The temperature of the fluidization air also has a minimal impact on the average coating thickness, with the highest fluctuation at about 1%. This small fluctuation in the average coating thickness is a result again of the bubble void fraction and overall fluidized bed void fraction being relatively stable to small fluctuations in temperature (see Figure 7.12).

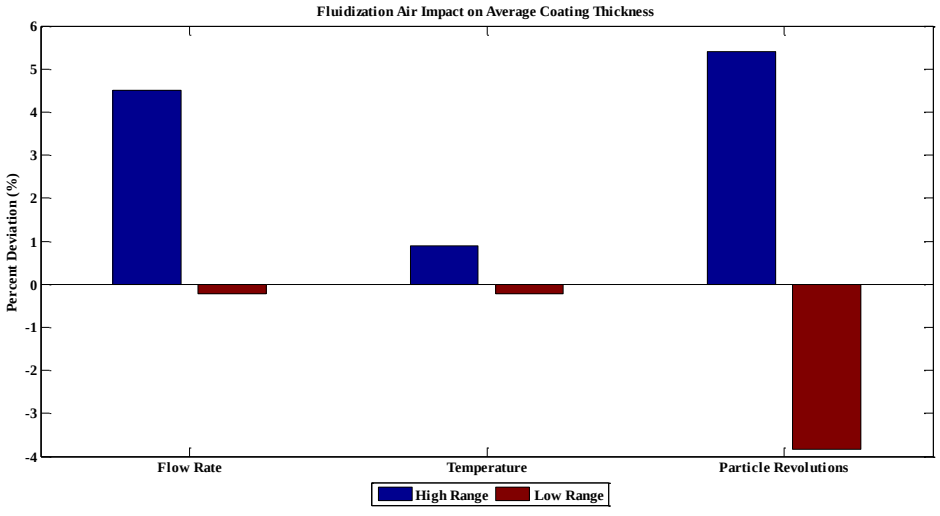

Figure 7.43 Average Coating Thickness Sensitivity to Fluidization Air Properties

The number of revolutions a particle makes has the largest impact on the average coating thickness with regards to the fluidization air properties. For this simulation, the number of revolutions made by the particles is 9460. A 10% fluctuation gives 10406 revolutions for the positive deviation and 8514 for the negative deviation. This change of 946 revolutions per coating operation yields 42 additional opportunities for the increase in revolutions and 42 less opportunities for the decrease in revolutions for the particle to be coated in the spray area (see Table 7.6 CISA%).

The next set of variables examined in the sensitivity analysis was the particle properties. Figure 7.44 shows the sensitivity of the average coating thickness to the particle properties.

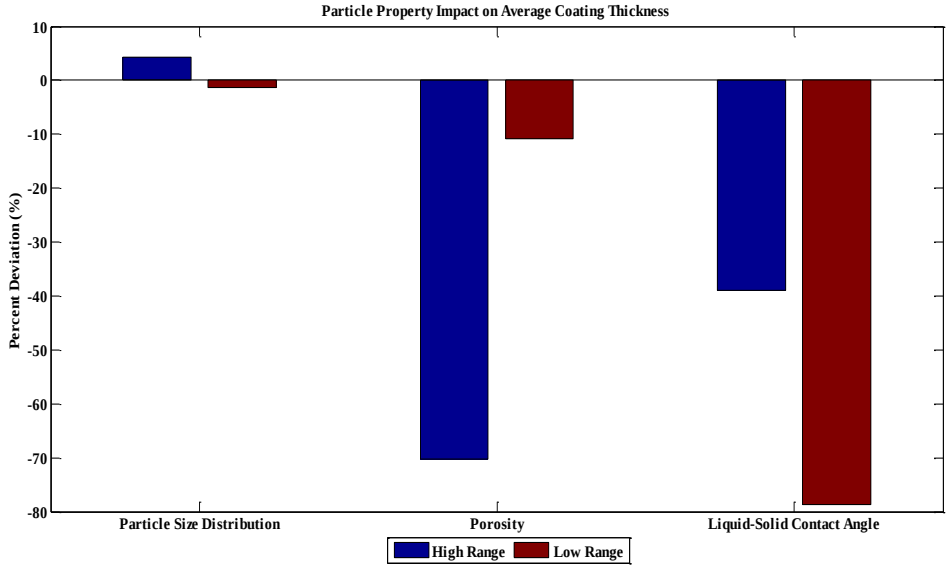

Figure 7.44 Average Coating Thickness Sensitivity to Particle Properties

For the particle size distribution impact, the high and low values for the particle size range were used as the respective modes. A larger particle size leads to a higher average coating thickness while a smaller particle size leads to a smaller average coating thickness. The reason for this is due to the change in the number of particles for the simulation. The base case simulation has $2.23e^{6}$ particles, while the high and low range particle size distributions have

$2.07e^6$ particles and $2.43e^6$ particles respectively. This is a -7.3% and 9.1% difference from the base case number of particles. With a smaller number of particles to coat, the average coating thickness should increase. Similarly, with a greater number of particles to coat, the average coating thickness should decrease.

The particle porosity has a very pronounced effect on the coating thickness in Figure 7.44. The particles in the base case simulation have no porosity at all. At 5% porosity the average coating thickness decreases 10% and at 35% porosity the average coating thickness decreases 70%. An inherent assumption with the porosity calculations for this sensitivity analysis is that all the particle pores are completely filled with the liquid coating solution before the particle surface gets coated. Surface tension and viscosity effects are neglected to simplify the simulation calculations and the sensitivity analysis. In addition, in a fluidized bed coating experiment, some particle pores get filled with coating, some particle pores are coated only on the surface, and some particle pores are not filled, covered, or coated.

The final particle property examined for the sensitivity analysis is the solid-liquid contact angle. For the coating thickness calculations presented in the previous section, the contact angle is assumed to be 0^o, complete spreading of the liquid droplet over the particle surface. The liquid droplet surface tension plays an important role in how far the droplet spreads over the particle surface before evaporation occurs. A 30^o solid-liquid contact angle results in a about a 40% reduction in the average coating thickness, while a 90^o solid liquid contact angle results in about an 80% reduction in the average coating thickness. Another assumption made here to simplify calculations is that each layer of coating is complete before the next layer begins.

The final set of variables examined for the magnitude of impact on the average coating thickness is the control volume properties. Figure 7.45 shows the sensitivity of the average coating thickness to the control volume properties of the simulation.

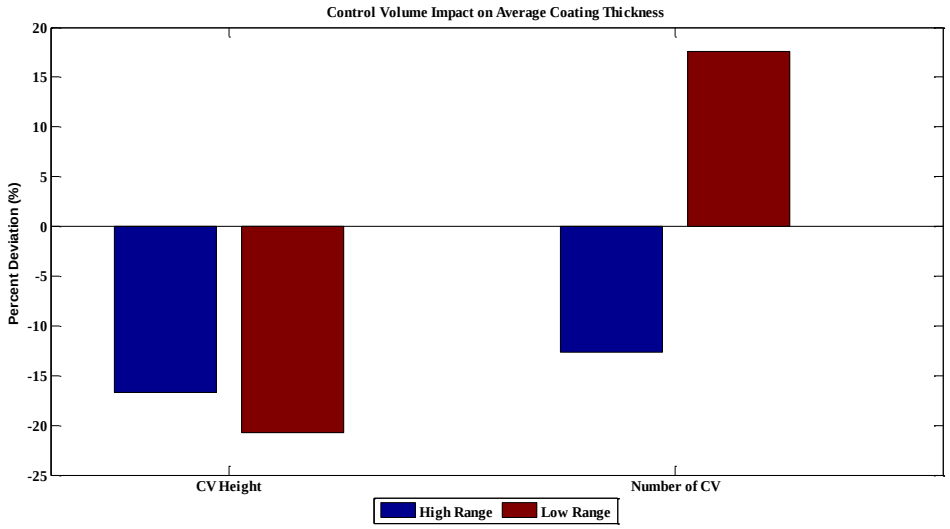

Figure 7.45 Average Coating Thickness Sensitivity to Control Volume Properties

As Figure 7.45 shows, the control volume height selected for the simulation has a significant impact on the average coating thickness. Changing the control volume height changes the number of control volumes for the simulation. This change then effects the hydrodynamic properties calculated for the fluidized bed operation (see Figure 7.14), i.e. bubble diameter and bubble rise velocity. In addition, changing the control volume height also changes the number of particles in each cell and the spray area cone for each control volume.

The number of control volumes selected for the simulation is important, once the control volume height has been designated. Choosing a larger number of control volumes for a simulation results in a lower average coating thickness. The reason for this is because it is assumed that the particle spends time in that section of the bed as well, changing the number of revolutions made for the coating operation. Choosing a lower number of control volumes also

impacts the average coating thickness, for the same reason as choosing too many control volumes – changing the number of particle revolutions made during the coating operation.

Since the gas hydrodynamics and particle motion are different in the Wurster orientation compared to the top spray orientation a sensitivity analysis was done on the Wurster orientation coating growth kinetics model regarding the parameters unique to the Wurster orientation. Table 7.18 shows the parameters of interest for the Wurster orientation sensitivity analysis.

Table 7.18 Parameters Tested for Wurster Orientation Sensitivity Analysis

Variable	Initial Condition	Low Value	High Value
Terminal Velocity	Varies	-5% IC	+5% IC
Revolutions	Varies	-5% IC	+5% IC
Partition Gap Height	1 cm	0.5 cm	1.5 cm
Control Volume Height	0.5 cm	0.25 cm	1 cm

Figure 7.46 shows the average coating thickness sensitivity to the parameters listed in Table 7.18 for the Wurster orientation experiments.

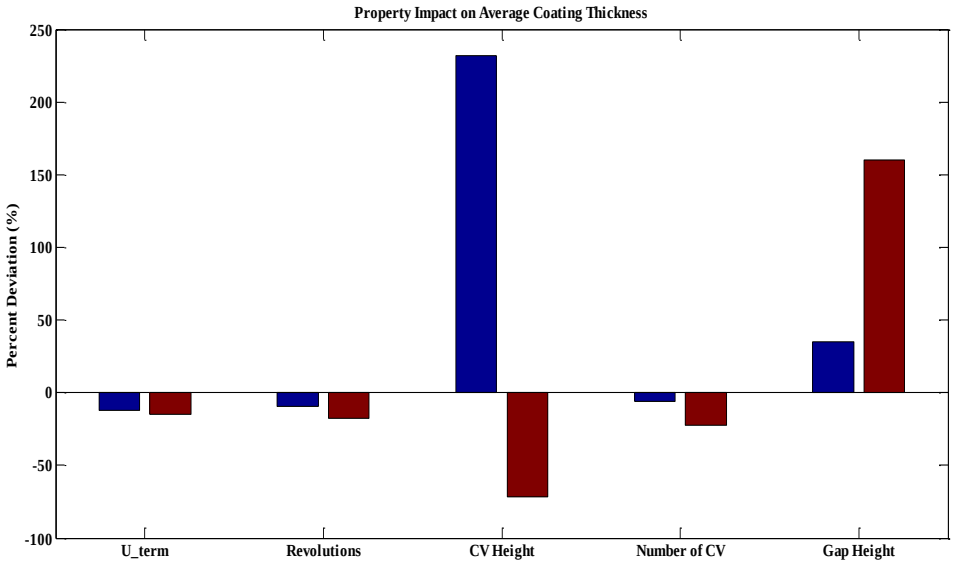

Figure 7.46 Average Coating Thickness Sensitivity for Wurster Orientation

As Figure 7.46 shows, the average coating thickness is highly sensitive to many parameters within the coating growth kinetics model. Similarly to the top spray orientation, the control volume height used in the simulation has the largest impact on the average coating thickness, with the largest differences at 232% and -72% for the high and low values respectively. The number of control volumes used in the simulation also impacts the average coating thickness. Having too many or too few control volumes will lead to a different number of times particles are in the spray cone area and subsequently coated because both probabilities change with the addition or removal of calculations. The average coating thickness also shows a high sensitivity to the Wurster tube gap height as well. A larger gap height allows for more particles to enter the tube simultaneously, while a lower gap height minimizes the number of particles entering the Wurster tube insert simultaneously.

The average coating thickness is also sensitive to the terminal velocity distribution of the particle size distribution as it plays a direct role in the particle circulation rate. A higher terminal velocity leads to more revolutions within the fluidized bed because the particles travel a shorter distance than smaller particles that have a lower terminal velocity. The number of revolutions a particle makes during the coating operation also has an impact on the average coating thickness, at about the same magnitude as the terminal velocity and for the same reason.

A sensitivity analysis performed on the coating growth kinetics model has yielded insight into what factors, experimental or simulation, play important roles in determining the average coating thickness for a coating operation. The coating growth kinetics model shows the highest sensitivity to the particle properties of porosity and the liquid-solid contact angle. The next factors with the largest impacts in the sensitivity analysis are the liquid properties of coating solution concentration and flow rate. The fluidization air properties were shown to have a slight

impact on the average coating thickness, but the simulation conditions regarding control volume properties were shown to be more significant. For the Wurster orientation, the average coating thickness is sensitive to changes in the following variables from highest to lowest impact: control volume height, Wurster tube gap height, number of control volumes, and the terminal velocity distribution and the number of revolutions made.

The sensitivity analysis has shown that experimental sources of error can have an impact on the coating growth kinetics calculations. In the next section the experimental sources of error will be discussed as well as steps taken to minimize them.

7.5 Experimental Sources of Error

There are several potential sources of error that can lead to misrepresentations of the experimental results. For this discussion, the experiments will be examined as three sequential phases: preparation, run, and post-analysis. The sources of error will be discussed along with steps taken to minimize them.

The preparation phase of the experiment involves several steps including: sieving the ammonium nitrate particles to get the desired particle size distribution, weighing the core particles along with transfer to the fluidized bed product bowl, weighing the coating material, and measuring out the desired volume of solvent (water) for the coating material.

There are two issues with regards to sieving the ammonium nitrate particles to obtain the desired particle size distribution for an experiment: the length of time for sieving and the degree of agitation used in the sieving. A sufficient time (~5 minutes) is needed to allow smaller particles to pass through the sieve meshes while entraining the larger particles. Smaller particles may still be entrained in the sieve after the sieving process due to static forces developed from frictional sliding. Particle breakage can also occur as a result of the degree of agitation used

during the sieving process in addition to the length of time the sieving is done. The broken particle fragments will elutriate from the fluidized bed thus distorting coating efficiency calculations done by weighing samples before and after coating. So, while two sieves have nominal sizes of 210 μm and 300 μm for example, there may be smaller particles (< 210 μm) entrained within the pan. To minimize the potential of breaking fragments of the ammonium nitrate particles during sieving, the sieves were not filled to more than one third of the pan volume, and a medium degree of agitation was used to separate the particle sizes.

The sieved particles and the coating material are both weighed separately on an analytical balance that has an accuracy of ±0.0001g in the next step of the preparation phase. This error is considered negligible for the due to the batch sizes used for experiments 50-100g for core particles and 5-10g for coating material. The error associated with this magnitude is 0.0001-0.0002% and 0.001-0.002% respectively.

Once the coating material is weighed, the volume of solvent desired for dissolving the coating material is measured out next in the preparation phase. The solvent volume is measured out in a graduated cylinder with markings at 2 ml increments, and large print markings at every 10 ml. The amount of solvent used ranged from 75-250 ml for the experiments of this work, yielding a potential error of 0.8-2.67% for over-pouring of solvent. A higher solvent volume for the coating solution can lead to an extended run phase in order to evaporate the extra solvent. To minimize this potential error, the solvent was measured out in smaller portions to the large markings at the 10 ml increments and an additional 10 ml graduated cylinder with markings at 1 ml increments was used as needed.

The last step in the preparation phase involves the transfer of the core particles to the fluidized bed product bowl and the transfer of the coating material into the solvent for

dissolution. It is possible that some of the core particles will not be transferred to the fluidized bed product bowl or that the coating material will not be transferred to the solvent. If this happens the coating efficiency calculations are already erroneous even if it less than 1%. If the coating efficiency calculations are erroneous, the coating thickness calculations will be off by the same amount as well. To ensure accuracy and minimize the error associated with transfer, beakers housing the core particles and the coating material were weighed before and after transfer to their respective containers

The next phase of the experiment is the run phase. Here potential error sources lie with flow rates (atomization air, fluidization air, and liquid) as well as air, particle, and liquid temperatures, and the relative humidity of the air.

The flow meter for the fluidization air has markings from 6 Nm^3/hr to 60 Nm^3/hr in 2 Nm^3/hr increments. Interpolation between the 2Nm^3/hr markings is difficult as the distance between markings is about 1 cm in length, with no additional scale markings to aid in determining the air flow rate. For this reason, fluidization air flow rates for experiments in both orientations were set to even number flow rates. The error here can be problematic for calculations and possibly scale up attempts depending on the set flow rate. For example, if the desired flow rate is 20 Nm^3/hr, but the actual flow rate is 20.8 Nm^3/hr, the error is 4%. This error increases at lower flow rates. For example, a desired flow rate of 16 Nm^3/hr and actual flow rate of 16.8 Nm^3/hr yields an error of 5%. To minimize this experimental error source, the fluidization air flow rate was monitored continuously throughout the experiment run to ensure no substantial fluctuations in flow rate occurred.

The next air flow rate that must be monitored throughout the experiment run is the atomization air flow rate. The line housing the atomization air is not connected to an inline

flow meter like the fluidization air. Therefore, calibrations were done by correlating the atomization air pressure with the velocity at the nozzle exit. Calibrations were done after every two or three experiments to ensure validity for calculation purposes. The relationship was found to be 1 liter/min for every bar of pressure for the atomization air. The repeated calibration checks found this relationship to be constant for the across the experiments done for this work.

The final flow rate that has potential to be a source of error for the experiments is the liquid coating solution flow rate. The liquid coating solution is pumped into the fluidized bed via a peristaltic pump into a two fluid nozzle. There are two ways to control the liquid coating solution flow rate for the peristaltic pump: choosing the proper diameter tubing to use in the experiment and controlling the number of rpms the pump head makes. Three different diameter silicone tubes were investigated for use in the delivery of the liquid coating solution to the spray nozzle: 0.5 mm, 1.6 mm, and 3.2 mm. Calibrations done with the three different diameter tubes at various rpm speeds showed the smallest diameter silicone tube, 0.5 mm, to be the only tube diameter that would deliver the liquid coating solution at the desired flow rates without over-wetting the fluidized bed. To ensure that the liquid coating solution delivery rate was essentially constant for the duration of the fluidized bed experiments, the liquid coating solution volume was measured at various time intervals and the liquid coating solution flow rate was calculated.

In addition to potential error sources arising from experimental flow rates, experimental temperature measurements can also be a source for error. For this work, the temperature of the fluidization air, the atomization air, the fluidized particles, and the liquid coating solution were of interest.

The fluidization air temperature set point can range from 25-80^{o}C. This set point has an accuracy of ±1^{o}C, this leads to an error ranging from 1.25-4%. To measure the temperature of the particle bed and the fluidization air before and after the fluidized bed j thermocouples with an accuracy of ±0.1^{o}C were used. Therefore the error range associated with the j thermocouples is 0.125-0.4%. Similarly to the recording of the liquid coating solution amount, the temperatures of the fluidization air before and after the fluidized bed were recorded along with the particle temperature within the fluidized bed. For the liquid coating solution, an alcohol based lab thermometer (0-100^{o}C with 2^{o}C markings) was used to determine temperature. Interpolation between the 2^{o}C markings was difficult as the distance between markings is about 1 mm in length. Therefore the error associated with liquid coating solution temperature can range from 2-8% depending on the coating solution temperature set point.

The last potential source of error in the run phase of the experiment is the relative humidity measurement. The relative humidity probe used for these experiments has an accuracy of ±3%. For example, an exit relative humidity of 45% may actually be 43.65-46.35%. The relative humidity was recorded at the same frequent intervals as the air, liquid coating solution, particle temperatures.

The post-analysis phase of the experiments also contains potential error sources to be aware of. In the post-analysis phase of the experiment, calorimetry and UV/Vis absorbance runs were used to determine the experiment coating efficiency and provide the basis for the coating growth calculations. There are several potential sources for error with the calorimetry experiments that can lead to incorrect experiment coating efficiencies including: solid sample size, the volume of liquid, and the equilibrium time.

The amount of solid sample used in each calorimetry experiment 0.5g. Recalling the balance accuracy as ±0.0001g, the error is then 0.02%, essentially negligible. The sample was put into the vials before weighing, so there is no error associated with the solids transfer from one container to the next for these experiments. There is an additional issue of concern for error with the amount of solid sample used, regarding uniformity of coating distribution. Using the results from one sample to represent the larger population can be problematic because the coating may not be uniformly distributed. For this reason, at least two calorimetry runs were used to determine the experiment coating efficiency.

The volume of liquid can also impact the coating efficiency calculations for the experiments. Two 3 ml syringes, with markings for every 0.2 ml, were used to introduce water into the vials (one for the sample and one for the reference) for the calorimetry experiments. One potential error source for the syringe is small air bubbles being trapped in the syringe, thus reducing the actual water volume in the syringe and impacting the heat of mixing observed for the experiment. To reduce this potential source of error, the syringe volume is minimized such that only water occupies the volume. In addition, any air bubbles trapped in the syringe are purged from the syringe during the minimization of the syringe volume. Another potential error source with the volume of liquid lies in the 0.2 ml markings on the syringe. The calorimetry experiments were done using 2 ml of water to determine the heat of mixing for the coated samples. Incorrect filling to the 2 ml marking could lead to an error as high as 10%, and this error would then lead to misrepresentation of the coating efficiency and ultimately the coating thickness distribution. In order to minimize this potential source of error, at least two calorimetry runs are used to determine the experiment coating efficiency.

The final source of error with regards to the calorimetry runs is the equilibrium time allowed for the experiments. The dissolution of PEG 3400 coated ammonium nitrate in water is endothermic and reasonably fast for the particle size ranges used (~15 minutes maximum). The calorimeter is very sensitive to fluctuations in heat (mW scale), so it must be allowed a certain amount of time, here called equilibrium time, to return to the reference state so the full heat of mixing can be ascertained. Cutting this equilibrium time short can lead to lower heat of mixing values and an overstatement of coating efficiency. For example, cutting the equilibrium time short such that the heat of mixing value is 127 J for an experiment with a batch size of 100g and a coating mass of 10g, rather than 130 J, leads to a 2.31% error. This 2.31% error in heat of mixing value leads to a significant difference in coating efficiency, 81.9% coating efficiency with the 127 J result versus 58.1% coating efficiency with the 130 J result, an error of 41%. For this reason all the calorimetry runs were 45 minutes in length, allowing ample time for the return to the reference state.

UV/Vis absorbance was used in addition to calorimetry to determine the experiment coating efficiency. There are a few potential sources of error using this technique as well including: solid sample size, the volume of deionized water used, the dissolution time allowed, and the concentration uniformity in the solution.

The potential source of error for the sample size with UV/Vis absorbance is similar to that of the calorimetry experiments which has been discussed previously. The coated sample size used for analysis was 0.5g to keep the absorbance between 0 and 1. The potential source of error for the volume of water used regarding the graduated cylinder markings is similar to that of the coating solution which has been discussed previously. Here however an extra 2 ml of water changes the ppm concentration. For example, 0.5 g in 100 ml of water gives a 5000 ppm

solution, while the same mass in 102 ml of water gives a 4902 ppm solution. The error is 1.96%. This error will again be carried forward to the coating thickness calculations.

Another area where potential error could impact the coating efficiency results is the dissolution time allowed prior to measuring the UV/Vis absorbance. If an insufficient amount of time is allowed for the dissolution of the coated particles there are some potential problems: the coated particles may not completely dissolve in the deionized water and the solute may not have enough time to diffuse throughout the deionized water. This will lead to inaccurate absorbance readings and thus inaccurate coating efficiency and coating thickness calculations. To minimize this potential error source, a dissolution time of two hours is used for each UV/Vis absorbance experiment. The deuterium lamp for the UV/Vis spectrometer requires two hours to warm up, so the solution of interest is prepared prior to warming up the lamp. This way, when the UV lamp is ready, the coated sample has had sufficient time to dissolve in the deionized water.

The final area where potential error could impact the coating efficiency results is the sample concentration uniformity. The concentration uniformity of the solution is partially a function of the dissolution time allowed which has been discussed previously. In addition to allowing for the coated sample to dissolve, an extra measure taken to ensure error minimization here is a thorough stirring of the sample solution prior to taking a UV/Vis absorbance measurement. For example, one absorbance measurement value of 0.32601 yields a coating efficiency of 67.9%. A second absorbance measurement for the same conditions of 0.32368, yields a coating efficiency of 91%. A 0.71% error in the absorbance measurement leads to a 34% difference in coating efficiencies. Multiple UV/Vis absorbance measurements were also taken in a very short time (< 1 minute) to verify a uniform concentration within the solution.

There are several potential sources of experimental error for this work. This discussion has shown the post-analysis phase of the experiment to be the most sensitive to potential error sources, as slight variations in calorimetry and UV/Vis absorbance results can have a major impact on the coating efficiency and subsequent coating thickness calculations. The route taken to minimize the potential error in both cases is multiple measurements with both techniques. In addition to potential experimental sources of error that can affect coating efficiency and coating thickness calculations, there are also numerical sources of error that must be considered. The numerical sources of error will be discussed in the next section.

7.6 Numerical Sources of Error

Due to the number of calculations involved in the development of this coating growth kinetics model for a coating thickness distribution, the potential for numerical error in these calculations must be considered. As seen in Chapter 4, there are 89 equations needed to calculate all the parameters needed for the coating growth kinetics models for the top spray and Wurster orientation. This does not include the additional dimensionless number calculations used for confirmation of operation in the particle coating regime and not the agglomeration regime. The following discussion will show how numerical error for certain parameters (minimum fluidization velocity, bubble diameter, bubble rise velocity, bed void fraction) can impact the final coating thickness distribution.

The correlation for the minimum fluidization velocity developed by Wen and Yu has a standard deviation of ± 34%. For the bubble diameter a nominal deviation of ±5% was taken. A 2% deviation was taken for the bed void fraction, particle residence time (τ) and the number of revolutions for the coating operation. Table 7.19 shows the average coating thickness for the previously mentioned variables at the high and low values.

Table 7.19 Numerical Deviation Impact on Calculated Average Coating Thickness

Variable	Low [μm]	High [μm]	Error [%]	
			Low	High
U_{mf}	4.25 ± 0.32	4.54 ± 0.34	-3.2	3.4
D_{bub}	4.40 ± 0.33	4.54 ± 0.34	0.2	3.4
ε_{bed}	4.64 ± 0.35	4.10 ± 0.31	5.7	-6.6
τ_c	4.61 ± 0.34	4.33 ± 0.33	5.0	-1.4
Revolutions	4.32 ± 0.33	4.49 ± 0.34	-1.4	2.3
Combined	4.55 ± 0.34	4.18 ± 0.32	3.6	-4.8

As Table 7.19 shows, the average coating growth thickness is most sensitive to changes in the fluidized bed void fraction followed by the minimum fluidization velocity. Changes in the fluidized bed void fraction alter the number of particles in each control volume and therefore the number of particles in the spray area in each control volume. Changes in the minimum fluidization velocity alter many properties almost all the other hydrodynamic properties needed for the coating growth kinetics model: bubble diameter, bubble rise velocity, fluidized bed void fraction, the particle residence time and the number of revolutions made. The combination of all deviations at bot levels yield errors slightly lower than the maximum for the high and low categories respectively.

Numerical error can be built into a model unexpectedly as well. An additional parameter was incorporated into the coating growth kinetics model after the initial mass balance to account for the number of droplets hitting a particle in each control volume. Overestimation of this parameter leads to erroneous results for the coating thickness distribution. To calculate the number of droplets hitting a particle in each control volume a nominal drop size must be used. Therefore as an initial attempt, the SMD of each respective droplet size distribution was used. The amount of coating for each particle is calculated and this total is summed for the entire particle size distribution. The mass of coating calculated for the particle size distribution is then compared to the extrapolated out for a coating mass for the entire batch size. If the coating

efficiency for the particle size distribution is within 1% of what the calculated batch coating efficiency is, the correct drop size has been selected. Table 7.20 shows the coating efficiency and error calculated for each top spray experiment with the overall balance and then based on the SMD and MMD values for each droplet size distribution.

Table 7.20 Top Spray Experiments Droplets Per Particle Coating Growth Kinetics

Experiment	CE* [%]	SMD		MMD		Drop Diameter Used+	Error [%]
		CE [%]	Error [%]	CE [%]	Error [%]		
1	62.4	193.0	209.4	111.2	78.3	1.2100	0.5
2	67.9	88.2	30.0	51.3	-24.4	0.9072	-0.1
3	58.2	94.7	62.7	53.4	-8.3	0.9700	0.5
4	70.4	59.0	-16.2	33.3	-52.8	0.7780	0.9
5	63.5	84.8	33.5	48.5	-23.7	0.9130	0.3
6	53.6	91.0	69.7	52.2	-2.7	0.9875	-0.2
7	60.8	72.3	18.9	41.8	-31.2	0.8830	0.6
8	63.8	95.8	50.3	55.3	-13.2	0.9550	-0.1
9	69.4	128.1	84.8	73.0	5.3	1.0200	-0.3
10	57.4	121.5	111.5	69.2	20.4	1.0600	0.4
11	68.3	65.2	-4.5	37.9	-44.5	0.8220	-0.4
12	58.9	100.3	70.5	57.4	-2.6	0.9927	-0.4
13	65.4	143.7	119.7	82.2	25.6	1.0800	-0.3
14	61.1	123.5	102.2	70.6	15.6	1.0496	0.0
15	69.0	137.1	98.9	78.4	13.7	1.0450	0.4

*CE: Coating Efficiency +Drop Diameter Used is a factor multiplied by the MMD

Figure 7.47 shows the data presented in Table 7.20 graphically. The corrected model predictions for coating efficiency in subplot A are all within 1% of the respective calculated coating efficiencies. As subplots B and C show, using the Sauter mean diameter or the mass median diameter leads to a misrepresentation of the coating efficiency. The largest difference for the Sauter mean diameter is 209.4% (Experiment 1) while the largest difference for the mass median diameter is 78.3% (Experiment 1).

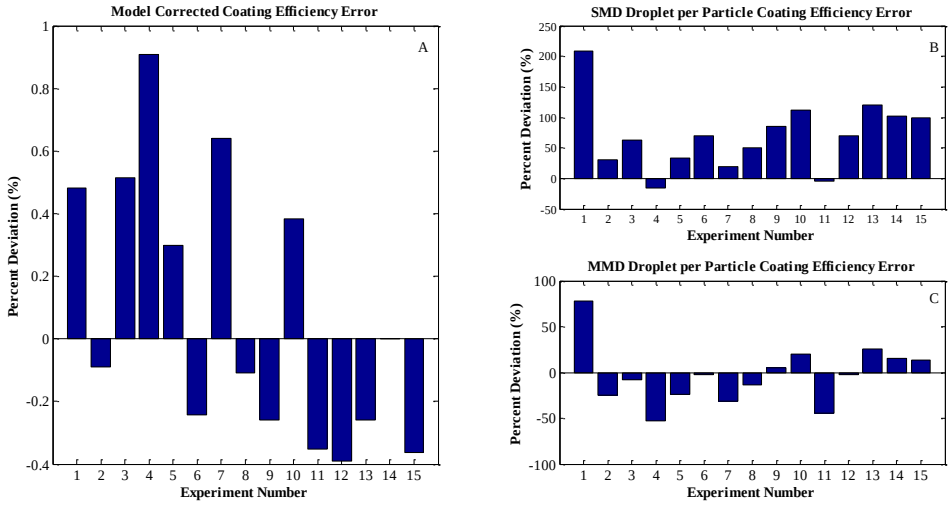

Figure 7.47 Top Spray Experiments Droplet Per Particle Balance Resulting Coating Efficiency Error

The trends for the Wurster orientation experiments are similar to those presented in Figure 7.47. Table 7.21 shows the droplet diameter used for the number of droplets per particle calculation in the coating growth kinetics model.

Table 7.21 Wurster Orientation Experiments Droplets Per Particle Coating Growth Kinetics

Experiment	**Calorimetry Experiment CE [%]**	**Drop Diameter Used [*MMD]**	**Error [%]**
1	45.0	1.407	0.0
2	40.1	1.761	0.8
3	47.8	1.650	-0.4
4	43.4	1.720	0.3
5	54.8	1.747	-0.5
6	56.5	1.760	-0.8
7	55.5	2.290	0.3
8	38.6	1.670	0.0
9	56.7	1.687	-0.7
10	68.3	1.728	-0.6
11	39.9	1.670	0.7
12	71.3	1.540	-0.9
13	30.4	1.680	-0.5
14	62.1	1.830	-0.2
15	55.8	1.410	-0.7

The discrepancies in the coating efficiency in Table 7.21 also lead to a discrepancy in the average coating thickness values. The calculated average coating thickness for the top spray experiments according the coating efficiency values in Table 7.20 is shown in Table 7.22. Figure 7.48 shows graphically the data presented in Table 7.22. As Table 7.22 and Figure 7.48 show, choosing the improper droplet size for the droplet per particle balance has a significant impact on the average coating thickness, ranging from -52% to +197%. For this reason reconciliation to the drop diameters listed in Tables 7.21 and 7.22 is needed to reduce the model calculated coating thickness error close to 1%.

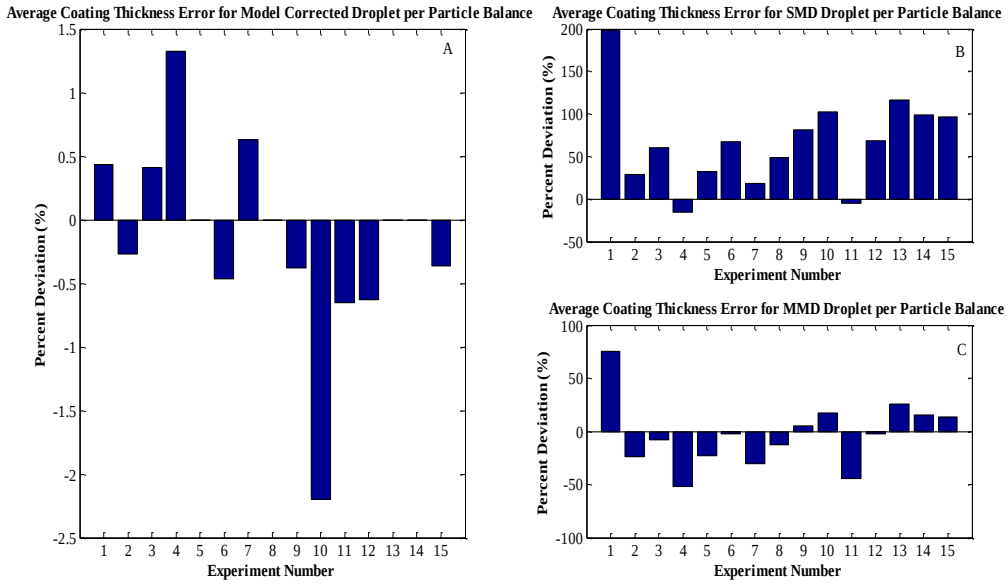

Figure 7.48 Average Coating Thickness Error Calculations Based on Droplet Per Particle Balance by A) Correct Droplet Size B) SMD C) MMD

Table 7.22 Average Coating Thickness Values for Top Spray Experiments Using Coating Efficiency Values Listed in Table 7.20

Experiment	Calculated Coating Thickness [µm]	SMD Coating Thickness [µm]	MMD Coating Thickness [µm]	Model Calculated Coating Thickness [µm]	SMD Error [%]	MMD Error [%]	Model Error [%]
1	2.32 ± 0.34	6.91 ± 0.95	4.07 ± 0.58	2.33 ± 0.34	197.8	75.4	0.4
2	3.67 ± 0.28	4.74 ± 0.36	2.78 ± 0.21	3.66 ± 0.28	29.2	-24.3	-0.3
3	2.42 ± 0.34	3.89 ± 0.66	2.22 ± 0.32	2.43 ± 0.35	60.1	-8.6	0.4
4	2.27 ± 0.34	1.91 ± 0.28	1.09 ± 0.16	2.30 ± 0.34	-15.9	-52.0	1.3
5	3.17 ± 0.22	4.20 ± 0.29	2.43 ± 0.17	3.17 ± 0.22	32.5	-23.3	0.0
6	2.16 ± 0.32	3.62 ± 0.52	2.10 ± 0.31	2.15 ± 0.32	67.6	-2.8	-0.5
7	3.18 ± 0.23	3.77 ± 0.27	2.20 ± 0.17	3.20 ± 0.23	-12.9	-30.8	0.6
8	2.57 ± 0.38	3.82 ± 0.56	2.24 ± 0.33	2.57 ± 0.38	48.6	-12.8	0.0
9	2.62 ± 0.38	4.76 ± 0.66	2.76 ± 0.40	2.61 ± 0.38	81.7	5.3	-0.4
10	2.73 ± 0.20	5.54 ± 0.39	3.20 ± 0.23	2.67 ± 0.20	102.9	17.2	-2.2
11	3.08 ± 0.24	2.94 ± 0.23	1.72 ± 0.14	3.06 ± 0.24	-4.5	-44.2	-0.6
12	3.20 ± 0.24	5.39 ± 0.39	3.12 ± 0.23	3.18 ± 0.24	68.4	-2.5	-0.6
13	3.04 ± 0.21	6.59 ± 0.44	3.81 ± 0.26	3.04 ± 0.21	116.8	25.3	0.0
14	4.03 ± 0.28	8.01 ± 0.53	4.65 ± 0.32	4.03 ± 0.28	98.6	15.4	0.0
15	2.74 ± 0.21	5.38 ± 0.40	3.11 ± 0.23	2.73 ± 0.21	96.4	13.5	-0.4

The droplet size used in the droplets per particle balance listed in Tables 7.20 and 7.21 is not a random parameter. However, regression attempts to relate the droplet size used in the droplet per particle balance to measureable variables for a fluidized bed operation failed to yield a clear relationship. The variables investigated in the regression attempt include: liquid flow rate, number of particles in batch, number of particles in spray area, average fluidized bed void fraction, and number of control volumes for simulation (i.e. fluidized bed height). More research will have to be conducted to ascertain the proper relationship between the droplet size used in the droplets per particle balance in the coating growth kinetics model and the measureable fluidized bed operating parameters.

Due to number of parameters needed to calculate the coating growth kinetics of a fluidized bed experiment, a summary of the modeling results will be presented next.

7.7 Summary of Modeling Results

A 1-D coating growth kinetics model was developed for a top spray and Wurster orientation fluidized bed to describe the coating growth kinetics of a particle size distribution. The goal was to be able to test a set of fluidized bed operating conditions for final coating thickness properties without having to run experiments.

The first part of the coating growth kinetics model involves an accurate description of the dynamic mass and energy balances as presented in 7.2-7.2.2. The inputs for the dynamic mass and energy balances include: fluidization and atomization air properties, particle properties, liquid properties, and fluidized bed geometry. The fluidization air properties needed include: flow rate, inlet temperature, and preheat relative humidity. The thermo-physical properties of air are then calculated including: density, specific heat capacity, thermal conductivity, and viscosity as a function of temperature and relative humidity. The atomization air properties needed

include: flow rate, inlet temperature, and relative humidity. The particle properties include: particle size, specific heat capacity, and thermal conductivity. The liquid properties needed include: flow rate, inlet temperature, and specific heat capacity. The fluidized bed properties needed include: diameter as a function of height (for tapered bowl geometry), wall thickness, specific heat capacity, thermal conductivity, and emissivity. The dynamic mass and energy balances involve discretizing the fluidized bed into equal height control volumes before doing calculations.

The outputs for the dynamic mass and energy balances include: temperature profiles of the fluidization air, the particles, and the fluidized bed wall, a fluidization air relative humidity profile, the fluidized bed height (via number of control volumes), and hydrodynamic properties of the fluidized bed. The hydrodynamic properties calculated include: bubble properties – diameter, velocity, and void fraction, the overall fluidized bed void fraction, and the particle circulation rate. Several dimensionless numbers are tabulated to determine heat and mass transfer characteristics. Moreover, dimensionless numbers developed specifically for determining if a fluidized bed operation is in the coating regime or agglomeration regime are calculated. A sensitivity analysis on the dynamic mass and energy balances showed the height of the control volume to have the biggest impact on the temperature profiles.

Once the dimensionless numbers illustrate that the operating conditions are in the coating regime and not the agglomeration regime, calculations for the coating growth kinetics can begin. The coating growth kinetics model developed for this work uses the hydrodynamic properties from the dynamic mass and energy balances as inputs. Additional inputs to the coating growth kinetics model include: a droplet size distribution, a particle size distribution, and nozzle

properties to calculate spray areas. The coating growth kinetics model developed for this work is an event driven stochastic model.

The main outputs of the coating growth kinetics model are: coating efficiency, final particle size distribution, and coating thickness distribution. Additional parameters calculated include the number of times a particle is in the spray cone area and the number of times a particle is coated in the spray cone area. Due to simplifications made for a 1-D modeling effort, the coating efficiency of each experiment in both top spray and Wurster orientations is overestimated. To make the model coating efficiency match the experimentally determined coating efficiency, a tunable parameter was incorporated into the calculations. This tunable parameter was found to be a function of the number of control volumes and the control volume height for the simulation. In other words, the height of the fluidized bed, and thus the fluidization air flow rate combined with the fluidized bed geometry has a direct impact on the magnitude of this tunable parameter. More research will need to be done in this area to generate a more clearly defined relationship nonetheless.

A second tunable parameter was incorporated into the coating growth model to match the model coating efficiency with the experimental coating efficiency in the form of a representative droplet size to calculate the number of liquid coating droplets that hit particles in the spray area. The droplet size used as the second tunable parameter is not random, similarly to the first tunable parameter previously described. However, no clearly evident relationship between this droplet size magnitude and the inlet variables was discernible. It is believed by the author that similarly to the first tunable parameter, the combination of the fluidization air flow rate and fluidized bed bowl geometry, and thus the fluidized bed height, plays a role in determining the magnitude of this second parameter.

CHAPTER 8

CONCLUSIONS AND RECOMMENDATIONS

The purpose of this chapter is to present the conclusions ascertained from this work. In addition, recommendations and future directions for extending this particular research will be given as well. The recommendations discussion will cover aspects regarding experiment design, the techniques used for post-experiment analysis, and elements to improve the coating growth kinetics model robustness.

8.1 Conclusions

Conclusions for this work can be classified into two categories: experimental and modeling conclusions. They will be addressed separately below.

8.1.1 Experiment Conclusions

The most important conclusion regarding the experiments is that various particle size ranges (210-600 μm) of ammonium nitrate can be coated in a top spray or Wurster orientation fluidized bed with PEG 3400 under various conditions (50-80^{o}C temperature set point and 12-26 m^3/hr fluidization air flow rate) with no particle agglomeration present in the final product. PEG 3400 was chosen as the coating material for a few reasons: it is a water soluble polymer, it is environmentally benign, when solid it does not absorb moisture from the air until the relative humidity is above 80%, and it has an amorphous crystalline structure. The amorphous crystalline structure of PEG 3400 in particular was important because ammonium nitrate

undergoes temperature induced crystalline structure changes where volume and therefore density change as well.

Several methods were used for confirmation that PEG 3400 was present in the final product both qualitative and quantitative. Qualitative measures confirming the presence of PEG 3400 in the final sample include: the addition of a colored dye to PEG 3400-water solution, FTIR spectra, SEM analysis and AFM analysis. The colored dye confirms that additional mass is now on or in the particle. Moreover, the hue of the colored dye is roughly the same for the entire batch. The FTIR spectra of the coated sample showed characteristic peaks of ammonium nitrate above 3000 $cm^{-}1$, indicating the presence of an N-H bond as well as the characteristic peaks of PEG 3400 just below 1500 cm^{-1} for the C-H bond.

SEM analysis showed that the ammonium nitrate particles were not completely symmetrical. In addition, SEM analysis showed the presence of pinholes in the PEG 3400 coating indicating either incomplete coating of the ammonium nitrate surface or the evolution of high capillary pressure during the coating operation. Higher magnification SEM pictures showed the presence of cracks within the coating layers again confirming incomplete coating of the core ammonium nitrate particles.

AFM analysis showed the average surface roughness of ammonium nitrate before the coating operation was 380 nm with a range of 169 nm, whereas after the coating operation the surface roughness was 419 nm with a range of 631 nm. The larger average surface roughness could be the result of gas-liquid-solid equilibrium phenomena such as capillary pressure evolution occurring during the coating operation, but more investigation into this particular aspect is needed to confirm this hypothesis. AFM analysis also showed the uncoated ammonium

nitrate particle surface to appear smooth, while the PEG 3400 coated ammonium nitrate particles had a cloud-like appearance.

Quantitative measures confirming the presence and amount of PEG 3400 in the final sample include isothermal calorimetry and UV/Vis absorbance. The use of isothermal calorimetry or UV/Vis absorbance as a method of determining the experiment coating efficiency is sensitive to the sample size taken so multiple samples were taken as a precaution against misrepresenting the coating efficiency. The coating efficiency determined by isothermal calorimetry ranged from 56-73% for the top spray experiments and 30-71% for the Wurster orientation experiments. The coating efficiency determined by UV/Vis absorbance ranged from 56-72% for the top spray experiments and 31-75% for the Wurster orientation experiments. The slight variation in coating efficiencies by the two methods is a result of the sensitivity of each method to the sample size used and the randomness of choosing a sample for analysis.

In addition to the conclusions for the experiments there are also conclusions that can be made about the fluidized bed modeling and the coating growth kinetics modeling done in this work. The modeling conclusions will be presented next.

8.1.2 Modeling Conclusions

Two different models were used for this work, one developed to describe the dynamic mass and energy balances for top spray orientation fluidized bed operations temperature profiles in a discretized form [1]and a stochastic event driven model to describe the coating growth kinetics in a top spray or Wurster orientation fluidized bed developed by the author. Conclusions regarding the 1-D dynamic mass and energy balances will be discussed first, then the stochastic coating growth model.

The 1-D dynamic mass and energy balance for the top spray orientation for temperature vs. time profiles developed by Hede et al. [1] was confirmed in this work with the largest experimental error attributed mostly to response time of the hygrometer. A sensitivity analysis on the 1-D dynamic mass and energy balance model showed the control volume height selected for discretization to have the highest impact on the model particle bed temperature, with an error of ± 20% during the preheat phase of operation. A closer examination of the fluidized bed properties showed the control volume height selection to have a role in almost every hydrodynamic property (except minimum fluidization velocity and void fraction at minimum fluidization), every heat transfer property, and every mass transfer property. The particle size chosen for the model simulation also has a high impact on the model fluidized bed temperature, with an error of ± 10% during the preheat phase. The reason for this is because the minimum fluidization and void fraction at minimum fluidization impact the rest of the fluidized bed hydrodynamic properties and therefore heat and mass transfer. The fluidization air temperature and flow rate have roughly the same impact on the model fluidized bed temperature, with errors of ± 5% during the preheat phase. The inlet relative humidity was found to have the least impact on the model fluidized bed temperature with an error of about ± 0.1% during the preheat phase.

In this work, a stochastic model was developed to describe the coating growth of a distribution of particles for a fluidized bed coating operation either in the top spray orientation or the Wurster orientation. The model calculates the particle residence time and the number of revolutions for the coating time based on the gas hydrodynamics involved with the orientation of the fluidized bed. Currently, the model over calculates the coating efficiency for fluidized bed operation in both orientations (65-89% for top spray and 37-85% for Wurster orientation) and therefore overstates the average coating thickness as well. The error between the model

prediction and the calorimetry results range from 11-30% for the top spray orientation and 11-23% for the Wurster orientation. The error between the model prediction and the UV/Vis results is 9-35% for the top spray experiments and 6-28% for the Wurster orientation experiments. One possible reason for the discrepancy between the model and the experiment results is the absence of a term accounting for spray drying that may occur during the course of operation.

Two tunable parameters were incorporated into the stochastic calculation sequence to make the model calculate the outputs correctly. The first tunable parameter is used specifically to make the experimental and calculated coating efficiency match each other to within ±1%. A regression analysis showed this parameter to be a function of the fluidized bed height, the fluidized bed void fraction, and therefore a function of the fluidization air flow rate and fluidized bed geometry.

The second tunable parameter added to the stochastic calculation is specifically to make the overall mass balance for the coating material deposited match the calculated coating mass of the stochastic simulation. This second tunable parameter takes form as a multiple of the droplet Sauter mean diameter. A regression analysis did not reveal a clear relationship between this parameter and the operating conditions of the fluidized bed experiments, yet this parameter value is not believed to be random. The author believes this parameter is a function of the fluidization air flow rate and fluidized bed geometry, similarly to the first tunable parameter.

Without the incorporation of the two tunable parameters previously described, the miscalculation of the coating efficiency also leads to errors for the coating thickness distribution of the coating growth kinetics model. The error associated with the coating thickness distribution is on the same order as the error for the coating efficiency with any differences resulting from the random nature of the coating growth kinetics model. An additional source of

error, regarding a mass balance of the number of droplets hitting a particle in the spray cone area, also exists within the model that must be minimized before the coating thickness distributions can be calculated. Failure to reconcile this number properly leads to highly erroneous model coating efficiency values and therefore coating thickness values, with errors ranging from -45% to 209% for average coating thickness values in the top spray orientation. This parameter was different for each experiment, being slightly higher the SMD for the droplet size distribution of each top spray experiment and ranging from 1.407-2.29 times the MMD for the droplet size distribution for the Wurster orientation experiments. For both experiment orientations this error was minimized to about ± 1% to match the model calculated coating efficiency.

A sensitivity analysis done for the coating growth kinetics model showed the liquid-solid contact angle and the particle porosity to have the largest impact on the average coating thickness value with errors around 70%. A higher liquid-solid contact angle means the droplet does not spread very well across the particle surface. This in turn means more droplets are needed to cover the core particle surface to ensure complete coverage. The liquid-solid contact angle is a thermodynamic property that can lead to unwanted particle agglomeration if the liquid coating solution addition rate is too high or the fluidization air flow rate is too low or a combination thereof. With regards to porosity, the more porous a particle is, the more coating material will be needed to achieve a desired coating thickness. However, there is an uncertainty issue here as how much of the particle pores actually get filled with coating material during a coating operation. There are a few different possibilities for porous particles: partial or incomplete pore filling, complete pore filling, or pore covering (i.e. pore is not filled or only partially filled). Which of the three possibilities previously mentioned actually happens is a function of the liquid coating solution properties (droplet size, viscosity, surface tension, contact

angle) , the fluidized bed hydrodynamic properties (the number of times a particle is in the spray area and the number of times a particle is coated in the spray area) and randomness.

In addition to the particle properties, the coating growth kinetics model was also shown to be sensitive to the liquid coating solution properties, in particular the coating solution concentration (± 50% error) and the coating solution flow rate (± 30%). The fluidization air properties were shown to have minimal impact on the average coating thickness with the largest factor being the fluidization air flow rate at a 5% error along with the number of revolutions made by the particles.

Similarly to the dynamic mass and energy balances the control volume has a significant impact on the coating growth kinetics model output. The control volume height sensitivity was shown to result in large errors as well, -20%. In addition choosing the wrong number of control volumes was shown to have an effect with a ± 15% error.

An additional sensitivity analysis was done for the Wurster orientation coating growth kinetics model due to the difference in particle and gas motion compared to the top spray orientation. The Wurster orientation coating growth kinetics model was shown to be most sensitive to the control volume height (with an error ranging from -72-232%) followed by the partition gap height (with an error ranging from 50-150%). Changes to both parameters alter the number of particles inside the Wurster tube insert and therefore change the coating distribution.

One final sensitivity analysis was done a few of the gas hydrodynamic properties (minimum fluidization velocity, bubble diameter, bed void fraction, and particle residence time) to assess the impact of numerical error on the average coating thickness in the top spray orientation. This sensitivity analysis showed that a ± 2% change in bed void fraction had the

largest effect on the average coating thickness (5.7% error for low bed void fraction value and -6.6% error for high bed void fraction value).

The coating growth kinetics model developed in this work can be used to estimate the coating thickness distribution of a fluidized bed operation in the top spray or Wurster orientation. Without any coating efficiency data, the model will over-predict the coating thickness distribution due to the lack of a term properly accounting for spray drying. However, as the sensitivity analyses have shown, several input parameters have a significant effect on the resultant coating thickness distribution. The sensitivity analyses also highlight the interaction between all the phases present in a fluidized bed operation.

With the conclusion of any major project there are always areas that, upon reflection, could be improved upon to yield more data and ideally provide a greater depth of understanding. The recommendations for this work will be discussed in the next section.

8.2 Recommendations

Recommendations for this work fall into two categories: experiment and modeling. Small or simple changes to the experimental setup can help strengthen the coating growth kinetics model developed in this work.

The first recommendation for improving this work is the addition of thermal hygrometers in the fluidized bed product bowl, the fluidized bed freeboard, and the fluidized bed exit. This will allow for real time data collection regarding the temperature and relative humidity profiles at various positions within the fluidized bed. Tracking and recording this data in real time would also be beneficial if scaling up the lab scale experiments was desired. From a modeling perspective, there would be additional data to compare against the model prediction for the

relative humidity within the product bowl, so reliance on the beginning and end point relative humidity is not so heavily relied on.

Another recommendation for improving this work is the addition of particle tracking method to the fluidized bed experimental setup. The particle tracking method can then be used to track particle motion and subsequently give experimental residence times inside the fluidized bed for a particle size range. Moreover, depending on the tracking method chosen, additional fluidized bed properties can be tracked as well (although not necessarily simultaneously) including: bubble diameter, bubble rise velocity, and droplet size distribution exiting the nozzle. Table 8.1 shows a listing of various tomography and radiography techniques as well as velocimetry techniques used in non-invasive fluidized bed particle tracking [2]. The main drawbacks to the methods listed in Table 8.1 involve either spatial or temporal resolution issues [2]. Other techniques for particle tracking include phosphorescence [42] and x-ray fluoroscopy [43].

The tracking techniques listed in Table 8.1 and the additional methods discussed after not only improve the experimental setup by increasing data acquisition they also improve the accuracy of the dynamic mass and energy balance model and the coating growth kinetics model. However, there are some areas where small adjustments can expand the capability of the coating growth kinetics model.

Table 8.1 Non-Invasive Particle Tracking Techniques

Tomography and Radiography		
Technique	**Properties Studied**	**Reference**
γ-ray and X-ray Transmission Tomography	Bubble Volume and Rise Velocity Particle Morphology (Radius of Gyration, Porosity, Fractal Dimension and Pre-Factor, Coordination Number, Coordination Angle) Solids Distribution Particle Pore Shape, Connectivity, and Distribution Fluidized Bed Voidage	[3-7]
X-ray Radiography	Fluidized Bed Voidage Bubble Hydrodynamics Reaction Rate of Shrinking Core Cubes in Fluidized Bed	[8-11]
Positron Emission Tomography	Particle Flow Dynamics	[12]
Nuclear Magnetic Resonance Imaging	Bubble Formation and Eruption at Fluidized Bed Surface Rotating Drum, Vibrating Fluidized Bed, Spouted Fluidized Bed Flows	[13, 14]
Electrical Capacitance Tomography	Bubble Hydrodynamics Bubble Velocity and Frequency Particle Moisture Content and Excitation Frequency Particle Motion in Spouted Fluidized Bed	[15-18]
Optical Tomography	Particle Volume Fraction	[19-21]
Microwave Tomography	Multiphase Density	[22]
Ultrasonic Tomography	Pneumatic Conveying	[23]

Table 8.1 Continued

Velocimetry		
Technique	**Properties Studied**	**Reference**
Positron Emission Particle Tracking (PEPT)	Particle Flow Pattern in Tapered Fluidized Bed Solids Velocity Profiles Transport Disengaging Height	[24-28]
Radioactive Particle Tracking Cinematography	Particle Circulation Pattern Particle Mixing Particle Flow Behavior to Determine Fluidization Regime	[29-32]
Laser Doppler Anemometry (LDA)	Flow Behavior Bubble Velocity Velocity in Fluidized Bed Freeboard Velocity Profiles in Plasma Fluidized Bed	[33-36]
Particle Image Velocimetry (PIV)	Distributor Plate Design Impact on Particle Motion Gas Hydrodynamics and Fluctuations Particle Elutriation	[37-40]
Fluorescent Particle Image Velocimetry (FPIV)	Interstitial Velocity	[41]

One last promising non-invasive tracking technique is focused beam reflectance measurement (FBRM) [44-46]. FBRM involves tracking the reflection of a focused laser beam to determine particle properties (i.e. size, shape, porosity, etc.). FBRM allows for real time measurement of the particle size distribution and therefore allows real time determination of which regime (coating or agglomeration) the fluidization operation is in. Moreover, the coating thickness can be determined directly as a function of time with the initial particle size distribution data. However, there are areas of concern regarding FBRM. One issue with FBRM is the location of the probe in the fluidized bed experimental setup. The view cell can be hindered, therefore skewing the measurements, if the fluidized bed conditions are not robust enough to ensure particle motion. The view cell hindrance can also be problematic if the particle bed is too wet causing particles to stick to the probe. Despite this challenge, FBRM would be a valuable addition to the experimental setup for two reasons: ensuring final product specifications are met (coating thickness distribution, no agglomeration present, etc.) and providing more data for comparison and cross-checking with the coating growth kinetics model.

First, it is recommended that the relationship between the fluidization air flow rate, fluidized bed height and the two tunable parameters be investigated. As noted in Chapter 7, the coating growth kinetics model has two tunable parameters integrated into the calculation sequence such that the model matches experimental data for coating efficiency. Additional experimental research is needed for a clearer definition of the relationships or mechanisms that account for the magnitude of each tunable parameter. Since this research has shown that the fluidized bed height plays a role in each tunable parameter, there is the possibility that these tunable parameters could be related to the fluidized bed pressure drop. Ideally, the effect of

spray drying could be modeled as a function of pressure drop and then included in the stochastic modeling sequence.

A second recommendation for the coating growth kinetics model is the incorporation of different particle geometries (see Figure 1.3) as part of the calculation algorithm. A spherical particle geometry used for this work but many different particle shapes can be coated in a fluidized bed (particularly in the Wurster orientation). Adding a catalog of particle geometries and automating the calculation sequence once specific size parameters have been entered can expand the flexibility of the coating growth kinetics model.

A third recommendation for the coating growth kinetics model is expansion to 2-D rather than 1-D. The 1-D modeling approach overestimates the experiment coating efficiency in both fluidized bed orientations. Incorporating radial effects into the calculations, like Equations 4.68 or 4.69 may reduce or potentially eliminate the 1-D model error for coating efficiency calculations.

The coating growth kinetics model can also be enhanced by integrating particle morphology calculations into it. This aspect involves a recommendation pertaining to the post experiment SEM and AFM analysis. One consistent challenge in fluidized bed processing is tracking the changes in particle morphology as a function of time. Taking samples without interrupting the fluidized bed operation for SEM and AFM analysis is one way to address this challenge. SEM pictures will show if the particle shape is changing and how while AFM analysis will show how the surface roughness changes. These changes in particle properties can then be correlated to the fluidized bed operating conditions and the phenomena causing them can be identified and quantified.

An additional recommendation regarding the SEM and AFM analysis pertains to ammonium nitrate for this work. SEM analysis at higher temperatures (above 32^{o}C and above 80^{o}C) may show some variation for the same sample with regards to the crystal structure change for the coated and uncoated samples. SEM analysis at these temperatures will allow for quantification of these changes. With regards to AFM analysis, measurements at elevated temperatures will show how the surface roughness changes quantitatively as well.

8.3 References

[1] Hede, P.D., Bach, P., & Jensen, A.D. (2009). Batch Top-Spray Fluid Bed Coating: Scale Up Insight Using Dynamic Heat and Mass Transfer Modelling, Chemical Engineering Science, 64, 1293-1317.

[2] Chaouki, J., Larachi, F., & Dudukovic, M. (1997) Nonivasive Tomographic and Velocimetric Monitoring of Multiphase Flows, Industrial Engineering and Chemistry Research, 36, 4476-4503

[3] Mudde, R.F. (2010) Double X-ray Tomography of a Bubbling Fluidized Bed, Industrial Engineering and Chemistry Research, 49, 5061-5065

[4] Dadkhah, M., Peglow, & Tsotsas, E. (2012) Characterization of the Internal Morphology of Agglomerates Produced in a Spray Fluidized Bed by X-Ray Tomography, Powder Technology, 228, 349-358.

[5] Farber, L., Tardos, G., & Michaels, J.N. (2003) Use of X-Ray Tomography to Study Porosity and Morphology of Granules, Powder Technology, 132, 57-63.

[6] MacCuaig, N., Seville, J.P.K., Gilboy, W.B., & Clift, R. (1985) Applications of Gamma Ray Tomography to Gas Fluidized Beds, Applied Optics, 24, 4083-4085.

[7] Patel, A.K., Waje, S.S., Thorat, B.N. & Mujumdar, A.S. (2008) Tomographic Diagnosis of Gas Maldistribution in Gas-Solid Fluidized Beds, Powder Technology, 185, 239-250.

[8] Romero, J. & Smith, D. (1965) Flash X-Ray Analysis of Fluidized Beds, AIChE Journal, 11, 595-600.

[9] Furui, S., Ozawa, M., & Umekawa, H. (2000) Flow Visualization of Fluidized Bed by X Ray Radiography, Journal of Visualization Society of Japan, 20, 347-350.

[10] Sarkar, P.S., Jilju, V., More, M.R., Sinha, A., Kamudu, M.V., Ramani, N.V.S., & Anadam, G. (2010) Development of an X-Ray Imaging System for Visualization and Quantitative Measurement of Fluidized Bed, Proceedings of the National Seminar & Exhibition on Non-Destructive Evaluation, 144-147.

[11] Dhanarathinam, R.S. & Kolar, A.K. (2013) Visualization and Characterization of Thermo-Physical Behavior of Wood During Devolatilization in a Hot Fluidized Bed Using X-Ray Radiography Technique, Fuel, 112, 208-223.

[12] Dechsiri, C., Van der Zwan, E.A., Dehling, H.G., & Hoffman, A.C. (2005) Dispersion of Particle Pulses in Fluidized Beds Measured by Positron Emission Tomography, AIChE Journal, 51, 791-801.

[13] Müller, C.R., Davidson, J.F., Dennis, J.S., Fennell, P.S., Gladden, L.F., Hayhurst, A.N., Mantle, M.D., Rees, A.C., & Sederman, A.J. (2007) Oscillations in Gas Fluidized Beds: Ultra-Fast Magnetic Resonance Imaging and Pressure Sensor Measurements, Powder Technology, 177, 87-98.

[14] Kawaguchi, T. (2010) MRI Measurement of Granular Flows and Fluid-Particle Flows, Advanced Powder Technology, 21, 235-241.

[15] Wiens, J. & Pugsley, T. (2006) Tomographic Imaging of a Conical Fluidized Bed of Dry Pharmaceutical Granule, Powder Technology, 169, 49-59.

[16] Makkawi, Y.T., & Wright, P.C. (2004) Electrical Capacitance Tomography for Conventional Fluidized Bed Measurements – Remarks on the Measuring Technique, Powder Technology, 148, 142-157.

[17] Wang, H.G. & Yang, W.Q. (2010) Measurement of Fluidized Bed Dryer by Different Frequency and Different Normalization Methods with Electrical Capacitance Tomography, Powder Technology, 199, 60-69.

[18] Takei, M., Zhao, Tong, & Yamane, K. (2009) Measurement of Particle Concentration in Powder Coating Process Using Capacitance Computed Tomography and Wavelet Analysis, Powder Technology, 193, 93-100.

[19] Magnusson, A., Rundqvist, R., Almstedt, A.E., & Johnsson, F. (2005) Dual Fibre Optical Probe Measurements of Solid Volume Fraction in a Circulating Fluidized Bed, Powder Technology, 151, 19-26.

[20] Cui, H., Mostoufi, N., & Chaouki, J. (2001) Gas and Solids Between Dynamic Bubble and Emulsion in Gas-Fluidized Beds, Powder Technology, 120, 12-20.

[21] Sobrino, C., Ellis, N., & de Vega, M. (2009) Distributor Effects Near the Bottom Region of Turbulent Fluidized Beds, Powder Technology, 189, 25-33.

[22] Hauschild, T. & Knöchel, R. (1993) Density Monitoring in Circulating Fluidized Beds Using a Microwave Sensor, 23rd European Microwave Conference, Paper B4.1, Madrid, Spain, 260-262.

[23] Brown, G.J., Reilly, D., & Mills, D. (1996) Development of an Ultrasonic Tomography System for Application in Pneumatic Conveying, Measurement Science and Technology, 7, 396-405.

[24] Schaafsma, S.H., Marx, T., & Hoffman, A.C. (2006*)* Investigation of the Particle Flowpattern and Segregation in Tapered Fluidized Beds, Chemical Engineering Science, 61, 4467-4475.

[25] Laverman, J.A., Fan, X., Ingram, A., van Sint Annaland, M., Parker, D.J., Seville, J.P.K., & Kuipers, J.A.M. (2012) Experimental Study on the Influence of Bed Material on the Scaling of Solids Circulation Patterns in 3D Bubbling Gas-Solid Fluidized Beds of Glass and Polyethylene Using Positron Emission Particle Tracking, Powder Technology, 224, 297-305.

[26] Hoomans, B.P.B., Kuipers, J.A.M., Mohd Salleh, M.A., Stein, M., & Seville, J.P.K. (2001) Experimental Validation of Granular Dynamics Simulations of Gas-Solid Fluidized Beds with Homogeneous in-Flow Conditions Using Positron Emission Particle Tracking, Powder Technology, 116, 166-177.

[27] Depypere, F., Pieters, J.G., & Dewettinck, K. (2009) PEPT Visualization of Particle Motion in a Tapered Fluidized Bed Coater, Journal of Food Engineering, 93, 324-336.

[28] Brems, A., Chan, C.W., Seville, J.P.K., Parker, D., & Baeyens, J. (2011) Modeling the Transport Disengagement Height in Fluidized Beds, Advanced Powder Technology, 22, 155-161.

[29] Khanna, P., Pugsley, T., Tanfara, H., Dumont, H. (2008) Radioactive Particle Tracking in a Lab-Scale Conical Fluidized Bed Dryer Containing Pharmaceutical Granule, Canadian Journal of Chemical Engineering, 86, 563-570.

[30] Upadhyay, R.K. & Roy, S. (2010) Investigation of Hydrodynamics of Binary Fluidized Beds via Radioactive Particle Tracking and Dual-Source Densitometry, Canadian Journal of Chemical Engineering, 88, 601-610.

[31] Tamadondar, M.R., Azizpour, H., Zarghami,R., Mostoufi, N. & Chaouki, J. (2012) Using Particle Trajectory for Determining the Fluidization Regime in Gas-Solid Fluidized Beds, Advanced Powder Technology, 23, 349-351.

[32] Fraguio, M.S., Cassanello, M.C., Larachi, F., & Chaouki, J. (2006) Flow Regime Transition Pointers in Three Phase Fluidized Beds Inferred from a Solid Tracer Trajectory, Chemical Engineering and Processing, 45, 350-358.

[33] Mathiesen, V., Solberg, T., & Hjertager, B.H. (2000) An Experimental and Computational Study of Multiphase Flow Behavior in a Circulating Fluidized Bed, International Journal of Multiphase Flow, 26, 387-419.

[34] Gautam, M., Jurewicz, J.T., Palmer, G.M., & Kale, S.R. (1993) Conditioned Sampled LDA Measurements of Throughflow Velocities Inside Two-Dimensional Fluidized Bed Bubbles, Flow Measurement and Instrumentation, 4, 109-118.

[35] Francke, E. & Amouroux, J. (1997) LDA Simultaneous Measurements of Local Density and Velocity Distribution of Particles in Plasma Fluidized Bed at Atmospheric Pressure, Plasma Chemistry and Plasma Processing, 17, 433-452.

[36] Levy, Y. (1986) LDA Technique for Measurements of Freeboards of Fluidized Beds, AIChE Journal, 32, 1579-1583.

[37] Agarwal, G., Lattimer, B., Ekkad, S., & Vandsburger, U. (2011*)* Influence of Multiple Gas Inlet Jets on Fluidized Bed Hydrodynamics Using Particle Image Velocimetry and Digital Image Analysis, Powder Technology, 214, 122-134.

[38] Chen, R.C. & Fan, L.S. (1992) Particle Image Velocimetry for Characterizing the Flow Structure in Three-Dimensional Gas-Liquid-Solid Fluidized Beds, Chemical Engineering Science, 47, 3615-3622.

[39] Rix, S.J.L., Glass, D.H., & Greated, C.A. (1996) Preliminary Studies of Elutriation from Gas-Solid Fluidized Beds Using Particle Image Velocimetry, Chemical Engineering Science, 51, 3479-3489

[40] Santana, D., Nauri, S., Acosta, A., Garcia, N., & Macias-Machin, A. (2005) Initial Particle Velocity Spatial Distribution from 2-D Erupting Bubbles in Fluidized Beds, Powder Technology, 150, 1-8.

[41] Northrup, M.A., Kulp, T.J., Angel, S.M., & Pinder, G.F. (1993) Direct Measurement of Interstitial Velocity Field Variations in a Porous Medium Using Fluorescent Particle Image Velocimetry, Chemical Engineering Science, 48, 13-21.

[42] Harris, A.T., Davidson, J.F., & Thorpe, R.B. (2003) Particle Residence Time Distributions in Circulating Fluidised Beds, Chemical Engineering Science, 58, 2181-2202.

[43] He, Z., We, B., Chandrasekaran, B., Bellehumeur, C., & Kantzas, A. (2007) X-Ray Fluoroscopy Measurements and CFD Simulation of Hydrodynamics in a Two Dimensional Gas-Solids Fluidized Bed, 2007 ECI Conference on The 12th International Conference on Fluidization – New Horizons in Fluidization Engineering. Paper 58, 481-488.

[44] Hu, X., Cunningham, J.C., & Winstead, D. (2008) Study Growth Kinetics in Fluidized Bed Granulation with at-line FBRM, International Journal of Pharmaceutics, 347, 54-61.

[45] Tok, A.T., Goh, X., Ng, W.K. & Tan, R.B.H. (2008*)* Monitoring Granulation Rate Processes Using Three PAT Tools in a Pilot-Scale Fluidized Bed, AAPS PharmSciTech, 9, 1083-1091.

[46] Arp, Z., Smith, B., Dycus, E., O'Grady, D. (2011) Optimization of a High Shear Wet Granulation Process Using Focused Laser Beam Reflectance Measurement and Particle Vision Microscope Technologies, Journal of Pharmaceutical Sciences, 100, 3431-3440.

APPENDICES

Appendix A Dynamic Mass and Energy Balance Step by Step Calculation Procedure

In order to calculate the dynamic mass and energy balances of a fluidized bed coating process, there are several parameters that must be defined a priori:

- Total Mass of Particles within the Batch
- Particle Diameter
- Air Temperature Prior to Heating
- Relative Humidity of Air Prior to Heating
- Volumetric Flow Rate of Air Prior to Heating
- Heated Air Temperature
- Temperature of Ambient Environment

Using the seven initial conditions listed above, the outcome of the mass and energy balances: air temperature, particle temperature, and wall temperature can be calculated. Table A1 shows the parameters listed above that are used in this step by step calculation procedure.

Table A1. Fluidized Bed Calculation Initial Conditions

Parameter	Value
Particle Mass (kg)	0.050
Average Particle Diameter (μm)	250
Air Temperature Prior to Heating (^{o}C)	25
Relative Humidity (%)	50
Air Volumetric Flow Rate Prior to Heating (m^3/hr)	15
Heated Air Temperature (^{o}C)	70
Ambient Environment Temperature (^{o}C)	25

The first part of this step by step calculation procedure is for the preheating segment of the fluidized bed coating operation. The adjustment for including the coating solution and atomization air will be addressed later.

Appendix A Continued

The total number of particles is calculated using the average particle diameter. The particles are assumed to be spherical, so the volume of a sphere is calculated and then transformed to mass by multiplying by the particle density as shown below. The total number of particles is then given as the total mass of the batch divided by the mass per particle as shown in Equation A1:

$$\text{N Particles} = \frac{0.05\ \text{kg}}{\frac{4\pi}{3}\left(\frac{250e^{-6}\text{m}}{2}\right)^3\left(1725\,\frac{\text{kg}}{\text{m}^3}\right)} = 3{,}542{,}927\ \text{Particles} \qquad \text{(A1)}$$

The total number of particles is then used as a checkpoint later to determine if an appropriate number of control volumes were selected for the calculation.

The next step is deciding on the height of the control volumes used to model each section of the fluidized bed. Selecting the height of the control volume is a balance between the scale of operation (laboratory, pilot, or commercial) and the computing time necessary for the program to run. The Mini Glatt fluidized bed is a laboratory scale fluidized bed, so a small control volume height of 0.5 cm is used as the control volume height.

The volume of each control volume is a small but important part of the dynamic mass and energy balances. The product bowl of the fluidized bed has a tapered geometry with the diameter increasing from bottom to top. The height of the product bowl is 11 cm. The diameter at the bottom of the bowl is 6.35 cm and the diameter at the top of the bowl is 14.605 cm. The diameter for the expansion chamber and filter house is constant at 14.605 cm. The product bowl diameter as a function of height is calculated as shown in Equation A2:

$$D_{bowl} = \frac{14.605\ \text{cm} - 6.35\ \text{cm}}{11\ \text{cm}} h_{bowl} + 6.35\ \text{cm} = 0.75045 h_{bowl} + 0.635 \qquad \text{(A2)}$$

Appendix A Continued

The diameter for the expansion chamber and filter house is constant at 14.605 cm. The height of the expansion chamber and the filter house are combined into one number as 34 cm. The volume of each control volume can now be calculated for the mass and energy balances. The volume of each control volume is calculated as a cylinder. For the constant diameter segments in the expansion chamber and the filter house the volume of each control volume is shown in Equation A3:

$$V_{cvcd} = \pi \frac{d^2}{4} h_{cv} = \pi \frac{(0.14605\ m)^2}{4} (0.005\ \text{m}) = 8.3765e^{-5} m^3 \qquad \text{(A3)}$$

The volume for each product bowl control volume is also calculated as a cylinder, but the diameter is changed with each control volume height to reflect the changing geometry. Table A2 shows the geometric characteristics of the product bowl as a function of height in 0.5 cm increments including: diameter, area, segment volume, and total volume.

Table A2. Product Bowl Geometry Characteristics

Height [cm]	**Diameter [m]**	**Area [m^2]**	**Volume [m^3]**	**Total Volume [cm^3]**
0.0	0.064	0.003167	-	-
0.5	0.067	0.003552	1.776E-05	17.8
1.0	0.071	0.003960	1.980E-05	37.6
1.5	0.075	0.004389	2.195E-05	59.5
2.0	0.079	0.004841	2.420E-05	83.7
2.5	0.082	0.005315	2.657E-05	110.3
3.0	0.086	0.005811	2.905E-05	139.3
3.5	0.090	0.006329	3.164E-05	171.0
4.0	0.094	0.006869	3.434E-05	205.3
4.5	0.097	0.007431	3.716E-05	242.5
5.0	0.101	0.008015	4.008E-05	282.6
5.5	0.105	0.008622	4.311E-05	325.7
6.0	0.109	0.009251	4.625E-05	371.9
6.5	0.112	0.009901	4.951E-05	421.4
7.0	0.116	0.010574	5.287E-05	474.3
7.5	0.120	0.011269	5.635E-05	530.6

Appendix A Continued

Table A2 Continued

8.0	0.124	0.011986	5.993E-05	590.6
8.5	0.127	0.012725	6.363E-05	654.2
9.0	0.131	0.013487	6.743E-05	721.6
9.5	0.135	0.014270	7.135E-05	793.0
10.0	0.139	0.015076	7.538E-05	868.4
10.5	0.142	0.015903	7.952E-05	947.9
11.0	0.146	0.016753	8.377E-05	1031.6

With the control volume height set and the fluidized bed geometry now properly accounted for, the next step is to calculate the thermo-physical properties (density, specific heat, thermal conductivity, and viscosity) of the fluidization air at the process conditions listed in Table A1. As noted in Chapter 4, the thermo-physical properties of air are a function of relative humidity and temperature. To determine the thermo-physical properties at the heated air temperature, the partial pressure of water vapor in the fluidization air at the preheat conditions must be calculated first.

The vapor pressure of water at the preheat condition is shown in Equation A4:

$$P^{sat}(25^{o}C) = 0.7073034146 - 2.703615165e^{-2}(25) + 4.36088211e^{-3}(25)^{2} - 4.662575642e^{-5}(25)^{3} + 1.034693708e^{-6}(25)^{4} = 2.43260 \text{ kPa} \quad \text{(A4)}$$

The partial pressure of water vapor, P_{WV}, in the air is the product of the relative humidity with the vapor pressure of water as shown in Equation A5:

$$P_{WV} = (0.5)2.4326 \text{ kPa} = 1.2163 \text{ kPa} \quad \text{(A5)}$$

The vapor pressure at the heated air temperature is calculated in the same manner as the preheated air in Equation A6:

$$P^{sat}(70^{o}C) = 0.7073034146 - 2.703615165e^{-2}(70) + 4.36088211e^{-3}(70)^{2} - 4.662575642e^{-5}(70)^{3} + 1.034693708e^{-6}(70)^{4} = 29.03346 \text{ kPa} \quad \text{(A6)}$$

Appendix A Continued

The relative humidity of the heated air is then given as the partial pressure of water over the vapor pressure of water at the heated air temperature as shown in Equation A7:

$$RH(70^oC) = \frac{1.2163\ kPa}{29.03346\ kPa} \times 100\% = 4.189\%\ RH \qquad (A7)$$

An additional enhancement factor is incorporated into the calculation for the thermo-physical properties of air. The enhancement factor, f(P,T) is a two parameter equation that is dependent only on temperature. The first parameter ξ_1 and the second parameter ξ_2 are shown below in Equations A8 and A9:

$$\xi_1 = 3.53624e^{-4} + 2.93228e^{-5}(70+273.15) + 2.61474e^{-7}(70+273.15)^2 + 8.57538e^{-9}(70+273.15)^3 = 0.005389595 \qquad (A8)$$

$$\xi_2 = \exp\left(\begin{matrix}-1.07588e^{1} + 6.32529e^{-2}(70+273.15) - 2.53591e^{-4}(70+273.15)^2 \\ + 6.33784e^{-7}(70+273.15)^3\end{matrix}\right) = 0.000620053 \qquad (A9)$$

The enhancement factor, f(P,T) is then calculated with ξ_1 and ξ_2 as shown below in Equation A10:

$$f(P,T) = \exp\left(0.005389595\left(1 - \frac{29.03346\ kPa}{101.325\ kPa}\right) + 0.000620053\left(\frac{29.03346\ kPa}{101.325\ kPa} - 1\right)\right) = 1.003408683 \qquad (A10)$$

The first thermo-physical property of humid air to be calculated is the density. The density of air is dependent on: the compressibility factor, relative humidity, temperature, and vapor pressure. The compressibility factor, Z_v is calculated using a two-parameter equation that is temperature dependent.

Appendix A Continued

The A and B parameters are given by Equations A11 and A12:

$$A = 0.7e^{-8}Pa^{-1} - 0.147184e^{-8}Pa^{-1}\exp\left(\frac{1734.29K^{-1}}{70+273.15}\right) = -2.23567e^{-7}Pa^{-1} \quad (A11)$$

$$B = 0.104e^{-14}Pa^{-2} - 0.335297e^{-17}Pa^{-2}\exp\left(\frac{3645.09K^{-1}}{70+273.15}\right) = -1.36585e^{-13}Pa^{-2} \quad (A12)$$

The compressibility factor is then given by Equation A13:

$$Z_v = 1 - 2.23567e^{-7}Pa^{-1}(29.03346\ kPa)\left(\frac{1000\ Pa}{1\ kPa}\right)$$

$$- 1.36585e^{-13}Pa^{-2}(29.03346\ kPa)^2\left(\frac{1000\ Pa}{1\ kPa}\right)^2 = 0.9933939 \quad (A13)$$

The density of humid air is calculated with Equation A14:

$$\rho_{air} = \frac{1}{0.9933939}\left(\frac{101325\ Pa}{8.314471e^{-3}\frac{Pa\ m^3}{mol\ K}(70+273.15)}\right)\left(28.963\frac{kg}{kmol}\right)$$
$$\left[1 - 1.003408683(0.04189)\left(1 - \frac{18.02\frac{kg}{kmol}}{28.963\frac{kg}{kmol}}\right)\left(\frac{29.03346\ kPa}{101.325\ kPa}\right)\right]$$
$$= 1.05305\ \frac{kg}{m^3} \quad (A14)$$

The next thermo-physical property to calculate is the viscosity. The viscosity of humid air is dependent on: dry air and water vapor viscosity respectively, relative humidity, temperature, vapor pressure, and two interaction parameters. The viscosity of water vapor is shown below in Equation A15:

$$\mu_{WV} = \frac{\left(8.058131868x10^{1} + 4.000549451x10^{-1}(70)\right)}{1000000} = 1.086e^{-4}\ Pa{\cdot}s \quad (A15)$$

Appendix A Continued

The viscosity of dry air is shown as Equation A16:

$$\mu_{DA} = \frac{\begin{pmatrix} -9.8601e^{-1} + 9.080125e^{-2}(70+273.15) - 1.17635575e^{-4}(70+273.15)^2 \\ + 1.2349703e^{-7}(70+273.15)^3 - 5.7971299e^{-11}(70+273.15)^4 \end{pmatrix}}{1000000} = 2.05069e^{-5}\ \text{Pa·s} \quad \text{(A16)}$$

The two interaction parameters to calculate are the air-vapor interaction parameter and the vapor-air interaction parameter. The air-vapor interaction parameter and the vapor-air interaction parameter are shown in Equations A17 and A18:

$$\Phi_{av} = \frac{\sqrt{2}}{4}\left(1+\frac{28.963\ \frac{kg}{kmol}}{18.02\ \frac{kg}{kmol}}\right)^{-0.5}\left[1+\left(\frac{2.05069e^{-5}\text{Pa·s}}{1.086e^{-4}\text{Pa·s}}\right)^{0.5}\left(\frac{18.02\ \frac{kg}{kmol}}{28.963\ \frac{kg}{kmol}}\right)^{0.25}\right]^2 = 0.4206 \quad \text{(A17)}$$

$$\Phi_{va} = \frac{\sqrt{2}}{4}\left(1+\frac{18.02\ \frac{kg}{kmol}}{28.963\ \frac{kg}{kmol}}\right)^{-0.5}\left[1+\left(\frac{1.086e^{-4}\text{Pa·s}}{2.05069e^{-5}\text{Pa·s}}\right)^{0.5}\left(\frac{28.963\ \frac{kg}{kmol}}{18.02\ \frac{kg}{kmol}}\right)^{0.25}\right]^2 = 3.5795 \quad \text{(A18)}$$

The viscosity of the humid fluidization air can now be calculated as shown in Equation A19:

$$\mu_a = \frac{\left[1-1.00341(0.04189)\left(\frac{29.03346}{101.325}\right)\right]1.086e^{-4}\ \text{Pa·s}}{\left[1-1.00341(0.04189)\left(\frac{29.03346}{101.325}\right)\right]+1.00341(0.04189)\left(\frac{29.03346}{101.325}\right)(0.4206)} + \frac{\left[1.00341(0.04189)\left(\frac{29.03346}{101.325}\right)\right]2.05069e^{-5}\text{Pa·s}}{\left[1.00341(0.04189)\left(\frac{29.03346}{101.325}\right)\right]+\left[1-1.00341(0.04189)\left(\frac{29.03346}{101.325}\right)\right](3.5795)} = 2.07709e^{-5}\ \text{Pa·s} \quad \text{(A19)}$$

The thermal conductivity of the fluidization air is calculated in a similar manner to the viscosity. The thermal conductivity of humid air is dependent on dry air and water vapor thermal conductivity respectively, relative humidity, temperature, vapor pressure, and two interaction parameters.

Appendix A Continued

The thermal conductivity of water vapor is shown in Equation A20:

$$\lambda_{WV} = \frac{\left(1.761758242\text{x}10^{1} + 5.558941059\text{x}10^{-2}(70)\right)}{1000} = 0.02232\,\frac{\text{W}}{\text{m}\cdot\text{K}} \qquad \text{(A20)}$$

The thermal conductivity of dry air is shown in Equation A21:

$$\lambda_{DA} = \frac{\begin{pmatrix}-2.276501e^{-3} + 1.2598485e^{-4}(70+273.15) - 1.4815235e^{-7}(70+273.15)^2 \\ + 1.73550646e^{-10}(70+273.15)^3 - 1.066657e^{-13}(70+273.15)^4 \\ +2.47663035e^{-17}(70+273.15)^5\end{pmatrix}}{1000}$$

$$= 0.029161\ \frac{\text{W}}{\text{m}\cdot\text{K}} \qquad \text{(A21)}$$

The thermal conductivity of humid air can now be calculated as shown in Equation A22:

$$\lambda_a = \frac{\left[1\text{-}1.00341(0.04189)\left(\frac{29.03346}{101.325}\right)\right]0.029161\frac{\text{W}}{\text{m}\cdot\text{K}}}{\left[1\text{-}1.00341(0.04189)\left(\frac{29.03346}{101.325}\right)\right] + 1.00341(0.04189)\left(\frac{29.03346}{101.325}\right)(0.4206)}$$

$$+ \frac{\left[1.00341(0.04189)\left(\frac{29.03346}{101.325}\right)\right]0.02232\frac{\text{W}}{\text{m}\cdot\text{K}}}{\left[1.00341(0.04189)\left(\frac{29.03346}{101.325}\right)\right] + \left[1\text{-}1.00341(0.04189)\left(\frac{29.03346}{101.325}\right)\right](3.5795)}$$

$$= 0.029088\,\frac{\text{W}}{\text{m}\cdot\text{K}} \qquad \text{(A22)}$$

The final thermo-physical property of humid air needed before any mass and energy balances can be calculated is the specific heat capacity. The specific heat capacity of air is dependent on dry air and water vapor specific heat capacities respectively, relative humidity, temperature, and vapor pressure. The specific heat capacity of water vapor is shown below in Equation A23:

$$C_{p,WV} = \left(1.86910989 - 2.578421578\text{x}10^{-4}(70) + 1.941058941\text{x}10^{-5}(70)^2\right)(1000)$$

$$= 1946.17\ \frac{\text{J}}{\text{kg}\cdot\text{K}} \qquad \text{(A23)}$$

Appendix A Continued

The specific heat capacity of dry air is shown in Equation A24:

$$C_{p,DA} = \frac{\left(1.03409 - 0.284887e^{-3}(70+273.15) - 0.7816818(70+273.15)^2 - 0.4970786e^{-9}(70+273.15)^3 + 0.1077024e^{-12}(70+273.15)^4\right)}{1000} = 1009.79\frac{J}{kg\cdot K} \quad (A24)$$

The numerator of the specific heat capacity of humid air can be calculated in Equation A25:

$$C_{p,a}\text{ numerator} = 1009.79\frac{J}{kg\cdot K}\left[1\text{-}1.00341(0.04189)\left(\frac{29.03346}{101.325}\right)\right]\left(28.963\frac{kg}{kmol}\right) + 1946.17\frac{J}{kg\cdot K}\left[1.00341(0.04189)\left(\frac{29.03346}{101.325}\right)\right]\left(18.02\frac{kg}{kmol}\right) = 29316.685\frac{J}{kmol\cdot K} \quad (A25)$$

The denominator of the specific heat capacity of humid air can be calculated in Equation A26:

$$C_{p,a}\text{ denominator} = \left(28.963\frac{kg}{kmol}\right)\left[1\text{-}1.00341(0.04189)\left(\frac{29.03346}{101.325}\right)\right] + \left(18.02\frac{kg}{kmol}\right)\left[1.00341(0.04189)\left(\frac{29.03346}{101.325}\right)\right] = 28.8312\ \frac{kg}{kmol} \quad (A26)$$

The specific heat capacity of humid air is Equation A25 divided by A26 and is shown below as Equation A27:

$$C_{p,a} = \frac{29316.685\ \frac{J}{kmol\cdot K}}{28.8312\ \frac{kg}{kmol}} = 1016.83\frac{J}{kg\cdot K} \quad (A27)$$

While relative humidity is used to determine the thermo-physical properties of humid air at the operating conditions, the absolute humidity is used in the mass and energy balances and converted to relative humidity.

Appendix A Continued

The relationship between relative humidity and absolute humidity, X_{air}, is shown in Equation A28:

$$X_{air} = \frac{\left(\frac{(0.04189)(29.03346\ \text{kPa})\left(\frac{18.02\ \frac{\text{kg}}{\text{kmol}}}{28.963\ \frac{\text{kg}}{\text{kmol}}}\right)}{101.325\ \text{kPa}} \right)}{\left(1 - \frac{(0.04189)(29.03346\ \text{kPa})}{101.325\ \text{kPa}}\right)} = 0.007557\ \frac{\text{kg } H_2O}{\text{kg Air}} \qquad \text{(A28)}$$

The next step involves calculations for the fluidized bed hydrodynamics. The fluid flow calculations here lead to heat and mass transfer characteristics. First, the volumetric flow rate must be corrected for expansion during heating. This is done by calculating the density of humid air at the preheat conditions listed in Table A1. The procedure for calculating the humid air density at the preheat conditions listed in Table A1 is the same as the procedure for calculating the heated humid air density that has previously been described in Equations A6-A14. Therefore, values for the variables of Equations A6-A14 are shown in Table A3.

Table A3. Parameter Values for Equations A6-A14 at Preheat Air Conditions

Parameter	Value
ξ_1	0.001226044
ξ_2	$8.87383e^{-5}$
Enhancement Factor	1.01110618
A	$-4.87403e^{-7}$
B	$-6.8284e^{-13}$
Z_v	0.9988103
ρ_a (kg/m^3)	1.25299

Appendix A Continued

The corrected volumetric flow rate can now be calculated with the humid air density at the preheat and heated conditions as shown in Equation A29:

$$V_{o,\,corr} = 15\frac{m^3}{hr}\left(\frac{1.25299\frac{kg}{m^3}}{1.05350\frac{kg}{m^3}}\right) = 17.84\ \frac{m^3}{hr} \quad (A29)$$

The superficial gas velocity is calculated using the corrected volumetric flow rate and the distributor plate diameter in Table A1 and the distributor plate porosity as shown in Equation A30:

$$U_o = \frac{17.84\ \frac{m^3}{hr}}{\pi\left(\frac{0.0635}{2}\right)^2\left(3600\frac{s}{hr}\right)(0.2)} = 7.824\ \frac{m}{s} \quad (A30)$$

The superficial velocity is assumed to be constant for the entire height of the control volume in each control volume. The superficial velocity in Equation A30 will be used shortly to determine the fluidization gas bubble properties – diameter, rise velocity, frequency, bed voidage, and particle circulation rate, but first the minimum fluidization velocity must be calculated to establish a lower bound for operation. The minimum fluidization velocity is a function of the Archimedes number. Equation A31 shows the calculation for the Archimedes number:

$$Ar = \frac{\left(9.81\frac{m}{s^2}\right)\left(250e^{-6}m\right)^3\left(1725\frac{kg}{m^3} - 1.0535\frac{kg}{m^3}\right)\left(1.0535\frac{kg}{m^3}\right)}{\left(2.07709e^{-5}\frac{kg}{m\cdot s}\right)^2} = 644.988 \quad (A31)$$

The minimum fluidization velocity is then calculated in dimensionless form as the Reynolds number using Equation A32:

$$Re_{mf} = \sqrt{33.7^2 + 0.0408(644.988)} - 33.7 = 0.3882 \quad (A32)$$

Appendix A Continued

The minimum fluidization velocity is then calculated from the result of Equation A32 in Equation A33:

$$U_{mf} = \frac{0.3882\left(2.07709e^{-5}\frac{kg}{m\cdot s}\right)}{\left(250e^{-6}m\right)\left(1.0535\frac{kg}{m^3}\right)} = 0.0306\ \frac{m}{s} \qquad (A33)$$

Along with the minimum fluidization velocity, another important parameter at the minimum fluidization condition is the void fraction. Equation A34 shows the void fraction at minimum fluidization with a particle sphericity of 1 :

$$\varepsilon_{mf} = 0.586(1)^{-0.72}\left(\frac{1}{644.988}\right)^{0.029}\left(\frac{1.0535\frac{kg}{m^3}}{1725\frac{kg}{m^3}}\right)^{0.021} = 0.4158 \qquad (A34)$$

The height of the fluidized bed at minimum fluidization can be calculated now with the total particle volume, the void fraction at minimum fluidization, and the product bowl volume as a function of height. The total particle volume is shown as Equation A35:

$$V_{part} = \frac{0.05\ kg}{1725\frac{kg}{m^3}} = 2.89855e^{-5}\ m^3 \qquad (A35)$$

The volume of the fluidized particle bed at minimum fluidization is then calculated as Equation A36:

$$V_{bed,\ mf} = \frac{2.89855e^{-5}m^3}{1\text{-}0.4158} = 4.9615e^{-5}\ m^3 \qquad (A36)$$

Through interpolation of the volumes listed in Table A2, the particle bed height at minimum fluidization that satisfies the result of Equation A36 is about 1.3 cm.

Appendix A Continued

The interpolation is shown in Equation A37:

$$h_{mf} = \frac{4.9615e^{-5}m^3 - 37.6e^{-5}m^3}{\left(\frac{59.5e^{-5}m^3 - 37.6e^{-5}m^3}{1.5\text{ cm} - 1.0\text{ cm}}\right)} + 1.0\text{ cm} = 1.274\text{ cm} \qquad (A37)$$

With the superficial gas velocity from Equation A30 and the minimum fluidization velocity of Equation A33, the properties of the gas bubbles formed at the porous fluidized bed distributor plate can be determined. The gas bubble diameter is shown in Equation A38:

$$D_{bub} = \frac{0.54}{\left(9.81\frac{m}{s^2}\right)^{0.2}}\left(7.824\frac{m}{s} - 0.0306\frac{m}{s}\right)^{0.4}(0.005 + 0.03)^{0.8} = 0.0535\text{ m} \qquad (A38)$$

The bubble rise velocity is a function of the superficial gas velocity and the bubble diameter as shown in Equation A39:

$$U_{br} = 7.824\frac{m}{s} - 0.0306\frac{m}{s} + 0.711\left(9.81\frac{m}{s^2}(0.0535\text{ m})\right)^{0.5} = 8.308\frac{m}{s} \qquad (A39)$$

The bubble frequency is also a function of the bubble diameter. The bubble frequency is shown as Equation A40:

$$f_{bub} = \frac{17.84\frac{m^3}{hr}}{\left(3600\frac{s}{hr}\right)\left(\frac{\pi}{6}\right)(0.0535\text{ m})^3} = 61.806\text{ s}^{-1} \qquad (A40)$$

The particle residence time for the control volume can now be calculated as well. The particle residence time for the control volume is shown in Equation A41:

$$\tau = \frac{0.013\text{ m}}{0.6\left(7.824\frac{m}{s} - 0.0306\frac{m}{s}\right)\left(1 - \frac{\left(7.824\frac{m}{s} - 0.0306\frac{m}{s}\right)}{8.308\frac{m}{s}}\right)} = 0.04488\text{ s} \qquad (A41)$$

Appendix A Continued

The particle circulation rate is the reciprocal of Equation A41 and is shown as Equation A42:

$$r = \frac{1}{0.04488\ s} = 22.281\ s^{-1} \qquad (A42)$$

The fluidization gas bubbles have a void fraction associated with them that plays a role in the overall void fraction of the fluidized bed. The bubble void fraction was used previously in the denominator of Equation A41 but is shown here as Equation A42:

$$\varepsilon_{bub} = \frac{\left(7.824\frac{m}{s} - 0.0306\frac{m}{s}\right)}{8.308\frac{m}{s}} = 0.938 \qquad (A42)$$

The overall bed void fraction for the control volume is then calculated in Equation A43:

$$\varepsilon_{bed} = 0.938 + 0.4158\left(1 - \frac{\left(7.824\frac{m}{s} - 0.0306\frac{m}{s}\right)}{8.308\frac{m}{s}}\right) = 0.9638 \qquad (A43)$$

The overall bed void fraction will be used shortly to determine the number of particles within the first control volume. The volume of the control volume is determined as a cylinder with a control volume height of 0.5 cm. The volume of the first control volume is shown in Equation A44:

$$V_{cell} = \pi\left(\frac{0.0635m}{2}\right)^2 (0.005\ m) = 1.5834e^{-5}\ m^3 \qquad (A44)$$

The volume occupied by the particles within the control volume is shown in Equation A45:

$$V_{part} = 1.5834e^{-5}m^3\ (1-0.9638) = 5.732e^{-7}\ m^3 \qquad (A45)$$

Appendix A Continued

The number of particles based on the average particle diameter listed in Table A1 is shown in Equation A46:

$$N_{part} = \frac{5.732e^{-7}m^3}{\frac{4\pi}{3}\left(\frac{250e^{-6}m}{2}\right)^3} = 70063 \quad (A46)$$

The mass of particles within the control volume is shown as Equation A47:

$$M_{part} = 70063\left(\frac{4\pi}{3}\left(\frac{250e^{-6}m}{2}\right)^3\right)\left(1725\,\frac{kg}{m^3}\right) = 9.8877e^{-4}\ kg \quad (A47)$$

The total area of the particles, estimated as perfect spheres, within the control volume is shown as Equation A48:

$$A_{part} = 4\pi\left(\frac{250e^{-6}m}{2}\right)^2 (70063) = 0.013757\ m^2 \quad (A48)$$

There are two Reynolds numbers needed for heat and mass transfer calculations, the particle Reynolds number and the gas Reynolds number. The particle Reynolds number is shown as Equation A49:

$$Re_{part} = \frac{\left(1.0535\frac{kg}{m^3}\right)\left(7.824\frac{m}{s}\right)(250e^{-6}m)}{2.07709e^{-5}\ Pa{\cdot}s} = 99.208 \quad (A49)$$

The gas Reynolds number uses the diameter of the fluidized bed rather than the particle diameter and is shown as Equation A50:

$$Re_{gas} = \frac{\left(1.0535\frac{kg}{m^3}\right)\left(7.824\frac{m}{s}\right)(0.0635\ m)}{2.07709e^{-5}\ Pa{\cdot}s} = 25198.912 \quad (A50)$$

Appendix A Continued

The Prandtl number is needed before convective heat transfer to the particles and the fluidized bed wall from the fluid can be calculated. The Prandtl number is shown as Equation A51:

$$Pr = \frac{\left(1016.83\frac{J}{kg\,K}\right)(2.07709e^{-5}\ Pa{\cdot}s)}{0.029088\ \frac{W}{m\,K}} = 0.72609 \qquad (A51)$$

The particle Nusselt number provides the convective fluid-to-particle heat transfer coefficient in dimensionless form. The particle Nusselt number is shown in Equation A52:

$$Nu_{part} = 2 + (0.72609)(0.43(99.208)^{0.5} + 0.06(99.208)^{0.667}) = 6.04483 \qquad (A52)$$

The convective heat transfer coefficient for fluid-to-particle heat transfer is shown as Equation A53:

$$\alpha_{part} = \frac{6.04483\left(0.029088\ \frac{W}{m\,K}\right)}{250e^{-6}m} = 703.328\frac{W}{m^2K} \qquad (A53)$$

The Nusselt number for the convective fluid-to-wall heat transfer is shown as Equation A54:

$$Nu_{wall} = 0.023(0.72609)^{0.4}(25198.912)^{0.8} = 67.1784 \qquad (A54)$$

The convective fluid-to-wall heat transfer coefficient is shown as Equation A55:

$$\alpha_{wall} = \frac{67.1784\left(0.029088\ \frac{W}{m\,K}\right)}{0.0635\ m} = 30.773\frac{W}{m^2K} \qquad (A55)$$

The result of Equation A55 is used to determine the thermal convective heat transfer resistance of the fluidization gas to the fluidized bed walls. The thermal convective heat transfer

resistance of the fluidization gas to the fluidized bed walls is the reciprocal of Equation A55 and is shown as Equation A56:

$$R_{conv} = \frac{1}{30.773 \frac{W}{m^2 K}} = 0.32496 \frac{m^2 K}{W} \quad (A56)$$

Equations A54-A56 represent heat transfer from the fluidization gas bubbles to the interior fluidized bed walls. There is also heat transfer from the fluidization gas to the interior fluidized bed walls via the gas-particle emulsion contact with the fluidized bed walls. Since there is sufficient gas-particle mixing when a stable fluidization pattern has developed, the gas-particle mixture is treated as an emulsion. Research on the gas-particle behavior has led to the development of heat transfer correlations treating the gas-particle mixture as an emulsion. Heat transfer from the gas-particle emulsion occurs via conduction. The ratio of gas film thermal boundary layer to the particle diameter is shown as Equation A57:

$$\tau_w = 0.3361 \left(\frac{0.142 \frac{W}{m\,K}}{0.029088 \frac{W}{m\,K}} \right)^{-0.1862} = 0.25018 \quad (A57)$$

The thermal conductivity of stationary gas around a submerged particle is shown as Equation A58:

$$\lambda_{aw} = 0.4158 \left(0.029088 \frac{W}{m\,K} \right) + (1\text{-}0.4158) \left(0.142 \frac{W}{m\,K} \right) \left[\frac{1}{0.25018 \left(\frac{0.142 \frac{W}{m\,K}}{0.029088 \frac{W}{m\,K}} \right) + \frac{1}{3}} \right] = 0.0655 \frac{W}{m\,K} \quad (A58)$$

Appendix A Continued

The heat transfer resistance from a particle-fluidized bed contact point is shown as Equation A59:

$$R_{pcd} = \frac{1}{\left[\frac{2\left(0.0655\frac{W}{m\,K}\right)}{250e^{-6}m} + 0.05\left(1016.83\frac{J}{kg\cdot K}\right)\left(1.0535\frac{kg}{m^3}\right)\left(7.824\frac{m}{s}\right)\right]}$$

$$= 0.0010637\frac{m^2K}{W} \qquad \text{(A59)}$$

In addition to particle-fluidized bed wall heat transfer, there is also heat transfer between particles during a particle-particle collision. The ratio of gas film thermal boundary layer to the particle diameter for contact between nearby particles is shown as Equation A60:

$$\tau_{mark} = 0.3116\left(\frac{0.142\frac{W}{m\,K}}{0.029088\frac{W}{m\,K}}\right)^{-0.2174} = 0.22075 \qquad \text{(A60)}$$

The thermal conductivity of the stationary gas in the fluidized bed is shown as Equation A61:

$$\lambda_{aw} = 0.4158\left(0.029088\frac{W}{m\,K}\right)$$

$$+ (1\text{-}0.4158)\left(0.142\frac{W}{m\,K}\right)\left[\frac{1}{0.22075\left(\frac{0.142\frac{W}{m\,K}}{0.029088\frac{W}{m\,K}}\right) + \frac{2}{3}}\right] = 0.0597\frac{W}{m\,K} \qquad \text{(A61)}$$

To calculate the heat transfer resistance of the emulsion packet, the specific heat capacity of the particles should also be known. The specific heat capacity of a solid is usually determined by experiment and sometimes assumed to be constant over a specific temperature range.

Appendix A Continued

The specific heat capacity for this work as a function of temperature is shown as Equation A62:

$$C_{p,part} = \left(\frac{1000\,\frac{J}{kJ}}{80.03\,\frac{g}{mol}}\right)(3.98 + 0.6219(298.15\text{ K}) - 6.3357e^{-4}(298.15\text{ K})^2)$$

$$= 1662.87\,\frac{J}{kg\text{ K}} \qquad \text{(A62)}$$

The heat transfer resistance of the emulsion packet is then shown as Equation A63:

$$R_{packet} = \frac{1}{\left[\frac{2}{\sqrt{\pi}}\left(\frac{0.0597\,\frac{W}{m\text{ K}}\left(1725\,\frac{kg}{m^3}\right)(1\text{-}0.4158)\left(1662.87\,\frac{J}{kg\cdot K}\right)(61.806\text{ s}^{-1})}{1\text{-}0.938}\right)^{0.5}\right]}$$

$$= 8.8743e^{-5}\ \frac{m^2K}{W} \qquad \text{(A63)}$$

The total heat transfer resistance to the interior fluidized bed wall is the summation of R_{pcd} and R_{packet} and is shown as Equation A64:

$$R_p = 0.0010637\,\frac{m^2K}{W} + 8.8743e^{-5}\ \frac{m^2K}{W} = 1.152443e^{-3}\ \frac{m^2K}{W} \qquad \text{(A64)}$$

In addition to convective heat transfer resistance within a fluidized bed operation, there is also conductive heat transfer resistance along the fluidized bed walls. The conductive heat transfer resistance along the fluidized bed walls is shown as Equation A65:

$$R_{cond} = \frac{0.005\text{ m} + 0.005\text{ m}}{2\left(14.6\,\frac{W}{m\text{ K}}\right)} = 3.4245e^{-4}\ \frac{m^2K}{W} \qquad \text{(A65)}$$

With all the internal heat transfer characteristics accounted for, the next step is to account for natural convection from the outer fluidized bed walls to the environment. Natural convection

heat transfer rates are dependent on the thermo-physical properties of the surrounding environment and the surface that heat is transferred to or absorbed from. The thermo-physical properties of the entire system are evaluated at the film temperature which is the average temperature between the environment (25°C) and the surface of interest (T_{part} = 25.01°C). The film temperature is shown in Equation A66:

$$T_{film} = \frac{25^{o}C + 25.01^{o}C}{2} = 25.005^{o}C \qquad (A66)$$

The procedure to calculate the thermo-physical properties of humid air at the film temperature is the same as previously outlined in Equations A4-A27. Therefore, the parameters needed to evaluate the thermo-physical properties at the film temperature are shown in Table A4 and the thermo-physical properties of humid air at the film temperature are shown in Table A5.

Table A4. Parameters for Humid Air Thermo-Physical Properties

Parameter	Value
Environment RH (%)	50
Vapor Pressure (kPa)	2.43344
ξ_1	0.001226
ξ_2	$8.8761e^{-5}$
Enhancement Factor	1.008572
A	$-4.87355e^{-7}$
B	$-6.827e^{-13}$
Z_v	0.99881
Φ_{av}	0.42963
Φ_{va}	3.39128
μ_{DA} (Pa s)	$1.8444e^{-5}$
μ_{WV} (Pa s)	$9.006e^{-5}$
λ_{DA} (W/m K)	0.025932
λ_{WV} (W/m K)	0.019112
$C_{p,DA}$ (J/kg K)	1006.32
$C_{p,WV}$ (J/kg K)	1874.75

Appendix A Continued

Table A5. Thermo-Physical Properties of Humid Air at Film Temperature

Parameter	Value
Film T RH (%)	49.983
ρ_a (kg/m^3)	1.25296
μ_a (Pa s)	1.86724e^{-5}
λ_a (W/m K)	0.025865
C_p (J/kg K)	1012.84

With the thermo-physical properties of humid air at the film temperature, the next step is to calculate the Prandtl number at the film temperature. The procedure for the Prandtl number at the film temperature is the same as previously outlined in Equation A51, however here the properties of humid air at the film temperature are used. The resultant Prandtl number at the film temperature has a value of 0.73118.

The Nusselt number for natural convection involves a correlation between the Prandtl number and the Grashof number. The Grashof number has an additional parameter called the coefficient of volumetric expansion shown as Equation A67:

$$\beta_a = \frac{1}{25.005+273.15} = 0.003354\text{K}^{-1} \tag{A67}$$

The Grashof number is shown as Equation A68:

$$\text{Gr} = \frac{0.003354\text{K}^{-1}\left(9.81\frac{\text{m}}{\text{s}^2}\right)(0.0635\text{ m})^3\left(1.25296\frac{\text{kg}}{\text{m}^3}\right)^2(25.01^{\text{o}}\text{C} - 25.00^{\text{o}}\text{C})}{(1.86724\text{e}^{-5}\text{ Pa}\cdot\text{s})^2} = 329.596 \tag{A68}$$

The Nusselt number for natural convection is shown as Equation A69:

$$\text{Nu}_e = 0.59[(0.73118)(329.596)]^{0.25} = 2.32463 \tag{A69}$$

Appendix A Continued

The natural convection heat transfer coefficient is shown as Equation A70:

$$\text{NHTC} = \frac{2.32463\left(0.025865\,\frac{\text{W}}{\text{m K}}\right)}{0.0635\text{ m}} = 0.9469\,\frac{\text{W}}{\text{m}^2\text{K}} \tag{A70}$$

The heat transfer resistance for the fluidized bed wall to the surrounding environment is the reciprocal of the result A Equation A70, shown as Equation A71:

$$R_{wall} = \frac{1}{0.9469\,\frac{\text{W}}{\text{m}^2\text{K}}} = 1.0568\,\frac{\text{m}^2\text{K}}{\text{W}} \tag{A71}$$

In addition to convection and conduction heat losses, there is also heat loss via radiation. Heat loss by radiation is very low when temperatures are below 400^{o}C as noted in Chapter 2. In order to calculate heat loss by radiation, the wall area must be calculated first which is shown as Equation A72:

$$A_{wall} = \pi(0.0635\text{ m})(0.005\text{ m}) = 9.975e^{-4}\text{m}^2 \tag{A72}$$

The heat loss via radiation is shown as Equation A73:

$$\begin{aligned} Q_{rad} &= 5.669e^{-8}\,\frac{\text{W}}{\text{m}^2\text{K}^4}(1)\left(9.975e^{-4}\text{m}^2\right)((25.01+273.15)^4 - (25+273.15)^4) \\ &= 5.9952e^{-5}\text{ W} \end{aligned} \tag{A73}$$

Two additional heat loss need to be calculated for the mass and energy balances. The first heat loss is gas-to-wall heat transfer loss which is shown as Equation A74:

$$\Phi_{loss,a} = \frac{9.975e^{-4}\text{m}^2(0.938)(70^{o}\text{C} - 25.01^{o}\text{C})}{0.32496\,\frac{\text{m}^2\text{K}}{\text{W}}} = 0.12954\text{ W} \tag{A74}$$

Appendix A Continued

The heat loss for particle-to-wall heat transfer is shown as Equation A75:

$$\Phi_{loss,p} = \frac{9.975e^{-4}m^2(1 - 0.938)(25.011^oC - 25.01^oC)}{1.152443e^{-3}\ \frac{m^2K}{W}} = 5.3664^{-5}W \qquad (A74)$$

The mass flow rate of air and the mass of air that is in a control volume at the operating conditions are two of the last three parameters left to calculate before the mass and energy balances can calculated for the particle preheating segment of the fluidized bed coating operation. The mass flow rate of air is shown as Equation A75:

$$G_a = \frac{17.84\ \frac{m^3}{hr}\left(1.0535\frac{kg}{m^3}\right)}{3600\frac{s}{hr}}\left(\frac{1}{1 + 0.007557}\right) = 5.18152e^{-3}\frac{kg}{s} \qquad (A75)$$

The mass of air that occupies the control volume at the operating conditions is shown as Equation A76:

$$M_a = 1.5834e^{-5}\ m^3\left(1.0535\frac{kg}{m^3}\right)(0.9638) = 1.6077e^{-4}\ kg \qquad (A76)$$

The last parameter to calculate is the fluidization gas residence time within the control volume. The fluidization gas residence time is needed to maintain all the terms in the mass and energy balances on the same magnitude scale. The fluidization gas residence time is shown as Equation A77:

$$GRT = \frac{1.5834e^{-5}\ m^3}{\left(\frac{17.84\ \frac{m^3}{hr}}{3600\frac{s}{hr}}\right)} = 3.1952^{-3}\ s \qquad (A77)$$

The mass and energy balances can now be calculated with all the parameters established for fluid flow and heat transfer. There is no liquid addition during the preheating segment of the

fluidized bed coating operation when the particles are heated up above ambient temperature. It is also assumed that the particles are dry (no moisture present on the surface) therefore there is no increase in the absolute air humidity. It is also assumed that the number of particles exiting the first control volume is equal to the number of particles entering the first control volume. Therefore, the mass of particles within the first control volume is treated as constant. These assumptions cut the number of equations to solve for the temperature profiles from six down to three.

There are mass and energy balances to solve during the particle preheating segment of a fluidized bed coating operation. There are three temperature profiles of interest during a fluidized bed coating operation: the fluidizing air temperature, the particle temperature, and the wall temperature. The energy balance for the fluidizing air temperature is shown as Equation A78:

$$\frac{1.6077e^{-4}\ \text{kg}\left(1016.83\frac{\text{J}}{\text{kg}\cdot\text{K}}\right)(70^{o}\text{C} - T_{a,out})}{1\text{s} - 0\text{s}} =$$

$$5.18152e^{-3}\frac{\text{kg}}{\text{s}}\left(1016.83\frac{\text{J}}{\text{kg}\cdot\text{K}}\right)(70^{o}\text{C} - T_{a,out})$$

$$- 703.328\frac{\text{W}}{\text{m}^2\text{K}}(0.013757\ \text{m}^2)(70^{o}\text{C} - 25.01^{o}\text{C})\left(3.1952^{-3}\text{s}\right) - 0.12954\ \text{W}\left(3.1952^{-3}\text{s}\right)$$

$$\therefore T_{a,out} = 69.73^{o}\text{C} \qquad \text{(A78)}$$

The energy balance for the particle temperature is shown as Equation A79:

$$\frac{9.8877e^{-4}\ \text{kg}\left(1662.87\frac{\text{J}}{\text{kg}\cdot\text{K}}\right)(T_p - 25^{o}C)}{1\text{s} - 0\text{s}} =$$

$$703.328\frac{\text{W}}{\text{m}^2\text{K}}(0.013757\ \text{m}^2)(70^{o}\text{C} - 25.01^{o}\text{C})\left(3.1952^{-3}\text{s}\right) - 5.3664^{-5}\text{W}\left(3.1952^{-3}\text{s}\right)$$

$$\therefore T_p = 25.85^{o}\text{C} \qquad \text{(A79)}$$

Appendix A Continued

The energy balance for the fluidized bed wall temperature is shown as Equation A80:

$$\frac{7850\frac{kg}{m^3}\left(9.975e^{-4}m^2\right)(0.0635\ m)\left(500\frac{J}{kg\cdot K}\right)(T_{wall}\ -\ 25.011^oC)}{1s-\ 0s}\ =$$

$$\left(\frac{9.975e^{-4}m^2(0.938)(70^oC-25.011^oC)}{0.32496\ \frac{m^2K}{W}}\right)+\left(\frac{9.975e^{-4}m^2(1-0.938)(25.01^oC-25.011^oC)}{1.152443e^{-3}\ \frac{m^2K}{W}}\right)$$

$$-\ 5.9952e^{-5}\ W\ -\ \frac{9.975e^{-4}m^2}{1.0568\frac{m^2K}{W}}\qquad \therefore T_{wall} = 25.0115^oC \qquad (A80)$$

This procedure is continued for the duration of the preheating segment of the fluidized bed coating operation. When the preheating segment is over a liquid coating solution is introduced as small droplets into the fluidized bed via a two-fluid nozzle. Additional parameters must be calculated to account for the additional air and liquid in the fluidized bed. The additional parameters are: the solvent (water) vapor diffusion coefficient, the latent heat of vaporization, mass transfer dimensionless numbers, mass transfer rates, and drying rates. In addition to Equations A78-A80 for the temperature profiles there are other mass balance equations that must be incorporated properly with the liquid coating solution and atomization air. The additional equations for the particle coating segment of the fluidized bed operation will be addressed now.

A few additional parameters for the coating solution addition before any calculations can be done. Table A6 shows the additional parameters needed and their respective values which are constant for the duration of the spraying segment of the fluidized bed coating operation.

Table A6. Coating Solution Parameters for Spraying Segment of Fluidized Bed Coating Operation

Parameter	Value
Atomization Air Pressure (bar)	0.4
Atomization Air Relative Humidity (%)	50
Atomization Air Temperature (^{o}C)	25
Coating Solution Density (kg/m^3)	1100
Coating Solution Flow Rate (ml/min)	1
Coating Solution Temperature (^{o}C)	25
Coating Solution Specific Heat Capacity (J/kg K)	4184
Dry Matter Content (kg Coating/kg Solvent)	0.1

For this example, the particles and wall have already been through the preheat segment of the fluidized bed coating operation. The particle temperature is taken as 55^{o}C and the wall temperature is taken as 52^{o}C. The fluidization air temperature is still at 70^{o}C.

The atomization air is split off from the fluidization air prior to heating, so it enters the spray nozzle with the same density as the fluidization air at the preheat condition, 1.25299 kg/m^3. The volumetric flow rate of atomization air in the spray nozzle is a function of the atomization air pressure as shown in Equation A81:

$$V_{at} = 447.7612 \frac{\left(\frac{mL}{min}\right)}{bar}(0.4\ bar) = 179.1 \frac{mL}{min} \qquad (A81)$$

The additional mass of air added to the fluidized bed in addition to the fluidization air is shown as Equation A82:

$$M_{at} = 179.1 \frac{mL}{min}\left(\frac{1\ min}{60\ s}\right)\left(\frac{m^3}{1000000\ ml}\right)\left(1.25299 \frac{kg}{m^3}\right) = 3.7403e^{-6}\ \frac{kg}{s} \qquad (A82)$$

In order to calculate the mass transfer rate, a few additional dimensionless numbers must be calculated first. Diffusion is an important part of the dimensionless numbers used to

determine the mass transfer characteristics of a fluidized bed operation. The diffusion coefficient of water in the vapor phase is shown as Equation A83:

$$D_{Water} = 24.2e^{-6}\frac{m^2}{s}\left[\frac{(70^oC+273.15)}{293.15}\right]^{1.75}\left(\frac{10^5\ Pa}{101325\ Pa}\right) = 3.1462e^{-5}\ \frac{m^2}{s} \qquad (A83)$$

The diffusion coefficient can now be used in the Schmidt number, the mass transfer equivalent to the heat transfer Prandtl number. The Schmidt number is shown as Equation A84:

$$Sc = \frac{2.07709e^{-5}\ Pa{\cdot}s}{\left(1.0535\frac{kg}{m^3}\right)\left(3.1462e^{-5}\ \frac{m^2}{s}\right)} = 0.6267 \qquad (A84)$$

The mass transfer coefficient can now be calculated in dimensionless form as the Sherwood number as Equation A85 and the mass transfer coefficient as Equation A86:

$$Sh_{part} = 2 + (0.6267)(0.43(99.208)^{0.5} + 0.06(99.208)^{0.667}) = 6.621 \qquad (A85)$$

$$\alpha'_{part} = \frac{6.621\left(3.1462e^{-5}\ \frac{m^2}{s}\right)}{250e^{-6}m} = 0.8332\frac{m}{s} \qquad (A86)$$

In order to determine the drying rate, the vapor pressure of the solvent (water in this case) must be calculated first at the particle temperature. The vapor pressure of water at 50°C is calculated in a similar manner as Equation A4 and has a value of 10.896 kPa. The solvent content of the particles within the control volume must also be calculated as well. The liquid coating amount is evenly divided among the coating control volumes for laboratory scale fluidized beds. The mass of coating solution in a control volume is dependent on the total number of control volumes selected for computation. In this example 15 control volumes was

selected for computational purposes. The mass of coating solution in each coating control volume is shown as Equation A87:

$$M_{coat,\,cv} = \frac{1\,\frac{ml}{min}\left(\frac{1\ min}{60\ s}\right)\left(\frac{m^3}{1000000\ ml}\right)\left(1100\,\frac{kg}{m^3}\right)}{15} = 1.222e^{-6}\ \frac{kg}{s} \qquad (A87)$$

The solvent content of the particles is shown as Equation A88:

$$W_p = \frac{1.222e^{-6}\ \frac{kg}{s}(1\ s)(1-0.1)}{9.8877e^{-4}\ kg} = 1.112e^{-3}\,\frac{kg\ H_2O}{kg\ Particles} \qquad (A88)$$

The drying rate is expressed in the same units as Equation A88 and is shown as Equation A89:

$$RD = \frac{0.8332\,\frac{m}{s}\left(\frac{0.013757\ m^2}{70063\ particles}\right)\left(1.112e^{-3}\,\frac{kg\ H_2O}{kg\ Particles}\right)(29033.46\ Pa - 10896\ Pa)}{\left(\frac{4\pi}{3}\left(\frac{250e^{-6}m}{2}\right)^3\right)\left(1725\,\frac{kg}{m^3}\right)\left(\frac{8.314472\ \frac{Pa\ m^3}{mol\ K}}{.01802\,\frac{kg}{mol}}\right)\left(\frac{50^oC+70^oC+273.15}{2}\right)}$$

$$= 1.521e^{-3}\,\frac{kg\ H_2O}{kg\ Particles} \qquad (A89)$$

The last parameter to calculate before the mass and energy balances can be put together is the solvent latent heat of vaporization.

Appendix A Continued

The heat of vaporization for water is shown as Equation A90:

$$Q_{lat} = 2059.10612\left(\frac{647.07\text{K} - 55^{o}\text{C} - 273.15}{647.07\ \text{K}}\right)^{0.333} + 6604.54101\left(\frac{647.07\text{K} - 55^{o}\text{C} - 273.15}{647.07\ \text{K}}\right)^{0.333+0.4567} + 7694.31324\left(\frac{647.07\text{K} - 55^{o}\text{C} - 273.15}{647.07\ \text{K}}\right)^{1-0.125+0.333} - 11318.02809\left(\frac{647.07\text{K} - 55^{o}\text{C} - 273.15}{647.07\ \text{K}}\right) - 4284.42966\left(\frac{647.07\text{K} - 55^{o}\text{C} - 273.15}{647.07\ \text{K}}\right)^{2} - 2598.60251\left(\frac{647.07\text{K} - 55^{o}\text{C} - 273.15}{647.07\ \text{K}}\right)^{3} = 2367.61\ \frac{\text{J}}{\text{kg}} \quad \text{(A90)}$$

The mass and energy balances for the liquid coating solution spraying segment can now be calculated with the additional parameters calculated from Equations A81-A90. The energy balance for the air (fluidization and atomization) is shown as Equation A91:

$$\frac{1.6077e^{-4}\ \text{kg}\left(1016.83\ \frac{\text{J}}{\text{kg}\cdot\text{K}}\right)\left(70^{o}\text{C} - T_{a,out}\right)}{1\text{s} - 0\text{s}} = \left(5.18152e^{-3}\ \frac{\text{kg}}{\text{s}} + \frac{3.7403e^{-6}\ \frac{\text{kg}}{\text{s}}}{15}\right)\left(1016.83\ \frac{\text{J}}{\text{kg}\cdot\text{K}}\right)\left(70^{o}\text{C} - T_{a,out}\right) - 703.328\ \frac{\text{W}}{\text{m}^2\text{K}}(0.013757\ \text{m}^2)(70^{o}\text{C} - 55^{o}\text{C})\left(3.1952^{-3}\text{s}\right) - 0.12954\ \text{W}\left(3.1952^{-3}\text{s}\right) - 1.521e^{-3}\ \frac{\text{kg}\ H_2O}{\text{kg Particles}}(9.8877e^{-4}\ \text{kg})\left(1946.17\ \frac{\text{J}}{\text{kg}\cdot\text{K}}\right)(70^{o}\text{C} - 55^{o}\text{C}) \quad \therefore T_{a,out} = 69.76^{o}\text{C} \quad \text{(A91)}$$

Appendix A Continued

The adjusted energy balance of the particles is shown as Equation A92:

$$\frac{9.8877e^{-4}\ \text{kg}\left(1684.44\frac{\text{J}}{\text{kg}\cdot\text{K}}\right)(T_p - 55^oC)}{1s - 0s} =$$

$$703.328\frac{\text{W}}{\text{m}^2\text{K}}(0.013757\ \text{m}^2)(70^o\text{C} - 55^o\text{C})(3.1952^{-3}\text{s}) - 5.3664^{-5}\text{W}(3.1952^{-3}\text{s})$$

$$- 1.222e^{-6}\ \frac{\text{kg}}{\text{s}}\left(4184\frac{\text{J}}{\text{kg}\cdot\text{K}}\right)(55^o\text{C} - 25^o\text{C}) - 1.222e^{-6}\ \frac{\text{kg}}{\text{s}}\left(2367.61\frac{\text{J}}{\text{kg}}\right)$$

$$\therefore T_p = 55.18^o\text{C} \qquad \text{(A92)}$$

The reason for the increase in the particle temperature even though the liquid coating solution is added is because the maximum drying rate is higher than the liquid coating solution addition rate. The maximum drying rate is shown as Equation A93:

$$DR_{max} = 1.521e^{-3}\frac{\text{kg } H_2O}{\text{kg Particles}}(9.8877e^{-4}\ \text{kg Particles}) = 1.504e^{-6}\ \text{kg } H_2O \qquad \text{(A93)}$$

The energy balance for the wall temperature is shown as Equation A94:

$$\frac{7850\frac{\text{kg}}{\text{m}^3}\left(9.975e^{-4}\text{m}^2\right)(0.0635\ \text{m})\left(500\frac{\text{J}}{\text{kg}\cdot\text{K}}\right)(T_{wall} - 52^o\text{C})}{1s - 0s} =$$

$$\left(\frac{9.975e^{-4}\text{m}^2(0.938)(70^o\text{C}-52^o\text{C})}{0.32496\ \frac{\text{m}^2\text{K}}{\text{W}}}\right) + \left(\frac{9.975e^{-4}\text{m}^2(1-0.938)(55^o\text{C}-52^o\text{C})}{1.152443e^{-3}\ \frac{\text{m}^2\text{K}}{\text{W}}}\right)$$

$$- 5.9952e^{-5}\ \text{W} - \frac{9.975e^{-4}\text{m}^2}{1.0568\frac{\text{m}^2\text{K}}{\text{W}}} \qquad \therefore T_{wall} = 52^o\text{C} \qquad \text{(A94)}$$

The wall temperature actually increases by 0.008^oC.

In addition to the energy balances to determine the temperatures of the air, particles, and wall there are two additional mass balances that must be done for a complete description of the system. One mass balance concerns the amount of moisture on the particle surface. The other

mass balance concerns the addition of moisture into the fluidization air. These two additional balances along with the balances for the three aforementioned temperatures help determine the thermo-physical properties of the next control volume. The particle moisture balance is shown as Equation A95:

$$\frac{9.8877e^{-4}\ kg\left(1.112e^{-3}\frac{kg\ H_2O}{kg\ Particles}-W_{p,out}\right)}{1s-0s}= 9.8877e^{-4}\ kg\left(1.112e^{-3}\frac{kg\ H_2O}{kg\ Particles}\right)$$
$$-9.8877e^{-4}\ kg\left(1.521e^{-3}\frac{kg\ H_2O}{kg\ Particles}\right)+1.222e^{-6}\ \frac{kg\ H_2O}{s}$$
$$W_{p,out}=2.8512e^{-4}\frac{kg\ H_2O}{kg\ Particles} \quad (A95)$$

The fluidization and atomization air moisture balance is shown as Equation A96:

$$\frac{1.6077e^{-4}\ kg\ \left(X_{a,out}-0.007557\frac{kg\ H_2O}{kg\ Air}\right)}{1s-0s}=$$
$$\left(5.18152e^{-3}\frac{kg}{s}+\frac{3.7403e^{-6}}{15}\ \frac{kg}{s}\right)\ \left(X_{a,out}-0.007557\frac{kg\ H_2O}{kg\ Air}\right)$$
$$+9.8877e^{-4}\ kg\left(1.112e^{-3}\frac{kg\ H_2O}{kg\ Particles}\right)\left(3.1952^{-3}s\right)\quad \therefore X_{a,out}=0.007556\ \frac{kg\ H_2O}{kg\ Air} \quad (A96)$$

Appendix B Coating Growth Kinetics Model Step by Step Sample Calculation Procedure

In order to calculate the particle coating growth kinetics inside a fluidized bed, there are some variables that must be defined a priori:

- Liquid Coating Solution Density, Surface Tension, and Viscosity
- Dry Matter Content of Liquid Coating Solution
- Mass Flow Rate of Liquid Coating Solution
- Mass Flow Rate of Atomization Air
- Atomization Air Pressure and Fluidized Bed Air Pressure
- Coating Density
- Liquid Coating Solution-Particle Contact Angle
- Nozzle Orifice Diameter and Spray Angle
- Nozzle Height Inside Fluidized Bed
- Height of Fluidized Bed
- Particle Diameter

Using the above listed variables along with some variables from the mass and energy balances and a few more calculated within the framework of this model, the coating growth kinetics can be ascertained. Table B1 shows the variables listed above that are used in this step by step calculation procedure.

Appendix B Continued

Table B1. Coating Growth Kinetics Calculation Initial Conditions

Parameter	Value
Liquid Coating Solution Density (kg/m^3)	1014.72
Liquid Coating Solution Surface Tension (N/m)	0.0587
Liquid Coating Solution Viscosity (Pa s)	20.45e^{-4}
Dry Matter Content (DMc)	0.1
Mass Flow Rate of Liquid Coating Solution (kg/s)	1.69e^{-5}
Mass Flow Rate of Atomization Air (kg/s)	9.86e^{-3}
Coating Density (kg/m^3)	1245
Liquid Coating Solution-Particle Contact Angle (^{o})	30
Atomization Air Pressure (bar)	0.5
Fluidized Bed Air Pressure (bar)	0.1
Nozzle Orifice Diameter (m)	0.0005
Nozzle Height Inside Fluidized Bed (m)	0.18
Nozzle Spray Angle (^{o})	20
Height of Fluidized Bed (m)	0.105
Particle Diameter (μm)	250

The variables from the mass and energy balances that are incorporated into the coating growth kinetics model are a result of the hydrodynamic calculations and include: the bed void fraction, the particle circulation rate, the superficial velocity, the fluidized bed area, and the fluidized bed bubble properties – diameter and rise velocity.

The first part of the step by step calculation for the coating growth kinetics is the average liquid coating solution droplet size. The liquid droplet Sauter mean diameter is dependent on the liquid coating solution properties, the atomization air properties and the nozzle properties, all of which are shown in Table B1. The Sauter mean diameter is also dependent on the Ohnesorge number which is shown as Equation B1:

$$\mathrm{Oh} = \frac{20.45e^{-4}\ \mathrm{Pa\ s}}{\sqrt{(0.0005\ \mathrm{m})\left(1014.72\frac{\mathrm{kg}}{\mathrm{m}^3}\right)\left(0.0587\frac{\mathrm{N}}{\mathrm{m}}\right)}} = 0.01185 \qquad \text{(B1)}$$

Appendix B Continued

The liquid coating solution droplet Sauter mean diameter is shown as Equation B2:

$$SMD = 0.35(0.0005\text{ m})\left[\frac{(0.5\text{ bar}-0.1\text{ bar})\left(101325\frac{\text{Pa}}{\text{bar}}\right)(0.0005\text{ m})}{0.0587\frac{\text{N}}{\text{m}}\left(1+\frac{1.69e^{-5}\frac{\text{kg}}{\text{s}}}{9.86e^{-3}\frac{\text{kg}}{\text{s}}}\right)^{2}}\right]^{-0.4}\left(1+2.5(0.01185)\right)$$

$$= 17.41e^{-6}\text{ m} \qquad \text{(B2)}$$

The liquid coating droplets are assumed to be spherical, so the volume of the droplet with the diameter calculated in Equation B2 is shown as Equation B3:

$$V_{drop} = \frac{4\pi}{3}\left(\frac{17.41e^{-6}\text{ m}}{2}\right)^{3} = 2.763e^{-15}\text{ m}^3 \qquad \text{(B3)}$$

The droplet size distribution is then generated using the Rosin-Rammler distribution, shown as Equation 2.20 in Chapter 2, and a random number generator for Q (n = 10000). The value used for q is 2.5 and the value for X is the mass median droplet diameter. The mass median droplet diameter, which is related to the Sauter mean diameter, is shown as Equation B4:

$$MMD = \frac{17.41^{-6}\text{m}}{0.83} = 20.98e^{-6}\text{m} \qquad \text{(B4)}$$

The result with the random number generator for Q is a distribution of liquid coating solution droplets shown as Figure 7.16 in Chapter 7. A sample calculation will be shown however to demonstrate how the droplet distribution is obtained. For example, Equation B5 shows the calculated droplet size for a random value of 0.7219 for Q, with q = 2.5 and X = 20.98 microns from Equation B4:

$$1 - 0.7219 = \exp\left(-\frac{d_{drop}}{20.98e^{-6}\text{m}}\right)^{2.5} \quad \therefore d_{drop} = 14.40^{-6}\text{m} \qquad \text{(B5)}$$

Appendix B Continued

The next step is to create a particle size distribution. In the absence of data describing a particle size distribution, a triangular distribution, as shown in Figure 4.12, can be used to generate the particle size distribution. In this case all that is needed are a maximum, minimum, and mode value for particle size, along with a random number generator (n = 10000). The random number generator is used to represent the cumulative distribution function (CDF) defined previously in Equation 4.76. As a sample calculation, the minimum, maximum, and mode particle sizes are taken as 355 microns, 425 microns, and 390 microns. The random number representing the particle CDF shall be taken as 0.9832. The calculated particle size is shown as Equation B6:

$$\text{Part D} = 425e^{-6}\text{m} - \sqrt{(1 - 0.9832)\left(425e^{-6}\text{m} - 355e^{-6}\text{m}\right)\left(425e^{-6}\text{m} - 390e^{-6}\text{m}\right)}$$

$$\therefore \text{Part D} = 418.58e^{-6}\text{m} \tag{B6}$$

With the droplet size distribution and particle size distribution now calculated the next step is to examine the spray area characteristics within the fluidized bed. The spray area of the liquid coating solution is determined by the spray pattern of the nozzle, the spray angle of the nozzle, and the distance between the nozzle tip and the distributor plate. The nozzle used in this work is a full cone nozzle. The spray diameter 1 cm from the nozzle tip is shown as Equation B7:

$$d_{spray} = 2(0.01\text{ m})\left(\tan\left(\frac{20}{2}\right)\right) = 0.00353\text{ m} \tag{B7}$$

The spray area, circular in shape, is then calculated as shown in Equation B8:

$$A_{spray} = \pi\left(\frac{0.00353\text{ m}}{2}\right)^2 = 9.7867e^{-6}\text{ m}^2 \tag{B8}$$

Appendix B Continued

The spray area as a function of distance from the nozzle tip is shown in Table B2.

Table B2. Nozzle Spray Area Characteristics

Height (cm)	Diameter (m)	Area (m^2)
0.0	0	0
1.0	0.00353	$9.7867e^{-6}$
2.0	0.00705	$3.9070e^{-5}$
3.0	0.01058	$8.7908e^{-5}$
4.0	0.01411	$1.5628e^{-4}$
5.0	0.01763	$2.4419e^{-4}$
6.0	0.02116	$3.5163e^{-4}$
7.0	0.02469	$4.7861e^{-4}$
8.0	0.02821	$6.2513e^{-4}$
9.0	0.03174	$7.9117e^{-4}$
10.0	0.03527	$9.7676e^{-4}$
11.0	0.03879	$1.1818e^{-3}$
12.0	0.04232	$1.4065e^{-3}$
13.0	0.04585	$1.6507e^{-3}$
14.0	0.04937	$1.9144e^{-3}$
15.0	0.05290	$2.1977e^{-3}$
16.0	0.05642	$2.5005e^{-3}$
17.0	0.05995	$2.8228e^{-3}$
18.0	0.06348	$3.1647e^{-3}$

The spray area increases with increasing distance from the nozzle. The percentage of the control volume within the spray area is a ratio of the spray area to the fluidized bed area. The percentage of the fluidized bed control volume within the spray area at the top of the fluidized particle bed is shown as Equation B9:

$$\% \text{ SA} = \frac{0.0012918 \text{ m}^2}{0.011269 \text{ m}^2} \times 100\% = 11.46\% \qquad \text{(B9)}$$

Table B3 shows the percentage of the control volume that is within the spray area as a function of distance from the nozzle.

Appendix B Continued

Table B3. Spray Area Characteristics of Fluidized Bed

Height (cm)	Area (m^2)	FB Area (m^2)	% SA
0.0	0	0	0
1.0	$9.7867e^{-6}$	0.016753	0.0584
2.0	$3.9070e^{-5}$	0.016753	0.2332
3.0	$8.7908e^{-5}$	0.016753	0.5247
4.0	$1.5628e^{-4}$	0.016753	0.9328
5.0	$2.4419e^{-4}$	0.016753	1.4576
6.0	$3.5163e^{-4}$	0.016753	1.8880
7.0	$4.7861e^{-4}$	0.016753	2.8569
8.0	$6.2513e^{-4}$	0.150756	4.147
9.0	$7.9117e^{-4}$	0.134866	5.866
10.0	$9.7676e^{-4}$	0.011986	8.149
11.0	$1.1818e^{-3}$	0.010574	11.176
12.0	$1.4065e^{-3}$	0.009251	15.204
13.0	$1.6507e^{-3}$	0.008015	20.594
14.0	$1.9144e^{-3}$	0.006869	27.871
15.0	$2.1977e^{-3}$	0.005811	37.822
16.0	$2.5005e^{-3}$	0.004841	51.653
17.0	$2.8228e^{-3}$	0.003960	71.288
18.0	$3.1647e^{-3}$	0.003167	99.930

With the spray area characteristics defined, the number of particles in each control volume needs to be calculated. The number of particles in each control volume is calculated in a similar manner to Equations A44-A46 in Appendix A. Since a particle size distribution is used the bed voidage is calculated by using bed voidage values for each particle size and averaged according to the particle size distribution CDF. Table B4 shows the following properties of the fluidized bed control volumes: diameter, volume, bed void fraction, and number of particles. In this example there are 19 control volumes.

Appendix B Continued

Table B4. Fluidized Bed Control Volume Properties

Control Volume	Diameter (m)	Volume (m^3)	Bed Voidage	Number of Particles
1	0.0635	$1.5835e^{-5}$	0.9680	15520
2	0.0673	$1.7761e^{-5}$	0.9632	20043
3	0.0710	$1.9798e^{-5}$	0.9581	25401
4	0.0748	$2.1946e^{-5}$	0.9529	31678
5	0.0785	$2.4205e^{-5}$	0.9475	38962
6	0.0823	$2.6574e^{-5}$	0.9419	47338
7	0.0860	$2.9053e^{-5}$	0.9361	56893
8	0.0898	$3.1643e^{-5}$	0.9302	67713
9	0.0935	$3.4344e^{-5}$	0.9241	79883
10	0.0973	$3.7155e^{-5}$	0.9179	93487
11	0.1010	$4.0077e^{-5}$	0.9116	108610
12	0.1048	$4.3110e^{-5}$	0.9051	125330
13	0.1085	$4.6253e^{-5}$	0.8986	143730
14	0.1123	$4.9506e^{-5}$	0.8920	163890
15	0.1160	$5.2871e^{-5}$	0.8853	185870
16	0.1198	5.6345	0.8785	209760
17	0.1235	5.9931	0.8717	235630
18	0.1273	6.3627	0.8649	263530
19	0.1310	6.7433	0.8579	293540

The next step involves taking the control volume particle circulation times calculated in the mass and energy balances previously and divide them by two. The particle circulation time calculated in the mass and energy balances represent the time spent from bottom to top and top to bottom summed together. The particle circulation time for each control volume for each particle size in the particle size distribution is calculated as shown with Equation A41 in Appendix A. Table B5 shows sample values for the particle circulation time for one particle size and 50% of the particle circulation time values.

Table B5. Particle Circulation Rates

Control Volume	Particle Circulation Time (s)	50% PCT (s)
1	0.0750	0.0375
2	0.0731	0.0366
3	0.0718	0.0359
4	0.0708	0.0354
5	0.0702	0.0351
6	0.0697	0.0349
7	0.0694	0.0347
8	0.0693	0.0347
9	0.0693	0.0347
10	0.0694	0.0347
11	0.0697	0.0349
12	0.0700	0.0350
13	0.0704	0.0352
14	0.0708	0.0354
15	0.0714	0.0357
16	0.0720	0.0360
17	0.0727	0.0364
18	0.0734	0.0367
19	0.0742	0.0371
Total	1.3526	0.6763

With the particle circulation time now tabulated, the number of revolutions a particle makes during the coating addition of the fluidized bed operation. For a coating addition time of one hour, the number of particle revolutions is given as Equation B10:

$$\text{Revolutions} = \frac{3600 \text{ seconds}}{1.3526 \frac{\text{seconds}}{\text{revolution}}} = 2716 \text{ Revolutions} \qquad \text{(B10)}$$

The total number of times a particle is in the spray area can now be calculated with the data listed in Table B3 and the number of revolutions from Equation B10. It should be noted that the particle is in each control volume twice for each revolution. The number of times a particle is in the spray area of each control volume of the fluidized bed is calculated using the binornd function in MatLab. The total number of opportunities to be in the spray area for each

control volume in this sample calculation is 5432. Table B6 shows the results for each control volume. The particle is in the spray area 32573 times out of 103208 potential opportunities, totaling 31.56% of the time.

Table B6. Number of Times in Spray Area

Control Volume	Number of Times	Percentage [%]
1	5135	94.53
2	4333	79.77
3	3662	67.42
4	3069	56.50
5	2658	48.93
6	2127	39.16
7	1885	34.70
8	1674	30.82
9	1448	26.66
10	1263	23.25
11	1049	19.31
12	879	16.18
13	775	14.27
14	602	11.08
15	561	10.33
16	481	8.85
17	334	6.15
18	332	6.11
19	306	5.63

With the number of times a particle is in the spray area calculated, the next step is to determine the probability that a particle is coated in the spray area, and subsequently the number of times the particle is coated in the spray area. The first variable to examine is the spray cone volume as it changes. Table B7 shows the spray area characteristics.

Appendix B Continued

Table B7. Spray Area Characteristics

Control Volume	Spray Area [$10e^{-3}m^2$]	Spray Cone Volume [$10e^{-4}m^3$]
1	2.991	1.7948
2	2.823	1.7499
3	2.659	1.6951
4	2.501	1.6452
5	2.347	1.5954
6	2.198	1.5455
7	2.054	1.4970
8	1.914	1.4458
9	1.780	1.3960
10	1.651	1.3461
11	1.526	1.2962
12	1.407	1.2464
13	1.292	1.1965
14	1.182	1.1467
15	1.077	1.0968
16	0.977	1.0470
17	0.882	0.9971
18	0.791	0.9473
19	0.706	0.8974

The difference in the spray cone volume for each control volume is $4.98e^{-6}$ m^3. Now the initial void fraction of the atomization air can be calculated. The atomization air void fraction just before it hits the first control volume of particles is given as Equation B11:

$$\varepsilon_{spray} = \frac{1\ \frac{ml}{min}\left(\frac{1m^3}{1000000\ ml}\right)(1\ min)}{0.8974e^{-4}m^3 - 4.98e^{-6}m^3} = 0.99980 \qquad (B11)$$

Now the probability a particle is coated in the spray area can be calculated as well as the amount of liquid coating solution that is deposited onto the particles within the first control volume. Equation B12 shows the calculation for the probability that a particle is coated in the spray area:

$$\text{Probability Coated} = \left(1 - \frac{0.8579}{0.9998}\right) \times 100\% = 14.19\% \qquad (B12)$$

Appendix B Continued

The amount of liquid coating deposited for the first control volume that the liquid droplets can come into contact with the particle bed is given by Equation B13:

$$\text{Liquid Deposited} = 1\,\frac{\text{ml}}{\text{min}}\,(0.1419) = 0.1419\,\frac{\text{ml}}{\text{min}} \qquad \text{(B13)}$$

The amount of liquid left for the next control volume is 0.8581 ml. This sequence is done for each control volume for the simulation. Once the values for liquid deposited in each control volume are calculated the overall coating efficiency of the fluidized bed coating experiment can be determined. Table B8 shows the values each control volume concerning the spray void fraction, the probability of being coated, and the amount of liquid deposited.

Table B8. Probability Coated and Liquid Deposited

Control Volume	ε_{spray}	Probability Coated [%]	Liquid Deposited[ml]	Liquid Left [ml]
1	0.9993	3.13	0.0062	0.1887
2	0.9993	3.62	0.0074	0.1949
3	0.9993	4.12	0.0088	0.2023
4	0.9993	4.64	0.0104	0.2111
5	0.9993	5.18	0.0123	0.2215
6	0.9992	5.74	0.0144	0.2338
7	0.9992	6.31	0.0169	0.2482
8	0.9991	6.89	0.0199	0.2651
9	0.9990	7.50	0.0233	0.2850
10	0.9989	8.11	0.0275	0.3083
11	0.9988	8.73	0.0324	0.3358
12	0.9986	9.36	0.0384	0.3682
13	0.9984	10.00	0.0456	0.4066
14	0.9983	10.65	0.0543	0.4522
15	0.9981	11.30	0.0650	0.5065
16	0.9978	11.96	0.0780	0.5715
17	0.9975	12.61	0.0943	0.6495
18	0.9971	13.27	0.1143	0.7438
19	0.9998	14.19	0.1419	0.8581

The total amount of liquid deposited is the sum of the liquid deposited column in Table B8, 0.8113 ml. The coating efficiency is shown as Equation B14:

Appendix B Continued

$$\text{Coating Efficiency} = \frac{(1\text{ ml} - 0.1887\text{ ml})}{1\text{ ml}} \times 100\% = 81.13\% \qquad \text{(B14)}$$

The coating efficiency calculated by the model is higher than the experimental coating efficiency as determined by calorimetry or UV/Vis absorbance. The actual experimental coating efficiency for this experiment is 67.9%. Therefore, a tunable parameter is incorporated into Equation B12 for each control volume to make the model match the experimental data. The regressed tunable parameter value for this sample calculation is 0.702004. The adjusted values for the amount of liquid deposited and liquid left are shown in Table B9.

Table B9. Corrected Liquid Deposited and Liquid Left

Control Volume	ε_{spray}	Liquid Deposited[ml]	Liquid Left [ml]
1	0.99890	0.0071	0.3208
2	0.99887	0.0084	0.3279
3	0.99884	0.0100	0.3363
4	0.99880	0.0116	0.3463
5	0.99876	0.0134	0.3579
6	0.99871	0.0155	0.3713
7	0.99865	0.0178	0.3868
8	0.99858	0.0204	0.4046
9	0.99850	0.0235	0.4250
10	0.99841	0.0269	0.4485
11	0.99831	0.0309	0.4754
12	0.99819	0.0355	0.5063
13	0.99805	0.0408	0.5418
14	0.99790	0.0469	0.5826
15	0.99771	0.0541	0.6295
16	0.99751	0.0625	0.6836
17	0.99726	0.0724	0.7461
18	0.99698	0.0840	0.8185
19	0.99980	0.0975	0.9025

The coating efficiency with the corrected values is 67.92%, just 0.02% off from the experimental value.

Appendix B Continued

Since the model calculated coating efficiency matches the experimentally observed coating efficiency, the next step is to calculate the number of times a particle is coated when it is in the spray area. Recall Table B6 gives a sample of the number of times a particle is in the coating area for each control volume. The data presented in Table B6 will be used to calculate the number of times the particle is coated in the spray area. This calculation is done in a similar manner as the determination of the number of times a particle is in the spray area. The binornd function in MatLab is used to determine the number of times a particle is coated in the spray area. Table B10 shows the results for each control volume.

Table B10. Number of Times in Coated in Spray Area

Control Volume	Number of Times	Percentage [%]
1	138	2.69
2	170	3.92
3	153	4.17
4	160	5.21
5	139	5.23
6	122	5.74
7	114	6.06
8	132	7.92
9	109	7.53
10	99	7.84
11	101	9.63
12	86	9.78
13	75	9.68
14	55	9.14
15	55	9.80
16	56	11.64
17	47	14.07
18	43	12.95
19	50	16.34

The total number of times the particle is coated in the spray area is 1904 times out of a potential 32573 times, or 5.85%. For the overall coating process, the particle is coated 1.84% of the time it is in the fluidized bed.

Appendix B Continued

The next step is a mass balance involving the number of droplets hitting a particle each time it is successfully coated in the spray area for each control volume. The correct droplet diameter must be chosen for this calculation; otherwise the coating thickness will be overstated when it is calculated later. As a check, the coating efficiency is calculated again to ensure that the correct droplet size is chosen. This calculation is done by using the Sauter mean diameter of the droplet size distribution as a starting point and then adjusting the droplet size until the calculated coating efficiency matches the experimental coating efficiency. Equation B15 shows a sample calculation for the top control volume for number of droplets per particle using the Sauter mean diameter droplet size for the simulation:

$$\text{NdropsPP} = \frac{0.1388e^{-6}\frac{m^3}{min}/60 \text{ seconds}}{\frac{4}{3}\pi\left(\frac{17.41e^{-6}m}{2}\right)^3\left(\frac{7.0571e^{-4}m^2}{0.0143m^2}\right)(296830 \text{ particles})} = 57.13 \qquad \text{(B15)}$$

This procedure is carried out for each control volume. Typically, using the Sauter mean diameter leads to an overstatement of the coating thickness because the number of droplets that hit the particle is overstated by Equation B15. Therefore a second tunable parameter is incorporated into this calculation to match the calculated coating efficiency with the experimental coating efficiency as shown in Equation B16:

$$\text{NdropsPP} = \frac{0.0975e^{-6}\frac{m^3}{min}/60 \text{ seconds}}{\frac{4}{3}\pi\left(1.093\times\frac{17.41e^{-6}m}{2}\right)^3\left(\frac{7.0571e^{-4}m^2}{0.0143m^2}\right)(296830 \text{ particles})} = 9.295 \qquad \text{(B16)}$$

The 1.093 term represents the tunable parameter in Equation B16. The value calculated by Equation B16 represents the number of droplets that hit a particle if it is actually coated when

it is in the spray area. When the proper droplet size is found (after confirmation with the coating efficiency calculation) the next step is to calculate the coating growth for a droplet that hits a particle. For this example, a droplet diameter of 25 microns will be used. The droplet volume is given by Equation B17:

$$V_{drop} = \frac{4\pi}{3}\left(\frac{25.0\ e^{-6}\ m}{2}\right)^3 = 8.1812e^{-15}\ m^3 \qquad (B17)$$

The droplet mass is given by Equation B18:

$$M_{drop} = \left(8.1812e^{-15}\ m^3\right)\left(1014.72\frac{kg}{m^3}\right) = 8.301e^{-12}\ kg \qquad (B18)$$

The mass of coating deposited on the particle is shown as Equation B19:

$$M_c = 8.301e^{-12}\ kg\left(\frac{0.1\frac{kg\ coat}{kg\ solvent}}{1+0.1\frac{kg\ coat}{kg\ solvent}}\right) = 7.546e^{-13}\ kg\ Coating \qquad (B19)$$

The volume of the coating material is given as Equation B20:

$$V_c = \frac{7.546e^{-13}\ \frac{kg\ coating}{particle}}{1245\frac{kg}{m^3}} = 6.061e^{-16}\ \frac{m^3\ coating}{particle} \qquad (B20)$$

The new particle diameter (for a 0^o contact angle) is given by Equation B21:

$$New\ D = 2\left(\frac{6.061e^{-16}m^3+\frac{4\pi}{3}\left(\frac{250\ e^{-6}\ m}{2}\right)^3}{\frac{4\pi}{3}}\right)^{\frac{1}{3}} = 250.006e^{-6}m \qquad (B21)$$

Appendix B Continued

The coating growth rate after the successful collision of a droplet with a particle is given by Equation B22:

$$CGR = \frac{250.006e^{-6}m - 250e^{-6}m}{2} = 3e^{-9}m \qquad (B22)$$

To determine the growth rate of the particle, the contact angle between the liquid coating solution and the particle must be known. Once the liquid coating droplet hits the particle, instantaneous spreading is assumed to occur in accordance with wetting thermodynamics and the contact angle. The droplet is then assumed to take the shape of an oblate spheroid. For this example a contact angle of 30^o between the liquid coating solution and the particle is assumed. The radius of coverage on the particle surface is shown as Equation B23:

$$A_{liq} = \left[\frac{3\left(6.061e^{-16}m^3\right)}{\pi}\frac{\sin^3(30^o)}{2 - 3\cos(30^o) + \cos^3(30^o)}\right]^{\frac{1}{3}} = 1.7785e^{-5}\ m \qquad (B23)$$

The height of the droplet on the surface of the particle is shown as Equation B24:

$$h_{drop} = 1.7785e^{-5}\ m\left(\frac{1-\cos 30^o}{\sin 30^o}\right) = 4.765^{-6}\ m \qquad (B24)$$

To calculate the growth rate, the surface area of the particle and coating must be calculated. The surface area of a particle is shown as Equation B25:

$$A_{part} = 4\pi\left(\frac{250e^{-6}m}{2}\right)^2 = 1.9635e^{-7}m^2 \qquad (B25)$$

The total surface area of the coating material deposited on the surface as a function of the contact angle is given by Equation B26:

$$A_{coat} = \pi\left[\left(1.7785e^{-5}\ m\right)^2 + \left(\left(\frac{6.061e^{-16}m^3}{8.1812e^{-15}\ m^3}\right)4.765^{-6}\ m\right)^2\right] = 9.941e^{-10}m^2 \qquad (B26)$$

Appendix B Continued

The total surface area for the particle now is the sum of Equations B25 and B26 which is $1.97344e^{-7}$ m^2. The particle growth rate is then given as Equation B27:

$$CGR = \left(\frac{1.97344^{-7}m^2}{4\pi}\right)^{0.5} - \frac{250e^{-6}}{2} = 6.323e^{-7}m \quad (B27)$$

With a coating growth rate model now in place the boundary conditions for applicability must now be determined. Dimensionless numbers play an important role in the boundary conditions in a similar fashion as the mass and energy balances. The Stokes Viscous number is used to determine if particles rebound or coalesce after a collision. The Stokes Viscous numbers are calculated for the entire particle size distribution, but the smallest and largest particle diameters will yield the minimum and maximum Stokes Viscous numbers.

The critical Stokes Viscous number is dependent on three parameters, the coefficient of restitution, e, h_{asp} and h_{liq}. The coefficient of restitution is taken to be 0.9. The particle asperity is given as Equation B28 and B29 for a particle size distribution of 200-350 μm:

$$h_{asp} = 0.01\left(\frac{200e^{-6}m}{2}\right) = 1.00e^{-6}m \quad (B28)$$

$$h_{asp} = 0.01\left(\frac{350e^{-6}m}{2}\right) = 1.75e^{-6}m \quad (B29)$$

The h_{liq} term is the same as h_{drop} in Equation B24. The Stokes Viscous numbers are shown as Equations B30 and B31:

$$St_v^* = \left(1+\frac{1}{0.9}\right)\ln\left(\frac{4.765^{-6}m}{1.00e^{-6}m}\right) = 3.296 \quad (B30)$$

$$St_v^* = \left(1+\frac{1}{0.9}\right)\ln\left(\frac{4.765^{-6}m}{1.75e^{-6}m}\right) = 2.115 \quad (B31)$$

Appendix B Continued

In order for particle rebound to be successful after a collision the Stokes Viscous number must be higher than the critical Stokes Viscous numbers calculated in Equations B30 and B31. The Stokes Viscous numbers are dependent on the particle and gas bubble diameter as well as the gas bubble velocity in the fluidized bed. The bubble diameter and bubble velocity calculations can be found in Appendix A as Equations A38 and A39. The collision velocity for the Stokes numbers is shown as Equations B32 and B33:

$$U_{coll} = \frac{12\left(8.308\ \frac{m}{s}\right)\left(100e^{-6}m\right)}{0.0535\ m} = 0.1863\frac{m}{s} \tag{B32}$$

$$U_{coll} = \frac{12\left(8.308\ \frac{m}{s}\right)\left(175e^{-6}m\right)}{0.0535\ m} = 0.3261\frac{m}{s} \tag{B33}$$

The Stokes Viscous numbers are shown as Equations B34 and B35:

$$St_v = \frac{8\left(1725\frac{kg}{m^3}\right)\left(100e^{-6}m\right)\left(0.1863\frac{m}{s}\right)}{9\left(2.045e^{-3}\ Pa\ s\right)} = 13.96 \tag{B34}$$

$$St_v = \frac{8\left(1725\frac{kg}{m^3}\right)\left(175e^{-6}m\right)\left(0.3261\frac{m}{s}\right)}{9\left(2.045e^{-3}\ Pa\ s\right)} = 42.79 \tag{B35}$$

The calculated values for the Stokes Viscous numbers in Equation B34 and B35 are both higher than the critical Stokes Viscous numbers in Equations B30 and B31, therefore no particle agglomeration will occur within the first control volume of the fluidized bed. The Stokes Viscous number is calculated for each control volume in the same manner outlined in Equations B32-B35 and compared to the critical Viscous Stokes numbers of Equations B30 and B31.

In addition to the Stokes Viscous number as a boundary condition, there is also the Flux Number. A fluidized bed process with a Flux Number greater than 3.5 will result in particle

coating rather than particle agglomeration. The Flux number is dependent on the liquid flux, bulk powder density, and excess gas velocity. The liquid flux is given as Equation B36:

$$q_{liq} = \frac{1\frac{ml}{min}\left(\frac{1\ min}{60\ s}\right)\left(\frac{1m^3}{1000000\ ml}\right)\left(1100\frac{kg}{m^3}\right)}{5.5187e^{-4}m^2} = 0.03322\frac{kg}{m^2 s} \quad \text{(B36)}$$

The bulk density of the solid is shown as Equation B37:

$$\rho_{bulk} = \frac{503423\ particles\left(\frac{4\pi}{3}\right)\left(125e^{-6}m\right)^3\left(1725\frac{kg}{m^3}\right)}{5.2871^{-5}m^3} = 1343.76\frac{kg}{m^3} \quad \text{(B37)}$$

The excess velocity is the difference between Equations A30 and A33 and is 7.7934 ms^{-1}. The Flux Number is shown as Equation B38:

$$FN = \log\left[\frac{1343.76\frac{kg}{m^3}\left(7.7934\frac{m}{s}\right)}{0.03322\frac{kg}{m^2 s}}\right] = 5.4986 \quad \text{(B38)}$$

The Flux Number is well above the requirement of 3.5, thus indicating that the operation will result in coating rather than agglomeration. The Flux Number is calculated for each control volume in the same manner outlined in Equations B36-B38.

A final check that for the coating growth model that helps ensure coating occurs rather than agglomeration is the Dimensionless Spray Flux. Ideally, the Dimensionless Spray Flux should be low to ensure against over-wetting and eventual fluidized bed collapse. The Dimensionless Spray Flux is shown as Equation B39:

$$DSF = \frac{3\left(1\frac{ml}{min}\right)\left(\frac{1\ min}{60\ s}\right)\left(\frac{m^3}{1000000\ ml}\right)}{2\left(5.5187e^{-4}\frac{m^2}{s}\right)\left(87e^{-6}m\right)} = 0.5207 \quad \text{(B39)}$$

The DSF as calculated in Equation B39 is well below 1. The DSF is calculated for each coating control volume as outlined in Equation B39. However, the Stokes Viscous number is the main dimensionless number used to determine the boundaries for coating growth applicability.

Appendix C Nomenclature

A	Area, Constant for Enhancement Factor, Constant for Compressibility Factor
ANN	Artificial Neural Network
A_{ann}	Annulus Area
A_{bed}	Fluidized Bed Area
A_{con}	Particle Contact Area
A_{liq}	Droplet Area on Particle Surface
A_p	Particle Surface Area
Ar	Archimedes Number
A_{wall}	Surface Area of Fluidized Bed Wall
a, b	Constants for Natural Convection Nusselt Number
a,b,c	Minimum, Maximum, and Mode for Particle Size Distribution
a*	Relative Particle Radius
B	Constant for Enhancement Factor, Constant for Compressibility Factor, Heat Transfer and Mass Transfer Numbers, Birth Term for Population Balance Equation
B_{agg}	Aggregation Birth Term for Population Balance Equation
B_{break}	Breakage Birth Term for Population Balance Equation
Bi	Biot Number
Bo	Bond Number
CDF	Cumulative Distribution Function
CF	Collision Frequency
CFD	Computational Fluid Dynamics

Appendix C Continued

CGR Coating Growth Rate

CV Control Volume

C_{coat} Coating Material Concentration

C_d Drag Coefficient

C_p Specific Heat Capacity at Constant Pressure

C_{pa} Air Specific Heat Capacity at Constant Pressure

C_{pm} Air-Water Vapor Specific Heat Capacity at Constant Pressure

C_{pp} Particles Specific Heat Capacity at Constant Pressure

C_{pv} Water Vapor Specific Heat Capacity at Constant Pressure

C_{pwall} Wall Specific Heat Capacity at Constant Pressure

C_{surf} Surface Concentration

C_∞ Bulk Concentration

c Number of Coating Control Volumes

c_i Fluctuation in Particle Velocity

D Diameter, Diffusion Coefficient, Death Term for Population Balance Equation

D_{agg} Aggregation Death Term for Population Balance Equation

D_{break} Breakage Death Term for Population Balance Equation

DEM Discrete Element Method

DF Drying Force

DM_c Dry Matter Content

D_{ab} Diffusion Coefficient

D_v Diffusion Coefficient

Appendix C Continued

d_{bed} Fluidized Bed Diameter

d_{b0} Initial Bubble Diameter

d_{bub} Bubble Diameter

$d_{bub,max}$ Maximum Bubble Diameter

d_d d_{drop} Droplet Diameter

d_{dsd} Droplet Diameter of Droplet Size Distribution

d_0 Orifice Diameter

$d_{0rifice}$ Orifice Diameter

d_{MMD} Mass Median Diameter

d_p Particle Diameter

$d_{prefilm}$ Prefilmer Diameter

d_{spray} Atomization Spray Diameter

d_s Fluidized Bed Wall Diameter

d_{SMD} Sauter Mean Diameter

d_{wall} Fluidized Bed Wall Thickness

E* Relative Young's Modulus

$E_{1,2}$ Young's Modulus of Component 1 or 2

e Coefficient of Restitution

F_{cap} Capillary Force

FDM Finite Difference Method

FN Flux Number

Fr Froude Number

Appendix C Continued

FVM Finite Volume Method

f Number Density Function

f_{ci} Particle-Particle Collision Force

f_{bub} Bubble Frequency

f_{coll} Collision Frequency

f_{fpi} Fluid-Particle Interaction Force

f(P,T) Enhancement Factor

G Growth Term for Population Balance Equation

G_a Mass Flow Rate of Air

G_{adh} Gibbs Free Energy of Adhesion

G_{at} Mass Flow Rate Atomization Air

G_{imm} Gibbs Free Energy of Immersion

G_{ls} Gibbs Free Energy of Solid-Liquid Spreading

G_{spr} Gibbs Free Energy of Spreading

Ga Galileo Number

G_{air} Mass Flux of Air

Gr Grashof Number

Gz Graetz Number

g Gravity

g_o Radial Distribution Function

H Meniscus Curvature

h Adhesion Probability, Distance From Nozzle, Droplet Height on Particle Surface, Droplet Penetration Depth into Pore

Appendix C Continued

h_{asp} Particle Asperity Height

h_{bed} Fluidized Bed Height

h_{conv} Convective Heat Transfer Coefficient

h_{liq} Liquid Droplet Height on Particle Surface

h_{mf} Fluidized Bed Height at Minimum Fluidization

h_s Control Volume Height

h_{stat} Static Particle Bed Height

I_i Moment of Inertia

K Constant

KTGF Kinetic Theory of Granular Flow

k Thermal Conductivity

k_a Dry Air Thermal Conductivity

k_{amark} Stagnant Gas Thermal Conductivity

k_{aw} Gas Thermal Conductivity Around a Particle

k_m Air-Water Vapor Thermal Conductivity

k_m Mass Transfer Coefficient

k_p Particle Thermal Conductivity

k_v Water Vapor Thermal Conductivity

L Latent Heat of Vaporization

L_c Characteristic Length

LES Large Eddy System

M_a Mass of Air

Appendix C Continued

M_c Coating Liquid Mass Flow Rate

MFP Mean Free Path

Mv Mass Ratio

M_{coat} Coating Mass

M_g Molecular Weight of Gas

M_{liq} Molecular Weight of Liquid

M_p Mass of a Single Particle

m* Relative Particle Mass

m_{air} Mass Flow Rate of Air

m_{harm} Harmonic Particle Mass

m_{liq} Mass Flow Rate of Liquid

N_{bed} Number of Particles in Fluidized Bed

N_{col} Energy Lost by Particle-Particle Collisions

N_{gen} Energy Generated by Rising Bubbles

N_i Number of Particles

N_{ij} Number of Particle-Particle Collisions

N_{or} Number of Orifices

N_p Number of Particles

N_{PISA} Number of Particles in Spray Area

N_{vis} Energy Lost by Viscous Dissipation

Nu Nusselt Number

Nu_e Environment Nusselt Number

Appendix C Continued

Nu_p Particle Nusselt Number

Nu_{wall} Wall Nusselt Number

n Number of Control Volumes

n_1,n_2 Number of Particles of Size 1 or 2

Oh Ohnesorge Number

PBE Population Balance Equation

PDF Probability Density Function

P_{actual} Actual Partial Pressure

P_{cap} Capillary Pressure

P_{CISA} Probability a Particle is Coated in Spray Area

P_{ev} Equilibrium Vapor Pressure

P_H Heywood Terminal Velocity Parameter

P_{ISA} Probability a Particle Is in Spray Area

P_p Probability of Success

Pr Prandtl Number

Pr_e Environmental Prandtl Number

P_{sat} Saturation Vapor Pressure

P_{sata} Saturation Vapor Pressure in Air

P_{satp} Saturation Vapor Pressure on Particle Surface

p Pressure

p_0 Collision Pressure

Q Fraction of Droplets

Appendix C Continued

Q_{cond} Conductive Heat Transfer Rate

Q_{conv} Convective Heat Transfer Rate

Q_H Heywood Terminal Velocity Parameter

Q_{lat} Latent Heat of Vaporization

Q_{mliq} Mass Flow Rate of Liquid

Q_{rad} Radiation Heat Transfer Rate

q Nozzle Constant

q_{air} Mass Flow Rate of Air

q_{liq} Mass Flow Rate of Liquid

q_{mliq} Mass Flux Rate of Liquid

R Fluidized Bed Expansion Ratio

R Universal Gas Constant

RANS Reynolds Averaged Navier Stokes

R_b Droplet Radius

R_{b0} Initial Droplet Radius

R_D Drying Rate

R_{cond} Fluidized Bed Wall Conductive Heat Transfer Resistance

R_d Relative Drop Size

R_g Individual Gas Constant

R_p Wall to Particle Heat Transfer Resistance

R_{packet} Emulsion Packet Heat Transfer Resistance

R_{packet} Emulsion Packet Heat Transfer Resistance

Appendix C Continued

R_{pcd} Particle Vertical Surface Heat Transfer Resistance in a Surrounding Gas

R_{rad} Radiation Heat Transfer Resistance

R_{wall} Fluidized Bed Wall to Environment Conductive Heat Transfer Resistance

Re Reynolds Number

Re_e Environmental Reynolds Number

Re_{mf} Reynolds Number at Minimum Fluidization

Re_{term} Reynolds Number at Terminal Velocity

Re_{wall} Reynolds Number for Gas to Wall Heat Transfer

RH Relative Humidity

RNG Renormalization Group

RSM Reynolds Stress Model

r_i Particle Exchange Rate

r_{drop} Droplet Radius

r_{harm} Harmonic Radius

S Saturation, Stage

SA_{coat} Coating Surface Area

SA_{part} Particle Surface Area

S_{ls} Spreading Coefficient

Sc Schmidt Number

Sh Sherwood Number

St_{def} Stokes Deformation Number

St_{tack} Stokes Tack Number

Appendix C Continued

St_v Viscous Stokes Number

s_0 Specific Particle Surface Area

T Temperature

T_{air} Fluidization Air Temperature

T_{bulk} Bulk Temperature

T_e Environment Temperature

T_i Torque

T_{part} Particle Temperature

T_{ref} Reference Temperature

T_s Surface Temperature

T_{sol} Liquid Coating Solution Temperature

T_{surf} Surface Temperature

T_{wall} Fluidized Bed Wall Temperature

T_{wb} Wet Bulb Temperature

t_{coll} Collision Time

U_0 Superficial Velocity

U_{12} Normal Velocity Component

U_{12Y} Critical Normal Velocity Component

U_{bu} Bubble Velocity

U_{bub} Bubble Velocity

U_c Transition Velocity

U_{cf} Complete Fluidization Velocity

Appendix C Continued

U_{ch} Choking Velocity

U_{coll} Collision Velocity

U_E Excess Velocity

U_f Fluid Velocity

U_g Gas Velocity

U_k Transition Velocity

U_l Liquid Velocity

U_{mb} Minimum Bubbling Velocity

U_{mf} Minimum Fluidization Velocity

U_{noz} Atomization Air Velocity Leaving Nozzle

U_{part} Particle Velocity

U_{reb} Rebound Velocity

U_{rel} Relative Velocity

U_{salt} Saltation Velocity

U_{slip} Slip Velocity

U_{slug} Slugging Velocity

U_t Terminal Velocity

U_{term} Terminal Velocity

U_{test} Test Velocity

U_{tr} Transition Velocity

V_{bed} Volume of Fluidized Bed

V_c Droplet Volume

Appendix C Continued

V_{c0} Initial Droplet Volume

V_{coat} Coating Volume

V_{dep} Volume of Liquid Deposited During Spraying

V_{drop} Droplet Volume

V_{left} Volume of Liquid Left Over From Spraying

$V_{liq,pore}$ Liquid Volume Inside Pore

V_M Liquid Molar Volume

V_{part} Particle Volume

V_{sol} Total Volume of Liquid Sprayed per Second

v_{crit} Critical Velocity

v_{rel} Relative Velocity

v_z Radial Velocity

v_{zmax} Maximum Radial Velocity

W_{adh} Adhesion Work

W_p Particle Moisture Content

WALE Wall Adapting Local Eddy Viscosity Model

We Weber Number

We_{air} Air Weber Number

X Rosin-Rammler Constant

X_{air} Fluidization Air Absolute Humidity

X_{at} Atomization Air Absolute Humidity

Y_d Yield Stress

Appendix C Continued

Y_i Coating Mass

Y_f Liquid Mass Fraction in Air

y Wurster Orientation Segment Height

Z_v Compressibility Factor

Greek Letters

α Angle of Taper

α_p Particle Convective Heat Transfer Coefficient

α_p' Particle Mass Transfer Coefficient

β Coefficient of Thermal Expansion, Mass Transfer Coefficient

β_a Drag Coefficient

γ Surface Tension

γ_{lv} Liquid-Vapor Surface Tension

γ_{sl} Solid-Liquid Surface Tension

γ_{sv} Solid-Vapor Surface Tension

Δ Change in Variable

δ Dimensionless Bubble Spacing

ε Surface Emissivity

ε_{bed} Void Fraction of Fluidized Bed

ε_{bu} Void Fraction of Gas Bubble

ε_{bub} Void Fraction of Gas Bubble

ε_{mf} Void Fraction at Minimum Fluidization

Appendix C Continued

ε_s Solids Fraction

ε_{spray} Void Fraction of Atomization Spray

ε_{sp} Particle Porosity

η Overall Droplet Deposition Efficiency

θ Contact Angle, Granular Temperature

θ_{wall} Material Emissivity

κ Tack Force Correction Factor

κ_w Mixing Constant

λ Evaporation Constant, Thermal Conductivity

λ_i Granular Flow Mean Free Path

λ_p Particle Thermal Conductivity

μ Fluid Viscosity

μ_{bulk} Bulk Fluid Viscosity

μ_a Dry Air Viscosity

μ_{air} Air Viscosity

μ_f Fluid Viscosity

μ_{film} Fluid Viscosity at Film Temperature

μ_l, μ_{liq} Liquid Viscosity

μ_m Air-Water Vapor Mixture Viscosity

μ_p Particulate Viscosity

μ_v Water Vapor Viscosity

μ_{wall} Fluid Viscosity at Wall

Appendix C Continued

ν	Dynamic Viscosity
$\xi_{1,2}$	Enhancement Factor Parameters
π	Mathematical Constant 3.14159
ρ_{air}	Air Density
ρ_{air}	Air Density
ρ_{coat}	Coating Density
ρ_{drop}	Liquid Density
ρ_f	Fluid Density
ρ_{film}	Fluid Density at Film Temperature
ρ_l, ρ_{liq}	Liquid Density
ρ_m	Air-Water Vapor Mixture Density
ρ_p,ρ_{part}	Particle Density
ρ_s	Solid Density
ρ_{wall}	Fluidized Bed Wall Density
σ	Boltzmann Constant
σ, σ_l	Surface Tension
τ_{ads}	Droplet Adsorption Time into Pore
τ_c	Particle Circulation Rate
τ_{col}	Particle-Particle Collision Time
τ_{mark}	Gas Film Thickness Around Particle Contact Point for Particle-Particle Contact
τ_w	Ratio of Gas Film Thickness Around a Particle to Particle Diameter
Φ_{aloss}	Heat Transfer Loss Air to Wall

Appendix C Continued

Φ_{ploss} Heat Transfer Loss Particles to Wall

$\upsilon_{1,2}$ Poisson's Ratio of Component 1 or 2

φ Particle Porosity

φ_{eff} Droplet Impingement Efficiency

ϕ_s Particle Sphericity

ϕ_{exp} Fluidized Bed Experimental Solids Fraction

ϕ_{fix} Fixed Bed Solids Fraction

ψ_a Dimensionless Spray Flux